

Dissertation zur Erlangung des Doktorgrades
der Fakultät für Chemie und Pharmazie
der Ludwig-Maximilians-Universität München

**New concepts for molecular photoswitches
in chemical biology: from molecular amplifiers
in photoacoustic imaging to ideal efficacy
switches for protein chromocontrol in tissues**

Markus Müller

aus

Memmingen

2024

Erklärung

Diese Dissertation wurde im Sinne von § 7 der Promotionsordnung vom 28. November 2011 von Herrn Prof. Dr. Oliver Thorn-Seshold betreut.

Eidesstattliche Versicherung

Diese Dissertation wurde eigenständig und ohne unerlaubte Hilfe erarbeitet.

München, den 21. Oktober 2024

.....
Markus Müller

Dissertation eingereicht am	<u>23.10.2024</u>
1. Gutachter:in:	Prof. Dr. Oliver Thorn-Seshold
2. Gutachter:in:	Prof. Dr. Andrea Rentmeister
Mündliche Prüfung am	<u>06.12.2024</u>

Abstract

This thesis comprises two parts with diverging research topics, that nevertheless share a common focus, on the interaction of light with a chromophore whose centrepiece is an N=N double bond.

Part I: Contrast agents for photoacoustic imaging. Seeing is understanding, and imaging technologies are crucial to visualise biological processes at levels ranging from the (sub-)cellular to the whole body. *Molecular imaging* is the subfield that focuses on noninvasively imaging enzyme activity, usually by monitoring small molecular contrast agents that are designed to reveal specific biological processes. Photoacoustic (PA) imaging is a technical method that adds relatively new opportunities to the imaging toolbox. In PA, a pulsed laser is used as a precisely-resolved input, to excite chromophores that locally dissipate photon energy as heat, which induces pressure waves in the ultrasound frequency domain that serve as the output signal detected. PA using near infrared (NIR) lasers enables non-invasive bioimaging even at penetration depths of several cm, while delivering spatial resolution on the micron level. However, contrast agents suitable for *molecular PA imaging* are rare, and unified criteria to define how to design optimal contrast agents specifically for PA do not exist yet.

The first part of this thesis addresses these deficits by providing a rational molecular blueprint for organic small molecule PA contrast agents that have three key features: they are *loud* (i.e. efficient conversion of photon energy to ultrasonic amplitudes), have high *photostability* (enabling long-term imaging experiments), and are *NIR active* (enabling deep tissue excitation).

To achieve loudness and photostability, we aimed to create ultrafast-nonradiatively-relaxing molecular PA contrast agents. PA imaging uses laser pulses of typically just ~10 nanoseconds; with excited state lifetimes in the picosecond region (ca. 10 to 100-fold shorter than current dyes), PA contrast agents might undergo multiple excitation-relaxation cycles in each pulse, so harvesting more energy from each laser pulse, and amplifying the ultrasound signal output. Ultrafast relaxation should also suppress excited state side-reactions, thus photostabilising the chromophores. To achieve NIR activity in combination with these features, I merged azobenzene or azoheteroarene molecular switches with NIR-absorbing cyanine dyes, to obtain **azohemicyanines (AzHCys)** combining the NIR absorbance of the cyanine with the ultrafast relaxation of the molecular switches. **AzHCys** served as proof-of-concept compounds to validate the conceptual hypotheses. We confirmed the desired photophysical properties by spectroscopy and showed their amplified PA signal generation on a commercially available PA imaging device. We also showed that the often-formulated PA design goal of "low fluorescence quantum yield" is poorly-correlated to performance, and should be replaced by the considerations of relaxation rate and pathway that we demonstrate. Lastly, we applied the water soluble derivative **wsT-AzHCy** *in vivo* with PA imaging by multispectral optoacoustic tomography (MSOT), and demonstrated it can be effectively unmixed (imaged) in tissue despite a non-ideal broadened absorption band (§1.3.2).

The essence of this PA contrast agent design, demonstrated with **AzHCys**, is not dependent on a specific chemical space. Therefore, I consolidated the concept by translating it from molecular switches to molecular rotors. For this, I designed and synthesized NIR-absorbing ultrafast-relaxing triarylmethane (**TAM**) dyes, which were subsequently used for excited state spectroscopy and PA imaging: confirming

the superior *loudness* of ultrafast relaxing chromophores, but on a chemically totally distinct motif (§1.3.3).

Taken together, this research provides a photophysically guided molecular blueprint for *loud and photostable* PA contrast agents that can lead to the development of effective PA dyes that unlock the full potential of PA imaging. In particular, the second-generation **TAM** dyes are promising candidates for incremental improvements towards specific tasks, because their modular and straightforward synthesis facilitates the required chemical tuning steps, while retaining the overall beneficial PA properties.

Part II: Photopharmacology tools for TRPC4/5 & efficacy photoswitches. TRPC4 and TRPC5 are proteins that are mainly expressed in the nervous system, that tetramerise to form ion channels with specific tissue-dependent functions. These functions were usually researched by genetic knockouts, and lately, by the application of selective pharmacological activators or inhibitors. However, ion channels are dynamic systems, and native signalling is not characterized by permanent activation or inhibition. Thus, *dynamic* pharmaceuticals that can be spatiotemporally controlled are required for high-precision modulation; and light, as a non-invasive stimulus, is an ideal trigger for them. "Photopharmacological" ligands that include a light-responsive moiety such as reversibly photoswitchable azobenzenes can thus deliver spatiotemporal control, for example if the photoisomers differ in binding affinity (thus transferring a light-determined structural effect to the biological target). Indeed, several other TRP channels have been studied in detail by means of photopharmacology, but never TRPC4/5.

TRPC4/5 share substantial structural overlap, and subtype-specific modulators are rare. One is the moderately potent TRPC5 agonist **BTD**. We created **BTDAzo** as a lit-active (*Z*-active) photoswitchable agonist with similarly good potency and selectivity as the parent compound **BTD**. **BTDAzo** enables excellent reversible activation of TRPC5, in overexpression cell culture model systems and in native tissue slices with endogenous expression levels. The selectivity over TRPC4 and suitable potency render **BTDAzo** a promising high-precision tool to study tissue-specific functions of TRPC5 (§2.3.2).

A curious result arising from this work was that, in electrophysiology, **BTDAzo** all-*E*→mostly-*Z* photoswitching gave good channel activation, but then mostly-*Z*→mostly-*E* switching fully returned activity to basal channel activity, *despite* the incomplete photoisomerisation with significant residual active *Z*-isomer. We suggested that the two photoisomers would have to bind competitively, with either (1) opposing efficacy modes or else (2) with the *E* isomer being biologically innocent.

We perceived that a second structural class of TRPC4/5 modulators, the highly potent xanthenes, offered a rational route to install such an efficacy switch: because minor chemical modifications were known to alter efficacy from an agonist to an inhibitor. Therefore, we decided to rationally develop an efficacy photoswitch based on those high-potency lead structures by introducing azobenzenes as structural modifications exactly at the known chemical tipping points. We discovered **AzPico** and **AzHC** as nanomolar *Z*-isomer-agonists yet *E*-isomer-inhibitors, and by application in biological experiments, we could for perhaps the first time demonstrate the far-reaching implications of what we term *ideal* efficacy photoswitches as high-precision tools aiming at *in vivo* photopharmacology. Crucially, the photoinduced effect now correlates only with the ratio of isomers (instead of the concentration of the

active isomer as for affinity photoswitches), so bioactivity photoswitching is independent of the concentration of the applied ligand. We argue this will uniquely enable photoswitching in complex tissue or *in vivo* because, despite inhomogeneous and time-dependent drug distributions, the effect is uniform due to the constancy of *E/Z* ratios established by any given light wavelength applied.

With that in mind, we applied **AzPico** in cultured neurons, chromaffin cells, tissue slices, and lastly to excised organ sections (a deep tissue setting), where it reproducibly and photoreversibly controls TRPC4&5 function and downstream biology even at low endogenous expression levels. A highlight was demonstrating the photocontrol of macroscopic gut motions (similar to peristalsis) by photoswitching nanomolar applied concentrations of **AzPico**. Controlling the tonic force in an endogenously-mimicking way requires careful channel activity control, to avoid overstimulation of the muscle; and we show that efficacy switching can be harnessed by using reproducibly-oversaturating concentrations but *tuned* switching wavelengths to moderate TRPC4 activation, which mimics natural pathways better than by maximal channel activation (§2.3.3).

Taken together, this research contributes to TRPC4/5 pharmacology with the introduction of potent, high-precision, and photoswitchable tool compounds suitable for progression to *in vivo* studies. Moreover, we aim to reinvigorate the field of photopharmacology by the detailed conceptual exploration and practical elucidation of the implications of ideal efficacy switches, as hitherto literature examples did not harness or consider the true power of efficacy switching.

Kurzusammenfassung

Diese Dissertation besteht aus zwei Teilen mit unterschiedlichen Forschungsthemen, wobei beide auf der Wechselwirkung von Licht und einem Chromophor mit einer N=N Doppelbindung aufbauen.

Teil I: Kontrastmittel für die photoakustische Bildgebung. Bildgebung ist entscheidend, um biologische Prozesse von der (sub-)zellulären Ebene bis hin zum gesamten Körper zu visualisieren. Die *molekulare Bildgebung* ermöglicht nicht-invasive Bildgebung von Enzymaktivitäten, indem molekulare Kontrastmittel abgebildet werden, die spezifische biologische Prozesse aufklären sollen. Die photoakustische (PA) Bildgebung ist eine moderne Technologie die neue Möglichkeiten eröffnet, da bei PA ein gepulster Laser als präzise aufgelöster Input verwendet wird, der Chromophore anregt, die anschließend lokal Photonenergie als Wärme abgeben, was wiederum Druckwellen im Ultraschallfrequenzbereich erzeugt, die als Ausgangssignal detektiert werden. Die PA-Bildgebung mit Nahinfrarot-(NIR)-Lasern ermöglicht eine nicht-invasive Bildgebung bei Eindringtiefen von mehreren Zentimetern, während sie eine räumliche Auflösung auf Mikrometer-Ebene liefert. Allerdings sind Kontrastmittel, die für die molekulare PA-Bildgebung geeignet sind, selten, und es gibt noch keine einheitlichen Kriterien für die Entwicklung von PA-Kontrastmitteln.

Der erste Teil dieser Dissertation beschäftigt sich mit diesen Defiziten, indem ein rationaler molekularer Bauplan für organische, kleine PA-Molekülkontrastmittel erarbeitet wird, der auf drei Aspekten beruht: Die Kontrastmittel sind *laut* (d.h. effiziente Umwandlung von Photonenergie in Ultraschall-Amplituden), haben eine hohe *Photostabilität* (was Langzeit-Bildgebungsexperimente ermöglicht) und sind NIR-aktiv (was eine Anregung in tiefem Gewebe ermöglicht). Um *Lautstärke* und *Photostabilität* zu erreichen, haben wir ultraschnell strahlungslos relaxierende molekulare PA-Kontrastmittel entwickelt. Die Laserpulse bei PA sind üblicherweise nur ca. ~10 Nanosekunden lang und mittels angeregter Zustände mit Lebensdauern im Pikosekundenbereich (ca. 10- bis 100-mal kürzer als bei aktuellen Farbstoffen) könnten PA-Kontrastmittel mehrere Anregungs-Relaxations-Zyklen pro Puls durchlaufen, sodass mehr Energie aus jedem Laserpuls umgewandelt und das Ultraschallsignal verstärkt wird. Ultraschnelle Relaxation sollte auch Nebenreaktionen des angeregten Zustands unterdrücken und somit die Chromophore *photostabilisieren*. Um NIR-Aktivität in Kombination mit diesen Merkmalen zu erreichen, habe ich Azobenzol- oder Azoheteroaren-Molekularschalter mit NIR-absorbierenden Cyanin-Farbstoffen kombiniert, um **Azohemicyanine (AzHCys)** zu erhalten, die die NIR-Absorption des Cyanins mit der ultraschnellen Relaxation der Molekularschalter verbinden. **AzHCys** dienen als Modellverbindungen zur Validierung der konzeptionellen Hypothesen. Wir zeigten die gewünschten photophysikalischen Eigenschaften durch Spektroskopie und ihre verstärkte PA-Signalgenerierung auf einem kommerziell erhältlichen PA-Bildgebungsgerät. Außerdem zeigten wir, dass das oft formulierte PA-Kriterium einer "geringen Fluoreszenzquantenausbeute" keine Relevanz für die PA-Signalintensität hat und durch die von uns gezeigten Überlegungen hinsichtlich strahlungsloser Relaxationsrate ersetzt werden sollte. Schließlich haben wir das wasserlösliche Derivat **wsT-AzHCy** für *in vivo* PA-Bildgebung durch multispektrale optoakustische Tomographie (MSOT) verwendet und konnten zeigen, dass trotz breiter Absorptionsbanden die spektrale Auftrennung in Gewebe effektiv funktioniert (§1.3.2).

Das PA-Kontrastmittel-Design ist nicht auf eine bestimmte chemische Struktur beschränkt, daher habe ich das Konzept konsolidiert, indem ich es von molekularen Schaltern auf molekulare Rotoren übertragen habe. Dazu entwarf und synthetisierte ich NIR-absorbierende, ultraschnell relaxierende Triarylmethan (TAM)-Farbstoffe, die anschließend für Spektroskopie im angeregten Zustand und PA-Bildgebung verwendet wurden, und konnte erneut eine erhöhte *Lautstärke* ultraschnell relaxierender Chromophore mittels eines chemisch völlig anderen Motivs zeigen (§1.3.3).

Zusammengefasst bietet diese Forschung einen photophysikalischen molekularen Bauplan für *laute* und *photostabile* PA-Kontrastmittel, die zur Entwicklung effektiver PA-Farbstoffe führen können und somit das volle Potenzial der PA-Bildgebung eröffnen. Insbesondere die TAM-Farbstoffe der zweiten Generation sind vielversprechende Kandidaten für schrittweise Verbesserungen in Richtung spezifischer Aufgaben, da ihre modulare und unkomplizierte Synthese die erforderlichen chemischen Modifikationen erleichtert, während die insgesamt vorteilhaften PA-Eigenschaften beibehalten werden.

Teil II: Photopharmakologische Werkzeuge für TRPC4/5 und Wirksamkeitsphotoschalter. TRPC4 und TRPC5 sind Proteine, die hauptsächlich im Nervensystem exprimiert werden und als Tetramere Ionenkanäle mit spezifischen, gewebsabhängigen Funktionen bilden. Diese Funktionen wurden bisher vorwiegend durch genetische Knockouts erforscht oder in letzter Zeit durch die Anwendung selektiver pharmakologischer Aktivatoren oder Inhibitoren. Allerdings sind Ionenkanäle dynamische Systeme, und die native Signalübertragung ist nicht durch eine permanente Aktivierung oder Inhibition gekennzeichnet. Daher werden dynamische Modulatoren benötigt, die räumlich und zeitlich kontrolliert werden können, um eine hochpräzise Modulation zu ermöglichen. Dabei ist Licht, als nicht-invasiver Impuls, ein idealer Auslöser für solche Wirkstoffe. „Photopharmakologische“ Liganden, die eine lichtempfindliche Komponente wie reversibel photoschaltbare Azobenzole enthalten, können eine räumlich-zeitliche Kontrolle bieten, insbesondere wenn sich die Photoisomere in ihrer Bindungsaffinität unterscheiden (und so einen lichtbestimmten Struktureffekt auf das biologische Ziel übertragen). Tatsächlich wurden mehrere andere TRP-Kanäle detailliert mittels Photopharmakologie untersucht, TRPC4/5 jedoch noch nicht.

TRPC4/5 sind strukturell sehr ähnlich und subtypspezifische Modulatoren sind selten. Einer davon ist der mäßig potente TRPC5-Agonist **BTD**. Wir entwickelten **BTDAzo** als lichtaktiven (Z-aktiven) photoschaltbaren Agonisten mit ähnlich guter Potenz und Selektivität wie die Ausgangsverbindung **BTD**. **BTDAzo** ermöglicht eine hervorragende reversible Aktivierung von TRPC5 in Überexpressionszellkulturmodellen und in nativen Gewebeschnitten mit endogenen Expressionsniveaus. Die Selektivität gegenüber TRPC4 und die geeignete Potenz machen **BTDAzo** zu einem vielversprechenden Präzisionswerkzeug zur Erforschung gewebespezifischer Funktionen von TRPC5 (§2.3.2).

Ein interessantes Ergebnis dieser Arbeit war, dass in der Elektrophysiologie das Schalten von **BTDAzo** von "komplett E" zu "überwiegend Z" eine gute Kanalaktivierung bewirkte, aber das Schalten von "überwiegend Z" zu "überwiegend E" die Aktivität vollständig auf die basale Kanalaktivität absenkte, trotz unvollständiger Photoisomerisierung und signifikantem Rest des aktiven Z-Isomers. Wir nehmen an, dass die beiden Photoisomere kompetitiv binden müssen, und zwar entweder (1) mit entgegengesetzten Wirksamkeiten oder (2) das E-Isomer ist biologisch harmlos.

Wir erkannten, dass eine zweite strukturelle Klasse von TRPC4/5-Modulatoren, die hochpotenten Xanthine, einen rationalen Ansatz zur Entwicklung eines Wirksamkeitsschalters bietet, da bekannt ist, dass geringfügige chemische Modifikationen die Wirksamkeit von einem Agonisten zu einem Inhibitor verändern können. Deshalb beschlossen wir, einen Wirksamkeitsphotoschalter auf Basis dieser hochpotenten Leitstrukturen zu entwickeln, indem wir Azobenzole als strukturelle Modifikationen genau an den bekannten chemischen Kipp-Punkten einführten. Wir entdeckten **AzPico** und **AzHC** als nanomolare *Z*-Isomer-Agonisten, jedoch *E*-Isomer-Inhibitoren, und konnten in biologischen Experimenten erstmals die weitreichenden Implikationen demonstrieren. Entscheidend ist, dass der photoinduzierte Effekt nun nur mit dem Verhältnis der Isomere korreliert (anstatt mit der Konzentration des aktiven Isomers wie bei Affinitäts-Photoschaltern), sodass die Bioaktivität unabhängig von der Konzentration des verabreichten Liganden geschaltet werden kann. Wir denken, dass dies auf einzigartige Weise die Schaltbarkeit in komplexem Gewebe oder *in vivo* ermöglicht, da trotz inhomogener und zeitabhängiger Wirkstoffverteilungen der Effekt aufgrund der Konstanz der *E/Z*-Verhältnisse bei jeder angewendeten Lichtwellenlänge einheitlich bleibt.

Mit diesem Ansatz verwendeten wir **AzPico** in kultivierten Neuronen, chromaffinen Zellen, Gewebeschnitten und schließlich in exzidierten Organabschnitten (tiefes Gewebe), wo es reproduzierbar und photoreversibel die Funktion von TRPC4/5 und nachgeschaltete Prozesse auch bei niedrigen endogenen Expressionsniveaus steuert. Ein Höhepunkt war der Nachweis der Photokontrolle makroskopischer Darmbewegungen (ähnlich der Peristaltik) durch das Photoschalten nanomolarer Konzentrationen von **AzPico**. Die Kontrolle der tonischen Muskelkraft in einer endogen nachgeahmten Weise erfordert eine sorgfältige Steuerung der Kanalaktivität, um eine Überstimulation des Muskels zu vermeiden und wir zeigen, dass der Wirksamkeitsschalter mit eigentlich übersättigender Konzentrationen mittels Schaltwellenlängen nivelliert werden kann, um schließlich TRPC4-Aktivierung zu moderieren. Diese Nivellierung imitiert die natürlichen Signalwege deutlich besser als eine maximale Kanalaktivierung (§2.3.3).

Zusammengefasst trägt diese Forschung zur TRPC4/5-Pharmakologie bei, indem potente, hochpräzise und photoschaltbare Werkzeugverbindungen eingeführt werden, die für die Weiterentwicklung zu *in vivo* Studien geeignet sind. Darüber hinaus zielt unsere Arbeit darauf ab, das Feld der Photopharmakologie aufzurütteln, indem wir die Implikationen idealer Wirksamkeitsschalter konzeptionell detailliert untersuchen und praktisch aufzeigen, da bisherige Literaturbeispiele die tatsächlichen Möglichkeiten von Wirksamkeitsschaltern nicht genutzt oder berücksichtigt haben

Parts of this work have been published in peer reviewed journals:

(1) Publication shown in **section 1.3.2**

Markus Müller, Nian Liu, Vipul Gujrati, Abha Valavalkar, Sean Hartmann, Pia Anzenhofer, Uwe Klemm, András Telek, Benjamin Dietzek-Ivanšić, Achim Hartschuh, Vasilis Ntziachristos, Oliver Thorn-Seshold*.

Merged Molecular Switches Excel as Optoacoustic Dyes: Azobenzene–Cyanines Are Loud and Photostable NIR Imaging Agents.

Angew. Chem. Int. Ed. **2024**, 63, e202405636 (<https://doi.org/10.1002/anie.202405636>) *VIP paper*

(2) Publication shown in **section 2.3.2**

Markus Müller, Konstantin Niemeyer, Nicole Urban, Navin K. Ojha, Frank Zufall, Trese Leinders-Zufall, Michael Schaefer, Oliver Thorn-Seshold*.

BTDAzo: A Photoswitchable TRPC5 Channel Activator.

Angew. Chem. Int. Ed. **2022**, 61, e202201565 (<https://doi.org/10.1002/anie.202201565>)

Parts of this work have been deposited on preprint servers and are currently in submission process

(3) Publication shown in **section 2.3.3**

Markus Müller[‡], Konstantin Niemeyer[‡], Navin K. Ojha, Sebastian A. Porav, Deivanayagabharathy Vinayagam, Nicole Urban, Fanny Büchau, Katharina Oleinikov, Mazen Makke, Claudia C. Bauer, Aidan V. Johnson, Stephen P. Muench, Frank Zufall, Dieter Bruns, Yvonne Schwarz, Stefan Raunser, Trese Leinders-Zufall, Robin S. Bon, Michael Schaefer*, Oliver Thorn-Seshold*.

Ideal efficacy photoswitches for TRPC4/5 channels harness high potency for spatiotemporally-resolved chromocontrol of TRPC function in live tissues.

BioRxiv, **2024** (<https://doi.org/10.1101/2024.07.12.602451>) *‡contributed equally as first authors*

(4) Publication shown in **section 1.3.3**

Markus Müller*, Abha Valavalkar, Vipul Gujrati, Jan P. Prohaska, Divyesh Shelar, Michaela Kaltenegger, Benjamin Dietzek-Ivanšić, Vasilis Ntziachristos, Oliver Thorn-Seshold*.

Molecular rotors as design template for NIR & SWIR optoacoustic contrast agents.

ChemRxiv, **2024** (<https://doi.org/10.26434/chemrxiv-2024-t6zqq>)

Table of Contents

Abstract	1
1 Part I: Optoacoustic imaging	11
1.1 Introduction	11
1.1.1 Photoacoustic effect and optoacoustic imaging	11
1.1.2 Listening to molecules - contrast agents for optoacoustic imaging	15
1.1.2.1 Theoretical background to photoacoustic signal generation	15
1.1.2.2 Types and examples of photoacoustic contrast agents	17
1.1.3 A focused introduction to azobenzenes as molecular photoswitches	21
1.1.3.1 Switching and spectral tuning of azobenzenes	22
1.1.4 Excursus: the colour blue in nature - inspiration for PA contrast agents?	25
1.2 Aims and objectives	27
1.3 Results and Discussion	28
1.3.1 Author Contributions	28
1.3.2 Publication One: NIR azobenzenes as contrast agents for PA imaging	29
1.3.3 Publication Two: Molecular rotors as NIR & SWIR PA contrast agents	41
2 Part II: Efficacy switches for optical control of TRPC4/5	50
2.1 Introduction	50
2.1.1 Transient Receptor Potential (TRP) Channels	50
2.1.1.1 Classification and importance of TRP channels	50
2.1.1.2 Transient receptor potential canonicals (TRPC) & the subfamily TRPC1/4/5	53
2.1.1.3 Pharmacological Modulators for TRPC1/4/5	56
2.1.1.4 The interplay of structure and pharmacology for TRPC1/4/5 drugs	58
2.1.2 Light as a trigger for biological function	60
2.1.2.1 Optogenetics	60
2.1.2.2 Photoremovable protecting groups (Photocages)	62
2.1.2.3 Photopharmacology	63
2.1.2.4 Efficacy switches – bringing a new horizon for ideal photopharmacology?	66
2.2 Aims and objectives	69
2.3 Results and Discussion	70
2.3.1 Author contributions	70
2.3.2 Publication One: BTDAzo is a photoswitchable TRPC5 agonist	71
2.3.3 Publication Two: Ideal efficacy switches for TRPC4/5 channels harness high potency for spatiotemporally-resolved chromocontrol of TRPC function in live tissue	81
3 Conclusions and Outlook	97
3.1 Research summary	97
3.2 Ongoing research and outlook: Optoacoustic Imaging	98
3.3 Ongoing research and outlook: Efficacy Switches and TRP Tools	103
3.4 General conclusion	105
4 Acknowledgements	107
5 Appendix	109
5.1 Supporting Information	109
5.1.1 Supporting Information for section 1.3.2 (AzoCyanines)	109
5.1.2 Supporting Information for section 1.3.3 (Triarylmethanes)	109
5.1.3 Supporting Information for section 2.3.2 (BTDAzo)	109
5.1.4 Supporting Information for section 2.3.3 (Efficacy switches AzPico&AzHC)	109
5.1.5 Experimental sections for unpublished preliminary results	325
5.1.5.1 Materials and methods	325
5.1.5.2 Synthetic procedures	325
5.1.5.3 UV/VIS Spectroscopy	329
5.2 List of Abbreviations	331
6 Bibliography	332

1 Part I: Optoacoustic imaging

1.1 Introduction

1.1.1 Photoacoustic effect and optoacoustic imaging

The first inquiries into the photoacoustic effect date back to the 19th century when Alexander Graham Bell invented the *photophone*, used to transmit vocal signals by reflecting sunlight from a moving mirror onto a receiver that consisted of a plain black surface absorbing light, coupled to an earpiece. In 1881, he described the underlying physical effect as *the production of sound by radiant energy*,¹ nowadays known as the photoacoustic effect (also called optoacoustic effect; these terms are used interchangeably throughout this thesis, with optoacoustic preferably referring to imaging and photoacoustic preferably describing photo-physical/-chemical processes). Absorption of photons means light energy is converted into thermal energy leading to a thermoelastic expansion of the surrounding matter and after the irradiation stops a period of cooling and thermoelastic collapse follows (Figure 1a).² The mechanical process of expansion and collapse forms an acoustic pressure wave transmitted from the source of the absorption events (Figure 1b). Short laser pulses in the low nanosecond region generate expansion waves with ultrasonic frequencies propagating through the sample volume, which can be sensed by ultrasound transducers placed either on the surface or above the sample.

Photoacoustic effect - mechanistic principle and optoacoustic imaging

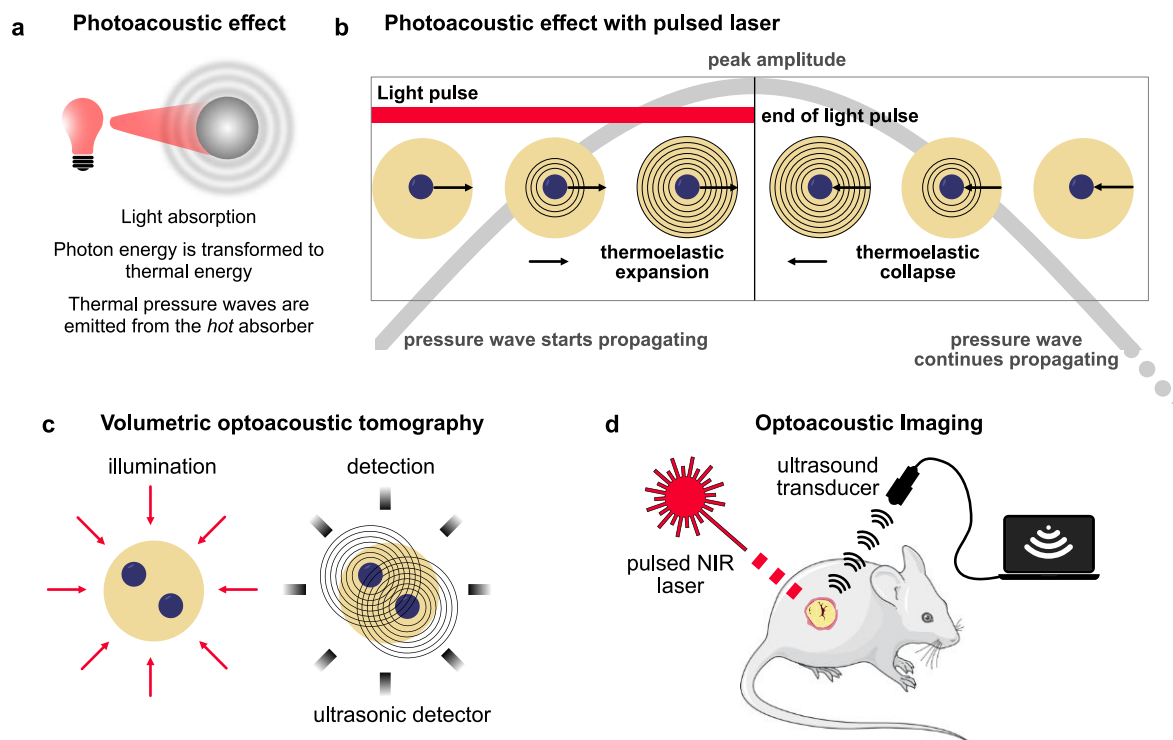


Figure 1. Photoacoustic effect and optoacoustic imaging. **a**) Principle of the photoacoustic effect: An object (blue dot) absorbs light and the energy is transferred to surrounding matter (yellow circle) as thermoelastic pressure wave (indicated as black circular lines with increasing size, and as grey waveform in background representing 1D propagation over time); end of irradiation results in thermoelastic collapse. **b**) Illumination source and ultrasonic detectors are placed as circular peripheral arrays to gain spatial resolution of different absorbers in 3D. Mathematical inversion methods are used for image reconstruction.³ **c**) Schematic optoacoustic *in vivo* imaging of a tumour in a mouse: A pulsed laser generates photoacoustic waves with ultrasonic frequencies that are detected with broadband ultrasound transducers and processed to 3D images.

This principle was used accordingly to generate low-resolution pictures of biological samples e.g. by Rosencwaig and Bowen in the 1970s and 1980s.^{2,4-6} A breakthrough came with the development of modern high power pulsed laser systems, because signal intensity at the detector correlates with the amount of absorbed light energy.⁷ Increasing output signal intensity and resolution unlocked the transformation from the photoacoustic (PA) effect to a powerful imaging modality now called optoacoustic (OA) imaging (Figure 1c,d).⁸ Over the last 20 years OA imaging has grown to a versatile imaging modality able to picture tissues, organelles or whole organs and with assistance of mathematical reconstruction models the images from OA tomography can be built into 3D structures (Figure 1c).^{3,7,9,10}

Ultrasound propagation through tissue is excellent and occurs without much scattering,⁷ therefore the crux for OA imaging remains the delivery of light, albeit with the advantage relative to fluorescence that for OA, light has only one way to travel, and can be applied with high power. Light, especially in the visible region scatters massively within tissue and loses directional information causing decrease in spatial resolution. The mean free path (MFP) describes the average distance between two scattering events and marks the threshold for transitioning from a ballistic light pathway to a conical spread. In tissue the MFP for light <700 nm lies typically around ~100 μm , and after ~ 1 mm most directional information is lost (Figure 2a); but light with higher wavelengths generally scatters less.³ OA imaging can reach penetration depths of several cm, but at the cost of a spatial resolution drop; according to Wang, the achievable spatial resolution with can be roughly estimated as ca. 1/200 of the desired imaging depth.⁷ Additionally, endogenous chromophores absorb light and cause not only limitations in resolution but also generate background signals. The level of absorption depends on the wavelength of the applied light. Blue light barely penetrates skin because it is completely absorbed by natural chromophores such as melanin (Figure 2b); while green light penetrates but is absorbed by (oxy-)hemoglobin; red light > 650 nm is the only part of visible light that can penetrate tissue well, marking the beginning of the *biological window*. Ideally, near-infrared (NIR) or short wave infrared (SWIR) light is used because of low tissue absorption (Figure 2b), although at higher wavelengths above 950 nm absorption of water, proteins or lipids increases¹¹⁻¹³ (note: the definitions in literature on visible, NIR, and SWIR are not consistent; here, visible refers to 400-700 nm, NIR to 700-1000 nm and SWIR to 1000-2000 nm, in line with the modern classification by Bawendi, Bruns and Sletten¹⁴⁻¹⁷). Despite the increased tissue absorption in the SWIR region, imaging resolution and tissue penetration are increased because of reduced SWIR scattering. Hence, there is no *ideal* narrow imaging wavelength region, but in general, deep tissue imaging is best operated within the NIR/SWIR window 700-2000 nm.

A major technological breakthrough for optoacoustic imaging was the introduction of multispectral optoacoustic tomography (MSOT) by Ntziachristos and coworkers.¹⁸ MSOT utilizes endogenous or exogenous contrast agents with known absorption profiles excited not only at their absorption maxima but also with additional excitation wavelengths, ideally located in parts of their spectra with distinct changes of $\epsilon(\lambda)$ for small deviations of λ (Figure 2c).^{19,20} Since there are no steep gradients in $\epsilon(\lambda)$ of tissue (Figure 2b), strong changes in each voxel's OA signal intensities at small deviations of λ can be assigned to the targeted contrast agent, whose voxel concentration can then be extracted accordingly.

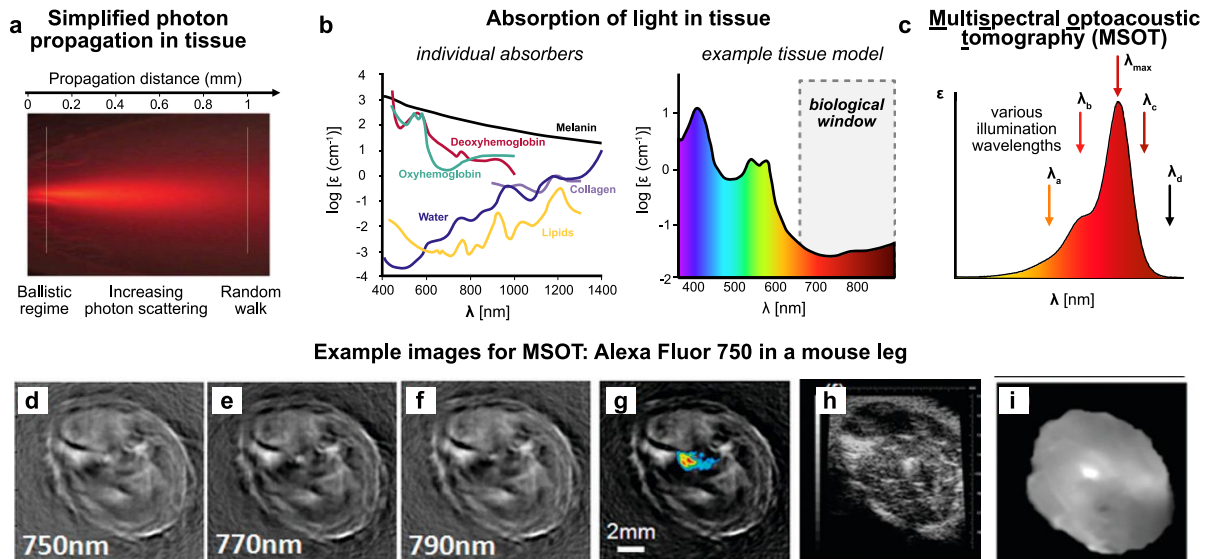


Figure 2. **a**) Schematic of photon propagation in tissue; the scale varies with tissue type and wavelength. **b**) Schematic representation of the absorption coefficient of light in tissue, as dependent on wavelength and composition of absorbers. **c**) Principle of multispectral optoacoustic tomography (MSOT): irradiation at several wavelengths with known absorptions resolves contrast agents from tissue. **d-i**) Example images for MSOT showcasing the imaging power with images of a mouse leg and the fluorophore Alexa Fluor 750¹⁸ **d-f**): MSOT images at 750 nm, 770 nm, 790 nm, **g**) spectrally resolved MSOT image showing Alexa Fluor 750 signal, **h**) ultrasonic image, **i**) fluorescence image confirming location of the fluorophore [images in **a** adapted with permission from ref⁸; **b** adapted and modified from ref²¹ and ref¹ with permission from Springer Nature; **d-i** adapted with permission from ref⁹ copyright 2010 American Chemical Society].

Current commercially available MSOT devices can perform spectral deconvolution for the individual OA(λ) spectra by correlating with one or several input $\epsilon(\lambda)$ to produce images with high sensitivity and resolution of the desired chromophore/s. Crucially, MSOT enables resolving tissue with background signal (e.g. blood distribution) separate to the distribution of exogenous contrast agents. The concept of MSOT was first reported by Ntziachristos and Razansky in 2007 and its power can be directly perceived from the images provided in that publication (reproduced in Figure 2d):¹⁸ an exogenous fluorophore (Alexa Fluor 750) was introduced into a mouse leg, imaged by MSOT, and after image processing, the tissue and fluorophore were well-resolved within the same image. Localization of the fluorophore was confirmed by fluorescence imaging and tissue images were crossvalidated with a conventional ultrasonic imager. The fluorophore signal was resolved with a resolution of 150 μm and detection limit was only 25 femtomole as total amount of dye. Haemoglobin and oxyhaemoglobin are the only endogenous absorbers suitable for MSOT, hence, endogenous MSOT imaging is mostly restricted to blood-supplied tissue. Examples for this include monitoring (oxy-)haemoglobin levels/ratios²² and resolving structures in animal brain²³ or blood vessels in humans.²⁴ Using NIR light enables non-invasive whole body imaging of small animals (e.g. mice) rendering it a very attractive technology for basic research. Additionally, the development of handheld devices is promoting MSOT towards routine applications in clinics.^{25–27}

While diverse optical imaging methods are backbone technologies for many biological research tasks and diagnostics in clinics, MSOT has some unique features that are missing in other commonly used methods, so MSOT as a technology may soon close some existing performance gaps. The most similar imaging technology is fluorescence imaging, also an optical method relying on dyes for signal generation. Fluorescence imaging was one of the main driving forces in chemical biology over the last decades: fluorophores must not only be genetically encoded fluorescent proteins,^{28,29} but they can also

be exogenous, acutely-applied small molecules that can be equipped by chemists to reveal biomarkers for certain conditions in health and disease, or tagged specifically onto proteins of interest (POIs) to visualize their location and distribution.^{30–33} MSOT shares the strengths of being able to exploit exogenous small molecule reporters.^{19,21} The main differences between the methods are (1) resolution (spatial and temporal) and (2) penetration depths. Fluorescence microscopy offers unmatched spatial resolution as exemplified by the development of super-resolution microscopy, which initially broke the diffraction barrier of light,³⁴ subsequently reached nanometre resolutions in cells^{35,36} i.e. the same scale as the individual fluorescent molecules that generate the photons, and continues to evolve with controlled systems allowing differentiation of individual emitters at the atomic level.³⁷ On top of the spatial resolution, fluorescence imaging provides also temporal resolution, as well as insights into dynamic processes by measuring fluorescence lifetimes.³⁸ Apart from basic research on the micron to nanometre scale, fluorescent probes are used on the macro scale for fluorescence guided surgery^{39–42} where fluorescence is either a visual assistance for a surgeon or the guidance for automatically performed surgeries by robots such as the FDA approved da Vinci Xi robot.^{43,44} The practical bottleneck in macro usage remains however, that even for NIR fluorescent dyes, the imaging depths are limited to at most a few mm because of high tissue attenuation and scattering of photons.⁴⁵ By contrast, MSOT delivers ca. 2-4 orders of magnitude lower spatial resolution than fluorescence imaging on comparable scales, and does not offer the option to monitor temporal processes, so it does not compete with fluorescence imaging for resolution-critical problems. Yet, the increased penetration depths of MSOT (low attenuation for ultrasound waves and only *one way* for photons to travel) in combination with its different scope of molecular contrast agents offer unique options for *in vivo deep tissue molecular imaging* that no other technology can achieve until today. Other frequently used clinical imaging modalities include X-ray, X-ray computer tomography (CT), magnetic resonance imaging (MRI), and positron emission tomography (PET). All of those provide the possibility of whole-body imaging in humans, though only PET can be used for molecular imaging (and this only in a few cases), and only MRI can be considered harmless (high energy X-rays can cause DNA alterations and PET needs radioactive material within the body); and particularly PET and MRI are very expensive technologies that are not suitable as high throughput modalities.^{19,46} While MSOT lacks their penetration depths for whole body imaging, it can rely on harmless electromagnetic/ultrasonic waves, is cheap, is ready for high throughput, and can be used for molecular imaging.

Evidently there is no *jack of all trades* macro-scale clinical imaging modality, but there is a distinct and broad performance gap between fluorescence imaging and other clinical imaging technologies that MSOT can fill: because it operates in penetration depths of mm – cm with mm resolution, without using ionizing radiation, and has the ability to image biomarkers: a truly unique combination in one package. Therefore, MSOT may be primed to become a favourite technology in basic research for whole-body animal imaging or tissue-specific imaging with max ca. 10 cm radial depth (e.g. whole primate brains have been imaged⁴⁷), as well as in clinics for diagnostics close to the body surface, such as breast cancer screenings.^{48,49}

1.1.2 Listening to molecules - contrast agents for optoacoustic imaging

The hardware technology in optoacoustic imaging is highly advanced but the development of molecular contrast agents has not kept pace with it. So far, most key contributions to MSOT arose from biomedical engineers: but the existence of easily-accessible, commercially-available NIR fluorophores (particularly the FDA-approved cyanine **ICG**) has led to a widespread use, or rather abuse, of such molecules that were optimized as fluorescence dyes instead of as optoacoustic imaging contrast agents. One can argue that to some extent this has even been baked into MSOT, with significant current hardware and processing choices apparently designed to get the most out of classical fluorophores, rather than ideal MSOT agents, which seems to hold the field back from realising some innovations. Nonetheless, chemists have picked up optoacoustic imaging as a worthwhile target within the last years, and the development of tailor-made MSOT contrast agents is growing into a vibrant field of its own.

1.1.2.1 Theoretical background to photoacoustic signal generation

The photoacoustic signal intensity for molecular contrast agents depends on a mixture of intrinsic molecular properties and externally dictated experimental parameters. Under one photon absorption and under limited photon flux the photoacoustic response of a contrast agent is according to Rochford, described by Eq. 1:⁵⁰

$$PA = \varepsilon_g \Phi_{nr} C_g \Gamma I \quad (1)$$

where ε_g is the ground-state molar extinction coefficient of the contrast agent, Φ_{nr} is the quantum yield for nonradiative decay, C_g is the ground-state concentration of contrast agent, I is the incident photon fluence, and Γ is the Grüneisen coefficient: a constant that quantifies a medium's ability to conduct sound efficiently, as defined by Eq. 2:⁵¹

$$\Gamma = \frac{V_s^2 \alpha}{C_p} \quad (2)$$

where V_s is the velocity of sound, α is the thermal expansion coefficient of the medium, and C_p is the specific heat capacity of the medium at constant pressure.

On a molecular level, the efficiency of this photoacoustic effect is based on efficient conversion of photon energy into thermal energy; for this, ε_g and Φ_{nr} are the relevant molecular properties, with ε_g giving the fraction of photon energy absorbed and Φ_{nr} the fraction of absorbed energy transformed into thermal output. Radiative decay and non-radiative decay are two competitive pathways for deexcitation from an excited state (Figure 3a), and energy dissipated radiatively does not add into the photoacoustic signal. However, absorption of a photon at $\varepsilon(\lambda)_{\max}$ promotes an electron from the ground state S_0 to a *hot vibrational* electronically excited state S_1 , and according to Kasha's rule photon emission only happens from the vibrational ground state of S_1 , therefore the radiative decay pathway does contribute some share to thermal energy dissipation (Figure 3a) which is not covered by Eq. 1. S_1 can also undergo spin forbidden intersystem crossing to a long-lived triplet state that can either decay again by emitting a photon (phosphorescence), or annihilate through triplet sensitization (= quenching). The most common quenching pathway is the formation of highly reactive singlet oxygen: a desired pathway in cell-killing photodynamic therapy^{52,53} but undesirable for any imaging technology.^{54,55}

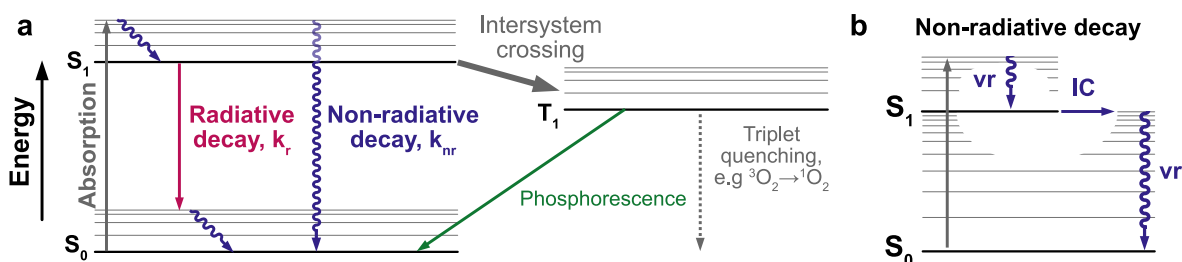


Figure 3. Jablonski diagram. **a)** Schematic representation of possible excited state relaxation pathways on a Jablonski diagram: radiative, non-radiative decay and intersystem crossing. **b)** Mechanism of non-radiative decay: vibrational relaxation (vr) to S_1 ground state, then internal conversion (IC) to a hot vibrational S_0 and vibrational relaxation to S_0 groundstate. IC is an energetical horizontal process.

Regarding the competitive nature of radiative [fluorescence] and non-radiative decay (Figure 3a), it is often recommended to use *bad fluorophores* with low fluorescence quantum yields Φ_{FL} as PA contrast agents, or when designing new lead compounds.^{19,21,56} The S_1 excited state decay follows a first order decay kinetic and is described by Eq. 3, with quantum yield Φ_{nr} by Eq. 4, and the half time τ by Eq. 5:

$$A(t) = A_0 e^{-Kt} \quad (3)$$

$$\Phi_{nr} = \frac{k_{nr}}{k_r + k_{nr}} \quad (4)$$

$$\tau = \frac{1}{k_r + k_{nr}} = \frac{1}{K} \quad (5)$$

where k_r is the rate constant for radiative decay and k_{nr} is the rate constant for non-radiative decay. To maximize Φ_{nr} requires $k_{nr} \gg k_r$ (Eq. 4), but note that this does not specify an *absolute* range for either rate. PA imaging uses irradiation with typically ~ 10 nanosecond pulsewidths. Rochford found a coherence between the *absolute* excited state lifetime (Eq. 5) and the PA signal intensity. Based on this finding Rochford postulated three categories of photoacoustic contrast agents:^{50,57}

- (1) Linear absorber (LA) \rightarrow linear PA emitter ($\tau \ll \tau_{Laser}$)

A contrast agent with an excited state lifetime significantly shorter than the laser pulse width rapidly decays to the ground state during a pulse, so any individual molecule can undergo subsequent excitations within the same pulse. A linear dependence of the PA signal intensity on the laser fluence is observed (closest match to Eq. 1).

- (2) Saturable absorber (SA) \rightarrow weak PA emitter ($\tau > \tau_{Laser}$)

A contrast agent with an excited state lifetime comparable to, or greater than, the laser pulse width can only be excited once per molecule per pulse. After reaching the saturation laser intensity PA signal does not increase further.

- (3) Reverse saturable absorber (RSA) \rightarrow nonlinear PA emitter ($\tau_g > \tau_{Laser}$, $\tau_e \ll \tau_{Laser}$)

A contrast agent with an excited-state lifetime comparable to, or greater than, the laser pulse width, concomitant with a nonzero excited-state absorption cross section, delivers a nonlinear increase in absorption and PA response as laser fluence increases.

Rochford promoted the idea of RSAs for the development of molecular contrast agents because RSAs can in theory emit the strongest PA signals. However, we will argue that this is problematic for several

reasons, including that to do so requires laser intensities above the limit set by the FDA for clinical optical imaging.¹⁹ The second best category identified were LAs which depend on fast excited state relaxation. In Rochford's empirical dataset the only LAs were dyes with lifetimes orders of magnitudes lower than the laser pulse width (e.g. crystal violet)⁵⁸, resulting in a rather black and white split between the categories of LA and SA.⁵⁷ In a recent preprint published on ChemRxiv during composing this thesis, Stains screened a set of rhodamines and found a rough correlation for the non-radiative decay rate k_{nr} to the photoacoustic signal intensity.⁵⁹ They defined an *acoustic loudness factor* (ALF) as the product of k_{nr} with the extinction coefficient (Eq. 6), positing it as a metric similar to brightness for fluorophores:

$$ALF = k_{nr} \cdot \varepsilon \quad (6)$$

Compared with the LA dyes used by Rochford, Stains' phosphonorhodamines have relatively slow k_{nr} , and hence the ALF may serve as a more subtle metric for them than a LA / SA split, to help researchers to develop rationally guided PA contrast agents. It should be noted that the first conceptual design and experimental results from this thesis were already cited in Stains' preprint and may have contributed to its development, since we had already introduced ultra-fast thermal relaxation as a design criterion exemplified with azobenzenes, driven by the hypothesis of several excitations per laser pulse, and presented it to the paper's authors in private as well as at a conference the year before their preprint. We had also introduced the half-time τ as a photophysical metric to characterize PA contrast agents, which is close to (but potentially more nuanced) than their use of k_{nr} (see chapter 1.3.2).

1.1.2.2 Types and examples of photoacoustic contrast agents

In general there are three different types of photoacoustic contrast agents: (1) molecular contrast agents, comprising organic small molecules as chromophores; (2) nanoparticles built by either inorganic moieties e.g. gold nanorods, or semiconductor quantum dots, or organic semiconducting materials; and (3) genetically encoded proteins, which are only rarely used (Figure 4).^{21,60–62} Gold nanoparticles have a particularly strong history because plasmonic resonance generates a strong PA response, and their spectral properties can be tuned from 500-1100 nm by modification of size, shape, and composition.^{21,63}

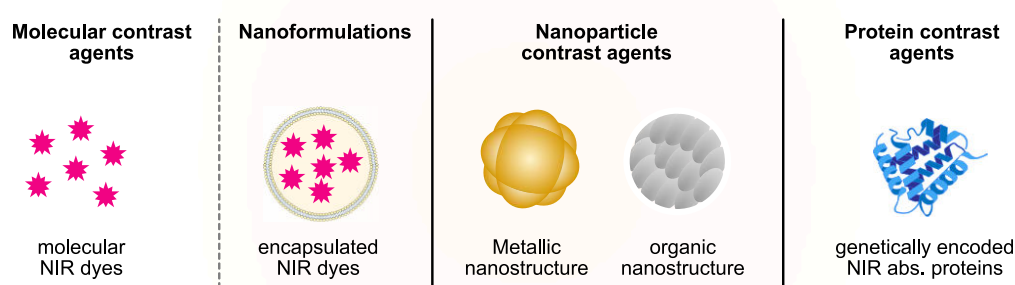


Figure 4. General types of photoacoustic contrast agents.

The separation from nanoparticles to molecular contrast agents is often fluid in the literature because molecular contrast agents can also be applied as nanoformulations, by encapsulating the chromophores in a matrix or within polymeric nanostructures, to facilitate solubility or targeted drug delivery. However, within this thesis only *completely dissolved, free molecules* are regarded as molecular contrast agents because only such systems can interact reliably with enzymes and biomarkers to function in molecular imaging. The state of the art in molecular agents will now be discussed in more detail.

Photoacoustic imaging is a relatively young discipline, starting in the early 2000s. Molecular NIR dyes available at that time were mostly fluorophores which were used since the 20th century and incrementally refined for specific needs.^{64,65} Early examples of repurposed fluorophores for PA imaging were mostly easy accessible commercial available dyes such as cyanine dyes, porphyrins, or methylene blue (example structures see Figure 5).⁶¹ The most prominent example is Indocyanine Green (**ICG**), a NIR fluorophore approved for hepatic function diagnosis by the FDA in 1959; as a cheap FDA-approved dye it also found immediate wide spread use in PA imaging,^{61,66,67} despite its many disadvantages such as fast clearance, tight binding to plasma proteins, formation of aggregates, and photoinstability.^{21,68–70}

Commercially available fluorophores used for photoacoustic imaging

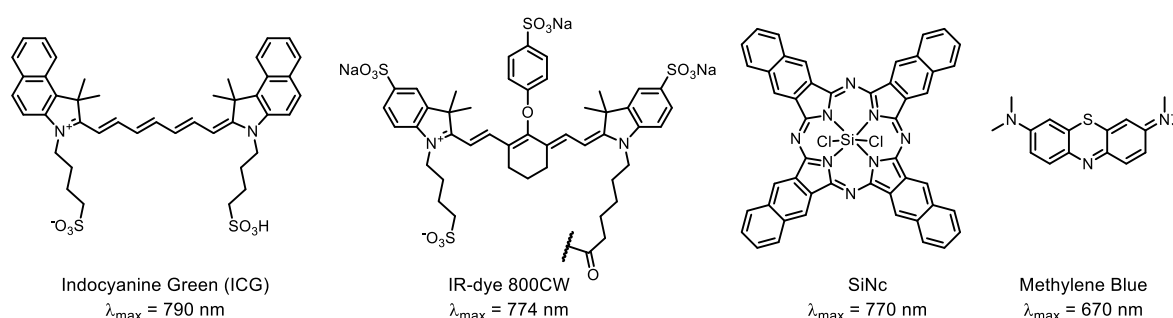


Figure 5. Example structures of commercially available NIR fluorophores repurposed for PA imaging in the early 2000s.⁶¹

In principle, any NIR-absorbing fluorophore can be repurposed for PA, but synthetic chemists have recognized the need for specific molecular contrast agents for PA, e.g. with strong nonradiative decay.^{50,56,71} One of the first reports of a non-radiatively-optimized PA contrast agent occurred by chance when Gambhir and co-workers created a dual wavelength protease probe with a fluorophore coupled to the quencher **BHQ3**; they found an unusually strong PA signal intensity for **BHQ3** after enzymatic cleavage. At that time they could not explain the strong signal and their rationale to use **BHQ3** was simply that it was a well-known fluorescence quencher mainly used for FRET (fluorescence resonance energy transfer) probes.⁷² Subsequently, Urano used fluorescence-quenched silicon rhodamines (**SiNQ**, Figure 6a) as PA contrast agents,⁷³ a motif based on his own finding that introduction of rotatable *N*-aryl residues on silarhodamines results in the formation of an excited state twisted intramolecular charged transfer (TICT) complex that quenches fluorescence.⁷⁴ A further example for fluorescence quenching as a design element for PA contrast agents is **PyBODIPY** by Banala, a BODIPY derivative with pyrroles functioning as a PeT (photoinduced electron transfer) quencher motif (Figure 6a).⁷⁵ A mechanistically different approach for designing PA contrast agents was discovered by Rochford and coworkers, who identified a fluorescent BODIPY derivative (Figure 6b) as a strong PA emitter despite its high fluorescence quantum yields.⁷⁶ They rationalized that under high laser fluence, non-linear excitation from S_1 to S_2 occurs, and this additional absorption cycle contributes constructively to the PA signal generation (the main finding that led to the classifications in section 1.1.2.1: though recall that such systems require a laser fluence above the limit set by the FDA for clinical optical imaging¹⁹).

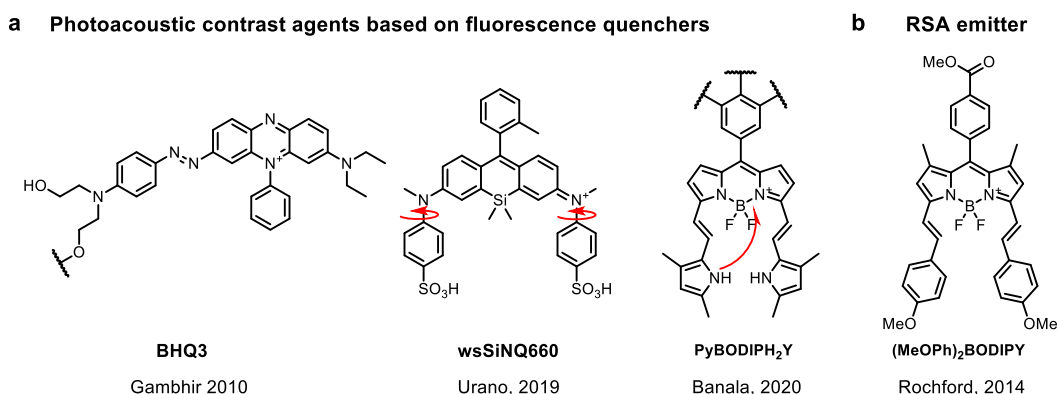


Figure 6. Optimised molecular photoacoustic contrast agents. **a)** Photoacoustic contrast agents based on fluorescence quenchers, **BHQ3**: red light absorbing azobenzenes are fluorescence quencher, **wsSiNQ606**: molecular rotation leads to formation of an intramolecular TICT state, **PyBODIPY**: pyrrole acts as PeT donor to the BODIPY core.^{72,73,75,77} **b)** Reverse saturable absorber (RSA) emitter by Rochford.⁷⁶

One of the main advantage of small molecules as contrast agents is the ability to reveal biomarkers in molecular imaging by a reaction-based shift of spectral properties, where ideally the product can be detected sensitively and with high confidence without crosstalk from the probe, whether in an absolute or a ratiometric sense (Figure 7). Therefore, achieving spectral separation from probe to product is crucial for the design of good molecular imaging probes.⁷⁸

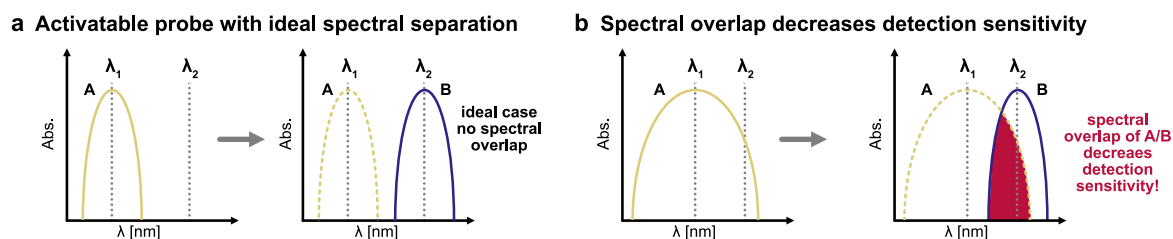


Figure 7. Spectral properties required for ideal activation in photoacoustic imaging without generation of background signals and loss in sensitivity. a) ideal case scenario with spectral separation. b) spectral overlap which results in loss of sensitivity.

One way to achieve such a strong spectral shift is using enzyme-removable electron withdrawing groups (EWGs) to increase the HOMO-LUMO gap of a probe relative to a product, by reducing electron density or blocking a push-pull system. Phenolic groups in NIR chromophores are a perfect molecular blueprint for masking with enzymatically cleavable EWGs. Therefore, it is not surprising that phenol-donor hemicyanine dyes (**HDs**, also called Changsha dyes), originally introduced for fluorescence imaging, were quickly adopted for molecular PA imaging.^{79,80} **HDs** are a merge between cyanines and xanthenes, yielding an asymmetric but modular core applicable for molecular imaging (Figure 8a). The field was mainly driven by Chan, Wu and Pu (Figure 8b-g) with notable claimed application examples including a GSH sensor,⁸¹ an alkaline phosphatase sensor,⁸² a β -galactosidase sensor,⁸³ a hypoxia theranostic,⁸⁴ a peroxynitrite sensor,⁸⁵ and a CYP450 reductase sensor:⁸⁶ though the cleavable groups that directed the nature of the imaged enzymes are, at best, proofs of concept that have long been known to have specificity and reactivity problems, so the prolific leveraging of a single dye core into a large paper output should not be over-interpreted. Chan also obtained higher PA intensities and a red-shift of the chromophore by replacing the oxygen bridge in the core by sulphur (Figure 8h).^{87,88}

Molecular imaging with hemicyanine dye (HD) probes

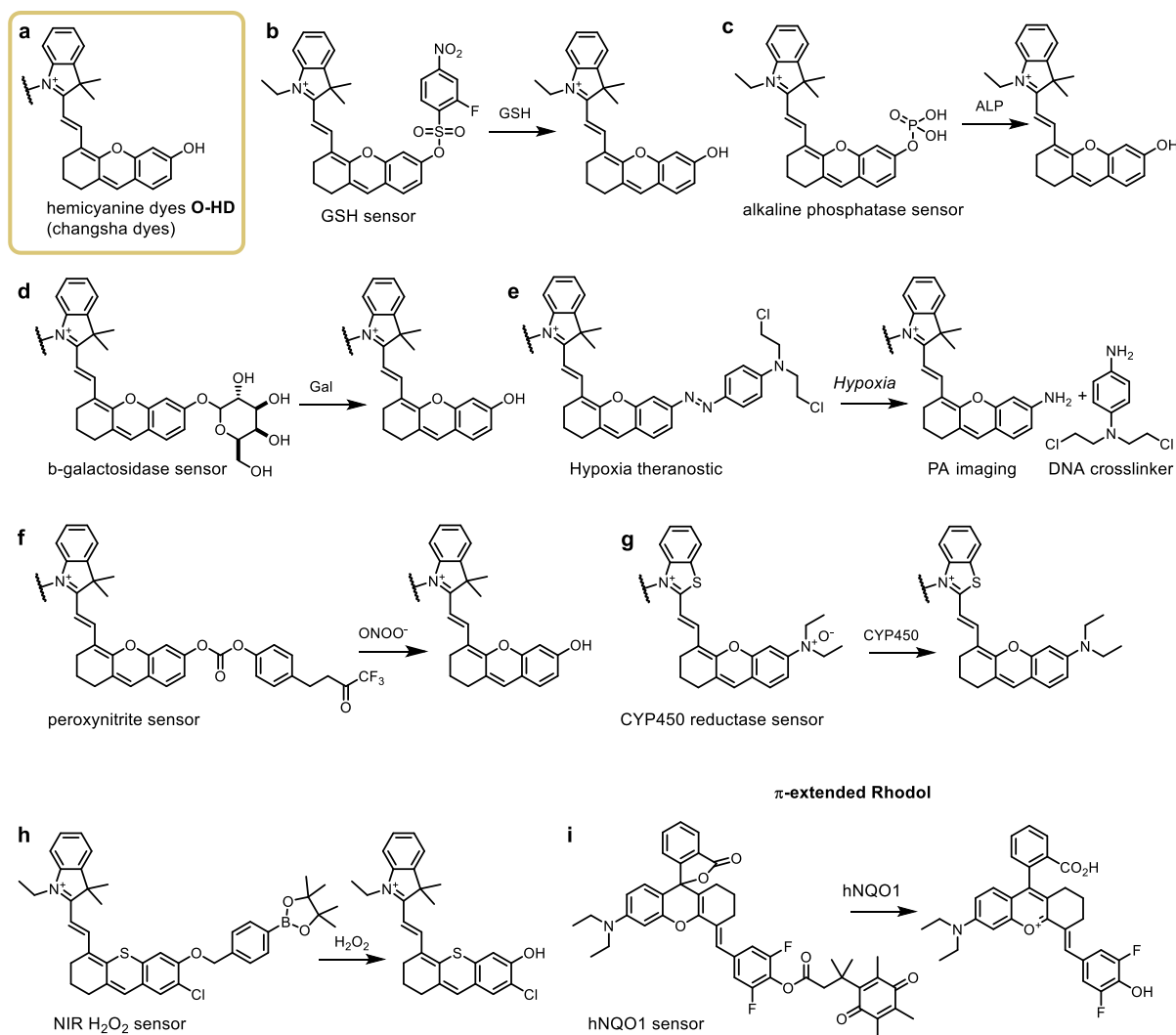


Figure 8. Molecular photoacoustic imaging probes harnessing fused dye core structures. **a**) Chemical structure of hemicyanine dyes (also called Changsha dyes); chromophore structure was used for numerous molecular probes.^{79,80} **b**) GSH sensor by Chan.⁸¹ **c**) alkaline phosphate sensor by Wu.⁸² **d**) β -galactosidase sensor by Pu.⁸³ **e**) hypoxia theranostics by Wu.⁸⁴ **f**) peroxynitrite sensor by Pu.⁸⁵ **g**) CYP450 reductase sensor by Wu.⁸⁶ **h**) Modular motif optimized for PA imaging by Chan, exemplified with a H_2O_2 sensor.⁸⁷ **i**) A hemirhodol as hNQO1 sensor by Jiang.⁸⁹

More conceptually exciting however was that merging fluorophore cores to obtain phenolic NIR dyes has proven viable beyond the **HDs**, with a similar approach giving hemirhodols for hNQO1 sensing (Figure 8i) that operate by triggered spirolactone opening.⁸⁹ Normal xanthenes present a problem, however: while spirolactonisation and donor-group-controlled open-closed equilibria are popular design strategies for xanthene fluorophores in the visible spectrum,^{90,91} NIR xanthenes tend to be very lipophilic and prefer closed neutral states instead of NIR-absorbing zwitterionic ones.^{30,31,92} Urano suggested one specific solution for some rather artificial conditions, by using a thioether as the spirocyclisation site, which undergoes irreversible oxidations by exogenous HOCl to a non-spirocyclising sulfonic acid:⁷³ a concept that was later adopted by Stains for phosphonorhodamines (Figure 9a).⁹³ Quite different scaffolds can also be used as molecular imaging probes for PA. The Chan group, which spearheaded molecular imaging with HDs, developed interesting EWG-unmasking designs to use with NIR azaBODIPYs in the context of *N*-oxide-based hypoxia sensors (Figure 9b).^{78,94} Intriguingly, asymmetric rigidification of the azaBODIPY core led to stronger photoacoustic signal generation and higher

ratiometric performance,⁹⁵ and introduction of Cu(II) sensitive motifs⁹⁶ enabled molecular Cu(II) imaging (Figure 9c),⁹⁷ which is also possible with cyanine derived Cu(II) chelators.⁹⁸

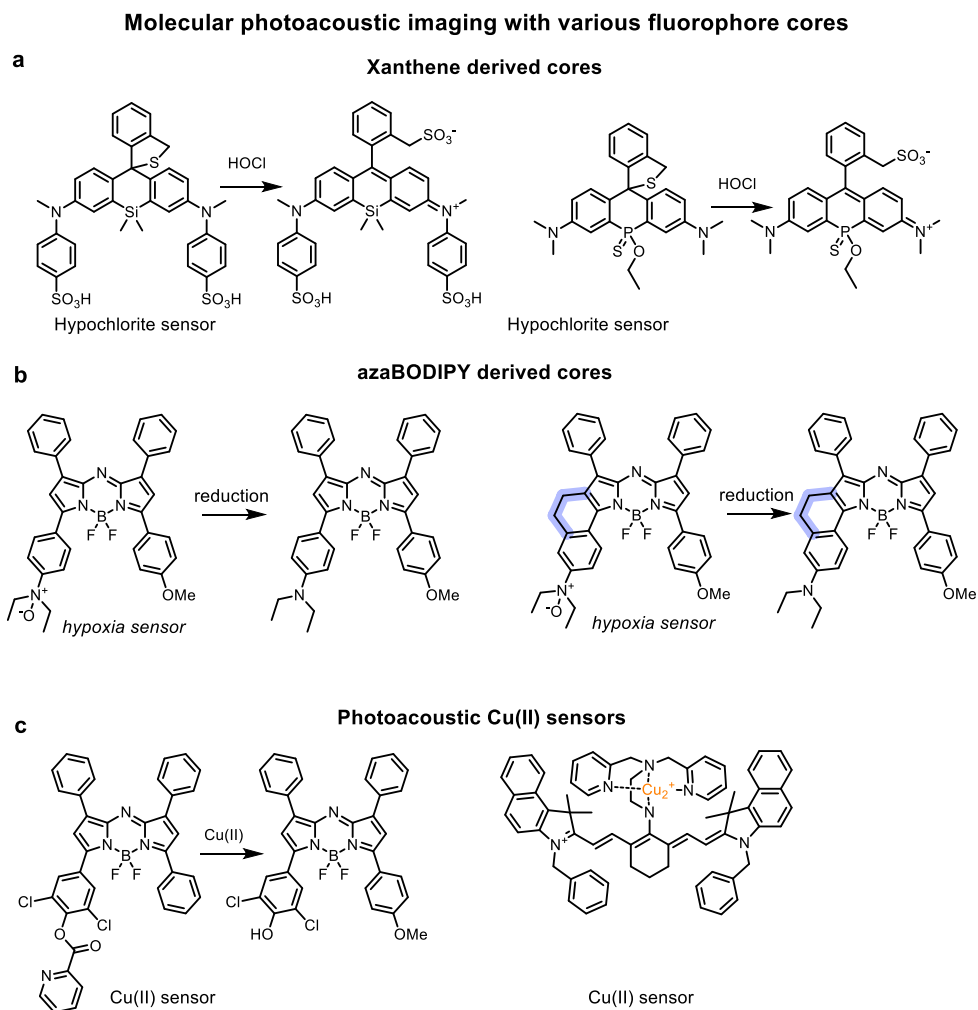


Figure 9. Molecular photoacoustic imaging sensors derived from various fluorophore cores. **a**) Xanthene derivatives as HOCl sensors.^{73,93} **b**) azaBODIPY based hypoxia sensors; asymmetric conformational restriction (highlighted in blue) increases photoacoustic signal.^{94,95} **c**) Photoacoustic Cu(II) sensors based on azaBODIPY and Cy7.5.^{97,98}

Taken together, one can state that the enzymatic unmasking strategies known from previous decades of fluorogenic and chromogenic imaging probe research, can apparently be applied to suitable PA contrast agents, to generate molecular PA imaging agents. The challenge remains, however, to innovate what the performance and design features of those *suitable PA contrast agents* should be.

1.1.3 A focused introduction to azobenzenes as molecular photoswitches

Molecules or materials that reversibly change their colour upon irradiation with light, as caused by structural and spectral changes, are said to be photochromic.⁹⁹ Often, a thermodynamically metastable state is generated that can switch back to the starting state either with light or via thermal relaxation. Several types of photoreactions are possible, such as *E*↔*Z*-isomerizations, electrocyclizations, cycloadditions, or intramolecular transfers.¹⁰⁰ From a conceptual viewpoint, triggering molecular *motions* with irradiation seems a good match to the requirements for PA contrast agents: however, molecular switches were never yet rationally considered as potential PA contrast agent motifs.

1.1.3.1 Switching and spectral tuning of azobenzenes

Azobenzenes were discovered in the 19th century¹⁰¹ and found immediate use as dyes and pigments, with a main focus on tuning them to achieve a range of colours.¹⁰² The era of molecular photoswitches started around 1937 when Hartley discovered the light-driven isomerization of *E*-azobenzene (*trans*-azobenzene) to *Z*-azobenzene (*cis*-azobenzene) after observing an apparent lack of reproducibility in spectral analysis when azobenzenes were exposed to sunlight.¹⁰³ *Z*-azobenzene is a metastable isomer and relaxes back to *E*-azobenzene either thermally or by irradiation with blue light (Figure 10a). The *E*-configuration of unsubstituted azobenzene is nearly planar and has a dipole moment of near zero whereas the *Z*-configuration is nonplanar, with a significant CNNC dihedral of 173.5°, a phenyl ring twist of ~55°, and a dipole moment of 3 Debye (Figure 10b).^{104,105} The strongest electronic transition band in/near the visible range for *E*-azobenzenes arises from the $\pi \rightarrow \pi^*$ transition located at λ_{\max} 320 nm; a much weaker band is found at λ_{\max} 450 nm (symmetry-forbidden $n \rightarrow \pi^*$). In *Z*-azobenzenes, the $n \rightarrow \pi^*$ transition is ~4× stronger than for *E*-azobenzenes, and the $\pi \rightarrow \pi^*$ transition undergoes a hypsochromic shift to λ_{\max} 270 nm, leading to distinct spectra for the two isomers (Figure 10c). Despite their significant spectral overlap, the difference in extinction coefficients still allows photoswitching azobenzenes between bulk population photoequilibria featuring majority-*E* or majority-*Z* composition (termed photostationary states, PSSs), where the *E*:*Z* ratio depends on each isomer's $\epsilon(\lambda)$ and photoisomerisation quantum yield. Quantum yields for $\pi \rightarrow \pi^*$ initiated photoisomerisations depend on the solvent and typically range from 10-20% for *E*→*Z* and 25-50% for *E*→*Z*. Intriguingly, the quantum yields for *E*→*Z* photoisomerisation are approximately doubled when initiated by the $n \rightarrow \pi^*$ transition.¹⁰⁶

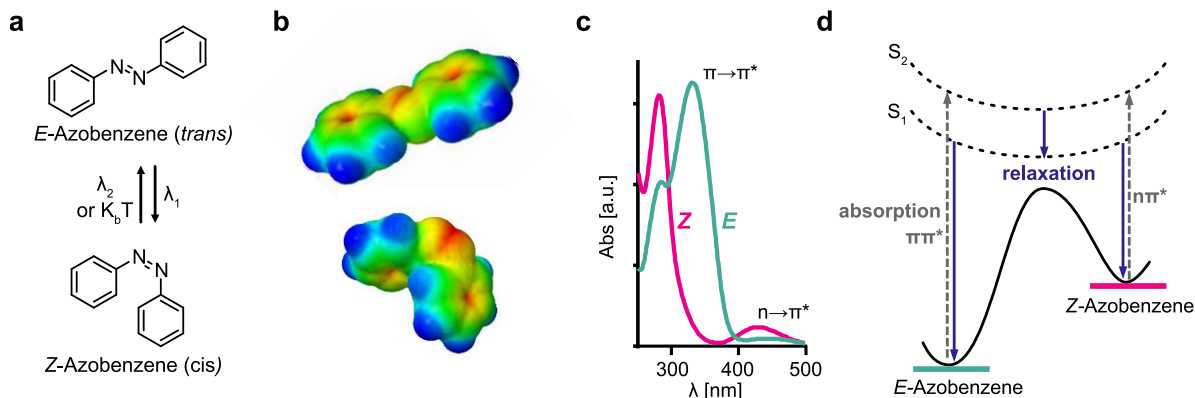


Figure 10. *E*↔*Z*-Isomerization of azobenzene. a) isomerisation of *E*- and *Z*-azobenzene. b) Electron density map for *E*- and *Z*-azobenzene, red: high electron density, blue: low electron density, derived from Molvis (LMU Munich¹⁰⁷). c) Absorption spectra of isolated *E*- and *Z*-azobenzene. d) Simplified energetic scheme for the *E*↔*Z*-photoisomerisation of azobenzenes.

For the sake of completeness, it must be stated that until recently, two general molecular motion mechanisms for azobenzene isomerization were contrasted belligerently in the literature: inversion and rotation, often stating that inversion would occur via the first excited singlet state S_1 ($n \rightarrow \pi^*$) but rotation via S_2 ($\pi \rightarrow \pi^*$). Since, after excitation to S_2 , internal conversion to S_1 can also occur, a mixture of isomerization mechanisms was usually understood to operate in practice (Figure 10d). This simplistic and binary picture has recently received strong experimental and theoretical challenges.¹⁰⁶ However, for the sake of this thesis, this history of passionate mechanistic debate is rather irrelevant. What matters are the experimentally accessible facts on which reports are unanimous: that the relevant timescales for relaxation from S_2 or S_1 to the groundstate are extremely fast, e.g. $\tau_{S_1} \sim 1$ ps and $\tau_{S_2} \sim 0.2$ ps.^{108–110} (The

rate of thermal $E \rightarrow Z$ "relaxation" is temperature, solvent, and substitution pattern dependant; typical half-lives range from hours to milliseconds,¹⁰⁵ while in extreme cases it may reach years¹¹¹ or subnanosecond timescales¹¹² at 25-40 °C, but this too will prove mostly irrelevant to this thesis.)

Azobenzene photoisomerization is usually driven by UV ($E \rightarrow Z$) and blue light ($Z \rightarrow E$). These wavelengths are poor for biological applications because of limited light penetration depths, and UV phototoxicity, therefore strategies to redshift their absorption were explored.¹¹³ To reduce the energy gap between HOMO and LUMO, typical organic dyes can either increase the π -system length, or introduce electron-donating groups (EDGs) and/or electron withdrawing groups (EWGs) on opposite ends of the π system to give *push-pull* systems with a strong intramolecular charge transfer character (Figure 11a-c).^{114,115} However, for azobenzenes, redshifting is more complicated. The main $\pi \rightarrow \pi^*$ transition used for $E \rightarrow Z$ -isomerization is in the UV and is not the HOMO-LUMO transition; extending the π system or creating strong push-pull systems can significantly redshift that $\pi \rightarrow \pi^*$ transition but it only moderately affects the visible $n \rightarrow \pi^*$ transition;¹¹⁶ and as consequence, these strategies can cause the two transition bands to overlap, and to occur at the same spectral region in both isomers: which reduces the completeness of photoisomerisation (though, in this thesis, that completeness will not always be a relevant feature), and in general accelerates thermal back-relaxation. A more specific way to not only redshift but also make the Z -state the thermally stable isomer was shown by Herges who introduced ring strain, in the form of the diazocine motif (Figure 11d).¹¹⁷ Intramolecular coordination of the azobenzene to a Lewis acid also shifts its absorption into the red, but the complexes are hydrolytically instable, preventing applications in aqueous environments (Figure 11e).¹¹⁸ The most reliable redshifting mechanism today uses four *ortho*-substituents to separate the $n \rightarrow \pi^*$ transitions of the two isomers, so enabling bidirectional switching with visible light;^{111,119,120} in some settings, *ortho*-alkoxy groups can also be used to stabilise a protonated azonium ion under neutral pH by coordination, for further red-shifting (Figure 11f).¹²¹ Apart from these direct substituent-based modifications affecting the $\pi \rightarrow \pi^*$ and $n \rightarrow \pi^*$ transitions, azobenzenes can also be indirectly photoswitched by sensitization¹²²⁻¹²⁵ or photoredox,¹²⁶ allowing a broad variety of excitation wavelengths (chosen to excite the catalyst) to be used.

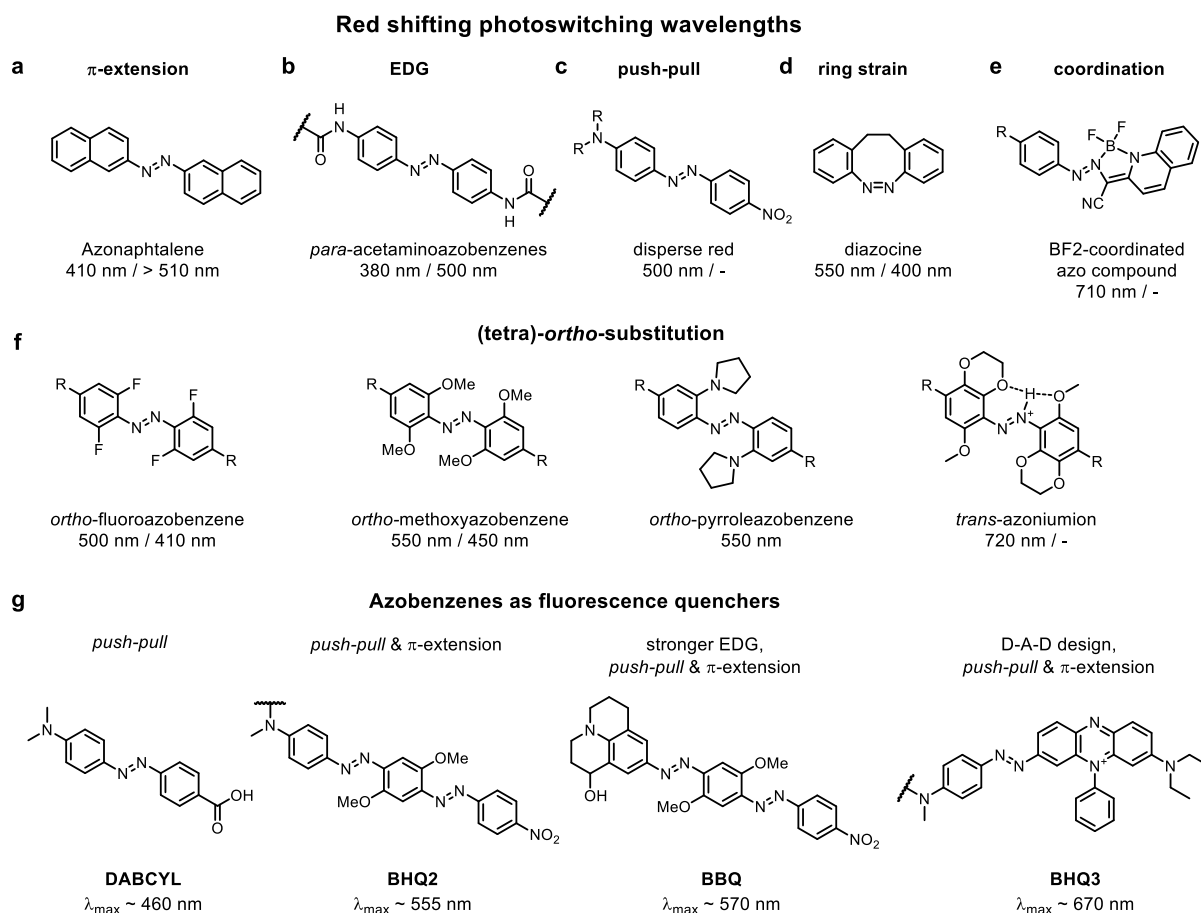


Figure 11. Redshifted azobenzenes. **a-f**) wavelengths used for photoisomerisation: λ_{irr} ($E \rightarrow Z$ / $Z \rightarrow E$), **a-e**) different strategies to red shift photoswitching wavelengths. **f**) *ortho*-substitution for bidirectional visible light photoswitching. **g**) Azobenzenes as fluorescence quencher.

At the time of this thesis, the combination of strong push-pull-systems with π -system elongation was known to result in azobenzenes with absorption *nearly*, but not quite, up to the NIR (Figure 11f,g). Such motifs were not used as molecular photoswitches and are much under-studied in the photoswitching field; but their intrinsically non-fluorescent deexcitation pathway was often harnessed to quench fluorescence in FRET probes. Some are commercialised under trade names like black hole quencher (BHQ) or blackberry quencher (BBQ).^{127,128} While we considered that such types of azobenzenes present ideal lead characteristics for photoacoustic contrast agents based on their ultrafast excited state relaxation via internal conversion, and while **BHQ3** was already found to be an unusually strong PA emitter⁷⁷, their absorption wavelengths appeared to have hit a limit below the useful region for PA.

1.1.4 Excursus: the colour blue in nature - inspiration for PA contrast agents?

“Je tiefer das Blau wird, desto mehr ruft es den Menschen in das Unendliche, weckt in ihm die Sehnsucht nach Reinem und schließlich Übersinnlichem“ — Wassily Kandinsky

The colour blue in our environment arises from absorption of non-blue light from white light and reflection of the blue fractions. Typically, blue chromophores have an absorption maximum in the red region and filter out yellow/green light with their absorption tail. Photoacoustic imaging requires contrast agents absorbing red/NIR light and as corollary PA dyes tend to appear deep blue (or green, if bands are narrow and if there are secondary maxima in the UV/blue region). Chemistry is an empirical natural science, and it is always worthwhile to get inspiration from nature when a new design for a problem is required. However, when it comes to red absorbing organic chromophores, nature does not have much to offer. Absorbing low energy photons with biomolecularly-accessible chromophores requires large and lipophilic π -systems that are complicated to produce and often unstable. Of course, nearly all plants using photosynthesis are green, but chlorophyll (or naturally accessible metalloporphyrins, with few exceptions) is not such a useful chromophore as it is relatively unstable, and its major spectral absorbance is within the blue region. The lack of blue pigments in nature is best seen through linguistics: Homer used the word blue in his epics exactly zero times, instead he described the colour of the sea with the same term as he used for wine; the bible also provides no examples for blue.¹²⁹ Historically, many intellectuals, led by William E. Gladstone, held that colour perception is an intellectual ability learned from red to blue, because less developed cultures miss the ability to name blue or green as colours. This theory is of course complete nonsense, and when modern linguistic research analysed the capability of different cultures to separate colours all of them set semantic separations at the same spectral lines. The only exception is between blue and green because a significant number of them only have one word for both colours, mainly because occurrence of the colour blue is rare and there is no need to name many blue objects in nature and the surrounding environment.

Natural pigment sources fall into three different categories: inorganic materials, animals, and plants. It is somewhat wishful thinking to search them deeply for design inspiration for contrast agents for red/NIR photoacoustic imaging. Inorganic materials such as Lapis lazuli or sapphire are not inspiring because their colour is caused by an exotic S_3^- radical anion (for Lapis lazuli)¹³⁰ or crystal distortions (for sapphire), with neither concept applicable to small molecules in solution. Animal blues are often very intense and shiny, but are mostly produced physically by light diffraction on gratings or photonic crystals, which are typically built of protein superstructures. It appears that producing fine-tuned nano structures for optical interference was evolutionarily more straightforward than producing organic dye structures. There are only rare exceptions, such as the copper containing protein hemocyanin which occurs in invertebrates (e.g. lobster blood)¹³¹ and the tree frog *Aplastodiscus leucopygius*,¹³² or biliverdin which is an oxidation product of haemoglobin that is instable in most mammals but naturally occurs in fish (e.g. parrotfish) and avian egg shells.¹³³ Nonetheless, the plants remain.

Roses are red, and cornflowers are blue. Intriguingly, both contain cyanidin as the core structure responsible for the colour, a scientific mystery Richard Willstätter started to tackle in the early 20th century but which took until 2006 for researchers to solve, by tracing the blue pigment in cornflowers to a complex consisting of six cyanidins, six flavones, one ferric ion, and one magnesium ion.¹³⁴ It is safe to assume that nearly all blue flowers use complexes of cyanidin or its structural analogue delphinidin to generate their blue appearance. But again, those complexes are large, chemically instable, and offer no fruitful inspiration for PA imaging. Indeed, the huge effort that nature undertakes to create blues emphasizes how challenging they are to access with small molecules.

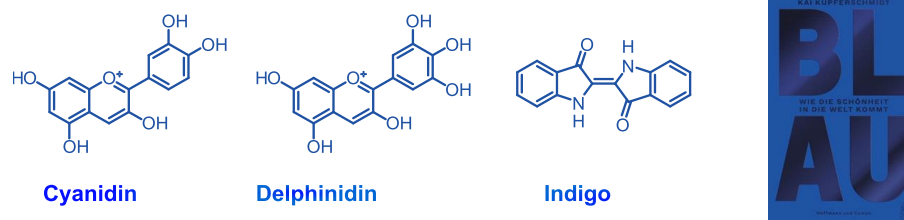


Figure 12. Chemical structures of cyanidin, delphinidin, and indigo. Cover of the book *Blau*, written by science magazine correspondent Kai Kupferschmidt, which served as main inspiration for this chapter.^{129,135}

Serendipitously, there is one (partial) exception: indigo (*Indigofera tinctoria*) and dyer's weed (*Isatis tinctoria*) contain a precursor for the intense blue dye indigo. Indigo has a long history in humanity, from early civilizations until today, and in the 19th century the German chemist Adolf von Baeyer solved its chemical structure, then developed a completely synthetic route to produce it, starting its transition from a natural product to an important synthetic dye. For a blue chromophore, indigo is relatively small, without an extended π -system which raises the question, why is indigo blue? The π -system of indigo consists of two pairs of donor-acceptor (D-A) pairs ($O=C-C=C-C-NH$) which are conjugated through the same double bond and the HOMO-LUMO gap is lowered by additive effects of the two individual D-A pairs even without an extended π system.¹³⁶ It is no accident that indigo is essentially a molecular photoswitch with ultrafast excited state relaxation,¹³⁷ and is the only colour-fast blue molecular organic dye in nature. The correlation between these features will be revisited below for NIR molecular photoswitches as chromophores for photoacoustic imaging: promising a blue miracle for imaging.

1.2 Aims and objectives

Photoacoustic (PA) imaging can localise exogenous contrast agents while simultaneously resolving surrounding tissue by endogenous contrast agents. However, general design criteria for small molecule PA contrast agents that are widely agreed on do not exist. The absence of widely applicable blueprints for the dye itself perpetuates the *status quo*, as molecular probes for specific biomarkers are built profusely but conservatively around non-PA-optimized motifs. Studies describing relevant molecular effects are rare, and none of them include molecular designs that can be used as a conceptual guidance.

PA contrast agents need to transform light energy to heat as efficiently as possible, and molecular photoswitches are characterized by light induced molecular rearrangement. This feature marks a promising starting point from a chemical design viewpoint because light-induced molecular motion is already an inherent feature. The field of photopharmacology (see part two of this thesis) traditionally uses photoisomerisation to control biological function, but herein, we want to focus on a different aspect of molecular photoswitches: the speed and pathway-simplicity of thermal relaxation from the excited state back to the ground state.

The aim of this thesis part is to demonstrate that *loud and photostable* PA contrast agents can be designed rationally, by harnessing the intrinsic photophysics of molecular photoswitches as a blueprint.

(section 1.3.2) Azobenzenes were picked as a proof of principle molecular switch scaffold because push-pull substitution results in ultra-fast non-radiative decay combined with little difference between *E* and *Z* spectra. Commercially available PA systems only operate in the NIR region, while azobenzenes traditionally strongly absorb only in the UV/blue; therefore, this work first aimed to design and synthesize azoaryl-derivatives with suitable NIR absorption, and then to evaluate their PA signal generation efficiency, and finally test the mechanistic design hypothesis of ultrafast relaxation with spectroscopic methods that are suitable to measure excited state dynamics.

(section 1.3.3) More generally, this thesis aimed to establish the general concept of fast thermal excited state relaxation as a widely applicable design criterion for future PA contrast agents. This requires the development and demonstration of a chemically entirely different motif that nonetheless delivers the same photophysical features and PA outcomes as an orthogonal validation to showcase how intrinsic properties are more important than specific molecules, and to inspire other chemists to join the challenge of modularly integrating such properties to deliver tailor-made PA contrast agents.

In the following chapters, I present my research towards these aims.

1.3 Results and Discussion

1.3.1 Author Contributions

The following projects are highly interdisciplinary, bridging the expertise of synthetic chemistry, chemical biology, engineering, and spectroscopy. While this section details my own scientific contributions and achievements that led to those papers, I want to emphasize the importance of my collaboration partners who constantly supported the scientific progress of my projects with their additional expertise and enabled a research project at this interdisciplinary scale with passion and commitment from all sides.

In the following I will briefly describe my contribution to each project:

Publication One: NIR azobenzenes as contrast agents for PA imaging

I helped to discuss and refine the mechanistic hypotheses, designed target compounds and their retrosynthesis, performed synthesis, structural characterization, UV/VIS, and fluorescence photocharacterization of Azocyanines and Azohemicyanines (primarily **Figs 1-2** and **Figs S1-S2**). I assisted in time-resolved fluorescence measurements; for transient absorption spectroscopy I was strongly involved in the first measurement collaboration (later aborted), then took an advisory role for the final collaboration which succeeded (Jena) (**Fig 4**). I assisted and performed photoacoustic phantom characterization, assisted with photoacoustic *in vivo* mouse imaging and coordinated image processing performed by collaborators (**Figs 3 & 5**). I coordinated data assembly, prepared figures, wrote a manuscript draft and assisted writing the final version of the manuscript.

Publication Two: NIR triarylmethane molecular rotors are privileged motifs for PA imaging

I originated the concept of using molecular rotors instead of only molecular switches for similar PA enhancement; designed the triarylmethane target compounds, and performed their synthesis (in part, supervising M.K. and J.P.P.), structural characterization, UV/VIS, and fluorescence photocharacterization (primarily **Figs 1-2**). I advised collaboration partners for transient absorption spectroscopy (**Fig. 3**). I performed photoacoustic phantom characterization, coordinated image processing performed by collaborators (**Fig. 4**) I coordinated data assembly, prepared figures, wrote a manuscript draft, and am assisting in writing the final version of the manuscript, where I will be co-corresponding author.

1.3.2 Publication One: NIR azobenzenes as contrast agents for PA imaging

In the following work we provide a rational approach, from a general concept through to concrete molecular design realisation, for how to construct efficient contrast agents for photoacoustic (PA) imaging, based on targeting intrinsic experimental parameters with tailored design.

PA imaging *in vivo* uses short laser pulses of 10 ns, at 10 Hz repetition rate, and the measured ultrasound signal intensity correlates with the amount of photon energy that is transformed to thermal energy within each pulse. We intended to create contrast agents with ultrafast excited state relaxation times, short enough to enable several excitation-relaxation cycles within one pulse of 10 ns. Such a design promises that the total number of photons that can be transformed to thermal energy by one single molecule gets increased and hence, increases the PA signal intensity. With a strong background in photopharmacology within the group (also see part 2 of this thesis) we envisioned azobenzenes as an auspicious chemical motif to serve as the PA emitter because the photophysics of azobenzenes match the desired criteria (explicitly, their ultra-fast non-radiative $S_1 \rightarrow S_0$ decay). However, PA imaging requires ideally NIR absorbing chromophores for maximal tissue penetration depths. Azobenzenes are mainly absorbing in the UV or visible range of the spectrum and the rare NIR absorbing examples are not compatible with PA requirements, such as solubility in aqueous environment; while most NIR-absorbing small molecules are fluorophores that were developed for deep tissue fluorescent imaging. Therefore, the first step was to create NIR absorbing chromophores that include an azobenzene motif. We embarked on this challenge by merging cyanine dyes – which exhibit the highest known extinction coefficients within the NIR range – in several structural combinations together with azobenzenes either (1) remotely as an extension to the cyanine dye (= Azocyanines, **AzCy**) or (2) incorporated into the cyanine π -system (= Azohemicyanines, **AzHCy**), and obtained chromophores with the desired NIR absorptivity in both cases (Paper 1, Figure 2, here page 33)

We showed that PA signal generation efficiency (SGE) of NIR absorbing **AzHCys** is $>3\times$ higher than the reference chromophore **ICG**, when measured at equal optical densities (OD) in a commercial *in vivo* imager: a *per-absorbable-photon* metric that classifies PA emission efficiency on a molecular level, subject to the practical settings currently used in translational research. This is an important result, because traditionally, low fluorescence quantum yields (Φ_{FL}) were the major design criterion for PA contrast agents, yet a $>200\%$ signal increase cannot be caused by only $\sim 10\%$ more radiative decay (quenching of the 10% fluorescence QY), therefore this "20 \times higher than expected" signal increase alerts the community that a different framework for predicting PA response is needed.

For unbiased design of molecular imaging probes, the extinction coefficient must also be considered, and we found strong spectral broadening for the asymmetric **AzHCys** that lowers the extinction coefficients, making them less attractive in comparison to the symmetric **ICG** because it decreases their *molar* SGE to ca. $\sim 0.8\times$ that of ICG under current standard settings (Paper 1, Figure 3, here page 34).

However, we highlight another benefit of the ultra-fast non-radiative-relaxing motifs that we consider outweighs their extinction coefficient: the **AzHCys** have nearly unlimited photostability, as we do not see even 0.5% decrease of PA signal over a time course of 30 minutes, whereas **ICG** photobleaches with halftime of ca. 5 minutes (at standard imager settings) *in a diffusible phantom model*. In PA imaging

typically ten pulses of one wavelength are averaged to give one frame; and for multispectral optoacoustic tomography (MSOT), frames from the whole absorption spectrum must be combined for unmixing to generate one image. For example, imaging with 10 nm steps from 700-900 nm requires 200 pulses (a common setting for *multispectral imaging*), i.e. taking 20 seconds for a single tomographic image. After only twelve such images, the signal intensity from ICG will photobleach, unpredictably, to below that of a less-strongly-absorbing but much more photostable **AzHCy**, in the phantom. However, *in vivo* imaging is different from phantom imaging: in the phantom, a cylindrical cuvette is imaged at a specific cross-section but with the residual cuvette volume serving as a reservoir for fresh unbleached contrast agent, which downplays its photobleaching kinetics in a way that *in vivo* molecular imaging (no diffusive replacement) would not. Therefore, the translational advantage of the photostability we introduce might even be underestimated based on the phantom half-life. At any rate, using photostable contrast agents promises reliable and practical *in vivo* imaging without the need of careful photon exclusion when setting up the experiment (including pre-acquisition imaging for transection adjustment). While the various mechanism/s for contrast agent photobleaching are not always unambiguous, and they are highly structure- and environment-dependent, we argue that long-lived excited states can be assigned as the *origin* of much photobleaching (particularly, but not only, by intersystem crossing to triplets subsequently forming singlet oxygen): that can now be circumvented by ultrafast relaxation.

To experimentally validate our photophysical hypothesis we conducted time-resolved photoluminescence and found excited state half-times (τ) of ~ 10 ps for **AzHCys** and ~ 400 ps for **AzCys**. Those values align with the SGE trend observed in PA imaging, but they are limited to monitoring the kinetics of S_n decay whereas our hypothesis explicitly requires relaxation fully back to S_0 (rather than e.g. crossing to a triplet, or isomerisation to a different groundstate species, etc). Therefore, we also applied transient absorption spectroscopy to test if the major (>90%) route is indeed $S_1 \rightarrow S_0$ relaxation: which for **AzHCys** was confirmed, with matching τ of ~ 4 ps. (Paper 1, Figure 4, here page 35)

AzHCys show broad absorption spectra. In MSOT, separating the signal of the contrast agent from the broad tissue background requires spectral information, where sharp peaks are generally easier to process (high signal to noise). To test the applicability of **AzHCys** for *in vivo* imaging despite this broadness, we used healthy mice, injected the water soluble **wsT-AzHCy** into the lateral tail vein, and imaged cross sections showing liver, kidney, and spleen, both before, and a challenging 120 min after, injection. The chromophore **wsT-AzHCy** is decorated with sulfonic acid groups for better solubility, and such small molecules are often either metabolized or excreted via liver/spleen or kidneys. Even 120 minutes later we observed **wsT-AzHCy** signal in the liver, spleen, and the gut, but not within the kidneys; while image processing gave negligible false positive signal before injection. This confirms that electronic image processing for spectral deconvolution and localization *in vivo* can be succeed on the broader **wsT-AzHCy**, as for other contrast agents (Paper 1, Figure 5, here page 36).

Our findings thus show a molecular blueprint for PA contrast agents guided by a photophysical rationale. For many years the logic of how to generate *loud* PA contrast agents has been uncertain. Herein we provided evidence for fast non-radiative decay as clear design criterion, that also allows repeated long-term imaging without loss of signal due to photobleaching, favouring true monitoring of biological processing (instead of external *photochemical* processing).

Merged Molecular Switches Excel as Optoacoustic Dyes: Azobenzene–Cyanines Are Loud and Photostable NIR Imaging Agents

Markus Müller, Nian Liu, Vipul Gujrati, Abha Valavalkar, Sean Hartmann, Pia Anzenhofer, Uwe Klemm, András Telek, Benjamin Dietzek-Ivanšić, Achim Hartschuh, Vasilis Ntziachristos, and Oliver Thorn-Seshold*

Abstract: Optoacoustic (or photoacoustic) imaging promises micron-resolution noninvasive bioimaging with much deeper penetration (> cm) than fluorescence. However, optoacoustic imaging of enzyme activity would require loud, photostable, NIR-absorbing molecular contrast agents, which remain unknown. Most organic molecular contrast agents are repurposed fluorophores, with severe shortcomings of photoinstability or phototoxicity under optoacoustic imaging, as consequences of their slow $S_1 \rightarrow S_0$ electronic relaxation. We now report that known fluorophores can be rationally modified to reach ultrafast $S_1 \rightarrow S_0$ rates, without much extra molecular complexity, simply by merging them with molecular switches. Here, we merge azobenzene switches with cyanine dyes to give ultrafast relaxation (< 10 ps, > 100-fold faster). Without even adapting instrument settings, these azohemicyanines display outstanding improvements in signal longevity (> 1000-fold increase of photostability) and signal loudness (> 3-fold even at time zero). We show why this simple but unexplored design strategy can still offer stronger performance in the future, and can also increase the spatial resolution and the quantitative linearity of photoacoustic response over extended longitudinal imaging. By bringing the world of molecular switches and rotors to bear on problems facing optoacoustic agents, this practical strategy will help to unleash the full potential of optoacoustic imaging in fundamental studies and translational uses.

Introduction

The idea of designing chromophores for ultrafast $S_1 \rightarrow S_0$ electronic relaxation has not yet been raised as a goal for optimising molecular NIR optoacoustic contrast agents, but we feel it will be crucial for successful translation of optoacoustic imaging. Here, we bring it to the community, by showing how a simple design lowers $S_1 \rightarrow S_0$ lifetimes by > 100-fold, and thus delivers substantial improvements to currently limited signal strength (here: > 7-fold) and dye photostability (> 1000-fold).

Optoacoustic imaging, interchangeably called photoacoustics or “PA”, adds new opportunities to the imaging toolbox. In PA, short laser pulses excite optical absorbers; when they locally dissipate the excitation energy as heat during the pulse, an expansion pressure wave results, that can be detected with low attenuation and high localisation by ultrasound transducers.^[1] With its unique optical-input/acoustic-output combination, PA offers attractive features that other imaging techniques do not: PA penetrates several cm through tissue, with resolution down to 150 μm , and can image endogenous or exogenous contrast agents (by MSOT,

[*] M. Müller, A. Telek, Dr. O. Thorn-Seshold
 Department of Pharmacy
 LMU Munich
 Butenandtstrasse 7, Munich 81377, Germany
 E-mail: oliver.thorn-seshold@cup.lmu.de

Dr. N. Liu, Dr. V. Gujrati, P. Anzenhofer, U. Klemm,
 Prof. Dr. V. Ntziachristos
 Institute of Biological and Medical Imaging
 Helmholtz Zentrum München
 Ingolstaedter Landstrasse 1, Neuherberg 85764, Germany

Dr. N. Liu, Dr. V. Gujrati, Prof. Dr. V. Ntziachristos
 Chair of Biological Imaging at the Central Institute for Translational
 Cancer Research (TranslaTUM)
 School of Medicine and Health
 Technical University of Munich
 Ismaninger Str. 22, Munich 81675, Germany

A. Valavalkar, Prof. Dr. B. Dietzek-Ivanšić
 Institute of Physical Chemistry
 University of Jena
 Lessingstraße 4, Jena 07743, Germany

A. Valavalkar, Prof. Dr. B. Dietzek-Ivanšić
 Research Department Functional Interfaces
 Leibniz Institute of Photonic Technology Jena
 Albert-Einstein-Straße 9, Jena 07745 Germany

S. Hartmann, Prof. Dr. A. Hartschuh
 Department of Chemistry
 LMU Munich
 Butenandtstrasse 8, Munich 81377, Germany

© 2024 The Author(s). Angewandte Chemie International Edition published by Wiley-VCH GmbH. This is an open access article under the terms of the Creative Commons Attribution Non-Commercial License, which permits use, distribution and reproduction in any medium, provided the original work is properly cited and is not used for commercial purposes.

multispectral optoacoustic tomography).^[2,3] Thus, PA has become valuable particularly in anatomical imaging, from basic research^[4] to image-guided surgery.^[5]

PA's ultrasound output has excellent tissue penetration; its depth limits come from its optical input. NIR light attenuates the least during tissue penetration,^[6] so PA adopted NIR dyes as exogenous contrast agents. Cyanine (Cy) dyes played a major role^[7] because of their strong NIR absorption and their rational wavelength tuning capacities, that had been developed for fluorescence.^[8] In particular, as the Cy dye indocyanine green (ICG; $\lambda_{\text{max}} \approx 780$ nm, Figure 1c) is FDA-approved for fluorescence imaging, it was rapidly adopted in PA and is still widely used.^[9,10]

Cyanines are still very actively researched: e.g. as SWIR (1–2 μm) fluorophores enabling deeper tissue penetration,^[11–13] or as hybrid “hemicyanines”^[14] that are easier to make into fluorogenic^[15] or acoustogenic^[16–18] probes. Other fluorophore and PA contrast agent structural scaffolds have been excellently reviewed.^[7,19–22]

However, there has been little rational development of contrast agents to optimise the specific properties needed for PA; in fact, principles for best PA are not even widely agreed upon. Thus, accessible fluorophores, such as Cy dyes, continue to be widely used even though the properties that make them good fluorophores lead to diverse problems when used in PA. These issues have been well-reviewed by Rochford.^[23] An optoacoustic signal is proportional to the fraction of absorbed optical energy which is dissipated as heat by vibrational relaxation (VR). An obvious drawback of good fluorophores is that they undergo fast VR from hot S_1 states to a cold S_1 state, but then emit the remaining energy as fluorescence: so overall they convert little energy to optoacoustic signal (Figure 1a).

Yet, most NIR fluorophores are “bad,” in the sense that their quantum yields are already low (e.g. 10%): so further

lowering^[24–27] or fully quenching^[28–30] fluorescence can only increase PA signal by 10%,^[31] unless other mechanisms are also involved.^[32] Two such mechanisms for PA enhancement are possible, and were well outlined by Rochford.^[23] In brief, since PA supplies energy during infrequent excitation pulses that have similar duration as typical S_1 state lifetimes (pulses \sim ns, \sim 10 Hz repeat rate), time-dependent effects become important:

(1) If relatively long-lived S_1 states can be excited further to S_n states during a PA pulse, these typically vibrationally relax rapidly back to S_1 . In theory, fast $S_1 \rightarrow S_n \rightarrow S_1$ cycling such “RSA” chromophores (reverse-saturable absorbers) can thus allow higher PA signal than ordinary chromophores using $S_0 \rightarrow S_1 \rightarrow S_0$ cycles (“SA”, saturable absorbers), since $S_n \rightarrow S_1$ is faster than $S_1 \rightarrow S_0$. RSAs have been widely reported in cell-free PA studies.^[23] However, RSA signal scales non-linearly with laser fluence, since the signal comes from doubly excited species ($S_0 \rightarrow S_1$ then $S_1 \rightarrow S_n$). Biologically allowed energy limits dictate such low fluence in deep tissue that in practice, RSAs are outperformed by ordinary PA emitters that simply absorb light more strongly.^[33,34] We also argue that cycling RSAs between S_1/S_n states may cause photoreactive damage to the chromophore or to biological tissues.

(2) Alternatively, if S_1 becomes very short-lived (lifetime \ll laser pulse length), in theory multiple $S_0 \rightarrow S_1 \rightarrow S_0$ excitation/VR cycles will be possible in a single pulse, also increasing the optoacoustic signal compared to ordinary chromophores (Figure 1b). Rochford named these “LA” chromophores (linear absorbers), since their PA signal should scale linearly to the excitation intensity, though only one was identified: the genotoxic 580 nm-absorbing dye crystal violet.^[23,35] We argue that if molecular NIR LAs can be made, they hold the

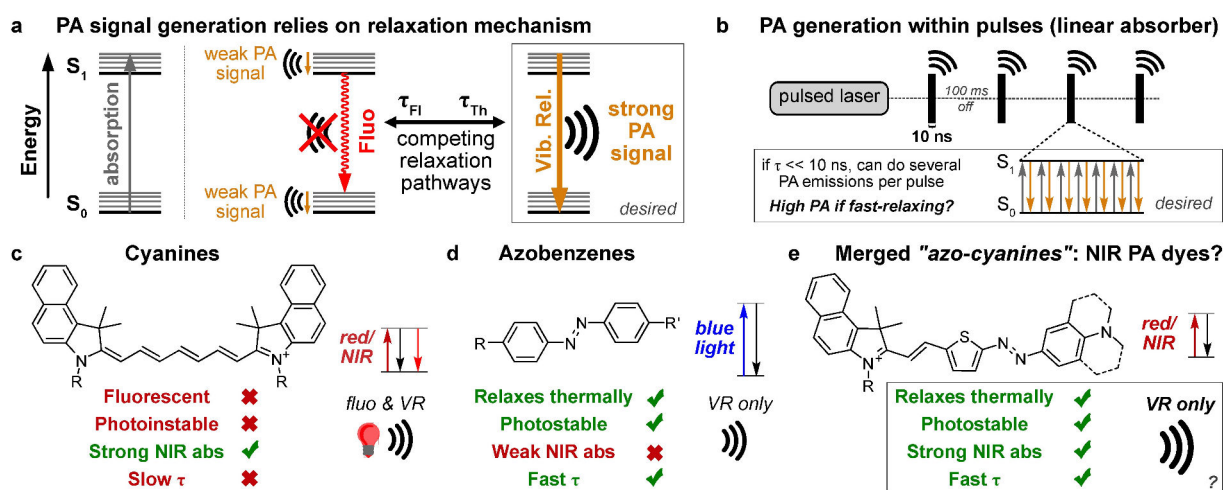


Figure 1. Design concept for molecular switch-based optoacoustic contrast agents. a) Energy dissipated as heat contributes to PA signal (internal conversion then vibrational relaxation); fluorescence does not. b) PA excitation is pulsed. For a linear absorber ($S_1 \rightarrow S_0$ relaxation half-life τ much shorter than the pulse), several $S_0 \rightarrow S_1 \rightarrow S_0$ excitation-relaxation cycles are possible within one pulse. c) Cyanine dyes have strong NIR absorption, but are poor PA agents as they are slow-relaxing and non-photostable. d) Azobenzenes have ultrafast nonradiative relaxation, but as UV/Vis-absorbers they are not useful for NIR PA. e) **Hypothesis:** merging azobenzenes and cyanines should give strong, photostable NIR-absorbing PA emitters.

key to successful molecular PA, for two reasons that we did not yet find discussed together:

(2a) Photostability is a major drawback for NIR fluorophores currently used in PA. A typical case is **ICG** which bleaches out in minutes (Figure 3d).^[36,37] This not only limits the imaging time-window, but makes a signal not quantitative for probe concentration, but only for its non-photo-bleached fraction. Instead, LAs should be very photostable, since rapid depletion of S_1 prevents excited-state photo-reactivity: thus LAs should allow long-term/longitudinal imaging, with accurate signal quantification, as is needed for molecular PA imaging.^[38]

(2b) LAs should give a predictable, useful response in biology, since they suffer only proportional signal decrease as the excitation power attenuates with depth (contrast this to nonlinear response of RSAs).

We recognised that molecular switches such as azobenzenes, which $S_1 \rightarrow S_0$ relax with picosecond halftimes and which, accordingly, have been exploited as enormously photostable dyes since >170 years,^[39,40] would be an ideal LA chemotype; and that this parallels Rochford's recognition of crystal violet (a molecular rotor) as an excellent LA. There were encouraging hints that *appropriate* azobenzenes could succeed in PA. The non-emissivity and photostability of azobenzenes makes them popular as fluorescence quenchers in FRET probes, if excitation energy can be transferred onto them;^[41] and in Gambhir's early work on acoustogenic probes, the complex azobenzene **BHQ3** was by chance found to be an "unusually strong" PA emitter, although the reasons for this were not explored and the work was not

pursued further.^[32] However, we knew of no biocompatible / water-soluble azobenzenes absorbing suitably in the ideal NIR window for PA (760–880 nm)^[42] that could be tested (Figure 1d).

We now show the feasibility of rationally creating LA-type, NIR-absorbing, highly photostable and loud PA chromophores allowing multiple excitations per pulse, by uniting good chromophores and good switches. Our proof of principle work unites the NIR absorption of Cy dyes (strong chance to enter S_1) with the relaxation of azobenzene-type molecular switches (for ultrafast $S_1 \rightarrow S_0$; Figure 1e).

Results and Discussion

Design, Synthesis, and Spectral Properties

Our first approach was to attach the phenylazo switch onto Cy5/7 fluorophores, at the middle (**M-AzCy5**) or the end (**E-AzCy5/7**; Figure 2). In the second approach, we replaced part of the π -system with the azobenzene, imagining that conjugating over its N=N would maximise relaxation rates. This gave azo-hemicyanines, with phenylazobenzene systems of two π -system lengths (**P-AzHCy1/2**). Like Nakamura, who used thiophenylazo bridges for redshifting,^[43] we also tested thiophenylazos with two donor group types (**T-AzHCy1/2**). Interestingly, Swager had suggested to use such scaffolds for PA imaging,^[44] but the lack of water solubility had presumably blocked it. To force water solubility, we also installed an extra sulfonate in **wsT-AzHCy** (Figure 2).

Their syntheses were direct. The middle phenylazo was installed by reacting the pentamethine with phenyldiazo-

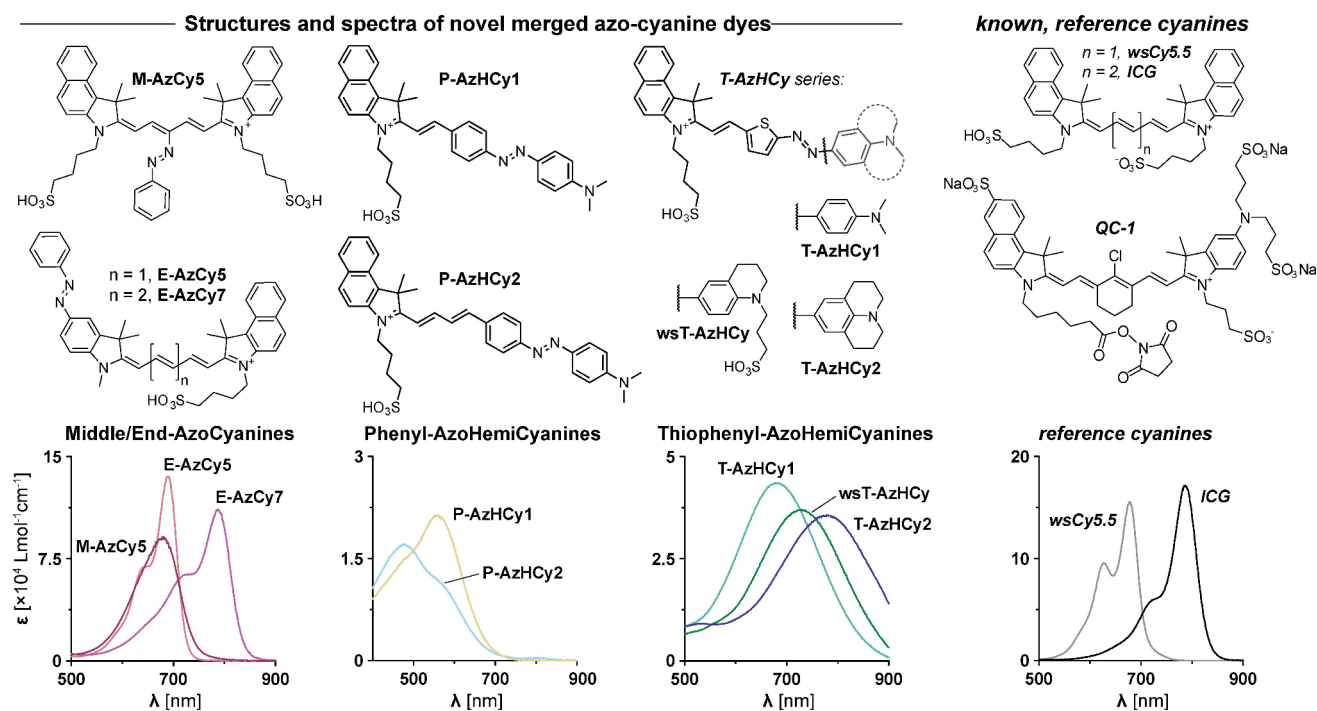


Figure 2. Structures and absorption spectra of azo-cyanines (dyes in 1 : 1 EtOH:PBS at 10 μ M, except ICG at 5 μ M; further details in Figure S1).

nium (**M-AzCy5**);^[45] the end phenylazos were installed onto the indolenin before the polymethines were synthesised by asymmetric Cy dye syntheses (**E-AzCy5/7**; Scheme S1). The azo-hemicyanines were synthesised by Knoevenagel condensation of the indolenin and the aldehydes (**P/T-AzHCy1/2**, **wsT-AzHCy**; Scheme S2).

The first requirement for these dyes was to reach strong NIR absorption, with λ_{max} desired as >720 nm for in vivo applicability. Middle/end azo-cyanine **M/E-AzCys** had similar absorption as the reference pentamethine **wsCy5.5** or heptamethine **ICG**, though were broadened and at lower intensity, as expected.^[46,47] The phenylazo-hemicyanine **P-AzHCy** types absorb in the cyan/green, so were not continued for further study. Pleasingly, the thiophenylazo-hemicyanine **T-AzHCy** types had strong absorption in the PA-adapted NIR window, with the λ_{max} value of 779 nm for **T-AzHCy2** being directly comparable to **ICG**; though again, their bands were broader and had lower extinction coefficients than the symmetric Cy dyes (Figure 2, Table 1).

The next requirement was to reach LA-type PA agents, by forcing an ultrashort-lived S_1 state. Low fluorescence is a necessary but insufficient proof of short S_1 lifetime. The **T-AzHCy** types had zero detectable fluorescence on our usual setup; **M-AzCy5** was almost nonfluorescent, but Φ_{FL} of **E-AzCy5/7** barely differed from their parents (Table 1; we return to the S_1 lifetimes later, at Table 2).

Azobenzenes can undergo $E \rightleftharpoons Z$ photoisomerizations^[48] that change their absorption profiles. For quantifying a PA contrast agent, such changes would be an undesirable. We tested the **T-AzHCy** types that were now our leads, and these did not change Vis/NIR absorption under strong LED illumination, which is promising but not yet conclusive (discussion at Figure S2, see also TA spectroscopy below).

Strength and Photostability of the Optoacoustic Signal

We now tested our hypothesis that azo-merged-cyanines with fast $S_1 \rightarrow S_0$ VR would have strong, photostable, optoacoustic signals.

We first determined PA response spectra. Pleasingly, the **T-AzHCys** and **M-AzCy** gave much stronger PA than **ICG**

Table 1: Absorption (1:1 EtOH:PBS) and fluorescence (EtOH).

	λ_{max} [nm]	ϵ [$\times 10^3$ $\text{M}^{-1} \text{cm}^{-1}$]	FWHM [nm]	Φ_{FL}
M-AzCy5	678	94	100	< 0.01
E-AzCy5	689	136	72	0.22
E-AzCy7	785	111	114	0.10
P-AzHCy1	557	48	162	not tested
P-AzHCy2	483	28	245	not tested
T-AzHCy1	685	44	189	$< 10^{-3}$
T-AzHCy2	779	35	220	$< 10^{-3}$
wsT-AzHCy	729	37	199	$< 10^{-3}$
wsCy5.5	679	156	82	0.31
ICG	787	172	56	0.13 (lit. ^[49])

across broad spectral ranges, despite all being tested at the same optical density: an indication that they function as LAs, not SAs (Figure 3a). For an ideal and quantitative LA, the photoacoustic response spectrum should match the absorption spectrum: and indeed, they had perfect spectral overlay, which suits them as scaffolds for strong, linear, quantitative PA imaging over a range of wavelengths (Figure S3; a counterexample is provided by SA **ICG**, whose spectra differ strongly; contributing to its PA response being nonlinear and environment-dependent).^[50]

To quantify the PA signal generation efficacy (SGE) robustly, we determined the PA-to-OD fits across the full OD range 0.1–0.5, which were linear for all species (Figure S4; comparison to cyanine-type reference compounds **wsCy5.5** and **QC-1** in Figures S5 and S6). Pleasingly, **wsT-AzHCy** and **T-AzHCy2** were excellently strong PA emitters, with SGE >3 times that of **ICG**. **M-AzCy5** was also a very strong PA emitter; **E-AzCy5/7** had the lowest SGE, similar to **ICG** (Figure 3b). Noteworthy, these PA signal enhancements up to +220% (Figure 3b) far surpass the +10% expected for pure fluorescence quenching: supporting the hypothesis of multiple excitations per pulse, which is expected to be a *fully general* advantage of the merged switch approach. (As a corollary of this: although the quantum yield Φ_{nr} for non-radiative decay following a single excitation is the typical way of rationalising photoacoustic efficiency, we can state that the enhanced photoacoustic signal does *not* directly arise from an increase in Φ_{nr} but rather is a time-dependent effect since multiple excitations are possible in a row).

Azo-cyanines have high photoacoustic signal & photostability

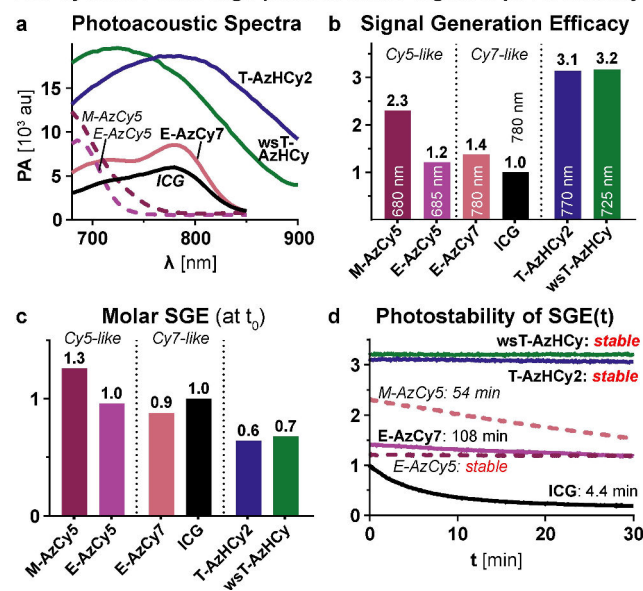


Figure 3. Optoacoustic properties in 1:1 PBS:EtOH. a) Photoacoustic spectra. b) PA signal generation efficacy (SGE) at constant OD, showing relative dye “loudness”. c) SGE adjusted to constant molarity (**ICG** set to 1). d) PA photostability determination. (a,d: measured at OD = 0.5 at λ_{max} [values given in panel b]; excitation in d performed at λ_{max}).

The photoacoustic performance enhancement for **AzHCy** over **ICG** is even greater when measured under more physiological conditions, i.e. with serum and without organic cosolvent: with SGE of **wsT-AzHCy** being >7 times that of **ICG** (Figure S7).

These *specific* azo-cyanines are band-broadened compared to symmetric cyanines; so if their SGEs are normalised by molarity, their lower extinction coefficients make their *starting* molar PA signal around 1–2 fold of that for the cyanines (Figure 3c, Figure S7). However, it is not the signal before imaging, but signal over time, that is the real challenge. Only PA agents that can be imaged *continually* and accumulate high photon count without bleaching can be useful molecular probes *in vivo*: otherwise, their signal is not quantitative, but bleaching unpredictably masks the true product concentration.^[7] Hoping that the ultrafast relaxation of the merged switches offers a *fully general* solution for stability enhancement, we now measured PA signal profiles over longer times, with typical settings for *in vivo* imaging (Figure 3d; i.e. laser pulses at 10 mJ/cm², 10 ns pulsewidth, 10 Hz repetition rate; *in vivo* image acquisition can take seconds to minutes per section at these settings). The results support our LA design principle excellently. For example, while the PA signal half-life ($t_{1/2}$) of **ICG** is only 4 min under these conditions, the **AzHCys** simply do not bleach (Figure 3d). Only by using the standard error of their PA signal over 30 minutes as a gross overestimate, could we even estimate a lowest possible bound for their bleaching half-life: with **wsT-AzHCy** as >140 hours, i.e. >1900 times more stable than **ICG**; isoelectronic **T-AzHCy2** was similar (Supporting Information 3.3). The mid-/end-attached **M-AzCy5/E-AzCy5/7** were also >10-fold more photostable than their cyanine congeners. The excellent **AzHCy** photostability is preserved with serum (discussion at Figure S7).

This direct access to **AzHCy** PA dyes that maintain a louder signal intensity for orders of magnitude longer than typical dyes, is the key value of our design: since it allows quantitative rather than only qualitative interpretation of signal intensity, throughout biologically relevant assay time-scales. Even focusing just on crude signal, the 3–7-fold higher SGE of **AzHCys** plus their *total* resistance to photobleaching let them surpass the higher extinction coefficients of photobleachable **ICG** to deliver far higher molar PA signal within a few minutes of imaging (i.e. a few frames, or less). We believe these photostability and SGE enhancements will be generally applicable in other dye/switch families too, enabling current dyes to withstand higher pulse energies in long-term imaging while also maintaining higher signal intensity: which is crucial for imaging low-turnover enzyme activity, by accumulating quantitative and stable signal over time.

Excited State Lifetimes and Evolution

The loud and photostable contrast agents we anticipated in these designs (Figure 1e) had been validated experimentally. Next, to see if the mechanisms we had anticipated were responsible for this performance, we tested if the excited

state lifetimes for the new PA contrast agents had been shortened far below the laser pulse length: needed to allow the several excitations per pulse that the SGE data suggested. First, we used time-resolved fluorescence spectroscopy^[51] on a high-sensitivity setup, to capture the weak **AzHCy** fluorescence (spectra in Figure S9). The time-resolved fluorescence data were used to extract S_1 decay time constants (Figure 4a). Matching our hopes, the most photostable compounds **T-AzHCy2** and **wsT-AzHCy** relaxed electronically with ultrafast time constants τ_{PL} of just approximately 10 ps: which is 10³-fold shorter than the PA laser pulse duration (10 ns). **M-AzCy5** and **E-AzCy5/7** had much longer time constants, ca. 540 and 370 ps respectively. This trend matches the involvement of the diazene in the π -s system (**T-AzHCy**: integral; **E/M-AzCy**: attached).

For multiple $S_0 \rightarrow S_1 \rightarrow S_0$ excitation/emission cycles per pulse, the depopulation of S_1 must be fast, as the luminescence data confirm, but the ground state must also be reached without other significant photoproducts.^[23,33] Therefore, we next used transient absorption (TA) spectroscopy to study the excited state evolution. Pleasingly, both **T-AzHCys** returned to the groundstate with ultrafast kinetics by a simple monoexponential $S_1 \rightarrow S_0$ path ($\tau_{TAS} \approx 4$ ps; the slower species **M-AzCy5** takes a biexponential path with overall half-time ca. 100 ps; Figure 4b–d, Figure S10). Although acquired in different solvents, the TA and luminescence lifetimes match. Thus, our “star” species show the set of properties we had targeted for loud, linear PA emitters (Table 2): ultrafast excited state decay to the groundstate allowing multiple $S_0 \rightarrow S_1 \rightarrow S_0$ cycles per pulse, associated to outstanding photostability and excellent SGE, just as desired for easy and reliable quantification in NIR photoacoustic imaging.

Time-resolved data: merged azo-cyanines have ultrafast $S_1 \rightarrow S_0$

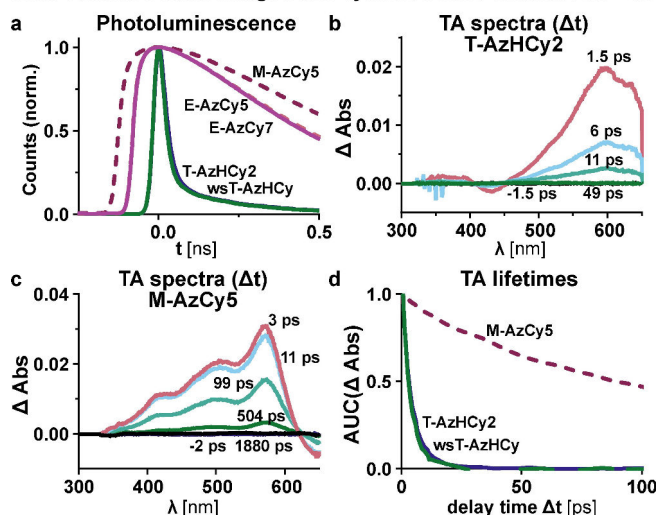


Figure 4. Time-resolved data. a) Fluorescence shows decay rates of singlet excited states. b–d) Transient absorption (TA) spectroscopy: **T-AzHCy2** relaxes fully to S_0 with $\tau_{TAS} \approx 4$ ps, but **M-AzCy5** has $\tau_{TAS} \approx 180$ ps. d) TA Δ Abs decays (fitted lifetimes given in Table 2).

Table 2: Summary of key optoacoustic parameters.

	Photoacoustic response			Elec. relaxation	
	λ_{SGE} [nm]	Signal (SGE)	stability $t_{1/2}$ [min]	τ_{PL}^a [ps]	τ_{TAS} [ps]
M-AzCy5	680	2.3	54	540 ^b	180 ^b
E-AzCy5	685	1.2	$\geq 4270^c$	386 ^b	not m.
E-AzCy7	785	1.4	108	363	not m.
T-AzHCy2	770	3.1	$\geq 1400^c$	13	4.0
wsT-AzHCy	740	3.2	$\geq 8400^c$	9	3.6
ICG (ref.)	780	1	4.4	10 ^{3;d}	not m.

[a] Major decay. [b] Complex fit. [c] Lower bounds. [d] Value from ref. [49]. "not m.": not measured.

In Vivo Imaging

The major goal of photoacoustics is to enable in vivo experiments. While the focus of this paper was to put forward a novel chemical concept that we believe can improve photoacoustic performance for many dye classes, we also wished to apply a specific example dye in vivo (choice: **wsT-AzHCy**), for a test of concept of whether ultrafast relaxation delivers real-world usability and utility in PA.

Our goals were to assess important conceptual features that should also be shared with other dyes developed along the azo-merged design: i) if the broad absorption of **wsT-AzHCy** still allows unmixing its signal from that of endogenous chromophores, during standard multispectral optoacoustic tomography (MSOT); ii) if the diazene-containing dye survives in vivo biochemistry/ADME long enough to allow practical use (we chose 120 min), since long survival is a necessary precondition to exploit its longterm photostability; iii) if such designs have promise for adaptation to molecular imaging agents, rather than being restricted to being *anatomical* stains. For example, if the dye is permanently bound to serum albumin, its signal will only map the bloodstream, making it an anatomical imaging agent; but if it non-uniformly distributes between organs, this offers hope that there are significant molecular interactions which may later be tuned by derivatisation e.g. for enzyme-responsive imaging.

In vivo MSOT imaging was thus performed before, and then 2 h after, intravenous (IV) injection of **wsT-AzHCy** into the lateral tail vein of healthy adult mice. Transverse image sections were chosen to visualize the organs where molecular dyes are typically accumulated: liver (Figure 5a,b), kidney and spleen (Figure 5c,d).

(i,ii) Spectral unmixing quantified strong specific **wsT-AzHCy** signal 2 h post injection, without significant background before injection. MSOT can therefore successfully separate the dye from endogenous background, and the azo-merged dye has a good survival time in vivo (Figure 5).

(iii) The **wsT-AzHCy** signal had a clear biodistribution to the gut, spleen, and liver, but exclusion from the kidneys (Figure 5b,d). This is a promising indication of molecular

MSOT imaging with ws-TAzHCy in healthy, live mice

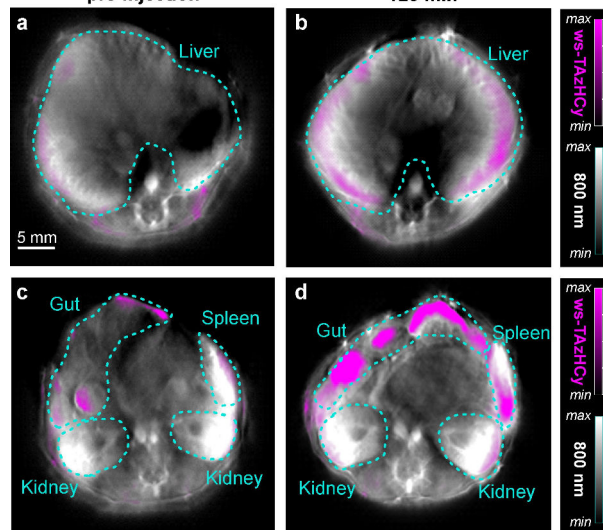


Figure 5. In vivo MSOT images. Transverse image sections of live, healthy mice, showing a,b) liver, c,d) kidney and spleen, each before and 120 min after IV injection of **wsT-AzHCy** (100 μ L, 0.5 mM) under the same image acquisition conditions. Imager: MSOT inVision 256-TF (iThera, Germany; 800 nm image is the anatomical imaging reference frame (essentially, blood content); **wsT-AzHCy** image is calculated by spectral deconvolution).^[52]

accessibility, that it may be possible to harness later for molecular imaging.

Taken together, this proof-of-concept experiment gave promising indications for the usability of photoacoustic contrast agents based on merged molecular switches in live animal imaging.

Conclusion

The great advances in biology have in large part been driven by chemical chromophores. Fluorophores, which easily enable quantitative imaging of live cell enzymatic activity, have for several decades been tuned e.g. for shallow in vivo imaging.^[53] The equipment and engineering necessary to instead harness the optoacoustic response of chromophores for deep in vivo imaging is now becoming available. Yet, to realise its promise for quantitative imaging in live animal as well as clinical settings, we must move beyond repurposing poorly adapted contrast agents such as fluorophores: we must rationally develop chemical design strategies for optoacoustic chromophores, tailored to the unique challenges and opportunities of PA.

Here, we have focused on the $S_1 \rightarrow S_0$ lifetime: one of the most powerful photophysical regulators of PA contrast agent performance, but which has been chemically almost ignored.

We showed that the rational integration of molecular switches into NIR-absorbing scaffolds can accelerate their $S_1 \rightarrow S_0$ transition by >100-fold. This gives a >1000-fold enhancement of PA signal photostability, while also convert-

ing even poorly quantifiable “saturable absorber” chromophores into “linear absorber” PA contrast agents that promise to be reliably and stably quantifiable at arbitrary illumination intensity, over arbitrarily long imaging time-courses. By permitting many $S_0 \rightarrow S_1 \rightarrow S_0$ cycles per pulse, **AzHCy** offer a simple organic chromophore method to multiply PA signal response: and even on current standard PA equipment, with relatively long pulse settings that are optimised around the weaknesses of current SAs, these ultrafast-relaxing **AzHCy** agents already provide 3–7 fold higher signal generation efficacy at the start of imaging. However, their linear response to excitation intensity offers an opportunity to harness shorter but more intense excitation pulses to deliver the same or higher PA signal intensity output, but with higher resolution and lower background, which no current NIR-active organic PA contrast agents can provide (since fast relaxation is needed to harness short pulses; Figure S12).

Conceptually, when we began this work, we did not locate an accessible analytical framework that would convincingly predict to colleagues how the multiple performance features that must *all* be balanced for high-performance PA, should all be improved to varying degrees by accelerating non-radiative $S_1 \rightarrow S_0$ decay: i.e. (1) photostability and (2) signal loudness in arbitrary settings, as we report here; but also, e.g., (3) signal loudness and (4) signal-to-background ratio and (5) excitation voxel resolution, each as a function of excitation pulse timing and intensity (Figure S12). During paper revisions, we were delighted that Brøndsted and Stains posted a preprint^[31] parametrising an Acoustic Loudness Factor ($ALF = k_{nr} \times \epsilon$) that, as we do, now *explicitly* prioritises non-radiative decay rates in which linear absorbers excel to guide PA dye optimisation (ALF corresponds to point 2, loudness in arbitrary settings, in our treatment). Since it is straightforward to determine ALF reliably even without PA equipment, we believe ALF will prove more useful than previous parametrisations that apply only to saturable absorbers and have oriented research into dead ends,^[31] even though ALF does not report other relevant aspects like photostability, ISC, and pulse-dependency effects.

Practically, since this rational merged-switch design hypothesis succeeded so directly, we predict that remastering molecular switches will become a powerful route to enhance the photophysically determined performance features of chromophores in a truly general sense. For example, the broadened NIR absorption of the nonfluorescent **AzHCys** (beyond 900 nm for **T-AzHCy2**, and easily tunable) makes them ideal candidate NIR fluorescence quenchers (another molecularly underrepresented class of imaging agent) e.g. for off \rightarrow ON, NIR, FRET probes. PA also faces other challenges for engineering the photophysics and biocompatibility of its chromophores,^[23] but we believe that they too can be solved in a modular way that can synergise with the benefits of ultrafast relaxation. Perhaps the most significant of these, is to introduce enzyme-responsive^[54,55] molecular PA imaging for the NIR/SWIR region.^[56,57] In this respect, Schnermann’s enzyme-activatable NIR cyanine template (CyBam)^[58] may offer an ideal model system to

synergise with the arylazo-cyanines developed here. We are convinced that the scope for other chromophore types, as well as other chemotypes of switches, or rotors and motors, will be broad enough to power much creative harmony: in optoacoustics and beyond.

Supporting Information

Synthesis, photophysics data, and NMR spectra (PDF). The authors have cited additional references within the Supporting Information.^[59–75]

Abbreviations

ADME	absorption, distribution, metabolism and excretion
ALF	acoustic loudness factor
FRET	fluorescence resonance energy transfer
IC	internal conversion
ISC	intersystem crossing
LA	linear absorber
MSOT	multispectral optoacoustic (or photoacoustic) tomography
NIR	near-infrared
PA	photoacoustic (or optoacoustic) signal generation or imaging
RSA	reverse-saturable absorber
SA	saturable absorber
SGE	signal generation efficiency
SWIR	short-wave infrared
VR	vibrational relaxation

Acknowledgements

This research was supported by funds from the Boehringer Ingelheim Stiftung (Exploration Grant to O.T.-S.) and the German Research Foundation (DFG: Emmy Noether grant number 400324123 to O.T.-S.; SFB 1032 number 201269156 project B09 to O.T.-S.; SFB TRR 152 number 239283807 project P24 to O.T.-S.; SPP 1926 number 426018126 project XVIII to O.T.-S.; CRC 1123 (Z1) to V.N.; SFB 1278 PolyTarget, project A03 to B.D.-I.). We thank Jan Felber (LMU) for assistance in PA imaging; Michaela Kaltenecker and Jan Philip Prohaska (LMU) for synthetic support and cordial discussions; Viktorija Glembockyte (LMU) for mechanistic discussions and advice on photophysical applications; and Eberhard Riedle (LMU) for motivation and discussions around using transient absorption spectroscopy for mechanistic studies. We acknowledge support from the Joachim Herz Foundation (Research Fellowship to M.M.). Open Access funding enabled and organized by Projekt DEAL.

Conflict of Interest

V.N. is a founder and equity owner of sThesis GmbH, iThera Medical GmbH, Spear UG and I3 Inc.

Data Availability Statement

The data that support the findings of this study are available in the Supporting Information, and related data are available from the corresponding author upon reasonable request.

Keywords: optoacoustic imaging · photoacoustic dyes · photoswitches · fluorescence · quenchers

- [1] V. Ntziachristos, *Nat. Methods* **2010**, *7*, 603–614.
- [2] V. Ntziachristos, D. Razansky, *Chem. Rev.* **2010**, *110*, 2783–2794.
- [3] A. Taruttis, V. Ntziachristos, *Nat. Photonics* **2015**, *9*, 219–227.
- [4] A. Karlas, M. A. Pleitez, J. Aguirre, V. Ntziachristos, *Nat. Rev. Endocrinol.* **2021**, *17*, 323–335.
- [5] C. Moore, J. V. Jokerst, *Theranostics* **2019**, *9*, 1550–1571.
- [6] S. L. Jacques, *Phys. Med. Biol.* **2013**, *58*, R37–R61.
- [7] V. Gujrati, A. Mishra, V. Ntziachristos, *Chem. Commun.* **2017**, *53*, 4653–4672.
- [8] A. P. Gorka, R. R. Nani, M. J. Schnermann, *Acc. Chem. Res.* **2018**, *51*, 3226–3235.
- [9] N. Beziere, N. Lozano, A. Nunes, J. Salichs, D. Queiros, K. Kostarelos, V. Ntziachristos, *Biomaterials* **2015**, *37*, 415–424.
- [10] J. Zhong, S. Yang, X. Zheng, T. Zhou, D. Xing, *Nanomedicine* **2013**, *8*, 903–919.
- [11] E. D. Cosco, J. R. Caram, O. T. Bruns, D. Franke, R. A. Day, E. P. Farr, M. G. Bawendi, E. M. Sletten, *Angew. Chem. Int. Ed.* **2017**, *56*, 13126–13129.
- [12] E. D. Cosco, A. L. Spearman, S. Ramakrishnan, J. G. P. Lingg, M. Saccomano, M. Pengshung, B. A. Arús, K. C. Y. Wong, S. Glasl, V. Ntziachristos, M. Warmer, R. R. McLaughlin, O. T. Bruns, E. M. Sletten, *Nat. Chem.* **2020**, *12*, 1123–1130.
- [13] V. G. Bandi, M. P. Luciano, M. Saccomano, N. L. Patel, T. S. Bischof, J. G. P. Lingg, P. T. Tsrunchev, M. N. Nix, B. Ruehle, C. Sanders, L. Riffle, C. M. Robinson, S. Difilippantonio, J. D. Kalen, U. Resch-Genger, J. Ivanic, O. T. Bruns, M. J. Schnermann, *Nat. Methods* **2022**, *19*, 353–358.
- [14] L. Yuan, W. Lin, Y. Yang, H. Chen, *J. Am. Chem. Soc.* **2012**, *134*, 1200–1211.
- [15] H. Li, H. Kim, F. Xu, J. Han, Q. Yao, J. Wang, K. Pu, X. Peng, J. Yoon, *Chem. Soc. Rev.* **2022**, *51*, 1795–1835.
- [16] M. Y. Lucero, J. Chan, *Nat. Chem.* **2021**, *13*, 1248–1256.
- [17] S. H. Gardner, C. J. Brady, C. Keeton, A. K. Yadav, S. C. Mallojjala, M. Y. Lucero, S. Su, Z. Yu, J. S. Hirschi, L. M. Mirica, J. Chan, *Angew. Chem. Int. Ed.* **2021**, *60*, 18860–18866.
- [18] S. Zhang, H. Chen, L. Wang, X. Qin, B.-P. Jiang, S.-C. Ji, X.-C. Shen, H. Liang, *Angew. Chem. Int. Ed.* **2021**, *61*, e202107076.
- [19] J. Weber, P. C. Beard, S. E. Bohndiek, *Nat. Methods* **2016**, *13*, 639–650.
- [20] X. Zhang, Y. Wu, L. Chen, J. Song, H. Yang, *Chem. Biomed. Imaging* **2023**, *1*, 99–109.
- [21] Z. Zhao, C. Chen, W. Wu, F. Wang, L. Du, X. Zhang, Y. Xiong, X. He, Y. Cai, R. T. K. Kwok, J. W. Y. Lam, X. Gao, P. Sun, D. L. Phillips, D. Ding, B. Z. Tang, *Nat. Commun.* **2019**, *10*, 768.
- [22] C. Xu, R. Ye, H. Shen, J. W. Y. Lam, Z. Zhao, B. Z. Tang, *Angew. Chem. Int. Ed.* **2022**, *61*, e202204604.
- [23] M. Hatamimoslehabadi, S. Bellinger, J. La, E. Ahmad, M. Frenette, C. Yelleswarapu, J. Rochford, *J. Phys. Chem. C* **2017**, *121*, 24168–24178.
- [24] C. S. L. Rathnamalala, N. W. Pino, B. S. Herring, M. Hooper, S. R. Gwaltney, J. Chan, C. N. Scott, *Org. Lett.* **2021**, *23*, 7640–7644.
- [25] N. Liu, V. Gujrati, J. Malekzadeh-Najafabadi, J. P. F. Werner, U. Klemm, L. Tang, Z. Chen, J. Prakash, Y. Huang, A. Stiel, G. Mettenleiter, M. Aichler, A. Blutke, A. Walch, K. Kleigrewe, D. Razansky, M. Sattler, V. Ntziachristos, *Photoacoustics* **2021**, *22*, 100263.
- [26] N. Liu, P. O'Connor, V. Gujrati, D. Gorpas, S. Glasl, A. Blutke, A. Walch, K. Kleigrewe, M. Sattler, O. Plettenburg, V. Ntziachristos, *Adv. Healthcare Mater.* **2021**, *10*, 2002115.
- [27] X. Zhou, Y. Fang, V. Wimalasiri, C. I. Stains, E. W. Miller, *Chem. Commun.* **2022**, *58*, 11941–11944.
- [28] T. Ikeno, K. Hanaoka, S. Iwaki, T. Myochin, Y. Murayama, H. Ohde, T. Komatsu, T. Ueno, T. Nagano, Y. Urano, *Anal. Chem.* **2019**, *91*, 9086–9092.
- [29] J. M. Merkes, T. Lammers, R. Kancherla, M. Rueping, F. Kiessling, S. Banala, *Adv. Opt. Mater.* **2020**, *8*, 1902115.
- [30] M. Laramie, M. Smith, F. Marmarchi, L. McNally, M. Henary, *Molecules* **2018**, *23*, 2766.
- [31] F. Brøndsted, H. Shield, J. Moore, X. Zhou, Y. Fang, C. Stains, *ChemRxiv* **2024**, DOI 10.26434/chemrxiv-2024-7cbk2.
- [32] J. Levi, S. R. Kothapalli, T.-J. Ma, K. Hartman, B. T. Khuri-Yakub, S. S. Gambhir, *J. Am. Chem. Soc.* **2010**, *132*, 11264–11269.
- [33] M. Frenette, M. Hatamimoslehabadi, S. Bellinger-Buckley, S. Laoui, J. La, S. Bag, S. Mallidi, T. Hasan, B. Bouma, C. Yelleswarapu, J. Rochford, *J. Am. Chem. Soc.* **2014**, *136*, 15853–15856.
- [34] R. E. Borg, M. Hatamimoslehabadi, S. Bellinger, J. La, F. Mithila, C. Yelleswarapu, J. Rochford, *Photochem. Photobiol.* **2019**, *95*, 280–292.
- [35] R. E. Borg, J. Rochford, *Photochem. Photobiol.* **2018**, *94*, 1175–1209.
- [36] S. S. Matikonda, D. A. Helmerich, M. Meub, G. Beliu, P. Kollmannsberger, A. Greer, M. Sauer, M. J. Schnermann, *ACS Cent. Sci.* **2021**, *7*, 1144–1155.
- [37] R. R. Nani, J. A. Kelley, J. Ivanic, M. J. Schnermann, *Chem. Sci.* **2015**, *6*, 6556–6563.
- [38] E. M. S. Stennett, M. A. Ciuba, M. Levitus, *Chem. Soc. Rev.* **2014**, *43*, 1057–1075.
- [39] H. M. D. Bandara, S. C. Burdette, *Chem. Soc. Rev.* **2012**, *41*, 1809–1825.
- [40] J. Garcia-Amorós, B. Maerz, M. Reig, A. Cuadrado, L. Blancafort, E. Samoylova, D. Velasco, *Chem. Eur. J.* **2019**, *25*, 7726–7732.
- [41] A. Chevalier, C. Massif, P.-Y. Renard, A. Romieu, *Chem. Eur. J.* **2013**, *19*, 1686–1699.
- [42] M. Dong, A. Babalhavaej, S. Samanta, A. A. Beharry, G. A. Woolley, *Acc. Chem. Res.* **2015**, *48*, 2662–2670.
- [43] S. Fuse, T. Oishi, K. Matsumura, Y. Hayashi, S. Kawauchi, H. Nakamura, *Org. Biomol. Chem.* **2019**, *18*, 93–101.
- [44] T. M. Swager, L. Delage-Laurin, *Synfacts* **2020**, *16*, 0152.
- [45] A. Treibs, R. Zimmer-Galler, *Justus Liebig's Ann. Chem.* **1959**, *627*, 166–181.
- [46] L. M. Tolbert, X. Zhao, *J. Am. Chem. Soc.* **1997**, *119*, 3253–3258.
- [47] S. Pascal, A. Haefele, C. Monnereau, A. Charaf-Eddin, D. Jacquemin, B. Le Guennic, C. Andraud, O. Maury, *J. Phys. Chem. A* **2014**, *118*, 4038–4047.
- [48] G. S. Hartley, *Nature* **1937**, *140*, 281–281.
- [49] M. Y. Berezin, S. Achilefu, *Chem. Rev.* **2010**, *110*, 2641–2684.
- [50] J. P. Fuenzalida Werner, Y. Huang, K. Mishra, R. Janowski, P. Vetschera, C. Heichler, A. Chmyrov, C. Neufert, D. Niessing,

- V. Ntziachristos, A. C. Stiel, *Anal. Chem.* **2020**, *92*, 10717–10724.
- [51] M. L. DiFrancesco, F. Lodola, E. Colombo, L. Maragliano, M. Bramini, G. M. Paternò, P. Baldelli, M. D. Serra, L. Lunelli, M. Marchioretto, G. Grasselli, S. Cimò, L. Colella, D. Fazzi, F. Ortica, V. Vurro, C. G. Eleftheriou, D. Shmal, J. F. Maya-Vetencourt, C. Bertarelli, G. Lanzani, F. Benfenati, *Nat. Nanotechnol.* **2020**, *15*, 296–306.
- [52] V. Gujrati, J. Prakash, J. Malekzadeh-Najafabadi, A. Stiel, U. Klemm, G. Mettenleiter, M. Aichler, A. Walch, V. Ntziachristos, *Nat. Commun.* **2019**, *10*, 1114.
- [53] J. B. Grimm, L. D. Lavis, *Nat. Methods* **2022**, *19*, 149–158.
- [54] H. Kobayashi, M. Ogawa, R. Alford, P. L. Choyke, Y. Urano, *Chem. Rev.* **2010**, *110*, 2620–2640.
- [55] F. Brøndsted, Y. Fang, L. Li, X. Zhou, S. Grant, C. I. Stains, *Chem. Eur. J.* **2024**, *30*, e202303038.
- [56] Z. Zhao, C. B. Swartzick, J. Chan, *Chem. Soc. Rev.* **2022**, DOI 10.1039/D0CS00771D.
- [57] Y.-F. Ou, T.-B. Ren, L. Yuan, X.-B. Zhang, *Chem. Biomed. Imaging* **2023**, *1*, 220–233.
- [58] S. M. Usama, F. Inagaki, H. Kobayashi, M. J. Schnermann, *J. Am. Chem. Soc.* **2021**, *143*, 5674–5679.
- [59] T. Ashida, T. Suzuki, TW201840738A, **2018**.
- [60] R. Tapia Hernandez, M. C. Lee, A. K. Yadav, J. Chan, *J. Am. Chem. Soc.* **2022**, *144*, 18101–18108.
- [61] K. Gutmiedl, C. T. Wirges, V. Ehmke, T. Carell, *Org. Lett.* **2009**, *11*, 2405–2408.
- [62] S. M. Pauff, S. C. Miller, *Org. Lett.* **2011**, *13*, 6196–6199.
- [63] A. Touthkine, WO2009152024A1, **2009**.
- [64] E. D. Cosco, I. Lim, E. M. Sletten, *ChemPhotoChem* **2021**, *5*, 727–734.
- [65] K. Rurack, M. Spieles, *Anal. Chem.* **2011**, *83*, 1232–1242.
- [66] D. Razansky, A. Buehler, V. Ntziachristos, *Nat. Protoc.* **2011**, *6*, 1121–1129.
- [67] L. Gao, Y. Kraus, A. Stegner, T. Wein, C. Heise, L. von Brunn, E. Fajardo-Ruiz, J. Thorn-Seshold, O. Thorn-Seshold, *Org. Biomol. Chem.* **2022**, *20*, 7787–7794.
- [68] S. Roberts, A. Strome, C. Choi, C. Andreou, S. Kossatz, C. Brand, T. Williams, M. Bradbury, M. F. Kircher, Y. K. Reshetnyak, J. Grimm, J. S. Lewis, T. Reiner, *Sci. Rep.* **2019**, *9*, 8550.
- [69] K. Cardinell, N. Gupta, B. D. Koivisto, J. C. Kumaradas, X. Zhou, H. Irving, P. Luciani, Y. H. Yücel, *Photoacoustics* **2021**, *21*, 100239.
- [70] R. Yin, F. Brøndsted, L. Li, J. L. McAfee, Y. Fang, J. S. Sykes, Y. He, S. Grant, J. He, C. I. Stains, *Chem. Eur. J.* **2024**, e202303331.
- [71] B. Du, C. Qu, K. Qian, Y. Ren, Y. Li, X. Cui, S. He, Y. Wu, T. Ko, R. Liu, X. Li, Y. Li, Z. Cheng, *Adv. Opt. Mater.* **2020**, *8*, 1901471.
- [72] M. Wranik, T. Weinert, C. Slavov, T. Masini, A. Furrer, N. Gaillard, D. Gioia, M. Ferrarotti, D. James, H. Glover, M. Carrillo, D. Kekilli, R. Stipp, P. Skopintsev, S. Brünle, T. Mühlethaler, J. Beale, D. Gashi, K. Nass, D. Ozerov, P. J. M. Johnson, C. Cirelli, C. Bacellar, M. Braun, M. Wang, F. Dworkowski, C. Milne, A. Cavalli, J. Wachtveitl, M. O. Steinmetz, J. Standfuss, *Nat. Commun.* **2023**, *14*, 903.
- [73] M. L. Landsman, G. Kwant, G. A. Mook, W. G. Zijlstra, *J. Appl. Physiol.* **1976**, *40*, 575–583.
- [74] T. Gokus, A. Hartschuh, H. Harutyunyan, M. Allegrini, F. Hennrich, M. Kappes, A. A. Green, M. C. Hersam, P. T. Araujo, A. Jorio, *Appl. Phys. Lett.* **2008**, *92*, 153116.
- [75] S. Liu, X. Zhou, H. Zhang, H. Ou, J. W. Y. Lam, Y. Liu, L. Shi, D. Ding, B. Z. Tang, *J. Am. Chem. Soc.* **2019**, *141*, 5359–5368.

Manuscript received: March 22, 2024

Accepted manuscript online: May 28, 2024

Version of record online: ■■, ■■

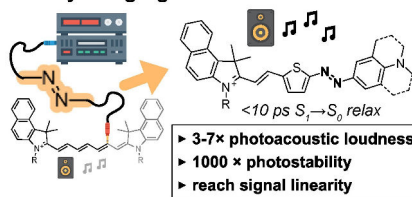
Research Article

Photoacoustics

M. Müller, N. Liu, V. Gujrati, A. Valavalkar, S. Hartmann, P. Anzenhofer, U. Klemm, A. Telek, B. Dietzek-Ivanšić, A. Hartschuh, V. Ntziachristos, O. Thorn-Seshold* e202405636

Merged Molecular Switches Excel as Photoacoustic Dyes: Azobenzene–Cyanines Are Loud and Photostable NIR Imaging Agents

Photoacoustic performance is amplified by merging molecular switches



The organic dyes used in photoacoustic imaging are often photobleachable and hard to quantify as they respond *non-linearly* to excitation intensity. However, a systematic method that uses molecular switches to shorten their nonradiative decay times to 4 ps converts them into reliably quantifiable *linear absorbers* that are up to > 1000-fold more photostable and several times better signal generators in photoacoustic imaging.

1.3.3 Publication Two: Molecular rotors as NIR & SWIR PA contrast agents

In the following work, we consolidate and extend the findings from **section 1.3.2**. The concept was based on using ultra-fast non-radiative $S_1 \rightarrow S_0$ relaxation to facilitate several excitation-relaxation cycles for one molecule within a laser pulse. Rather than using molecular switches again, we here translated the findings to molecular rotors as the ultrafast dissipator. Red light absorbing triphenylmethanes such as crystal violet or malachite green were already shown to be excellent PA emitters with low picosecond excited life-times. However, triphenylmethanes are not commonly used as dyes in imaging (the closest contender is coomassie blue, a ubiquitous chromogenic stain for proteins in wet lab work); and there are no NIR-absorbing triphenylmethanes: which is a key prerequisite for PA imaging.

Previously, we had taken a NIR absorbing fluorophore core and engineered it by merging it with an azobenzene switch to reach the desired PA properties. Here, I proposed to start with a rotor scaffold that already had nearly the desired spectral absorbance, then to simply adjust it by targeted red-shifting. Malachite Green has a λ_{\max} of 620 nm which is already close to the NIR. I envisioned that elongation of the π -system would result in the desired red-shift, so I integrated either one or two thiophenyl-bridging units (choosing thiophene to keep the rotor-like aryl residue properties, while hoping to find similar redshifting as in the π -extension designs of our previous work) (Preprint, Figure 1, here page 44).

Pleasingly, the newly generated triarylmethanes (TAMs) **TAM(I)** and **TAM(II)** showed the desired NIR absorption properties with λ_{\max} of ~ 770 nm for the single bridged **TAM(I)** and λ_{\max} of 920 nm for the double bridged **TAM(II)**, i.e. a shift of ~ 150 nm per thiophenyl bridging unit. ϵ was found to be solvent dependent with tendency for higher values in apolar solvents, or when serum proteins were present (e.g. adding FBS to an aqueous salt buffer) (Preprint, Figure 2, here page 45).

Next, our collaborators probed the TAM excited state dynamics via transient absorption spectroscopy (TAS) and found the NIR variants did keep the desired relaxation half-times in the low picosecond range. Together with the almost exclusively non-radiative decay pathway, this matched the desired photophysical design properties. Innovatively, our collaborators now also carried out TAS in live cells (a first for the method used), showing that the ultra-fast TAM relaxation is not diminished by the complex cellular environment (which often facilitates surface adsorption or aggregation and subsequently can cause drastic changes in chromophore properties), and confirming successful cellular uptake (Preprint, Figure 3, here page 46).

We showed that the *per absorbable photon* PA signal generation efficiency (SGE at same OD) of **TAM(I)** and **TAM(II)** is $5\times$ higher than for standard reference **ICG**, indicating a $5\times$ more efficient transformation of theoretically absorbable photon energy into PA signal under current standard commercial *in vivo* imager settings. Regarding a *per molecule* metric, although **TAMs** have $\sim 2.5\times$ lower ϵ than **ICG**, their molar SGE is nonetheless still $\sim 1.9\times$ higher under these settings, which highlights the rewards of harnessing optimized PA emissivity even if some ϵ is sacrificed. Moreover, the **TAM** signal stability under continuous pulsed laser irradiation is excellent, and we could not detect signal reduction in a mixture of organic solvent and buffer, a crucial requirement for reliable long-term imaging and in our opinion a pre-requisite that any PA probes must have, but which **ICG** does not (Preprint, Figure 4, here Page 47).

In conclusion, we now demonstrated with a second ultrafast-relaxing structural motif, molecular rotors, how to realise effective PA contrast agents which firmly leave fluorophore inspired designs for fluorescence imaging. These findings consolidate our design hypothesis that accelerating non-radiative decay rates universally results in *louder and more photostable* PA contrast agents that can expect to benefit from a variety of practical and applications advantages when applied *in vivo*, even without adjusting PA settings away from the current standards that are optimised towards essentially ICG-like emitters. On a chemical design level, in our previous paper we had back-engineered probably the most PA-popular fluorophore to fill what we identified as the most urgent PA imaging needs, whereas now with the **TAMs** we had started with unpopular molecular scaffolds that we had however hypothesised to already have the performance features that should be most crucial to effective PA imaging. Fine tuning of such a validated scaffold, with the modular and easy synthesis that TAMs afford, now offers promise towards **TAMs** or similar molecular rotors that can be ideal blueprints for high-performance PA agents as well as enzyme-responsive variants: for longitudinal, high sensitivity *in vivo* molecular imaging.

Molecular rotors are loud, highly photostable, NIR/SWIR-active molecular optoacoustic contrast agents

Markus Müller^{a,b*}, Abha Valavalkar^{c,d}, Vipul Gujrati^{e,f}, Jan P. Prohaska^a, Divyesh Shelar^{e,f}, Michaela Kaltenecker^b, Benjamin Dietzek-Ivanšić^{c,d}, Vasilis Ntziachristos^{e,f}, Oliver Thorn-Seshold^{a,b*}

[a] Faculty of Chemistry and Food Chemistry, Technical University of Dresden, Bergstrasse 66, Dresden 01069, Germany.

[b] Department of Pharmacy, LMU Munich, Butenandtstrasse 7, Munich 81377, Germany.

[c] Leibniz Institute of Photonic Technology Jena, Research Department Functional Interfaces, Albert-Einstein-Straße 9, Jena 07745 Germany.

[d] Institute of Physical Chemistry, University of Jena, Lessingstraße 4, Jena 07743, Germany.

[e] Institute of Biological and Medical Imaging, Helmholtz Zentrum München, Ingolstädter Landstraße 1, Neuherberg 85764, Germany.

[f] Chair of Biological Imaging at the Central Institute for Translational Cancer Research (TranslaTUM), School of Medicine and Health, Technical University of Munich, Ismaninger Str. 22, Munich 81675, Germany.

Correspondence to: oliver.thorn-seshold@tu-dresden.de; markus.mueller2@tu-dresden.de.

ABSTRACT: Optoacoustic or photoacoustic imaging (PA) combines optical excitation with acoustic readout, for non-invasive *in vivo* imaging at up to several centimetres' penetration depth, and down to micron resolution. Conceptually, many chromophore types can be used for simple anatomical PA, where signal generation is the only requirement: but few can perform the more complex task of molecular imaging of enzyme activity in practice, for which the many requirements include enzymatic signal switch-on. Here, we leverage molecular rotors to give a rational blueprint for high-performance small molecule PA contrast agents in the NIR/SWIR biotransparency window that offer straightforward adaptation for molecular imaging. According to our hypothesis, the ultrafast non-radiative $S_1 \rightarrow S_0$ kinetics (k_{nr}) of triphenylmethane rotors would be the chemical key to their PA signal (loudness) being strong, linear against imaging intensity, and outstandingly photostable. After we identified a route to shift typically the green/red absorbance of triarylmethanes into the NIR/SWIR, we showed that they are indeed >1000-fold more photostable as well as >5-fold louder than typical reference chromophores for PA. Pioneering femto-second transient absorption spectroscopy results in live cells, as a bridge from spectroscopy to biology, supported our conceptual approach of maximising k_{nr} to optimise the several key practical aspects of PA performance. Much like molecular switches, molecular rotors had only been used in a limited scope of imaging modalities to date. This approach now shows the potential of rotors for quantitative longitudinal PA; and more broadly, the results will guide the future of *mechanism-based design* in rationally improving dye performance in a range of basic and translational imaging methods.

Motivation: Nearly all organic small molecule contrast agents used in optoacoustic imaging (also called photoacoustic imaging, PA) are fluorophores or their structural derivatives. For many years, the usual design dogma has been that low fluorescence quantum yields (Φ_{FL}) in fluorophore derivatives suffice to make them strongly-performing as PA contrast agents, since low radiative decay rates mean that most light input is nonradiatively converted to thermal acoustic output.¹ Yet, this argument misses crucial logical steps, such that Φ_{FL} -based design misdirects focus away from key design tasks and opportunities for *effective* PA contrast agents. Here, we add experimental evidence from a new molecular structure class, that supports an emerging paradigm focused on the non-radiative relaxation rate k_{nr} as the key to several time-dependent effects in PA: not just *initial* PA signal strength,²⁻⁶ but also for the less-discussed yet even more critical aspects of long-term signal photostability, linearity of signal response, and practical PA hardware choice.⁴

Photoacoustic imaging is a non-invasive technique that uses laser pulses to excite chromophores (input), then images the ultrasound-frequency thermoelastic pressure waves (readout) generated when they relax and locally

dissipate the absorbed energy as heat (**Fig 1a**).⁷ The ultrasound is detected outside the sample, to reconstruct images of the tissue distribution of photon absorption by the chromophore.⁸ Ultrasound has excellent tissue penetration, so it is usually the tissue scatter/absorbance of excitation light that limits resolution and imaging depth. Near-infrared (NIR, 700-1000 nm) or short-wave infrared (SWIR, 1000-2000 nm) light are best suited for deep tissue penetration (NIR: least absorption, SWIR: least scatter).⁹⁻¹¹ Typically, the optical/acoustic combination of PA promises tissue imaging resolutions down to 150 μm and imaging depths of several centimetres: well-suited towards *in vivo* use.¹² Spectral unmixing by MSOT (multispectral optoacoustic tomography) also allows imaging multiple chromophores in distinct channels; notably, this provides a way to selectively trace exogenous contrast agents, e.g. for targeted molecular imaging by PA.¹⁰

PA dye quality: As PA advances into clinical translation,¹³ unlocking the functional imaging of enzymes or biomarkers is being hotly pursued.¹⁴⁻¹⁶ Organic small molecules are ideal for molecular imaging, as fluorescent probes have shown;^{17,18} and organic NIR fluorophores were widely repurposed for PA.^{1,19-21} Among these, low- Φ_{FL} NIR cyanines

such as indocyanine green (**ICG**) were often used for their strong, sharp absorption;^{1,19,21-24} the ease of derivatising NIR hemicyanines to create enzyme-activatable probes²⁵⁻²⁷ or reach low Φ_{FL} ,^{28,29} has also driven their use. Yet, there are still no widely-accepted guidelines to rationally design PA dyes for high performance in practice. Briefly, early papers e.g. by Rochford suggested excited state relaxation half-times (τ) can affect PA signal strength if the laser fluence is high enough to allow each dye molecule to absorb and relax multiple times during a laser pulse (thus, with $\tau \ll$ laser pulse width of typically ~ 10 ns, the full potential of the excitation pulse can be harnessed): but designs to enforce low

τ were not given.³⁰ Our recent work showed that fast non-radiative relaxation rates k_{nr} (i.e. low τ) increase *initial* PA signal intensity even under standard *in vivo* imaging conditions, but added that fast k_{nr} also ensures practical benefits of *long-term* signal photostability (favouring longitudinal MSOT *in vivo*), and linear response of signal to excitation intensity (towards quantitative imaging *in vivo*); a rational design giving $\tau \sim 4 - 10$ ps by building in azobenzene molecular switches was shown.⁴ Brøndsted and Stains also centred attention on k_{nr} as a key factor, by presenting the "acoustic loudness factor" ALF ($= k_{nr} \times \epsilon$) as a metric to guide the optimisation of dyes for PA signal intensity.⁵

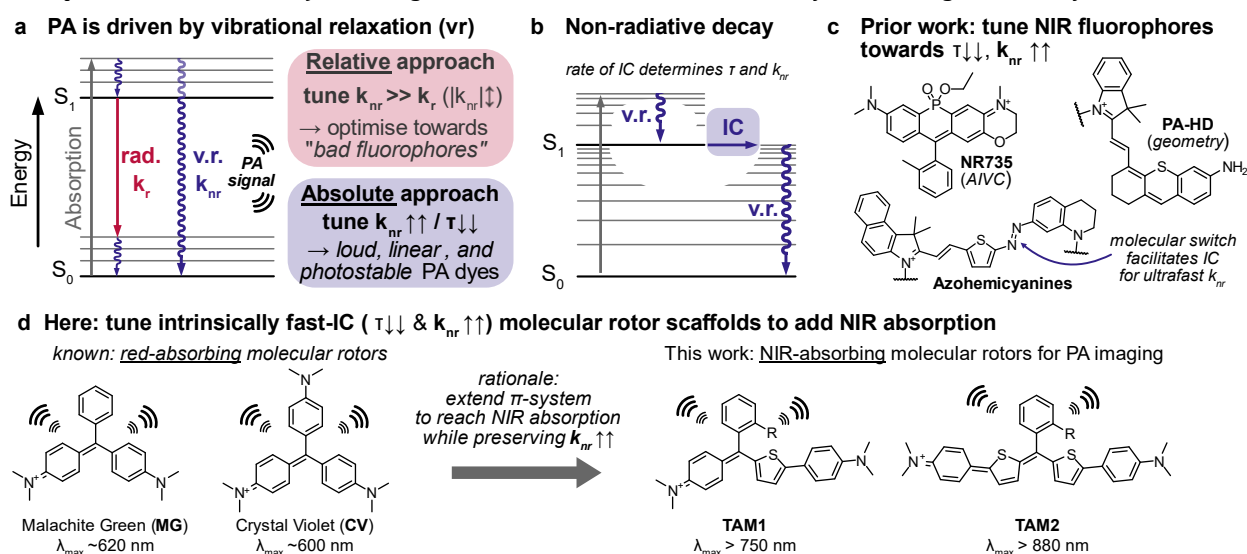


Figure 1. Contrast agents for PA imaging. **a**) The relative rates of radiative (*rad.*, k_r) vs non-radiative (vibrational relaxation *vr*, k_{nr}) decay determine Φ_{FL} . Most prior PA work aimed at "bad fluorophores" (low Φ_{FL}), yet this covers a wide range of k_{nr} values, so may not rationally optimise PA signal. The absolute value of k_{nr} (or, the overall excited state half-time τ), is a direct metric to guide PA optimisation that can also be quantified more robustly than Φ_{FL} . **b**) Non-radiative decay consists of fast *vr*, then a rate-limiting internal conversion (IC) from $S_1 \rightarrow S_0$, before another fast *vr*. **c**) Prior PA contrast agents that aimed to optimise IC and k_{nr} (AIVC = asymmetry induced vibronic coupling). **d**) Current design idea for shifting molecular rotor absorbance to the NIR, to then harness their fast IC for effective PA contrast agents.

Design Priorities: Since internal conversion (IC) is the rate-limiting step in non-radiative decay (**Fig 1b**), designs for fast IC may be key to rationally improving PA dyes. Recent designs applied asymmetry induced vibronic coupling (**NR735**),⁵ excited state geometry changes (**PA-HD**),^{31,32} or conical intersections of molecular switches (**azohemicyanines**),⁴ onto known NIR fluorophores (**Fig 1c**; see also **Supporting Note 1**). Yet, even these few PA dyes designed for rational k_{nr} minimisation *were still built from established NIR fluorophores*, by later introducing motifs to suppress Φ_{FL} . This seems to be the wrong priority order for optimising PA signal! Here, we wished to break from the usual NIR-fluorophore-based design space: instead jumping to a new chemical space of scaffolds that lock in the picosecond k_{nr} photophysics which we hypothesise as key for PA, and leave NIR/SWIR absorption for later steps of design tuning.

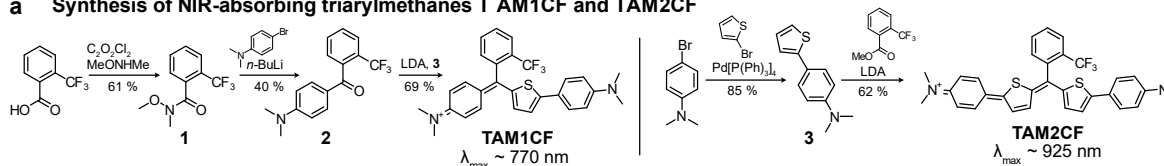
Rotor PA dyes: We selected triarylmethanes, such as Malachite Green (**MG**) or Crystal Violet (**CV**), as a scaffold lead class (**Fig 1d**). As molecular rotors, their non-radiative

decay can be ultrafast ($\tau = 3$ ps for **MG**, 10 ps for **CV**),³³ and though these rates are viscosity dependent (τ can reach 50 ps)³⁴ they still set a starting point for k_{nr} that is 20-300 faster than traditional fluorophores (matching this ultrafast rate, when **CV** was screened in a panel of commercially available dyes,³ it was found to be a linear and strong PA emitter: for detail see ref⁴). Triarylmethanes (TAMs) have a long history as dyes, and are frequently used as visible colorants in art, food coloring, and biology (non-selective Coomassie protein stain); but our literature search could not identify any TAMs with λ_{max} in the biotransparency window >750 nm, in biologically-relevant media. Yet, as TAM absorption maxima are already ~ 610 nm, incremental tuning to the NIR/SWIR seemed plausible. We began tuning by π -extending the donor/acceptor-system with thiophene bridges,^{35,36} which are still rotatable aryl residues,^{37,38} to design **TAM1H** and **TAM2H** (**Fig 1d**, R=H). The π -extension shifts their λ_{max} to 750 nm (**TAM1H**, one thiophene) or 880 nm (**TAM2H**, two thiophenes), i.e. well into the NIR. However, the NIR-

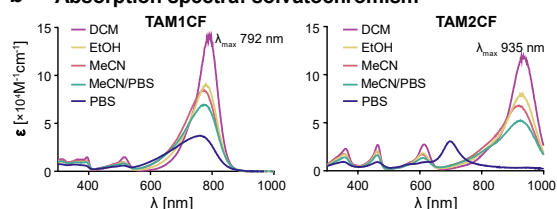
absorbing **TAM1/2H** open forms were prone to nucleophilic addition at the central methine carbon, giving UV-absorbing π -interrupted forms (even hydroxide adds;

Supporting Note 2 Fig S1-2): so we aimed to delete this lability before proceeding.

a Synthesis of NIR-absorbing triarylmethanes **TAM1CF and **TAM2CF****



b Absorption spectra: solvatochromism



c Absorption spectra: biologically mimicking buffer

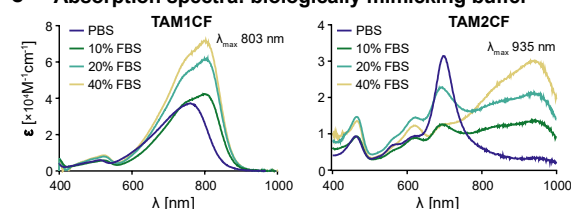


Figure 2. a) Synthesis of NIR-absorbing **TAM1/2CF**. **b-c)** Absorption spectra of **TAM1/2CF** shift with solvent polarity and with serum proteins.

Rotor PA Dyes for Biological Media: A short, modular TAM synthesis with good to moderate yields over only three linear steps (**Fig 2a**) helped to scan substituent effects at the pendant phenyl ring. We settled on $R=CF_3$ as a moderately bulky *ortho*-substituent, i.e. **TAM1CF** and **TAM2CF**. They are exclusively in the NIR-absorbing open form in aqueous buffers in the pH range 3–11, and resist biological nucleophiles such as GSH (10 mM, 300 eq; **Fig S1-S2**). They are solvatochromic, with strongest extinction coefficients and greatest bathochromic shifts in less polar media. In those settings, **TAM1CF** reached up to $\epsilon=140,000 \text{ M}^{-1}\text{cm}^{-1}$ at $\lambda_{\text{max}} = 792 \text{ nm}$; and **TAM2CF** up to $\epsilon=120,000 \text{ M}^{-1}\text{cm}^{-1}$ at $\lambda_{\text{max}} = 935 \text{ nm}$ with significant absorption into the SWIR: positioning these scaffold types well for PA (**Fig 2bc**, **Table 1**). Hydrophobic binding components typical of biological systems (blood proteins from foetal bovine serum (FBS), heterogeneous mixtures from malt, etc) beneficially shifted their aqueous absorption spectra towards those seen in less polar solvents (**Fig S3**). NIR fluorophores are often poorly water soluble, and prone to aggregate even at low concentrations unless solubilising groups are added. Though **TAM1/2CF** have no particular solubilising features, **TAM1CF** was perfectly soluble up to 400 μM in PBS (highest tested concentration, since far above the $\sim 5 \mu\text{M}$ useful for PA), giving confidence in its practical applicability (**Fig S4**).

Table 1: Environment-dependent absorption of **TAM1/2CF**.

	TAM1CF		TAM2CF	
	λ_{max} [nm]	$\epsilon [\times 10^3 \text{ M}^{-1}\text{cm}^{-1}]$	λ_{max} [nm]	$\epsilon [\times 10^3 \text{ M}^{-1}\text{cm}^{-1}]$
PBS	761	37	698 ^c	31 ^c
PBS/MeCN ^a	775	69	926	52
MeCN	773	85	921	68
EtOH	780	91	924	79
CH_2Cl_2	792	140	935	120
PBS + FBS ^b	803	72	935	29

^a Volumetric ratio 1:1; ^b values taken from dataset containing 40% FBS; ^c aggregation in pure PBS causes chromophore collapse.

Mechanistics: We focused on **TAM1CF** to study the excited state relaxation pathways and rates of the π -extended TAM in biologically-appropriate aqueous solutions. In brief, **TAM1CF** has $\Phi_{\text{FL}} < 0.01$ in water \pm FBS (**Table S1**), so non-radiative relaxation dominates even if hydrophobic binding proteins are available. Transient absorption spectroscopy (TAS) showed an excited state species (absorption peak $\sim 530 \text{ nm}$) whose nature is unchanged by the presence of human serum albumin (HSA; no spectral change; **Fig 3ac**). In water, **TAM1CF** had an ultrafast $\tau = 5 \text{ ps}$; this slowed to $\sim 60 \text{ ps}$ with HSA, but that is still >100 -fold faster than PA pulse durations (**Fig 3bd**). **TAM2CF** had similar relaxation speed (e.g. $\tau \sim 5 \text{ ps}$ in water, **Fig S5**).

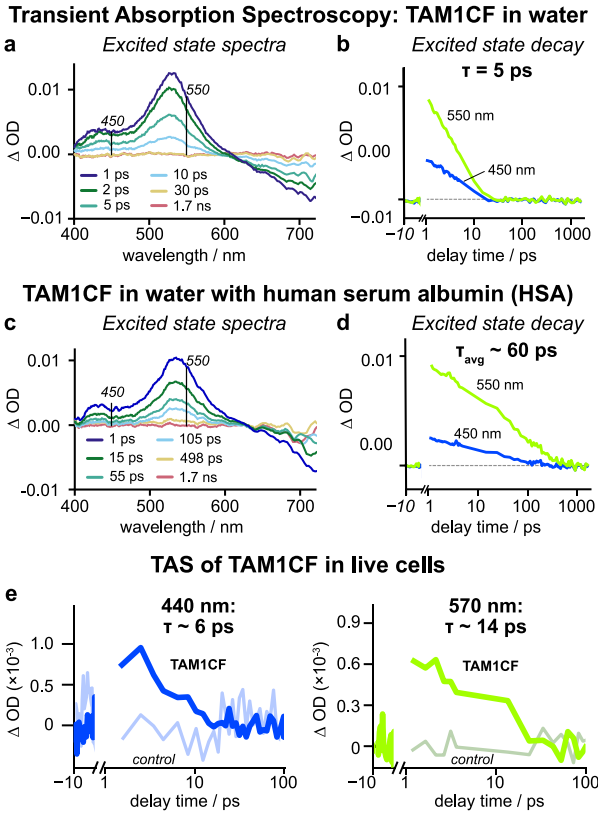


Figure 3. Excited state dynamics of **TAM1CF** in deionised water (**a,b**), deionised water with 100 μM HSA (**c,d**), and in human MCF7 cells (**e**). (**a,c**) Excited state absorption spectra and (**b,d,e**) excited state decay kinetics are coherent with a single excited state species that decays to the ground state on a timescale of picoseconds (for discussion of the decay slowing with HSA, see Supporting Information; all spectra and decay kinetics are corrected to offset pump scatter; "controls" in panel **e** are data for cells with 0 μM **TAM1CF**).

To predict TAM behaviour in complex biological environments with a better model than homogeneous aqueous solutions, we used *in cellulo* TAS³⁹⁻⁴¹ to study relaxation in human cells. In cells, the decay of the excited state absorption (570 nm and 440 nm) occurs on a ~ 10 ps cellular decay timescale (**Fig 3e**). 2D cell culture monolayer data is inherently more noisy than 3D volume data from solution experiments, but the match of these proof of concept rates to those in solution can suggest that **TAM1CF** is overall free (not aggregated/bound) in cells.

Testing PA performance: We next tested the photoacoustic properties of **TAM1/2CF**. We compared their performance to **ICG**, which has high ϵ giving it strong initial molar PA signal strength, and remains commonly-used^{1,19} despite not being ideal for PA^{4,42} (the field also lacks any other agreed comparators or referencing methods). We ran all experiments both in 1:1 MeCN:PBS as a spectroscopically clean system, and in PBS +20% FBS as a more biologically-mimicking system. Photoacoustic signal generation efficacies from different molecules can be compared on a *per photon absorbed* basis, i.e. PA signal intensity at same

absorbance (SGE), to reflect mechanistically on how efficiently different chemotypes convert absorbed energy to PA signal output. They can also be compared on a *per molecule* basis, i.e. signal at same concentration (molar SGE), which also depends on the dye ϵ . Except for linear emitter PA dyes, such as **TAM1/2**, both SGE and molar SGE will depend heavily on the excitation pulse intensity and length: therefore, we determined PA properties with standard settings for small animal imaging on a commercial MSOT device.

PA response: **TAM1/2CF**'s photoacoustic response correlate well to their absorption spectra (**Fig 4c**, **Fig S7**), allowing a mechanism-based interpretation of their PA properties⁴ (and notably, **TAM2**'s response even extends appreciably into the SWIR, which has been difficult for PA dyes to access). The remarkable feature is the TAMs' initial signal response strength, being $\sim 3\text{-}5\times$ the SGE of **ICG** (**Fig 4a**, **Fig S6**). **ICG** already has a low fluorescence quantum yield of ca. 0.05, i.e. 95% of its absorbed energy should be converted to heat. If PA agent performance were best understood from Φ_{FL} , TAMs would have $1.05\times$ the SGE of **ICG**, not $5\times$. We instead interpret this enhancement as a consequence of their ultrafast decay, enabling more excitations per pulse than fluorophore-derived systems, by our model of absolute k_{nr} driving PA performance.⁴ This is coherent with the TAM's more moderate performance in FBS-containing media, as it slows their relaxation (**Fig 4a**; though note that differences of background complicate direct comparisons). The molar SGEs (signal per molecule) are offset by the higher ϵ value for **ICG** (**Fig 4b**), though the TAMs remain competitive.

PA stability: There are additional requirements beyond SGE for *in vivo* PA dyes. The most important may be photostability: for repeated imaging, especially needed for MSOT, dyes must dissipate high cumulative energy without bleaching (full discussion in **Supporting Note 3**): and ultrafast relaxation to S_0 should prevent undesired photochemical reactions, whether in S_1 or after intersystem crossing (e.g. O_2 sensitisation).^{43,44} Exposing **TAM1/2CF** to continuous MSOT laser pulsing gave no detectable signal decrease in MeCN/PBS over 30 minutes (i.e. $t_{1/2} > 20$ h), whereas **ICG** photobleaches with $t_{1/2} = 4$ min under comparable conditions.⁴ TAM photostability was reduced with FBS (**TAM1CF**: $t_{1/2} = 6$ min, **TAM2CF**: $t_{1/2} > 2$ h), again matching the trends for k_{nr} ; but overall, the signal strength and stability particularly of the NIR/SWIR **TAM2CF** are remarkable.

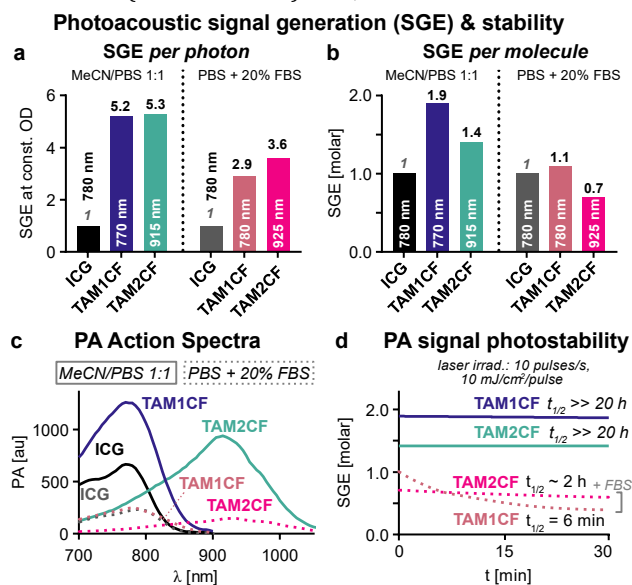


Figure 4. Photoacoustics. **a,b)** PA signal generation efficiency (SGE) as per absorbable photon, or per molecule, metrics relative to ICG (SGE set to 1). **c)** PA spectral response. **d)** PA signal photostability. (**a-d**: 5 μ M dyes; pulses 10 mJ/cm², 10 ns, 10 Hz).

Summary: Exploring novel scaffolds to maximise non-radiative decay rates k_{nr} seems promising as a route towards loud, photostable, linear-response PA contrast agents both on a theoretical level, and in practice with molecular rotors. We presented the first NIR/SWIR-absorbing TAMs, designed to harness their ultrafast relaxation for strong and photostable PA signal generation in the biotransparency window: in which they succeed remarkably. By providing TAMs as an unrelated second chemotype designed on the same k_{nr} -based logic as azohemicyanines,⁴ this work strengthens the case for understanding practical PA performance (not just initial SGE, but also photostability) in terms of k_{nr} ; and demonstrates a new molecular blueprint for reaching these ultrafast k_{nr} values with NIR absorbers.

Outlook for TAMs in PA: TAMs are an attractive molecular starting point for further PA dye development in many ways, including some in which azohemicyanines were stalled⁴. (1) TAM synthesis is easy and modular (**Fig 2a**), allowing straightforward chemical tuning by varying each aryl group independently. (2) Imaging in the SWIR region was a breakthrough for deep tissue fluorescence imaging, because of lower scattering;^{11,45} the structure and synthesis of SWIR TAMs e.g. **TAM2CF** are however vastly simple. We expect that further rational red-shifting of TAMs will easily reach PA agents with maxima > 1000 nm. This threshold is important: the maximal clinically permissible laser power exposure at >1000 nm is greater than in the NIR; and since TAMs' ultrafast k_{nr} makes them linear absorbers, they can convert higher laser power directly into higher PA signal.^{3,30} (3) TAMs avoid the metabolic liability of using azobenzene molecular switches for fast-relaxing dyes (the electrophilic, reducible, N=N bond), so they might prove still better

performant *in vivo*. (4) A major aim of MSOT *in vivo* is to monitor biological function with probes that respond to enzyme activity or biomarker dynamics, e.g. by undergoing a strong bathochromic absorption jump upon an enzymatic reaction. The TAM motif offers a dramatic spectral jump of +550 nm upon central leaving group expulsion (**Fig S1**). This can surely be addressed by techniques known from e.g. lactone-opening-based xanthene probes, to deliver enzyme-triggered PA probes with outstanding sensitivity (turn-on from zero background), as well as ratiometric PA probes. (5) The higher ϵ of TAMs in apolar environments suggests that TAM structural tuning has room to also increase ϵ in polar solvents, and thus increase the SGE.

Finally, we note that most PA agent designs today are based on choosing high- ϵ NIR-absorbing fluorophores then dialling back their fluorescence by rotor substituents or vibronic motifs.^{5,29,46,47} Given the central importance of k_{nr} to PA performance, we suggest that this order should be inverted: only tuning properties such as ϵ and λ_{max} after first choosing a scaffold that intrinsically delivers this key need of ultrafast non-radiative decay.

Supporting Information

Supporting Notes 1-3, synthesis, photophysics, PA evaluation, and NMR spectra (PDF)

Acknowledgements

This research was supported by funds from the Boehringer Ingelheim Stiftung (Exploration Grant *High-Resolution Enzyme Activity Imaging* to O.T.-S.) and the German Research Foundation (DFG: Emmy Noether grant number 400324123 to O.T.-S.; SFB 1032 number 201269156 project B09 to O.T.-S.; SFB TRR 152 number 239283807 project P24 to O.T.-S.; SPP 1926 number 426018126 project XVIII to O.T.-S.; CRC 1123 (Z1) to V.N.; SFB 1278 PolyTarget project A03 to B.D.-I.). We thank Viktorija Glembockyte and Achim Hartschuh (LMU) for engaging mechanistic discussions and advice on photophysical applications. We acknowledge support from the Joachim Herz Foundation (Research Fellowship to M.M.).

Author contributions

M.M. designed targets; designed and performed synthesis; performed, assisted, and coordinated photocharacterisation; and assisted PA experiments. J.P.P. and M.K. performed synthesis and photocharacterisation under the supervision of M.M.. A.V. performed transient absorption spectroscopy and assisted in drafting the manuscript, as supervised by B.D.-I.. V.G. and D.S. performed PA experiments, as supervised by V.N.. O.T.-S. designed the concept and supervised all other experiments. M.M. and O.T.-S. coordinated data assembly and wrote the manuscript.

Conflict of Interest

V.N. is a founder and equity owner of sThesis GmbH, iThera Medical GmbH, Spear UG and I3 Inc. All other authors declare no potential conflicts of interest.

REFERENCES

- Weber, J., Beard, P. C. & Bohndiek, S. E. Contrast agents for molecular photoacoustic imaging. *Nat. Methods* **13**, 639–650 (2016).
- Frenette, M. *et al.* Shining Light on the Dark Side of Imaging: Excited State Absorption Enhancement of a Bis-styryl BODIPY Photoacoustic Contrast Agent. *J. Am. Chem. Soc.* **136**, 15853–15856 (2014).
- Hatamimoslehadi, M. *et al.* Correlation of Photophysical Properties with the Photoacoustic Emission for a Selection of Established Chromophores. *J. Phys. Chem. C* **121**, 24168–24178 (2017).
- Müller, M. *et al.* Merged Molecular Switches Excel as Photoacoustic Dyes: Azobenzene–Cyanines Are Loud and Photostable NIR Imaging Agents. *Angew Chem Int Ed* e202405636 (2024) doi:10.1002/anie.202405636.
- Brøndsted, F. *et al.* Acoustic Loudness Factor: An Experimental Parameter for Benchmarking Small Molecule Photoacoustic Probes. (2024) doi:10.26434/chemrxiv-2024-7cbk2.
- Zhao, Z. *et al.* Highly efficient photothermal nanoagent achieved by harvesting energy via excited-state intramolecular motion within nanoparticles. *Nat Commun* **10**, 768 (2019).
- Wang, L. V. & Hu, S. Photoacoustic Tomography: In Vivo Imaging from Organelles to Organs. *Science* **335**, 1458–1462 (2012).
- Wang, L. V. & Yao, J. A practical guide to photoacoustic tomography in the life sciences. *Nat Methods* **13**, 627–638 (2016).
- Smith, A. M., Mancini, M. C. & Nie, S. Second window for in vivo imaging. *Nat. Nanotechnol.* **4**, 710–711 (2009).
- Ntziachristos, V. & Razansky, D. Molecular Imaging by Means of Multispectral Photoacoustic Tomography (MSOT). *Chem. Rev.* **110**, 2783–2794 (2010).
- Wong, K. C. Y. & Sletten, E. M. Extending optical chemical tools and technologies to mice by shifting to the shortwave infrared region. *Curr. Opin. Chem. Bio.* **68**, 102131 (2022).
- Ntziachristos, V. Going deeper than microscopy: the optical imaging frontier in biology. *Nat. Methods* **7**, 603–614 (2010).
- Assi, H. *et al.* A review of a strategic roadmapping exercise to advance clinical translation of photoacoustic imaging: From current barriers to future adoption. *Photoacoustics* **32**, 100539 (2023).
- Taruttis, A. & Ntziachristos, V. Advances in real-time multispectral photoacoustic imaging and its applications. *Nat. Photon* **9**, 219–227 (2015).
- Zhao, Z., Swartzchick, C. B. & Chan, J. Targeted contrast agents and activatable probes for photoacoustic imaging of cancer. *Chem. Soc. Rev.* (2022) doi:10.1039/D0CS00771D.
- Karlas, A., Pleitez, M. A., Aguirre, J. & Ntziachristos, V. Photoacoustic imaging in endocrinology and metabolism. *Nat. Rev. Endocrinol.* **17**, 323–335 (2021).
- Kobayashi, H., Ogawa, M., Alford, R., Choyke, P. L. & Urano, Y. New Strategies for Fluorescent Probe Design in Medical Diagnostic Imaging. *Chem. Rev.* **110**, 2620–2640 (2010).
- Grimm, J. B. & Lavis, L. D. Caveat fluorophore: an insiders' guide to small-molecule fluorescent labels. *Nat Methods* **19**, 149–158 (2022).
- Gujrati, V., Mishra, A. & Ntziachristos, V. Molecular imaging probes for multi-spectral photoacoustic tomography. *Chem. Commun.* **53**, 4653–4672 (2017).
- Knox, H. J. & Chan, J. Acoustogenic Probes: A New Frontier in Photoacoustic Imaging. *Acc. Chem. Res.* **51**, 2897–2905 (2018).
- Wu, Y., Zeng, F., Zhao, Y. & Wu, S. Emerging contrast agents for multispectral photoacoustic imaging and their biomedical applications. *Chem. Soc. Rev.* **50**, 7924–7940 (2021).
- Lozano, N., Al-Ahmady, Z. S., Beziere, N. S., Ntziachristos, V. & Kostarelos, K. Monoclonal antibody-targeted PEGylated liposome-ICG encapsulating doxorubicin as a potential theranostic agent. *International Journal of Pharmaceutics* **482**, 2–10 (2015).
- Moore, C. *et al.* Activatable Carbocyanine Dimers for Photoacoustic and Fluorescent Detection of Protease Activity. *ACS Sens.* **6**, 2356–2365 (2021).
- St. Lorenz, A., Buabeng, E. R., Taratula, O., Taratula, O. & Henary, M. Near-Infrared Heptamethine Cyanine Dyes for Nanoparticle-Based Photoacoustic Imaging and Photothermal Therapy. *J. Med. Chem.* **64**, 8798–8805 (2021).
- Lucero, M. Y. & Chan, J. Photoacoustic imaging of elevated glutathione in models of lung cancer for companion diagnostic applications. *Nat. Chem.* **13**, 1248–1256 (2021).
- Wu, Y. *et al.* Activatable probes for diagnosing and positioning liver injury and metastatic tumors by multispectral photoacoustic tomography. *Nat. Commun.* **9**, 3983 (2018).
- Zhen, X. *et al.* Macrotheranostic Probe with Disease-Activated Near-Infrared Fluorescence, Photoacoustic, and Photothermal Signals for Imaging-Guided Therapy. *Angew. Chem. Int. Ed.* **57**, 7804–7808 (2018).
- Merkles, J. M. *et al.* Photoacoustic Imaging Probes Based on Tetrapyrroles and Related Compounds. *International Journal of Molecular Sciences* **21**, 3082 (2020).
- Ikeno, T. *et al.* Design and Synthesis of an Activatable Photoacoustic Probe for Hypochlorous Acid. *Anal. Chem.* **91**, 9086–9092 (2019).
- Borg, R. E. & Rochford, J. Molecular Photoacoustic Contrast Agents: Design Principles & Applications. *Photochem. Photobiol.* **94**, 1175–1209 (2018).
- Gardner, S. H. *et al.* A General Approach to Convert Hemicyanine Dyes into Highly Optimized Photoacoustic Scaffolds for Analyte Sensing**. *Angew. Chem. Int. Ed.* **60**, 18860–18866 (2021).
- Zhang, S. *et al.* A General Approach to Design Dual Ratiometric Fluorescent and Photoacoustic Probe for Quantitatively Visualizing Tumor Hypoxia Levels in Vivo. *Angew. Chem. Int. Ed.* **61**, e202107076 (2021).
- Sundström, V., Gillbro, T. & Bergström, H. Picosecond kinetics of radiationless relaxations of triphenyl methane dyes. Evidence for a rapid excited-state equilibrium between states of differing geometry. *Chemical Physics* **73**, 439–458 (1982).
- Doust, T. Picosecond fluorescence decay kinetics of crystal violet in low-viscosity solvents. *Chemical Physics Letters* **96**, 522–525 (1983).
- Wu, W. *et al.* 2X-Rhodamine: A Bright and Fluorogenic Scaffold for Developing Near-Infrared Chemigenetic Indicators. *J. Am. Chem. Soc.* **146**, 11570–11576 (2024).
- Rathnamalala, C. S. L. *et al.* Thienylpiperidine Donor NIR Xanthene-Based Dye for Photoacoustic Imaging. *Org. Lett.* **23**, 7640–7644 (2021).
- Noack, A. & Hartmann, H. Preparation and Spectroscopic Characterisation of Some 5-Methylmercapto- and 5-Dimethylamino-substituted Tris-(2-thienyl)methinium Perchlorates. *Chem. Lett.* **31**, 644–645 (2002).
- Noack, A., Schröder, A. & Hartmann, H. Synthesis and spectral characterisation of a series of new heterocyclic triphenylmethane analogues. *Dyes and Pigments* **57**, 131–147 (2003).
- Yang, T. *et al.* Excited-State Dynamics in Borylated Aryli-soquinoline Complexes in Solution and in Cellulo. *Chem. Eur. J.* **29**, e202203468 (2023).
- Yang, T. *et al.* Monitoring excited-state relaxation in a molecular marker in live cells—a case study on astaxanthin. *Chem. Commun.* **57**, 6392–6395 (2021).
- Chettri, A. *et al.* Using Biological Photophysics to Map the Excited-State Topology of Molecular Photosensitizers for Photodynamic Therapy. *Angew. Chem. Int. Ed.* **62**, e202301452 (2023).
- Fuenzalida Werner, J. P. *et al.* Challenging a Preconception: Photoacoustic Spectrum Differs from the Optical Absorption Spectrum of Proteins and Dyes for Molecular Imaging. *Anal. Chem.* **92**, 10717–10724 (2020).

Müller (Thorn-Seshold) *et al.*, 2024: Molecular Rotors as High-Performance NIR/SWIR Optoacoustic Contrast Agents

43. Glembockyte, V., Lincoln, R. & Cosa, G. Cy3 Photoprotection Mediated by Ni²⁺ for Extended Single-Molecule Imaging: Old Tricks for New Techniques. *J. Am. Chem. Soc.* **137**, 1116–1122 (2015).
 44. Nani, R. R., Kelley, J. A., Ivanic, J. & Schnermann, M. J. Reactive species involved in the regioselective photooxidation of heptamethine cyanines. *Chem. Sci.* **6**, 6556–6563 (2015).
 45. Cosco, E. D. *et al.* Flavylium Polymethine Fluorophores for Near- and Shortwave Infrared Imaging. *Angew. Chem. Int. Ed.* **56**, 13126–13129 (2017).
 46. Myochin, T. *et al.* Development of a Series of Near-Infrared Dark Quenchers Based on Si-rhodamines and Their Application to Fluorescent Probes. *J. Am. Chem. Soc.* **137**, 4759–4765 (2015).
 47. Zhou, E. Y., Knox, H. J., Liu, C., Zhao, W. & Chan, J. A Conformationally Restricted Aza-BODIPY Platform for Stimulus-Responsive Probes with Enhanced Photoacoustic Properties. *J. Am. Chem. Soc.* **141**, 17601–17609 (2019).
-

2 Part II: Efficacy switches for optical control of TRPC4/5

2.1 Introduction

2.1.1 Transient Receptor Potential (TRP) Channels

2.1.1.1 Classification and importance of TRP channels

Sensory receptors and ion channels define the way an organism recognises the environment. Transient receptor potential (TRP) proteins form tetrameric TRP ion channels which are cellular sensors fundamental to the integration and processing of a wide range of external sensory stimuli, such as temperature, taste, and pain, as well as roles in metabolic sensing, electrolyte homeostasis, immune system homeostasis, controlling lysozyme formation, and more.¹³⁸ Considering their versatility and broad occurrence in different species one can describe them as a *Molecular Swiss Army Knife*.¹³⁹

The story of TRPs started in 1969 when Cosens & Manning discovered a visual mutant in *Drosophila*,¹⁴⁰ but it took another six years until the mutant gene was named as TRP (pronunciation *TRiP*). The name was chosen by Minke because the mutant gene produced transient signals during strong and prolonged stimuli with light, instead of the expected sustained response.¹⁴¹ In several small steps TRP was first identified as a transmembrane protein¹⁴² that was thought to be a Ca²⁺ transporter, before experiments in 1992 showed that TRP is a Ca²⁺ permeable ion channel.^{143–145} Three years later the first human homologue of TRP (TRPC1) was found independently by two groups,^{146,147} a finding that started the discovery of a whole new superfamily of ion channels.

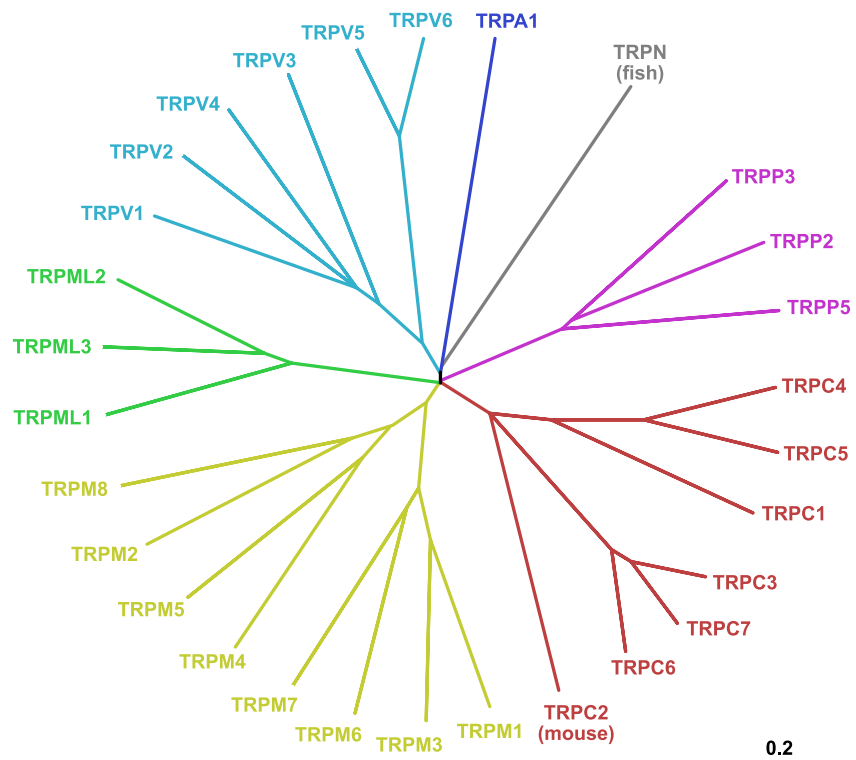


Figure 13 Phylogenetic tree of the TRP channel family.¹⁴⁸

All TRP channels are non-selective cation channels. There are 28 known mammalian TRP proteins (27 in humans as well other mammals, one in mice but not humans) and one additional TRP in fish (Figure 13), which are categorized by sequence and topological similarities into six subcategories.^{138,149} Canonicals (TRPC) are the closest relatives to the original *Drosophila* TRP; then come the vanilloids (TRPV), melastatins (TRPM), ankyrins (TRPA), mucolipins (TRPML), and polycystins (TRPP, TRPP3 is also termed polycystic kidney disease 2-like 1 protein, PKD2L1). The TRP ion channels themselves are often assembled as homotetramers, though in some cases as functional heterotetramers. Crucially, the functions of even the exact same channel in different cell types or tissues can be drastically different.

The best popularly-known member of the TRP family is the *capsaicin receptor* TRPV1.¹⁵⁰ Capsaicin is the *hot* ingredient in chili peppers and elicits a sensation of burning pain by activating neurons that transmit noxious stimuli to the central nervous system. TRPV1 is also activated by elevated temperatures in the noxious range and was the first ion channel shown to be connected with the ability to sense the environment. In total, there are currently 10 temperature sensing members of the TRP family (TRPV1-4, TRPM2-5, TRPM8, and TRPA1) called the thermoTRPs; TRPV1-4 can sense elevated temperatures in different ranges, whereas TRPM8 and TRPA1 sense cold temperatures, and activation of TRPA1 results in what humans experience as painfully cold.^{151,152} Perception of the environment is a key skill for every organism. David Julius and Ardem Patapoutian received a shared Nobel Prize in medicine in 2021 for their ground-breaking work on elucidating how we sense the temperature of the environment, and the role of TRP channels as gatekeepers for integrating external temperature stimuli (alongside the sensory basis of touch as mechanosensation via piezo channels).^{153–155}

A driving force for those discoveries was the identification of natural product ligands in our environment that exploit the obvious connection of TRPs to the sensory nervous system. TRPV1 is activated by deterrents such as capsaicin or the more potent resiniferatoxin (a natural product found in *Euphorbia* in northern Africa¹⁵⁶). TRPM8 is activated by menthol, a natural product found in *Mentha arvensis* and long known for its cool sensation (Figure 14). Intriguingly, TRPA1 is also a chemical nociceptor, able to sense electrophiles from the environment by channel activation after covalent modification of a hyperreactive cysteine.^{157,158} E.g. TRPA1 is activated by natural occurring electrophiles such as in wasabi (allyl isothiocyanate) or cinnamon (cinnamaldehyde), and gives another example for TRP channels involved in taste. These "popular" examples all show the importance of TRP channels as peripheral sensory receptors, but TRP channel functionality is much wider; one recent finding is that TRPM2 expressed in hypothalamic neurons not only *senses* temperature, but additionally functions as gatekeeper to *regulate* body temperature.¹⁵⁹

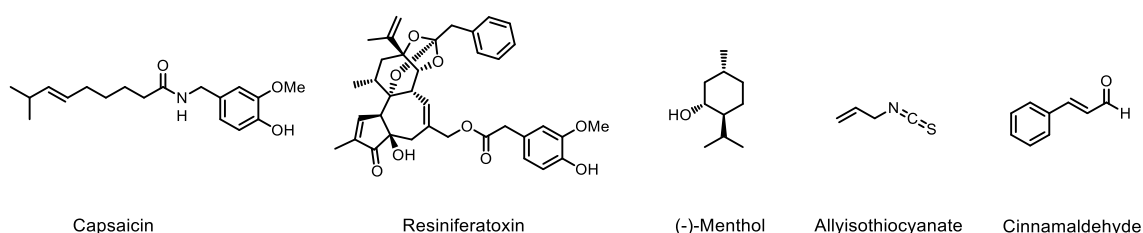


Figure 14. Chemical structures of natural products modulating TRPV1: capsaicin, resiniferatoxin, TRPM8: menthol, and TRPA1: allyl isothiocyanate, cinnamaldehyde.

Since TRP channels are organised into families by sequence not function, members within the same family often do not have similar physiological roles, e.g. not all TRPV members are thermosensitive, and only TRPM5/8 sense cold temperatures. However, from a structural perspective, TRP channels are very similar. They are C4-symmetric TRP protein tetramers, with each protein comprising six transmembrane domains (S1-S6), where the channel pore region is located between S5 and S6 (Figure 15a). The distinct segments of the subfamilies are mostly located at the intracellular C-terminal region, whereas the S6 transmembrane region is the most conserved region, indicating its importance within the gating mechanism.¹⁶⁰ S1-S4 show similarities to voltage-gated ion channels, but the absence of positively charged arginine residues indicates the generally weak voltage sensitivity of TRP channels; nonetheless, S1-S4 has been termed the "voltage sensing-like domain" (VSLD).¹⁶¹ The VSLD has a hydrophobic binding pocket that is commonly occupied by lipids and cationic cofactors.¹⁶²

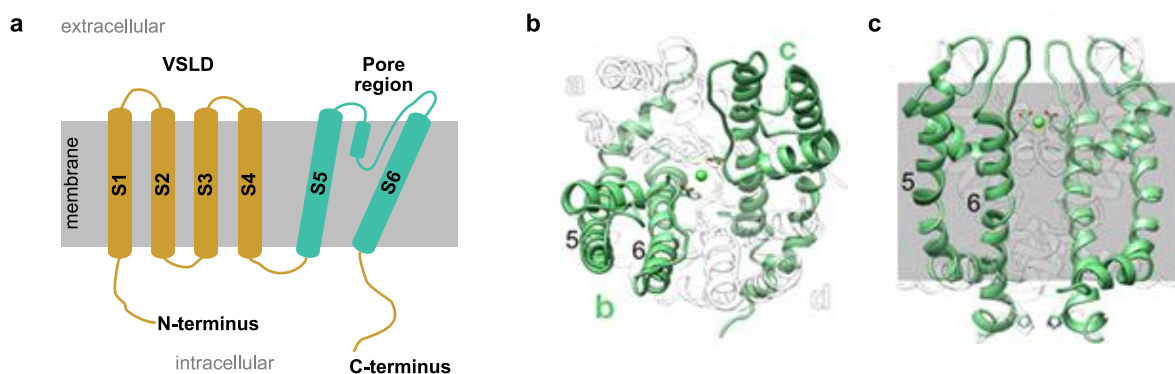


Figure 15. General structure of TRP channels. **a**) Representation of the structure of a monomeric unit of TRP channels: six transmembrane domains (S1-S6), S1-S4 form VSLD, S5-S6 the pore region. **b,c**) Example 3D structures from TRPV5 highlighting the pore region formed by S5 and S6 of two monomers, (PDB: 6B5V, modified and reproduced from ref¹⁶³ with permission from Springer Nature).

Obtaining high-resolution 3D structures for membrane proteins has proved challenging for structural biology. X-ray crystallography and nuclear magnetic resonance (NMR) spectroscopy essentially both failed to elucidate complete TRP channel structures, for a variety of reasons. For example, first, membrane proteins are difficult to produce in large quantities and high purity; second, TRP channels are tetramers built of individual domains (structurally-independent folding units) which often hinders crystallization because of the lack of structurally organised repeating parts, the essential requirement for crystallisation; third, NMR in structural biology is limited to relatively small and organized structures, so as very large proteins (typically >100 kD per monomer) tetrameric TRP structures are inaccessible by NMR.¹⁶⁴ TRPV1 was at the frontier of structural exploration and the first high resolution structures were derived by X-ray crystallography but only of individual domains.^{165,166} Later, low resolution Cryo-EM structures of the whole protein complex were obtained.¹⁶⁷ When in 2013 a technology leap in Cryo-EM made it possible to generate 3D structures of near-atomic-resolution structures by direct fitting of atomic models into experimentally observed density maps,¹⁶⁸ a high resolution structure of TRPV1 soon followed: a milestone, as the first 3D structure of a membrane protein with nearly atomic resolution.^{169,170} Remarkably, the structures of the closed channel (no ligand), and the open channel in complexes with resiniferatoxin or spider toxin (DkTx), were reported back to back. These landmark publications set the direction for structural biology of membrane proteins, and within the last decade Cryo-EM allowed researchers to gain insights into 3D structures of many different TRP channels with multiple ligands.¹⁶³

Admittedly, while such structural data can lead to a better understanding on a molecular level, Cryo-EM only delivers a snapshot of a highly dynamic system: and in particular, there remain no structures of most TRP channels in their open channel state (it has thus been suggested that agonists often do not stabilize the open state, but merely increase the opening probability).¹⁶²

Returning to the still ambiguous physiological roles of TRP channels, one aspect that has driven much pharmacological research recently has been that the noxious sensor TRP channels (TRPV, TRPM, TRPA) involved in *sensing* pain, may also be targets for *desensitising* it (e.g. for chronic pain treatment). Indeed, in early animal models, permanent activation of TRPV1 with capsaicin was found to desensitize pain recognition at the local nociceptor.¹⁵⁸ This finding generated huge interest from the pharmaceutical industry because current therapeutic options are often opioids which act in the brain and therefore cause strong addictive side effects. Treating pain directly at the nociceptor, crucially the source of pain at the opposite end of the signalling cascade, promised to be an effective and non-addictive strategy. But unfortunately, side effects related to suppressing the sensory roles of TRP channels, e.g. frequent burns, as well as wider expression of TRPs than originally believed, have so far prevented the successful development of TRP drugs.^{158,171} Furthermore, TRP channel pathology is complex, species-dependant, and subtle changes can cause huge effects in functionality. For example, in field of noxious stimuli, TRPV1 is not activated by capsaicin in birds¹⁷² (though introducing a single point mutation reverts chicken TRPV1 to capsaicin sensitivity¹⁷³), and TRPV1 does not act as noxious temperature sensor in mammals adopted to hot environments, such as camels.¹⁷⁴ In brief, it can be accurately said that the 27 TRP channels in humans have partially or majorly unknown functionalities, but that their role is much broader than only signal transduction: TRP channels are the sensory apparatus for individual cells, not only for the organism, and they respond to a variety of stimuli from both within and outside the cell.¹³⁸

2.1.1.2 Transient receptor potential canonicals (TRPC) & the subfamily TRPC1/4/5

TRPC1 was the first TRP discovered in mammals,^{146,147} but unlike other TRP subfamilies, which were discovered by function, naturally occurring ligands, or genetic correlation to disease, the mammalian TRPC members were merely identified because of sequence homology with the prototype *Drosophila* TRP¹⁷⁵ (TRPCs are the closest homologs to *D.m.* TRP, with 30-35% sequence identity). There are seven members of TRPC among mammals, but TRPC2 is only a pseudogene in humans. The others are categorized into two groups: TRPC3/6/7 and TRPC1/4/5. TRPCs have not had much time in the research spotlight and there is relatively little known about their physiological roles.

The activation mechanism of TRPC channels has been debated among researchers and their activation mechanism was either described as receptor operated (receptor operated Ca²⁺ influx, ROCE) or as store operated (store operated calcium entry, SOCE).¹³⁸ The second hypothesis, SOCE, supposed a direct activation by endoplasmic reticulum Ca²⁺ depletion and thereby an involvement of TRPCs in the essential cellular process of replenishing intracellular Ca²⁺ stores during signalling events.¹⁷⁶ However, the mechanisms of Ca²⁺ recognition in TRPC channels are complex and the SOCE concept was doubted from the beginning.^{138,176,177} Now, after identification of other pathways that mediate the Ca²⁺-release-activated Ca²⁺ (CRAC) current,^{178–180} the idea of SOCE seems unlikely. The Ca²⁺ dependence of TRPC function has rather been attributed to indirect downstream mechanisms such as calmodulin, protein kinase C, and phospholipase C (PLC). One common hallmark of TRPCs described as receptor operated

channels is the activation by diacylglycerol (DAG).^{181,182} The G-protein coupled PLC produces the secondary messengers DAG and inositol-1,4,5-trisphosphate (IP3) by cleavage of phosphatidylinositol-4,5-bisphosphate (PIP₂), which is an important messenger itself (Figure 16). Interestingly, TRPC4/5 were long considered DAG-insensitive, but only because DAG *alone* is not sufficient for activation (interplay with the Na⁺/H⁺ exchanger regulatory factor (NHERF) controls their DAG sensitivity¹⁸²).

TRPC1/4/5 bear extracellular cysteine residues in close proximity to each other that are able to form disulfides, but only TRPC5 and TRPC1:TRPC5 can be activated by reduction of the disulfide bond by reducing agents such as dithiothreitol (DTT) or the redox enzyme thioredoxin (TRX). The reduction site is predicted as an extracellular loop adjacent to the ion-selectivity filter of TRPC5 and may therefore play an important role in activation of TRPC5 by extracellular redox states.¹⁸³

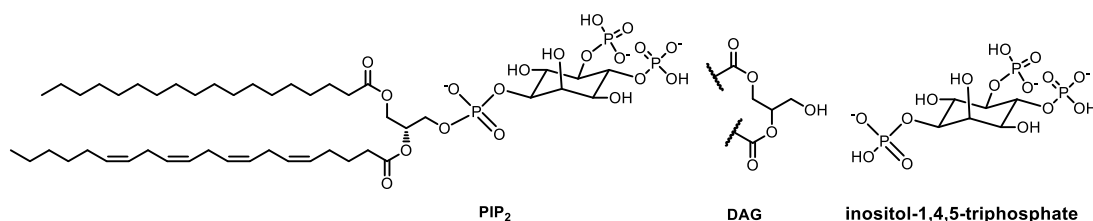


Figure 16 Structures of PIP₂ and its metabolites DAG and inositol-1,4,5-trisphosphate.

The large interest in Cryo-EM lead to an exponential growth in the number of high resolution 3D structures of proteins¹⁸⁴ and within five years after the first disclosure of TRPV1, researchers had adapted the method for many other TRPs, with near-simultaneous TRPC3/4/5/6 reports by several groups.^{185–190} The general constitution of TRP channels shown in Figure 15 also holds for TRPCs. Their structures are divided into a transmembrane domain comprising six transmembrane helices with S1-S4 forming a VSLD that is partially exposed to the intracellular space and offers interaction sites for ligands, as well as a cytoplasmic domain, and a smaller extracellular domain (Figure 17a). The pore helix is formed between S5 and S6 (also called the upper gate) and on the opposite site of the transmembrane domain lies the bundle crossing (also called the lower gate, see Figure 17b). TRPC members are moderately Ca²⁺-selective (also permeable for: Na⁺, Zn²⁺, Mn²⁺, Ba²⁺);¹⁹¹ the first filter step on the upper gate is performed by a pore surrounded by negatively charged glutamate residues, and at the second filter step on the most narrow section of the upper gate all TRPC share a glycine residue indicating a purely size dependent filter mechanism. Only channel-closed TRPC Cryo-EM structures have ever been found, with the lower gate clogged at the bottom with asparagine residues pointing into the pore (except for TRPC3 where an asparagine is present but pointing in the opposite direction; Figure 17b).¹⁹¹

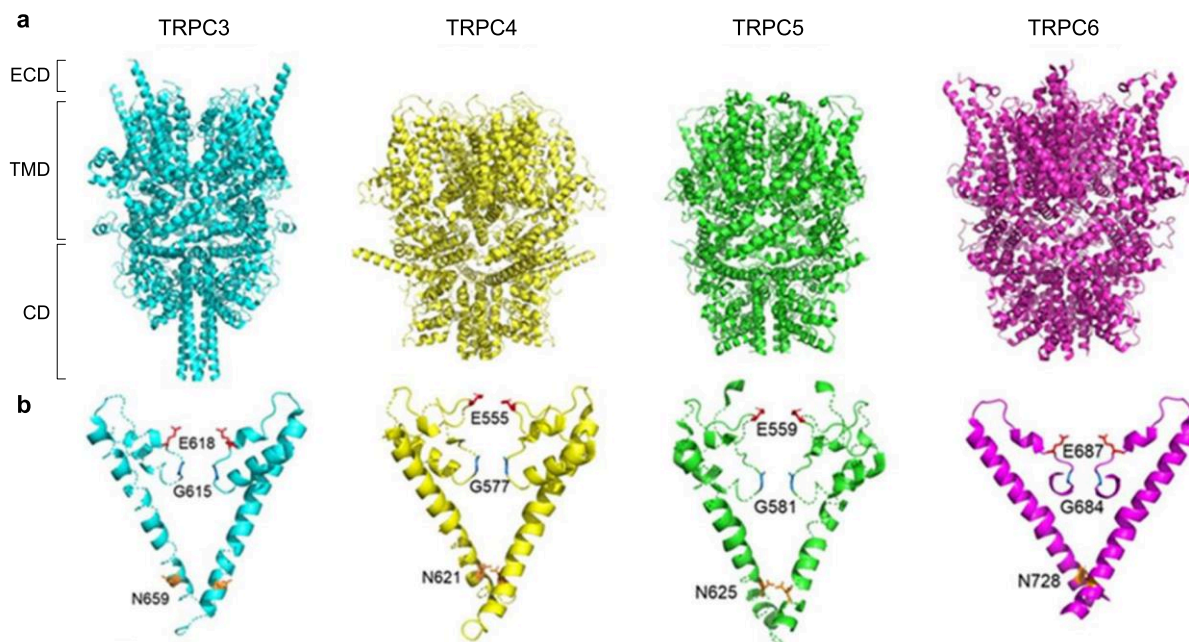


Figure 17. TRPC3/4/5/6 structures. a) 3D-model of homomeric Cryo-EM structures of tetrameric TRPC3 (PDB: 7DXB), TRPC4 (PDB: 5Z96), TRPC5 (PDB: 6AEI), and TRPC6 (PDB: 7DXF); (ECD: extracellular domain, TMD: transmembrane domain, CD: cytoplasmic domain). b) S6 helix and amino acids of conserved LWF motif. *Figure adapted from Baron et al¹⁷⁶ with permission from Elsevier.*

TRPC1/4/5

The Cryo-EM structures in Figure 17 are all derived from purified homologue tetrameric TRPCs; however, among the subfamily TRPC1/4/5, TRPC1 stands out because it does not form functional homomeric channels: it only participates functionally as part of TRPC1/4/5 heteromers. Homo- vs heteromerisation remains a problem for understanding TRPs *in vivo*; e.g. there are 21 theoretically possible TRPC1/4/5 channels (see Figure 18a), and in tissues with mixed expression levels, the composition of any individual channels remains enigmatic.¹⁹²

Not only composition, but also function, is difficult to study. For example, point mutations at the pore region have massive effects on channel functionality and selectivity, therefore the properties of heteromeric channels can be completely different than the homomeric ones.¹⁷⁶ And indeed, homomeric TRPC4/5 show significant rectifying I-V curves in both directions, but introduction of TRPC1 and formation of heteromeric channels leads to a truncated inward current (Figure 18b) which indicates a reduced cell excitability;¹⁹² coherent with this result, TRPC1 presence in mixed TRPC1/4/5 channels reduces their Ca²⁺ permeability.¹⁹³ Intriguingly, TRPC1 expression is ubiquitous, whereas TRPC4 and TRPC5 are mainly expressed in the nervous system; since the formation of heteromeric channels over homomeric channels is apparently preferred (although dependent on the expression ratio), TRPC1 expression seems to function as negative regulator to TRPC4/5.¹⁹⁴

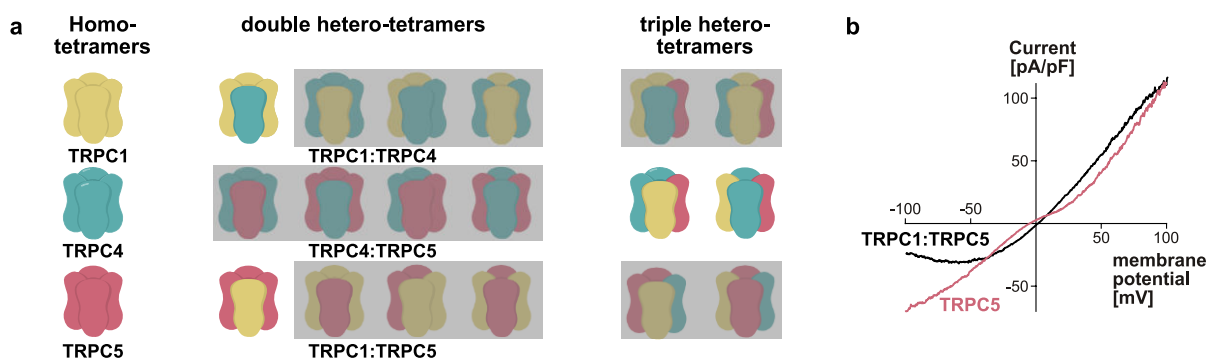


Figure 18. a) Possible compositions of tetrameric TRPC1/4/5 as homomers and heteromers; grey overlay on combinations that have not been identified yet, other combinations were found by *Kollewe et al*¹⁹⁵. b) I/V curves of TRPC5 vs TRPC1:TRPC5.

TRPC1/4/5 in disease

TRPC1/4/5 are mainly expressed in the central nervous system (CNS) and have been extensively associated with mental disorders. For example, early behavioural studies with TRPC4/5 knockout mice gave positive results in models supposed to predict anxiolytic and antidepressant action,^{196,197} TRPC4 deficient mice displayed reduced cocaine self-administration without deficits in learning for natural rewards,^{158,198} and TRPC5 modifications are connected to Huntington disease.^{194,199} Currently Boehringer Ingelheim runs clinical trials with TRPC4/5 blockers to treat anxiety disorders.

Other tissue localisations are also therapeutically relevant for TRP drugs though. For example, focal segmental glomerulosclerosis (FSGS) is a condition ultimately leading to kidney failure. TRPC5 activity mediates progress of FSGS, but a selective TRPC5 channel blocker suppressed severe proteinuria (a symptom of FSGS) putting TRPC5 in the spotlight for treatment of kidney disease.^{200,201} Goldfinch Bio is currently running a clinical trial to treat proteinuric kidney disease.

Currently, these are the only two targets in clinical development, but in two recent studies TRPC5 was identified as mediator in pain signalling,^{202–204} and treatment of pain by controlling TRPC5 is a promising new target, as it may promise therapeutic options without addictive side-effects.¹⁵⁸

2.1.1.3 Pharmacological Modulators for TRPC1/4/5

Pharmacological investigations require potent and selective modulators and for TRPC channels such small molecules are still scarce. Only a decade ago, Bon and Beech formulated the provocative question of whether the pursuit for such ligands is "a mirage or a pot of gold".²⁰⁵ Ten years on, substantial progress has been made, but especially for TRPC1/4/5, selective modulators are very challenging because of the proteins' structural similarities as well as the diversity of channels they may form.

While many drug classes have been inspired by natural products,²⁰⁶ nature did not provide many blueprints for TRPC1/4/5, and even fewer examples for natural products selectively targeting TRPC4 or TRPC5. The most famous is (-)-Englerin A (**EA**, Figure 19), a natural product derived from the bark of the *Phyllanthus engleri* tree naturally occurring in north-east Africa. In a natural product screen, **EA** was identified as an active ingredient that very cell-line-selectively inhibited growth of renal cancer cells²⁰⁷ but the mechanism remained elusive until Waldmann and Beech discovered TRPC4 and TRPC5 as the molecular targets.²⁰⁸ This discovery was fuelled by a huge interest in the total synthesis community which recognised **EA** not only as attractive synthetic target but as a target for structural synthetic

modifications to elucidate its activity.^{209–212} **EA** acts as an agonist for TRPC4/5, and also activates heteromeric channels containing TRPC1, with low nanomolar potencies. As **EA** only targets the subfamily of TRPC1/4/5, it quickly became the gold standard for pharmacological tools. Very interestingly, subtle changes in the structural core of **EA** abolished the activity or even flipped it from an agonist to an inhibitor/competitive binder of **EA** (Englerin B and Englerin Analogue 54, Figure 19; this efficacy flip will be relevant later).^{208,213} Its initially discovered anti-kidney-cancer effect could not however be translated into clinics because of its metabolic instability and toxic side effects.

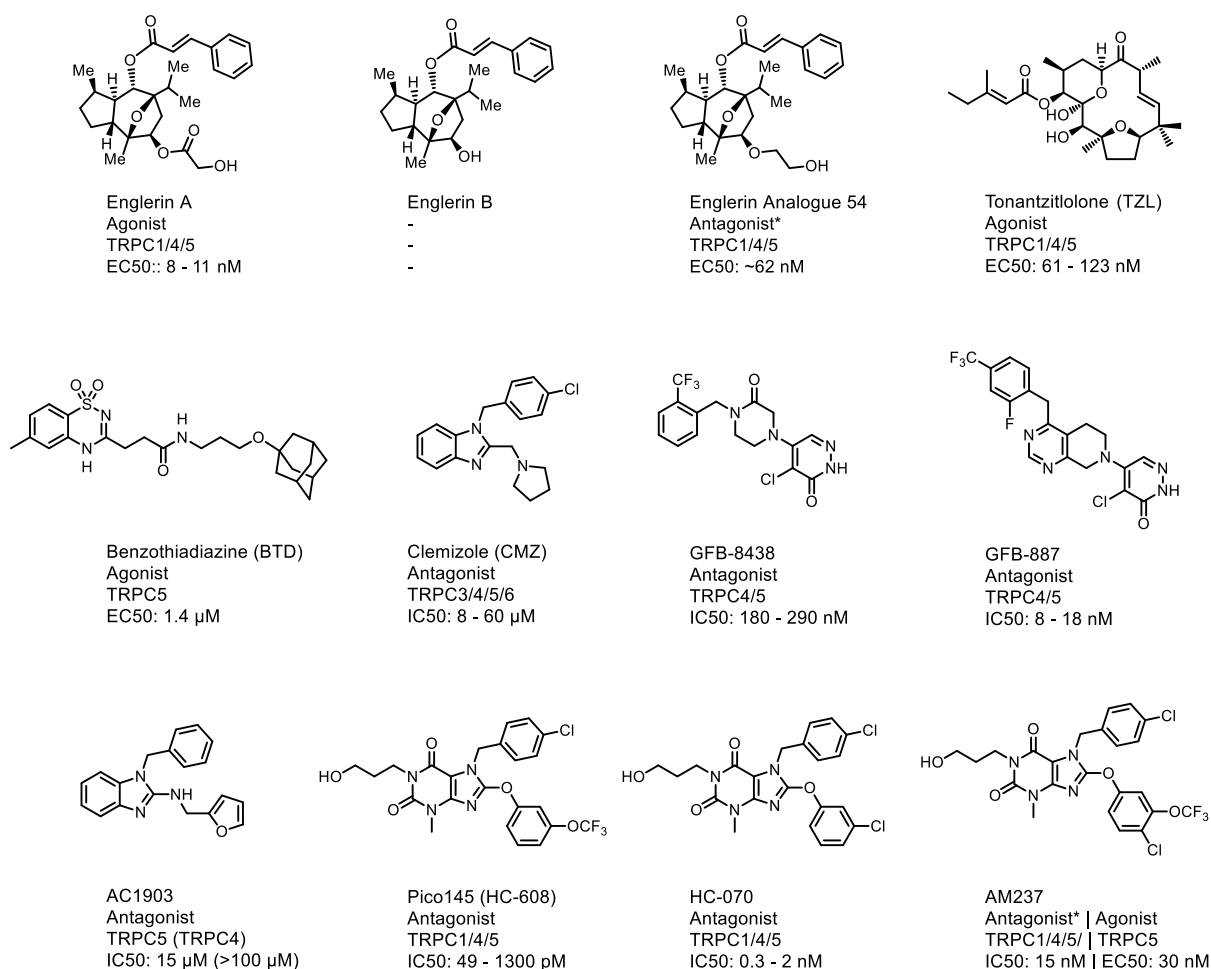


Figure 19. Chemical structures and pharmacological properties of known TRPC1/4/5 modulators.

Other TRPC1/4/5-acting compound leads were scarce. Tonantzitolone (**TZL**, Figure 19) is another potent natural product agonist for TRPC1/4/5, similarly to **EA** identified because of its effect against renal cancer cells, which was also connected to TRPC1/4/5. TRPC4 or TRPC5-specific modulators are particularly rare; Schaefer's identification of **BTD** as a moderately potent but highly selective agonist for TRPC5 over TRPC4 in a high throughput screening was therefore a highlight in this field.²¹⁴ Within the same screening, Schaefer also identified more promiscuous compounds, such as Clemizole (**CMZ**) or even methylprednisolone as having some inhibitory preference for TRPC5,²¹⁵ but **CMZ** later turned out to be unselective among the TRPC family and methylprednisolone has many other targets.²¹⁶ Other researchers also identified e.g. the **CMZ**-like **AC1903** as a moderately potent but remarkably selective inhibitor for TRPC5 over TRPC4 in a study aiming to find a treatment for progressive kidney disease.²⁰⁰

The major breakthroughs in selective and potent inhibitors came from pharmaceutical industry: Hydra Biosciences and Boehringer Ingelheim found small molecules built around a xanthine core structure as potent inhibitors for TRPC5.^{217,218} The early patent then served as a fruitful source for potent and selective inhibitor types, and within a big collaborative effort led by Beech and Muraki, the particularly promising compound **Pico145** was characterized in detail where it was found to not only inhibit TRPC5 but also TRPC4, with potencies ranging from 49 pM for TRPC1/4 heteromers to 1.3 nM for TRPC5 homomers, with reliable effects on any heteromers.²¹⁹ The rise of xanthine-based inhibitors proceeded with **HC-070** (a xanthine derivative that only differs from **Pico145** by substitution of an OCF₃ group on the southern phenyl ring by a chlorine, Figure 19), which, like **Pico145**, had remarkable selectivity: with inactivity against hundreds of other enzymes, receptors, transporters and especially other ion channels including other TRP channels.²¹⁸ That led to a widespread use of **Pico145** and **HC-070** as tool compounds, in turn driving a better understanding of TRPC biology especially in the CNS.²²⁰ Intriguingly, the activity flip observed in **EA** after subtle structural changes, is mirrored within the xanthine family. **AM237** has the same structural backbone as **Pico145** and only has an additional chlorine substituent in the 4-position at the southern ring (Figure 19); this flips the activity on homomeric TRPC5 from antagonistic to agonistic, still with low nanomolar potency. Remarkably, for TRPC4 or heteromeric channels **AM237** still functions as an antagonist against activation with **EA**.²²¹ The binding site of **EA** remained elusive, and while inhibitory assays and results should always be compared carefully because the mode of TRPC4/5 activation might differ,^{219,221–223} but several studies had basically suggested a shared binding site of **EA** and the xanthine based inhibitors.

Although xanthines such as **Pico145** and **HC-070** are selective and very potent inhibitors, their poor solubility and high affinity to serum proteins constrains their pharmacological use. A team at Goldfinch Bio therefore pursued a novel class of TRPC5 inhibitors based on a pyridazinone core, whose structural optimization led to the potent inhibitor **GFB-8438** (Figure 19) with much more desirable pharmacological properties, for *in vivo* use against FSGS. Further lead optimisation resulted in the more potent **GFB-887** with an only recently disclosed structure, which was used in clinical trials.²²⁴

Here, only a selection of reliable ligands was given (there are a plethora of other, unselective, and at best moderately potent modulators for TRPC channels in the literature^{225,226}) but since the most reliable tool compounds were derived from industry leads, the disclosure of structure of **GFB-887** together with the lead candidate of Boehringer Ingelheim (which is currently in clinical trials but without a disclosed structure) will boost research on TRPC4/5 channels simply by providing better tool compounds.

2.1.1.4 The interplay of structure and pharmacology for TRPC1/4/5 drugs

TRPC4/5 drug discovery started without structural guidance, merely driven by the discovery of selective and potent ligands. The disclosure of high resolution Cryo-EM apo structures happened soon afterwards; and following that, the binding sites for several previously reported inhibitors were elucidated by obtaining Cryo-EM complexed structures.^{227–229} In brief, these studies revealed that there are two major binding sites for ligands in TRPC4/5, that Chen defined as inhibitor binding pocket A (IBP-A) and IBP-B.²²⁹ **GFB-8438** and **CMZ** both bind at IBP-A which is located at the intracellular site of the VSLD (see Figure 15 and Figure 20). IBP-B is located in the pore domain, sandwiched at the subunit interface between monomers and closely located to the extracellular side. Both xanthines **Pico145** and **HC-070**

bind to IBP-B; their only difference is the orientation of the OCF₃/CI residues which point in opposite directions (Figure 20).^{227,229} In the apo structure of TRPC5, densities were observed at the location of IBP-B that were assigned to a lipid binding site for a bound phospholipid; also however, the recent study by Chen suggests IBP-B as binding pocket for (uncharged lipid) DAG.^{229,230} This finding is very interesting because so far no ligand binding sites for agonists on TRPC4/5 had been identified. Nevertheless, DAG activates TRPC4/5 (for details see section 2.1.1.2) and also the xanthine **AM237** can at least activate homomeric TRPC5, which indicates IBP-B as the key regulatory site for TRPC4/5 and not only as an inhibitory site blocking channel opening. Somewhat less prominently, in TRPC4/5 there is a conserved motif adjacent to IBP-B that is also present in other TRP channels where e.g. for TRPC3/6 and TRPV1 the motif was identified as ligand binding site:^{170,187} thus it was classified by Chen as IBP-C (even without known ligands for TRPC4/5 at this day).

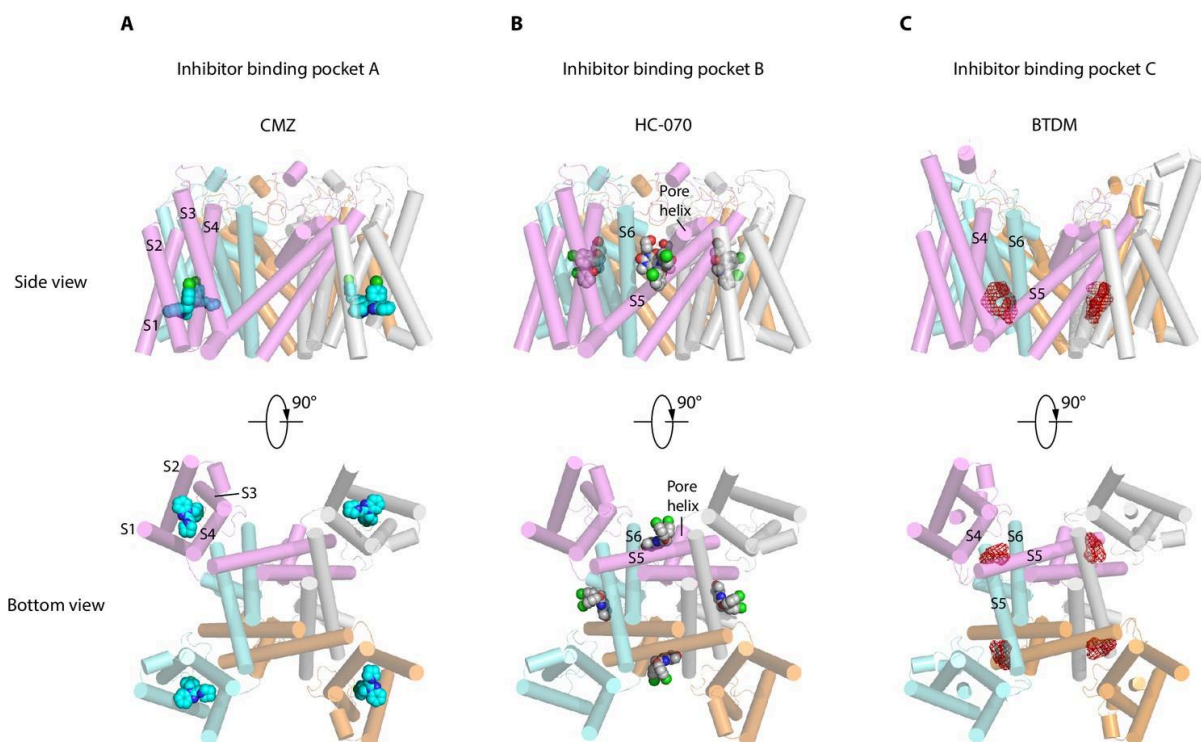


Figure 20. Inhibitor-binding pockets of TRPCs in transmembrane domain (TMD). The TRPC structures are shown as cylinder and bound ligands shown as spheres or mesh **A**) TRPC5 in complex with **CMZ** indicating IBP-A. **B**) TRPC5 in complex with **HC-070** indicating IBP-B, same binding pocket as for **Pico145**. **C**) TRPC6 in complex with **BTDM** indicating IBP-C a closely related binding pocket with confirmed ligands for TRPC6, TRPV1. Figure was adapted from ref²²⁹.

In conclusion, the pursuit of selective and potent ligands for TRPC4/5 is no mirage, but the race for the pot of gold is still ongoing. The knowledge of protein structures with ligand binding sites should now offer major opportunities for drug discovery, and IBP-B as the key regulatory binding pocket adjacent to the pore helix may be the most promising target.

Still, given that the roles of TRPC4/5 are highly tissue-dependant, and likely to be temporally-modulated, the high spatiotemporal precision of *photopharmacology* tools may be crucial for research unravelling these several functions, and the next chapter will accordingly discuss photopharmacology.

2.1.2 Light as a trigger for biological function

Light is not only the fundamental source of energy for nearly all surface-living organisms, but also a carrier of information that can be received upon absorption. Thus, controlling light emission in space and time enables an indirect spatiotemporal control over the light-receiving parts; and because most living beings depend on interactions with light, light-responsive systems are ubiquitous.

In a controlled experimental setting, the combination of (a) light responsive biological tools with specific functionality, and (b) controlled illuminations, offers spatiotemporal control over these functionalities. This is highly desirable for studying dynamic systems such as ion channels,²³¹ signalling receptors,²³² the cytoskeleton,^{233,234} protein degradation,²³⁵ etc. because functionally "static" drugs provide a static response, so dynamic response parts might be lost either because of the flooded response or fatigue. There are three major strategies to obtain photocontrol over drug activity, the general principles of which I will illustrate by the example of targeting an ion channel (Figure 21): (1) **optogenetics**, using genetically encoded light responsive ion channels that change conformation e.g. to a conducting state after illumination; (2) **photocaged drugs**, i.e. druglike small molecules which are inactive but release an active ligand after irradiation; and (3) **photopharmacology**, which *typically* switches a ligand between a binding and not-binding state by incorporation of molecular photoswitches into the ligand core structure. All three approaches have their own advantages and limitations, and researchers can pick their desired tool based on problem and objective.

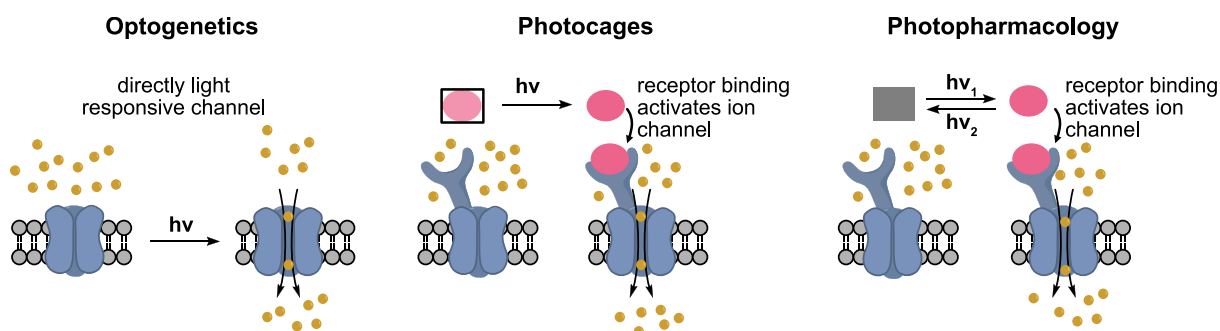


Figure 21. A triumvirate of general optical control methods for ion channels: optogenetics, photocages & photopharmacology.

2.1.2.1 Optogenetics

Optogenetics is the combination of optical tools and genetic engineering to control processes in biological systems, ranging from defined events in cells to behaviour in animals.²³⁶ Opsins are light-responsive proteins that undergo a conformational change after illumination and initiate a signalling process. All opsins are dependent on the chromophore retinal and its light-induced isomerization but intriguingly there are two different isomerization mechanisms. (1) In higher eukaryotes opsins are mainly responsible for vision²³⁷ and primarily function as G protein-coupled-receptors (GPCRs). 11-*cis*-retinal isomerizes to the all-*trans* configuration that triggers the signalling cascade (Figure 22a), then all-*trans*-retinal dissociates from its opsin partner, then is recycled by enzymatic isomerization by retinal isomerase²³⁸ to once more bind to an opsin. (2) In algae, prokaryotes, and fungi, all-*trans*-retinal is photoisomerized to 13-*cis*-retinal and then thermodynamically relaxed back to all-*trans*-retinal without breaking the covalent bond with the protein (Figure 22b). This reversible reaction occurs rapidly and it is this second class of opsin that led to the development of optogenetic tools, driven by the early example

where genetic encoding into specific neurons enabled optical control of their activity.^{239,240} Among the opsins, *channelrhodopsins* are cation permeable channels used to induce polarization and action potential, whereas *halorhodopsins* are chloride transporters that are used to block polarization and signalling events (Figure 22c,d).

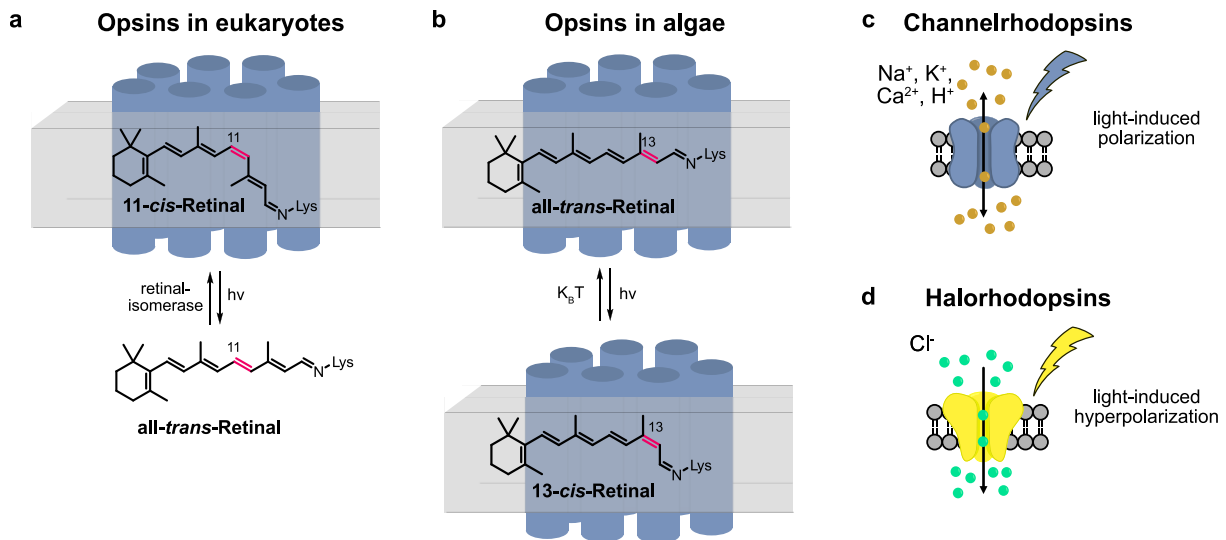


Figure 22. Basics of optogenetics. **a)** Opsins in higher eukaryotes: Photoinduced isomerisation of 11-*cis*-retinal to all-*trans*-retinal induces signalling cascade; all-*trans*-retinal dissociates from the opsin, 11-*cis*-retinal is regenerated enzymatically and then binds again to opsin. **b)** Opsins in algae: Photoinduced isomerisation of all-*trans*-retinal to 11-*cis*-retinal induces signalling cascade and thermodynamically stable all-*trans*-retinal is recovered by spontaneous relaxation while bound to opsin. **c)** Channelrhodopsins are unselective cation permeable ion channels activated by light and operate by the mechanism shown in **b)**. **d)** Halorhodopsins are chloride permeable ion channels activated by light and operate by the mechanism shown in **b)**.

The origin of optogenetics lie with *Drosophila*, but when Gero Miesenböck fused light responsive rhodopsins to a G-protein subunit to sensitize *vertebrate* neurons to light, the field entered a vast new domain.²⁴¹ Shortly after his initial pioneering work, researchers led by Georg Nagel and Peter Hegemann isolated and identified channelrhodopsin from green algae,²⁴² and they showed that channelrhodopsins are ion channels directly activated by light that can induce depolarization in cells simply by illumination.²⁴³ Next, Karl Deisseroth expanded the use of channelrhodopsins into neurons and showed light-induced neuron firing.²⁴⁴ These consecutive reports truly marked the beginning of a new era in neuroscience, and optogenetics had revolutionized neuroscience within a decade, because activation currents of channelrhodopsins are strong and therefore genetic engineering into specific brain areas to elucidate function became a standard method in neuroscience. Researchers could probe neural circuits, identify neural substrates of behavior,^{240,245–248} and *in vivo* applications became accessible upon the development of redlight-responsive rhodopsins.^{249–251} Apart from neuroscience, optogenetics is primed to have a similar impact in other fields, including cardiology, cell biology and plant sciences,^{252,253} or even as a therapeutic: because in a recent study the introduction of a light sensitive channel into the eye of a blind patient lead to partial recovery of visual function.²⁵⁴ However, the main drawback of optogenetics is the need for genetic engineering, which is often complicated (in case of the blind patient achieved with a virus), not applicable for all research questions, and most importantly, the resulting signals are not necessarily comparable to *endogenous* signalling cascades. Therefore, orthogonal strategies or tools to study endogenous systems are required and synthetic organic chemistry together with chemical biology offers several solutions at hand.

2.1.2.2 Photoremovable protecting groups (Photocages)

Photoremovable or photocleavable protecting groups (= photocages) are chromophores that undergo a photoreaction resulting in chemical bond scission after irradiation with light. Transferring the concept from synthesis into biological application means *caging* of a suitable functional group in a drug to modify its binding properties, typically blocking its pharmacological effects until irradiation with light releases the original drug. Popular photocages range from metal complexes to small molecule chromophores,^{255–257} and are known with photoresponses from the UV to the NIR.²⁵⁸

The *ortho*-nitrobenzyl motif was a key driver in the development of photocages. It was first developed as protecting group for synthetic chemistry by Woodward²⁵⁹ and Barton.²⁶⁰ Later, *ortho*-nitrobenzyls were transferred to biology by photocaging ATP.²⁶¹ The motif is an attractive photocage as it tolerates a broad scope of functional groups as caging targets.²⁵⁸ Wavelengths in the UV/blue²⁶² (Figure 23b), but technically also NIR (as a photon-inefficient, two-photon process²⁶³) can be applied for uncaging.

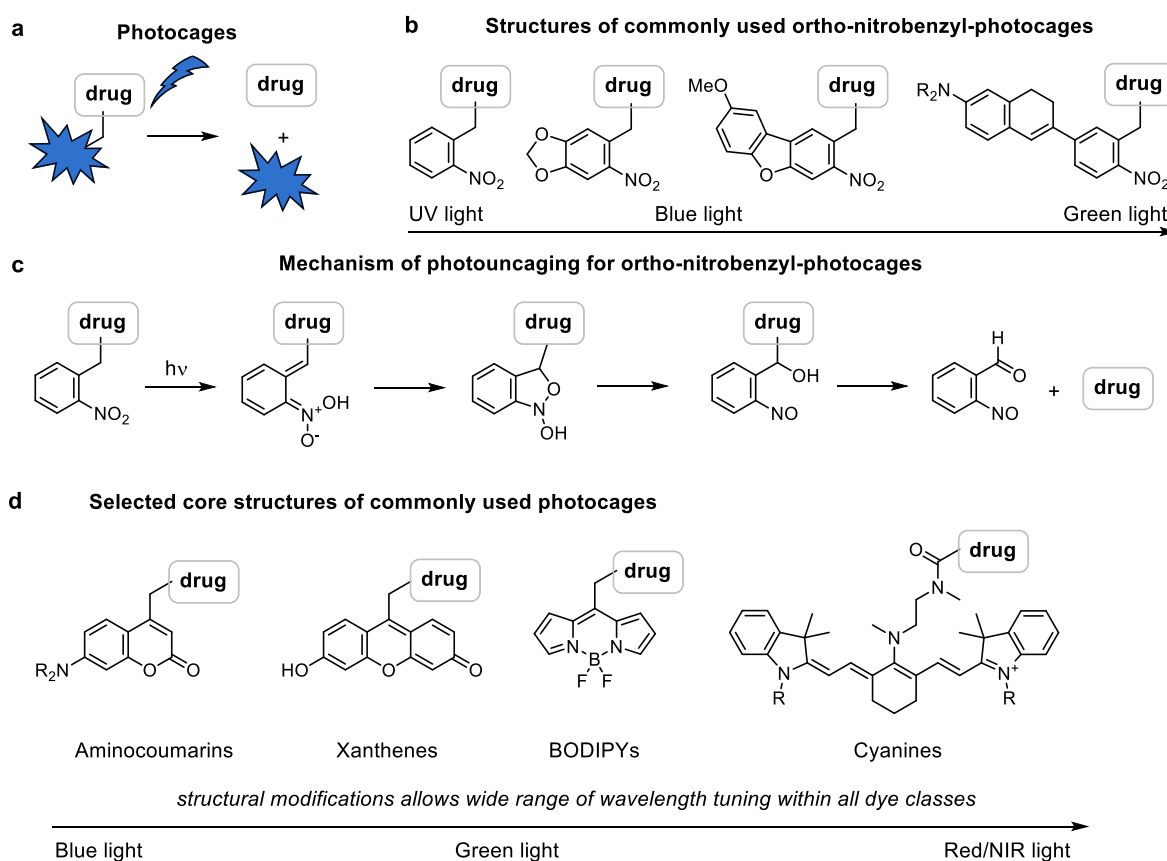


Figure 23. Examples for photocages. **a**) Schematic representation of photomediated release of a drug. **b**) *Ortho*-nitrobenzyls are widely used photocages and their spectroscopic properties can be tuned. **c**) Mechanism for the photo mediated release of *ortho*-nitrobenzyl protected cargos. **d**) Fluorophore core structures are modified as photocages and cover the whole range of the visible spectrum. Shown are selected examples representing four core structures of commonly used fluorophores as photocages: (amino)coumarins, xanthenes, BODIPYs and cyanines.

The photomediated bond cleavage at *ortho*-nitrobenzyls is not a concerted reaction and involves several intermediates (Figure 23c) which often leads to slow kinetics and long irradiation times, and toxic nitrosobenzene is formed as side product after release of the active drug.²⁶⁴

Therefore numerous alternatives were developed using modified fluorophores, such as coumarins,²⁶⁵ xanthenes,²⁶⁴ BODIPYs²⁶⁴ or cyanines^{266,267} (Figure 23d). Fluorophores are frequently used as imaging

tools in biology and therefore their photophysical and biological properties were optimized for biocompatibility, that can be somewhat retained as cages.^{30,32}

Photocages are valuable tools for controlled light-dependent release of active drugs, and the modular nature of the cage structure allows researchers to pick a suitable one for each problem individually, such as photocaged mRNA, photoactivated click-reagents, or antimetabolites.^{268–271} However, compared to optogenetics the process is not reversible and diffusion of released drugs limits spatial control.

2.1.2.3 Photopharmacology

Here, the term photopharmacology will be used restrictively to describe the *reversible* modulation of biological activity by means of *reversibly* optically controlled molecular switches. Photoswitching of ligands which contain a molecular photoswitch *typically* results in different potencies of the two isomers (Figure 24a, b). The most popular strategy is *cis/trans* isomerization of double bonds within a photoswitchable ligand to change the ligand 3D structure and binding affinity to the protein of interest²⁷² (Figure 24c, shows a *cis*-active photoswitchable ligand).

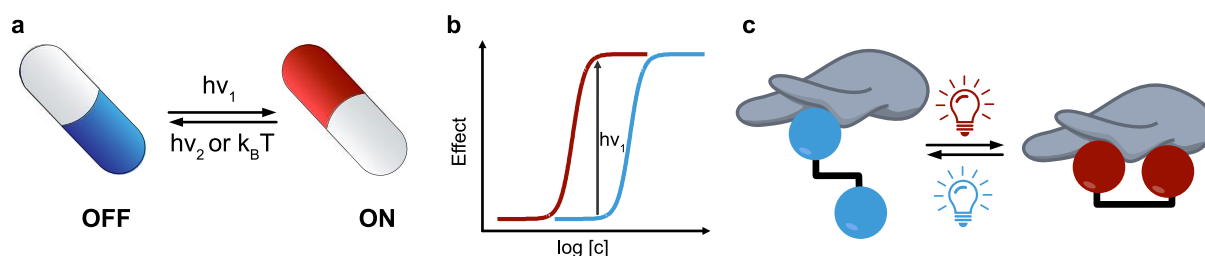


Figure 24. Principle of photopharmacology. **a)** Schematic representation of photoswitching activity of a drug. **b)** Schematic dose response curves of two photoisomers of the same drug with different agonistic potencies. **c)** Photoswitching the binding site affinity by photoisomerization of a double bond within a drug.

Azobenzenes in photopharmacology

Among the previously introduced chemical variety of molecular photoswitches (see section 1.1.3), azobenzenes are the most frequently used in photopharmacology.^{105,273} In 1968, Erlanger reported the first use of an azobenzene derivative as photoswitchable ligand for the enzyme chymotrypsin²⁷⁴ and later extended his work to photo-regulated acetylcholine receptor channels.^{275–277} Surprisingly, it took over 30 years until Erlanger’s pioneering work was picked up again in the mainstream. Modern photopharmacology was substantially re-started by the work of Trauner, Kramer and Isacoff, who showed the direct optical control of potassium channels and glutamate receptors by covalent tethering of photoswitchable ligands.^{231,278} Their semantic descriptors ranged from “Photoregulation”,²⁷⁴ to “Chemical Optogenetics”,²³¹ “Optochemical Genetics”,²⁷⁹ to finally settle on “Photopharmacology”.²⁸⁰

There are two common strategies to introduce a photoswitch into a pharmaceutically active compound. The self-evident approach is to mimic structural motifs found in drugs by near-isosteric replacement with e.g. an azobenzene, to give *azosteres*. This strategy, also called *azologisation*, usually targets stilbenes, *N*-aryl benzamides, benzyl phenyl (thio)ethers, benzyl anilines, and 1,2-diaryl ethanes (Figure 25a).^{273,281,282} Alternatively to pursuing *azosteres*, photoswitchable ligands can instead be developed serendipitously (or rationally by analysis of SAR tables or knowledge of the binding site) through extending the ligand with e.g. an azobenzene on an aryl already present (often aiming at a position that tolerates a range of substituents or that addresses empty space within the binding pocket).

E-azobenzenes are planar and rigid structures without intrinsic dipole moment, whereas *Z*-azobenzenes are twisted and rotatable structures with intrinsic dipole moment. Therefore, the likelihood that both isomers have the same affinity towards the binding pocket is very low. This strategy is called *azoextension* and there are many examples either adding the photoswitch as a new residue showcased by azo-propofol²⁸³ and azoflaxin,²⁸⁴ or by replacement of existing substituents e.g. for the photoswitchable Quinolone 2²⁸⁵ that was based on ciproflaxin (Figure 25b). Azobenzenes are lipophilic motifs prone to bind lipophilic sites, and membrane proteins are thus especially promising targets, as demonstrated for the TRPV1 targeting photoswitchable derivatives of capsaicin and capsazepine (Figure 25c),^{286,287} since both compounds share a vanillin-like headgroup, plus a lipophilic tail part that tolerates the photoswitch.

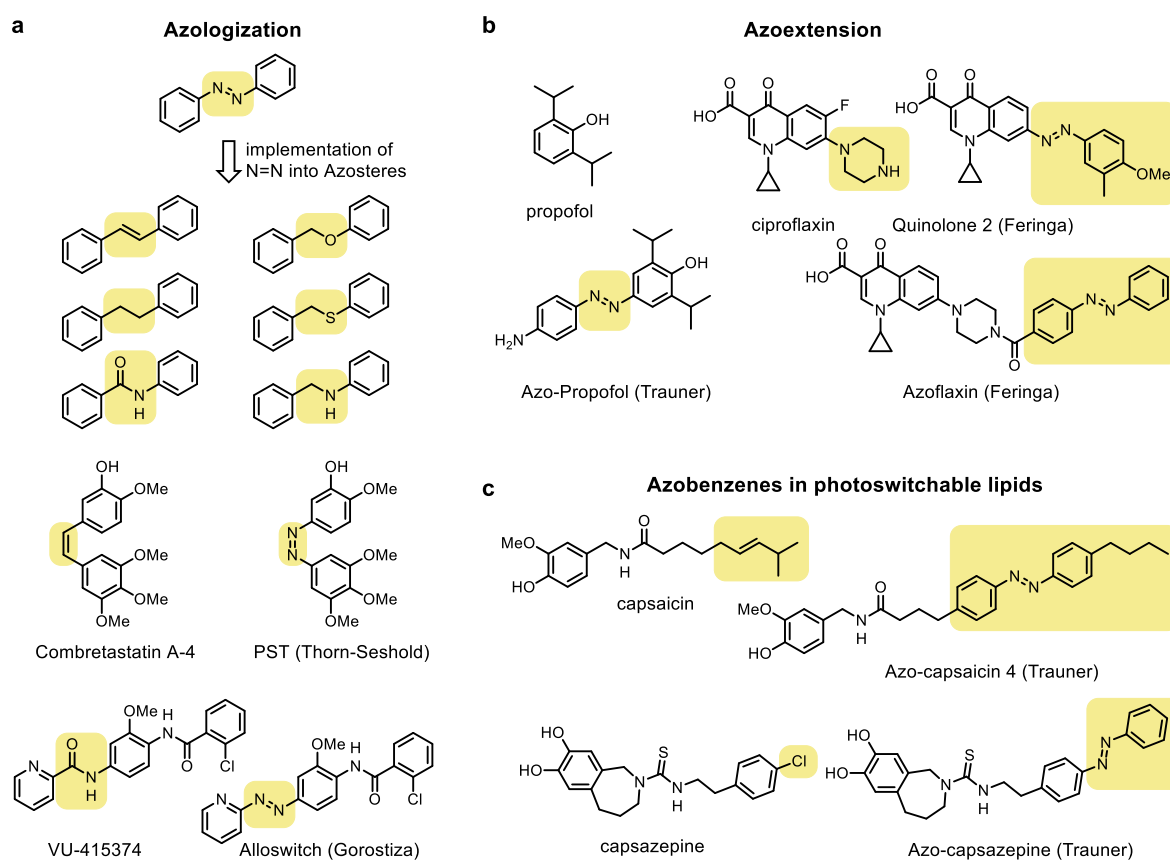


Figure 25. Common strategies for implementation of azobenzene photoswitches into pharmacophores. **a** Azologisation: The diazenyl switch is incorporated into the pharmacophore replacing a functional group with similar size bridging two aryl residues.^{273,281,282} **b** Azoextension: The structure of the pharmacophore is extended with an azobenzene at an existing aromatic ring; existing substituents might be replaced.^{283–285} **c** Azobenzenes are advantageous in binding lipophilic sites illustrated by the photoswitchable TRPV1 agonists of capsaicin and capsazepine.^{286,287}

More broadly though, azobenzenes are not common chemical motifs in drug discovery. They are usually flagged as potential pan assay interference compounds (PAINS), in part due to their photoresponsive nature and potential for N=N reduction.^{273,288,289} Therefore, screening azobenzene-containing compounds in the hope of finding novel ligands with optimized pharmacological properties is unusual, and the *true* successes (such as they are) of the high-quality probes scattered among the above-mentioned designs primarily rely on the prior availability of high-quality ligands, as the incorporation of azobenzene switches usually does not benefit the affinity or selectivity for a given target.

This leads to a situation where the core structure of the parent compound is mostly responsible for biological effects, and the isomerization of the photoswitch merely determines the level of disruptive binding properties. Photopharmacological agents are mostly tool compounds, and the difference in performance between the isomer photoequilibria that can be applied *in practice* through photoswitching must outweigh the pharmacological deficit caused by switch inclusion. Hereby, one key aspect to consider is the specific nature of the photoswitch. First, completeness of photoswitching depends on the relative absorptions of the two isomers, and thus primarily on their band separation. That can be incrementally tuned by substituents on the azobenzene,^{282,290,291} or by introducing heteroaryl-photoswitches such as arylazopyrazoles that yield near-quantitative photoswitching²⁹² (Figure 26a, b). Second, a short thermal half-life of the thermodynamically metastable Z-isomer can limit applicability because of undesired fast back relaxation, but this can be solved chemically e.g. (in a perhaps overly-compensating way) by introducing *ortho*-fluoro substituents that can increase thermal half-lives to years (Figure 26c).¹¹¹ For practical reasons, incremental fine tuning is often realised by modification of the phenyl substitution pattern. Küllmer and Arndt synthesised and characterised a small compendium of azobenzenes showcasing the incremental effects of substitution pattern on PSS values and thermal back isomerisation (representative examples are shown in Figure 26d).²⁹¹ For some applications, introducing thermally fast relaxing motifs by design is a fruitful strategy. Illumination can be carried out very precisely on a spatial scale of microns, but diffusion of activated ligands over time can (depending on assay setups) prevent this from translating to precise spatiotemporal control, especially on a *subcellular* level. Photoswitches with very short half-lives can work towards such resolution, because after diffusion out of the illuminated area, the ligand switches back to its inactive form.²⁹³

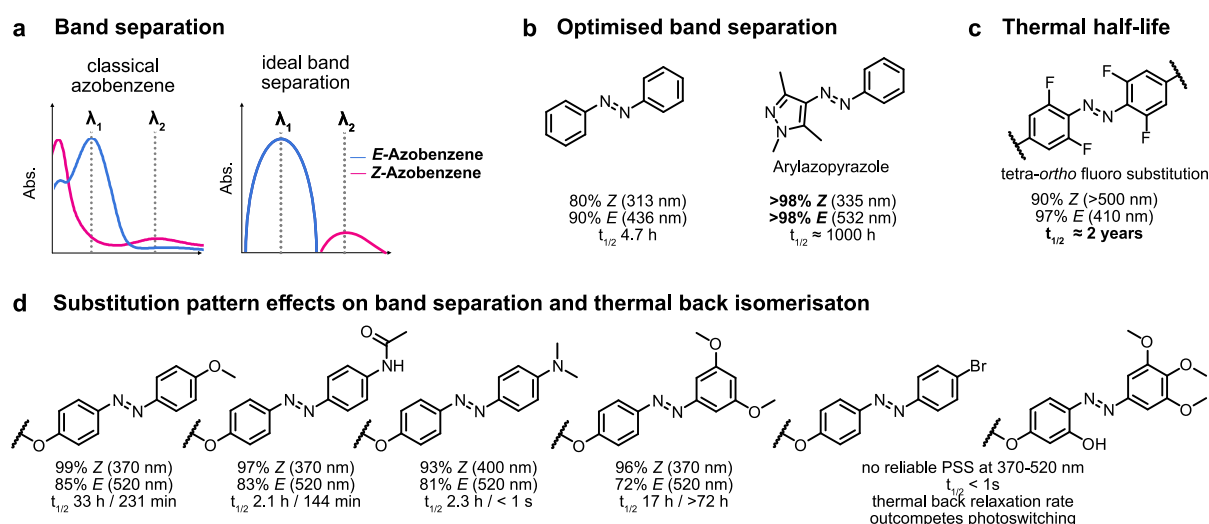


Figure 26. Optimization of photoswitch properties. **a)** Actual overlap of absorption bands in azobenzenes and ideal band separation of *E/Z*-isomers. **b)** Example structures for optimized band separation and higher bidirectional photoswitching. **c)** Tuning of thermal half-life by structural modification. **d)** Influence of substitution pattern on PSS values and thermal back isomerisation, $t_{1/2}$ values are as determined "in MeCN / in PBS".²⁹¹

TRP Channel photopharmacology

That azobenzene photoswitches are a perfect match for lipids or lipid-like compounds has been demonstrated across many targets, not only the TRPV1 modulators introduced above (Figure 25c).^{286,287} Intriguingly though, TRP channels offer biologically-driven examples of the complexity of using even apparently simple photochemical tools. For example, *trans*-azo-capsazepine was found to function as

an antagonist of voltage-activated TRPV1, but it was found to be a *cis*-antagonist when used against capsaicin-activated TRPV1. This also introduces some of the complexity specific to TRP channel pharmacology, but also shows that photoswitchable probes have the potential to gain spatiotemporal control over systems even where the mechanisms underlying it are completely unclear at the time.²⁹⁴

TRPC1/4/5 channels still lacked any suitable photoswitchable probes for spatiotemporal control before this thesis was started. However, lipid-like azobenzene tools were studied for other TRPCs even 10 years ago. TRPC channels all respond to the endogenous secondary messenger DAG (for details see section 2.1.1.2) and consequently, the first attempts for photoswitchable modulators were based on integration of azobenzenes into the lipid tail of DAG.^{295,296} These PhoDAGs enabled elucidation of DAG signalling pathways based on TRPC induced conductance, such as in mouse vomeronasal sensory neurons and sensory neurons of olfactory epithelium, showcasing another prime example of TRP channel involvement in sensory signalling.^{296,297} Inspired by this early success, Groschner developed a modified DAG structure (OptoDARg) that comprises two arachidonic acid mimicking tails each containing an azobenzene photoswitch. Gating mechanisms of TRPC channels are still elusive and much debated in the community; OptoDARg however provided a glimpse into the temporal gating mechanism of TRPC3: lipid-signalling by TRPC3 involves a “lipid gating fenestration” located within the pore region of the channel and the lipid recognition is controlled by a single glutamine residue.²⁹⁸ Later on, lipid-independent photoswitchable agonists for TRPC3/6 were introduced, based on a benzimidazole scaffold from GSK, and these were used to induce currents in native tissue such as endothelial cells and hippocampal neurons.²⁹⁹

2.1.2.4 Efficacy switches – bringing a new horizon for ideal photopharmacology?

Traditionally, most photopharmacology aimed for high photoconversion completeness between two isomers that had high potency difference based on binding affinity differences.²⁸⁹ Increasing potency differences between isomers can be seen as a semi-traditional medicinal chemistry optimization task based on structure-activity relationships (SAR), even if this task is almost never actually performed in the photopharmacology literature. However, even for a hypothetical ideal case with one binding isomer and one completely innocent isomer (Figure 27a), the incompleteness of photoswitching always results in residual effects at higher concentrations (Figure 27b). Crucially, biological effects are typically observed during *logarithmic* changes in concentration, thus photoswitches can usually only be used to exert photoreversible biological effects within a narrow concentration window called the *functional dynamic range* (FDR),^{300,301} characterized by a biologically-significant change in the more-active isomer concentration. FDR widening might therefore be realised with azoheteroarene photoswitches allowing near quantitative photoisomerization of up to 98% in both directions,^{292,302,303} but their application is only possible if the biological target tolerates incorporation of heteroarenes: and the already challenging (read: nearly impossible) task of generating one active and one *completely inactive* isomer is often impeded by this choice. Thus, traditional development of photoswitchable ligands is always a compromise between optimizing potency differential and optimizing photoconversion, to maximise a change of functional effect at switching wavelengths that are applicable in practice in an assay.

An alternative ideal scenario without such compromises, that this thesis will explore in depth, is to photoswitch efficacy instead of potency. In efficacy switching, the photoswitchable ligand is switched

between two states with (i) opposing activity (antagonist \leftrightarrow agonist) or else (ii) the biologically innocent isomer binds competitively; and the overall effect on the target thus relies on competitive binding between photoisomers (Figure 27c,d). We define *ideal* efficacy switching where the isomers have similar, and very high, affinity: hence, as long as the ligand is applied at high enough concentration to saturate its target, the isomer bound (and thus the bioactivity applied) is determined solely by the photo-determined ratio of the isomers and not by the overall drug concentration applied. Essentially, for such a scenario, the FDR is infinitely extended and transformed into a parallelised *dynamic range* (DR) solely dependent on the applied wavelength (i.e. light colour) and its resulting PSS ratio: hence we proposed the neologism **chromocontrol** to describe this mode of protein activity switching (Figure 27d). In our opinion, this feature should make efficacy switches ideal candidates for complex biological systems or *in vivo* application, because their effect no longer depends on strictly controlling drug biodistribution (as is essentially done in cell culture experiments); however, we were almost unable to find any prior theoretical treatments showing the potential of such ideal efficacy switching, and therefore we had to work out much of the ideas ourselves (see chapter 2.3.3).

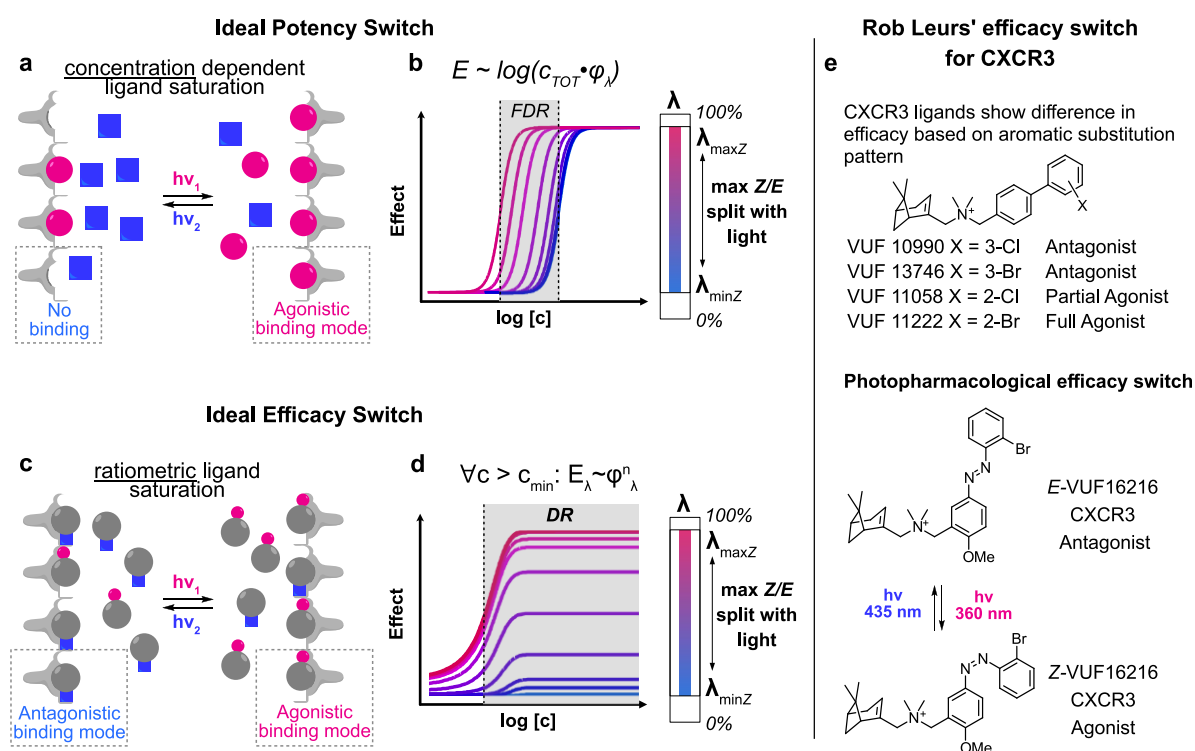


Figure 27. Model of an ideal potency switch and ideal efficacy switch. **a)** Binding model: a potency switch comprises one active isomer (agonistic activity) and one completely inactive isomer without affinity to the binding site. **b)** Dose response curves corresponding to **a** for varying PSS; c_{TOT} = total concentration, ϕ_λ = wavelength dependent percentage of active isomer. **c)** Binding model: an efficacy switch comprises two active isomers with the same affinity but opposite efficacy – one isomer acts as antagonist, one as agonist. **d)** Dose response curves corresponding to **c** for varying PSS; ϕ_λ^n = wavelength dependent ratio of isomers. **e)** Rational design for the photoswitchable efficacy switch VUF16216 based on efficacy SAR on CXCR3 by Leurs and coworkers.^{304,305}

In practice, Gorostiza, Ciruela and coworkers discovered the first efficacy-like-photoswitch of which we are aware, through chance: finding a photoswitchable ligand for G-protein coupled adenosine receptors that cycled between a partial agonistic state and a thermodynamically short-lived fully antagonistic state.³⁰⁶ Later, Leurs and coworkers were the first to report an efficacy photoswitch by design, targeting the peptidergic GPCR CXCR3.³⁰⁴ Based on an intriguing efficacy switch within their parent ligand class caused by subtle modifications on the aryl substituents, they could transfer this

remarkable functional effect to reversible photoswitching between the antagonistic Z-isomer and the agonistic E-isomer of an azobenzene substituted analogue (Figure 27e).^{304,305}

As far as we know, less than ten other examples build the entire history of published efficacy photoswitches, though none approach the model of ideality described above which is required for concentration-independence. These include studies from Feringa who used a photoswitchable ligand to interfere with bacterial communication,³⁰⁷ Frank who used photoswitchable Δ^9 -tetrahydrocannabinol derivatives to control cannabinoid receptor 1 (CB₁R) signaling,³⁰⁸ Decker who used a known efficacy switch in CB₂R targeting modulators developed by AstraZeneca,³⁰⁹ or other modulators for receptor efficacy,^{304,309,310} and again Gorostiza who controlled cardiac function with a photoswitchable muscarinic receptor agonist.³¹¹ Those examples are still not completely clear though, because the concept of an efficacy switch was not the focus of the studies, and therefore the assay setups *indicate* an efficacy photoswitch but do not prove it (nor did they seek to prove it or explore its potential).

In our analysis, the perfect targets for efficacy switches are proteins which inherently cycle between different conformations with different physiological activity (e.g. for ion channels conducting vs non-conducting). Combined with the existence of an allosteric binding site where ligands control the equilibrium between the two states, we consider the blueprint for efficacy switches is already there in nature. Targeting of drug efficacy "cliffs" as an essential parameter in tool development should, we think, result in photoswitchable tools that enable ligand-concentration-independent chromocontrol over a target. For protein targets that are anyway in dynamic structural-functional equilibria, such as opened-closed ion channels, modulating the efficacy cliff means to modulate the rates of conformational change into one direction resulting in a new equilibrium.³¹² Given that TRP channels are receptor operated channels and that endogenous messengers (often lipids) control their activity in both directions by binding to allosteric sites, over the course of this thesis we came to consider them particularly promising biological targets for the rational, systematic development of ideal efficacy photoswitches.

2.2 Aims and objectives

The success of many research projects in pharmacology/biology that aim to understand molecular connections and functions of individual proteins depends on the availability of high-quality probes. Unlike for the popular TRPV1/TRPM8 channels whose studies have recently been recognised with a Nobel prize, the detailed physiological and tissue-specific roles for the TRPC1/4/5 channels remain largely undiscovered. High quality probes for them were only discovered within the last decade, now offering new possibilities to study TRPC1/4/5 in controlled settings. However, ion channels are dynamic systems that change conformation between a closed state and an open conduction state. Endogenously, transient messengers such as lipid derivatives precisely control the transition rates between open and closed states; applying static probes results in an irreversible shift of this equilibrium, without baselining or recovery, and often incurring fatigue. Photoswitchable tools offer a workaround since they offer the possibility to reversibly switch their inherent activity profile by application of light, and so to modulate the protein equilibrium dynamically, which may more easily capture or probe the natural signalling pathways.

Photoswitchable modulators have been applied with great success for many receptors and ion channels, including TRP channels: but photoswitchable modulators for TRPC1/4/5 were not existent. Therefore, this thesis aimed to create photoswitchable modulators on the structural basis of recently discovered agonists and antagonists. Subtype specific, or highly potent, scaffolds were of particular interest as lead structures and azobenzenes were the preferable photoswitchable scaffold. Thus, I aimed to combine known high-quality TRPC1/4/5 ligands with azobenzenes, synthesize relevant compounds, evaluate them photochemically, and use them to assess TRPC1/4/5 pharmacology.

In the following chapters, I present my research towards these aims.

2.3 Results and Discussion

2.3.1 Author contributions

The following projects are again highly interdisciplinary, bridging the expertises of synthetic chemistry, chemical biology, biology, pharmacology, electrophysiology, structural biology, and neuroscience. While this section mainly outlines my personal scientific contributions and achievements in those papers, I want to again emphasize the importance of my collaboration partners who constantly supported the scientific progress of my projects with their diverse expertise, especially Michael Schaefer and his coworkers who were part of the project from early screenings to establishing the efficacy switch concept and application in deep tissue. A research project at this interdisciplinary scale would not have been possible without passion and commitment from all sides.

In the following I will briefly describe my contribution to each project:

Publication One: BTDAzo is a photoswitchable TRPC5 agonist

I helped to design target compounds, performed synthesis, structural characterization, UV/VIS, and photocharacterization of **BTDAzo** and derivatives. I advised collaboration partners with photoswitching trouble shooting for applications in cell biology and tissue slices. I coordinated data assembly, prepared figures, and assisted in writing the manuscript.

Publication Two: Elucidating the power of efficacy switches by means of the highly potent TRPC4/5 photoswitches AzPico and AzHC

I independently co-designed target compounds, and performed synthesis, structural characterization, UV/VIS, and photocharacterization of **AzPico**, **AzHC** and derivatives. I advised collaboration partners as intersection between the individual groups. I coordinated data assembly, prepared figures, helped develop the conceptual framework for understanding ideal efficacy photoswitching, and wrote the manuscript together with my supervisor Oliver Thorn-Seshold.

2.3.2 Publication One: BTDAzo is a photoswitchable TRPC5 agonist

TRPC4/5 are close homologues and the majority of probes that actuate them are not subtype selective. One exception is the only moderately potent but very TRPC5 selective agonist **BT**D which serves as a lead core structure in the following work. The binding mode of **BT**D on TRPC5 is elusive and prevented rational design, therefore we chose azo-extension approaches, by installing azobenzene photoswitches on various points of the lead structure **BT**D. The biologically most promising candidate **BTDAzo** comprised a hitherto unstudied phenylazo-benzothiadiazine photoswitch that pleasingly showed excellent bidirectional photoswitching, reaching up to 94 % *Z* (380 nm) and 87 % *E* (520 nm) without photoinstability over many cycles. Its thermal *Z*→*E* relaxation was significantly slower than timescales of channel switching experiments, therefore the applied wavelengths and the corresponding PSS solely determine the experimental outcome (Paper Figure 2, here page 75).

We identified **BTDAzo** as a reversibly photoswitchable agonist for TRPC5 via calcium influx imaging on a plate reader assay (the other analogues were found to be either inactive or not reversible and were not pursued further). **BTDAzo** showed several good to outstanding features. Firstly, **BTDAzo** is lit active, a good feature for photopharmaceuticals because activation can be precisely phototriggered, without background activity during incubation. Secondly, calcium influx photomodulation is reversible over many cycles, which is very good. Thirdly, the potency of *Z**-**BTDAzo** (asterisk* refers to a PSS composition, not the pure isomer) is quite good in an absolute sense (1.5 μM), but excellent in a relative sense, since the potency of **BT**D itself is 1.4 μM, and potency retention is very rare in photopharmacology; this not only is suggestive for mechanistic aspects, but also underscores the utility of **BTDAzo**. Excellently, **BTDAzo** is selective for TRPC5 and TRPC1:5 over TRPC4, as was **BT**D (Paper Figure 3, here page 76).

The plate reader setup was limited to fixed wavelengths of mounted LEDs, therefore we also used a monochromated continuous light source and measured Ca²⁺ influx on single cells with a microscope to determine cellular action spectra. Intriguingly, we found a striking *mismatch* of cellular Ca²⁺ influx action spectra to the PSS values in cuvette, when modelling channel activity as purely dependent on *Z* isomer concentration. We next showed that **BTDAzo** photomodulates TRPC5 currents by patch clamp electrophysiology, a non-optical readout. The I/V curves show photoswitching between a conducting state for *Z**-**BTDAzo** and *complete* recovery to basal activity for *E**-**BTDAzo**, and photoswitching currents were reproducible over > 60 cycles. In terms of photoswitching power, such features are truly outstanding: but again this represents a striking *mismatch* to cell-free PSS values (which indicated *incomplete* photoswitching at the used wavelengths, hence substantial background activation would be expected). We suggest that competitive binding between the two isomers might explain this phenomenon, and started to explore this by competing *E*-**BTDAzo** against the parent compound **BT**D where we indeed found an inhibitory effect of *E*-**BTDAzo** on **BT**D induced Ca²⁺ signals: a result that is highly suggestive of an efficacy switch mechanism, and which would (if true) greatly enhance the value of **BTDAzo** as an ion channel tool compound (Paper Figure 3 / Figure S7, here pages 76 and 215).

These TRPC5 studies so far had all been demonstrated on cellular systems which were genetically modified to over-express TRPC5. Since TRPC5 is expressed in a subset of brain dopamine neurons

where it contributes to crucial signalling events including reproductive hormone signalling, our collaborators next assayed **BTDAzo** for photocontrol of mouse brain tissue slices: where Ca^{2+} signals were indeed photocontrolled, though now from endogenous TRPC5 expression levels (Paper Figure 4, here page 78).

In summary, we developed the first photoresponsive modulator for TRPC5, with excellent selectivity over the closest homologue TRPC4, and unexpectedly excellent bidirectional photoswitching of bioactivity in cells (switching from basal activity to full activation of TRPC5 currents/ Ca^{2+} signals). Furthermore, we demonstrate the usability of this tool in complex tissue with low TRPC5 expression levels, and thus consider **BTDAzo** a valuable tool for spatiotemporally precise TRPC5 studies.

Photopharmacology

BTDAzo: A Photoswitchable TRPC5 Channel Activator**

Markus Müller, Konstantin Niemeyer, Nicole Urban, Navin K. Ojha, Frank Zufall, Trese Leinders-Zufall, Michael Schaefer, and Oliver Thorn-Seshold*

Abstract: Photoswitchable reagents can be powerful tools for high-precision biological control. TRPC5 is a Ca²⁺-permeable cation channel with distinct tissue-specific roles, from synaptic function to hormone regulation. Reagents giving spatiotemporally-resolved control over TRPC5 activity may be key to understanding and harnessing its biology. Here we develop the first photoswitchable TRPC5-modulator, **BTDAzo**, to address this goal. **BTDAzo** can photocontrol TRPC5 currents in cell culture, as well as controlling endogenous TRPC5-based neuronal Ca²⁺ responses in mouse brain slices. **BTDAzos** are also the first reported azobenzothiadiazines, an accessible and conveniently derivatised azoheteroarene with strong two-colour photoswitching. **BTDAzo**'s ability to control TRPC5 across relevant channel biology settings makes it suitable for a range of dynamically reversible photoswitching studies in TRP channel biology, with the aim to decipher the various biological roles of this centrally important ion channel.

Introduction

The twenty-eight Transient Receptor Potential (TRP) channels have crucial roles in sensing and integrating a wide range of stimuli.^[1] Better-known members include TRPV1

(heat) and TRPM8 (cold) for which a 2021 Nobel Prize was awarded, and TRPA1 (electrophiles). As these channels are expressed in many tissues but play different biological roles in these tissues,^[2] potentially with time-dependent aspects, a range of photoswitchable ligands have been actively developed to elucidate their tissue- and time-specific roles through spatiotemporally precise modulation.^[3] Notable photoswitchable TRP ligands include analogues of diacylglycerols (PhoDAGs)^[4,5] and of small polar GSK ligands^[6] for TRPC2,3,6; azo-vanilloids (azCA4,^[7] red-azCA4^[8]) for TRPV1; and TRPswitch^[9] for TRPA1.

TRPC5 is implicated in a range of tissue-dependent roles in physiology as well as in disease, with brain functions from synaptic plasticity and hormone regulation to potential importance in metabolic medicine.^[2,10–12] TRPC1,4 and 5 share substantial structural overlap which drives the typically poor channel selectivity of TRPC1/4/5 ligands; however, drug discovery for TRPC5 has recently yielded a treasure trove of valuable ligands.^[13,14] Weak antagonists were first identified from screening,^[15] before Christmann, Beech, Waldmann and co-workers identified TRPC5 as one of the targets of the potent but nonselective TRPC4/5-targeting natural product agonist **Englerin A**^[16,17] (Figure 1a). Moderately potent synthetic agonist **BTD** was also

[*] M. Müller, Dr. O. Thorn-Seshold

Department of Pharmacy, LMU Munich
 Butenandtstrasse 7, 81377 Munich (Germany)
 E-mail: oliver.thorn-seshold@cup.lmu.de

K. Niemeyer, N. Urban, Prof. Dr. M. Schaefer
 Rudolf-Boehm-Institute of Pharmacology and Toxicology, Leipzig
 University
 Härtelstraße 16–18, 04107 Leipzig (Germany)

Dr. N. K. Ojha, Prof. Dr. F. Zufall, Prof. Dr. T. Leinders-Zufall
 Center for Integrative Physiology and Molecular Medicine, Saarland
 University
 Kirrbergerstraße 100, 66421 Homburg (Germany)

[**] A previous version of this manuscript has been deposited on a preprint server (<https://doi.org/10.26434/chemrxiv-2022-hvh6b>).

© 2022 The Authors. Angewandte Chemie International Edition published by Wiley-VCH GmbH. This is an open access article under the terms of the Creative Commons Attribution Non-Commercial License, which permits use, distribution and reproduction in any medium, provided the original work is properly cited and is not used for commercial purposes.

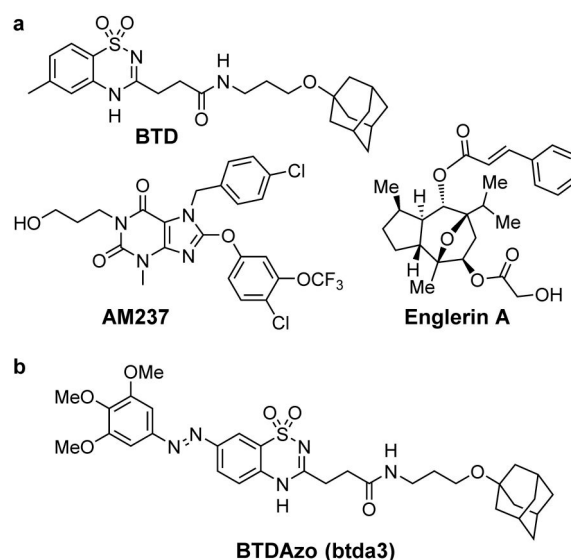


Figure 1. Design (see Supporting Information for high-resolution vectorial copies of all main text Figures). a) Known TRPC5 agonists **BTD**, **Englerin A**, **AM237**. b) **BTDAzo**, the best photoswitchable agonist of the series **btda1–btda7** (cf. Figure S1).

identified by Schaefer, with the unusual feature of excellent selectivity for TRPC5 and no activity on TRPC4.^[18] Boehringer-Hydra disclosed high-potency xanthine antagonist leads intended to treat anxiety,^[19,20] that Muraki, Beech and co-workers characterised as effective TRPC5 modulator tool compounds;^[21] Bon, Muraki and co-workers characterised these xanthines further to identify compounds with intriguing selectivity and mixed agonist-antagonist profiles (e.g. **AM237**; Figure 1a)^[22] as well as identify the Pico145 binding site.^[23,24]

However, no photoswitchable TRPC5 ligands have yet been reported, which could help to study its tissue- and time-resolved biological roles. We therefore wished to create TRPC5-selective photoswitchable ligands, with minimal effects on TRPC1/4 channels, as high spatiotemporal-precision tools with useful biochemical selectivity. **BTD** represented a good basis structure for this goal. Although its potency is moderate (EC_{50} $1.4 \pm 0.3 \mu\text{M}$), it selectively activates homomeric TRPC5 or heteromeric TRPC[1/4/5] channel complexes that contain TRPC5 subunits, while not activating homomeric TRPC4: making it a more selective tool than e.g. **AM237** or **Englerin A**. We set out to create a photoswitchable analogue of **BTD** for applications in researching the role of endogenous TRPC5 in mammalian cells and tissue slices.

Results and Discussion

Design and Synthesis

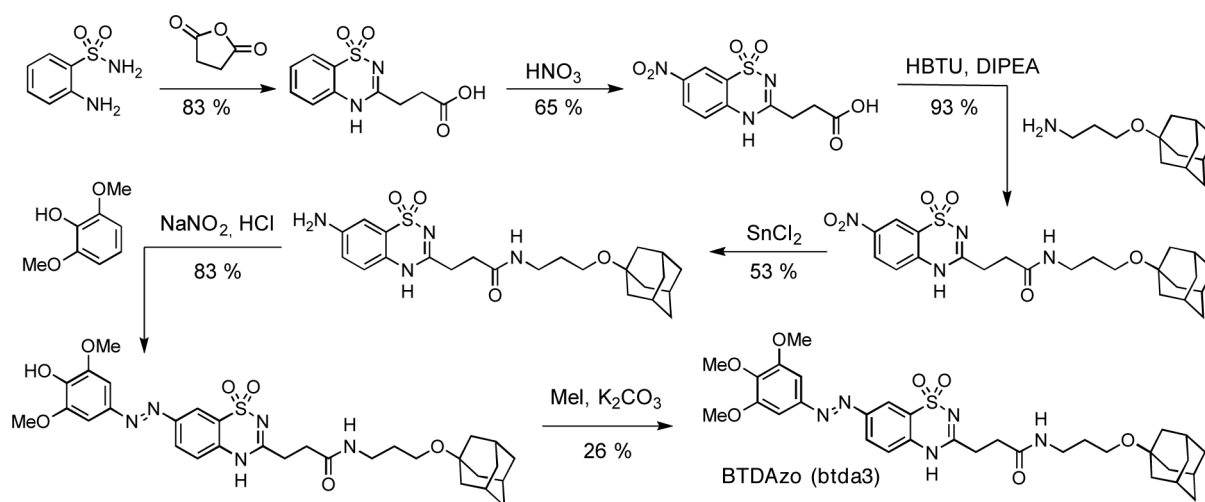
The TRPC5 binding mode of **BTD** is unknown, and structure-activity-relationship data are limited (the 4-methyl group on the benzothiadiazine can be deleted, but shorter spacers between the adamantane and benzothiadiazine abolish activity).^[18] We tested applying the bidirectional photoswitch azobenzene to the **BTD** scaffold at each end, presuming that one end could be sterically tolerated.

Firstly, we extended the azobenzene from the benzothiadiazine ring, though in *para* to the nitrogen. This was chosen hoping that this unknown azoheteroarene that is electronically similar to a *para*-anilide, could provide similarly desirable photoswitching properties, as are necessary for creating an effective photopharmaceutical: i.e. bidirectional photoswitching with near-UV and blue-green light each achieving high photostationary states (PSSs).^[25] We varied the azophenyl substitution pattern to scan for different polarities, PSSs, and *Z*→*E* spontaneous relaxation rates: comparing unsubstituted, with *para*-methoxy and trimethoxy (improved PSSs), and *para*-hydroxy (faster relaxation) designs **btda1**–**btda4** (Figure S1). Secondly, we replaced the hydrophobic adamantyl group with the azobenzene: retaining the oxyether attachment site because of its beneficial effects on photoswitching,^[26] and employing an unsubstituted, *para*-methoxy, or a bulky bis-isopropyl azobenzene to increasingly mimic the hydrophobicity of the adamantyl, in case this (rather than sterics) were the driving force of **BTD** binding. This yielded designs **btda5**–**btda7** (Figure S1).

The seven candidates **btda1**–**btda7** were assembled over three to six least linear steps, with good yields in all steps for except the final *O*-methylations of **btda2** and **btda3**; representative synthesis of **btda3** is shown in Scheme 1. **btda1**–**btda7** were typically obtained in 10 mg batches and excellent purity, sufficient for biological evaluations (see Supporting Information for details).

Photoswitchability

Pleasingly, the as-yet unstudied phenylazo-benzothiadiazine (**btda1**–**btda4**) proved to be an excellent photoswitch, with performance recalling that of *para*-anilides. As expected for mono/bis-*para*-alkoxy azobenzenes,^[26] **btda5**–**btda7** also had high PSS ratios and efficient photoswitching. As **btda3** later gave the best biological performance, it was renamed **BTDAzo**, and studied in detail. Like classical azobenzenes, the *E*-isomer is thermodynamically preferred, and all-*E*



Scheme 1. Synthesis of **BTDAzo** (**btda3**).

populations are reached by maintaining DMSO solution stocks at 60 °C overnight. **BTDAzo** could be reversibly photoswitched between majority-*E* and majority-*Z* populations, reaching solvent-dependent PSSs with up to 94% *Z* (380 nm) and 87% *E* (520 nm) in apolar solvents that mimic the expected cellular lipid environment for this hydrophobic compound (Figure 2a–c; Figure S2). The spectral separation between *E* and *Z* bands that results in the *Z* absorption minimum being located at the same wavelength as the *E* absorption maximum (Figure 2d) is the driver of the high-*Z* PSS.

Photoswitching in aqueous media was also strong and was photoreversible over many cycles with no photoinstability noted (Figure 2e). *Z*→*E* thermal relaxation below 40 °C was significantly slower than the timescales of channel switching experiments (Figure S3). PSS spectra and discus-

sions of photochemistry for other **btda** derivatives are given in the Supporting Information in Figures S3 and S4.

Cellular TRPC5 Photopharmacology

We initially screened **btda1**–**btda7** as photoswitchable TRPC5 agonists in cells, using human embryonic kidney cell line HEK293 stably transfected to express a mouse TRPC5-CFP fusion protein (HEK_{mTRPC5-CFP}). HEK_{mTRPC5-CFP} cell suspensions were loaded with the fluorescent Ca²⁺ indicator dye precursor Fluo-4/AM, washed, and dispensed into black pigmented clear-bottom 384-well microplates to monitor ion channel opening in a custom-made fluorescence imaging plate reader device. By adding serially diluted compounds to single wells, this is a convenient high-throughput method to obtain concentration-response curves before and during controlled application of ultraviolet light to the bottom of the microplate. We wished to use alternating cycles of moderate intensity 360/447 nm light for substantial *E*⇌*Z* photoswitching. The fluorescent Ca²⁺ indicator Fluo-4 was either excited at 447 nm for combined detection and off-switching, or at low intensities at 470 nm to achieve a lower impact on **btda** photostationary states due to the small extinction coefficients in the cyan (Figure S4).

BTDAzo (**btda3**) was the best hit from this screening: it gave highly repeatable, bidirectional Ca²⁺ influx signals with low basal activity as the relaxed *E* isomer and robust responses upon photoswitching with 365 nm light (Figure 3a). **BTDAzo** showed several outstanding features. Firstly, the potency of **Z-BTDAzo** (EC₅₀ 1.5 μM for the mostly-*Z* PSS at 365 nm; for simplicity now referred to as “*Z*-potency”; Figure 3b) was as good as that of its parent molecule **BTDA** (EC₅₀ 1.4 μM);^[18] potency matching is only very rarely achieved in photopharmacology.^[27] Secondly, not only was all-*E*-**BTDAzo** at 50 μM fully inactive on TRPC5 (Figure 3b), and nearly non-responsive to 470 nm imaging (initial 60 s of Figure 3a), but using 440 nm light to photo-switch 50 μM **BTDAzo** that had previously been in the mostly-*Z*-state reduced channel currents to below those seen with mostly-*Z* **BTDAzo** at just 1.5 μM. **BTDAzo**'s combination of activity exclusively in the *Z*-isomer, with efficient *Z*→*E* photoswitching at 440 nm in cells, helps give it such effective bidirectional *photoswitching of bioactivity*: although the actively antagonistic effect of its *E*-isomer was later identified as a third important factor (see below). Thirdly, no “biological fatigue” was seen, as photoswitching of **BTDAzo** was highly repeatable over many cycles. Thus **BTDAzo** could be a robust tool for complex studies (particularly since, as a lit-active photoswitch, it avoids background bioactivity in non-illuminated cells). The other **btidas** were not good tool compounds: **btda1,2,4** gave much slower bulk photoresponses, while **btda5**–**btda7** were inactive (see Figure S5 and Supporting Information).

Since the plate imaging device uses single-color light-emitting diodes for Fluo-4 detection as well as for **BTDAzo** photoswitching, no continuous spectral information could be gathered in this assay. We therefore used single-cell Ca²⁺ imaging with a Xenon lamp-equipped monochromator as

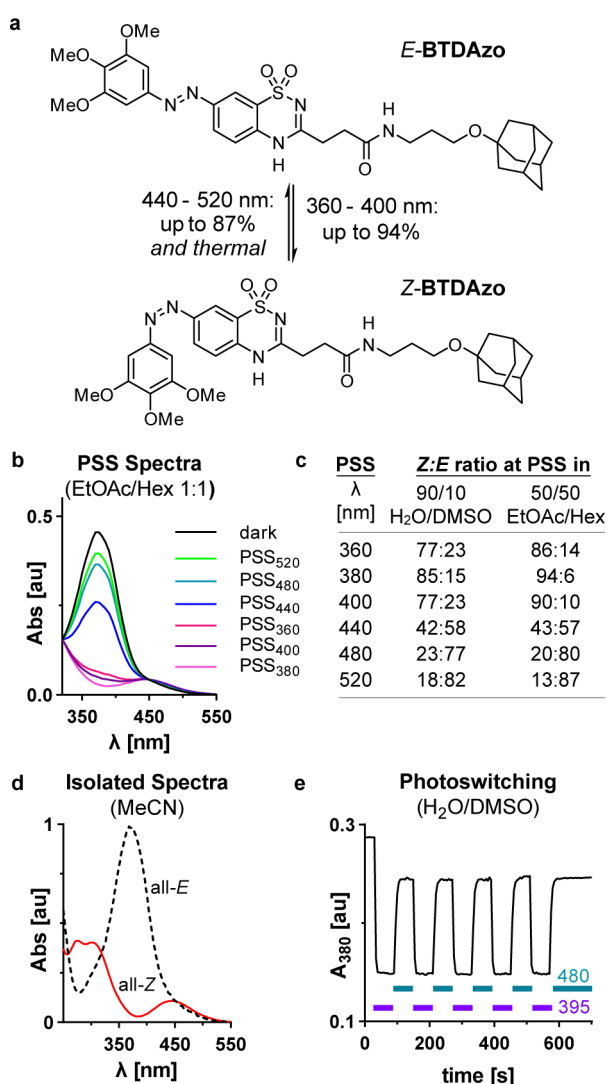


Figure 2. Photocharacterisation. a) *E*⇌*Z* isomerisations of **BTDAzo**. b) *Z*:*E* ratios at PSS depending on environment. c) PSS spectra of **BTDAzo** in H₂O/DMSO. d) Spectra of pure *E*- and *Z*-**BTDAzo** (inline HPLC detection). e) **BTDAzo** can be reversibly photoswitched between PSS states.

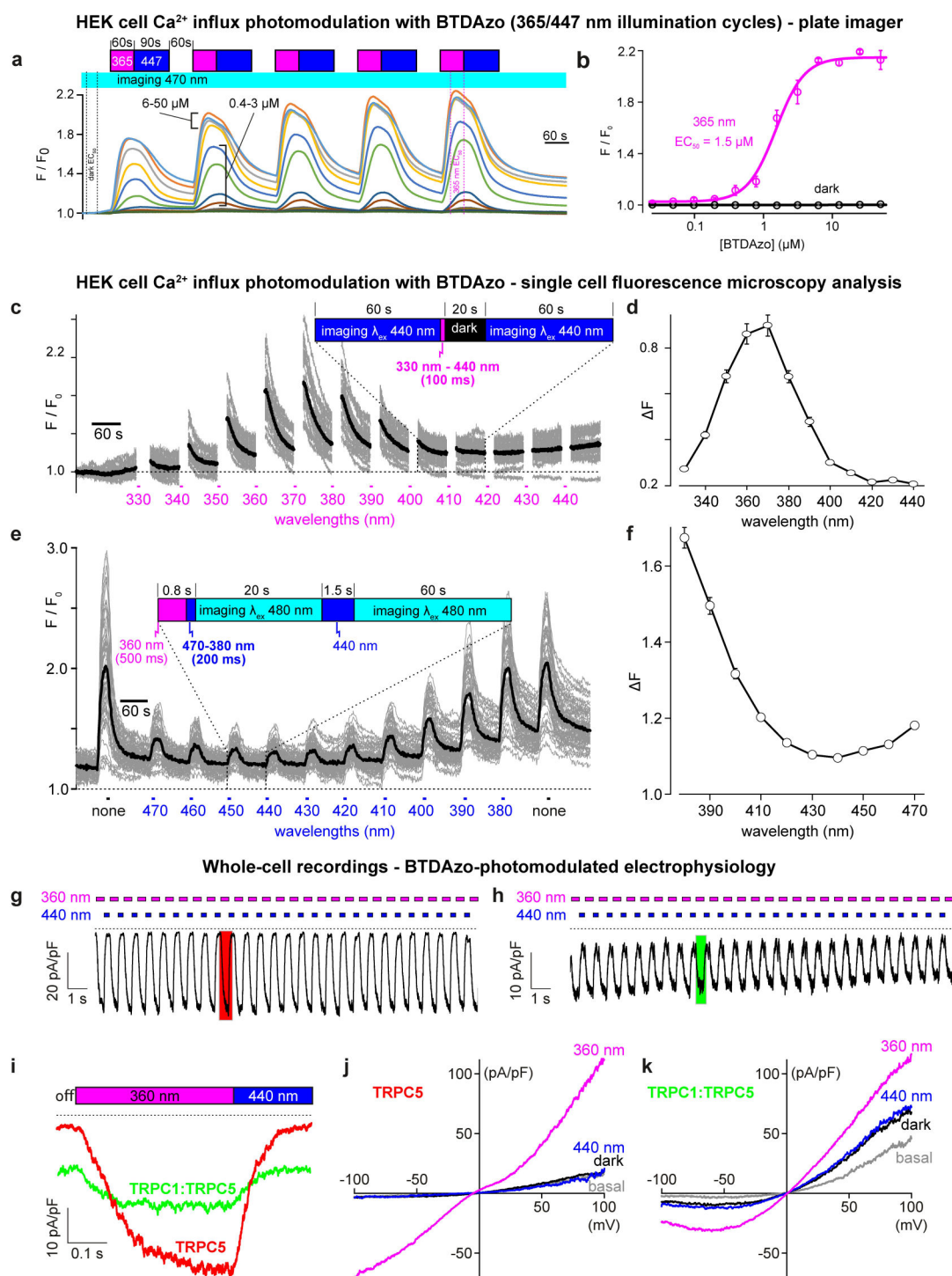


Figure 3. Cellular TRPC5 photoswitching with BTDAzo (see Supporting Information for high-resolution vectorial copies of all main text Figures). a), b) Reversible Ca²⁺ influx modulation with BTDAzo under cycles of 365/447 nm illumination, and peak amplitudes (mostly Z-BTDAzo), as detected in Fluo-4-loaded HEK_{mTRPC5-CFP} cell suspensions by fluorescence plate imager (values in b are means ± S.E., averaged over the time periods illustrated between dotted vertical lines in panel a). For additional information see Figure S5. c)–f) Microfluorometric single cell analysis (60 grey traces: single cells; black trace: averaged signal) of TRPC5 activation measured with a monochromator-equipped Xenon light source. c), d) Cellular action spectrum for stimulation of Ca²⁺ influx into single HEK_{mTRPC5-CFP} cells by E→Z BTDAzo isomerisation. e), f) Cellular action spectrum for preventing Ca²⁺ influx, by Z→E BTDAzo isomerisation at various wavelengths immediately after E→Z isomerisations. g)–i) Electrophysiological whole-cell recordings of TRPC5 currents in voltage clamp (V_h = −80 mV) mode. g) Ionic currents in a TRPC5-expressing HEK293 cell during 60 consecutive cycles of 360/440 nm illumination in the presence of 10 μM BTDAzo. Dotted line shows zero current level (half of each time course shown). h) Ionic currents in TRPC5/TRPC1-co-expressing HEK293 cell, as in panel g. i) Magnification of single on-off cycles taken from the traces shown in (g), (h) as indicated by the coloured boxes. j)–k) I/V curves of whole cell currents in voltage-clamped TRPC5- or TRPC5/TRPC1-expressing cells exposed to 360 nm and 440 nm light with 10 μM BTDAzo in the bath solution. Note the distinct shape of the I/V curve in panel k, with smaller inward current component. All data from a minimum of 3 independent experiments, each run in technical duplicates.

excitation light source to study the cellular action spectra (channel current dependency on wavelength) and cellular power spectra (channel current dependency on applied photon flux), and to optimise assay illumination protocols. $E \rightarrow Z$ action spectra showed optimal photo-switch-on response to ca. 360–370 nm (Figure 3c, d) when measured in flux-limited conditions designed to minimise photobleaching (power spectrum Figures S6a and S6b). $Z \rightarrow E$ action spectra showed optimal photo-switch-off response to ca. 420–460 nm (Figure 3e, f) in flux-limited conditions (power spectrum Figures S6c and S6d). The striking action spectrum peak sharpness (Figure 3d), and the mismatch between the poor photoswitching completion in homogeneous polar media such as DMSO:water (Figure 1c) and the excellent performance in cells, indicate that cell-free measurements are only approximately predictive of the cellularly-relevant photoswitching of this lipophilic photoswitch (discussions in Supporting Information at Figure S4 [relaxation timescales] and Figure S6 [action spectra]). The power spectra additionally highlight that bulk $E \rightarrow Z$ and $Z \rightarrow E$ photoswitching in the cellular setting proceed at comparable rates (50 % conversion at 30 mJ cm^{-2} for 360 nm and 50 mJ cm^{-2} for 440 nm; Figure S6); this is a reminder that the ratio of E/Z extinction coefficients is more important for photoswitching performance in microscopy, than are their absolute magnitudes (ca. tenfold lower at 440 nm than at 360 nm).

We next performed patch clamp experiments, a non-optical current readout that can orthogonally confirm and characterise the specificity of channel modulation. In the presence of $10 \mu\text{M}$ **BTDAzo**, on/off-photoswitching of ionic currents in TRPC5-expressing cells was fully reproducible over 60 cycles (Figure 3g) with 360 nm rapidly opening then 440 nm almost fully reclosing channels to baseline conductivity (Figure 3i). The efficient channel closure following 440 nm illumination was seen over the entire current-voltage plot range (Figure 3j).

An interesting question raised by this result is: why are TRPC5 currents so efficiently shut down to baseline by photoswitching at 440 nm (Figure 3g), when photoswitching at this wavelength is not complete (ca. 42 % Z remaining in cell-free tests either in polar protic or apolar aprotic media)? One hypothesis is that the E -isomer which is inactive on the channel (Figure 3b, “dark” curve) binds TRPC5 competitively to the Z -isomer and so prevents channel opening, potentially with complex stoichiometry from the tetrameric nature of the channel. To begin exploring this without the complications of uncertain photostationary states, we competed E -**BTDAzo** against the parent activator **BTD**. We found that it indeed shuts down **BTD**-induced Ca^{2+} currents, providing initial support for this hypothesis (Figure S7).

BTD is a strong tool compound because of its high selectivity for TRPC5-containing channels,^[18] while most other TRPC5 ligands also target TRPC4. To begin testing whether **BTDAzo** retains this TRPC5-selectivity, we imaged TRPC4-expressing HEK293 cells in FLIPR, and pleasingly saw no TRPC4-mediated photostimulation of Ca^{2+} influx responses under any of the **BTD** derivatives applied at concentrations up to $50 \mu\text{M}$, including **BTDAzo** (Figure S8).

We did not assay and so cannot exclude that TRPC1/C4 channels might be activated by **BTDAzo**, so the selectivity we assess of **BTDAzo** for TRPC5 vs. TRPC4 is based on data for TRPC4:C4 channels only (note however that **BTD** itself does not activate TRPC1/C4). Patch clamp recordings in TRPC1/TRPC5 co-expressing cells exposed to $10 \mu\text{M}$ **BTDAzo**, however, showed strong and reversible photo-control (Figure 3h, i) of inward and outward currents, with a characteristic shape of the I/V curve that is known to result from the assembly of TRPC1 and TRPC5 channel subunits into heteromeric channel complexes (Figure 3k). This finding is reminiscent of the parent compound **BTD**, which also activates heteromeric TRPC1/C5 channel complexes.

Taken together, we conclude that **BTDAzo** is a fully reversible, binary “fully-off \rightleftharpoons fully-on” performing photo-switchable agonist for cellular TRPC5 channels.

Tissue Slice Photopharmacology—Hypothalamic Mouse Dopamine Neurons

We now wished to use **BTDAzo** to probe the role of TRPC5-dependent responses in dopamine (i.e. tyrosine hydroxylase-positive, Th^+) neurons of the hypothalamic arcuate nucleus (ARC) (Figure 4a). TRPC5 contributes to both spontaneous oscillatory activity and persistent activation after stimulation with the maternal signalling hormone prolactin^[28] making TRPC5 essential for normal prolactin homeostasis of the body (Figure 4a).^[11]

We took slices through the ARC of mice expressing the Ca^{2+} indicator GCaMP6f in Th^+ neurons (Figure 4b, c) to test whether **BTDAzo** illumination could achieve photo-control over Ca^{2+} responses at endogenous TRPC5 expression levels. In Th^+ neurons, with sparse endogenous expression of TRPC5, long-lasting oscillatory Ca^{2+} signals are seen with delayed onset after prolactin receptor or after direct TRPC5 stimulation. These are a secondary response which is due to Ca^{2+} entry through voltage-gated channels, that are activated after sustained depolarising Na^+ and Ca^{2+} influx through TRPC5; and therefore, the measured Ca^{2+} responses are seen as trains of more frequent and higher-intensity spikes, as compared to baseline.

Spontaneous Ca^{2+} response trains in Th^+ neurons after treatment with **BTDAzo** and 355 nm photoactivation matched those upon treatment with either prolactin or **BTD** (Figure 4d, f). Genetic deletion of the TRPC5 channel in the $\text{Th-GCaMP6f-}\Delta\text{Trpc5}$ mouse prevented the increase in Ca^{2+} activity in Th^+ neurons (Figure 4g), indicating the channel selectivity of **BTDAzo** in the slice setting. The area under the curve (AUC) of the Ca^{2+} signals quantifies that **BTDAzo** does not induce changes under 488 nm illumination alone, but needs both isomerisation with 355 nm light and TRPC5 expression to generate Ca^{2+} rises ($p < 0.0001$) (Figure 4h, i; Figures S9a–S9c); and the delay time before the increase of Ca^{2+} activity was inversely correlated to the UV photon flux applied, matching expectations for a photo-controlled tool (Figure S9d, e).

Thus, **BTDAzo** can be used in complex tissue slice settings as a highly selective direct activator of the TRPC5

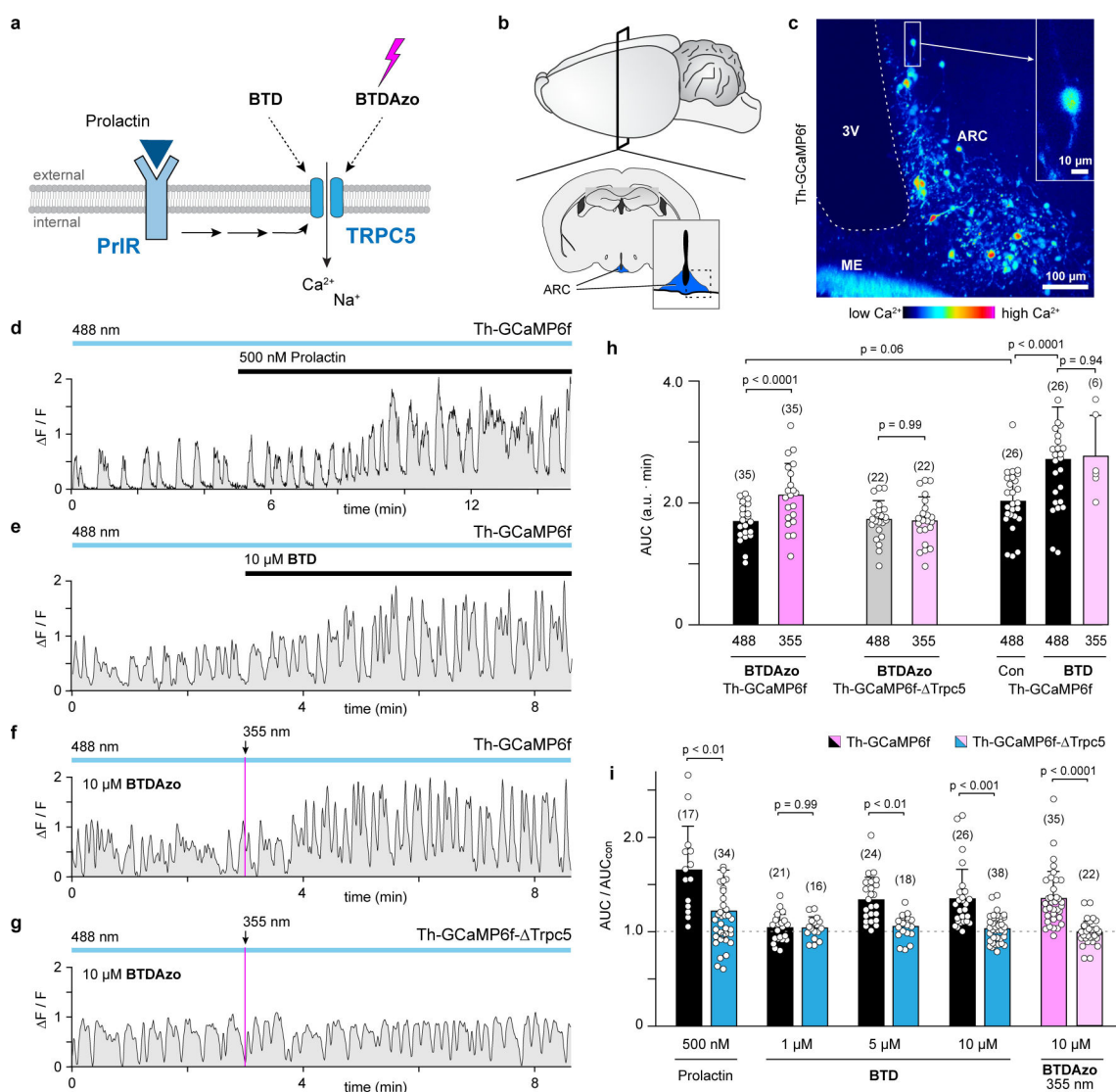


Figure 4. BTDAzo photocontrols endogenous TRPC5-dependent Ca²⁺ responses in mouse brain (see also Figure S9). a) Cascade model for TRPC5-dependent cation channel activation in Th+ neurons of the hypothalamic arcuate nucleus (ARC) after stimulation of the prolactin receptor (PrIR). b) Cartoon of the coronal brain slice, and region of the ARC (blue). Dashed box indicates the ARC region in (c). c) Pseudocoloured image of Th+ neurons expressing GCaMP6f in a mouse brain slice. Inset: Zoom on a GCaMP6f neuron from the dorsomedial region of the ARC. (3V, third ventricle; ME, median eminence). d)–g) Original traces of spontaneous Ca²⁺ responses in Th+ neurons of Th-GCaMP6f mice, stimulated with prolactin (d), BTDAzo (e), or BTDAzo followed by E→Z isomerisation using 355 nm UV laser stimulation (f: total UV exposure time, 14.1 ms; response delay, 48 s). f), g) Panel (g) shows data for the TRPC5-deficient Th+ neuron of Th-GCaMP6f-ΔTrpc5 mouse (total UV exposure time, 14.5 ms). h) Area under the curve (AUC) of Ca²⁺ signals when applying BTDAzo under 488 or 355 nm in wildtype or Trpc5 deficient Th+ neurons, compared with wildtype cosolvent only (Con) or BTDAzo controls. Two-way ANOVA: F(3, 158) = 3.011, p < 0.05. i) Wildtype or knockout AUCs normalized to their controls (cosolvent or 488 nm stimulation of BTDAzo) show prolactin, BTDAzo, and BTDAzo after 355 nm photoswitching stimulate TRPC5-dependent Ca²⁺ increases. Kruskal-Wallis ANOVA: χ²(9) = 95.24, p < 0.00001. [h, i]: number of cells is indicated in parentheses above each bar; for full description of material methods and statistics, see Supporting Information.]

channel complex, that acts only upon E→Z photoswitching to measurably increase sustained influxes of Ca²⁺ mimicking those seen with the endogenous upstream activating hormone, prolactin.

Conclusion

Photopharmaceuticals are proving to be powerful and flexible tools to non-invasively manipulate and study biological processes, with the high temporal and spatial resolution that is appropriate to their biology.^[29,30]

We here report the first photoswitchable ligand for the ion channel TRPC5. BTDAzo can reversibly photoswitch cellular channel activity between opened (conducting) and

full baseline states, and its potency and selectivity for TRPC5 against the typical cross-hit channel TRPC4 are additional promising features for future research. Its channel activation is potent enough to be applicable not only in overexpression systems, but in brain tissues with sparse endogenous TRPC5 expression levels, and its pharmaceutical properties make it suitable for tissue slice use. Following the proof-of-concept brain slice assay we have tested, we consider **BTDAzo** as a valuable tool to investigate the various roles of TRPC5 (and so distinguish them from the distinct roles of TRPC4) in brain function, including their potential in the study and treatment of metabolic disease.^[12]

We believe this is also the first report of azobenzothiadiazines as photoswitches for cell biology. It can give favourably complete bidirectional photoswitching with rapid response under biologically available wavelengths, and its easy synthesis and handling recommend it for use towards other photopharmaceuticals.

Challenges for the ongoing development and use of TRPC5 photopharmaceuticals in focus in our group include i) improving ligand potency, and ii) improving solubility and bioavailability, which should broaden the scope of applications of these ligands towards real-time in vivo uses.^[31] Nevertheless, **BTDAzo** is a reliable, potent TRPC5 photoswitch that can easily find applications in cell culture and slice use towards a better understanding of this truly remarkable protein.

Acknowledgements

We thank the German Research Foundation (DFG: SFB TRR 152 number 239283807 projects P10 to F.Z./T.L.-Z., P18 to MS, P24 to O.T.-S.; Emmy Noether number 400324123 to O.T.-S.) for funding. Open Access funding enabled and organized by Projekt DEAL.

Conflict of Interest

The authors declare no conflict of interest.

Data Availability Statement

The data that support the findings of this study are available from the corresponding author upon reasonable request.

Keywords: Agonists · Cation Channels · Ligand Design · Photopharmacology · Prolactin Signaling

- [1] “Mammalian Transient Receptor Potential (TRP) Cation Channels”: V. Flockerzi, B. Nilius in *Handbook of Experimental Pharmacology*, Vol. 222 (Eds.: B. Nilius, V. Flockerzi), Springer, Berlin, **2014**, pp. 1–12.
- [2] S. Sharma, C. R. Hopkins, *J. Med. Chem.* **2019**, *62*, 7589–7602.
- [3] S. Curcic, O. Tiapko, K. Groschner, *Pharmacol. Ther.* **2019**, *200*, 13–26.

- [4] T. Leinders-Zufall, U. Storch, K. Bleyemehl, M. Mederos y Schnitzler, J. A. Frank, D. B. Konrad, D. Trauner, T. Gudermann, F. Zufall, *Cell Chem. Biol.* **2018**, *25*, 215–223.e3.
- [5] T. Leinders-Zufall, U. Storch, M. Mederos y Schnitzler, N. K. Ojha, K. Koike, T. Gudermann, F. Zufall, *STAR Protocols* **2021**, *2*, 100527.
- [6] O. Tiapko, N. Shrestha, S. Lindinger, G. G. de la Cruz, A. Graziani, C. Klec, C. Butorac, W. F. Graier, H. Kubista, M. Freichel, L. Birnbaumer, C. Romanin, T. Glasnov, K. Groschner, *Chem. Sci.* **2019**, *10*, 2837–2842.
- [7] J. A. Frank, M. Moroni, R. Moshourab, M. Sumser, G. R. Lewin, D. Trauner, *Nat. Commun.* **2015**, *6*, 7118.
- [8] D. B. Konrad, J. A. Frank, D. Trauner, *Chem. Eur. J.* **2016**, *22*, 4364–4368.
- [9] P.-Y. Lam, A. R. Thawani, E. Balderas, A. J. P. White, D. Chaudhuri, M. J. Fuchter, R. T. Peterson, *J. Am. Chem. Soc.* **2020**, *142*, 17457–17468.
- [10] “Mammalian Transient Receptor Potential (TRP) Cation Channels”: A. V. Zholos, in *Handbook of Experimental Pharmacology*, Vol. 222 (Eds.: B. Nilius, V. Flockerzi), Springer, Berlin, **2014**, pp. 129–156.
- [11] T. Blum, A. Moreno-Pérez, M. Pyrski, B. Bufe, A. Arifovic, P. Weissgerber, M. Freichel, F. Zufall, T. Leinders-Zufall, *Proc. Natl. Acad. Sci. USA* **2019**, *116*, 15236–15243.
- [12] R. S. Bon, D. J. Wright, D. J. Beech, P. Sukumar, *Annu. Rev. Pharmacol. Toxicol.* **2022**, *62*, 427–446.
- [13] A. Minard, C. C. Bauer, D. J. Wright, H. N. Rubaiy, K. Muraki, D. J. Beech, R. S. Bon, *Cells* **2018**, *7*, 52.
- [14] H. N. Rubaiy, *Br. J. Pharmacol.* **2019**, *176*, 832–846.
- [15] J. M. Richter, M. Schaefer, K. Hill, *Mol. Pharmacol.* **2014**, *86*, 514–521.
- [16] Y. Akbulut, H. J. Gaunt, K. Muraki, M. J. Ludlow, M. S. Amer, A. Bruns, N. S. Vasudev, L. Radtke, M. Willot, S. Hahn, T. Seitz, S. Ziegler, M. Christmann, D. J. Beech, H. Waldmann, *Angew. Chem. Int. Ed.* **2015**, *54*, 3787–3791; *Angew. Chem.* **2015**, *127*, 3858–3862.
- [17] M. J. Ludlow, H. J. Gaunt, H. N. Rubaiy, K. E. Musialowski, N. M. Blythe, N. S. Vasudev, K. Muraki, D. J. Beech, *J. Biol. Chem.* **2017**, *292*, 723–731.
- [18] H. Beckmann, J. Richter, K. Hill, N. Urban, H. Lemoine, M. Schaefer, *Cell Calcium* **2017**, *66*, 10–18.
- [19] S. Just, B. L. Chenard, A. Ceci, T. Strassmaier, J. A. Chong, N. T. Blair, R. J. Gallaschun, D. del Camino, S. Cantin, M. D’Amours, C. Eickmeier, C. M. Fanger, C. Hecker, D. P. Hessler, B. Hengerer, K. S. Kroker, S. Malekiani, R. Mihalek, J. McLaughlin, G. Rast, J. Witek, A. Sauer, C. R. Pryce, M. M. Moran, *PLoS One* **2018**, *13*, e0191225.
- [20] “Substituted Xanthines and Methods of Use Thereof”: B. L. Chenard, R. J. Gallaschun, WO2014143799A3, **2014**.
- [21] H. N. Rubaiy, M. J. Ludlow, M. Henrot, H. J. Gaunt, K. Miteva, S. Y. Cheung, Y. Tanahashi, N. Hamzah, K. E. Musialowski, N. M. Blythe, H. L. Appleby, M. A. Bailey, L. McKeown, R. Taylor, R. Foster, H. Waldmann, P. Nussbaumer, M. Christmann, R. S. Bon, K. Muraki, D. J. Beech, *J. Biol. Chem.* **2017**, *292*, 8158–8173.
- [22] A. Minard, C. C. Bauer, E. Chuntharpursat-Bon, I. B. Pickles, D. J. Wright, M. J. Ludlow, M. P. Burnham, S. L. Warriner, D. J. Beech, K. Muraki, R. S. Bon, *Br. J. Pharmacol.* **2019**, *176*, 3924–3938.
- [23] D. J. Wright, K. J. Simmons, R. M. Johnson, D. J. Beech, S. P. Muench, R. S. Bon, *Commun. Biol.* **2020**, *3*, 704.
- [24] C. C. Bauer, A. Minard, I. B. Pickles, K. J. Simmons, E. Chuntharpursat-Bon, M. P. Burnham, N. Kapur, D. J. Beech, S. P. Muench, M. H. Wright, S. L. Warriner, R. S. Bon, *RSC Chem. Biol.* **2020**, *1*, 436–448.
- [25] V. A. Gutzeit, A. Acosta-Ruiz, H. Munguba, S. Häfner, A. Landra-Willm, B. Mathes, J. Mony, D. Yarotski, K. Börjesson,

- C. Liston, G. Sandoz, J. Levitz, J. Broichhagen, *Cell Chem. Biol.* **2021**, 28, 1648–1663.
- [26] M. Borowiak, W. Nahaboo, M. Reynders, K. Nekolla, P. Jalinot, J. Hasserodt, M. Rehberg, M. Delattre, S. Zahler, A. Vollmar, D. Trauner, O. Thorn-Seshold, *Cell* **2015**, 162, 403–411.
- [27] O. Thorn-Seshold, J. C. M. Meiring in *Microtubules: Methods and Protocols* (Ed.: H. Inaba), Springer US, New York, **2022**, pp. 403–430.
- [28] A. Costa-Brito, I. Gonçalves, Cecília R. A. Santos, *Neural Regen. Res.* **2022**, 17, 1695–1702.
- [29] J. Broichhagen, J. A. Frank, D. Trauner, *Acc. Chem. Res.* **2015**, 48, 1947–1960.
- [30] M. J. Fuchter, *J. Med. Chem.* **2020**, 63, 11436–11447.
- [31] X. Gómez-Santacana, S. Pittolo, X. Rovira, M. Lopez, C. Zussy, J. A. R. Dalton, A. Faucherre, C. Jopling, J.-P. Pin, F. Ciruela, C. Goudet, J. Giraldo, P. Gorostiza, A. Llebaria, *ACS Cent. Sci.* **2017**, 3, 81–91.

Manuscript received: January 28, 2022

Accepted manuscript online: June 17, 2022

Version of record online: July 27, 2022

2.3.3 Publication Two: Ideal efficacy switches for TRPC4/5 channels harness high potency for spatiotemporally-resolved chromocontrol of TRPC function in live tissue

In our previous work on **BTDAzo** we showed agonistic efficacy for the *E*-isomer and an inhibitory efficacy for the *Z*-isomer. On a chemical level, TRPC4/5 modulators with a xanthine backbone developed by Hydra Biosciences and Boehringer Ingelheim share the potential for a similar efficacy switch because subtle modifications at a specific position change the efficacy mode of the modulators. Namely, the inhibitors **Pico145** and **HC-070** and the agonist **AM237** only differ in their substitution pattern on a phenyl ring. Inspired by the success of **BTDAzo** and the existing knowledge on an efficacy cliff including chemical motifs to modulate it, we now aimed to design an *ideal* efficacy photoswitch based on the much more potent xanthine motif (pico- or nanomolar, instead of micromolar as for **BTDAzo**). Also, as TRPC4 targeting photoswitchable modulators did not exist, we hoped to capture further tool compound value by addressing that gap. We created the photoswitchable variants **AzPico** and **AzHC** by introduction of an azobenzene to the parent compounds at the position we assumed for an efficacy switch. Pleasingly, **AzPico** showed nanomolar agonist efficacy for the *Z*-isomers after irradiation with UV light on TRPC4/5 and **AzHC** showed similar effect and potency but only on TRPC5 (Preprint Figure 1, here page 86).

Experimentally creating such high potency photoswitchable tool compounds is already a major achievement. Nevertheless, we further pursued the *concept* of an ideal efficacy photoswitch. The basic ideas are not necessarily novel, and efficacy switches of various grades have been shown in the literature (see section 2.1.2.4), but its implications on bioactivity photoswitching had been neglected. Therefore, we developed a model for ideal efficacy switching assisted by literature evidence and our own previous findings. First, we examined dose response curves at different wavelengths that do not plateau at the same effect levels. This implies that despite incomplete photoswitching and variable absolute concentrations of residual active isomer, there is no change in bioactivity as long as the *E/Z* ratio is maintained. We conclude that the reason is competitive binding on the same binding site, with the two *E/Z*-photoisomers either having (i) opposing activity (e.g., activator/inhibitor), or (ii) one isomer is biologically innocent, but prevents the other from acting by its competitive binding. The drug-concentration-independence but solely wavelength-determined bioactivity that results from this is our first major conceptual finding: where photopharmacology traditionally aimed for a narrow functional dynamic range (FDR) defined by concentration, PSSs, and affinity differences of *E/Z*-isomers, ideal efficacy switches now deliver an open-ended dynamic range (DR) with reproducible operation at any concentration above a threshold. We validated this hypothesis via calcium influx imaging on a plate reader assay and indeed showed an inhibitory effect for the *E*-isomers against englerin-A activated TRPC4/5 (Preprint Figure 1, here page 86). The plate reader assay was limited to mounted LED wavelengths, and only measures intracellular calcium levels with slow response. Therefore, we used single cell patch clamp electrophysiology which directly records currents, and a fully tuneable light source, to examine **AzHC/AzPico** function in more detail. The I/V curves show photoswitching between a conducting state for *Z**-**AzPico** and *complete* recovery to basal activity for *E**-**AzPico**, with reproducible photoswitching currents over >36 cycles. We attribute the match between *E**-**AzPico** and

basal activity to the efficacy switch property that prevents channel activation by residual Z*-**AzPico** even though photoswitching is not complete. Next, we measured cellular action spectra for inward currents (IC) and found a sharp peak with a maximum at 350/360 nm which matches maximum PSS values measured in cuvette. We modelled I/V action spectra against $\log[Z/E]$ and $\log[Z]$ and as expected found matching curve shapes for the ratio $[Z/E]$ and no concentration correlation. This is the second conceptual outcome for efficacy photoswitching: the level of effect can be set solely by the wavelength. Consequently, a maximum effect can only be achieved by application of wavelengths which generate optimal PSS values because poor photoisomerisation cannot be compensated by overdosing (Preprint Figure 2, here page 87). Though potentially restrictive (e.g. the plater reader assay's fixed wavelengths had not captured optimal switching), it would later prove crucial for fine-tuning bioactivity.

Affinity switches aim for preferably big affinity differences between *E*- and *Z*-isomers and until today there were only two examples of any photopharmaceutical:protein complex pairs with high resolution 3D structures of each photoswitch isomer bound.^{313,314} In contrast, efficacy switches retain affinity for the binding site for both isomers and two separate collaboration partners obtained high resolution Cryo-EM structure pairs: of *E/Z*-**AzPico** in complex with TRPC4, and *E/Z*-**AzHC** in complex with TRPC5. All four structures show a closed channel, even for the bound agonists. Intriguingly, the xanthine part binds in the same place and only the photoswitch changes the position within the binding site for both cases. For the *Z*-isomers the distal phenyl ring switches into a pocket and interacts with a tyrosine residue that did not interact with the *E*-isomers. Those structures are the first TRPC4/5 structures with a bound agonist, but with a closed pore, detailed analysis of the agonist-antagonist switch is rather tentative. However, we can consolidate the hypothesis of competitive binding because the xanthine part occupies the same space within the binding pocket (Preprint Figure 3, here page 88).

The high potency and ideal efficacy switch properties of **AzPico** and **AzHC** enabled collaborators to demonstrate their usability in a range of endogenous systems expressing TRPC4 and/or TRPC5, such as cultured hippocampal neurons, chromaffin cells (which secrete dopamine after stimulation), tissue slices from the arcuate nucleus extracted from mouse brains, and lastly whole organ segments where intestine motility and peristalsis could be photoswitched on a macroscopic scale (Preprint Figures 4-6, here pages 89,90,92). Intriguingly, 30 nM of **AzPico** resulted in intestine overstimulation when 365 nm LEDs were used for photoswitching, but a 385 nm LED gave physiological stimulation even when applying 300 nM **AzPico**. This is a consequence of the ideal efficacy switch delivering *chromocontrol* over bioactivity, not dose-control. We consider this as major advantage for efficacy switches because in complex tissue or *in vivo*, drug distribution is complex and not uniform: but *E/Z*-ratios will always be reproducibly induced by fixed wavelengths, supplying a constant bioeffect in any settings (Preprint Figure 6, here page 92).

In summary, we developed ideal efficacy photoswitch tool compounds for TRPC4/5 with nanomolar potency; **AzPico** is also the first photoswitchable tool for TRPC4. The ideal efficacy switch property allowed applications in complex endogenous systems, and we anticipate that **AzPico** and **AzHC** will be a valuable addition to the toolbox of TRP channel biology by helping decipher tissue specific roles through spatial and temporal modulation. More generally, we elucidated *chromocontrol* as the reproducible, assay-independent, key functional outcome for ideal efficacy photoswitches.

Ideal efficacy photoswitches for TRPC4/5 channels harness high potency for spatiotemporally-resolved control of TRPC function in live tissues

Markus Müller^{1‡}, Konstantin Niemeyer^{2‡}, Navin K. Ojha³, Sebastian A. Porav^{4,5}, Deivanayagabharathy Vinayagam,⁶ Nicole Urban², Fanny Büchau², Katharina Oleinikov³, Mazen Makke³, Claudia C. Bauer^{4,5}, Aidan V. Johnson^{4,5}, Stephen P. Muench^{5,7}, Frank Zufall³, Dieter Bruns³, Yvonne Schwarz³, Stefan Raunser⁶, Trese Leinders-Zufall³, Robin S. Bon^{4,5}, Michael Schaefer^{2,*}, Oliver Thorn-Seshold^{1,*}

ABSTRACT: Directly probing the endogenous biological roles of target proteins with high spatial and temporal resolution, as non-invasively and reproducibly as possible, is a shared conceptual goal for research across many fields, as well as for targeted therapies. Here we describe the rational conceptual design and test-case practical implementation of a photopharmacological paradigm to empower high-performance photomodulation studies *in vivo*. TRPC4/5 ion channels are involved in many spatiotemporally resolved circuits, from pain and anxiety, to reproductive signaling, digestion, and obesity. To unpick their biology requires spatiotemporally precise tools, which were lacking. We developed "ideal efficacy photoswitch" ligands to control their diverse functions *in situ*. These *E*↔*Z*-photoswitchable ligands bias TRPC[4]/5 channel activity with exquisite photocontrol, from strong agonism under 360 nm, to low agonism at 385 nm, to strong antagonism at 410-460 nm. Cryo-EM structures of both TRPC4 and TRPC5 with both *Z*-agonists and *E*-antagonists support the rationale for efficacy switching through competitive *E/Z* isomer binding. Crucially, since the *E/Z* ratio is exclusively determined by the light wavelength applied, **their channel photocontrol is exclusively wavelength-dependent, yet drug-concentration-independent: so is reproducible from cell culture to >millimetre-depth tissues.** Indeed, we were able to photocontrol both direct and downstream TRPC4/5 biology in cell lines or primary cells in culture, from calcium flux, to primary neuron excitability and adrenaline release; and even in tissues, photoswitching small intestine motility and peristalsis. The TRPC4/5 ligands we develop will thus unlock a range of high-precision investigations in TRP biology. More broadly, we propose that the success of this efficacy photoswitch program, from concept to tissue level translation, is mainly a consequence of how biology has evolved proteins for efficacy control. We therefore foresee that a variety of functionally responsive protein targets, not only sensory and signaling ion channels and receptors, will be amenable to similarly high-performance photocontrol even *in vivo*, if a new generation of reagent development adopts this paradigm of **ideal efficacy photoswitching.**

Introduction

The 27 human Transient Receptor Potential (TRP) proteins can assemble to form tetrameric TRP ion channels, which have varied and highly tissue-dependent roles in cellular physiology: from sensing and signaling to mineralostasis.^{1,2} Several environment-sensing TRP channels such as TRPV1 (heat), TRPM8 (cold), or TRPA1 (electrophiles), are well-studied. For many other TRP channels their roles and significance remain unclear, even if their links with diseases make them hotly pursued as therapeutic targets.³⁻⁵ TRP canonicals (TRPC) are a subfamily of non-selective Na⁺/Ca²⁺-permeable cation channels; including the structurally similar TRPC4 and TRPC5.⁶⁻⁸ TRPC4/5 are mainly expressed in the central nervous system (CNS), gut, and kidneys, and are functionally linked with pain,⁹⁻¹¹ reproductive signaling,¹² anxiety and depression,^{13,14} kidney disease,¹⁵ and digestion;¹⁶ and striking discoveries are still ongoing e.g. linking TRPC5 loss to postpartum depression and obesity.¹⁷ TRPC4/5 form both homotetrameric, and heterotetrameric functional channels that can also include TRPC1.¹⁸

Insights into TRPC4/5 relevance were initially derived from knockout mice because potent and selective modulators were lacking.¹⁹ Recently, small-molecule modulators of TRPC4/5 have become available as tool compounds,²⁰ starting with the nanomolar-potency natural product (-)-**Englerin A (EA)**,²¹ a TRPC1/4/5 activator,^{22,23} and complemented by TRPC4/5 inhibitors developed as drug candidates.^{24,25} However, TRP functionality varies according to tissue localisation (spatial), and TRPs are best studied if their activity is reversibly modulated on short timescales (temporal); therefore, photoresponsive chemical tools, whose activity can be spatiotemporally patterned by light, are particularly well-adapted to resolve TRP biology.²⁶ In general, photoswitchable TRP ligands have been impactful: with azo-cap-saicins for TRPV1,^{27,28} TRPswitch for TRPA1,²⁹ OptoBI for TRPC3,³⁰ and azo-diacylglycerols (PhoDAGs and Opto-DAGs) for TRPC2/3/6.³¹⁻³³ However, there is no photoresponsive ligand for TRPC4, and the sole compound for Trpc5 (**BTDAzo**, a lipophilic photoswitchable agonist) has low potency and is almost inactive on human TRPC5³⁴.

The highly potent and selective TRPC4/5 drug leads from industry, e.g., TRPC5-targeting pyridazinones GFB-8438 and GFB-887 developed by GoldfinchBio, and TRPC4/5-targeting xanthines **HC-070** (in clinical trials as BI-1358894) and **Pico145** (also named HC-608) developed by Hydra/Boehringer (**Figure 1a**), have already driven major progress in basic TRPC4/5 research (**Supporting Note 1**). In this work, we sought to create photoswitchable analogues of

them, to add spatiotemporal resolution on top of their potency and selectivity, and so make powerful tools for TRP studies in complex biological systems. We particularly sought to address TRPC4, given its lack of photoswitchable tools. Crucially, we were drawn to the xanthenes for conceptual reasons, since their structure-activity relationships (SAR) reveal activators and inhibitors with high structural similarity,^{35,36} which in turn suggested the rare opportunity to harness an efficacy tipping point to obtain high-performance *efficacy switch* tools. We now report the design and experimental validation of this concept, use these tools for light-controlled high-spatiotemporal-precision elucidation of the separate roles of TRPC4 and/or TRPC5 from cell culture through to endogenous organ sections, and argue more broadly for the adoption of this efficacy switch paradigm as a way to unlock high precision *in vivo* photocontrol of a range of biological systems.

Results

Design Concept: Efficacy Switching (Figure 1e-j)

Azobenzenes are the best-explored chemical scaffolds for fully reversible structural photoswitching ($E \rightleftharpoons Z$ isomerisation),³⁷ and we determined to employ them in ligands to photoswitch TRPC4/5 bioactivity. However, azobenzene $E \rightleftharpoons Z$ photoswitching is never complete in both directions: it operates between mostly- Z and mostly- E photostationary states (PSSs, typically ca. 90% Z for the most- Z -PSS [Z^*], and 80% E for the most- E -PSS [E^*]).

Affinity Switching is the typical rational design concept for photopharmacology (ca. >95% of all photoswitches reported), where differences in binding affinity based on steric clash/fit drive a difference in potency of E/Z -isomers; so net $E \rightleftharpoons Z$ photoswitching modulates the biological activity applied. However, due to the typically 20% residual Z isomer in the mostly- E -PSS, even an *ideal* affinity switch that has a completely non-binding E -isomer but a high-agonist-potency Z -isomer (**Figure 1e**) suffers substantial background activity after $Z \rightarrow E$ photo-switching-off. Conceptually, this is covered in the general result that bidirectional photocontrol of an affinity switch can only deliver a narrow *functional dynamic range of bioactivity* (FDR),^{38,39} i.e. the bioactivity window between best-photoswitched-on and best-photo-switched-off states (**Figure 1f**; the FDR is limited by its PSSs in both directions). Worse still, the applied bioactivity of an affinity switch under a fixed wavelength is *extremely* sensitive to its concentration (**Figure 1j**), such that both dose and wavelength must be dynamically balanced to deliver a given effect. This is problematic or impossible for tissue or *in vivo* work, due to highly variable reagent concentrations (ADME-PK, distance from blood vessels, inter-animal variability, etc). We conjecture that this explains why affinity switches' applicability for bidirectional photocontrol has been mainly limited to highly controlled cell culture settings⁴⁰.

Efficacy Switching is the design concept we harness in this work. We formulate the goal⁴¹ of an efficacy photoswitch to be, that E/Z photoisomers have different modes of bioactivity on the target, while still binding competitively with similar affinity. Ideally, E/Z isomers have either (i) opposing activity (e.g., activator/inhibitor), or (ii) one isomer is biologically innocent, but prevents the other from acting by its competitive binding (**Figure 1h**). Here, the novelty of installing such a nanomolar, ideal efficacy switch on TRPC4/5-binding scaffolds will be the chemical highlight of this paper, and is the key feature that allows their *in vivo* biological applications. First however, it will be crucial to trace the logic of efficacy switching, to see why its opportunities and advantages arise, since this conceptual issue of *how* a compound exerts its photocontrol has not received proper formal attention (especially compared to e.g. how much literature is devoted to easily-measured but less critical aspects such as incremental tuning of photoresponse wavelengths and PSSs).

For an ideal efficacy switch, above a threshold concentration where its target nears saturation by an E/Z mixture, there is no more concentration-dependency of bioactivity. The only variable controlling bioactivity is the E/Z ratio of the competitively-binding isomers: i.e., (1) the PSS entirely controls the bioactivity. Setting the PSS by choosing the wavelength of light applied is far easier and more reproducible than controlling drug biodistribution or concentration: making efficacy switches ideal to tackle complex environments despite variable biodistribution, and suiting them to easy translation between model systems. Also, (2) efficacy switches thus access an *open-ended dynamic range* (DR), where switching between ON and full baseline states is identically possible at *any* concentration above the threshold, as long as light is applied efficiently (**Figure 1gi**). These features should make efficacy photoswitches much better-suited for robust use in biology, from cell culture through to *in vivo* (**Figures 3-6**). However, only about ten cases of efficacy photoswitching have been published (chemokine, adenosine, cannabinoid, and serotonin receptors). Key contributions include those of Decker, Leurs, Gorostiza, and coworkers (discussed in **Supporting Note 2**).⁴²⁻⁵¹ With the exception of Leurs' micromolar chemokine photoswitch ligand VUF16216,^{43,48} efficacy switching on the other known targets can be considered "non-ideal" in that (**a**) the ligand efficacies were switched between more- and less-activating, rather than activating and inhibiting, and (**b**) the isomers' affinity was rather different, which compromises the concentration-independence of ideal efficacy switching. It is also certain that other efficacy switches have been created, but simply not reported as such; e.g., we also published a reagent with excellent dynamic range of bioactivity photocontrol despite its $E \rightleftharpoons Z$ photoswitching incompleteness, but had not understood the full consequences of that performance at the time³⁴ (while re-parsing recent photopharmacology papers, we believe we have found many more instances of unsuspected efficacy switches; **Supporting Note 2** discusses this further with some examples from Fuchter, Groschner, Pepperberg, Trauner, etc⁵²⁻⁵⁶).

We give this level of detail since we believe that efficacy photoswitching is *the* mode needed to reach the naively popular picture of "solely wavelength-controlled bioactivity" that has motivated much of photopharmacology, but, we did not find it collected accessibly in the literature elsewhere. The conceptual importance of this framework goes deeper than pharmacology though. As one example, we highlight that there are *target-driven* reasons to choose efficacy switching for proteins which are natively poised for steeply nonlinear dose-response switching between metastable states, such as receptors and ion channels with multiple binding sites. These ought to be ideal platforms where competitive binding of similar-affinity *E/Z* isomers with opposing modes of action ought to deliver a concentration-independent, *true binary photoswitch for protein activity*, even though ligand photoswitching is never complete. A separate theoretical paper will treat these aspects in detail⁵⁷; but for now, we set out to test this concept in practice, by creating such "ideal efficacy switch" reagents for TRPC4/5.

Xanthine Efficacy Switches: Design and Synthesis (Figure S3)

Xanthines **Pico145** (also called **HC-608**) and **HC-070**⁵⁸ are TRPC1/4/5 antagonists with picomolar potency⁵⁹ and remarkable selectivity against hundreds of enzymes, receptors, transporters and other ion channels (including other TRP channels).²⁴ Excitingly, the very similar **AM237**⁵⁸ is instead a nanomolar *agonist* of homotetrameric TRPC5, despite also being a nanomolar antagonist of homotetrameric TRPC4 (for full details of the pharmacology, see **Supporting Note 1**).³⁵ The structures of these different-efficacy compounds are nearly identical (**Pico145**: *m*-OCF₃, **HC-070**: *m*-Cl; **AM237**: *m*-OCF₃, *p*-Cl; **Figure 1a**). This suggests that the *meta/para* positions are suitable as an "ideal efficacy tipping point": small modifications may flip the efficacy mode (activator/inhibitor) *without* changing the binding affinity. Thus, the xanthines seemed an outstanding starting point for ideal efficacy switches that are *also* highly potent, and so can be reliably applied *in vivo*.

In brief, we synthesised a series of xanthines "extended" with bidirectionally switchable azobenzenes (**Figure S3**). Noteworthy, with a simple -NNPh motif in *para* (where **AM237** has a -Cl), we obtained **AzPico** (*m*-OCF₃) and **AzHC** (*m*-Cl; **Figure 1b**) which were soon identified as the most biologically useful candidates in our panel of eight. From here onwards we will focus only on them, leaving the others to **Supporting Note 3**. **AzPico/AzHC** could be reversibly photoswitched between PSSs of ca. 82%*E* around 410 nm and 95%*Z* around 360 nm (**Figure 1cd** and **Table S3**).

Parallel-Throughput Photocontrol Assessment in Cells by FLIPR (Figure 1k-n)

We initially screened for photoswitchability of activity in cells, using a fluorometric imaging plate reader (FLIPR) calcium flux assay, with HEK293 cells stably expressing mouse TRPC4 β or mouse TRPC5. The parallel-throughput FLIPR setup is limited to use fixed LEDs at 365 nm (good-*Z*) and 447 nm (suboptimal-*E*), during imaging at 490 nm (so imaging counteracts both PSSs). Therefore, these FLIPR results will underestimate the true photocontrol the reagents can access, as shown later.

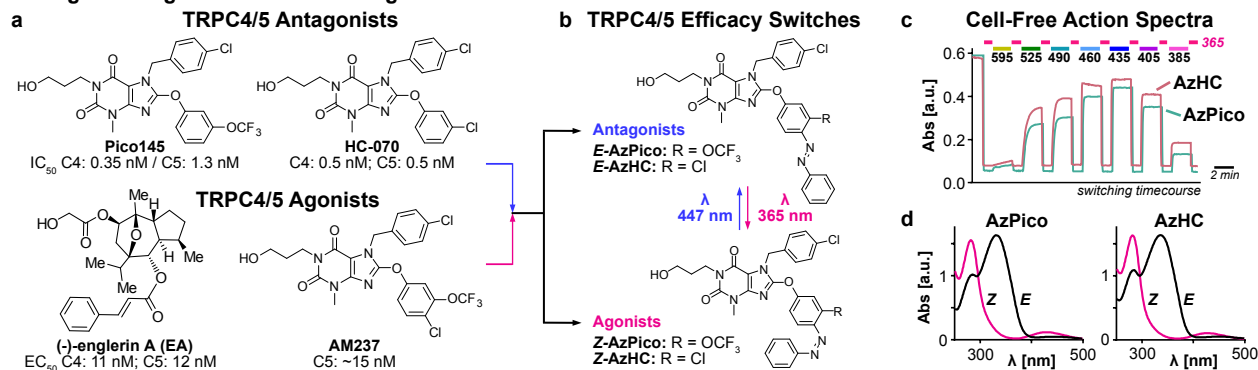
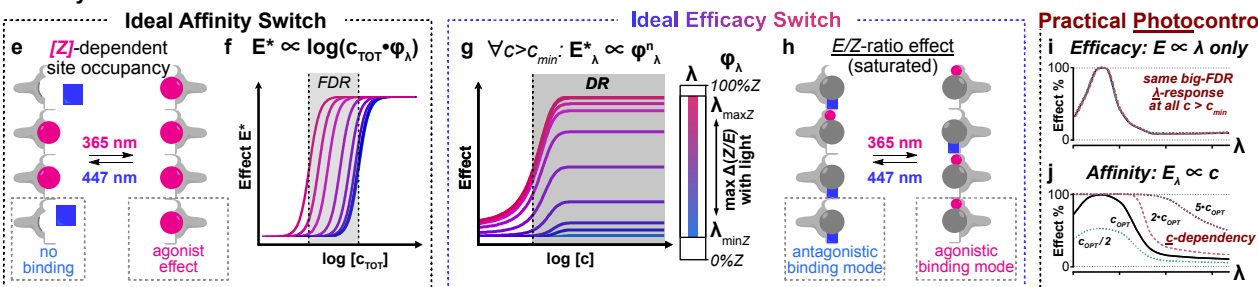
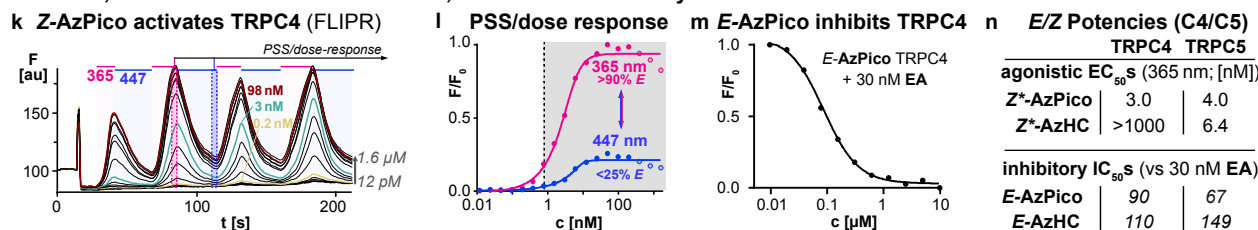
• Reagent Design and Photoswitching

• A Key Role for Mechanism

• In Cells, AzPico and AzHC are Nanomolar, Ideal TRPC4/5 Efficacy Switches


Fig. 1 | Efficacy photoswitches for TRPC4/5. **a**, Known TRPC4/5 modulators. **b**, Photoswitchable TRPC4/5 modulators **AzPico** and **AzHC**. **c-d**, Photoisomerisation action spectra and E/Z isomer absorption spectra of **AzPico** and **AzHC**. **e,f**, For an ideal affinity switch, only one isomer binds the target. Within the FDR window, binding site occupancy and thus biological effect E^* depend on the total switch concentration c_{TOT} and the PSS fraction of active isomer ϕ_λ . **g,h**, For an ideal efficacy switch, both isomers bind, with similar affinities, but with different efficacies. The dynamic range (DR) where the biological effect E^* is PSS-dependent but concentration-independent covers all $c > c_{min}$. **i,j**, Photocontrol in practice: for an efficacy switch, small variations in PSS(λ) sensitively control performance (whereas in affinity switches they are unimportant); but even large variations in concentration, which would ruin the performance of an affinity switch, are irrelevant. **k,l**, Reversible Ca²⁺ influx modulation with **AzPico** under 365/447 nm cycles, as timecourse and peak amplitudes. **m**, **E-AzPico** binds competitively to **EA**. **n**, EC₅₀ and IC₅₀ values of E/Z -**AzPico** & **AzHC** on TRPC4 and TRPC5 (**k-n**, Fluo-4-loaded HEK_{mTRPC4/5} cells).

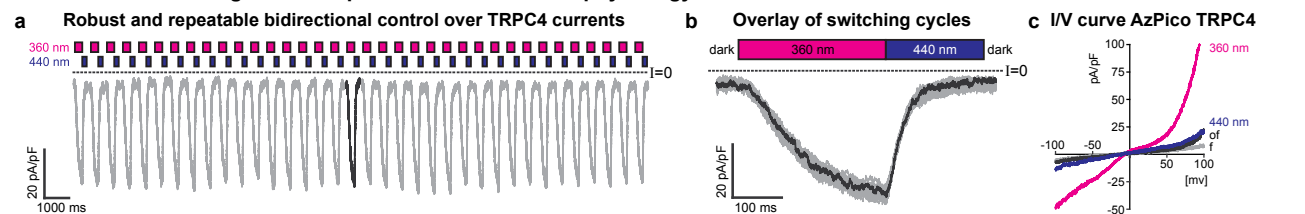
E-AzPico from 12 μ M to 1.6 μ M gave no effect with TRPC4 or TRPC5; upon 365 nm illumination, strong agonism was evident with Ca²⁺ influx rapidly evoked at low nanomolar concentrations; and this was rapidly photoreversible with 447 nm illumination, over many cycles (**Figure 1k**). The remarkable observation that the maximum and minimum calcium signals are dose-independent over a concentration range of >100-fold (from nM to μ M), even though the concentration of the agonistic Z isomer likewise increases by >100-fold in this range, confirms it as an *ideal efficacy switch* (TRPC4 in **Figure 1g**; TRPC5 in **Figure S2 (E)** and **Figure S13 (Z)**). Pleasingly, it inherits the high potency of its parent **Pico145**, with 365 nm EC₅₀ of just 3.0 nM on TRPC4 and 4.0 nM on TRPC5 (**Figure 1n**). **AzHC** was also a Z-agonistic ideal efficacy switch for TRPC5 with a 365 nm EC₅₀ of 6.4 nM. Excitingly though, Z-**AzHC** was completely inactive on TRPC4 into the μ M range (**Figure S13**). Competition assays supported that these compounds are indeed efficacy switches (**Figure 1m** and **Supporting Note 1**).

Taken together, this pair of reagents are uniquely potent efficacy switches; **AzPico** is the first photoswitchable tool to address TRPC4; and although **AzPico** acts on TRPC5 as well, it can be applied comparatively to the TRPC5-selective **AzHC** to test the cellular role of TRPC4: making them an outstanding reagent pair for probing these otherwise difficult to resolve channels. Their retention of the nanomolar potency of their optimised parent compounds is also a rarity among photopharmaceuticals, because the extra moiety needed for photoisomerisation usually sacrifices potency.

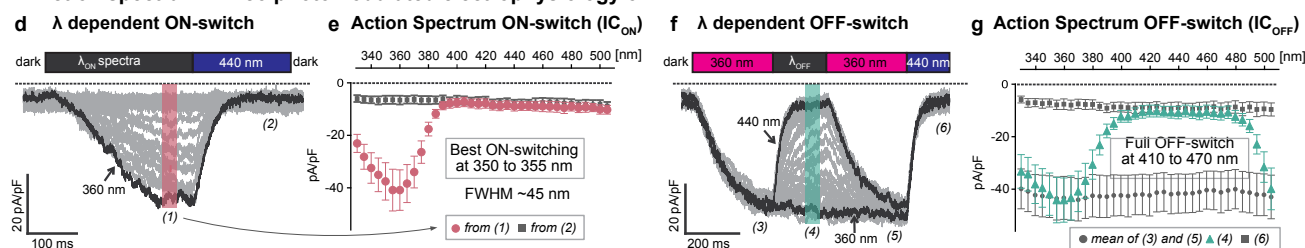
Photomodulated electrophysiology (Figure 2)

We next performed electrophysiological patch clamp experiments (ephys), to characterise the action and specificity of channel modulation in more detail. Though its throughput is lower, ephys is more powerful than FLIPR in several respects: (i) the non-optical ephys readout does not cause unwanted photoswitching, unlike FLIPR; (ii) ephys readouts linearly and temporally resolve ionic currents through the activated channels, unlike the delayed and attenuated fluorometric Ca^{2+} influx analyses in FLIPR; (iii) the ephys setup can use narrow-bandwidth monochromated light at any wavelength. These features allow measuring the full power of the photoswitch reagents.

• Whole-cell recordings - AzPico photomodulated electrophysiology on TRPC4



• Action spectra - AzPico photomodulated electrophysiology on TRPC4



• Efficacy switch action spectra - Correlation of [Z-AzPico] and functional effect

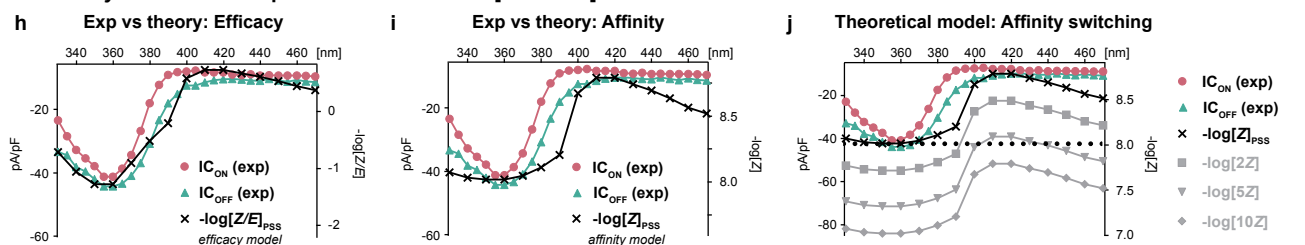


Fig. 2 | AzPico-photocontrolled electrophysiology of TRPC4. **a-g**, Electrophysiological whole-cell recordings of TRPC4 currents in voltage clamp mode (**a,b,d-g**: $V_h = -80$ mV; **c**: V_h scan) in HEK293 cells with 10 nM **AzPico** during photoswitching. **a-b**, Reproducibility of 36 consecutive photoswitching cycles of 360/440 nm (**a**: time-course; **b**: overlay of all cycles). **c**, I/V curves show that 440 nm drives almost full return to baseline currents throughout the applied voltage range. **d-g**, Spectral scans to extract the wavelength dependency of channel current photoswitch-on (**d-e**, cycles of $\lambda_{ON}/440$ nm) and photoswitch-off (**f-g**, 360 nm/ λ_{OFF}). **h-j**: Ephys action spectra of **AzPico** match PSS-informed expectations for an efficacy switch (**h**), not an affinity switch (**i**): important, since an affinity switch would have severe concentration dependency (**j**). Full legend at **Figure S24**.

We thus recorded wavelength-dependent action spectra of **AzPico** and **AzHC** under fast photoswitching in ephys in TRPC4 / TRPC5-expressing cells (**Figure 2**, **Figure S14**). They now fulfilled the potential of ideal efficacy switches. For example, **AzPico** reversibly photomodulated TRPC4 currents over >36 consecutive cycles with a fully constant activation profile, without fatigue (**Figure 2ab**). Current/voltage (I/V) curves show a strong activation of ion flux at best- Z (360 nm) PSS; yet, only at nonphysiological voltages (<-80 mV or $>+60$ mV) could any small differences between basal activity and good- E (440 nm) PSS be detected (**Figure 2c**): making them truly off/on TRPC modulators.

The repeatability of on/off photocycling allowed us to extract action spectra for both (1) photoactivation (**Figure 2de**) and (2) photodeactivation (**Figure 2fg**) *in situ* in live cells. Channel currents were optimally photoswitched-on in a sharp wavelength range of 340-370 nm; and *full* photoswitch-off was triggered over the broad range of 400-480 nm (best: 430 nm). Such action spectra conclusively match the highly wavelength-sensitive model expected from cell-free PSS measurements for an ideal efficacy switch (bioactivity $\propto -\log_{10}([Z]/[E])$), but mismatch the model for an affinity switch (bioactivity $\propto -\log_{10}([Z])$) (match/mismatch is visible even for single concentration data: **Figure 2hi**).

Importantly, we recall that only the efficacy switch mechanism allows these reagents to deliver binary off/on bioactivity, that is identically wavelength-dependent at any concentration (**Figure 1ghi**, **Figure 2h**); e.g., if they were classical affinity switches, even doubling their concentration would prevent photo-switching-off cell currents (**Figure 2j**; **Supporting Note 1**). Thus, the concentration-scan, fixed-wavelength FLIPR plus the fixed-concentration, wavelength-scan ephys (**Figures 1kl**, **2egh**, **S14**) show that **AzHC** and **AzPico** are ideal efficacy switches, whose E/Z -competitive binding controls TRPC4/5 currents with exquisite wavelength-sensitivity and concentration independence.

Paired Pairs of Cryo-EM TRPC4/5:*E/Z* Structures Indicate Activation Mechanism (Figure 3)

As **AzHC** and **AzPico** should bind TRPC4/5 with high affinity in both *E*- and *Z*-forms, this offers a rare opportunity for structural photopharmacology to elucidate the basis of efficacy switching (to date, there are only two protein-ligand structure pairs with an azobenzene reagent bound as both *E*- and *Z*-isomers^{49,60}); and potentially to understand the remarkable differential of TRPC4 activity induced by the *-Cl*/*-OCF₃* swap. Single-particle cryo-electron microscopy (cryo-EM) studies of TRPC4^{61–63} and TRPC5^{64–67} have already given important insights into the structures of these channels and their complexes with lipids, metals, proteins, and small-molecule modulators. These include TRPC5 structures with **Pico145**⁶⁶ and **HC-070**,⁶⁴ binding in near-identical pose to the same lipid binding pocket, adjacent to the pore helices. However, no channel-open structures are known, and all reported ligand structures are with inhibitors.³⁶

We now studied TRPC5:*E/Z*-**AzHC** and TRPC4:*E/Z*-**AzPico** complexes by cryo-EM, hoping to acquire the "paired pair" of both inhibited and activated structures for both channels. This work was run fully independently for TRPC4 at one site, and TRPC5 in another; yet the results aligned, giving confidence in their interpretations. We could determine all four structures at high resolution: **hTRPC5:*E*-AzHC** (2.6 Å), **hTRPC5:*Z*-AzHC** (2.9 Å), **TRPC4_{DR}:*E*-AzPico** (3.0 Å), and **TRPC4_{DR}:*Z*-AzPico** (3.1 Å), without imposing symmetry during data processing (**Figure 3**; **Figures S15–S19**; **Tables S4–S7**; hTRPC5 = human TRPC5, TRPC4_{DR} = zebrafish TRPC4). We used 365 nm for *Z*-ligand structures, and either dark or 440 nm for *E*-structures, and excluded DTT from buffers to avoid diazene reduction.

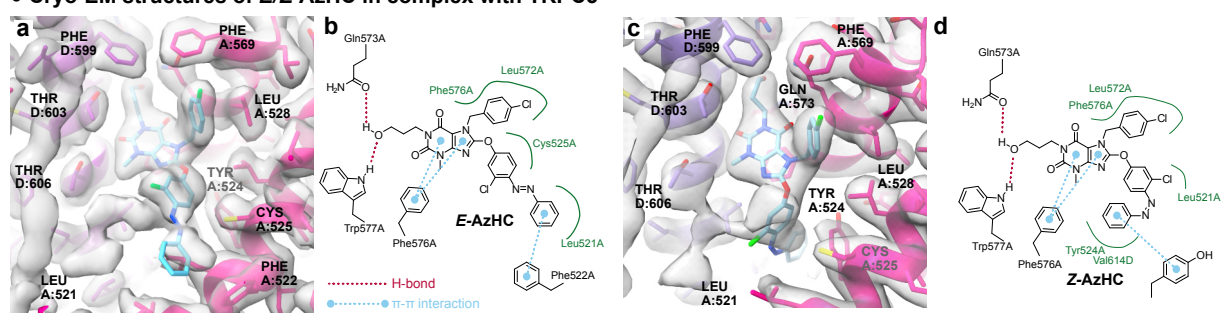
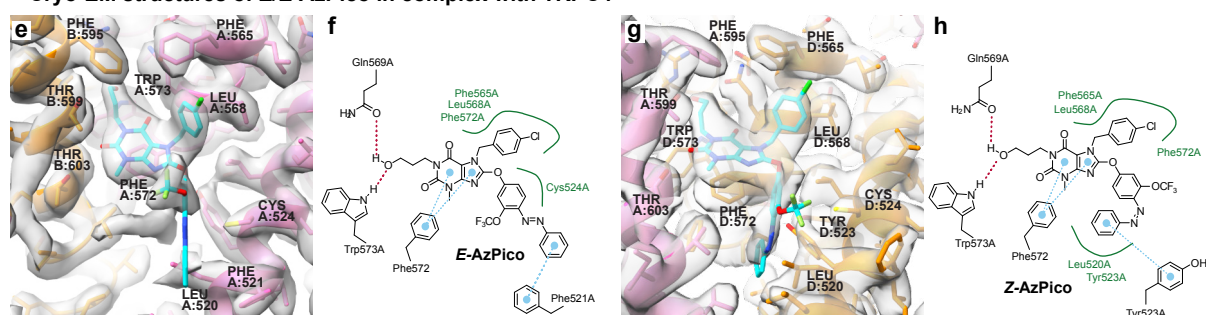
• Cryo-EM structures of *E/Z*-AzHC in complex with TRPC5**• Cryo-EM structures of *E/Z*-AzPico in complex with TRPC4**

Fig. 3 | Structures of TRPC4/5 in complex with *E/Z*-isomers of efficacy photoswitches. a-b, hTRPC5:*E*-AzHC (2.6 Å, PDB xx, EMDB xx), with 2D map of ligand-protein interactions. **c-d**, hTRPC5:*Z*-AzHC (2.9 Å, PDB xx, EMDB xx). Note the flip of the distal azobenzene ring. **e-g**, TRPC4_{DR}:*E/Z*-AzPico (*E*: 3.0 Å, PDB 9FXL, EMDB 50850; *Z*: 3.1 Å, PDB 9FXM, EMDB: 50851). Full legend at **Figure S25**.

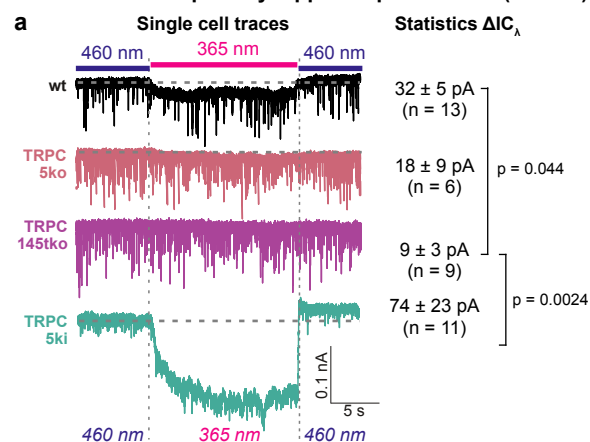
Supporting Note 4 contains full discussions of the structural biology results, but in brief, *E/Z*-**AzHC/AzPico** could be built into the expected lipid/xanthine binding site, with near-identical positions as for **Pico145**⁶⁸ for the conserved ligand portion, and differences between the *E* and *Z* isomers only at the azobenzene. E.g., the distal ring of *E*-**AzHC** is projected outwards to make a π - π interaction with Phe522 of TRPC5, while in *Z*-**AzHC**, it folds deeply inwards to make a π - π interaction with Tyr524; **AzPico** behaves similarly on TRPC4 (**Figure 3**; **Figures S4, S6**). Most protein residues in the ligand binding site are in similar positions in the *E/Z* structures; the exceptions are that for hTRPC5, Phe520 is flipped "in" or "out" depending on whether the antagonistic *E* or agonistic *Z* isomer is bound (**Figure S4b**), while in TRPC4_{DR} the cognate Phe (521) is much less shifted, though its neighbouring Leu520 is significantly displaced. All *E* and *Z* structures had the channel pore closed (see **Figures S5** and **S7**, which suggest potential reasons for this), so caution in interpreting the agonist structures is needed; nevertheless, these data offer the first structural insight into how closely related xanthenes can have opposite effects on TRPC4/5 function (i.e. inhibition vs. activation). With these binding modes confirmed, we tested whether the selective activation of TRPC5 but not TRPC4 by *Z*-**AzHC** could be the result of their binding sites' single amino acid difference (TRPC5 has Val579 where TRPC4 has Ile575 at the cognate position). However, neither the TRPC5→C4 mutation (V579I) nor the TRPC4→C5 mutation (I575V) changed their activity profiles for *E/Z*-**AzHC** or for control activator **AM237**. This suggests that the basis for *Z*-**AzHC**'s TRPC5-selective activation is more complex than the immediate residues it contacts (**Supporting Note 4**).

Photoswitching endogenous TRPC4/5 in primary cells to photoreversibly actuate cell function (Figure 4)

We next moved to test whether **AzPico** can directly photocontrol endogenous TRPC4/5, using autaptic hippocampal neurons (neurons cultured in isolation which only make synapses back onto themselves, as a model for simultaneously monitoring pre- and post-synaptic responses). 365/460 nm cycles reversibly activated inward currents in wildtype (**wt**) neurons, just as was seen in heterologously TRPC4/5-[over]expressing HEK cells (**Figure 2**). These **wt** neurons consist of a fraction of cells expressing TRPC channels that can be directly activated by **AzPico**, plus about 50% of neurons that do not express TRPC channels.⁶⁹ Matching expectations, average currents were larger when acquired exclusively from TRPC5-bearing cells (**5ki**); strongly depressed with TRPC5 single knockout (**5ko**); and almost abolished with TRPC1/C4/C5 triple knockout (**145tko**); supporting that TRPC[1/4/5] channels are the central contributor to **AzPico**'s photomodulation of membrane conductance (**Figure 4a**).⁷⁰ This shows that **AzPico** can optically control the activity of native TRPC[1/4/5] channels in primary nerve cells, without channel over-expression.

We then tested the photopharmacology of **AzPico** in isolated primary chromaffin cells (the neuroendocrine cells in the adrenal gland that secrete adrenaline by exocytosis in response to electrical activation; these functionally express TRPC1/4/5 channels).⁷¹ 360 nm illumination of **AzPico** photoreversibly triggered robust inward currents that caused an increase in membrane capacitance (CM) in **wt** cells, indicative of exocytosis (**Figure 4b**). Neither response was observed in **145tko** cells, confirming the TRPC-specificity of this photopharmacology. By supporting that direct activation of endogenous TRPC channels in chromaffin cells can trigger exocytosis, this again suggests how **AzPico** may be used to exert functional control over endogenous biology: here, for optically-controlled release of adrenaline.

• **Photocontrol of primary hippocampal neurons (AzPico)**



• **Photocontrol of primary chromaffin cells (AzPico)**

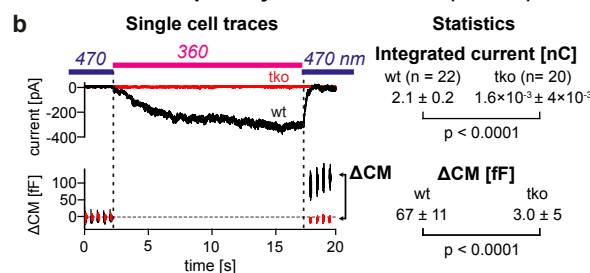


Fig 4 | AzPico (30 nM) photoswitchably evokes currents in primary neuronal and neuroendocrine cells with endogenous TRPC levels (single cell traces at left, group statistics at right). **a**, photoswitching-based current differentials ΔI_C in hippocampal neurons (currents at 365 nm relative to 460 nm). **b**, photoswitch-based currents and net charge transfer (top) correlate to membrane capacitance changes ΔCM (bottom), indicating that phototriggering of TRPC[1/4/5] leads to exocytosis (details at **Figure S20**).

TRPC4/5 photoswitches are effective in tissue slices and can reveal channel-specific biology (Figure 5)

We believed that **AzHC** and **AzPico**'s efficacy switch mechanism and high potency should make them effective photocontrol reagents for deeper tissues, and moved to test it. The hypothalamic arcuate nucleus (ARC; **Figure 5a**) is a signaling centre in the brain where most dopamine (Th⁺) neurons are known to express TRPC5, which contributes to spontaneous oscillatory burst-firing activity and Ca²⁺ burst responses,³⁴ but also to sustained activation following stimulation with the hormone prolactin (a mechanism of reproductive signaling that has been conserved for >300 million years).^{12,34} The temporal distinction between these activation modes is striking, and suggests using either **AzHC** or **AzPico** as a time-resolved TRPC5 probe. However, we remain ignorant even of whether the most closely related congener TRPC4 plays a role in this circuitry, so we were particularly drawn to apply these reagents *comparatively*, hoping that their intersecting C4/C5 selectivities could deliver new information about TRPC4 biology in endogenous systems.

We therefore took 275 μm thick mouse brain slices through the dorsomedial ARC (**Figure 5a**), and imaged the Ca²⁺ indicator GCaMP6f in Th⁺ neurons while photoswitching **AzHC** or **AzPico**, to study TRPC[4/5] photoactuation *in situ*. Ca²⁺ influx should be seen across several independent parameters: from time-resolved aspects such as longer Ca²⁺ burst durations and lower Ca²⁺ burst frequency, to simply larger areas under the curve of the fluorescent Ca²⁺ signal (AUC), which translate into a "response index" above 1 (details at **Figure S21**). Pleasingly, we again found that **AzHC** and **AzPico** can strongly photoswitch Ca²⁺ responses at endogenous TRPC levels by all these metrics. A single ≥ 23 ms pulse of 355 nm light (*E*→*Z*) induced dramatically sustained high-Ca²⁺ signals lasting up to ≥ 3 min (42% of cells; **Figure 5bdgh**). TRPC5 is sufficient for this signal, since TRPC5 knockout slices do not respond to **AzHC** photoswitching (**Figure 5ce**). However, **Z-AzPico** Ca²⁺ photoresponses are maintained despite TRPC5 knockout, providing the first functional evidence for a role of TRPC4 or TRPC1/C4 in the Ca²⁺ response in dorsomedial Th⁺ neurons of the ARC (**Figure 5f-h, Figure S21cd**), which can now be further explored¹².

This discovery underscores the utility of this pair of photoswitches for deconvoluting the roles of TRPC4 from TRPC5. We also stress how important it was for these studies, that the reagents are high-potency as well as ideal-efficacy photoswitches. This allowed internally baselining signals after compound application (to overcome expression heterogeneity), then photoswitching activity on from zero background at a precisely defined time in a fully reproducible wavelength-dependent manner (all needed for reliable statistics). Temporally-modulated studies beyond the scope of this report are already underway, motivated by the xanthenes' sustained (low frequency) Ca²⁺ bursts, that contrast to the photoswitchable TRPC5 activator **BTDAzo** (burst frequency barely affected, **Figure 5h**). This points to a rich interplay of pharmacology and spatiotemporally-resolved biology in complex tissues, that photoswitchable reagents are uniquely poised to tackle.

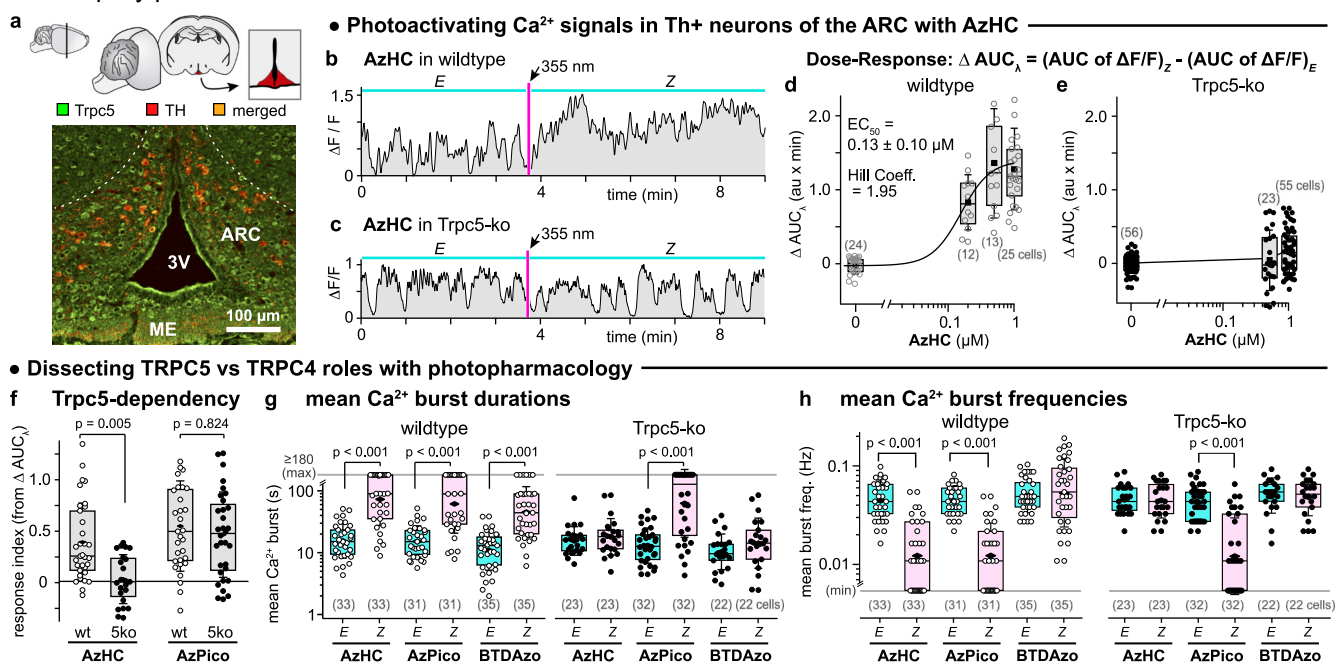


Fig 5 | AzHC and AzPico are potent photoswitchable activators of TRPC-dependent Ca²⁺ responses in mouse hypothalamus. **a**, Coronal brain slice: cartoon with ARC region in red, and microscopy image with Trpc5 immunostained in green, Th⁺ neurons in red. **b-h**, Ca²⁺ responses in Th⁺ neurons of Th-GCaMP6f (wildtype or wt) or Th-GCaMP6f- Δ Trpc5 (Trpc5-ko or 5ko) mice. **b,c**, Single-cell Ca²⁺ traces before ("E") and after ("Z") a 355 nm pulse. **d,e**, $\Delta \text{AUC}_\lambda$: light-dependency of the area under the curves as acquired in (**b,c**). **f**, **AzHC** only photocontrols TRPC5-dependent Ca²⁺ responses; **AzPico** can photocontrol Ca²⁺ responses by another route (likely TRPC4). **g,h**, mean Ca²⁺ burst durations and frequencies in wt and 5ko upon *E*→*Z* photoswitching. (**AzHC/AzPico** at 500 nM except in dose-response; **BTDAzo** at 10 μM ; **d-h**: each point is 1 cell, (n) cells per group; box plots show interquartile ranges, median (line), mean (black rhombus), and SD whiskers; **f-h**: Kruskal-Wallis ANOVA, Dunn's *p* values. For min/max values and all other details, see **Figure S21**; expanded legend at **Figure S27**.)

Photoswitching tissue-level physiology: TRPC4-based photocontrol of intestinal motility (Figure 6)

After observing these ideal efficacy switch reagents photocontrol channel currents in thin endogenous tissue slices by microscopic imaging, we next aimed to test their capabilities by photoactuating macroscopic downstream processes in thick tissue sections. Landmark papers by Freichel⁷² and Zholos¹⁶ argued by irreversible suppression experiments that TRPC4 activation should be a critical component controlling peristalsis of the small intestine, occupying a downstream position relative to muscarinic acetylcholine receptors (mAChR, the target of atropine). Intestinal segment contractions are macroscopically coordinated oscillatory motions overlaid on a "tonic" baseline contractile force. A sub-threshold slow oscillatory pacemaker potential is amplified by mAChR via phospholipase C (PLC) and TRPC4 activation to surpass the threshold potential of voltage-gated Ca²⁺ channels, leading to peristaltic contractions (**Figure 6a**). We therefore expected that direct TRPC4 activation by *Z*-**AzPico** might hijack the pacemaker signal to drive oscillatory contractility, even if upstream signaling by mAChR were blocked, and determined to test this and thus to directly elucidate the role of TRPC4 activation in intestinal contractility in endogenous tissues for the first time.

We took fresh 8-12 mm long segments of mouse small intestine (jejunal and ileal), added low atropine concentrations (300 nM) to paralyse their spontaneous motility, and monitored their contractility by macroscopic video imaging while photoswitching **AzPico** (**Figure 6b**). Indeed, even with just 10 nM **AzPico**, UV illumination initiated vigorous motions, that were stopped rapidly by applying 447 nm light, then restarted with UV, and the on↔off photocontrol could be cycled many times (**Figure 6c**, **Movie S1**). No intestinal light responses were evident without **AzPico**; and, highlighting the tissue-specificity involved, **AzPico**-treated colon segments also had no photoresponse.

We next analysed intestinal contractility quantitatively, monitoring contractile muscle force in 3 mm long ileal or jejunal segments by myography during **AzPico** photoswitching with UV and blue light (**Figure 6d**). With moderate **AzPico** concentrations (e.g. 3 nM), 365 nm UV not only increased tonic forces, but also doubled oscillatory forces (1.9×) yet *without* changing oscillatory frequency: indicating that *Z*-**AzPico** "rides" the circuit driving typical contractility. Subsequent 447 nm blue light immediately reversed this and returned to basal tension; and 365/447 nm cycling could be repeated many times (**Figure 6e**). We assign this intestinal photocontrol to TRPC4 since (i) segments of TRPC4-deficient mice⁷³ never responded to *E/Z*-**AzPico** (**Figure 6f**), while (ii) tonic and oscillatory force photoreponses in TRPC5-deficient mice were indistinguishable from those in matched control mice with the same genetic background.

Our findings thus support that TRPC4 activation is not only necessary, but also sufficient, to convert sub-threshold oscillatory signals into effective peristaltic motility in the small intestine. On an applied level, we note that the **AzPico**-induced, optically tunable re-activation of atropine-paralysed intestinal segments also bears the potential of designing experimental therapies to treat medical conditions of insufficient intestinal motility, such as toxic or post-operative paralytic ileus. On a more conceptual level, we feel it is the full and rapid photoreversibility of both gross motility and myographic readouts, assessed on the tissue level in wildtype samples, which gives such high confidence of the molecular TRPC4-specificity of intestinal contractility. We stress however that this simple and direct result is *only* possible for the ideal efficacy photoswitch, whereas classical high-affinity compounds such as (-)-**Englerin A** or **Pico145** practically cannot be washed out, so internally-baselined, reversible experimentation without fatigue-based rundown or gross toxicity⁷⁴ has been impossible before now. We also highlight that this is the first instance of a small molecule photoswitch being used to elucidate a target by hypothesis-driven research, instead of being created and used *after* target identification.

However, given the *in vivo* potential of ideal efficacy photoswitches, we are certain this will not be the last such case. To motivate this, we highlight a rare but practical example of true *light rather than dose control* that such photoswitches finally enable. Our protocols had converged to use 365 nm for high-completion *E*→*Z* switching and best channel activation; however, with moderate to high concentrations of **AzPico** (30 nM), this resulted in rictus-like intestinal tensioning and rundown, presumably via overstimulation (**Figure 6g**). On reflection, this seems to be a regular biological situation: that a desired, physiological effect is only reached when a target protein is *partially but not fully stimulated*. This could be avoided in a classical way by titrating down the **AzPico** concentration to 3 nM (**Supporting Section 7.1.1**): but the power of the efficacy switch mechanism allows a much simpler workaround. To stringently test the ideal model shown in **Figure 1g-i**, we now fully saturated tissues using 300 nM **AzPico**, but adopted 385 nm instead for UV illuminations. This 20 nm wavelength shift perfectly reproducibly drove only partial channel activation (even under saturating illumination), and so returned the physiology-like oscillatory intestinal contractions we sought, by a fully reproducible *doubly saturating* compound+light treatment protocol (**Figure 6h**). No affinity photoswitch can work when both light and compound dosage are maximised: at least one if not both of them are always limiting for biological performance. Now, we show that adopting this paradigm shift to *ideal efficacy photoswitching* can empower deep tissue or *in vivo* research, while overcoming the traditionally assumed irreproducibility of compound-and-light-dosing. Demonstrating this even on TRPC4/5 as non-linearly-responsive targets with time-and-dose-dependent bioactivity, gives an additional impression of the power that ideal efficacy photoswitching can bring to biology: whether on simple spatiotemporally-differentiated targets, or (here) as integrated in increasingly complex circuitries of biological sensing, signaling, and control.

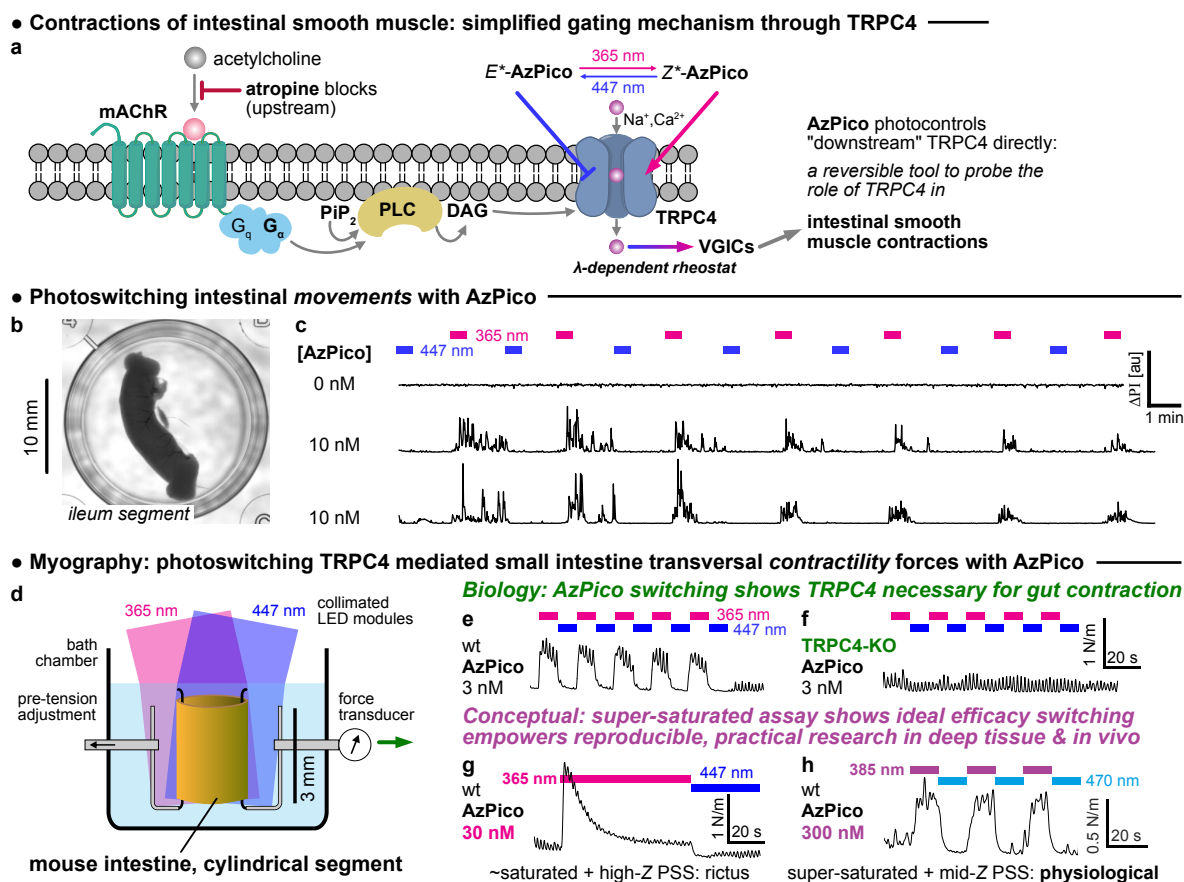


Fig 6 | AzPico photocontrol of intestinal contractility shows the key role of TRPC4, and power of ideal efficacy switching. **a**, simplified molecular mechanism for TRPC4-dependent intestinal contractility⁷⁵, that was now directly testable using **AzPico** (*E*/*Z** indicate *E/Z*-rich-PSSs). **b,c** (see also **Movie S1**), intestinal segments (mouse ileum) whose motility was blocked by atropine but were treated with **AzPico**, were driven into phases of fast macroscopic motions by UV photoswitching (longitudinal as well as ring muscle contractility), then returned to immobility by blue light, reversibly over many cycles. **d-f**, physiological-like ring contractility is reversibly stimulated and suppressed by alternating UV/blue illumination of segments treated with **AzPico**, in a TRPC4-dependent manner. **g,h**, the ideal efficacy switch paradigm allows fully reproducible control of deep tissue bioactivity, by leveraging the *saturation* of dose-and-photon-flux (hard to titrate) but the *selection* of wavelength (easy to choose) (see also **Figure S22**; full legend at **Figure S28**).

Summary

We rationally developed **AzHC** and **AzPico** as ideal efficacy photoswitches for TRPC[4]/5. Their photoisomerisation flips them between *E* inverse agonists and *Z* agonists, with both forms having excellent binding affinity: resulting in a pair of lit-active low-nanomolar-potency tools that can be used together to elucidate TRPC5-selective or TRPC4-selective biology. To date, there have only been two reports of protein-ligand structures where both *E*- and *Z*-isomers of the same azobenzene reagent were bound;^{49,60} we now report two more, with both TRPC4 and TRPC5 *E/Z* structure pairs, which will help progress design rules for efficacy switches on other targets. Unlike nearly all photopharmaceuticals, the bioactivity of **AzHC/AzPico** is fully determined by the illumination wavelength used, not their concentration. This suits them to reliable and reproducible operation across diverse model systems, from over-expression in HEK cells, to endogenous expression in primary neurons or primary adrenalin-secreting cells, to mouse brain slices, and finally intact segments of intestine, where they elegantly and directly substantiated a long-unsolved hypothesis for TRPC4-dependent contractility.

Importantly for the TRPC field, the demonstrations of highly effective *tissue-level photoresponse* under exposure to low concentrations of **AzPico** / **AzHC** mark these reagents as exceptionally effective optical tools for precisely and reversibly manipulating endogenous TRPC-dependent¹⁷ biology *in situ*. Their likely applications thus stretch far beyond the muscular and neuronal applications shown here, towards elucidating TRPC4/5's rich and largely still cryptic biology. Finally, the rapid macroscopic photoswitchability of **AzPico**'s downstream secondary and tertiary effects (i.e. not only channel opening and ion flux, but also of the integration and control of the native cascade which ultimately controls tissue-scale muscle movement) is highly unusual, if not unique, in photopharmacology (**Figure 6**).

For biology as well as chemistry in general, we have thus shown that the paradigm of efficacy photoswitching can be rationally chemically designed as well as rationally biologically exploited, and that it at last achieves a >20-year-old dream of photopharmacology: delivering robust pharmacological control of endogenous systems, that is *purely* and effectively controlled by light without needing to bow to the vagaries of drug dosing and distribution. This is the feature combination that suits it so excellently to the challenges of deep tissue and *in vivo* work. We have introduced some general biological target considerations as well as general chemical design concepts to ground the widespread introduction of efficacy photoswitching.⁵⁷ In brief, our perception has been that the targets which are of the highest

possible *importance* for studying *in vivo* with the resolution that efficacy switches allow, are also the targets which are the most *likely* to be addressable by this spatiotemporally precise paradigm. We refer to these as "poised targets", such as ion channels, receptors, sensory or signaling integrators, etc: covering many of the proteins that need to rapidly and spatiotemporally modulate their functions, in order to support life. That match of need to opportunity is of course not accidental; it simply reflects how biology has evolved and perfected its own ligand- (or protein-)based regulatory mechanisms to operate in complex environments.

We particularly encourage chemists to take up an awareness of this possibility, to start rigorously testing for it even where it was not a design aim,^{52,53,55,56} and to work towards rationally using the efficacy photoswitching paradigm to generate a cornucopia of *in vivo*-competent reagents, rather than remaining locked to affinity photoswitching approaches. We foresee that such efficacy photoswitches can unlock a new era for photocontrolled biology, in ways that deeply impact not only chemical or cell culture proof of principle studies, but translate seamlessly across to basic physiology and medical research, to noninvasively probe and modulate endogenous pathways in deep tissues and *in vivo*.

AUTHOR INFORMATION

‡ M.M. and K.N. declare equal first authorship contributions, with the right to present their author positions in either order in publication lists.

Addresses:

¹Department of Pharmacy, Ludwig-Maximilians University of Munich, DE.

²Rudolf-Boehm-Institute of Pharmacology and Toxicology, Leipzig University, DE.

³Center for Integrative Physiology and Molecular Medicine, Saarland University, DE.

⁴Leeds Institute of Cardiovascular and Metabolic Medicine, LIGHT Laboratories, University of Leeds, UK.

⁵Astbury Centre for Structural Molecular Biology, University of Leeds, UK.

⁶Department of Structural Biochemistry, Max Planck Institute of Molecular Physiology, Dortmund, DE.

⁷School of Biomedical Sciences, University of Leeds, UK.

Corresponding Authors:

* michael.schaefer@medizin.uni-leipzig.de;

* oliver.thorn-seshold@cup.lmu.de

ORCID:

Navin K. Ojha: 0000-0001-9225-4267

Sebastian A. Porav 0000-0003-4238-0083

Deivanayagarathy Vinayagam 0000-0001-7862-9499

Nicole Urban: 0000-0001-5516-7922

Claudia C. Bauer 0000-0003-4278-4803

Aidan V. Johnson 0000-0003-0303-9106

Stephen P. Muench 0000-0001-6869-4414

Frank Zufall: 0000-0002-4383-8618

Stefan Raunser 0000-0001-9373-3016

Trese Leinders-Zufall: 0000-0002-0678-362X

Robin S. Bon: 0000-0003-1733-3680

Michael Schaefer: 0000-0003-3662-4387

Oliver Thorn-Seshold: 0000-0003-3981-651X

Caption to Movie S1

Movie S1: Photocontrol over gross motility of intestinal segments by alternating 365/447 nm illumination in the presence of 10 nM **AzPico**.

Funding

This research was supported by funds from the **German Research Foundation** (DFG: SFB TRR 152

number 239283807 projects P24 to O.T.-S., P18 to M.S., P02 to S.R., P10 to F.Z. and T.L.-Z., P07 to Y.S. and D.B.; SFB 1032 project B09 number 201269156, SPP 1926 project number 426018126, and Emmy Noether grant 400324123 to O.T.-S.; SFB 894 project A17 to F.Z. and T.L.-Z.); the **Biotechnology and Biological Sciences Research Council** (BB/P020208/1 to R.S.B.); the **British Heart Foundation** (PG/19/2/34084 to C.C.B.); and the **Max Planck Society** (to S.R.).

Large-scale tissue culture at the University of Leeds was performed in the Asbury Protein Production Facility, funded by the University of Leeds and the Royal Society (WL150028). CryoEM work at Leeds was performed at the Astbury Biostructure Laboratory, funded by the University of Leeds and Wellcome Trust (108466/Z/15/Z; 221524/Z/20/Z; 218785/Z/19/Z).

Author Contributions

As related to **Figure 1a-j, 2h-j**: M.Müller designed targets and performed synthesis and photochemical evaluation, as supervised by O.T.-S.; M.Müller and O.T.-S. performed mechanistic analysis and modelling.

As related to **Figures 1k-n, 2a-g, 6**: K.N. and F.B. performed all experiments as designed and supervised by N.U. and M.S.. M.S. analysed data and drafted the corresponding manuscript sections and figures.

As related to **Figure 3a-d**: S.A.P. performed protein expression/purification, cryoEM data collection, processing, and model building and data analysis; C.C.B. designed and cloned TRPC4 and TRPC5 plasmids; A.V.J. performed intracellular calcium recordings and analysed data; S.A.P. and A.V.J. made figures; S.P.M. and R.S.B. designed and supervised experiments and obtained funding; R.S.B. wrote sections of the manuscript with input from S.A.P., C.C.B., A.V.J. and S.P.M..

As related to **Figure 3e-h**: D.V. performed protein expression/purification, cryoEM data collection and processing, under the supervision of S.R.

As related to **Figure 4**: K.O. and M.Makke performed all experiments related to chromaffin cells and hippocampal neurons, that were designed, supervised, and analysed by Y.S. and D.B., who drafted the corresponding manuscript sections and figures.

As related to **Figure 5**: N.K.O., F.Z., and T.L.Z. designed, performed, analysed, and drafted the

manuscript for all experiments related to mouse hypothalamus.

M.S. and O.T.-S. designed the study.

M.Müller and O.T.-S. performed overall data and figure assembly, and wrote the manuscript with input from all authors.

Acknowledgements

M.Müller thanks the Joachim Herz Foundation for fellowship support. A.V.J. thanks the BBSRC for a White Rose DTP PhD studentship. Professor Eric Gouaux (Vollum Institute) is kindly acknowledged for providing the BacMam vector. Marc Freichel (Heidelberg) is kindly acknowledged for providing the TRPC4- and TRPC5-KO mice. O.T.-S. thanks Rob Leurs, Michael Decker, Pau Gorostiza, Wiktor Szymanski, and James Frank, for feedback on the prior reports of efficacy switches.

Data and materials availability

All data needed to evaluate the conclusions in the paper are present in the paper and/or the Supplementary Materials. Data are also deposited and freely available on BioRxiv and Figshare (*dois upon paper acceptance*).

Cryo-EM structures are deposited as:

TRPC4_{DR}:E-AzPico, 3.0 Å, PDB 9FXL, EMD 50850;

TRPC4_{DR}:Z-AzPico, 3.1 Å, PDB 9FXM, EMD 50851;

hTRPC5:E-AzHC, 2.6 Å, PDB xxxx, EMD xxxx;

hTRPC5:Z-AzHC, 2.9 Å, PDB xxxx, EMD xxxx.

Conflict of Interest

R.S.B. is co-founder and partner of the pharmaceutical start-up company CalTIC GmbH. R.S.B. and S.A.P. have received funding from CalTIC GmbH. The other authors declare no conflict of interest.

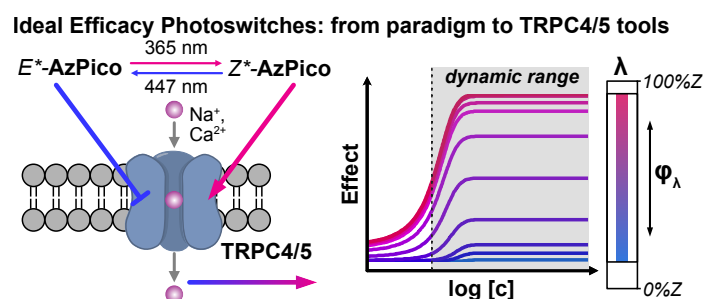
REFERENCES

- Clapham, D. E. TRP channels as cellular sensors. *Nature* **426**, 517–524 (2003).
- Flockerzi, V. & Nilius, B. TRPs: Truly Remarkable Proteins. in *Mammalian Transient Receptor Potential (TRP) Cation Channels: Volume I* (eds. Nilius, B. & Flockerzi, V.) 1–12 (Springer, Berlin, Heidelberg, 2014). doi:10.1007/978-3-642-54215-2_1.
- Kaneko, Y. & Szallasi, A. Transient receptor potential (TRP) channels: a clinical perspective. *British Journal of Pharmacology* **171**, 2474–2507 (2014).
- Koivisto, A.-P., Belvisi, M. G., Gaudet, R. & Szallasi, A. Advances in TRP channel drug discovery: from target validation to clinical studies. *Nat Rev Drug Discov* **21**, 41–59 (2022).
- Zhang, M. *et al.* TRP (transient receptor potential) ion channel family: structures, biological functions and therapeutic interventions for diseases. *Sig Transduct Target Ther* **8**, 1–38 (2023).
- Clapham, D. E., Runnels, L. W. & Strübing, C. The trp ion channel family. *Nature Reviews Neuroscience* **2**, 387–396 (2001).
- Zholos, A. V. TRPC5. in *Mammalian Transient Receptor Potential (TRP) Cation Channels* (eds. Nilius, B. & Flockerzi, V.) vol. 222 129–156 (Springer Berlin Heidelberg, Berlin, Heidelberg, 2014).
- Freichel, M., Tsvilovsky, V. & Camacho-Londoño, J. E. TRPC4- and TRPC4-Containing Channels. in *Mammalian Transient Receptor Potential (TRP) Cation Channels* (eds. Nilius, B. & Flockerzi, V.) vol. 222 85–128 (Springer Berlin Heidelberg, Berlin, Heidelberg, 2014).
- Sadler, K. E. *et al.* Transient receptor potential canonical 5 mediates inflammatory mechanical and spontaneous pain in mice. *Science Translational Medicine* **13**, eabd7702 (2021).
- Bernal, L. *et al.* Odontoblast TRPC5 channels signal cold pain in teeth. *Science Advances* **7**, eabf5567 (2021).
- Koivisto, A.-P., Voets, T., Iadarola, M. J. & Szallasi, A. Targeting TRP channels for pain relief: A review of current evidence from bench to bedside. *Current Opinion in Pharmacology* **75**, 102447 (2024).
- Blum, T. *et al.* Trpc5 deficiency causes hypoprolactinemia and altered function of oscillatory dopamine neurons in the arcuate nucleus. *Proc. Natl. Acad. Sci. USA* **116**, 15236–15243 (2019).
- Riccio, A. *et al.* Decreased Anxiety-Like Behavior and Gαq/11-Dependent Responses in the Amygdala of Mice Lacking TRPC4 Channels. *J. Neurosci.* **34**, 3653–3667 (2014).
- Riccio, A. *et al.* Essential Role for TRPC5 in Amygdala Function and Fear-Related Behavior. *Cell* **137**, 761–772 (2009).
- Zhou, Y. *et al.* A small-molecule inhibitor of TRPC5 ion channels suppresses progressive kidney disease in animal models. *Science* (2017) doi:10.1126/science.aal4178.
- Dryn, D. O., Melnyk, M. I., Bon, R. S., Beech, D. J. & Zholos, A. V. Pico145 inhibits TRPC4-mediated mICAT and postprandial small intestinal motility. *Biomedicine & Pharmacotherapy* **168**, 115672 (2023).
- Li, Y. *et al.* Loss of transient receptor potential channel 5 causes obesity and postpartum depression. *Cell* doi:10.1016/j.cell.2024.06.001.
- Dietrich, A., Fahlbusch, M. & Gudermann, T. Classical Transient Receptor Potential 1 (TRPC1): Channel or Channel Regulator? *Cells* **3**, 939–962 (2014).
- Bon, R. S. & Beech, D. J. In pursuit of small molecule chemistry for calcium-permeable non-selective TRPC channels – mirage or pot of gold? *Br. J. Pharmacol.* **170**, 459–474 (2013).
- Sharma, S. & Hopkins, C. R. Review of Transient Receptor Potential Canonical (TRPC5) Channel Modulators and Diseases. *J. Med. Chem.* **62**, 7589–7602 (2019).

21. Ratnayake, R., Covell, D., Ransom, T. T., Gustafson, K. R. & Beutler, J. A. Englerin A, a Selective Inhibitor of Renal Cancer Cell Growth, from *Phyllanthus engleri*. *Org. Lett.* **11**, 57–60 (2009).
22. Akbulut, Y. *et al.* (–)-Englerin A is a Potent and Selective Activator of TRPC4 and TRPC5 Calcium Channels. *Angew. Chem. Int. Ed.* **54**, 3787–3791 (2015).
23. Radtke, L. *et al.* Total Synthesis and Biological Evaluation of (–)-Englerin A and B: Synthesis of Analogues with Improved Activity Profile. *Angewandte Chemie International Edition* **50**, 3998–4002 (2011).
24. Just, S. *et al.* Treatment with HC-070, a potent inhibitor of TRPC4 and TRPC5, leads to anxiolytic and antidepressant effects in mice. *PLoS ONE* **13**, e0191225 (2018).
25. Yu, M. *et al.* Discovery of a Potent and Selective TRPC5 Inhibitor, Efficacious in a Focal Segmental Glomerulosclerosis Model. *ACS Med. Chem. Lett.* **10**, 1579–1585 (2019).
26. Curcic, S., Tiapko, O. & Groschner, K. Photopharmacology and opto-chemogenetics of TRPC channels—some therapeutic visions. *Pharmacol. Ther.* **200**, 13–26 (2019).
27. Frank, J. A. *et al.* Photoswitchable fatty acids enable optical control of TRPV1. *Nat. Commun* **6**, 7118 (2015).
28. Stein, M., Breit, A., Fehrentz, T., Gudermann, T. & Trauner, D. Optical Control of TRPV1 Channels. *Angewandte Chemie International Edition* **52**, 9845–9848 (2013).
29. Lam, P.-Y. *et al.* TRPswitch—A Step-Function Chemo-optogenetic Ligand for the Vertebrate TRPA1 Channel. *J. Am. Chem. Soc.* **142**, 17457–17468 (2020).
30. Tiapko, O. *et al.* Lipid-independent control of endothelial and neuronal TRPC3 channels by light. *Chem. Sci.* **10**, 2837–2842 (2019).
31. Leinders-Zufall, T. *et al.* PhoDAGs Enable Optical Control of Diacylglycerol-Sensitive Transient Receptor Potential Channels. *Cell Chem. Bio.* **25**, 215–223.e3 (2018).
32. Leinders-Zufall, T. *et al.* A diacylglycerol photoswitching protocol for studying TRPC channel functions in mammalian cells and tissue slices. *STAR Protocols* **2**, 100527 (2021).
33. Lichtenegger, M. *et al.* An optically controlled probe identifies lipid-gating fenestrations within the TRPC3 channel. *Nature Chemical Biology* **14**, 396–404 (2018).
34. Müller, M. *et al.* BTDAzo: A Photoswitchable TRPC5 Channel Activator**. *Angew Chem Int Ed* **61**, (2022).
35. Minard, A. *et al.* Potent, selective, and subunit-dependent activation of TRPC5 channels by a xanthine derivative. *Br. J. Pharmacol.* **176**, 3924–3938 (2019).
36. Bauer, C. C. *et al.* Xanthine-based photoaffinity probes allow assessment of ligand engagement by TRPC5 channels. *RSC Chem. Biol.* **10**.1039.D0CB00126K (2020) doi:10.1039/D0CB00126K.
37. Fuchter, M. J. On the Promise of Photopharmacology Using Photoswitches: A Medicinal Chemist's Perspective. *J. Med. Chem.* **63**, 11436–11447 (2020).
38. Thorn-Seshold, O. & Meiring, J. C. M. Photocontrolling Microtubule Dynamics with Photoswitchable Chemical Reagents. in *Microtubules: Methods and Protocols* (ed. Inaba, H.) 403–430 (Springer US, New York, NY, 2022). doi:10.1007/978-1-0716-1983-4_26.
39. Thorn-Seshold, O. Photoswitchable Cytotoxins. in *Molecular Photoswitches* 873–919 (2022). doi:10.1002/9783527827626.ch36.
40. Hüll, K., Morstein, J. & Trauner, D. In Vivo Photopharmacology. *Chem. Rev.* **118**, 10710–10747 (2018).
41. Colquhoun, D. Binding, gating, affinity and efficacy: The interpretation of structure-activity relationships for agonists and of the effects of mutating receptors. *British Journal of Pharmacology* **125**, 923–947 (1998).
42. Agnetta, L. *et al.* A Photoswitchable Dualsteric Ligand Controlling Receptor Efficacy. *Angewandte Chemie International Edition* **56**, 7282–7287 (2017).
43. Gómez-Santacana, X. *et al.* A toolbox of molecular photoswitches to modulate the CXCR3 chemokine receptor with light. *Beilstein J. Org. Chem.* **15**, 2509–2523 (2019).
44. Steinmüller, S. A. M., Tutov, A., Hislop, J. N. & Decker, M. Bridging the Binding Sites 2.0: Photoswitchable Dualsteric Ligands for the Cannabinoid 2 Receptor. *ACS Chem. Neurosci.* **14**, 3737–3744 (2023).
45. Hansen, M. J., Hille, J. I. C., Szymanski, W., Driesen, A. J. M. & Feringa, B. L. Easily Accessible, Highly Potent, Photocontrolled Modulators of Bacterial Communication. *Chem* **5**, 1293–1301 (2019).
46. Gerwe, H., He, F., Pottier, E., Stove, C. & Decker, M. Enlightening the “Spirit Molecule”: Photomodulation of the 5-HT_{2A} Receptor by a Light-Controllable N,N-Dimethyltryptamine Derivative. *Angewandte Chemie International Edition* **61**, e202203034 (2022).
47. Riefolo, F. *et al.* Optical Control of Cardiac Function with a Photoswitchable Muscarinic Agonist. *J. Am. Chem. Soc.* **141**, 7628–7636 (2019).
48. Gómez-Santacana, X. *et al.* Photoswitching the Efficacy of a Small-Molecule Ligand for a Peptidergic GPCR: from Antagonism to Agonism. *Angewandte Chemie International Edition* **57**, 11608–11612 (2018).
49. Arkhipova, V. *et al.* Structural Aspects of Photopharmacology: Insight into the Binding of Photoswitchable and Photocaged Inhibitors to the Glutamate Transporter Homologue. *J. Am. Chem. Soc.* **143**, 1513–1520 (2021).
50. Westphal, M. V. *et al.* Synthesis of Photoswitchable Δ^9 -Tetrahydrocannabinol Derivatives Enables Optical Control of Cannabinoid Receptor 1 Signaling. *J. Am. Chem. Soc.* **139**, 18206–18212 (2017).
51. Panarello, S., Rovira, X., Llebaria, A. & Gómez-Santacana, X. Photopharmacology of G-Protein-Coupled Receptors. in *Molecular Photoswitches* 921–944 (2022). doi:10.1002/9783527827626.ch37.
52. Morstein, J. *et al.* Optical control of sphingosine-1-phosphate formation and function. *Nature Chemical Biology* **15**, 623–631 (2019).
53. Lam, P.-Y. *et al.* TRPswitch—A Step-Function Chemo-optogenetic Ligand for the Vertebrate TRPA1 Channel. *J. Am. Chem. Soc.* **142**, 17457–17468 (2020).
54. Tiapko, O. *et al.* Lipid-independent control of endothelial and neuronal TRPC3 channels by light. *Chem. Sci.* **10**, 2837–2842 (2019).
55. Yue, L. *et al.* Robust photoregulation of GABA_A receptors by allosteric modulation with a propofol analogue. *Nature Communications* **3**, 1095 (2012).
56. Morstein, J. *et al.* Optical Control of Lysophosphatidic Acid Signaling. *J. Am. Chem. Soc.* **142**, 10612–10616 (2020).
57. Photoswitching in 2030: What Concepts Do We Need To Reach Impactful Photopharmacology? *article in preparation*.
58. Chenard, B. & Gallaschun, R. Substituted xanthines and methods of use thereof. (2014).
59. Rubaiy, H. N. *et al.* Picomolar, selective, and subtype-specific small-molecule inhibition of TRPC1/4/5 channels. *J. Biol. Chem.* **292**, 8158–8173 (2017).
60. Pospich, S. *et al.* Cryo-EM Resolves Molecular Recognition Of An Optojasp Photoswitch Bound To Actin Filaments In Both Switch States. *Angewandte Chemie International Edition* **60**, 8678–8682 (2021).
61. Vinayagam, D. *et al.* Electron cryo-microscopy structure of the canonical TRPC4 ion channel. *eLife* **7**, e36615 (2018).
62. Duan, J. *et al.* Structure of the mouse TRPC4 ion channel. *Nat Commun* **9**, 3102 (2018).
63. Vinayagam, D. *et al.* Structural basis of TRPC4 regulation by calmodulin and pharmacological agents. *eLife* **9**, e60603 (2020).
64. Song, K. *et al.* Structural basis for human TRPC5 channel inhibition by two distinct inhibitors. *eLife* **10**, e63429 (2021).

65. Won, J. *et al.* Molecular architecture of the Gai-bound TRPC5 ion channel. *Nat Commun* **14**, 2550 (2023).
66. Wright, D. J. *et al.* Human TRPC5 structures reveal interaction of a xanthine-based TRPC1/4/5 inhibitor with a conserved lipid binding site. *Commun. Biol.* **3**, 704 (2020).
67. Duan, J. *et al.* *Cryo-EM Structure of the Receptor-Activated TRPC5 Ion Channel at 2.9 Angstrom Resolution.* <http://biorxiv.org/lookup/doi/10.1101/467969> (2018) doi:10.1101/467969.
68. Wright, D. J. *et al.* Human TRPC5 structures reveal interaction of a xanthine-based TRPC1/4/5 inhibitor with a conserved lipid binding site. *Communications Biology* **3**, 704 (2020).
69. Schwarz, Y. *et al.* TRPC channels regulate Ca²⁺-signaling and short-term plasticity of fast glutamatergic synapses. *PLOS Biology* **17**, e3000445 (2019).
70. Bröker-Lai, J. *et al.* Heteromeric channels formed by TRPC1, TRPC4 and TRPC5 define hippocampal synaptic transmission and working memory. *The EMBO Journal* **36**, 2770–2789 (2017).
71. Jenny Bröker-Lai, José Rego Terol, Christin Richter, Ilka Mathar, Angela Wirth, Stefan Kopf, Ana Moreno-Pérez, Michael Büttner, Linette Liqi Tan, Mazen Makke, Gernot Poschet, Julia Hermann, Volodymyr Tsvilovsky, Uwe Haberkorn, Philipp Wartenberg, Michael Berlin, Roger Ottenheijm, Koenraad Philippaert, Moya Wu, Tobias Wiedemann, Stephan Herzig, Anouar Belkacemi, Rebecca Levinson Terral, Nitin Agarwal, Juan E. Camacho Londoño, Bert Klebl Klaus Dinkel, Frank Zufall, Peter Nussbaumer, Ulrich Boehm, Rüdiger Hell, Peter Nawroth, Lutz Birnbaumer, Trese Leinders-Zufall, Rohini Kuner, Markus Zorn, Dieter Bruns, Yvonne Schwarz and Marc Freichel. TRPC5 controls the adrenaline-mediated counter regulation of hypoglycemia. *EMBO J* (2024).
72. Tsvilovsky, V. V. *et al.* Deletion of TRPC4 and TRPC6 in Mice Impairs Smooth Muscle Contraction and Intestinal Motility In Vivo. *Gastroenterology* **137**, 1415–1424 (2009).
73. Freichel, M. *et al.* Lack of an endothelial store-operated Ca²⁺ current impairs agonist-dependent vasorelaxation in TRP4^{-/-} mice. *Nature Cell Biology* **3**, 121–127 (2001).
74. Ying Cheung, S. *et al.* TRPC4/TRPC5 channels mediate adverse reaction to the cancer cell cytotoxic agent (-)-Englerin A. *Oncotarget; Vol 9, No 51* (2018).
75. Zholos, A. V., Melnyk, M. I. & Dryn, D. O. Molecular mechanisms of cholinergic neurotransmission in visceral smooth muscles with a focus on receptor-operated TRPC4 channel and impairment of gastrointestinal motility by general anaesthetics and anxiolytics. *Neuropharmacology* **242**, 109776 (2024).

Table of Contents Graphic



3 Conclusions and Outlook

3.1 Research summary

Part I: A rational photophysics-based design for effective optoacoustic imaging contrast agents

Optoacoustic (OA) imaging allows non-invasive imaging and exogenous contrast agents are crucial components to resolve biological processes and indirectly track biomarkers. Small molecules with near infrared (NIR) absorption have been a pillar of modern chemical biology as fluorescent probes, and these are now being repurposed for OA imaging.

This thesis investigated rational molecular designs for OA contrast agents based on photophysical tuning, primarily focusing on achieving ultrafast electronic relaxation and demonstrating its advantages.

We first demonstrated that NIR-absorbing *AzoHemicyanines* are *loud* OA contrast agents compared to the repurposed fluorophore standard, **ICG**. Their ultra-fast relaxation ($S_1 \rightarrow S_0$) was a key driving force for strong OA signal emission intensity on a *per photon* metric, and was caused by the implementation of molecular switches in the chromophore. Additionally, the ultra-fast relaxation resulted in indefinite signal stability under constant irradiation, a critical feature for reliable long-term imaging experiments which most current repurposed fluorophores cannot provide. The results presented in **section 1.3.2** also included an *in vivo* application that validated how spectral deconvolution against endogenous contrast agents in native tissue succeeds with band-broadened, switch-merged designs.

We next showed that the desired properties of OA signal strength and photostability could also be realised with rather different molecular motifs, by reaching the same crucial photophysical property of ultrafast relaxation. We showed that molecular rotors, namely, NIR absorbing triarylmethanes (TAMs) are *loud* and photostable OA contrast agents also based on ultra-fast $S_1 \rightarrow S_0$, now enabled by their intrinsic molecular motility. These results are presented in **section 1.3.3** and support the rational approach of ultra-fast excited state relaxation as a molecular blueprint for effective OA contrast agents.

Part II: Developing efficacy photoswitches and applying them to chromocontrol TRPC4/5

Photopharmacology allows optical control over biological functionality by photoswitching the properties of photoisomerisable chemical probes. Photopharmaceutical probes are especially valuable for dynamic systems, because static drugs can only induce static effects, whereas photopharmaceuticals allow spatiotemporally targeted and reversible control. Particularly, ion channels or receptors can profit from dynamic modulation as it may better reflect their native signalling dynamics.

This thesis investigated the optical control of TRPC4 and TRPC5, two closely related non-selective cation channels with largely unknown but tissue dependent functions. We based our work on the introduction of azobenzene photoswitches to established pharmacological tool compounds or drugs, aiming to harness the pharmacology of the parent compounds while simultaneously adding a photocontrollable dynamic part in terms of the azobenzene photoswitch.

We first demonstrated optical control over TRPC5 with the photoswitchable activator **BTDAzo**, that had excellent selectivity over the closest homologue TRPC4, and unexpectedly excellent bidirectional bioactivity photoswitching in cells (between basal activity and full activation of TRPC5 currents/ Ca^{2+}

signals). These results are presented in **section 2.3.2** and demonstrate the usability of this tool in complex tissue with low TRPC5 expression levels, and thus show that **BTDAzo** is a valuable tool for spatiotemporally precise TRPC5 studies.

Retrospectively, we rationalised **BTDAzo's** excellent bidirectional biological control as being due to an efficacy photoswitch mechanism, with competitive binding of the opposing efficacy photoisomers (e.g. antagonist vs agonist). We modelled the performance exerted by ideal efficacy photoswitches and mapped their implications for practical photopharmacology, crucially finding that their biological effect is controlled purely by the *E/Z* isomer ratio which is controlled purely by the applied wavelength, and coining the term *chromocontrol* to describe this. We then further developed the experimental concept of ideal efficacy photoswitching by rationally targeting a known efficacy cliff within the class of xanthene ligands for TRPC4/5. The results presented in **section 2.3.3** demonstrate how the ideal efficacy photoswitches **AzPico** and **AzHC** for TRPC4 and TRPC5 can address a range of complex biological systems such as cultured neurons, chromaffin cells, mouse brain slices, and small intestine segments, with fully reproducible and sensitively-tunable, photoreversible chromocontrol over channel activity.

3.2 Ongoing research and outlook: Optoacoustic Imaging

Molecular imaging probes based on the TAM motif

In the first part of this thesis, it was shown how fast kinetics of non-radiative decay rates increase PA signal intensities on a molecular level, and structural guidance to obtain such contrast agents was given. However, the true power of molecular contrast agents is the ability to recognize and image biomarkers and enzyme activity; so the logical next step is to combine biomarker-responsive groups with our newly developed *loud, photostable* scaffolds. Contrast agents for molecular PA imaging should change their absorption spectra upon enzymatic reaction; and their sensitivity for the analyte will be determined by the spectral separation between probe and product (section 1.1.2.2, Figure 7. Spectral properties required for ideal activation in photoacoustic imaging without generation of background signals and loss in sensitivity. a) ideal case scenario with spectral separation. b) spectral overlap which results in loss of sensitivity. Figure 7). NIR absorbing TAMs are thus promising motifs, for their absorption jump of ~400/600 nm by addition/removal of a nucleophile at the central carbon (see also part I: section 1.3.3, and Figure 28). As the prior art in hemicyanines shows, once a suitable activatable PA chromophore is established, it will be adopted readily for the field.

Major Outlook 1: Molecular imaging probes for H₂O₂

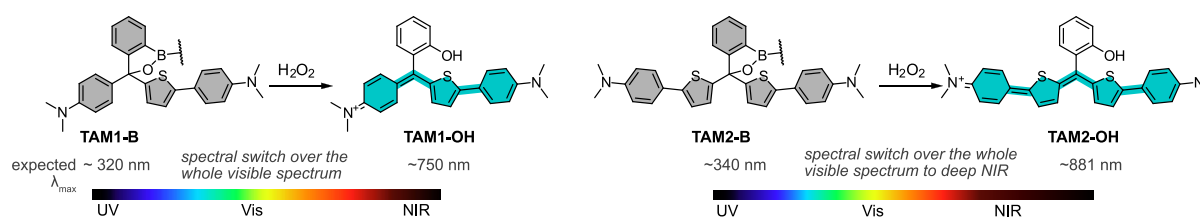
Hydrogen peroxide is regarded as a critical signalling molecule involved in the reversible oxidation of proteins, and increased concentrations are a sign for disordered redox homeostasis and oxidative stress.³¹⁵ Phenylboronates or borinates act as sensors for H₂O₂ by forming phenols after oxidation,^{316,317} with many fluorogenic probes using this effect.³¹⁸ I recognised boronate spirocycles incorporated into the TAM core structure as a chance for sensitive molecular H₂O₂ PA sensors, and I designed the responsive TAM concept shown in Figure 28a.

In my approach, the probe exists preferably in a UV absorbing form with a central sp³-carbon (**TAM1/2-B**); only after the oxidation-hydrolysis-elimination cascade, is the NIR-absorbing TAM

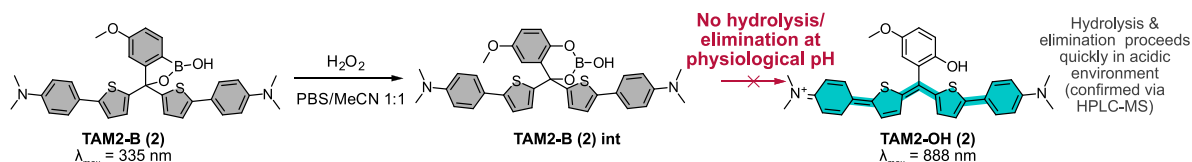
structure containing a phenol at the outlying phenyl ring (**TAM1/2-OH**) released. The previous results with related compounds promise sharp absorption peaks with a reaction-induced spectral shift to the NIR (expectations for **TAM1/2**: λ_{\max} shift from 320 nm to 750 nm; **TAM1/2**: λ_{\max} 340 nm to 880 nm).

Preliminary results validate the design proof of concept and confirm an impressive spectral shift from $\lambda_{\max} = 335$ nm to 888 nm (Figure 28b), a shift that leaps over the whole visible spectrum. However, for application the probe needs to be fine-tuned, because the intermediate 6-membered borate-lactone (**TAM1/2-B (2) int**) is stable under physiological pH and only releases the NIR absorbing TAM under acidic conditions (HPLC-MS analysis with acidic modifier shows only **TAM1/2-OH (2)** as product, UV/VIS at pH 7.4 only a UV absorbing species).

a Boronic/Borinic acid probes for PA imaging



b Preliminary results



c Proposed structural modifications

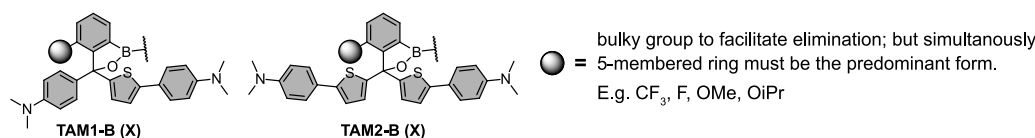


Figure 28. TAM based H_2O_2 sensors. a) Structural design of TAM H_2O_2 sensors: boronic/borinic acid forms a 5-membered spirocycle absorbing in the UV region and an oxidation-hydrolysis cascade releases the NIR absorbing TAM PA contrast agent. b) Preliminary results indicate that the intermediate 6-membered borate ester is stable against hydrolysis at physiological pH; addition of acid hydrolyses the boric acid as detected in HPLC-MS with acidic modifier. c) Proposed structural modifications towards a high sensitivity probe operated at physiological pH.

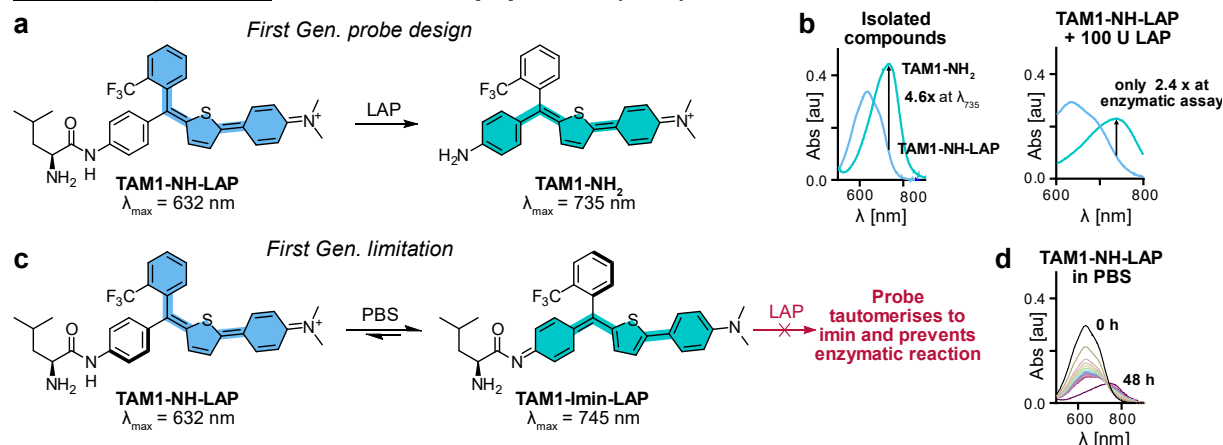
For colleagues who may take over this project idea in the future, I would therefore suggest introducing bulky residues at the 6' position on the outlying phenyl ring to generate steric clash facilitating the desired ring opening (Figure 28c). I expect a narrow window for fine-tuning because such modifications might also interfere with the stability of the starting borate lactone, and formation of a zwitterionic boronate structure would reduce sensitivity. Summarised, the combination of spirocyclic boronates (or borinates) as sensing motif with TAMs as loud PA emitter can promise an unprecedented bathochromic shift for a bioactive probe, that may ultimately be useful for molecular PA imaging of oxidant dynamics.

Major Outlook 2: Modular design of molecular imaging probes using the TAM scaffold

To gain access to a broader set of biomarkers I envisioned a different turn-on mechanism. Attachment of removable electron withdrawing groups (EWG) onto the TAM scaffold induces a hypsochromic shift and spectral separation for imaging purposes. I chose a leucine-amide as a model substrate because the amide bond can be cleaved by leucine aminopeptidase and the enzyme is rather promiscuous as long as the substrate is a N-terminal primary amine.³¹⁹ To obtain preliminary results I

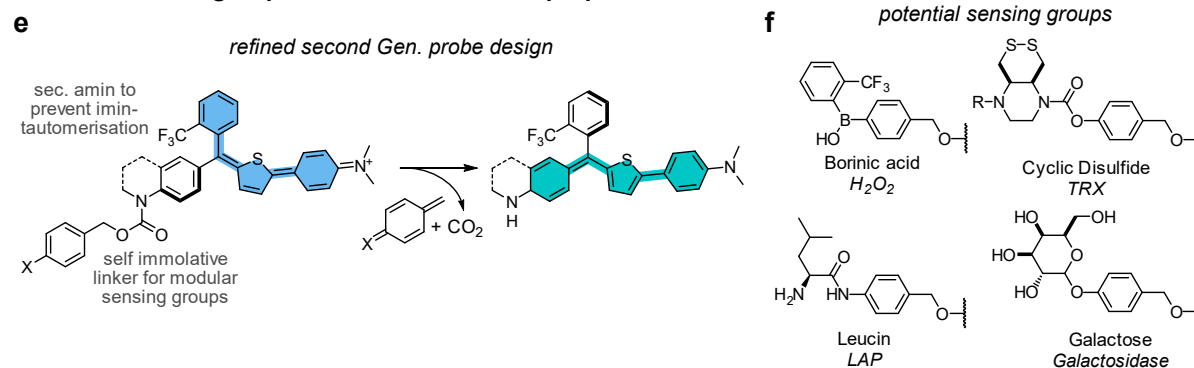
synthesized **TAM1-NH-LAP** and **TAM1-NH₂** as model substrates (Figure 29a). The hypsochromic shift is only ~100 nm, so there is significant spectral overlap (extinction coefficient ratio is 5× at the product λ_{\max} , or 20× at 800 nm though with ~4-fold-lower ϵ : Figure 29b). Initial enzyme assays and hydrolysis controls indicated probe tautomerism between two forms (Figure 29b,c,d) that decreased the already low sensitivity, resulting in an unreliable probe. Secondary amines might resolve this undesired side-effect, but would require an extended self-immolative spacer (Figure 29e); that would however open up the sensing chemical space towards a plethora of different sensing groups e.g. H₂O₂,³¹⁷ the redox enzyme TRX,³²⁰ LAP,³¹⁹ and β -galactosidase³²¹ (Figure 29f).

Preliminary results: Leucin amino peptidase (LAP) as model substrate



Design strategies towards modular high contrast molecular probes

Removable EWG groups modulate absorption properties



Removable EWG groups modulate pK_{Cycle} of an unusual pyran-phenol cyclisation equilibrium

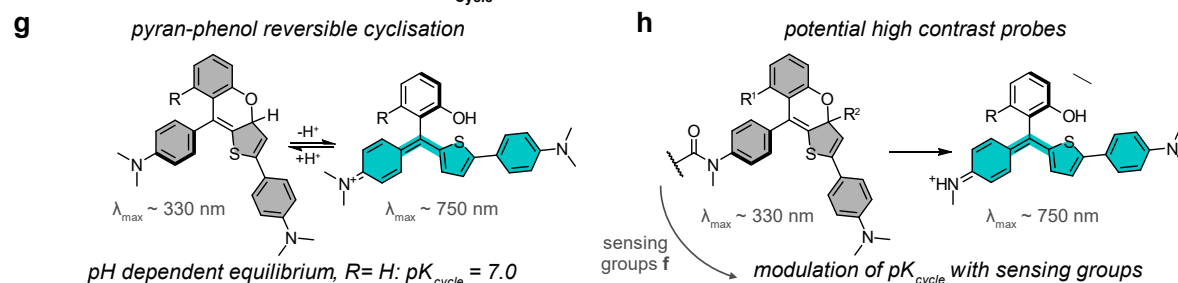


Figure 29. Design of modular probes suitable for various types of biochemical analytes. a-d) Preliminary results for the generation of a leucine aminopeptidase (LAP)-responsive TAM PA probe. a) chemical structures. b) Absorption spectra of isolated **TAM1-NH-LAP** and **TAM1-NH₂** and before and after enzymatic reaction. c) Potential mechanism of probe inactivation by tautomerisation. d) Change in absorption properties over time of **TAM1-NH-LAP** in PBS.. e) design concept to increase sensitivity by removal of a possible tautomerisation mechanism. f) Exemplary sensing groups for different types of biochemical analytes. g) structural basis of a potential high sensitivity probe; Note: the mechanism via pyran ring formation is assigned tentatively based on preliminary experimental results. h) Potential modular high sensitivity probes for molecular PA imaging with TAM scaffolds.

During evaluation of the **TAM1/2-OH** scaffolds (Figure 28a) I found an intriguing pH dependent spectral switch from UV to NIR that I tentatively assigned to the reversible formation of an 6-membered pyran (Figure 29g, for details see section 5.1.5). The pH dependency of the spectral switch can be chemically modulated by the pKs of the phenol indicating the nucleophilicity of the negatively charged phenolate as driving force for ring closure. In case this hypothesis holds true, it ought to be possible for pK_{cycle} to be modulated by changing pKs of the phenol and the electrophilicity of the carbon.

Therefore, I would propose again an introduction of electron withdrawing cleavable groups to increase the electrophilicity of the carbon and induce pyran formation with a maximum absorption in the UV-region. Cleavage of the EWG by the targeted biomarker could induce ring opening and formation of a strong NIR chromophore that I expect could be visualized by PA imaging.

No matter what the exact structural basis for opening a TAM pyran, I would argue that it is clear that this modular concept and its unprecedentedly large wavelength switch to the NIR is an ideal starting point for high sensitivity molecular PA contrast agent development.

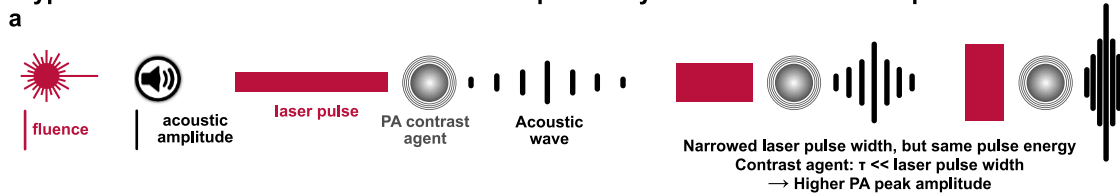
Related Outlook 1: Benchmarking imaging hardware on fast-relaxing contrast agents

Our ultra-fast relaxing PA chromophores can now be used to review potentially biased settings used on commercial PA devices (standard: 10 ns pulse width). PA signal intensity scales with the laser fluence, thus with constant pulse energies but shorter pulses, the PA peak amplitude must increase (Figure 30a). This result was already observed for gold nanospheres,³²² and now the availability of loud PA contrast agents with defined photophysical properties will allow to test and potentially shift towards instrument settings with much improved imaging outcomes, instead of benchmarking performance with re-purposed fluorophores that cannot cope well with shorter pulses due to saturation.

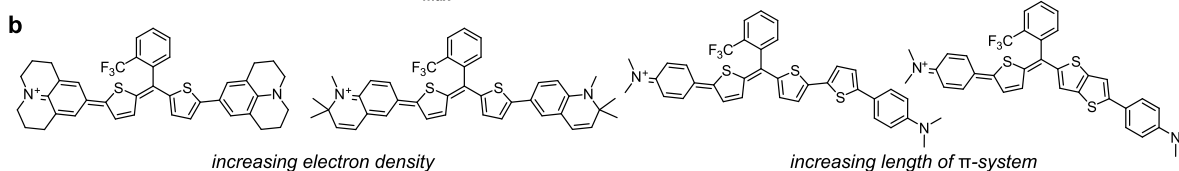
Related Outlook 2: PA imaging in the SWIR region

Red-shifting absorbance/emission of optical probes to reduce both absorption and scattering in tissues, for higher resolution and deeper tissue penetration, was a pivotal aim over decades.³⁰ For wavelengths reaching the SWIR region, the picture is more complicated, because tissue absorption increases (dependent on composition) but scattering continues to reduce. In PA imaging, the signal intensity correlates with the excitation intensity; in addition to absorbance and scattering, there is another limit to excitation intensity, set by the maximum permissible exposure (MPE) limit. The American National Standards Institute defines the MPE as 20 mJ/cm² for single nanosecond pulse exposures (or 200 mW/cm² for averaged power deposition) in the visible region, but this gradually increases to 100 mJ/cm² (or 1000 mW/cm²) in the SWIR region.¹⁹ Thus, the development of SWIR contrast agents with linear absorber properties may allow harnessing these higher maximum SWIR laser powers; and our first generation of TAMs may provide an excellent starting point for loud SWIR agents (Figure 30b).

Hypothesis: Ultra-fast relaxers enable *louder* probes by reduction of the laser pulse width



Molecular designs for red shifting λ_{\max} into the SWIR region



FRET Probes for NIR Fluorophores

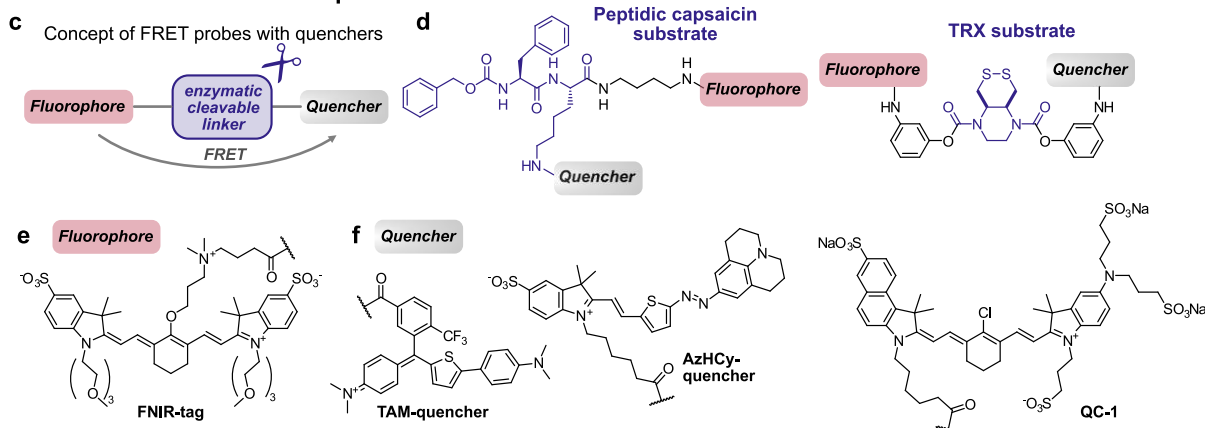


Figure 30. a) Narrowing laser pulse width with constant pulse energy should produce higher PA amplitudes for suitably fast-relaxing contrast agents. b) Molecular designs to reach the SWIR region with TAMs. c) Concept of FRET probes with quenchers. d) Potential FRET probes to monitor enzymatic activity of cathepsins or thioredoxin with NIR dyes. e) FNIR-tag is the preferred NIR dye for FRET applications. f) Structures of quenchers for FRET pairs based on the TAM, AzHCy scaffold and the non-ideal commercially available dye QC-1.

Major Outlook 3: Repurposing PA dyes as FRET quenchers in the NIR & SWIR

Small molecule dark quenchers for fluorescence resonance energy transfer (FRET) are widely used as acceptors in FRET probes to detect biochemical activities. Suitable NIR quenchers are rare and IRDye QC-1 (Figure 30f, LICORbio) offers hitherto the longest quenching wavelength. The distributor indicates a quenching range from 500-800 nm, but since the absorption tail reaches ~950 nm the maximum quenching limit is most likely somewhere in between 800-900 nm. Efficient quenchers other than QC-1 are desirable because despite several solubilizing groups, QC-1 aggregates in aqueous buffer and biological media, is chemically instable, expensive, and the synthesis is complicated. AzHCys and TAMs have been used in biological media without compromising PA properties, therefore I proposed using AzHCys and TAMs as uniquely long-absorbing tunable FRET quenchers.

FRET quenching efficiency depends on the distance between donor and acceptor. Using a cleavable motif between donor and acceptor enables turn-on probes (Figure 30c): e.g. hypothetically, NIR FRET pairs to monitor proteases such as cathepsins,⁴⁴ or the redox protein thioredoxin³²⁰ (Figure 30c-f). Additionally, there are currently no FRET quenchers suitable for SWIR probes. TAMs of type II already absorb significantly >1000 nm and so might be suitable candidates. Admittedly, we have no data on their fluorescence/quenching properties, because SWIR imaging requires specialized

instrumentalization such InGaAs detectors; but I have begun trying to establish collaborations for testing such potential SWIR FRET probes.

Related Outlook 3: Photostabilisation of fluorophores

The main part of this thesis and the previous outlook focus on non-radiative decay and its various implications. In the publication covered in section 1.3.2, remote placement of the azobenzene photoswitch as in **E-AzCy5** resulted in incomplete fluorescence quenching and insubstantially-enhanced PA performance: but the PA signal intensity for **E-AzCy5** under continuous pulsed laser irradiation remained unchanged for 30 min, a feature entirely lacking in Cy5-derived fluorophores. This indicates greater photostability of **E-AzCy5** than Cy5. In single molecule super resolution fluorescence microscopy, photon budget is a limiting factor for resolution; and despite the reduced quantum yield for **E-AzCy5**, its greatly increased photostability may compensate or even outperform the photon budget of a corresponding Cy5. Applications of **E-AzCy5** in single molecule microscopy are thus being pursued by collaboration partners with the required instrumentation, as part of our group's work on photostabilisation of fluorophores through ultrafast triplet state quenching.

3.3 Ongoing research and outlook: Efficacy Switches and TRP Tools

Efficacy Switches

We thoroughly characterized the ideal efficacy switches **AzPico** and **AzHC** and reported their implications for photoswitching. I anticipate strong feedback from the small but closely linked field of photopharmacology, because on a conceptual level we offer a new and successful design strategy for protein control without the usual needs of incremental fine-tuning. I also expect that many previous tools will be identified retrospectively as efficacy switches, and then even revisited or rationally enhanced. For example we already identified studies in literature with dose-response curves that plateau at different effect levels per wavelength, or unusual bidirectional effects despite incomplete photoswitching.^{299,323–326} Those studies share rare successful applications either *in vivo* or in complex tissues, so highlighting the power of efficacy switching for chromocontrol independent of drug distribution.

We believe that the most suitable biological targets are those that naturally occur in two different states (e.g. conducting and non-conducting for ion channels), that can be stabilised by the efficacy switch. Typically, the equilibrium between the two states is carefully controlled and neither full activation nor full deactivation reflect natural signalling. Efficacy switching will allow fine-tuning a range of wavelength-dependent equilibria, particularly with multi-ligand-binding systems such as tetrameric channels; and associated to that, a range of functionally distinct biological states (regimes), not just switching between maximum and minimum effects. Addressing desired regimes reproducibly will hopefully allow to study functions in a more natural way, allowing to observe subtle physiological responses or downstream effects (as shown in section 2.3.3). It may even be that high-intensity illumination at a fixed PSS may reveal the dynamic effects of *protein switching rates*, rather than static binding to a defined *E/Z* ratio. With efficacy switches, such effects can now be systematically explored.

TRPC4/5 Photopharmacology

Efficacy switches are inherently eligible for *in vivo* application because complex tissue distribution can be compensated, and the next step with **AzPico** and **AzHC** is to study effects of TRPC4/5 *in vivo*. TRPC4/5 are mainly expressed in the brain, where hijacking endogenous TRPC4/5 signalling promises insights into natural signalling pathways and mechanisms. The main challenge will be photon delivery into brain tissue, as both photoswitches are ideally operated with 360-450 nm light which does not penetrate skin or bones. To overcome such barriers with optogenetics, LED light sources are regularly implanted into the brains of mice, to locally irradiate them with UV light,³²⁷ and wireless controllable light sources for the brain have been particularly well-developed,^{327,328} these could be applied here. TRPC4 is also an essential part of the enteric nervous system, which operates independently from the brain to govern the function of the gastrointestinal tract. With **AzPico** we now offer a high precision tool to study TRPC4 within the enteric nerve system *in vivo*; and applying light to the intestine with micro implants, μ LEDs, or even ingested programmable LEDs is a much simpler prospect than for the brain. A potential *in vivo* experiment could involve tracing the gastrointestinal progress of SWIR microparticles during localised photoswitching of TRPC4 activity, to clarify the role of TRPC4 in digestion.

Additional tools for TRPC4/5 Photopharmacology

AzPico and **AzHC** are valuable tools because their UV light induced *agonist* activity of the *Z*-isomers is switched back to basal activity by blue light because of competitive binding of the *E*-isomers. For a photoswitchable inhibitor such an activity profile is suboptimal if the aim is to switch between fully *blocked* and basal activity. To complete the toolbox of photoswitchable TRPC4/5 modulators I thus suggest to create photoswitchable *inhibitors* based on the GFB inhibitors developed by Goldfinch Biosciences (Figure 31). Cryo-EM structures of TRPC4 in complex with **GFB-8438** revealed the binding site located in the VLSD region, a different binding site than the one **AzPico** and **AzHC** are located. The 3D structures show that the pyridazinone ring is buried within the binding pocket and CF_3 -phenyl has more empty space adjacent. Therefore, I suggest to introduce diazenyl photoswitches at that particular ring at different positions (Figure 31c).

Potential photoswitchable inhibitors based on the GFB-inhibitor scaffold

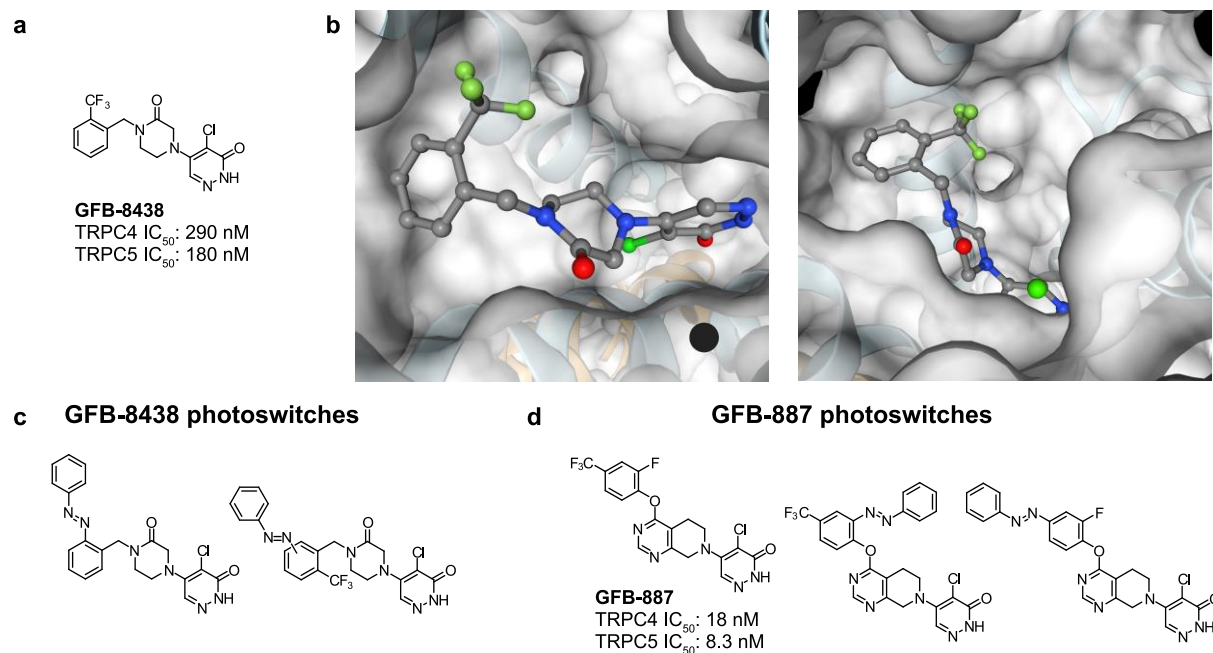


Figure 31. Potential photoswitchable TRPC4/5 inhibitors based on the GFB-inhibitors. a) Structure and potencies of **GFB-8438**. b) **GFB-8438** in complex with TRPC4 (PDB: 7b0s, snapshots created with proteins.plus). c) Potential suitable photoswitches for **GFB-8438**. d) Potential suitable photoswitches for **GFB-887**, a more potent analogue used in clinical studies.

Recently, the structure and pharmacological properties of the clinical candidate **GFB-887** were disclosed. The potency on TRC4/5 is ~10-20× higher than **GFB-8438** and the pyridazinone is a conserved structural element. I assume that the orientation within the binding pocket is similar and therefore suggest introducing diazenyl photoswitches on the aryl ring at the opposite side of the compound (Figure 31d).

Final remark on photopharmacology

Achieving reversible on↔off photocontrol of biological activity has typically focused on the ‘photo’ part, rather than on the ‘pharmacology’ part of photopharmacology. I expect that our conceptual innovation in ideal efficacy switching of TRPC4/5 will be extended to many other protein targets, and the evolution from photocontrol to chromocontrol will embrace the full pharmacological value of optical tools to study endogenous systems in complex tissue or *in vivo*.

3.4 General conclusion

On first glance, optoacoustics (OA) and photopharmacology have no overlap as fields, except that the projects pursued here started with using azobenzenes as a common structural motif to interact with light in both contexts, in ways that we identify as solving key problems in each field. OA has struggled to find contrast agents that convert the available pulsed excitation energy efficiently and photostably to an OA signal. For this, the optical properties of contrast agents needed to be tailored for nanosecond pulses; and shifting $S_1 \rightarrow S_0$ into the picosecond regime allowed several excitation cycles per molecule within one pulse. The timescale of this photophysical requirement is rather special for OA imaging (though other optical imaging fields needing ultrafast relaxation are being explored by my lab colleagues); however, it matched well to the performance of molecular switches, as well as rotors. Photopharmacology, instead, has had the long-standing goal to provide robust optical control over

endogenous targets in their natural environment, regardless of non-uniform drug distribution and local concentration effects. The conceptual rules of ideal efficacy photoswitching now allow chromocontrol towards deep tissue settings, suggesting efficacy switches as go-to method for *in vivo* photopharmacology. Although very different properties are exploited in these two project areas, i.e. either fast $S_1 \rightarrow S_0$ electronic relaxation or else reproducible bidirectional $E \rightleftharpoons Z$ photoisomerisation, the general underlying idea is in both cases to provide high-precision (= **light-stimulated**), high-performance (= **conceptually-optimised**) tools for chemical biology by rationally installing the photopharmaceutical or photophysical properties required. Formulating and understanding the general conceptual rules driving those property requirements has been the key to the tool development work performed here; and the conceptual photochemical advances developed may now serve as future design blueprints in their fields.

4 Acknowledgements

First, I would like to express my gratitude to my supervisor, Prof. Dr. Oliver Thorn-Seshold, for giving me the opportunity to pursue my doctoral thesis in his group. Thank you for your unwavering support, motivation, and especially for the opportunity to stay abroad in Berkeley during my PhD. I deeply appreciate the engaging scientific discussions and the freedom you provided to independently pursue projects, allowing me to grow as a researcher. It has been a great honour to be part of your group and to contribute to shaping the LMU era.

Secondly, I am very grateful to Prof. Dr. Andrea Rentmeister for agreeing to be the second reviewer of this thesis, and I would also like to thank the rest of my defense committee: Prof. Dr. Michael Schaefer, Prof. Dr. Ivan Huc, Prof. Dr. Thomas Gudermann, and Prof. Dr. Achim Hartschuh.

Next, I would like to thank my former and current chemistry lab mates - Li, Adrian, Alex, Jan, Ben, Lukas, Philipp, Carina, and Martin R. - for promoting a culture of scientific enthusiasm in the lab and for the exceptional times we shared outside of it. I would also like to extend my gratitude to our refreshing medical doctors Lena, Carmen, and Lüc and my previous colleagues Annabel, Martin M., Elena L., and Elena F.R. To all of you: The constant exchange of ideas and your motivation over the past five years were invaluable. Discussing scientific challenges atop mountains or over my favourite Bavarian drink made this journey truly remarkable.

Thanks goes to my interns and students, Andrés, Dimitrii, Michaela, and Jan-Philip for assisting me in the lab, all the best for your future. Also to Master students and/or Hiwis Brandy and Jimmy it was a pleasure to have you around.

I would like to express my gratitude to all my collaborators; your expertise and willingness to work with my compounds elevated my research from purely chemistry to truly remarkable cross-disciplinary work. A special thanks goes to Michael Schaefer, my main collaborator within the TRiP consortium. You were part of my PhD journey from the very beginning, from the initial screenings to the major discoveries we made together towards the end of my project. I also extend special thanks to Vipul Gujrati for introducing me to the fascinating world of optoacoustic imaging.

I am also very grateful for the excellent support from the members of the analytical department, particularly the NMR facilities. Special thanks to Claudia Glas, Dr. Lars Allmendinger, and Claudia Ober for providing me enough spectrometer time to identify all the carbons in my *ionic grease*. I would also like to thank Michi Geyer for his invaluable help with practically any issue that arose. A big thank you to Dr. Christoph Müller, who made teaching duties an enjoyable experience.

During my time at LMU the TS group was supported by Prof. Wanner, his follower Prof. Merk and Prof. Ivan Huc. Thank you for sharing your laboratories which were the origin for all my compounds and measurements.

Next, I would like to express my gratitude to Prof. Evan Miller from the University of California, Berkeley. Thank you for giving me the opportunity to pursue a PhD externship in your group. It was a fantastic experience to stay in Berkeley and work on a truly creative and exciting project, which allowed

me to expand my skillset with microscopy and patch clamping. I also want to extend my thanks to the entire Miller group for their support, not only in the lab but also in helping me arrive into a new country.

Next, I would like to thank the funding agencies that supported me financially and made my daily work, and more, possible. Many thanks to TRR152 and the Boehringer-Ingelheim Foundation for funding my research projects, BaCaTec for enabling my PhD externship in Berkeley, and the Joachim Herz Foundation for their flexible support, which facilitated my externship, attendance at conferences, and the opportunity to meet and exchange ideas with scholars from various disciplines.

Finally, I want to express my deep gratitude to my family, especially to my parents, Lydia and Rudolf, who have supported my journey as a chemist from my apprenticeship to my PhD (even if some still refer to PhD research as just *going to school*). I could always focus on my path, knowing that you had my back no matter what.

Lastly, my heartfelt thanks go to my partner Anja. Thank you for your patience, your unwavering support during the downs, and for sharing in my excitement during the ups. "*Wie war dein Tag?*" "*Hab was Blaues gemacht.*" This entire journey over the last 5 years is truly entangled with you and sharing my life with you during this period made a real difference to remain balanced, creative and productive.
Danke

5 Appendix

5.1 Supporting Information

5.1.1 Supporting Information for section 1.3.2 (AzoCyanines)

Supporting information to the publication: Merged Molecular Switches Excel as Optoacoustic Dyes: Azobenzene–Cyanines Are Loud and Photostable NIR Imaging Agents (page 110-169).

5.1.2 Supporting Information for section 1.3.3 (Triarylmethanes)

Supporting information to the publication: Molecular rotors are loud, highly photostable, NIR/SWIR-active molecular optoacoustic contrast agents (page 170-189).

5.1.3 Supporting Information for section 2.3.2 (BTDAzo)

Supporting information to the publication: BTDAzo: A Photoswitchable TRPC5 Channel Activator (page 190-248).

5.1.4 Supporting Information for section 2.3.3 (Efficacy switches AzPico&AzHC)

Supporting information to the publication: Ideal efficacy photoswitches for TRPC4/5 channels harness high potency for spatiotemporally-resolved control of TRPC function in live tissues (page 249-324).

Supporting Information

Merged Molecular Switches Excel as Optoacoustic Dyes: Azobenzene–Cyanines Are Loud and Photostable NIR Imaging Agents

*M. Müller, N. Liu, V. Gujrati, A. Valavalkar, S. Hartmann, P. Anzenhofer, U. Klemm,
A. Telek, B. Dietzek-Ivanšić, A. Hartschuh, V. Ntziachristos, O. Thorn-Seshold**

Supporting Information for:
Merged Molecular Switches Excel as Optoacoustic Dyes:
Azobenzene–Cyanines Are Loud and Photostable NIR Imaging Agents

Markus Müller^a, Nian Liu^{b,c}, Vipul Gujrati^{b,c}, Abha Valavalkar^{d,e}, Sean Hartmann^f, Pia Anzenhofer^b, Uwe Klemm^b, András Telek^a, Benjamin Dietzek-Ivanšić^{d,e}, Achim Hartschuh^f, Vasilis Ntziachristos^{b,c}, Oliver Thorn-Seshold^{a*}

[a] Department of Pharmacy, LMU Munich, Butenandtstrasse 7, Munich 81377, Germany; *oliver.thorn-seshold@cup.lmu.de

[b] Institute of Biological and Medical Imaging, Helmholtz Zentrum München, Ingolstädter Landstraße 1, Neuherberg 85764, Germany.

[c] Chair of Biological Imaging at the Central Institute for Translational Cancer Research (TranslaTUM), School of Medicine and Health, Technical University of Munich, Ismaninger Str. 22, Munich 81675, Germany.

[d] Institute of Physical Chemistry, University of Jena, Lessingstraße 4, Jena 07743, Germany.

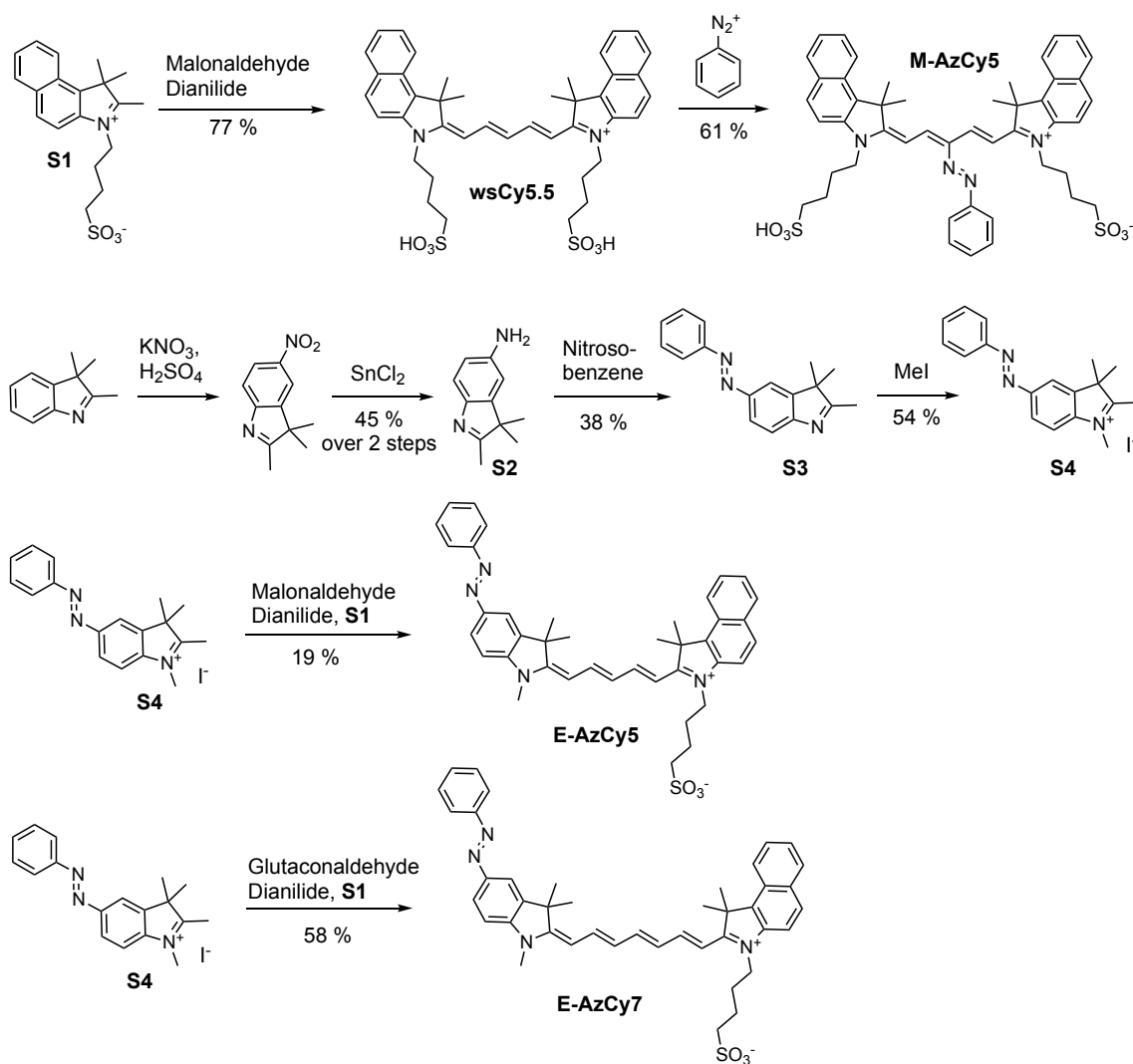
[e] Leibniz Institute of Photonic Technology Jena, Research Department Functional Interfaces, Albert-Einstein-Straße 9, Jena 07745 Germany.

[f] Department of Chemistry, LMU Munich, Butenandtstrasse 8, Munich 81377, Germany.

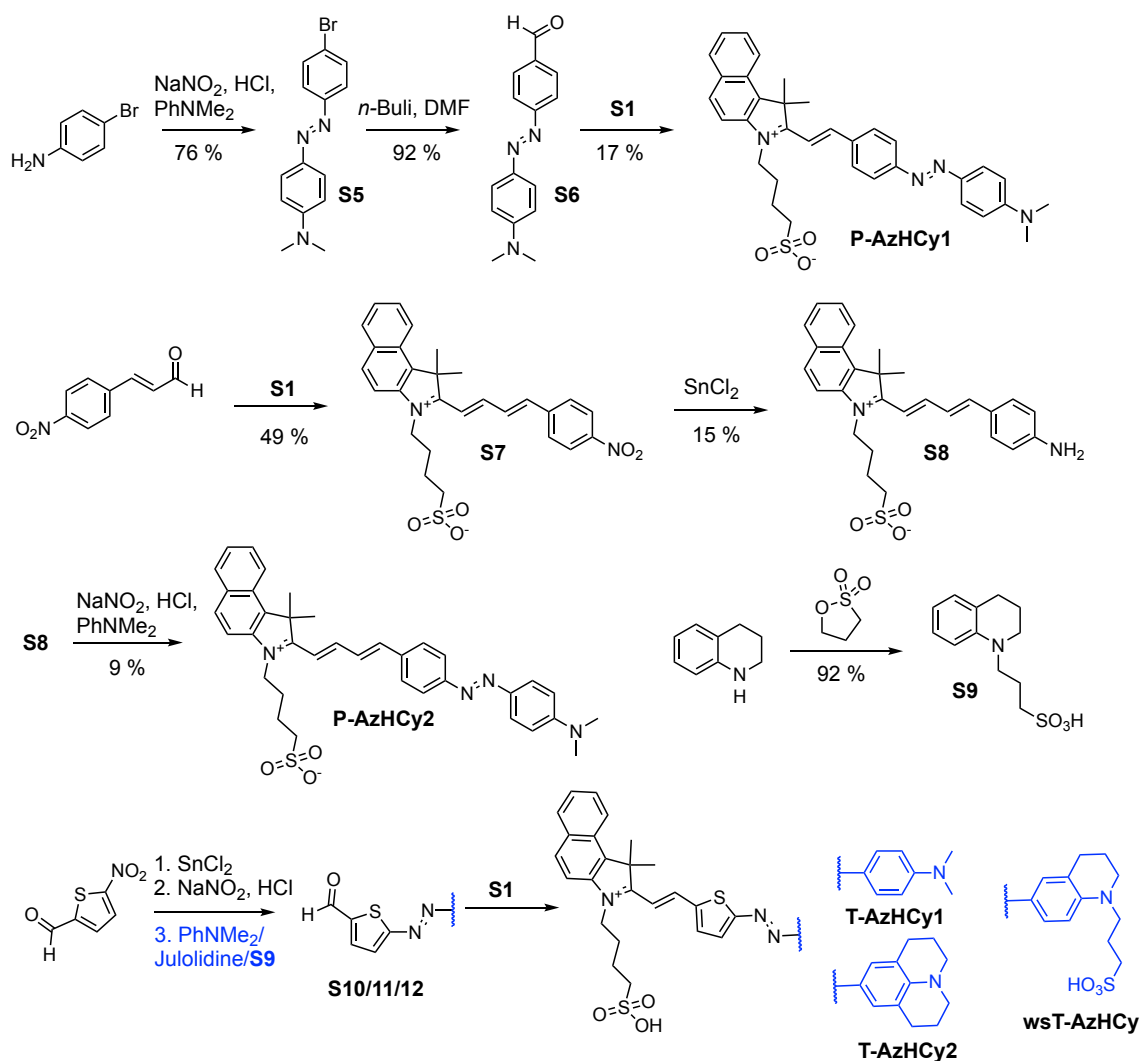
1	Chemical Synthesis	S2
1.1	Synthesis Overviews	S2
1.2	Materials and Methods	S3
1.3	Synthetic Procedures	S4
2	Photocharacterization	S14
2.1	Standard Absorption and Fluorescence Methods	S14
2.2	Fluorescence Properties.....	S14
2.3	Photoswitching	S15
3	Photoacoustics	S17
3.1	MSOT set-up and data acquisition	S17
3.2	Determination of optoacoustic signal generation efficacy	S18
3.3	Photostability of the PA signal	S19
3.4	Reference photoacoustic measurements: QC-1, IR 820.....	S20
3.5	Photoacoustic properties in biological media	S21
3.6	Comparison of photoacoustic measurements: wsCy5.5	S23
4	Time-resolved fluorescence spectroscopy	S24
5	Transient Absorption Spectroscopy	S25
6	<i>in vivo</i> optoacoustic measurements in mouse	S25
7	Outlook for switch-integrated PA agents	S27
8	References	S28
9	Appendices	S29
9.1	NMR Spectra	S29
9.2	HRMS Spectra.....	S49
9.3	Photoluminescence Data.....	S50
9.4	Vectorial copies of the images in the main text	S57

1 Chemical Synthesis

1.1 Synthesis Overviews



Scheme S1. Synthetic overview for **AzoCyanines**.



Scheme S2. Synthetic overview for **AzoHemiCyanines**.

1.2 Materials and Methods

Reagents and conditions. Unless stated otherwise, (a) all reactions and characterisations were performed with unpurified, undried, non-degassed solvents and reagents, used as obtained, under closed air atmosphere without special precautions; (b) “hexane” used for chromatography was distilled from commercial crude isohexane fraction by rotary evaporation; (c) “flash column chromatography” refers to purification on a Biotage Selekt system, using prepacked silica cartridges purchased from Biotage or phenomenex; (d) procedures and yields are unoptimized; (e) yields refer to isolated chromatographically and spectroscopically pure materials; (f) all eluent and solvent mixtures are given as volume ratios unless otherwise specified; (g) thin-layer chromatography (TLC) was run on 0.25 mm Merck silica gel plates (60, F-254) with UV light (254 nm) as a visualising agent.

Nuclear magnetic resonance (NMR) spectroscopy. Standard NMR characterisation was by ^1H - and ^{13}C -NMR spectra on a Bruker Ascend 400 (400 MHz & 101 MHz for ^1H and ^{13}C respectively) and on a Bruker Ascend 500 (500 MHz & 126 MHz for ^1H and ^{13}C respectively). Chemical shifts (δ) are reported in ppm calibrated to residual non-perdeuterated solvent as an internal reference. Peak descriptions singlet (s), doublet (d), triplet (t), quartet (q), multiplet (m) and broad (br) are used. NMR spectra are given in the appendix at the end of this document.

High resolution mass spectrometry (HRMS). HRMS was carried out by the Zentrale Analytik of the LMU Munich using ESI ionisation on a Thermo Finnigan LTQ FT Ultra Fourier Transform Ion Cyclotron Resonance Spectrometer.

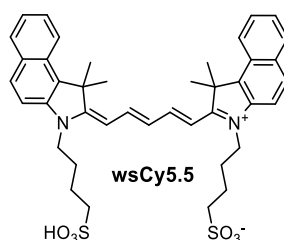
High performance liquid chromatography (HPLC) coupled to mass spectrometry (MS).

Analytical HPLC-MS was performed on an Agilent 1100 SL with (a) a binary pump to deliver H₂O:MeCN eluent mixtures containing 0.1% formic acid at a 0.4 mL/min flow rate, (b) YMC-Triart C18 column (3.0 µm; 50 mm × 3 mm) maintained at 40 °C, (c) an Agilent 1100 series diode array detector, (d) an Agilent LC/MSD iQ mass spectrometer. Typical run conditions were a linear gradient of H₂O:MeCN from 90:10 to 0:100 (first 5 min), then 0:100 for 2 min for flushing; then the column was (re)equilibrated with 90:10 eluent mixture for 2 min.

Preparative HPLC. Preparative HPLC was performed on an Agilent 1200 SL with (a) a binary pump to deliver H₂O:MeCN eluent mixtures containing 0.1% formic acid at 20 mL/min flow rate, (b) Agilent-Zorbax C18 column (10.0 µm; 250 mm × 30 mm) maintained at room temperature, (c) an Agilent 1200 series diode array detector, and (d) Agilent 1200 series fraction collector.

1.3 Synthetic Procedures

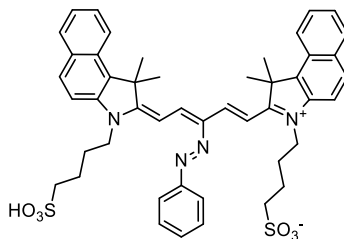
wsCy5.5



The compound was synthesized according to a literature procedure.^[1]

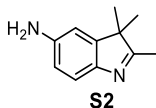
A screw cap vial was charged with commercial **S1** (1,1,2-trimethyl-3-(4-sulfobutyl)-benz[e]indolium, inner salt; 691 mg, 2.0 mmol, 2.0 eq), malonaldehyde dianilide hydrochloride (259 mg, 1.0 mmol, 1.0 eq), sodium acetate (410 mg, 5.0 mmol, 5.0 eq) and acetic anhydride (5 mL), the vial was sealed, and the mixture stirred at 120°C for 2 h. The resulting slurry was diluted with EtOH until everything seemed dissolved and stirred at room temperature for 30 minutes. Solvents were removed under reduced pressure and the crude product was purified by rp-flash chromatography (H₂O:MeCN, 95:5 to 55:45) to afford **wsCy5.5** (560 mg, 0.77 mmol) as deep blue solid.

The compound was **literature-known**, but without spectroscopic data,^[1] which are now given: **¹H NMR** (400 MHz, DMSO-*d*₆) δ [ppm]: 8.53 – 8.38 (m, 2H), 8.24 (d, *J* = 8.6 Hz, 2H), 8.10 – 7.99 (m, 4H), 7.77 (d, *J* = 8.9 Hz, 2H), 7.70 – 7.63 (m, 2H), 7.50 (dd, *J* = 8.2, 6.9 Hz, 2H), 6.66 (t, *J* = 12.3 Hz, 1H), 6.43 (d, *J* = 13.8 Hz, 2H), 4.24 (t, *J* = 7.4 Hz, 4H), 2.57 – 2.52 (m, 4H), 1.96 (s, 12H), 1.92 – 1.71 (m, 8H). **¹³C NMR** (101 MHz, DMSO-*d*₆) δ [ppm]: 173.5, 152.8, 139.8, 133.1, 131.3, 130.3, 129.9, 127.7, 127.6, 125.9, 124.7, 122.1, 111.7, 103.1, 50.7, 50.65, 43.5, 26.8, 26.3, 22.4. **HRMS** C₄₁H₄₆N₂O₆S₂ [MH⁺] calc. 727.2871, found 727.2875.

M-AzCy5**M-AzCy5**

Aniline (6.3 μL , 69 μmol , 1.0 eq) was dissolved in MeCN (0.5 mL) and cooled to 0°C, then TFA (7.9 μL , 103 μmol , 1.5 eq) followed by isoamyl-nitrite (10 μL , 76 μmol , 1.1 eq) were added, and the mixture was stirred for 20 minutes. The diazonium solution was added dropwise to a precooled solution of **wsCy5.5** (50 mg, 69 μmol , 1.0 eq) and NaOAc (11 mg, 138 μmol) in MeCN (0.5 mL) and water (0.5 mL) at 0°C. The mixture was stirred for 30 min at 0°C, warmed to room temperature, MeCN was removed under vacuum and the crude product was purified by rp-flash chromatography (H₂O:MeCN, 90:10 to 40:60) followed by preparative HPLC (H₂O/MeCN, 90:10 to 2:98 over 20 minutes, then 5 minutes 98% MeCN) to afford **M-AzCy5** (7 mg, 8.4 μmol , 12 %) as a blue solid.

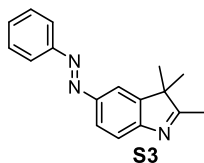
¹H NMR (500 MHz, DMSO-*d*₆) δ [ppm]: 8.50 (d, *J* = 14.1 Hz, 2H), 8.38 (d, *J* = 8.6 Hz, 2H), 8.15 (d, *J* = 8.9 Hz, 2H), 8.12 (d, *J* = 8.1 Hz, 2H), 7.97 (d, *J* = 8.9 Hz, 2H), 7.92 – 7.86 (m, 2H), 7.75 – 7.66 (m, 4H), 7.66 – 7.55 (m, 4H), 7.47 (t, *J* = 7.4 Hz, 1H), 4.50 – 4.36 (br, 4H), 2.63 (t, *J* = 7.3 Hz, 4H), 2.09 (s, 12H), 2.04 – 1.96 (m, 4H), 1.93 – 1.87 (m, 4H). **¹³C NMR** (126 MHz, DMSO-*d*₆) δ [ppm]: 177.7, 152.7, 139.3, 136.3, 135.0, 131.9, 130.5, 130.1, 129.9, 129.8, 127.9, 127.4, 125.5, 125.5, 122.5, 121.7, 112.2, 101.0, 51.7, 50.7, 44.8, 26.9, 26.4, 22.7. **HRMS** C₄₇H₅₁N₄O₆S₂ [MH⁺] calc. 831.3245, found 831.3257.

S2: 2,3,3-trimethyl-3H-indol-5-amine**S2**

The procedure was conducted according to a modified literature procedure.^[2]

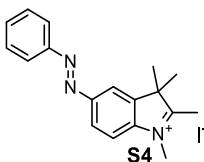
A solution of commercial 2,3,3-trimethyl-indolenin (2.9 g, 18.2 mmol, 1.0 eq; buy freshly and store carefully) in conc. H₂SO₄ (9 mL) was cooled to 0°C before KNO₃ (1.84 g, 18.2 mmol, 1.0 eq) was added carefully in small portions. The reaction mixture was stirred for 1 h at 0°C followed by 1 h at room temperature and then poured on ice. The mixture was vigorously stirred in an ice bath and neutralized by slow addition of 6 M NaOH. The neutralized solution was extracted with EtOAc (2 × 200 mL), the combined organic layers were dried over anhydrous Na₂SO₄, filtered, and concentrated. The obtained brown solid was dissolved in 6 M HCl (60 mL), SnCl₂ (11.1 g, 58.8 mmol, 4.0 eq) was added and the reaction mixture was heated to reflux for 2 h. After cooling to room temperature, the mixture was neutralized with 6 M NaOH, extracted with EtOAc (2 × 200 mL). The combined organic layers were dried over anhydrous Na₂SO₄, filtered, concentrated, and purified by flash chromatography (gradient: hexane:EtOAc, 2:8 to 0:1) to afford **S2** (1.37 g, 7.85 mmol, 54 %) as yellow solid.

Spectral data match the literature (**known compound**)^[2]: **¹H NMR** (400 MHz, CDCl₃) δ : 7.30 (d, *J* = 8.0 Hz, 1H), 6.66 – 6.57 (m, 2H), 3.65 (br, 2H) 2.21 (s, 3H), 1.26 (d, 6H).

S3: 2,3,3-trimethyl-5-(phenyldiazenyl)-3H-indole

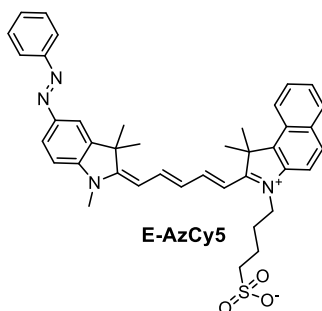
A mixture of **S2** (410 mg, 2.35 mmol, 1.0 eq) and nitrosobenzene (252 mg, 2.35 mmol, 1.0 eq) in AcOH (20 mL) was stirred at room temperature for 14 h. The mixture was neutralized with sat. aq. NaHCO₃ and extracted with EtOAc (2 × 50 mL). The combined organic layers were dried over anhydrous Na₂SO₄, filtered, concentrated, and purified by flash chromatography (hexane:EtOAc, 2:8) to afford **S3** (234 mg, 0.89 mmol, 38 %) as red oil.

¹H NMR (500 MHz, CDCl₃) δ: 7.96 (dd, *J* = 8.1, 1.9 Hz, 1H), 7.94 – 7.90 (m, 2H), 7.87 (d, *J* = 1.9 Hz, 1H), 7.66 (d, *J* = 8.2 Hz, 1H), 7.55 – 7.49 (m, 2H), 7.48 – 7.43 (m, 1H), 2.33 (s, 3H), 1.38 (s, 6H). ¹³C NMR (126 MHz, CDCl₃) δ: 191.0, 156.5, 152.9, 150.7, 146.8, 130.9, 129.2, 126.0, 122.8, 120.3, 114.1, 54.2, 23.2, 15.9. HRMS C₁₇H₁₈N₃ [MH⁺] calc. 264.1495 found 264.1498.

S4: 1,2,3,3-tetramethyl-5-(phenyldiazenyl)-3H-indol-1-ium iodide

A pressure vial was charged with **S3** (150 mg, 0.57 mmol, 1.0 eq), iodomethane (355 μL, 5.7 mmol, 10 eq) and MeCN (6 mL). The vial was sealed and stirred at 50°C for 48 h. The reaction mixture was cooled down, poured into Et₂O (12 mL) and left in the fridge to precipitate for 2 h. The resulting precipitate was collected by filtration, washed with Et₂O to afford **S4** (86 mg, 0.31 mmol, 54 %) as brown solid.

¹H NMR (500 MHz, DMSO-*d*6) δ: 8.33 (br, 1H), 8.22 – 8.10 (m, 2H), 7.99 – 7.92 (m, 2H), 7.68 – 7.61 (m, 3H), 4.03 (s, 3H), 2.82 (s, 3H), 1.62 (s, 6H). ¹³C NMR (126 MHz, DMSO- *d*6) δ: 198.3, 152.2, 151.9, 143.9, 143.1, 132.2, 129.7, 124.8, 122.8, 116.3, 116.3, 54.4, 35.0, 21.6, 14.5. HRMS C₁₈H₂₀N₃ [M⁺] calc. 278.1652, found 278.1656.

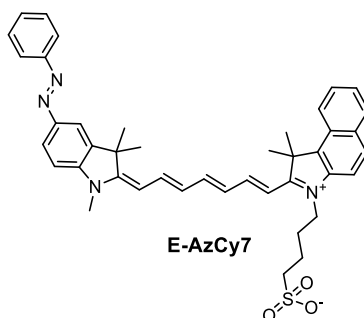
E-AzCy5

A screw cap vial was charged with **S1** (17 mg, 50 μmol mmol, 1.0 eq), malonaldehyde dianilide hydrochloride (13 mg, 50 μmol, 1.0 eq), and acetic anhydride (0.5 mL). The vial was sealed, and the mixture stirred at 110°C for 2 h. The solvent was removed under reduced pressure

and **S4** (20 mg, 50 μmol , 1.0 eq), sodium acetate (10 mg, 125 μmol , 2.5 eq), and EtOH (0.5 mL) were added. The vial was sealed and the mixture stirred at 80°C for 1 h. The solvent was removed under reduced pressure and the crude product was first purified by flash chromatography (CH_2Cl_2 :MeOH, 9:1) and then further purified by rp-flash chromatography (H_2O :MeCN, 90:10 to 2:98) to afford **E-AzCy5** (6.0 mg, 9.1 μmol , 18%) as blue solid.

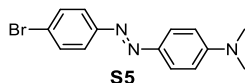
^1H NMR (500 MHz, DMSO-*d*6) δ 8.57 – 8.46 (m, 1H), 8.36 – 8.23 (m, 2H), 8.16 – 8.04 (m, 3H), 7.98 (dd, J = 8.4, 1.9 Hz, 1H), 7.91 – 7.85 (m, 3H), 7.75 – 7.68 (m, 1H), 7.64 – 7.52 (m, 4H), 7.46 (d, J = 8.5 Hz, 1H), 6.74 – 6.63 (m, 2H), 6.21 (d, J = 13.4 Hz, 1H), 4.36 (t, J = 7.7 Hz, 2H), 3.58 (s, 3H), 2.54 – 2.51 (m, 2H), 1.96 (s, 6H), 1.92 – 1.84 (m, 2H), 1.83 – 1.73 (m, 8H). **^{13}C NMR** (126 MHz, DMSO-*d*6) δ : 176.5, 170.2, 154.7, 152.2, 151.8, 148.6, 146.0, 141.8, 139.3, 134.6, 131.8, 130.9, 130.5, 130.0, 129.5, 127.9, 127.3, 126.8, 126.7, 125.4, 122.4, 122.3, 114.5, 112.2, 110.3, 105.9, 102.9, 51.5, 50.5, 47.8, 44.3, 40.4, 27.3, 26.5, 26.4, 22.4. **HRMS** $\text{C}_{40}\text{H}_{43}\text{N}_4\text{O}_3\text{S}$ [MH^+] calc. 659.3050, found 659.3078.

E-AzCy7



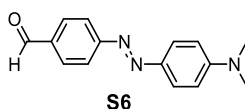
A screw cap vial was charged with **S1** (15 mg, 43 μmol , 1.0 eq), Glutaconaldehydedianil hydrochloride (12 mg, 43 μmol , 1.0 eq), and acetic anhydride (0.5 mL). The vial was sealed, and the mixture stirred at 110°C for 2 h. The solvent was removed under reduced pressure and **S4** (18 mg, 43 μmol , 1.0 eq), sodium acetate (9 mg, 108 μmol , 2.5 eq), and EtOH (0.5 mL) were added. The vial was sealed and the mixture stirred at 80°C for 1 h. The solvent was removed under reduced pressure and the crude was purified by flash chromatography (CH_2Cl_2 :MeOH, 9:1) to afford **E-AzCy7** (17.0 mg, 25 μmol , 58%) as a green solid.

^1H NMR (500 MHz, DMSO-*d*6) δ 8.33 (d, J = 8.6 Hz, 1H), 8.19 – 8.09 (m, 3H), 7.99 (d, J = 1.9 Hz, 1H), 7.97 – 7.92 (m, 2H), 7.89 – 7.85 (m, 2H), 7.82 – 7.67 (m, 3H), 7.63 – 7.56 (m, 3H), 7.56 – 7.50 (m, 1H), 7.36 (d, J = 8.5 Hz, 1H), 6.87 (d, J = 14.4 Hz, 1H), 6.70 (t, J = 12.6 Hz, 1H), 6.55 (t, J = 12.6 Hz, 1H), 6.13 (d, J = 13.0 Hz, 1H), 4.39 (t, J = 7.7 Hz, 2H), 3.50 (s, 3H), 3.34 (s, 3H), 2.54 (t, J = 7.3 Hz, 2H), 1.95 – 1.86 (m, 8H), 1.85 – 1.76 (m, 2H) 1.68 (s, 6H). **^{13}C NMR** (126 MHz, DMSO-*d*6) δ 176.8, 166.5, 154.9, 153.1, 152.2, 148.0, 146.2, 141.2, 139.2, 135.3, 132.0, 130.7, 130.6, 129.9, 129.4, 127.9, 127.2, 127.2, 126.7, 126.3, 125.7, 122.6, 122.2, 114.6, 112.4, 109.5, 107.8, 102.5, 51.6, 50.5, 46.9, 44.8, 30.5, 27.5, 26.7, 26.4, 22.4. **HRMS** $\text{C}_{42}\text{H}_{45}\text{N}_4\text{O}_3\text{S}$ [MH^+] calc. 685.3207, found 685.3217.

S5: 4-((4-bromophenyl)diazenyl)-*N,N*-dimethylaniline

4-bromoaniline (344 mg, 2.0 mmol, 1.0 eq) was dissolved in MeCN (20 mL) and cooled to 0°C, then TFA (228 μ L, 3.0 mmol, 1.5 eq) followed by isoamyl nitrite (322 μ L, 2.4 μ mol, 1.2 eq) were added, and the mixture was stirred for 20 minutes. The diazonium solution was added dropwise to a precooled mixture of *N,N*-dimethylaniline (255 μ L, 2.0 mmol, 1.0 eq) and NaOAc (328 mg, 4 mmol, 2 eq) in MeCN (10 mL) at 0°C. The mixture was stirred for 30 min at 0°C, warmed to room temperature, and MeCN was removed under vacuum, then the crude product dissolved in EtOAc (100 mL) was washed with sat. aq. NaHCO₃ (3 \times 100 mL) and brine (100 mL). The organic layer was dried over anhydrous Na₂SO₄, filtered, and concentrated to afford **5** (462 mg, 1.52 mmol, 76 %) as red solid which was used without further purification.

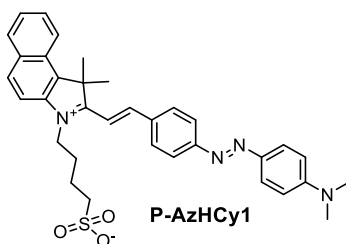
Spectral data are in accordance with the literature (**known compound**)^[3]: ¹H NMR (400 MHz, CDCl₃) δ [ppm]: 7.87 (d, *J* = 9.2 Hz, 2H), 7.72 (d, *J* = 8.8 Hz, 2H), 7.59 (d, *J* = 8.7 Hz, 2H), 6.75 (d, *J* = 9.2 Hz, 2H), 3.10 (s, 6H). ¹³C NMR (101 MHz, CDCl₃) δ [ppm]: 152.8, 152.2, 143.6, 132.2, 125.3, 123.9, 123.4, 111.6, 40.5.

S6: 4-((4-(dimethylamino)phenyl)diazenyl)benzaldehyde

This known compound was prepared according to a literature procedure.^[3]

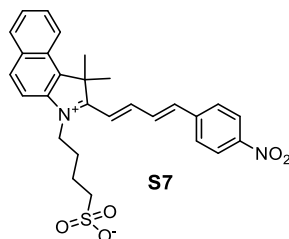
N-butyllithium (1.04 mL, 1.6 M in hexane, 1.66 mmol, 1.1 eq) was added dropwise to a solution of **S5** (460 mg, 1.51 mmol, 1.0 eq) in THF abs. (15 mL) at -78°C, the mixture was stirred for 5 min, then DMF abs. (141 μ L, 1.81 mmol, 1.2 eq) was added dropwise and the reaction was stirred 4 h in the dry ice bath. After warming to room temperature, the reaction was quenched with sat. aq. NH₄Cl and extracted with EtOAc (3 \times 100 mL). The combined organic layers were dried over anhydrous Na₂SO₄, filtered, concentrated, and purified by flash chromatography (hexane:EtOAc, 8:2) to afford **S6** (353 mg, 1.39 mmol, 92 %) as orange oil.

Spectral data are in accordance with the literature (**known compound**)^[3]: ¹H NMR (400 MHz, CDCl₃) δ [ppm]: 10.06 (s, 1H), 8.08 – 7.83 (m, 6H), 6.77 (d, *J* = 9.2 Hz, 2H), 3.12 (s, 6H). ¹³C NMR (101 MHz, CDCl₃) δ [ppm]: 191.9, 157.1, 153.2, 144.0, 136.3, 130.9, 125.9, 122.8, 111.6, 40.5.

P-AzHCy1

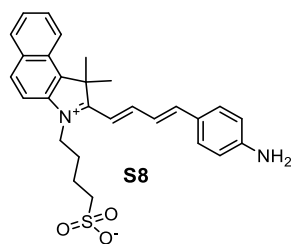
S1 (35 mg, 0.10 mmol, 1.0 eq) and **S6** (25 mg, 0.1 mmol, 1.0 eq) were dissolved in EtOH (1 mL) and stirred at 80 °C for 45 minutes. After cooling to room temperature the mixture was purified by rp-flash chromatography (H₂O:MeCN, 95:5 to 50:50) to afford **P-AzHCy1** (10 mg, 0.017 mmol, 17 %) as a red oil.

¹H NMR (500 MHz, DMSO-*d*6) δ [ppm]: 8.67 – 8.55 (m, 1H), 8.51 – 8.40 (m, 3H), 8.30 (d, *J* = 9.0 Hz, 1H), 8.26 – 8.18 (m, 2H), 7.98 – 7.85 (m, 5H), 7.84 – 7.79 (m, 1H), 7.78 – 7.70 (m, 1H), 6.88 (d, *J* = 9.3 Hz, 2H), 4.88 (t, *J* = 8.1 Hz, 2H), 3.11 (s, 6H), 2.58 (t, *J* = 7.1 Hz, 2H), 2.11 – 2.01 (m, 8H), 1.89 (t, *J* = 7.2 Hz, 2H). ¹³C NMR (126 MHz, DMSO-*d*6) δ [ppm]: 182.1, 155.0, 153.2, 151.7, 143.0, 138.8, 138.5, 135.3, 133.3, 132.1, 131.1, 130.1, 128.4, 127.3, 126.7, 125.6, 123.2, 122.3, 113.5, 112.6, 111.7, 53.8, 50.1, 46.8, 27.3, 25.6 22.2. **HRMS** C₃₄H₃₇N₄O₃S [MH⁺] calc. 581.2581 found 581.2584.

S7: 4-(1,1-dimethyl-2-((1*E*,3*E*)-4-(4-nitrophenyl)buta-1,3-dien-1-yl)-1*H*-benzo[*e*]indol-3-ium-3-yl)butane-1-sulfonate

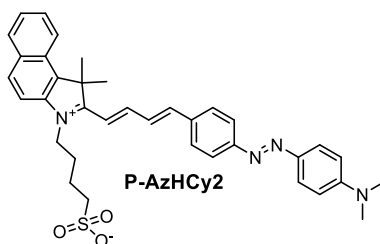
S1 (87 mg, 0.25 mmol, 1.0 eq) and 4-nitrocinnamaldehyde (44 mg, 0.25 mmol, 1.0 eq) were dissolved in EtOH (2.5 mL) and stirred at 80 °C for 45 minutes. After cooling to room temperature the mixture was purified by rp-flash chromatography (H₂O:MeCN, 95:5 to 5:95) to afford **S7** (62 mg, 0.123 mmol, 49 %) as a red oil.

¹H NMR (500 MHz, DMSO-*d*6) δ [ppm]: 8.48 – 8.40 (m, 2H), 8.35 – 8.26 (m, 3H), 8.24 – 8.18 (m, 2H), 7.97 – 7.90 (m, 2H), 7.85 – 7.77 (m, 2H), 7.77 – 7.71 (m, 2H), 7.62 (d, *J* = 15.5 Hz, 1H), 4.69 (t, *J* = 7.9 Hz, 2H), 2.57 (t, *J* = 7.2 Hz, 2H), 2.09 – 2.02 (m, 2H), 1.99 (s, 6H), 1.91 – 1.80 (m, 2H). ¹³C NMR (126 MHz, DMSO-*d*6) δ [ppm]: 181.7, 152.1, 147.8, 143.9, 141.8, 138.8, 138.5, 133.3, 133.0, 131.2, 130.1, 129.0, 128.5, 127.4, 126.7, 124.4, 123.3, 118.1, 113.5, 53.7, 50.3, 47.1, 27.4, 25.3, 22.3. **HRMS** C₂₈H₂₈N₂O₅S⁺ [MH⁺] calc. 505.1792, found 505.1792.

S8: 4-(2-((1E,3E)-4-(4-aminophenyl)buta-1,3-dien-1-yl)-1,1-dimethyl-1H-benzo[e]indol-3-ium-3-yl)butane-1-sulfonate

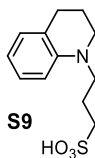
S7 (62 mg, 0.123 mmol, 1.0 eq) and tin(II) chloride (93 mg, 0.49 mmol, 4.0 eq) were dissolved in EtOH (2 mL) and stirred 1 h at 60 °C. The reaction mixture was cooled to room temperature and purified by rp-flash chromatography (H₂O:MeCN, 90:10 to 0:100) to afford **S8** (9 mg, 0.019 mmol, 15%) as a blue solid.

¹H NMR (400 MHz, methanol-*d*₄) δ [ppm]: 8.42 – 8.32 (m, 2H), 8.21 (d, *J* = 9.0 Hz, 1H), 8.13 (d, *J* = 8.2 Hz, 1H), 7.97 (d, *J* = 9.0 Hz, 1H), 7.85 – 7.80 (m, 2H), 7.80 – 7.76 (m, 1H), 7.72 – 7.61 (m, 2H), 7.52 (dd, *J* = 15.2, 10.6 Hz, 1H), 7.36 – 7.25 (m, 3H), 4.74 – 4.59 (m, 2H), 3.04 – 2.89 (m, 2H), 2.28 – 2.14 (m, 2H), 2.10 – 2.00 (m, 8H). ¹³C NMR (126 MHz, methanol-*d*₄) δ 183.4, 155.8, 149.3, 139.8, 139.7, 135.1, 134.4, 132.8, 131.9, 131.3, 129.7, 129.7, 129.6, 128.7, 128.4, 124.1, 122.3, 115.6, 113.6, 55.1, 51.3, 47.8, 28.2, 26.6, 23.3. HRMS C₂₈H₃₀N₂O₃S⁺ [MH⁺] calc. 475.2050, found 475.2048.

P-AzHCy2

S8 (65 mg, 0.137 mmol, 1.0 eq) was dissolved in MeOH (5 mL) and cooled to 0°C, then HCl (273 μL, 0.547 mmol, 2M in water, 4 eq) and NaNO₂ (68 μL, 0.137 mmol, 2M in water, 1.0 eq) were added and stirred for 30 minutes. The diazonium solution was then added dropwise to a precooled solution of *N,N*-dimethylaniline (17 μL, 0.137 mmol, 1 eq) and sodium acetate (45 mg, 0.547 mmol, 4.0 eq) at 0°C. The mixture was stirred for 30 min at 0°C, warmed to room temperature, and directly purified by rp-flash chromatography (H₂O:MeCN, 90:10 to 40:60) to afford **P-AzHCy2** (12 mg, 20 μmol, 14 %) as a black solid.

¹H NMR (400 MHz, DMSO-*d*₆) δ [ppm]: 8.50 – 8.39 (m, 2H), 8.27 (d, *J* = 9.0 Hz, 1H), 8.23 – 8.15 (m, 2H), 7.92 – 7.77 (m, 8H), 7.74 – 7.69 (m, 1H), 7.68 – 7.59 (m, 1H), 7.50 (d, *J* = 15.3 Hz, 1H), 6.85 (d, *J* = 9.3 Hz, 2H), 4.65 (t, *J* = 7.9 Hz, 2H), 3.08 (s, 6H), 2.58 (t, *J* = 7.2 Hz, 2H), 2.04 – 1.96 (m, 8H), 1.91 – 1.80 (m, 2H). ¹³C NMR (126 MHz, DMSO-*d*₆) δ [ppm]: 181.4, 153.6, 153.5, 152.9, 146.9, 142.9, 138.5, 138.3, 136.4, 133.2, 131.1, 130.0, 130.0, 129.5, 128.4, 127.2, 126.8, 125.2, 123.2, 122.7, 116.0, 113.4, 111.7, 53.5, 50.4, 48.6, 46.7, 27.3, 25.6, 22.4. HRMS C₃₆H₃₉N₄O₃S [MH⁺] calc. 607.2737, found 607.2744.

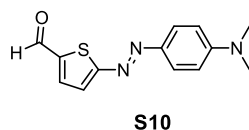
S9: 3-(3,4-dihydroquinolin-1(2H)-yl)propane-1-sulfonic acid

The synthesis was conducted by a modified literature procedure for a related substance.^[4]

A mixture of 1,2,3,4-tetrahydroquinoline (502 μ L, 4.0 mmol, 1.0 eq) and 1,3-propanesultone (977 mg, 8.0 mmol, 2 eq) was stirred for 16 h at room temperature. Ethanol (5 mL) was added, and the mixture was stirred for 72 h at room temperature followed by addition of acetone (10 mL). The mixture was cooled to 8°C for 48 h and the resulting precipitate was collected to afford **S9** (938 mg, 3.67 mmol, 92 %) as colourless solid.

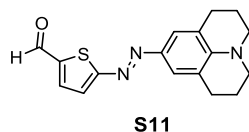
Spectral data are in accordance with the literature (known compound)^[5].

¹H NMR (500 MHz, D₂O) δ [ppm]: 7.54 – 7.35 (m, 4H), 3.81 – 3.62 (m, 4H), 3.04 – 2.94 (m, 4H), 2.31 – 2.18 (m, 4H). ¹³C NMR (126 MHz, D₂O) δ [ppm]: 136.2, 132.4, 132.2, 130.7, 128.5, 123.5, 57.5, 49.6, 48.5, 24.8, 21.2, 16.5. HRMS C₁₂H₁₇NO₃S [MH⁺] calc. 256.1002, found 256.1000.

S10: 5-((4-(dimethylamino)phenyl)diazenyl)thiophene-2-carbaldehyde

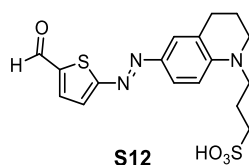
The synthesis was conducted according to a literature procedure.^[6]

A mixture of 5-nitrothiophene-2-carbaldehyde (157 mg, 1.0 mmol, 1.0 eq) and tin(II)chloride (569 mg, 3.0 mmol, 3.0 eq) in conc. HCl (3 mL) and THF (3 mL) was stirred at 60 °C for 1 h. The mixture was cooled to 0°C, NaNO₂ solution (0.5 mL, 2 M in water, 1.0 mmol, 1.0 eq) was added dropwise and the mixture was stirred for 1 h at 0°C. The diazonium salt solution was transferred into a solution of *N,N*-dimethylamine (128 μ L, 1 mmol, 1.0 eq) and sodium acetate (2.5 g) in EtOH (7.5 mL) and water (7.5 mL) at 0°C and stirred for 1 h at 0°C. The mixture was diluted with brine (100 mL), extracted with CH₂Cl₂ (2 \times 100 mL), the combined organic layers were dried over anhydrous Na₂SO₄, filtered, concentrated and purified by column chromatography (CH₂Cl₂) to afford **S10** (65 mg, 0.25 mmol, 25 %) as a purple solid which was used directly without further purification.

S11: 5-((2,3,6,7-tetrahydro-1*H*,5*H*-pyrido[3,2,1-*ij*]quinolin-9-yl)diazenyl)thiophene-2-carbaldehyde

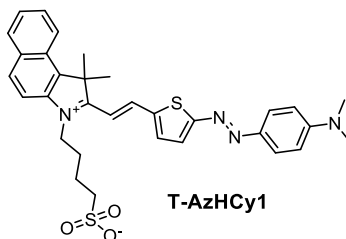
The synthesis was conducted according to a literature procedure.^[6]

A mixture of 5-nitrothiophene-2-carbaldehyde (157 mg, 1.0 mmol, 1.0 eq) and tin(II)chloride (569 mg, 3.0 mmol, 3.0 eq) in conc. HCl (3 mL) and THF (3 mL) was stirred at 60 °C for 1 h. The mixture was cooled to 0°C, NaNO₂ solution (0.5 mL, 2 M in water, 1.0 mmol, 1.0 eq) was added dropwise and the mixture was stirred for 1 h at 0°C. The diazonium salt solution was transferred into a solution of julolidine (173 mg, 1 mmol, 1.0 eq) and sodium acetate (2.5 g) in EtOH (7.5 mL) and water (7.5 mL) at 0°C and stirred for 1 h at 0°C. The mixture was diluted with brine (100 mL), extracted with CH₂Cl₂ (2 × 100 mL), the combined organic layers were dried over anhydrous Na₂SO₄, filtered, concentrated and purified by column chromatography (CH₂Cl₂) to afford **S11** (89 mg, 0.30 mmol, 30 %) as a dark purple oil that was used directly without further purification.

S12: 3-(6-((5-formylthiophen-2-yl)diazenyl)-3,4-dihydroquinolin-1(2*H*)-yl)propane-1-sulfonic acid

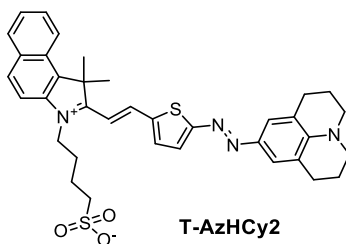
The synthesis was conducted by a modified literature procedure for a related substance.^[6]

A mixture of 5-nitrothiophene-2-carbaldehyde (314 mg, 2.0 mmol, 1.0 eq) and tin(II)chloride (1.14 g, 6.0 mmol, 3.0 eq) in conc. HCl (6 mL) and THF (6 mL) was stirred at 60 °C for 1 h. The mixture was cooled to 0°C, NaNO₂ solution (1 mL, 2 M in water, 2.0 mmol, 1.0 eq) was added dropwise and the mixture was stirred for 1 h at 0°C. The diazonium salt solution was transferred into a solution of **S9** (357 mg, 1.4 mmol, 0.7 eq) and sodium acetate (5 g) in EtOH (15 mL) and water (15 mL) at 0°C and stirred for 1 h at 0°C. Solvents were removed under vacuum, the residue adsorbed on silica, dry loaded on a silica column and purified by column chromatography (CH₂Cl₂:MeOH 85:15 to 75:25 as stepwise gradient), followed by rp-flash chromatography (H₂O:MeCN, 90:10 to 2:98) to afford **S12** (218 mg, 0.55 mmol, 28 %) as purple solid which was used without further purification.

T-AzHCy1

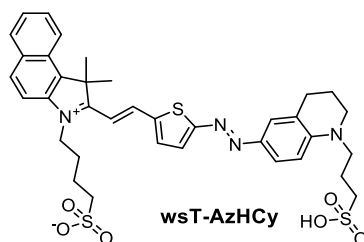
A screw cap vial was charged with **S1** (87 mg, 0.25 mmol, 1.0 eq), **S10** (65 mg, 0.25 mmol, 1.0 eq) and acetic anhydride (2.5 mL), sealed and the mixture was stirred at 115°C for 60 min. After cooling to room temperature MeOH (5 mL) was added, stirred for 1 h, then solvents were removed and the residue was purified by flash chromatography (CH₂Cl₂:MeOH, stepwise gradient 90:10 to 80:20) to afford **T-AzHCy1** (64 mg, 0.11 mmol, 43 %) as a blue solid.

¹H NMR (400 MHz, DMSO-*d*₆) δ [ppm]: 8.71 (d, *J* = 15.8 Hz, 1H), 8.41 (d, *J* = 8.5 Hz, 1H), 8.29 – 8.23 (m, 2H), 8.20 (d, *J* = 8.2 Hz, 1H), 8.14 (d, *J* = 9.0 Hz, 1H), 7.80 – 7.76 (m, 4H), 7.71 (t, *J* = 7.5 Hz, 1H), 7.41 (d, *J* = 15.9 Hz, 1H), 6.90 (d, *J* = 9.4 Hz, 2H), 4.77 (t, *J* = 7.7 Hz, 2H), 3.15 (s, 6H), 2.59 – 2.52 (m, 2H), 2.05 – 1.97 (m, 8H), 1.88 – 1.78 (m, 2H). **¹³C NMR** (101 MHz, DMSO-*d*₆) δ [ppm]: 180.8, 172.0, 167.5, 153.6, 145.2, 142.6, 139.2, 139.1, 138.6, 138.2, 133.1, 131.1, 130.1, 128.9, 128.4, 127.1, 126.8, 123.0, 113.4, 112.4, 110.3, 53.5, 50.4, 46.4, 27.5, 25.7, 22.3, 21.1. **HRMS** C₃₂H₃₄N₄O₃S₂Na [MNa⁺] calc. 609.1965, found 609.1993.

T-AzHCy2

A screw cap vial was charged with **S1** (34 mg, 0.10 mmol, 1.0 eq), **S11** (31 mg, 0.10 mmol, 1.0 eq) and acetic anhydride (1 mL), sealed and the mixture was stirred at 115°C for 30 min. After cooling to room temperature MeOH (5 mL) was added, stirred for 1 h, then solvents were removed and the residue was purified by rp-flash chromatography (H₂O:MeCN, 90:10 to 0:100) to afford **T-AzHCy2** (10 mg, 0.016 mmol, 16%) as a black solid.

¹H NMR (500 MHz, DMSO-*d*₆) δ [ppm]: 8.65 (d, *J* = 15.6 Hz, 1H), 8.38 (d, *J* = 8.5 Hz, 1H), 8.23 (d, *J* = 9.0 Hz, 1H), 8.21 – 8.16 (m, 2H), 8.09 (d, *J* = 9.0 Hz, 1H), 7.78 (t, *J* = 7.7 Hz, 1H), 7.68 (t, *J* = 7.5 Hz, 1H), 7.60 (d, *J* = 4.3 Hz, 1H), 7.38 (s, 2H), 7.26 (d, *J* = 15.7 Hz, 1H), 4.71 (t, *J* = 7.7 Hz, 2H), 2.76 (t, *J* = 6.3 Hz, 4H), 2.54 – 2.53 (m, 2H), 2.03 – 1.96 (m, 8H), 1.93 – 1.87 (m, 6H), 1.84 – 1.75 (m, 4H). **¹³C NMR** (126 MHz, DMSO-*d*₆) δ [ppm]: 180.3, 169.1, 148.2, 145.1, 142.1, 140.2, 138.8, 137.9, 137.8, 133.0, 131.1, 130.1, 128.4, 127.3, 126.9, 126.9, 126.5, 123.0, 122.2, 113.2, 109.0, 53.2, 50.5, 50.0, 46.1, 27.4, 27.0, 25.9, 22.4, 20.7. **HRMS** C₃₆H₄₁N₄O₆S₃ [MH⁺] calc. 639.2458, found 639.2466.

wsT-AzHCy

A screw cap vial was charged with **S1** (34 mg, 0.10 mmol, 1.0 eq), **S12** (39 mg, 0.10 mmol, 1.0 eq) and EtOH (1 mL), sealed and the mixture was stirred at 70°C for 60 min. Solvents were removed and the residue was purified by rp-flash chromatography (H₂O/MeCN, gradient 90:10 to 65:35) followed by preparative HPLC (H₂O:MeCN, 90:10 to 2:98 over 20 minutes, then 5 minutes 98% MeCN) to afford **wsT-AzHCy** (3 mg, 0.04 mmol, 4%) as a blue solid.

¹H NMR (500 MHz, DMSO-*d*₆) δ [ppm]: 8.69 (d, *J* = 15.7 Hz, 1H), 8.40 (d, *J* = 8.5 Hz, 1H), 8.28 – 8.16 (m, 3H), 7.97 – 7.90 (m, 1H), 7.81 – 7.74 (m, 1H), 7.72 – 7.67 (m, 2H), 7.60 (dd, *J* = 9.0, 2.3 Hz, 1H), 7.53 (d, *J* = 2.4 Hz, 1H), 7.36 (d, *J* = 15.6 Hz, 1H), 6.91 (d, *J* = 9.2 Hz, 1H), 4.76 (t, *J* = 7.6 Hz, 2H), 3.64 – 3.56 (m, 2H), 3.51 – 3.46 (m, 2H), 2.79 (t, *J* = 6.3 Hz, 2H), 2.57 – 2.51 (m, 2H), 1.94 – 1.84 (m, 4H), 1.84 – 1.70 (m, 4H), 1.31 – 1.17 (m, 2H). **¹³C NMR** (126 MHz, DMSO-*d*₆) δ [ppm]: 180.5, 168.4, 150.2, 145.2, 142.4, 139.4, 138.7, 138.3, 137.9, 133.0, 131.0, 130.0, 128.3, 128.0, 127.0, 126.8, 123.4, 123.2, 123.1, 113.3, 111.1, 110.7, 109.6, 53.3, 50.5, 49.5, 48.5, 46.2, 27.5, 27.3, 26.7, 25.7, 22.7, 22.3, 20.9. **HRMS** C₃₆H₄₁N₄O₆S₃ [MH⁺] calc. 721.2183 found 721.2192.

2 Photocharacterization

2.1 Standard Absorption and Fluorescence Methods

UV-VIS. UV-Vis spectra were recorded on an Agilent Cary 60 UV-Vis spectrophotometer using 1 cm quartz or PMMA cuvettes. All measurements were performed at room temperature in non-degassed solvents at a concentration of 10 μM, unless stated otherwise.

Fluorescence. Fluorescence spectra were recorded on an Agilent Cary Eclipse 3500 fluorescence spectrometer using 1 cm quartz cuvettes. All measurements were performed at room temperature in non-degassed solvents at absorbance <0.1, unless stated otherwise.

Approximate quantum yields. Samples were measured against a fluorescence standard with a known quantum yield Φ_F. For this purpose, absorbance and fluorescence were subsequently measured from the same sample. The fluorescence quantum yield is then calculated according to equation (1), with: *f_x(λ_{ex})* = absorbance factor (derived from equation (2) and *A_x(λ_{ex})* = measured absorbance), and ∫_{λ_{Em}} *F_s(λ_{Em})* = area under the curve fluorescence measurement.

$$\Phi_F^i = \Phi_F^s \frac{f_s(\lambda_{Ex}) \int_{\lambda_{Em}} F_i(\lambda_{Em})}{f_i(\lambda_{Ex}) \int_{\lambda_{Em}} F_s(\lambda_{Em})} \quad (1)$$

$$f_x(\lambda_{Ex}) = 1 - 10^{-A_x(\lambda_{Ex})} \quad (2)$$

2.2 Fluorescence Properties

The newly synthesized chromophores are separated in two categories according to whether we could detect significant fluorescence with standard settings on our fluorimeter: (1) residually fluorescent dyes (AzCy), and (2) quenched dyes (AzHCy). To obtain approximate *upper limit* quantum yield values for category 2 we increased the sensitivity of the fluorimeter by

maximising the photomultiplier voltage (standard: 400 V, max: 1 kV). Integration of that signal mostly captures noise (with intensity values at or above 0), so that integration gives an upper limit for the quantum yield (e.g. " $<10^{-3}$ ").

All measurements for quantum yields were carried out in ethanol. To match the spectral properties of analytes, we used **ICG**^[7,8] as reference fluorophore for: **E-AzCy7**, **T-AzHCy2**, **wsT-AzHCy**, and **Cy5**^[9] for: **wsCy5.5**, **E-AzCy5**, **M-AzCy5**, **T-AzHCy1**.

Fluorescence spectra for residual fluorescent dyes are shown in **Fig. S1**, spectra for quenched dyes were obtained with a more sensitive experimental setup (see part **Photoluminescence**).

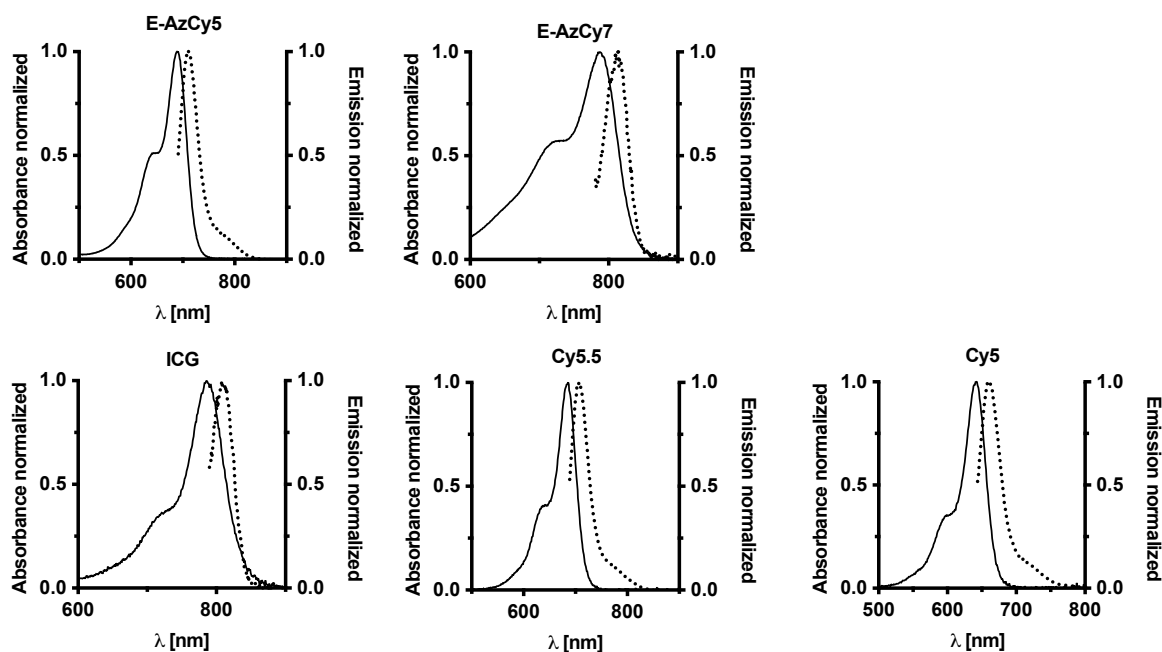


Fig. S1. Absorbance-Emission Spectra of residual fluorescent dyes **E-AzCy5** & **E-AzCy7** (top) and reference fluorophores **ICG**, **Cy5.5**, and **Cy5** (bottom).

2.3 Photoswitching

Aim: Azobenzenes undergo $E \rightleftharpoons Z$ photoisomerizations^[10] that change their absorption profiles; and for quantifying a PA contrast agent, such changes would be undesirable. Therefore, the photoswitching properties of compounds **M-AzCy5**, **E-AzCy5**, **E-AzCy7**, **T-AzHCy1**, **T-AzHCy2**, **wsT-AzHCy**, **3**, and **4** were investigated in a straightforward way, to study the potential for bulk photoisomerization under unfocussed illumination.

General procedure: The LED-illumination / UV-Vis-readout setup for testing photoisomerisation was similar to that reported elsewhere^[11]. In brief, LEDs at nominal wavelengths in the range 365 - 770 nm with FWHM < 30 nm, delivering intensity on the order of 2 mW/mm^2 in the sample plane (readout beam for UV-Vis), were shone from above into cuvettes of the UV-Vis spectrophotometer with a solution height of typically < 5 mm above the readout beam (itself ca. 2 mm in diameter). All compounds were illuminated at LEDs for 365 nm as well as near their long-wavelength absorption maximum (e.g. 660 nm for **M-AzCy5**), in MeCN solution, at $23 \text{ }^\circ\text{C}$, observing typically 250 - 900 nm.

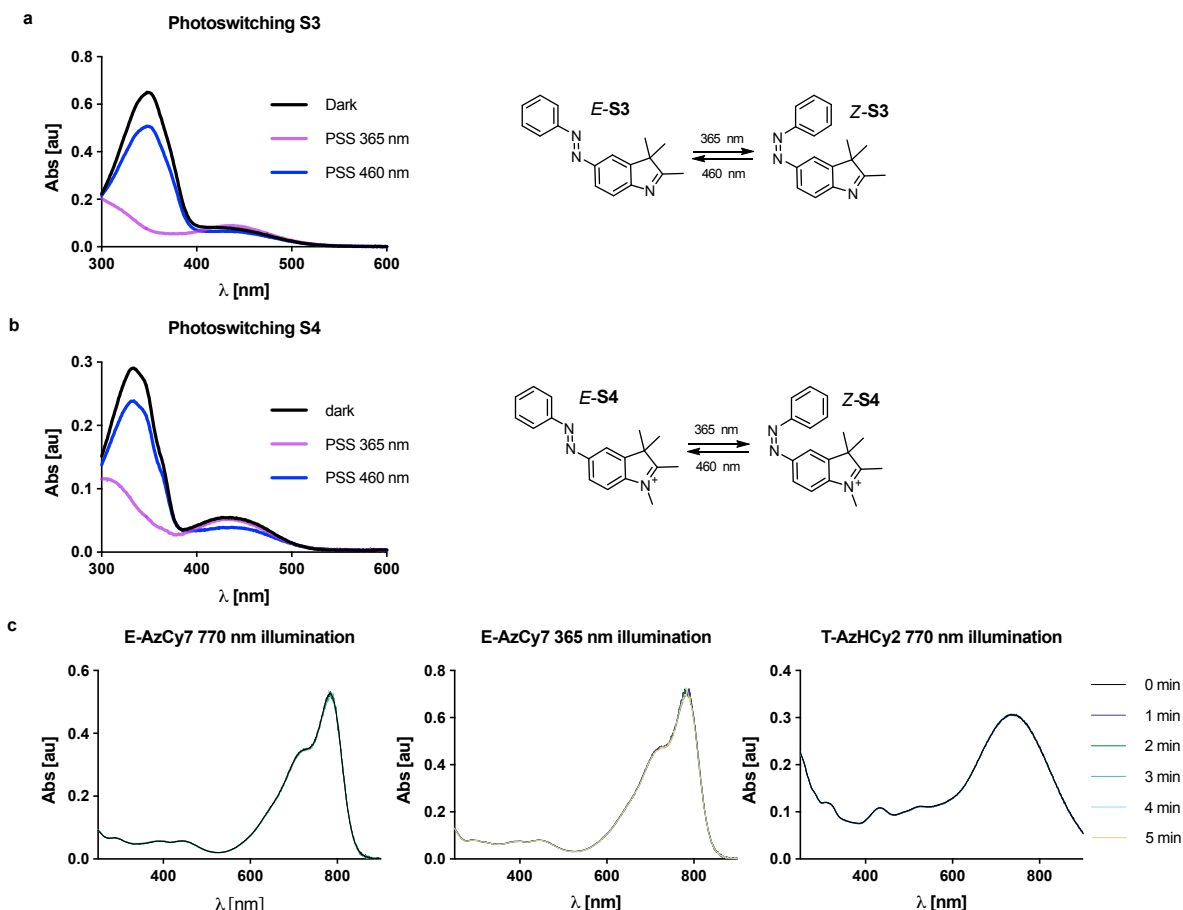


Fig. S2. (a,b) $E \rightleftharpoons Z$ -azobenzene photoswitching for **S3** and **S4**. (c) No observed photoswitching for **E-AzCy7** at 770 nm or at 365 nm and no observed photoswitching for **T-AzHCy2** at 770 nm.

Results: **S3** and **S4** were photoswitched at 365 or 460 nm to their photostationary states within <5 s (**Fig S2**), confirming bulk population $E \rightleftharpoons Z$ photoswitching with a Z-photoisomer that is slowly-relaxing relative to the applied intensity and the readout timescale.

M-AzCy5, **E-AzCy5**, **E-AzCy7**, **T-AzHCy1**, **T-AzCy2** and **wsT-AzCy** did not show changes in their absorption profiles in the 250 - 900 nm range over minutes of illumination (**Fig S2c**).

Discussion: This observation is *consistent with* our hopes that the dye species would not undergo appreciable $E \rightleftharpoons Z$ -photoisomerisation-based changes of absorption profile that would reduce their ability to act as quantitative reporters in PA. It is *not conclusive*, because although we can exclude that *under these illumination conditions* the Z photoisomer is formed and maintained at appreciable amounts that are different to the starting amount ($>1\%$ isomerisation should be detectable), we cannot exclude that the vastly higher intensities during a PA pulse would form significant Z-isomer during the pulse, so impacting quantitation. Such unwanted formation of Z during the pulse is not inconsistent with these UV-Vis observations if (i) spontaneous $Z \rightarrow E$ isomerisation is fast (half-life est. < 1 ms); and/or (ii) E and Z photoisomers have near-identical absorption profiles (we consider this unlikely in the <400 nm range); and/or (iii) photostationary states, optionally including those under ambient lighting conditions, are very E-rich and the E:Z ratio is relatively invariant with wavelength; mixtures of these possibilities are plausible (e.g. there is fast relaxation but the photoisomers have very similar absorption spectra). However, we note that as long as an E:Z photostationary state would be reached rapidly within a PA pulse (e.g. within the first 10% of the pulsewidth),

quantitative interpretation of the overall signal will be >90% accurate, no matter the difference in PA response between the isomers.

We consider it most likely that the azobenzene *E/Z*-geometry barely affects the absorption profile in the red/NIR region, or the electronic relaxation rate, of **E-AzCy** / **M-AzCy** compounds, thus likely also has little impact on their PA response. In keeping with ongoing research on different systems, we also consider it most likely that red/NIR photostationary states of all **AzCy** and **AzHCy** are very *E*-rich if not all-*E*. We note that if *Z*→*E* isomerisation is a more important cause of not observing *E*→*Z* isomerisation in UVVis than nearly-all-*E* PSSs, then the *Z*→*E* half-life should be < ms (which would not be surprising, since $\tau \sim 500$ ps is reported in acetonitrile for *Z*→*E* of push-pull-type compounds that are similar to truncated **AzHCy** species^[12]). Finally, the TA spectroscopy (**Fig 4**, **Fig S7**) indicates that the **T-AzHCys** and **M-AzCy5** relax back to their starting spectrum (which we assign from the LED experiments as \sim all-*E*) after excitation; we estimate that spectral differences of 5% *would* be visible, thus 5% is our (very) upper bound for the "photochemical difference brightness" ($\Phi_{E \rightarrow Z} \times [\Delta \text{Abs}_{E-Z}(\lambda) / \text{Abs}_E(\lambda)]$) which would be the main route that could confound simple PA quantification. Therefore, we remain confident of these compounds' ability to act as well-quantifiable PA chromophores, unharmed by potential for *E*↔*Z*-azo-photoisomerisation (we rather believe that, within this class, photostability is by far the more important problem to work on; separately, we note that the popular RSA-type dyes inherently face quantitation problems due to their nonlinear signal-to-intensity response).

3 Photoacoustics

3.1 MSOT set-up and data acquisition

Phantom data were acquired^[13] using a commercially available MSOT scanner (MSOT256-TF, iThera Medical GmbH, Munich, Germany). Nanosecond-pulsed light was generated from a tunable optical parametric oscillator (OPO) laser and delivered to the sample through a ring-type fiber bundle. The wavelength range used for imaging was from 680 to 900 nm, with a step size of 10 nm. The sample absorbs the light, generating an acoustic signal that propagates through the sample and is detected outside. In our experiments, we detected the acoustic signals using a cylindrically focused transducer consisting of 256 elements. The transducer array provided a coverage of 270° at multiple laser wavelengths. Photoacoustic images were reconstructed using a back-projection reconstruction method available in the viewMSOT software and subsequently analyzed using the same software.

To scan the dye samples,^[14,15] we used a cylindrical agar phantom equipped with 3 mm diameter holes for sample placement. The phantom was made up of 1.3% (w/w) agar (Sigma-Aldrich, St. Louis, MO, USA) to provide solidity, and 6% (v/v) intralipid emulsion (20%, Sigma-Aldrich) to ensure uniform illumination of the sample by light diffusion. The intralipid was added to decrease the scattering coefficient to 10 cm^{-1} , simulating scattering in biological tissue. To enable transversal plane imaging at a single position, approximately in the middle of the phantom, MSOT data were acquired as described above and values plotted (**Fig S3**).

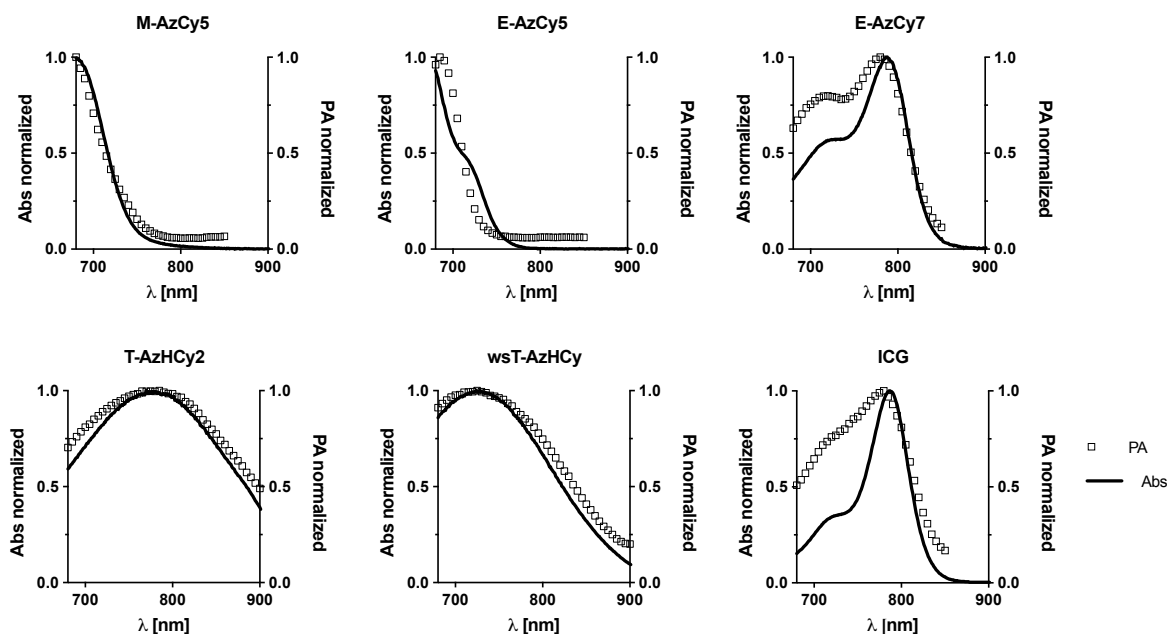


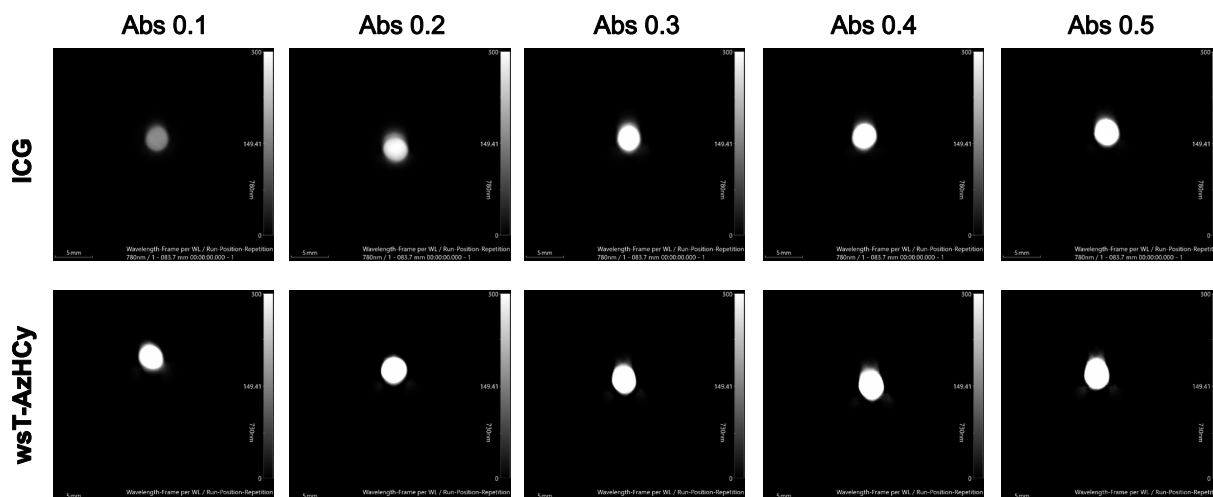
Fig. S3: Overlay of absorbance and photoacoustic signal generation spectra.

Note on the broadened signals in **Fig. S3**: Ideal multiplexing needs individual spectra to be well-separated for deconvolution, so broad spectra complicate convolution.

3.2 Determination of optoacoustic signal generation efficacy

Optical absorbance for all compounds were adjusted to 0.1, 0.2, 0.3, 0.4 and 0.5 respectively and the optoacoustic signal response was determined for each absorbance value. Optoacoustic generation efficacy is calculated by the slope of the linear regression (**Fig. S4**).

Exemplary Phantom Images of ICG and wsT-AzHCy



Linear regression to determine signal generation efficacy

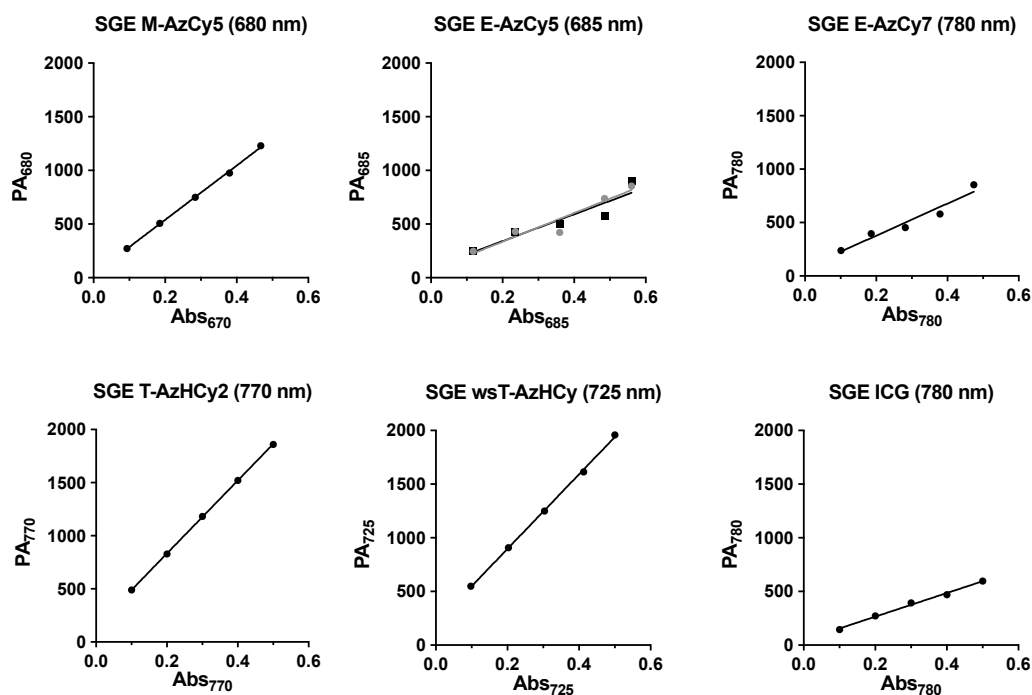


Fig. S4: Top: Exemplary phantom images for the dilution series with absorptions from 0.1-0.5. Bottom: Determination of optoacoustic signal generation efficacy (SGE, also called OGE). Values for **E-AzCy5** were determined as duplicates (grey and black).

3.3 Photostability of the PA signal

The photostability data (Fig 3d) do not allow fitting a decrease of PA signal for **T-AzHCy2**, **wsT-AzHCy**, and **E-AzCy5** because linear fits to the data are horizontal lines (no photobleaching). To give some meaningful numbers, we calculate lowest possible bounds for their photobleaching halftimes (23 and 140 hours respectively) by taking the standard error of the data (the scatter around PA = 1, over all experimental time) and using this as a very conservative upper bound for the amount of photobleaching that could have occurred during the 30 min observation, then forcing a monoexponential decay fit to that value. Optical absorbance for all samples used in photostability experiments was adjusted to 0.5.

3.4 Reference photoacoustic measurements: QC-1, IR 820

QC-1 (LI-COR Biosciences, NE, USA, structure see **Fig S5a**) is a commercially available NIR-quencher developed for FRET applications. One previous report used **QC-1** or **ICG** coupled to the water-soluble peptide pHLIP and found comparable photoacoustic intensities at the same concentrations,^[16] despite that **QC-1**'s more quenched fluorescence should be beneficial for PA imaging. Another report found slightly superior PA intensities for **QC-1** bound to BSA compared to commercially available fluorophores **IRDye 800CW** and **CF770**.^[17] Since **QC-1** was also designed to make the cyanine scaffold into a fast-relaxing nonfluorescent dye (TCSPC decay time ca. 2 ps on our setup), we thought to compare its photoacoustic properties, as an additional reference compound, to those of Azo-Cyanines.

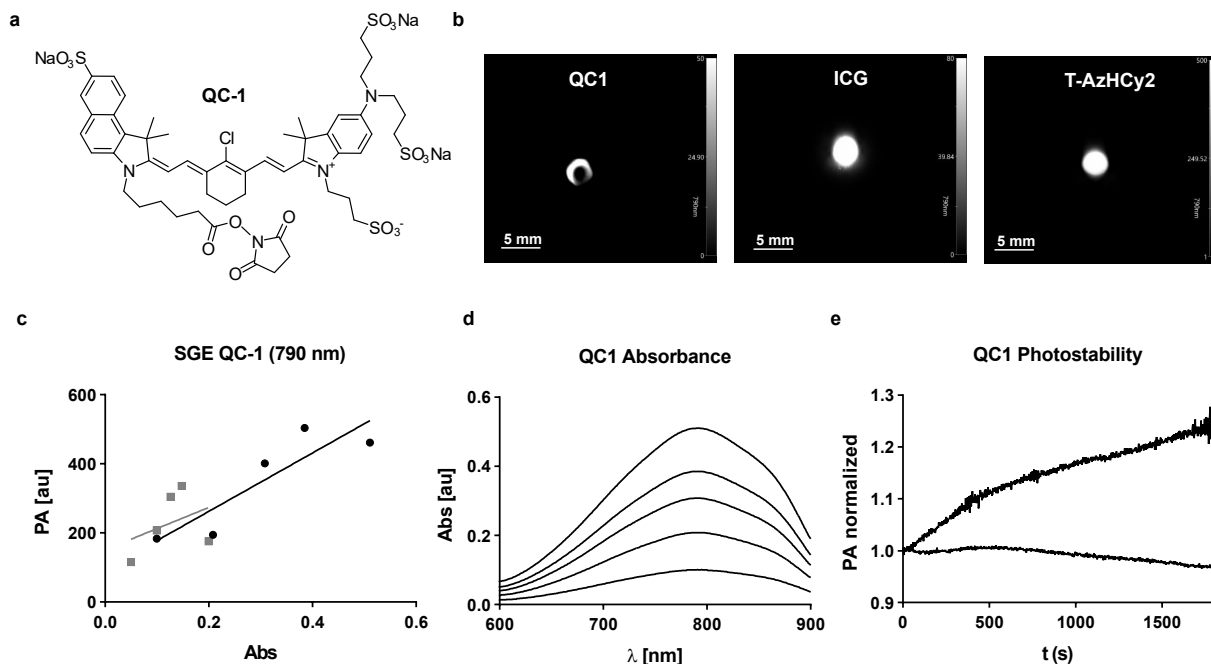


Fig. S5. (a) **QC-1**. (b) photoacoustic phantom images of **QC-1**, **ICG** and **T-AzHCy2**. (c) determination of signal generation efficacy for OD ranges from 0.1-0.5 (black) and 0.05-0.2 (grey). (d) absorbance spectra of **QC-1** samples used for PA imaging in PBS/EtOH 1:1. (e) photostability of **QC-1** with OD 0.5 and OD 0.2 samples.

However, in our phantom setup **QC-1** did not yield reliable PA results or high performance:

(1) The PA image was donut-shaped, with uneven signal distribution indicating high concentrations at the outer surface of the sample holder and low ones inside: a red flag for potential imaging in heterogeneous media (**Fig S5b**). For comparison, the phantom images of e.g. **ICG** and **T-AzHCy2** have signal intensity homogeneously distributed throughout the whole sample (**Fig S5b**). We note that donut-shaped images are seen regularly with experimental dyes that are not yet optimal for practical use in PA (see e.g. Fig 6d in ref^[18] or Fig. 6a in ref^[19]).

(2) There is no linear dependence between **QC-1** cuvette absorption and phantom photoacoustic signal intensity, so the basis for calculating a robust signal generation efficacy is missing (**Fig S5c**, compare section 3.2). This is puzzling since, in cuvette, the absorption spectra of **QC1** increased linearly with concentration (**Fig S5d**, concentration series aiming for OD = 0.1, 0.2, 0.3, 0.4, 0.5 at 790 nm), which would seem to contraindicate aggregation. To test whether lower concentrations might avoid aggregation and result in a linear dependence we used a second series of phantom samples with ODs ranging from 0.05 - 0.2 (**Fig S5c** in grey) but again did not find a linear correlation.

Interestingly, the intensities derived for **QC1** are lower than the ones for **ICG** for same ODs; i.e. its quenched fluorescence does not have a positive effect under these conditions.

(3) The standard photostability experiment using a sample with absorption of 0.5 gave an increase in signal of ~20% after 30 minutes. Using a more dilute sample (0.2) gave a decrease in signal but the shape of the curve did not allow a fit, therefore more complex proceedings might be the reason for this unusual behaviour (**Fig S5e**).

Since **QC-1** had only been hoped to serve as reference compound, in view of its unreliability making it unsuitable as reference in any type of experiment, we did not pursue it further.

Aggregates and nanoparticles: For our purpose of designing molecular contrast agents the formation of aggregates is undesired, but as it was raised in review, we mention that optimising PA properties of aggregates within nanoparticles is a recently explored topic, and most notably worked out with reducing excited state lifetimes by inducing intramolecular motion within nanoparticles.^[20] We consider nanoparticles an orthogonal approach in the field of PA contrast agents (e.g. they cannot easily respond to an enzymatic stimulus, whereas small molecule agents can perform molecular imaging); and we refer interested readers to recent works.^[21,22]

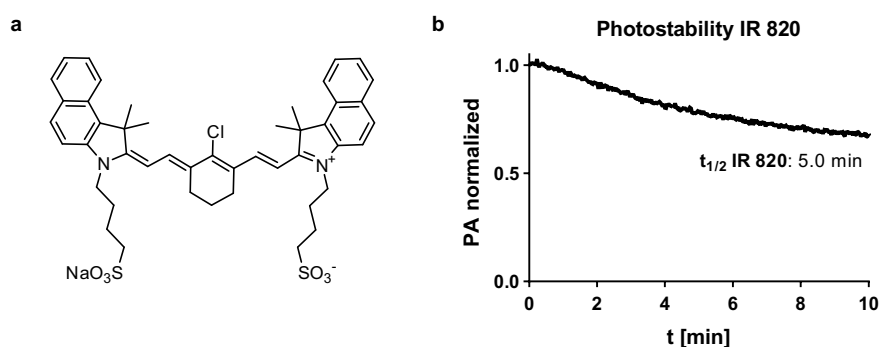


Fig. S6. (a) IR 820. (b) standard photostability experiment of IR 820 with absorption of 0.5 in EtOH/PBS.

IR 820 (Sigma Aldrich, **Fig. S6a**) is a commercially available NIR-dye for fluorescence imaging applications which was previously used for PA imaging in complex with BSA,^[23] and it has a similar signal generation efficacy compared to **ICG**.^[24] We wanted to test its photostability as an additional control experiment. We found a half-life of only 5 min (**Fig S6b**, compare: **ICG** 4 min). This makes us confident of the suitability of the comparisons we have drawn in the manuscript, between highly bleachable cyanines, and highly photostabilised azo-cyanines. (*Cyanines tend to photobleach by forming new molecular species that also absorb but with different optical properties.*^[25] *Because, for molecular imaging, we wish to study the quantifiability of a defined molecular probe, we therefore report an unconstrained monoexponential fit to this data [plateau ca. 0.6] since that reports on the photobleaching of the probe itself, and does not falsely weigh in signal from alternative bleach-product species.*)

3.5 Photoacoustic properties in biological media

The photophysical and photoacoustic properties reported in the main text of this manuscript were all measured in mixtures of aqueous buffer with organic solvents (except: fluorescence and TAS in pure organic solvents), so as to analyse true *molecular* properties in molecular solution. However, for future use in a biological setting, the surrounding will be more complex and therefore, we wanted to test how the trends of our findings would translate from photophysical driven phantom images in the presence of organic solvents, towards images derived in physiological media. We thus chose to investigate our strongest PA emitters **T-AzHCy2**, **wsT-AzHCy** and **ICG** as a reference, in 10% FBS (fetal bovine serum, 10 v/v % in PBS) solution, to provide a mixture of proteins, peptides, metabolites etc as a complex environment that mimics potential future applications.

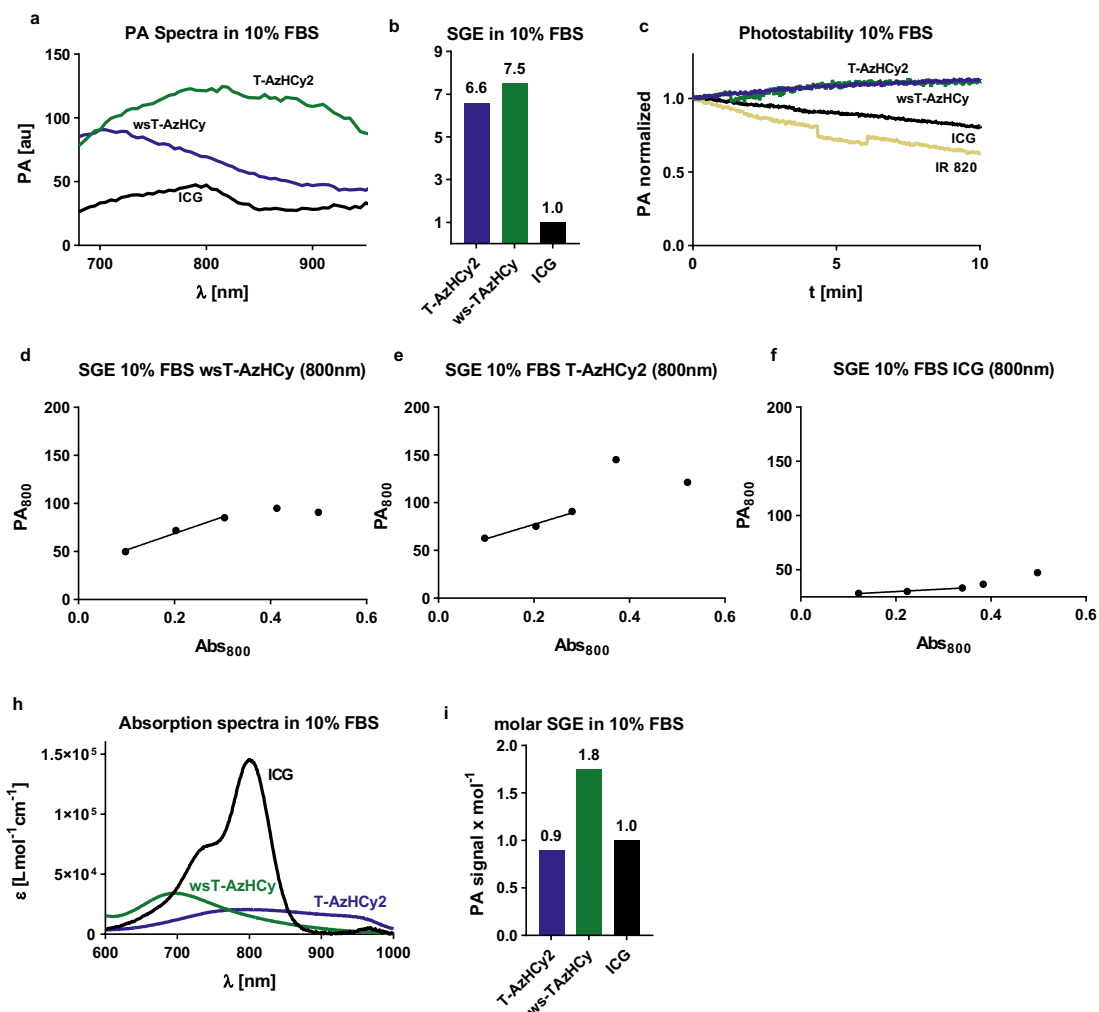


Fig. S7. (a) PA spectra of **T-AzHCy2**, **wsT-AzHCy** and **ICG** in 10% FBS, all concentrated to OD=0.5 at their maximum wavelengths. (b) Signal generation efficacy at constant OD in 10% FBS. (c) PA photostability determination. (d-f) Determination of optoacoustic signal generation efficacy from linear fitting of PA response. (g) absorption spectra of **T-AzHCy2**, **wsT-AzHCy** (10 μM) and **ICG** (2.5 μM) in 10% FBS. (h) Relative molar SGE (i.e. SGE adjusted to constant molarity; **ICG** set to 1). *The divet in the IR-820 trace in (c) corresponds to a time range where an air bubble entered the measurement zone.*

Table S1: PA and spectral properties in FBS

	λ_{max} [nm]	ϵ [$\times 10^3$ $\text{M}^{-1}\text{cm}^{-1}$]	FWHM [nm]	SGE (at const OD)	SGE (molar)	$t_{1/2}$ [min]
T-AzHCy2	797	21	292	6.6	0.9	<i>fully stable</i>
wsT-AzHCy	697	34	157	7.5	1.8	<i>fully stable</i>
ICG^{a)}	800	146	122	1	1	21

a) values for 2.5 μM

The photoacoustic action spectrum for **T-AzHCy2**, **wsT-AzHCy** and **ICG** are broadened compared to phantom images in EtOH/PBS (**Fig 3a**), indicating aggregation with proteins (**Fig. S7a**); and generally the noise levels are increased.

Very pleasingly, the enhanced signal generation efficacy for **T-AzHCy2** and **wsT-AzHCy** in 10% FBS compared to **ICG** is even stronger (6.5x/7.5x vs 3.1x/3.2x in EtOH/PBS respectively, see **Fig S7b** and **Fig. 3b**) Our analysis in mixed EtOH/PBS buffer system yielded a linear coherence between absorbance and PA signal over the analysed range (absorbance 0.1 – 0.5), however, matching this expectation, with 10% FBS, at higher concentrations the linear

dependence was not valid anymore, and this only allowed us to analyse absorbances from 0.1 – 0.3 in a linear fashion (see **Fig. S7d-f**). Also, as is known, cyanines such as ICG suffer nonlinear signal suppression effects, by aggregation and/or by adsorption on protein surfaces, which also modify their $\epsilon(\lambda)$ profiles significantly. This is why serum results are not as straightforward to measure as in pure media; and why "molar SGE in serum media" should not be trusted (see below). The mechanistically crucial point remains, how much signal is generated upon absorption of a fixed amount of light (SGE at constant OD): and this we calculate for the serum case using the more reliable, initial linear fit regions at low OD (also has already been prominently studied^[26]) - we use OD 0.1 – 0.3.

At such reliable absorbance values, the superiority of our fused molecular switches against **ICG** is higher still than in solution. Whether this reflects increased fluorescence quantum yield of **ICG** upon adsorption (i.e. lower nonradiative yield) and/or longer fluorescence lifetimes, is an open question. We note also, that unlike the adsorption-based hindering of *extrinsic nonradiative quenching* of **ICG**, adsorption should not hinder the *intrinsic* nonradiative quenching provided to **T-AzHCys** by the azobenzene motifs. Even if this quenching partly occurs through isomerisation, which is not suggested from our data (see section 2.3), isomerisations should not be blocked by protein adsorption: e.g. a recent pioneering study^[27] showed *Z*→*E* isomerization of azobenzenes within a protein binding pocket that "ought not" really accommodate the *E* isomer.

Next, we monitored PA signal stability over time (**Fig S7c**) and found half-lives in the presence of FBS of 21 minutes for **ICG** and 6 minutes for **IR 820**. **T-AzHCy2** and **wsT-AzHCy** gave similar results as **QC-1** (see SI section 3.4) with increasing PA signal over time, hence no half-life could be determined by exponential fitting, but we consider them as stable in FBS solution.

To evaluate the SGE on a per molecule scale we determined the extinction coefficients in 10% FBS (**Fig. S7h**) and subsequently normalized the SGE values on molarity. Intriguingly, the molar extinction coefficients of **ICG** and **T-AzHCy2** drop compared to buffer EtOH solution because of signal broadening; but the intensity and shape of **wsT-AzHCy** remains rather constant which may support our design logic of installing extra water solubility (see **Table S1** and **Table 1**). Therefore, the calculated molar SGE of **wsT-AzHCy** is 1.8x higher than the molar SGE of **ICG**, with FBS.

Note: The extinction coefficient of ICG in protein-containing media is not a constant but highly dependent on the absolute concentration^[28] and thus, there will always be a bias by the chosen concentration; so the molar SGE values we report should not be considered as constants, although we do argue that the trend we show is reliable. A 2.5 μ M solution of ICG in FBS (that has OD ca. 0.35) gave a PA signal that was within the measuring range of our PA samples, so that was chosen as the reference point.

3.6 Comparison of photoacoustic measurements: wsCy5.5

PA properties of **wsCy5.5** measured on a different PA device are reproduced below (**Fig S8**). Exact comparison of SGE and photostability are not possible between the different devices, so the data is only presented in the SI as additional information. Generally, compared to **ICG** the SGE of **wsCy5.5** is lower, and it is also not photostable enough for long term imaging.

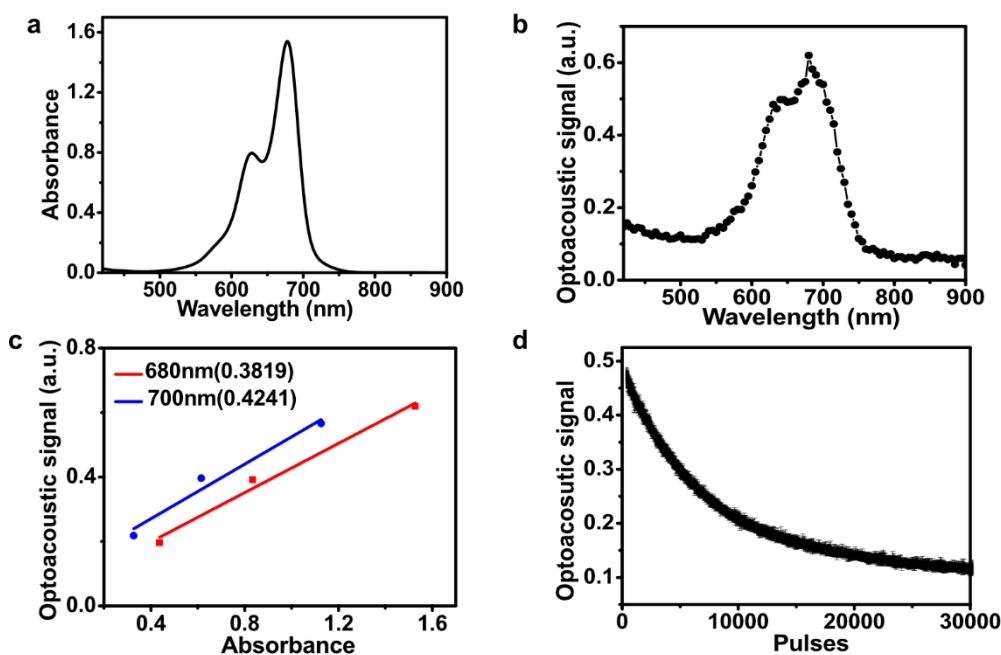


Fig. S8. (a,b) Optical spectrum and optoacoustic spectrum of **wsCy5.5**. (c) Optoacoustic signal intensity of **wsCy5.5** at different concentrations and different wavelengths. Slope value used to calculate OGE. (d) Optoacoustic signal changes of **wsCy5.5** during 680 nm pulsed laser irradiation (30 mJ/cm², 30000 pulses, 50 Hz).

4 Time-resolved fluorescence spectroscopy

Time Correlated Single Photon Counting (TCSPC) was measured using a tuneable pulsed Ti:Al₂O₃ laser (<200 fs pulsewidth, Coherent Mira 900-F, repetition rate 76 MHz, excitation wavelength 700 nm for **M-AzCy5**, **E-AzCy5**, **E-AzCy7** and **wsCy5.5**, 730nm for **T-AzHCy2** and **wsT-AzHCy**), and DMSO dye solutions (ca. 10 mM).

After filtering out the laser fundamental with a longpass filter (Thorlabs FELH0750), the detection was done using an avalanche photodiode (MPD PDM Series.). The fitting of the decay curves for the TCSPC was performed using *FluoFit* software (v.4.6.6.0, PicoQuant GmbH, 2014). Curves and fits derived from FluoFit, including IRF correction (instrument response curve). Curves in **Fig 4a** are uncorrected decay curves. Further details on the TCSPC setup can be found in ref^[29]. Fluorescence spectra for quenched dyes are shown in **Fig S9**.

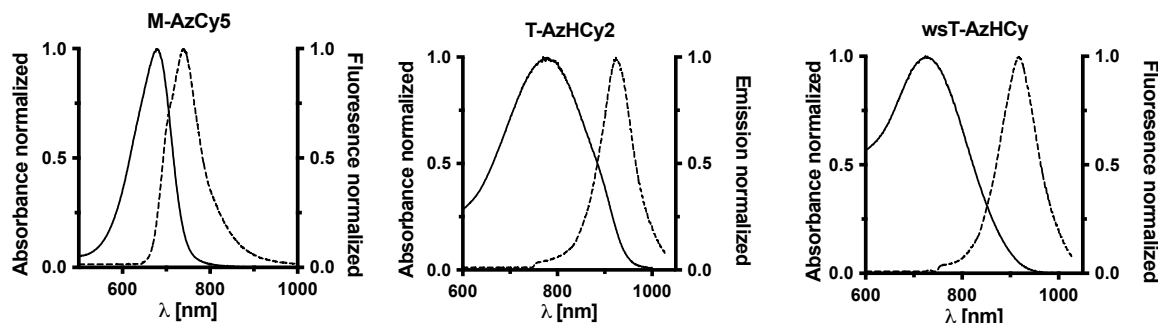


Fig. S9. Absorbance and fluorescence emission spectra. Fluorescence spectra derived from picosecond TCSPC setup.

5 Transient Absorption Spectroscopy

The femtosecond-TA data were acquired on a custom-built setup. Briefly, a regenerative Ti:sapphire amplifier (Astrella, Coherent, USA) has been used as pump laser delivering pulses of 5 mJ pulse energy at 1 kHz pulse repetition rate. The output of the laser is divided by a beam splitter. The first part is focused into a rotating CaF₂ plate to generate a broadband white light supercontinuum beam covering 300 to 700 nm. This broadband pulse is subsequently split into two parts, which are used as reference and probe pulse. A second fraction of the Ti:Sa output is used to pump an optical parametric amplifier (TOPAS prime, Light conversion, Lithuania) for generating pulses of about 100 fs pulse duration. The output of the amplifier is tunable across the UV-Vis-NIR spectral range. The repetition rate of the pump pulses is then reduced to 500 Hz by a mechanical chopper. A Berek compensator and a polarizer are used to adjust the polarization difference of pump and the white light probe pulse to the magic angle of 54.7°. The probe pulse is focused into a quartz cuvette of 10 mm path length by a concave mirror of 500 mm focal length. The spectra of probe and reference pulses are acquired by a 150 mm focal length Czerny-Turner spectrograph (SP2150, Princeton Instruments) equipped with two CCD arrays (Pascher Instruments AB, Sweden). The TA data analysis was performed on data acquired after 150 fs delay time, and includes a spectral preprocessing to correct for the chirp of the broadband pulse. The pump (excitation) wavelength used was 700 nm; solutions were acquired in a 1 cm cuvette at an OD between 0.1 and 0.2, in 1:1 ethanol:PBS.

After spectral plotting for $\Delta\text{Abs}(t)$ (**Fig 4b,c; Fig S10**), and confirming that single-wavelength-intercept data at $\lambda_{\text{max}\Delta}$ supported monoexponential fitting, we then integrated the absorption bands to find $\text{AUC}(\Delta\text{Abs})$ (difference peak areas over time; **Fig 4d**) and fitted these as monoexponentials to obtain the TA lifetimes, since this is a more robust quantification of rate of decay to the groundstate. Unconstrained monoexponential fits were excellent for **T-AzHCy2** and **wsT-AzHCy**, but for **M-AzCy5** the monoexponential fits were not so satisfactory even with constraining to plateau at zero ($\tau = 160$ ps for single wavelength 587 nm, 180 ps for AUC); a zero-plateau-constrained, two-phase AUC fit instead gives $\tau_1 = 64$ ps, $\tau_2 = 307$ ps, with pre-exponential factors $A_1:A_2 = 49:51$, which fits the data excellently (**Fig S10**). For simplicity, **Table 2** in the main text summarises this situation as simply "180 ps".

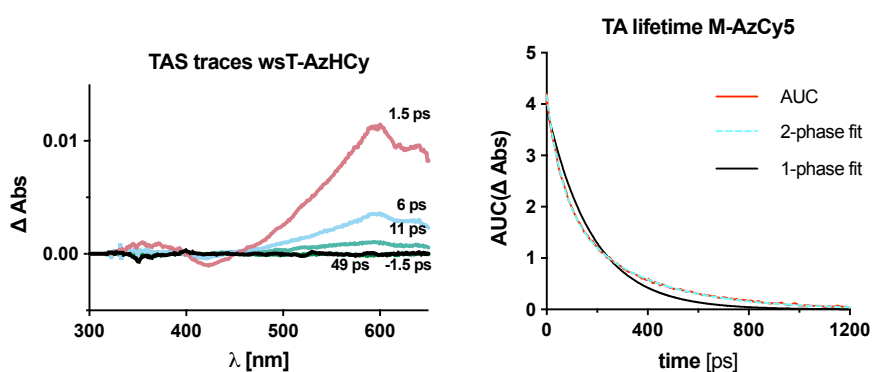


Fig. S10. TA spectra of **wsT-AzHCy** at selected time points; and **M-AzCy5** curve fitting.

6 *in vivo* optoacoustic measurements in mouse

6-week-old AthymicNude-Fox1nu mice ($n=2$) were injected with **wsT-AzHCy** dissolved in PBS containing 5 % DMSO as co-solvent (100 μL , 0.5 mM). *In vivo*, optoacoustic images were acquired at pre-injection and 120 minutes post-injection timepoints, on an MSOT inVision 256-TF (iThera Medical, Munich, Germany).^[14] The averaged optoacoustic signals of major organs were analysed using ViewMSOT 4.0 software (iThera Medical, Munich). Mice were sacrificed

at the end of the experiment. Ethical approval for all the animal experiments reported here was obtained from the Government of Upper Bavaria (#ROB-55.2-2532.Vet_02-18-120).

Indeed, as pointed out by reviewer 1, the accumulation of **wsT-AzHCy** signal in the gut, spleen, and liver (**Fig 5, Fig S11**), distinctly contrasts to its absence in the kidneys. We suppose that serum protein binding (cf. indications from **Fig 3 vs Fig S7**) is one mechanism for this biodistribution pattern. However, since the main point of this paper is to determine whether the new design principle for ultrafast-electronic-relaxation gives higher photostability and good signal generation, and since future generations of enzyme imaging PA probes based on this principle will release a different molecular cargo (as dictated by their target enzymes), we do not try to characterise this effect further nor to test biosafety of any **AzHCys**. Additional *in vivo* images with **ws-TAzHCy** from the second mouse, and with **ICG** for comparison (mice 3-4), are shown in **Fig. S11**. **ICG** shows weaker signal intensity in organs compared to **wsT-AzHCy**, in both mice the strongest signal accumulation occurs in the gut (**Fig S11hl**), signal accumulation in the liver was faint for mouse 1 (**Fig S11f**) and strong for mouse 2 (**Fig S11j**).

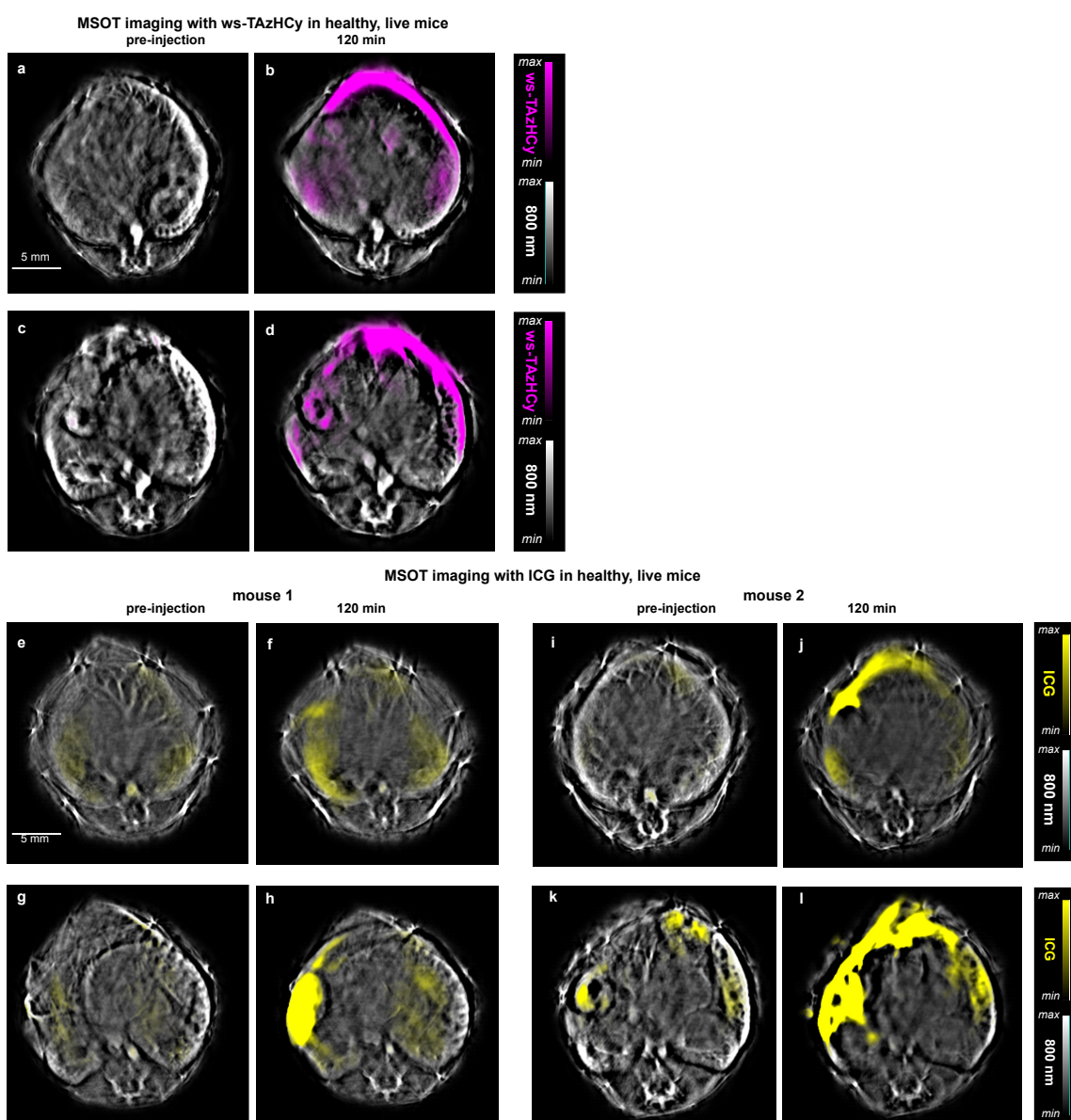


Figure S11. (a-d) *In vivo* MSOT images of the second mouse. Transverse image sections of live, healthy mice, showing liver (a,b), kidney and spleen (c,d), before and 120 min after IV injection of **wsT-AzHCy** (100 μ L, 0.5 mM). (e-h) *In vivo* MSOT images of the first mouse with **ICG**. Transverse image sections of live, healthy mice, showing liver (e,f), kidney and spleen (g,h), before and 120 min after IV injection

of **ICG** (100 μL , 0.5 mM). (i-I) In vivo MSOT images of the second mouse with **ICG**. Transverse image sections of live, healthy mice, showing liver (i,j), kidney and spleen (k,l), before and 120 min after IV injection of **ICG** (100 μL , 0.5 mM).

7 Outlook for switch-integrated PA agents

We only provide a limited set of compounds here, so to confirm or characterise the generality of using molecular switches for creating high-performance LA-type PA agents needs more study. Additionally, we only studied the excited to ground state decay of the chromophore: but to generate a photoacoustic signal more processes are involved, e.g. how excited vibrational/rotational states couple with surrounding solvent molecules to produce a thermal wave, which may be very different for intrinsically motile photoswitches as compared to the often rigidified chromophore scaffolds employed to date. However, our observations support that molecular switches should be considered as major design element for future generations of higher-photostability, louder, and above all *linear* photoacoustic contrast agents.

Figure S12 also sketches two outlook opportunities of ultrashort $S_1 \rightarrow S_0$ electronic relaxation times τ_{LA} that were briefly raised in the Conclusion. The excitation pulse length τ_{pulse} and power in PA/MSOT imaging need not remain fixed at the values used in today's commercial *in vivo* (τ_{pulse} ca. 10 ns, as we used here) or tissue slice (τ_{pulse} ca. 1 ns) imagers. Simplistically, during an excitation pulse, a chromophore dissipates power proportional to its number n of dissipation cycles ($S_0 \rightarrow S_1 \rightarrow S_0$), as determined by its nonradiative relaxation time τ_{relax} (for linear absorber τ_{LA} , for saturable absorber τ_{SA}) and the excitation power density (which together with $\epsilon(\lambda)$ controls t_x , the average lifetime of S_0 states before excitation) as per e.g. $n = \tau_{\text{pulse}} / (\tau_{\text{relax}} + t_x)$:

For long pulses at low power, where t_x is high, n approaches $\tau_{\text{pulse}} / t_x$: so the difference of n between LAs and SAs is small (current *in vivo* settings, as used in this paper).

As pulses are shortened and power density increased to compensate it, t_x approaches zero, so power dissipation approaches $\tau_{\text{pulse}}/\tau_{\text{relax}}$: and the difference of power dissipation between LAs and SAs now approaches $\tau_{\text{SA}}/\tau_{\text{LA}}$ (ca. 200-fold with typical LA/SA rates; that SA absorbers saturate at higher power is of course indicated by their name, but short pulses can also cause saturation, depending on signal gating aspects). Some benefits of pulse shortening may include that (a) dissipating even identical energy in shorter pulses may greatly change (magnify) the PA *signal* when LAs generate it; (b) *background* may also be reduced by shortening if the background chromophores respond as SAs to the excitation applied; and (c) for special purposes e.g. outside PA, shorter excitation voxel lengths may also be relevant.

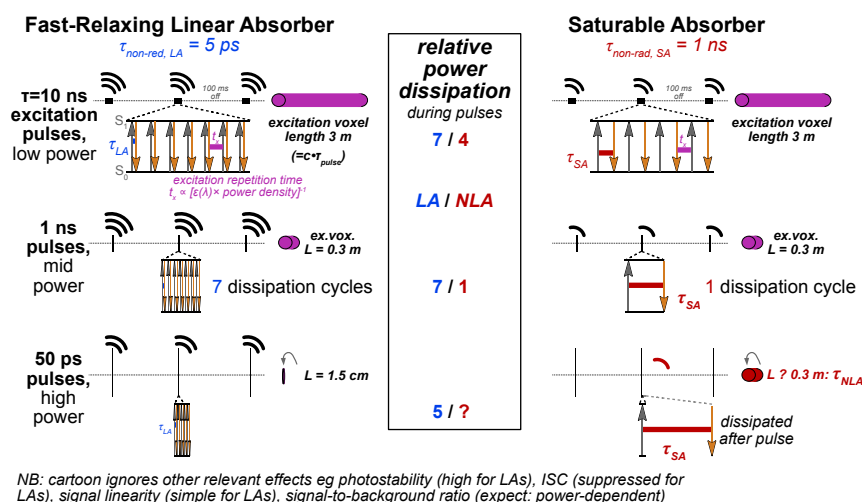


Figure S12. Time- and power-dependent effects that can give LA chromophores additional advantages.

8 References

- [1] T. Ashida, T. Suzuki, Colored Resin Composition, Color Filter, and Image Display Device Capable of Having Excellence in Contrast and Light Resistance, **2018**, TW201840738A.
- [2] R. Tapia Hernandez, M. C. Lee, A. K. Yadav, J. Chan, *J. Am. Chem. Soc.* **2022**, 144, 18101–18108.
- [3] K. Gutsmedl, C. T. Wirges, V. Ehmke, T. Carell, *Org. Lett.* **2009**, 11, 2405–2408.
- [4] S. M. Pauff, S. C. Miller, *Org. Lett.* **2011**, 13, 6196–6199.
- [5] A. Toutchkine, Oxazine Dyes with Improved Aqueous Solubility, **2009**, WO2009152024A1.
- [6] S. Fuse, T. Oishi, K. Matsumura, Y. Hayashi, S. Kawauchi, H. Nakamura, *Org. Biomol. Chem.* **2019**, 18, 93–101.
- [7] E. D. Cosco, I. Lim, E. M. Sletten, *ChemPhotoChem* **2021**, 5, 727–734.
- [8] K. Rurack, M. Spieles, *Anal. Chem.* **2011**, 83, 1232–1242.
- [9] “Quantum Yield [Cy5 (Cyanine-5)] | AAT Bioquest,” can be found under https://www.aatbio.com/resources/quantum-yield/cy5_cyanine_5, n.d.
- [10] G. S. Hartley, *Nature* **1937**, 140, 281–281.
- [11] L. Gao, Y. Kraus, A. Stegner, T. Wein, C. Heise, L. von Brunn, E. Fajardo-Ruiz, J. Thorn-Seshold, O. Thorn-Seshold, *Org. Biomol. Chem.* **2022**, 20, 7787–7794.
- [12] J. Garcia-Amorós, B. Maerz, M. Reig, A. Cuadrado, L. Blancafort, E. Samoylova, D. Velasco, *Chemistry – A European Journal* **2019**, 25, 7726–7732.
- [13] D. Razansky, A. Buehler, V. Ntziachristos, *Nat Protoc* **2011**, 6, 1121–1129.
- [14] V. Gujrati, J. Prakash, J. Malekzadeh-Najafabadi, A. Stiel, U. Klemm, G. Mettenleiter, M. Aichler, A. Walch, V. Ntziachristos, *Nat Commun* **2019**, 10, 1114.
- [15] N. Beziere, N. Lozano, A. Nunes, J. Salichs, D. Queiros, K. Kostarelos, V. Ntziachristos, *Biomaterials* **2015**, 37, 415–424.
- [16] S. Roberts, A. Strome, C. Choi, C. Andreou, S. Kossatz, C. Brand, T. Williams, M. Bradbury, M. F. Kircher, Y. K. Reshetnyak, J. Grimm, J. S. Lewis, T. Reiner, *Sci Rep* **2019**, 9, 8550.
- [17] K. Cardinell, N. Gupta, B. D. Koivisto, J. C. Kumaradas, X. Zhou, H. Irving, P. Luciani, Y. H. Yücel, *Photoacoustics* **2021**, 21, 100239.
- [18] X. Zhou, Y. Fang, V. Wimalasiri, C. I. Stains, E. W. Miller, *Chem. Commun.* **2022**, 58, 11941–11944.
- [19] R. Yin, F. Brøndsted, Y. He, Y. Fang, C. Stains, **2023**, DOI 10.26434/chemrxiv-2023-lx0g8.
- [20] Z. Zhao, C. Chen, W. Wu, F. Wang, L. Du, X. Zhang, Y. Xiong, X. He, Y. Cai, R. T. K. Kwok, J. W. Y. Lam, X. Gao, P. Sun, D. L. Phillips, D. Ding, B. Z. Tang, *Nat Commun* **2019**, 10, 768.
- [21] C. Xu, R. Ye, H. Shen, J. W. Y. Lam, Z. Zhao, B. Z. Tang, *Angew. Chem. Int. Ed.* **2022**, 61, e202204604.
- [22] S. Liu, X. Zhou, H. Zhang, H. Ou, J. W. Y. Lam, Y. Liu, L. Shi, D. Ding, B. Z. Tang, *J. Am. Chem. Soc.* **2019**, 141, 5359–5368.
- [23] B. Du, C. Qu, K. Qian, Y. Ren, Y. Li, X. Cui, S. He, Y. Wu, T. Ko, R. Liu, X. Li, Y. Li, Z. Cheng, *Advanced Optical Materials* **2020**, 8, 1901471.
- [24] N. Liu, V. Gujrati, J. Malekzadeh-Najafabadi, J. P. F. Werner, U. Klemm, L. Tang, Z. Chen, J. Prakash, Y. Huang, A. Stiel, G. Mettenleiter, M. Aichler, A. Blutke, A. Walch, K. Kleigrew, D. Razansky, M. Sattler, V. Ntziachristos, *Photoacoustics* **2021**, 22, 100263.
- [25] S. S. Matikonda, D. A. Helmerich, M. Meub, G. Beliu, P. Kollmannsberger, A. Greer, M. Sauer, M. J. Schnermann, *ACS Cent. Sci.* **2021**, DOI 10.1021/acscentsci.1c00483.
- [26] J. P. Fuenzalida Werner, Y. Huang, K. Mishra, R. Janowski, P. Vetschera, C. Heichler, A. Chmyrov, C. Neufert, D. Niessing, V. Ntziachristos, A. C. Stiel, *Anal. Chem.* **2020**, 92, 10717–10724.
- [27] M. Wranik, T. Weinert, C. Slavov, T. Masini, A. Furrer, N. Gaillard, D. Gioia, M. Ferrarotti, D. James, H. Glover, M. Carrillo, D. Kekilli, R. Stipp, P. Skopintsev, S. Brünle, T. Mühlethaler, J. Beale, D. Gashi, K. Nass, D. Ozerov, P. J. M. Johnson, C. Cirelli, C. Bacellar, M. Braun, M. Wang, F. Dworkowski, C. Milne, A. Cavalli, J. Wachtveitl, M. O. Steinmetz, J. Standfuss, *Nat Commun* **2023**, 14, 903.
- [28] M. L. Landsman, G. Kwant, G. A. Mook, W. G. Zijlstra, *Journal of Applied Physiology* **1976**, 40, 575–583.
- [29] T. Gokus, A. Hartschuh, H. Harutyunyan, M. Allegrini, F. Hennrich, M. Kappes, A. A. Green, M. C. Hersam, P. T. Araujo, A. Jorio, *Applied Physics Letters* **2008**, 92, 153116.

9 Appendices

Author Contributions

M.M. designed targets; designed and performed synthesis; performed, assisted, and coordinated photocharacterisation; coordinated data assembly; and assisted manuscript drafting. A.T. performed synthesis under the supervision of M.M.

N.L., V.G., P.A. and U.K. performed all photoacoustics experiments, as supervised by V.N.

A.V. performed transient absorption spectroscopy, as supervised by B.D.-I.

S.H. performed photoluminescence measurements. A.H. performed and supervised photoluminescence measurements.

O.T.-S. designed the concept and experiments, supervised all other experiments, coordinated data assembly and wrote the manuscript.

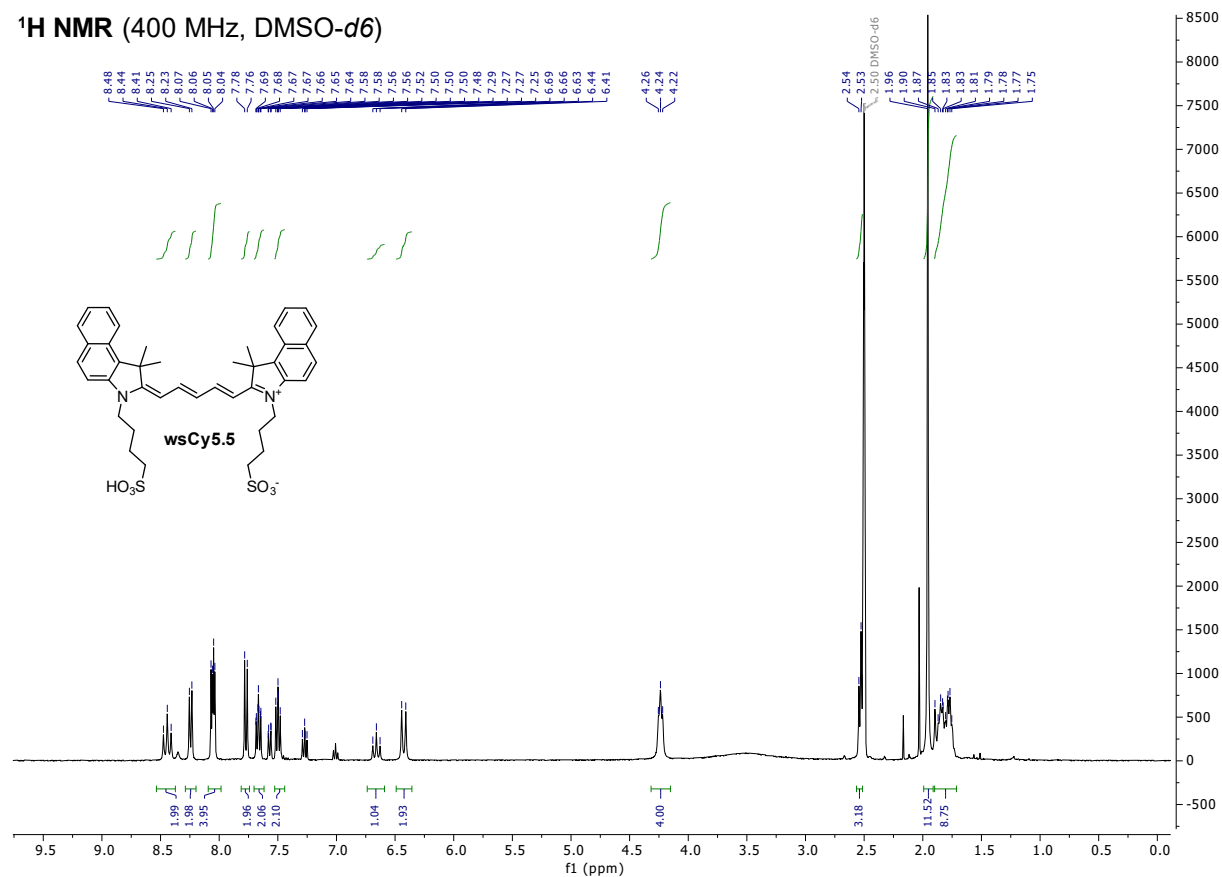
9.1 NMR Spectra

¹H and ¹³C NMR spectra are reproduced on the following pages:

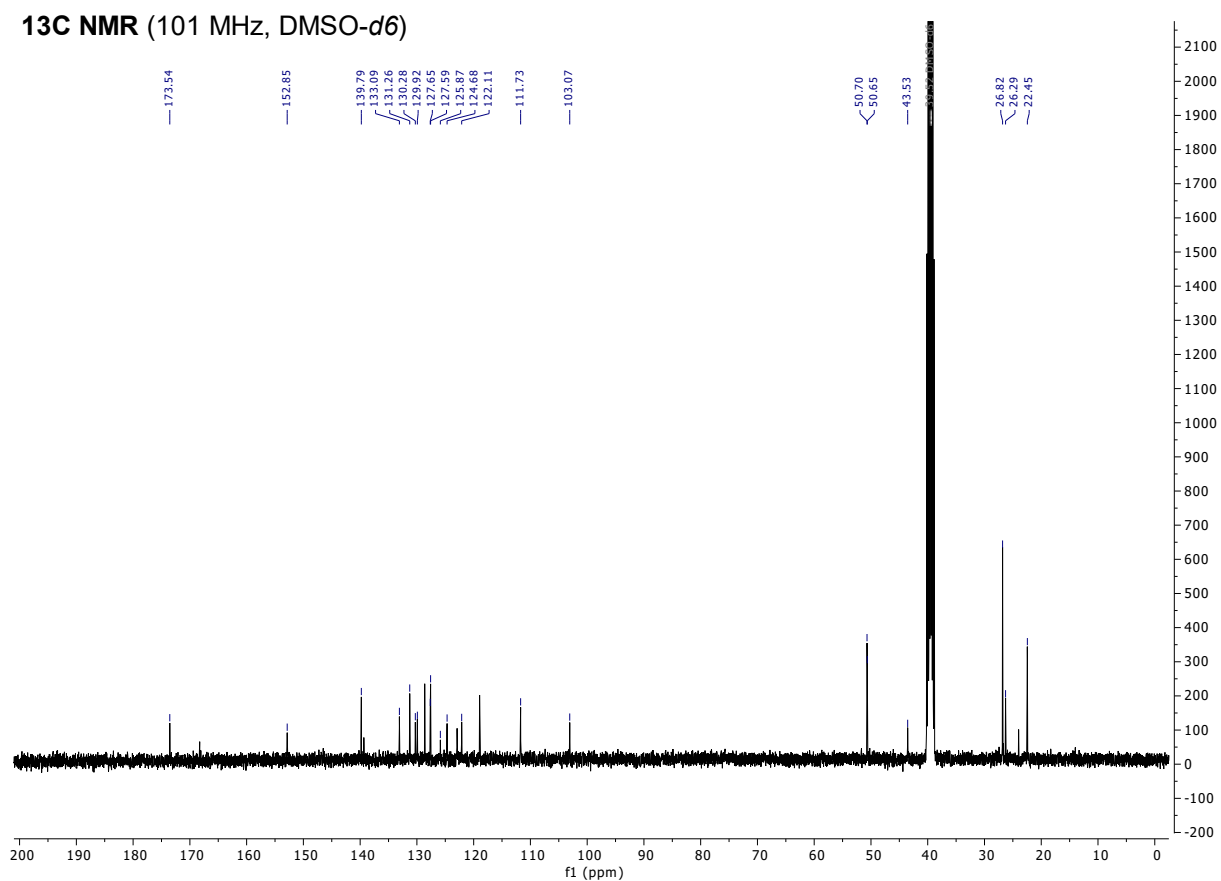
wsCy5.5	S30
M-AzCy5	S32
S2	S33
S3	S34
S4	S35
E-AzCy5	S36
E-AzCy7	S37
S5	S39
S6	S40
P-AzHCy1	S41
S7	S42
S8	S43
P-AzHCy2	S44
S9	S45
T-AzHCy1	S46
wsT-AzHCy	S47
T-AzHCy2	S48

wsCy5.5

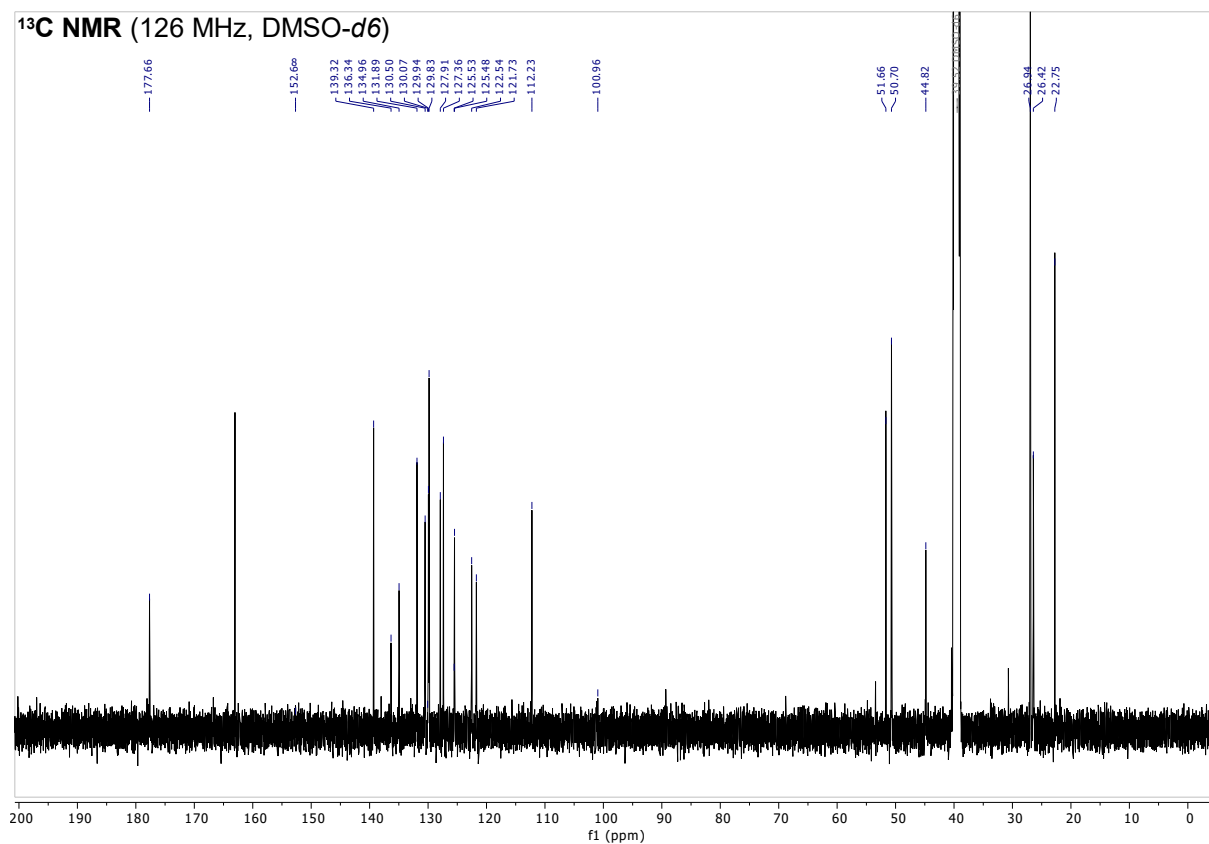
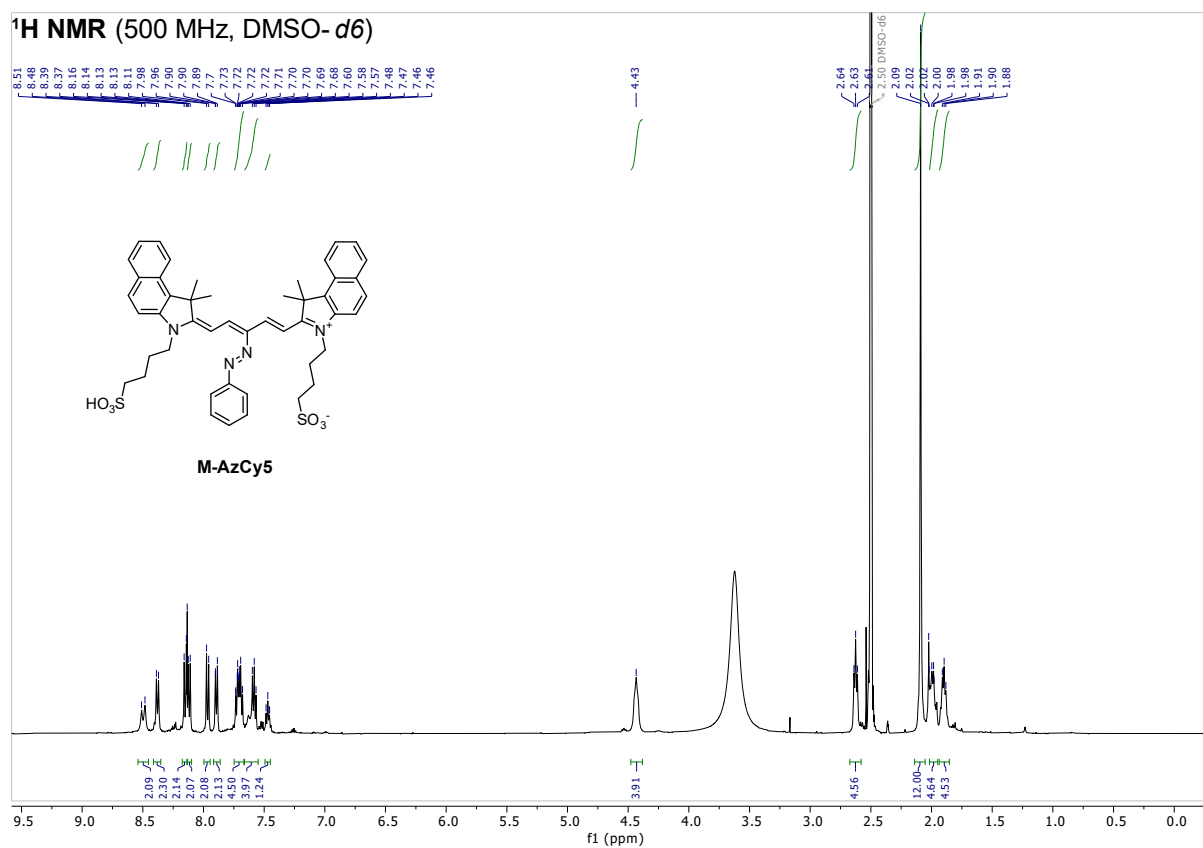
¹H NMR (400 MHz, DMSO-d₆)



¹³C NMR (101 MHz, DMSO-d₆)

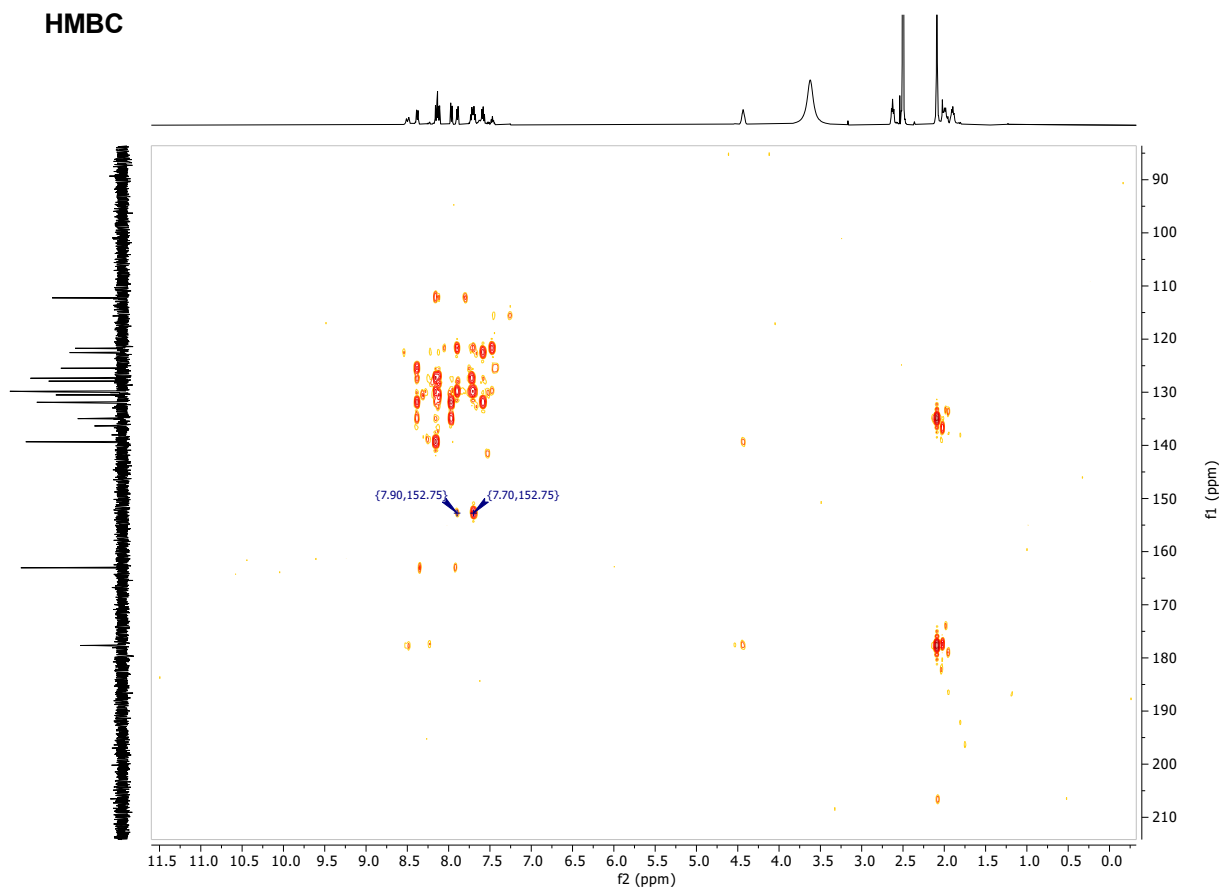


M-AzCy5



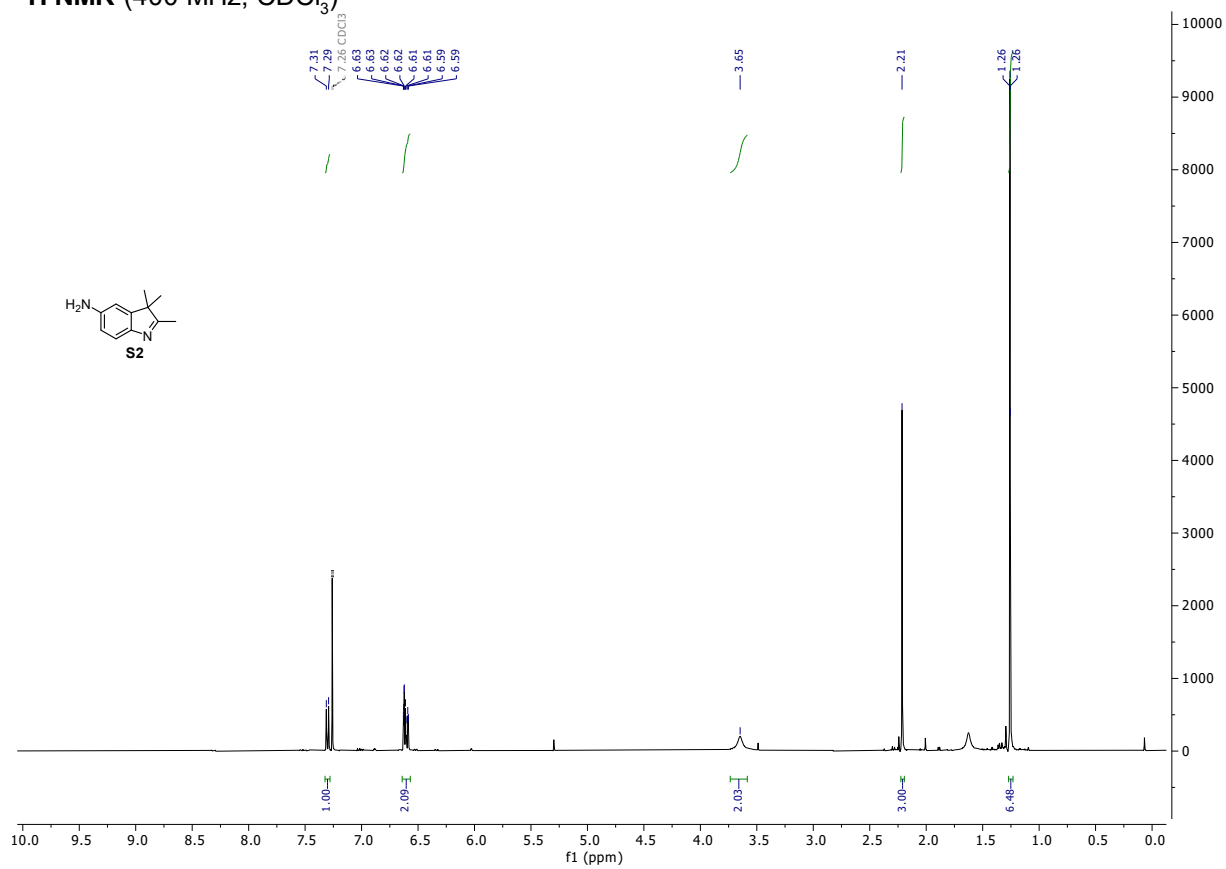
Note to M-AzCy5: quat. carbon adjacent to the N=N double bond at 158 ppm is only clearly visible as cross peak in HMBC, see next page.

HMBC



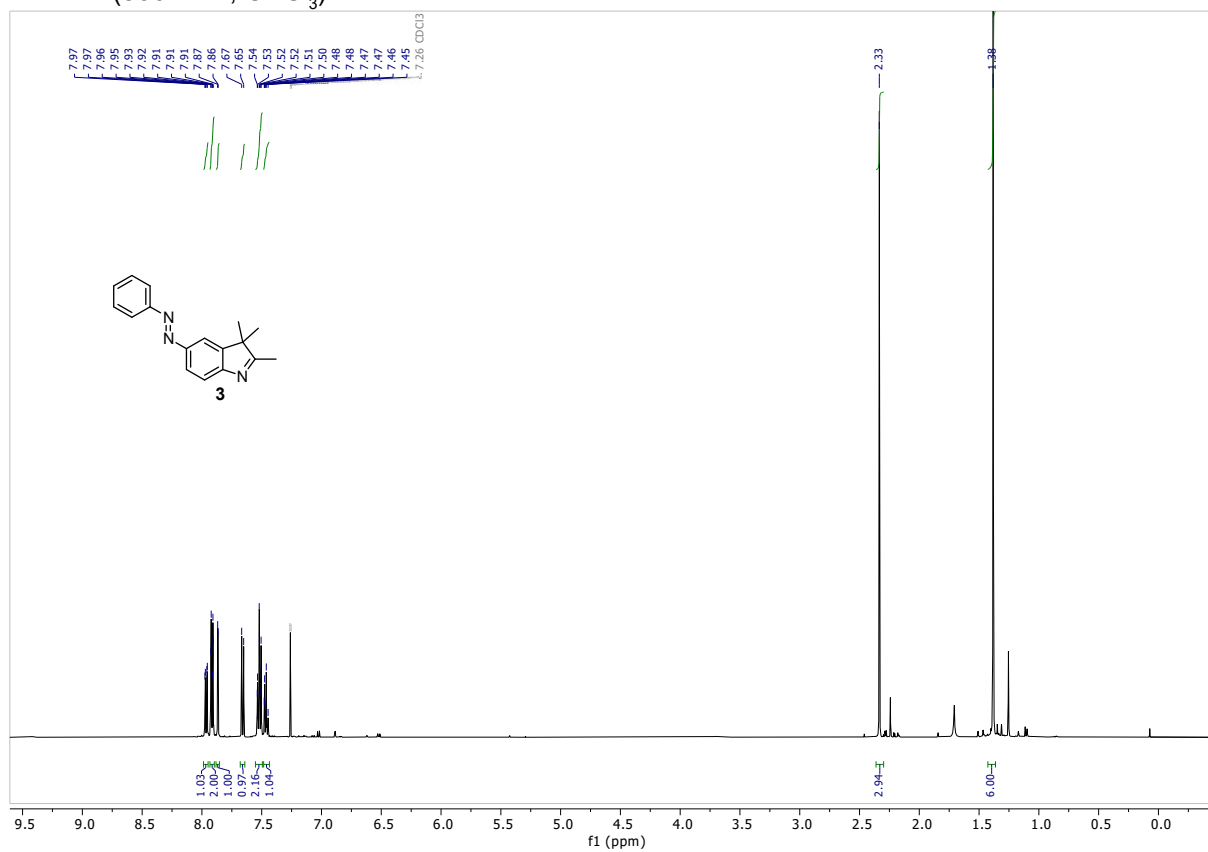
S2

¹H NMR (400 MHz, CDCl₃)

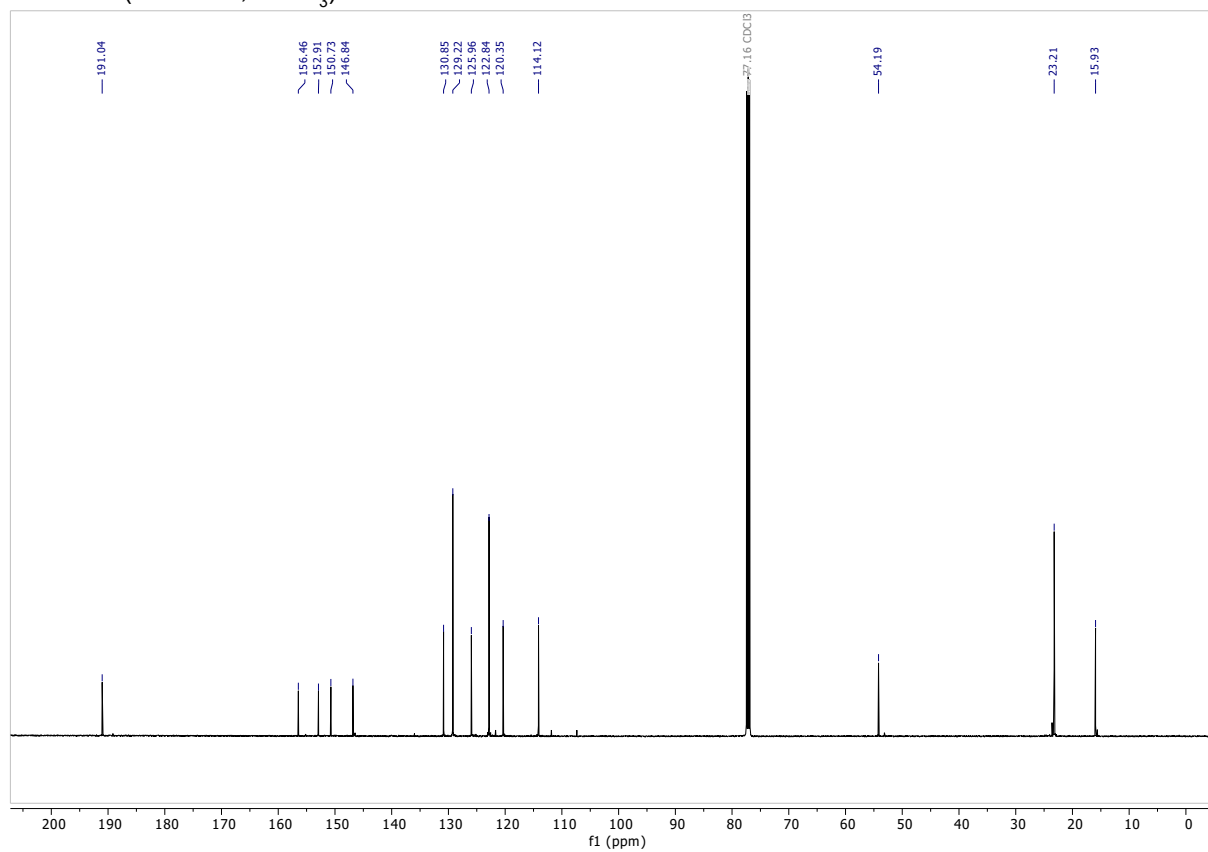


S3

¹H NMR (500 MHz, CDCl₃)

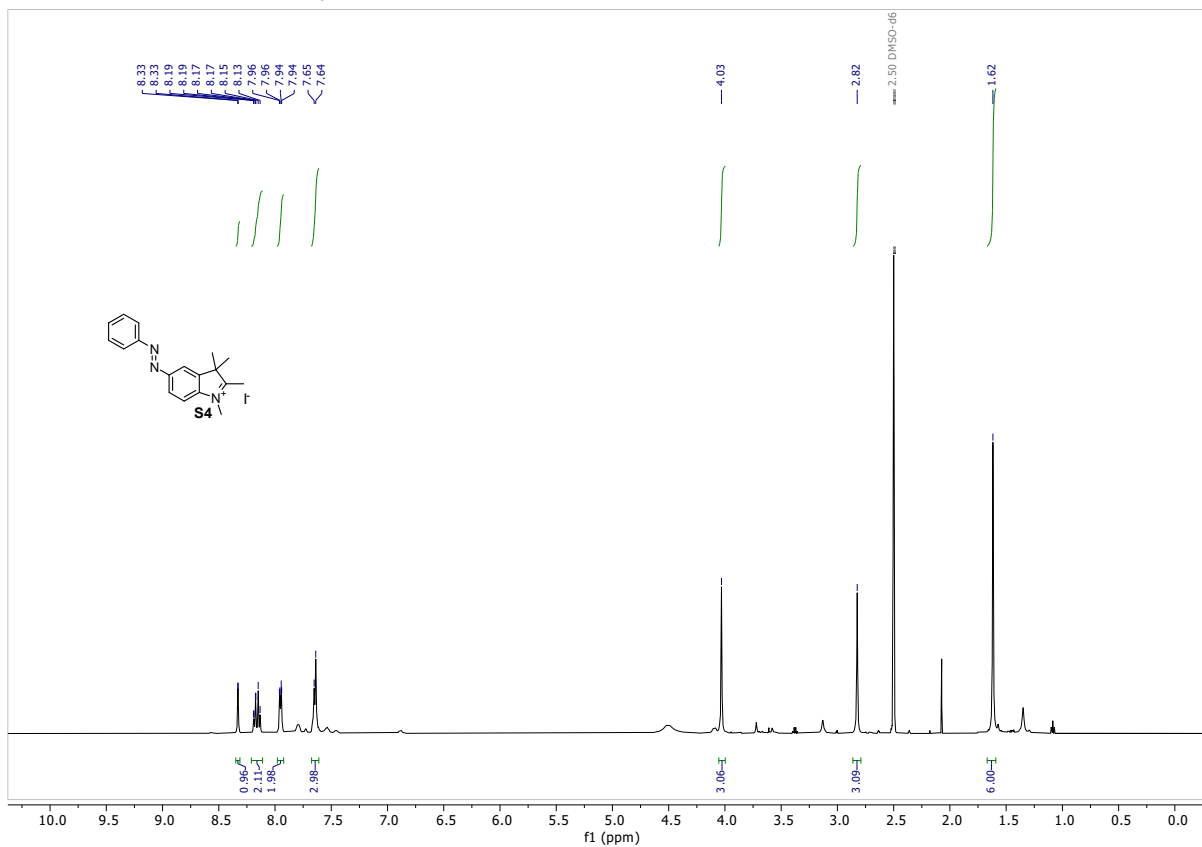


¹³C NMR (126 MHz, CDCl₃)

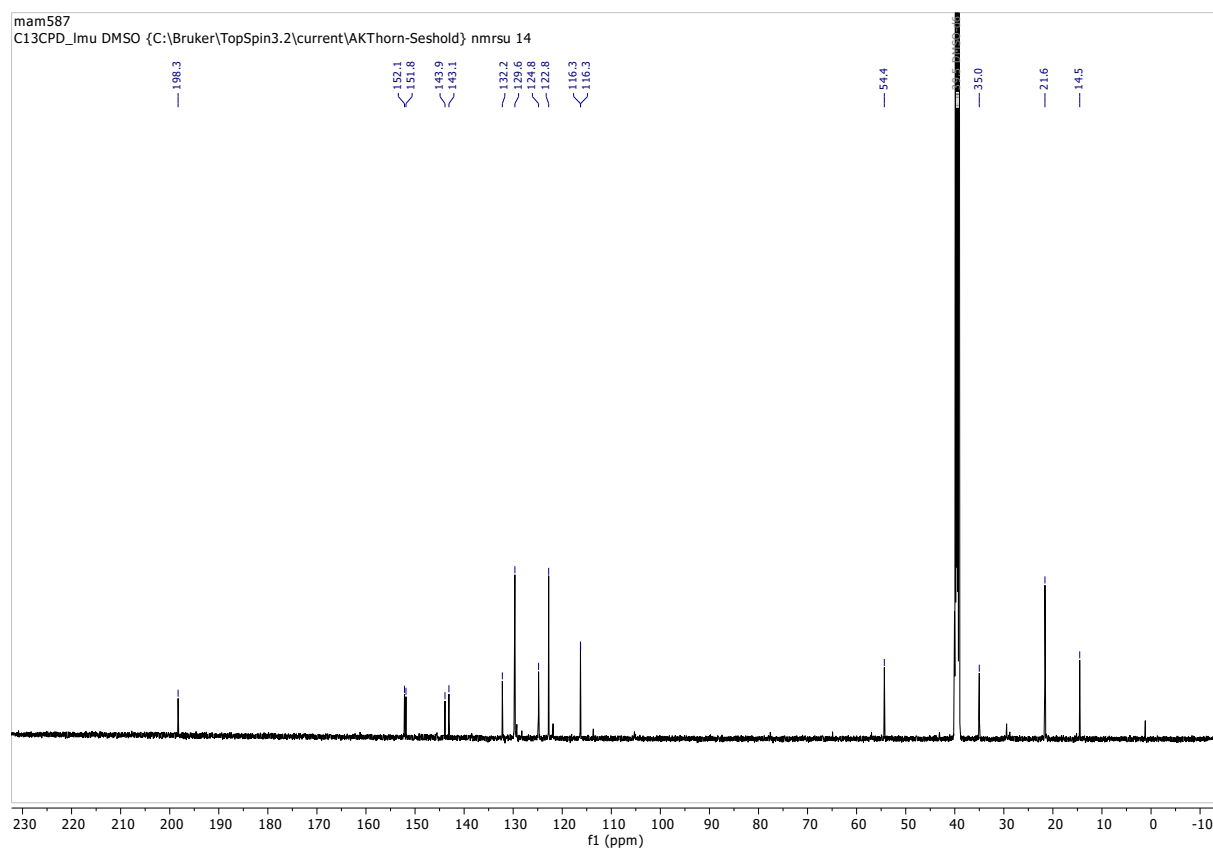


S4

¹H NMR (500 MHz, CDCl₃)

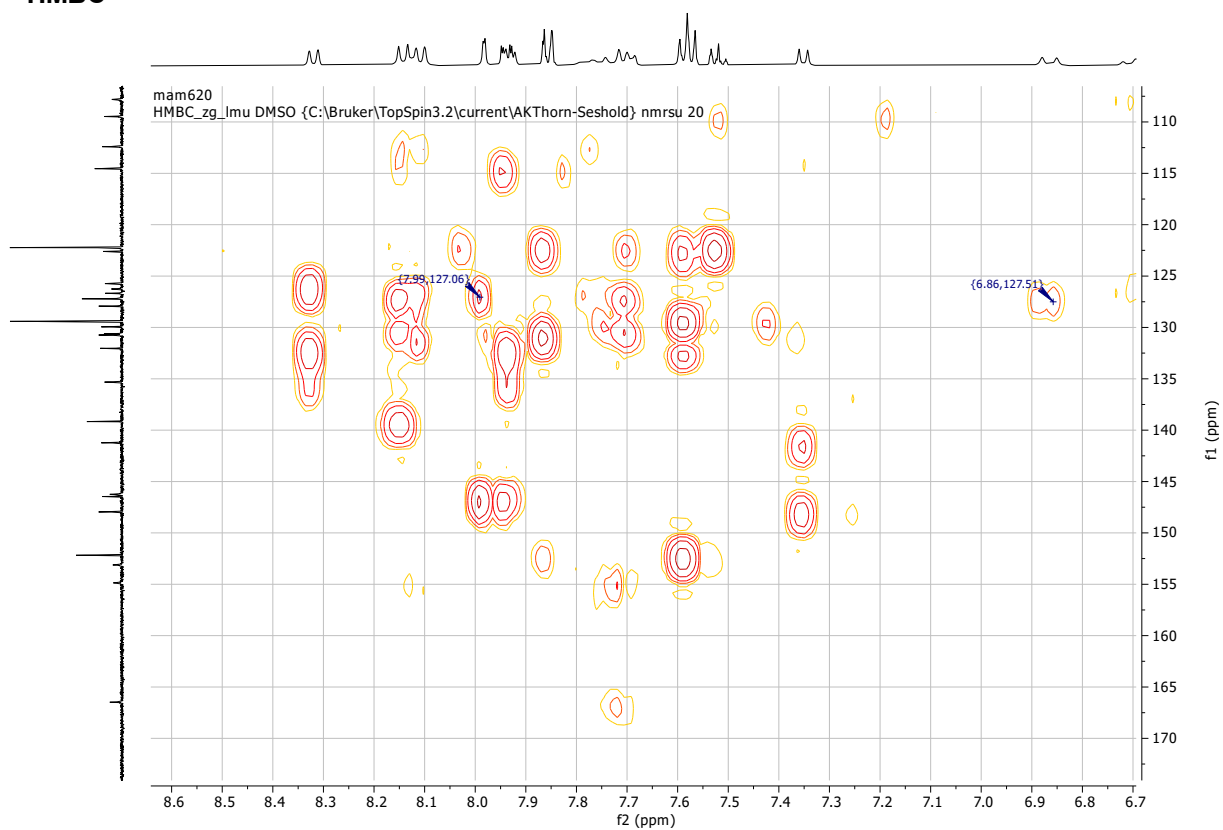


¹³C NMR (126 MHz, CDCl₃)



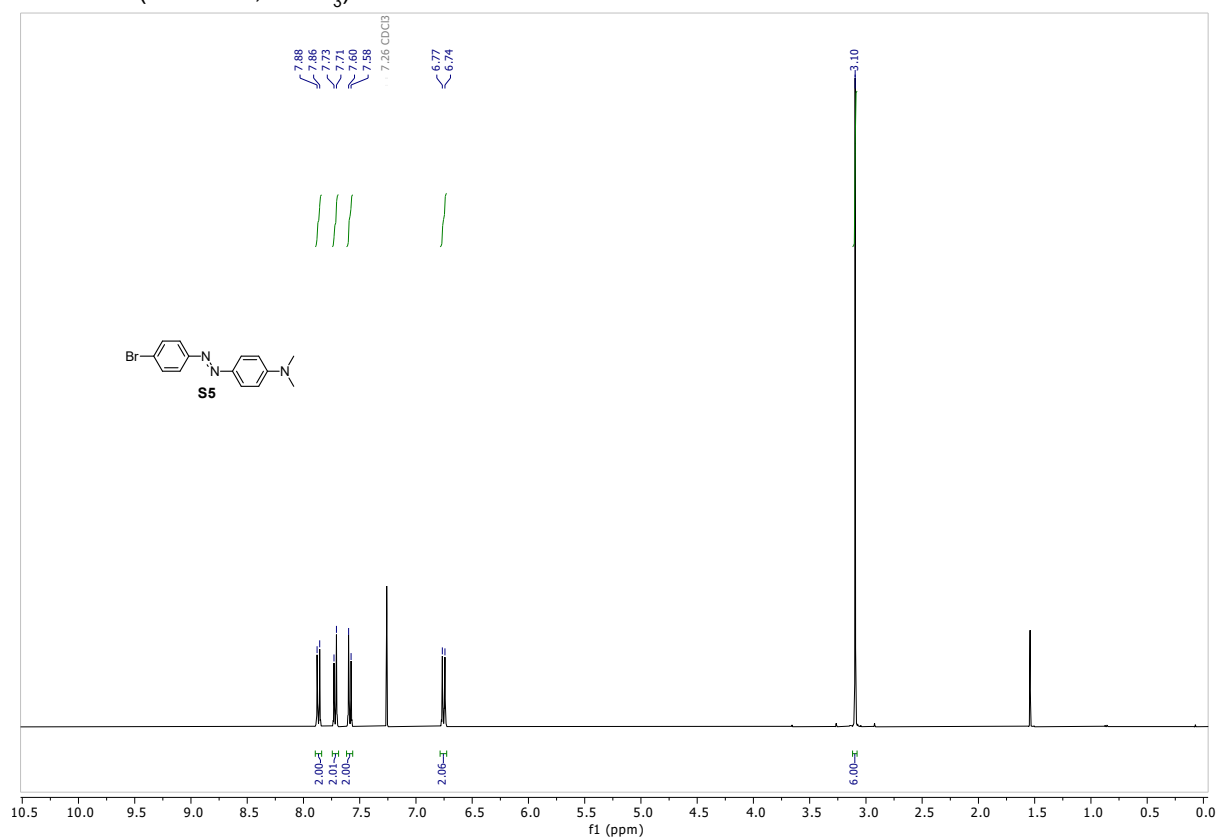
Note to **E-AzCy7**: ^{13}C : Double signal at 127.2, confirmed since: (a) 2 distinct crosspeaks in HMBC, to aromatic protons at 7.99 ppm and to protons in the methine chain at 6.86 ppm; (b) Integrates as 2. Peak does not split in a 800 MHz spectrometer.

HMBC

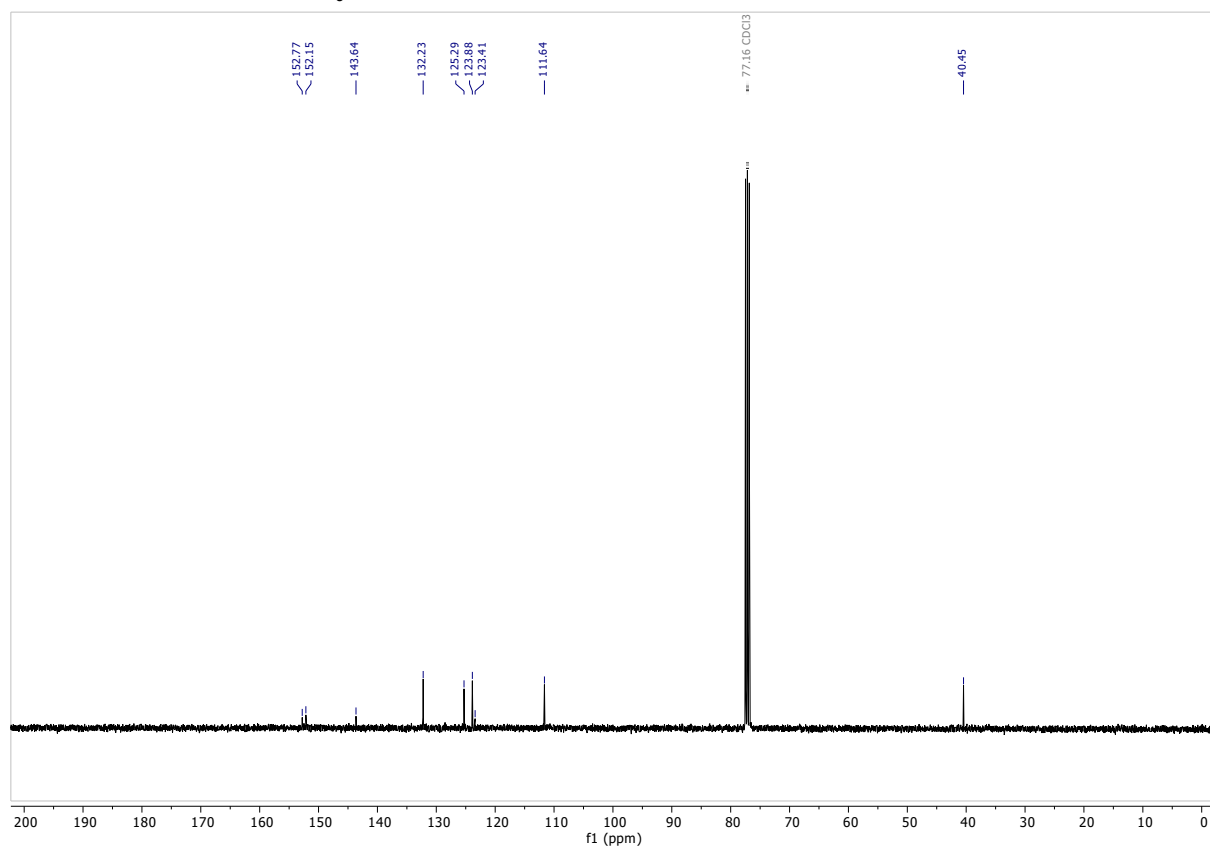


S5

¹H NMR (400 MHz, CDCl₃)

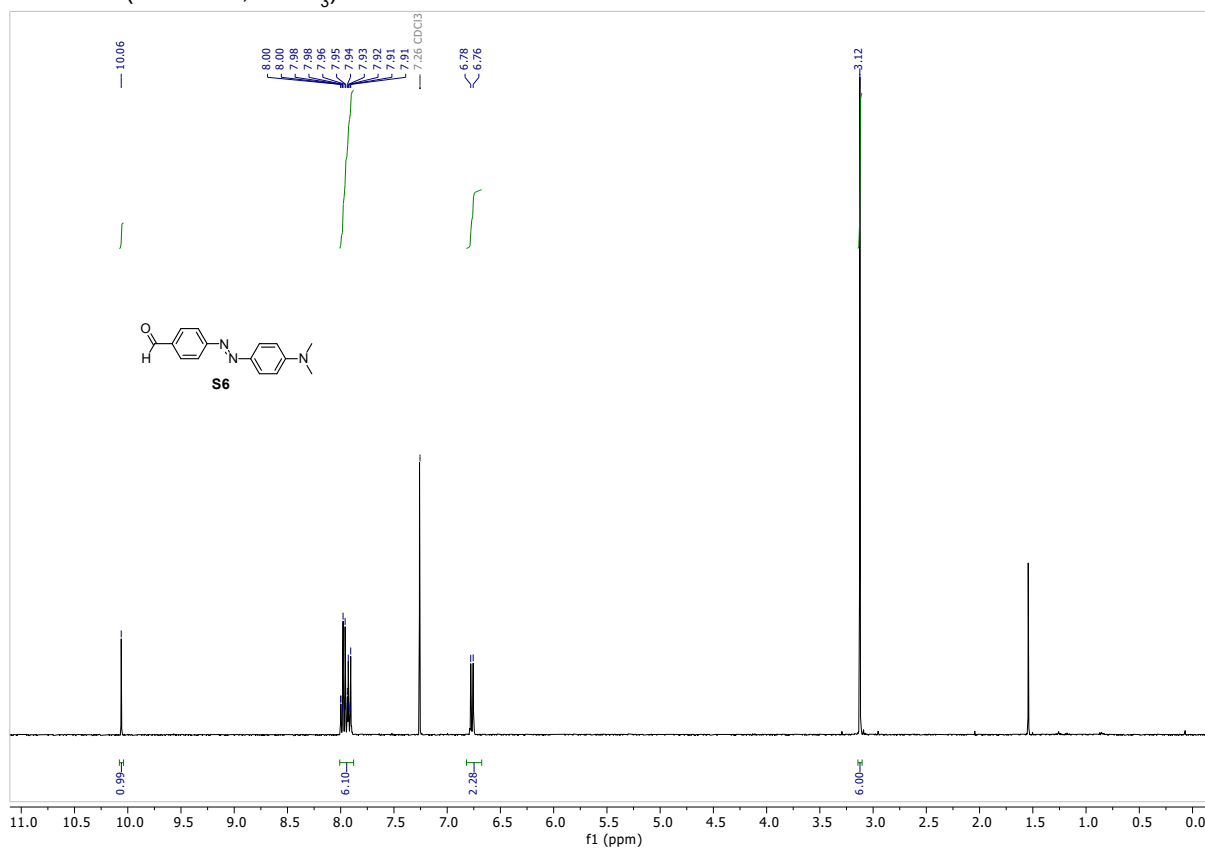


¹³C NMR (101 MHz, CDCl₃)

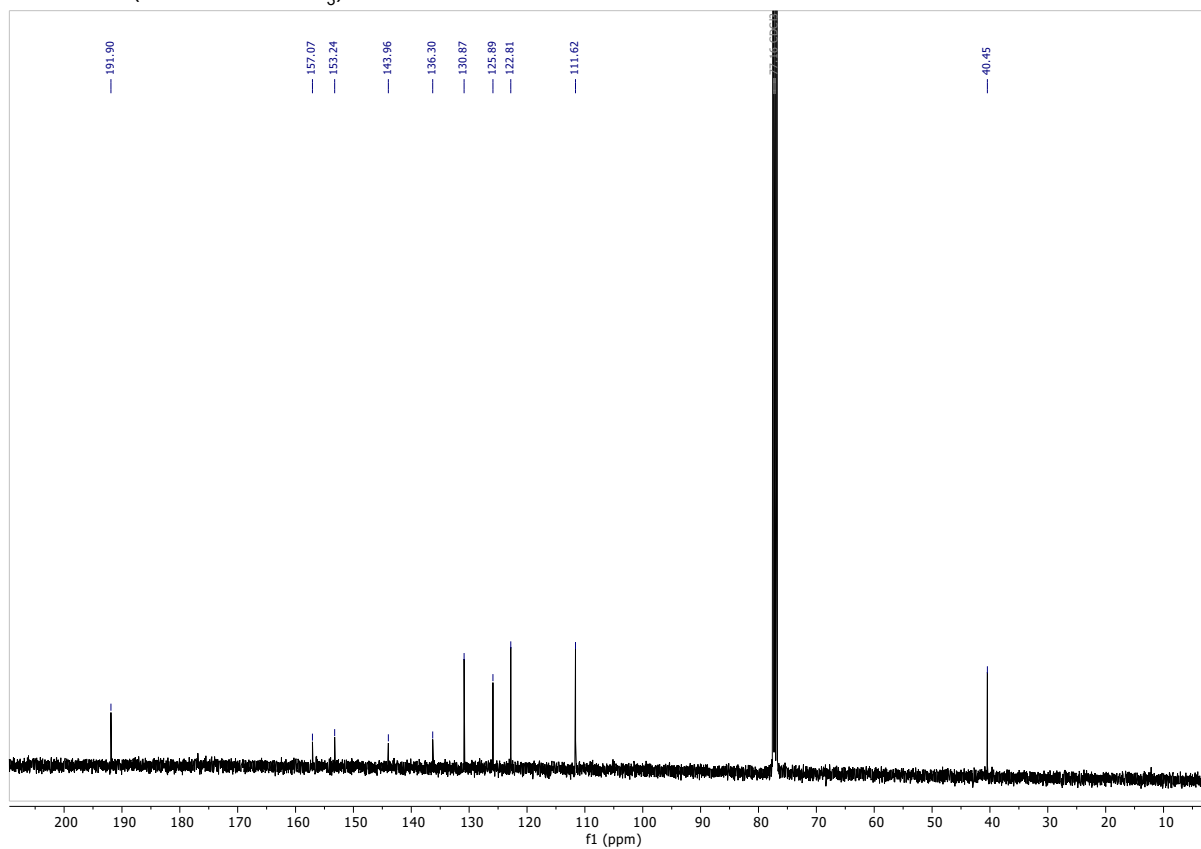


S6

¹H NMR (400 MHz, CDCl₃)

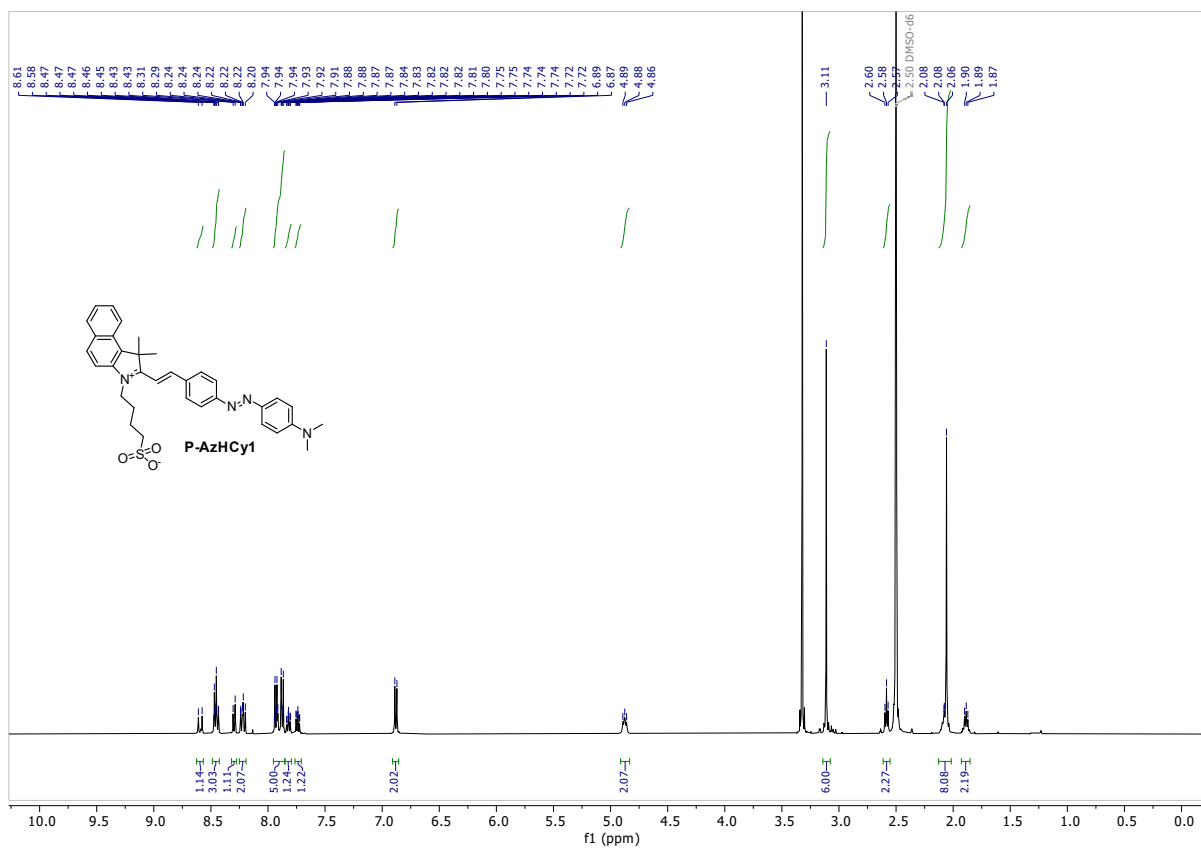


¹³C NMR (101 MHz, CDCl₃)

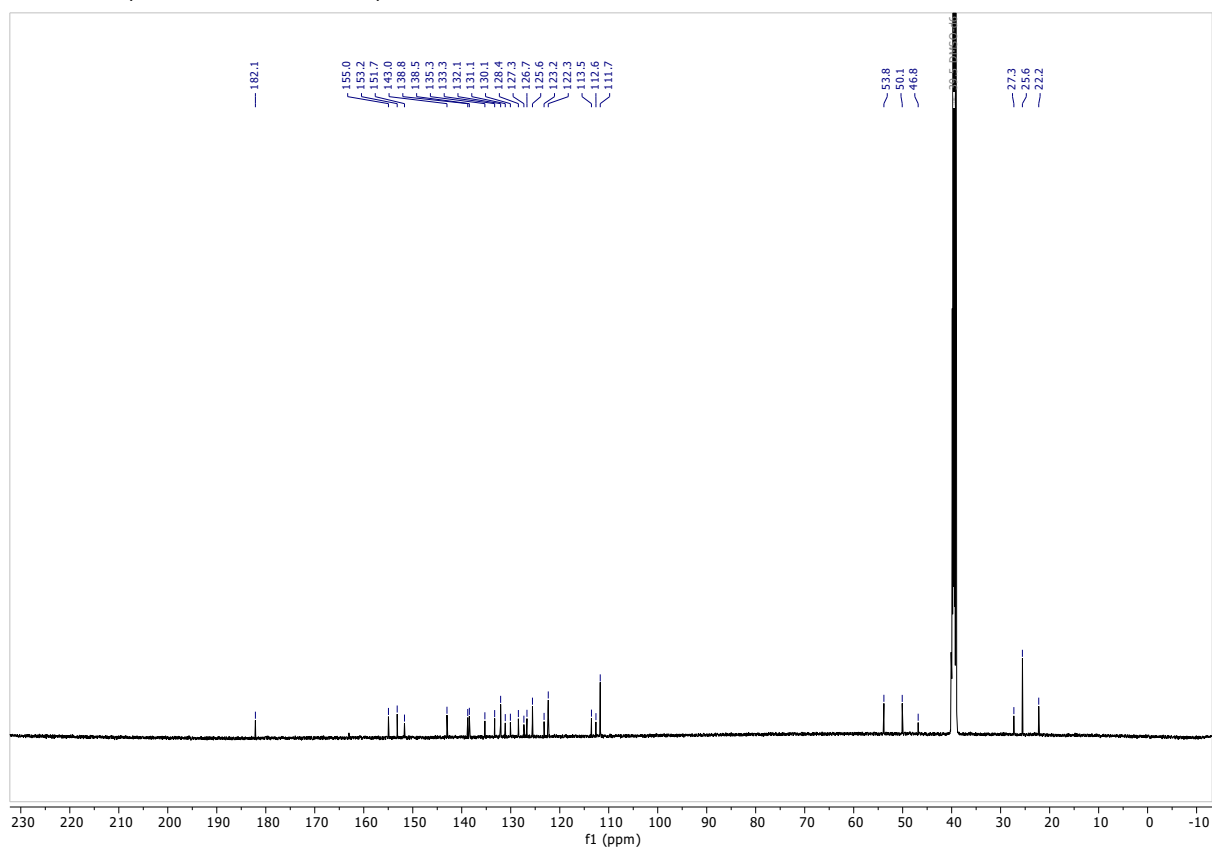


P-AzHCy1

¹H NMR (500 MHz, DMSO-*d*₆)



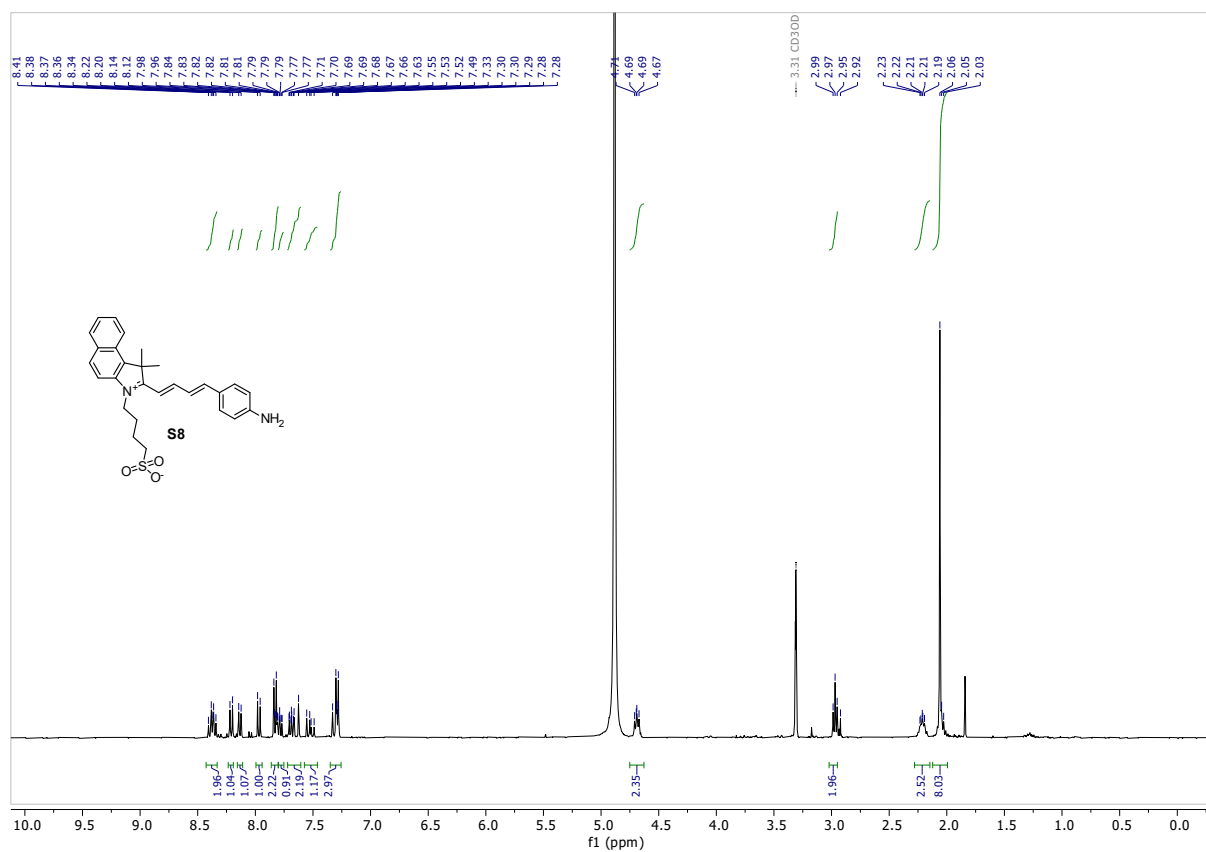
¹³C NMR (126 MHz, DMSO-*d*₆)



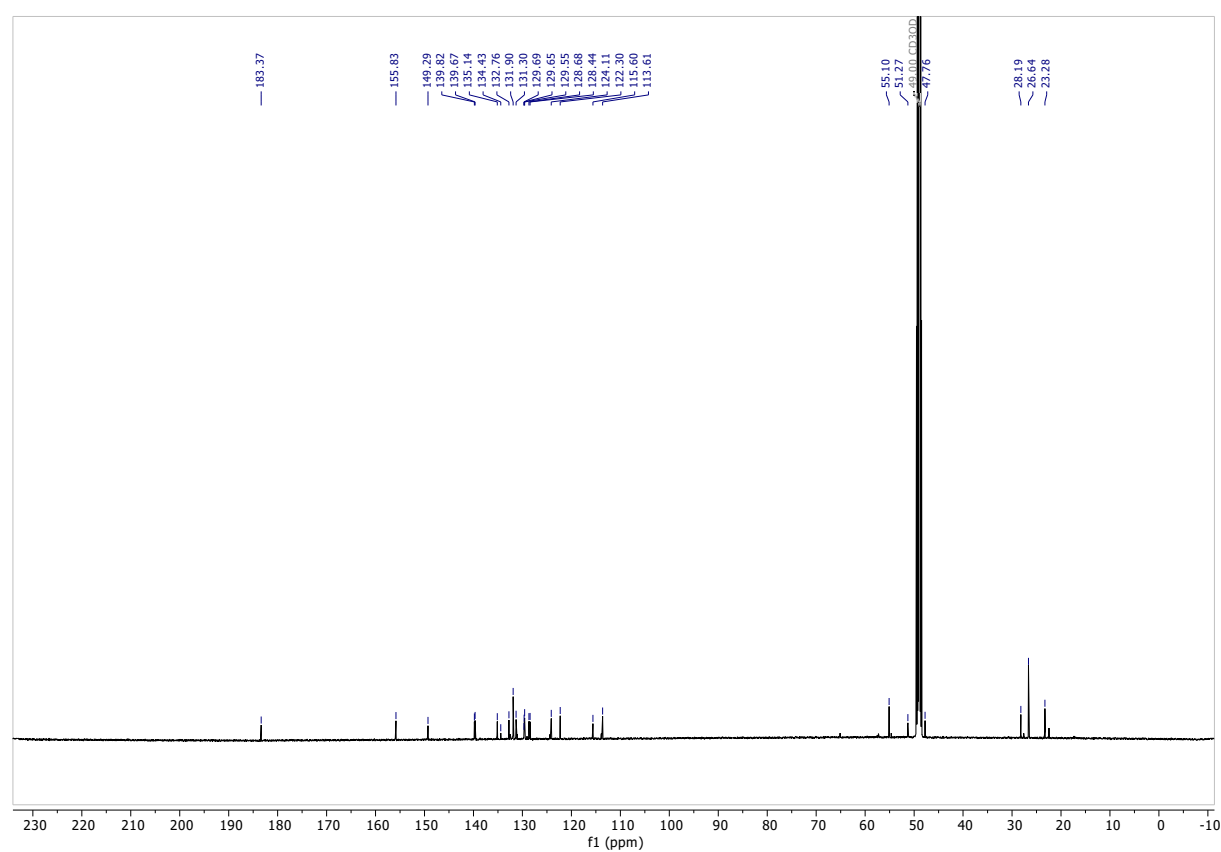
Note to **P-AzHCy1**: ¹³C: One carbon signal lies under the DMSO peak and is not resolved.

S8

¹H NMR (400 MHz, MeOD)

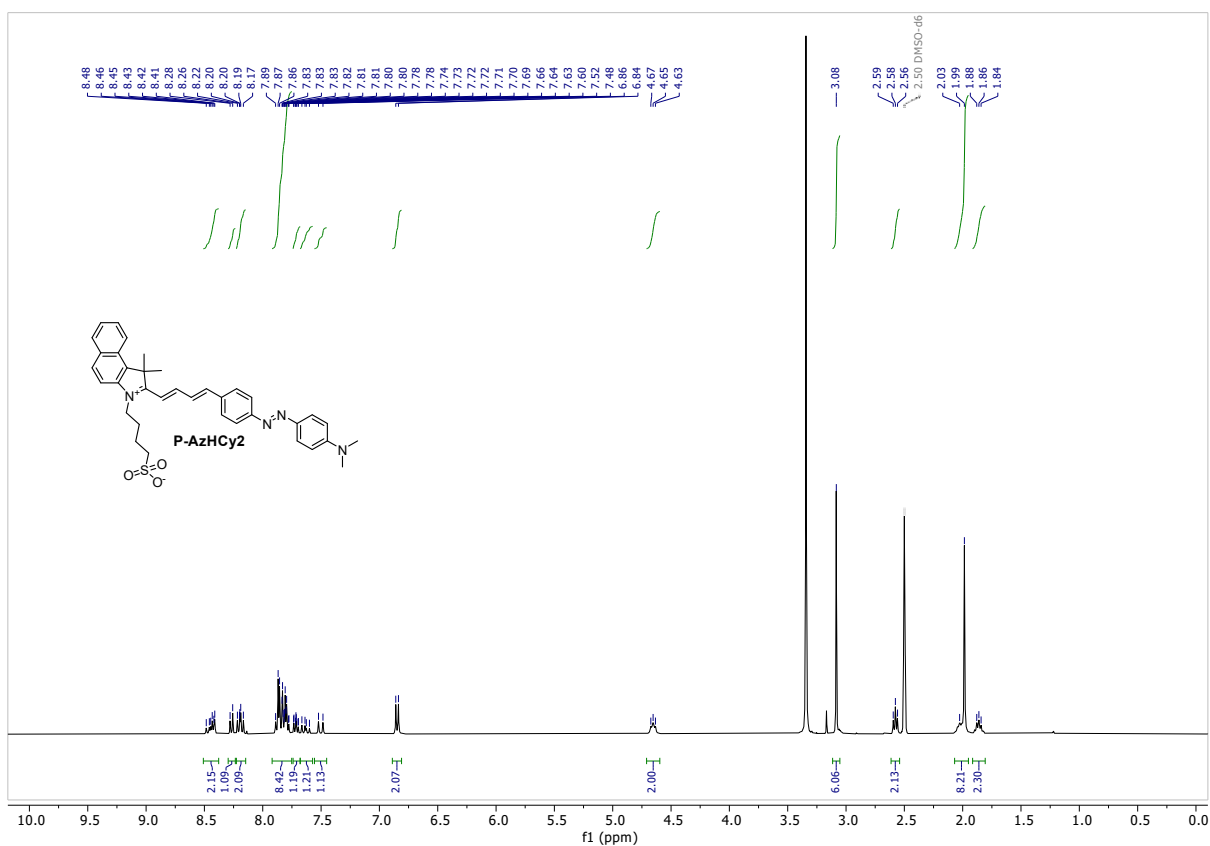


¹³C NMR (101 MHz, MeOD)

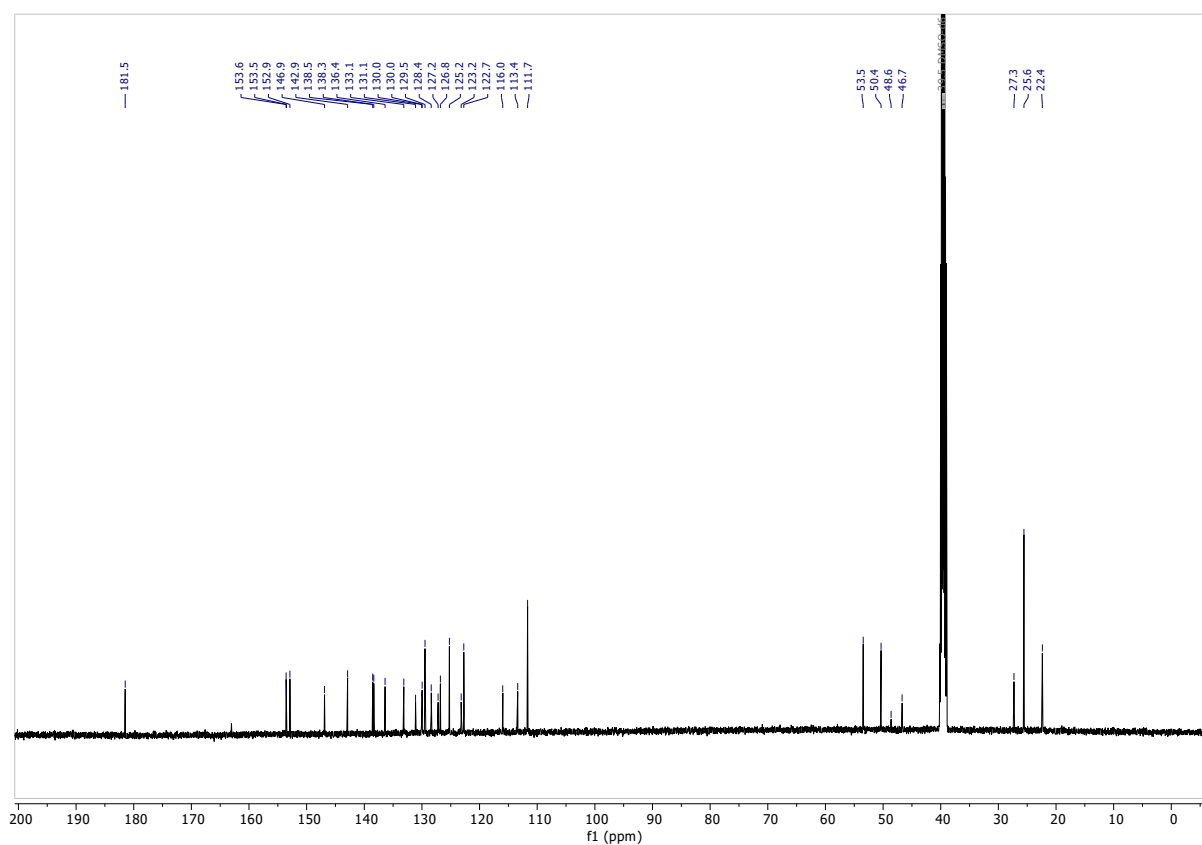


P-AzHCy2

¹H NMR (500 MHz, DMSO-d₆)

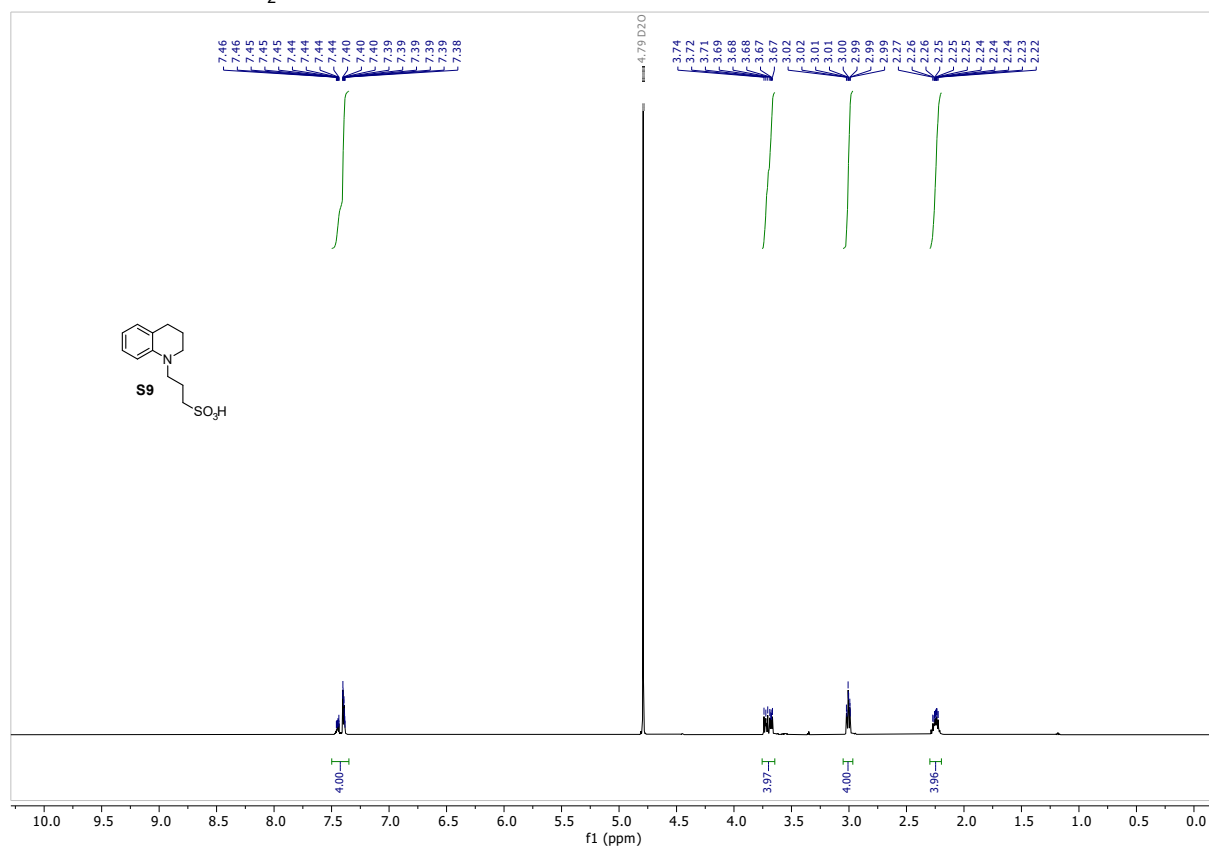


¹³C NMR (126 MHz, DMSO-d₆)

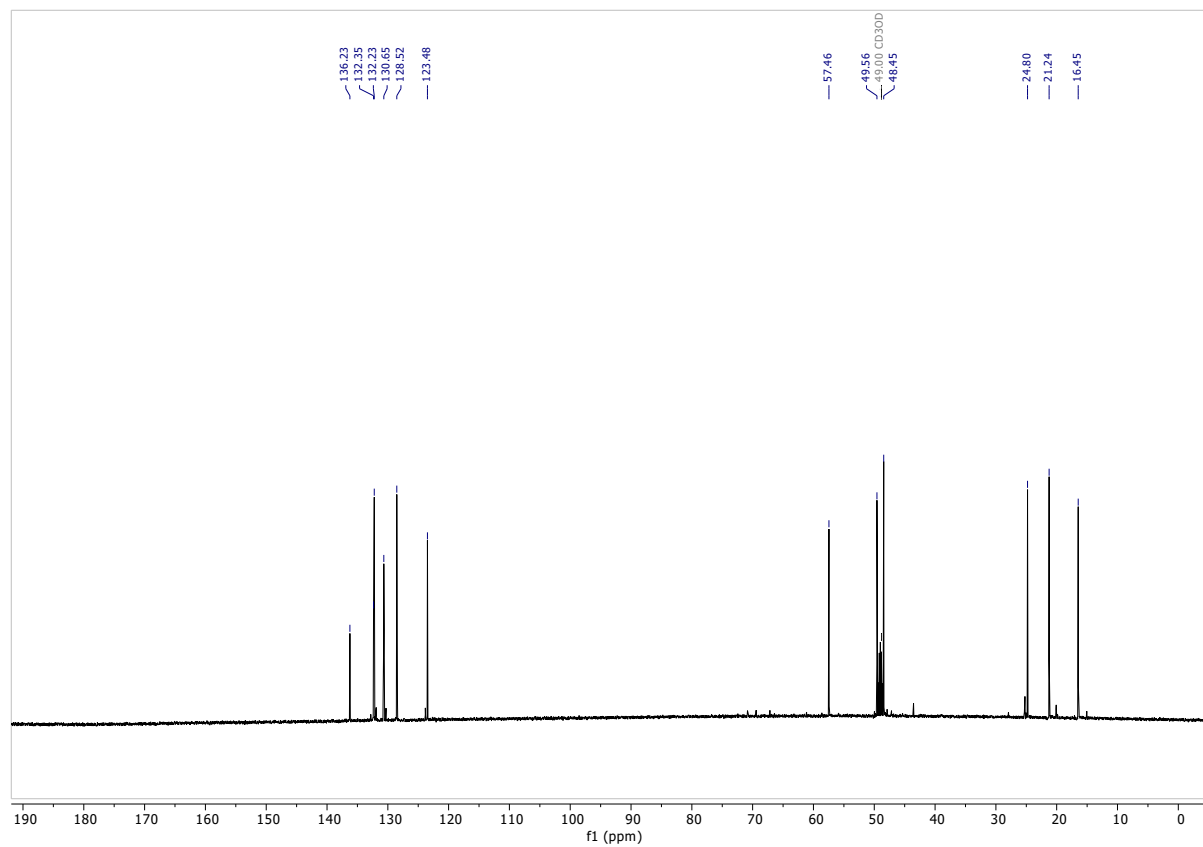


S9

¹H NMR (500 MHz, D₂O)

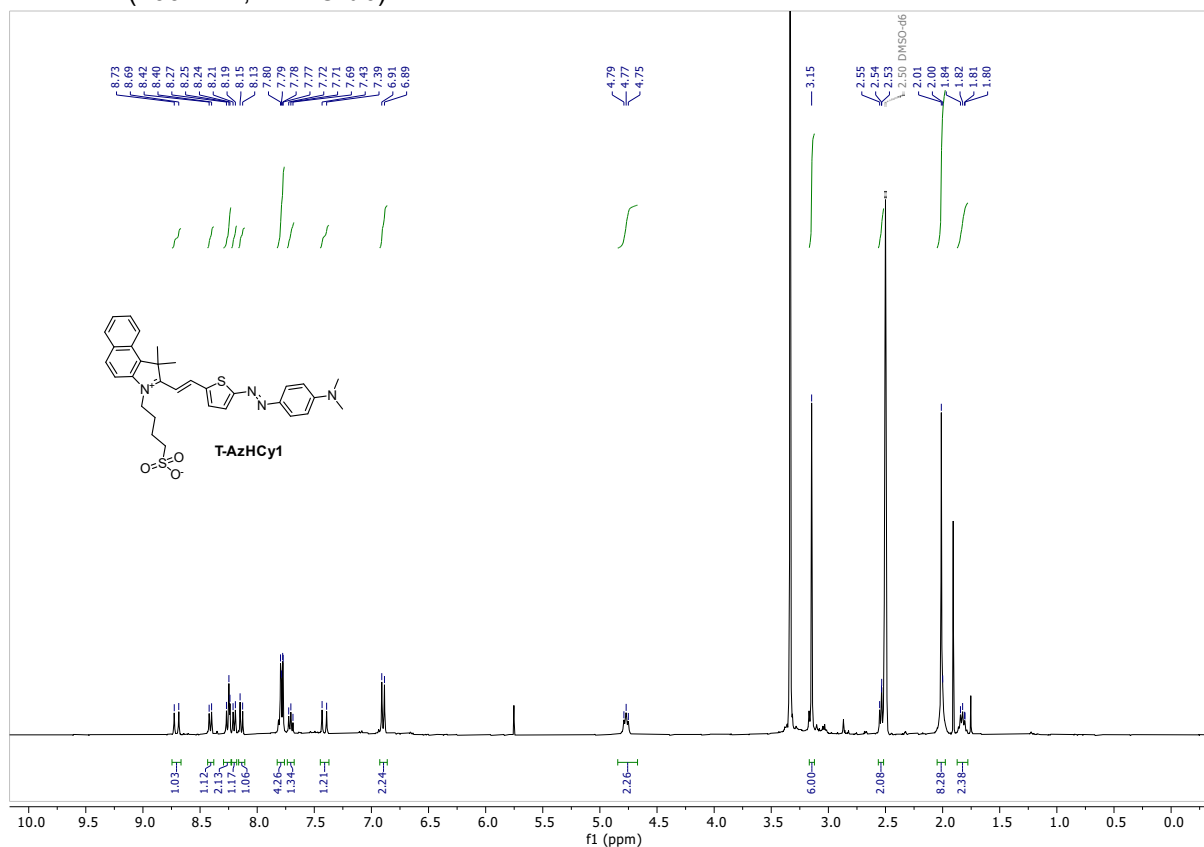


¹³C NMR (126 MHz, D₂O + MeOD)

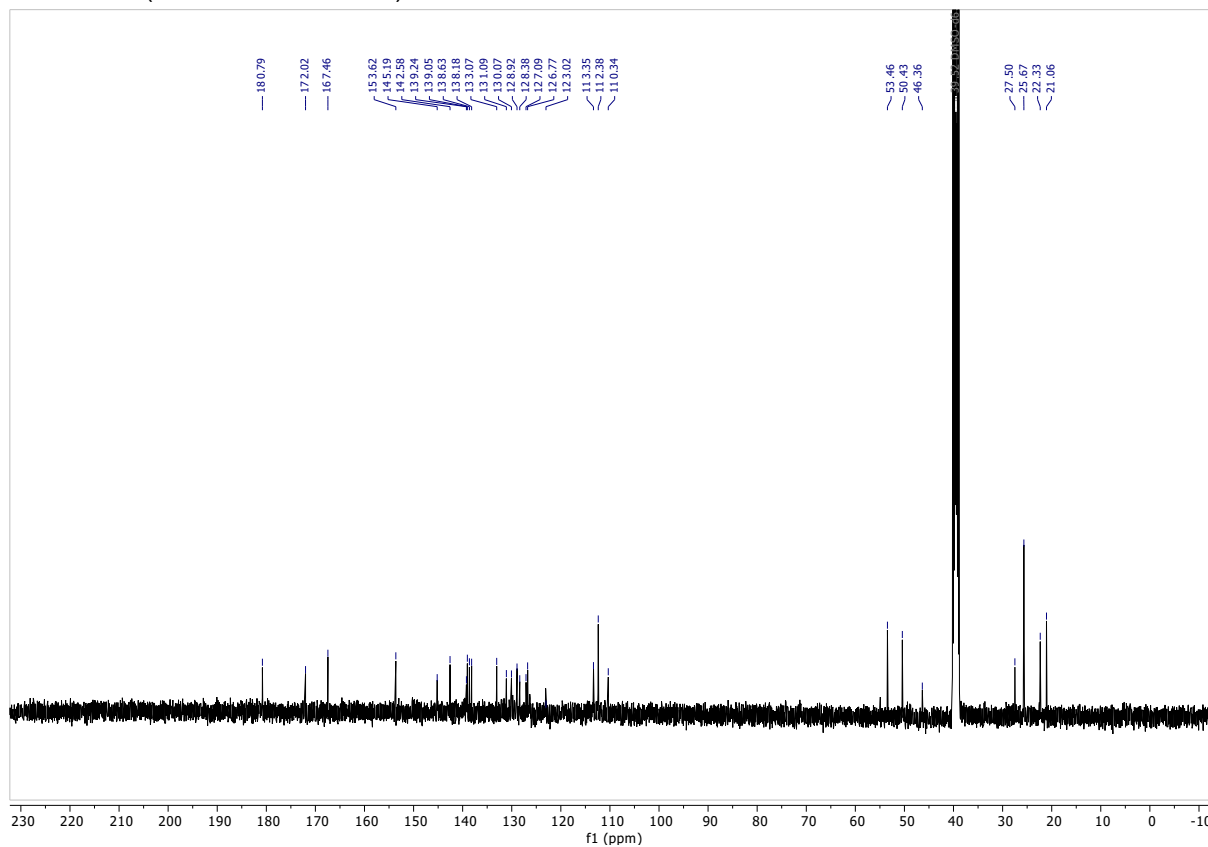


T-AzHCy1

¹H NMR (400 MHz, DMSO-d₆)

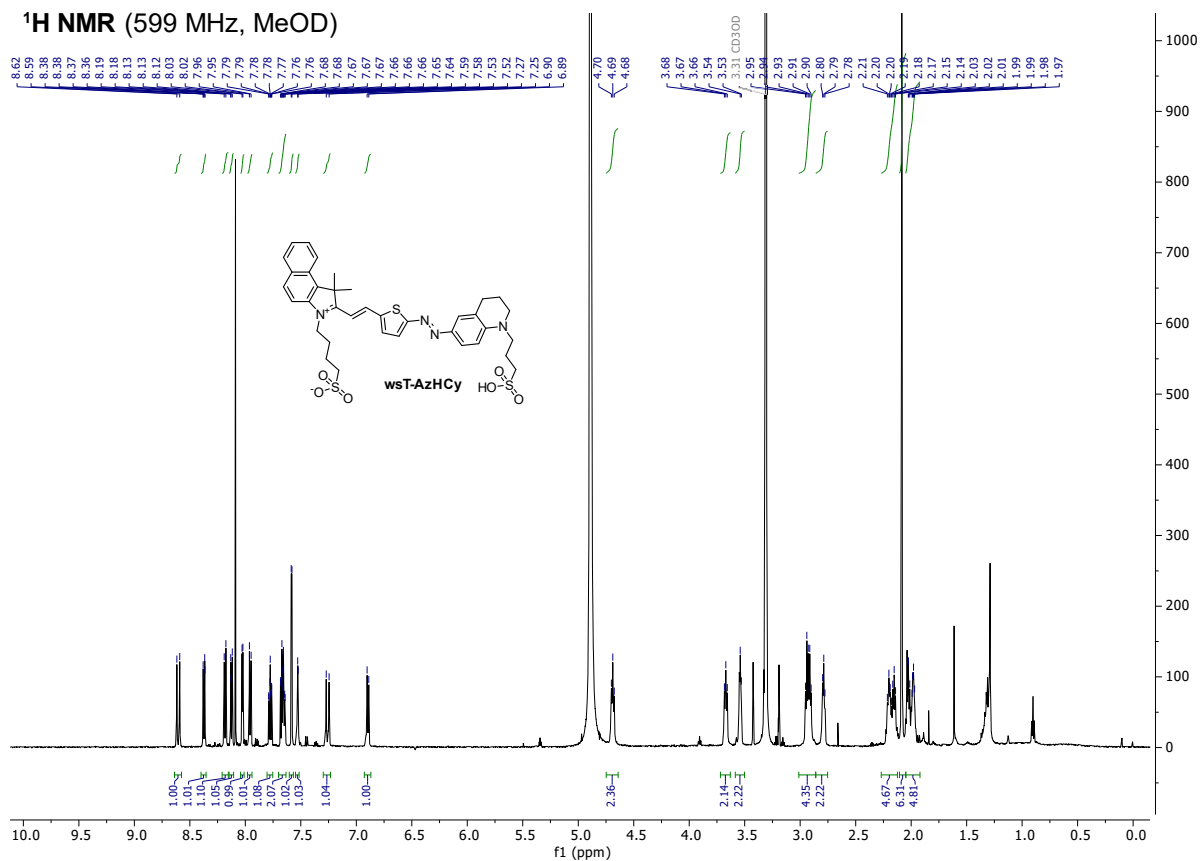


¹³C NMR (101 MHz, DMSO-d₆)

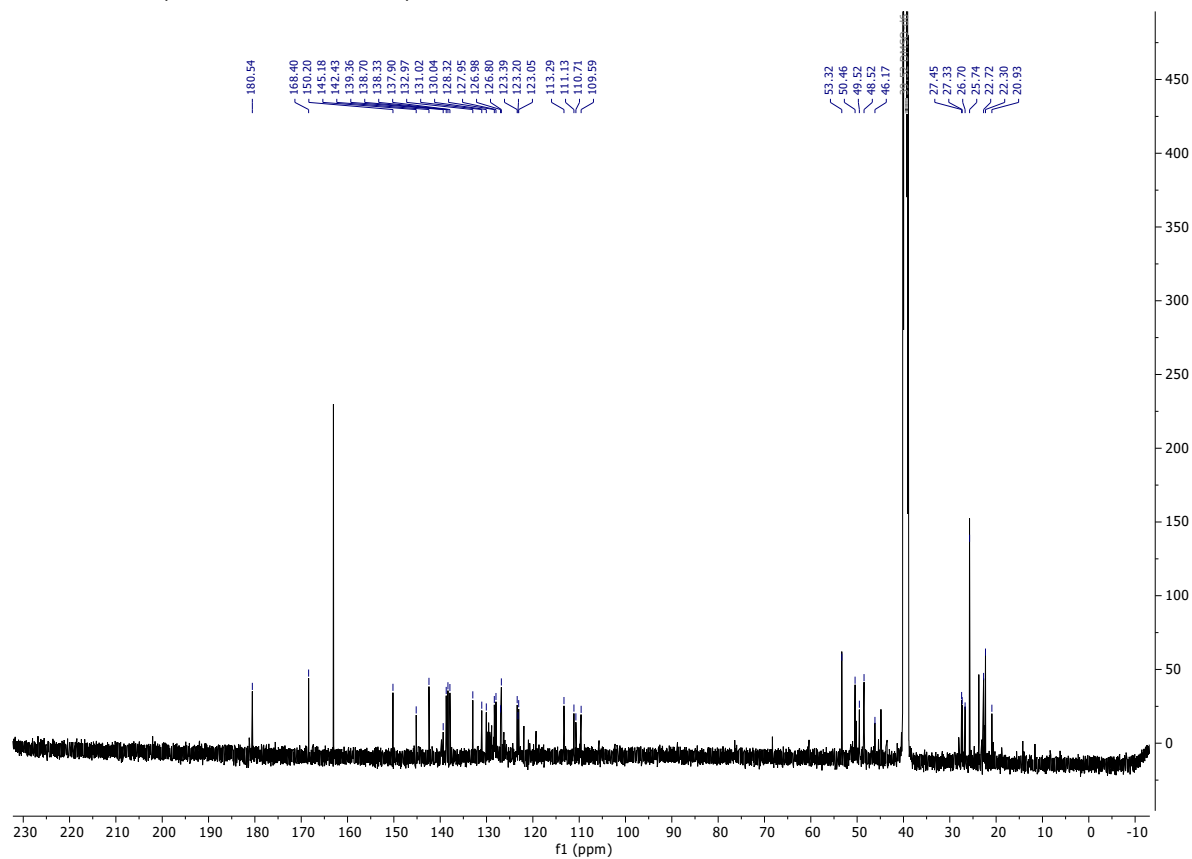


wsT-AzHCy

¹H NMR (599 MHz, MeOD)

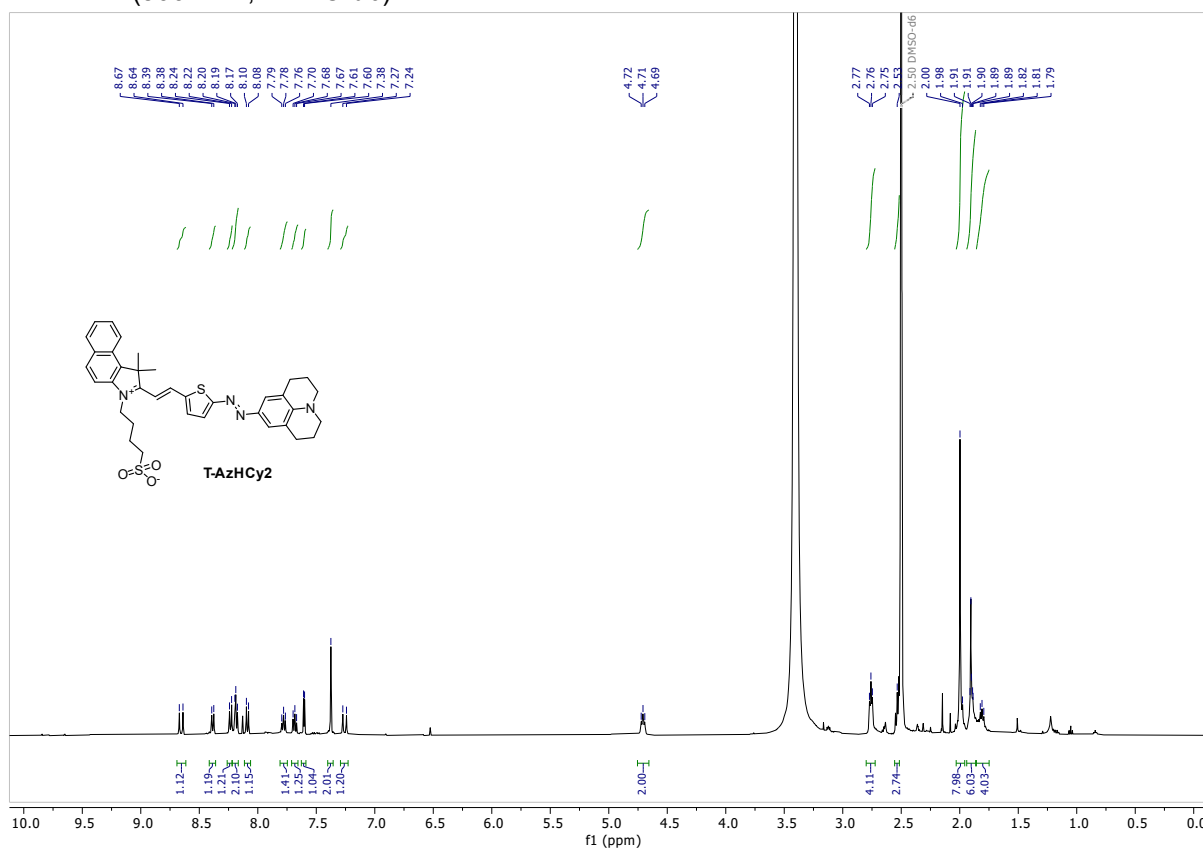


¹³C NMR (126 MHz, DMSO-d₆)

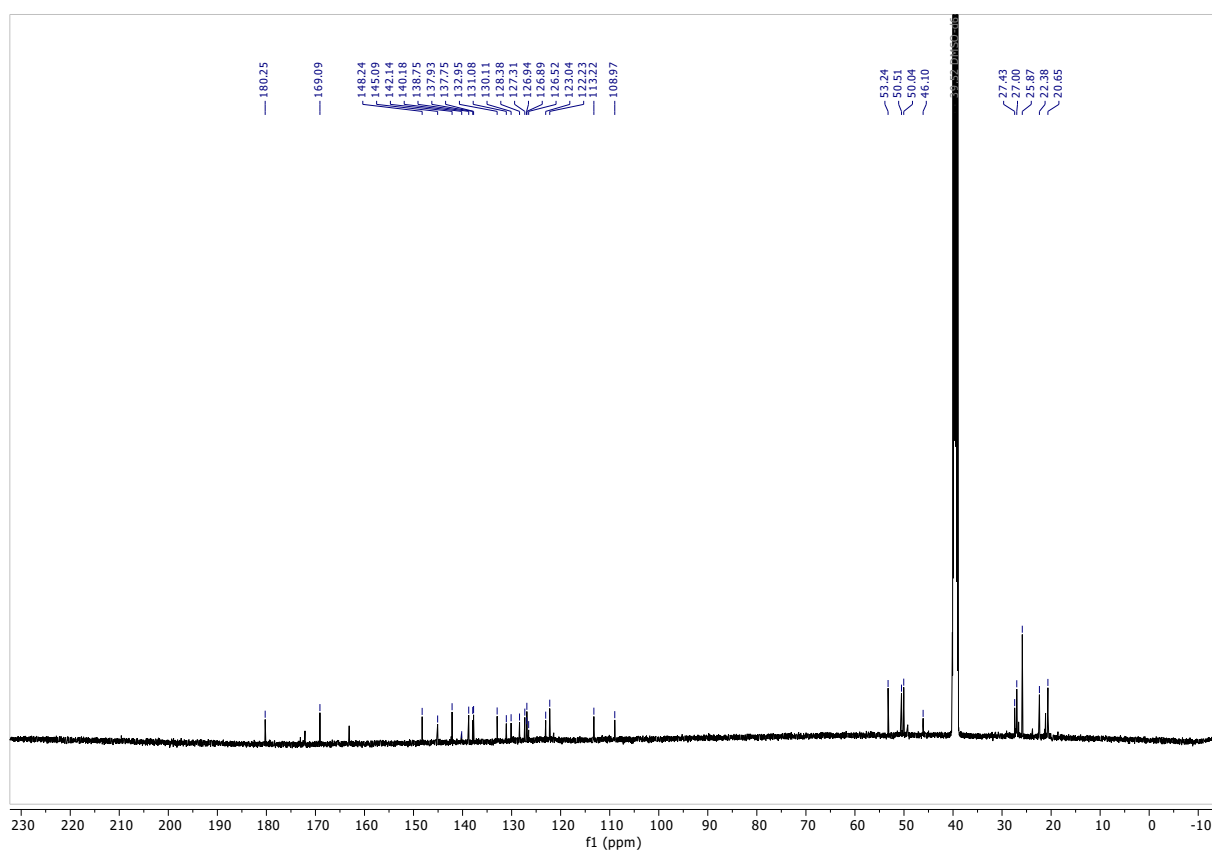


T-AzHCy2

¹H NMR (500 MHz, DMSO-d₆)

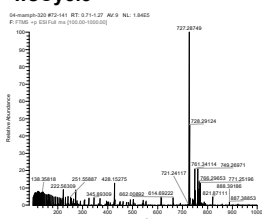


¹³C NMR (126 MHz, DMSO-d₆)

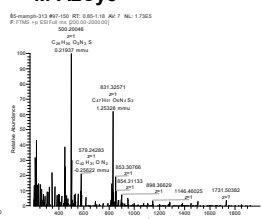


9.2 HRMS Spectra

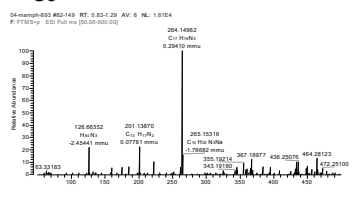
wsCy5.5



M-AzCy5



S3




9.3 Photoluminescence Data

PL decay curves and fitting parameters are reproduced on the following pages.

wsCy5.5 S50
 M-AzCy5 S51
 E-AzCy5 S52
 E-AzCy7 S53
 T-AzHCy2 S54
 wsT-AzHCy S55
 QC-1 S56

Data in *Main Plot* are vertically shifted for visibility and plotted on a vertical \log_{10} axis (blue), with the instrument response factor also plotted (red; relevant for AzHCy); time axis is arbitrary but excitation is usually around 0.5 ns.

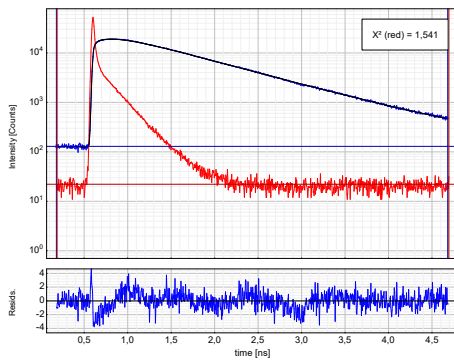
wsCy5.5 reference fluorophore, lifetime ~ 908 ps

PicoQuant FluoFit 12.05.2023 

wsCy5.5

Model: Exp. [Reconv.] (Exponential)
 Plotted Data Set #0 Decay: ".\WsCy55_exc700_gain10.sdt" (0)
 Plotted Data Set #0 IRF: ".\IRF_glass_exc700_gain10.sdt" (0)
 χ^2 (reduced): 1,5409 ; Fitted Data Points: 920

Main Plot



$$I(t) = \int_{-\infty}^t \text{IRF}(t') \sum_{i=1}^n A_i e^{-\frac{t-t'}{\tau_i}} dt'$$

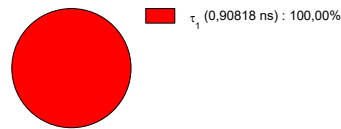
Parameter	Value	Conf. Lower	Conf. Upper	Conf. Estimation
A_1 [Cnts]	28497.2	-76.0	+76.0	Fitting
τ_1 [ns]	0,90818	-0,00196	+0,00196	Fitting
Bkgr. dec. [Cnts]	129.10	-5.77	+5.77	Fitting
Bkgr. str. [Cnts]	22.13	-1.09	+1.09	Fitting
Shift IRF [ns]	0,012001	-0,000435	+0,000435	Fitting

PicoQuant FluoFit 12.05.2023 

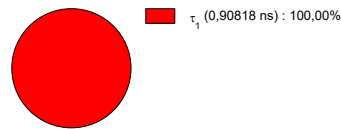
Average Lifetime:

$\tau_{Av,1}$ = 0,90818 ns (intensity weighted)
 $\tau_{Av,2}$ = 0,90818 ns (amplitude weighted)

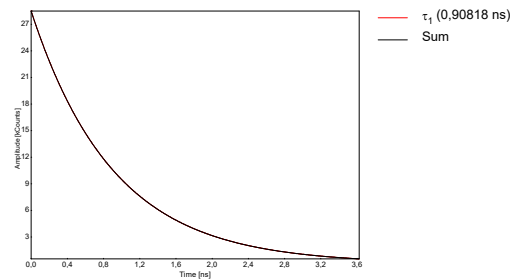
Fractional Intensities of the Positive Decay Components:



Fractional Amplitudes of the Positive Decay Components:



Fitted Decay and Exponential Components:



M-AzCy5, lifetime ~ 544 ps

PicoQuant FluorFit 14.12.2021



M-AzCy5 mono exponential fit

Model: Exp. [Reconv.] (Exponential)

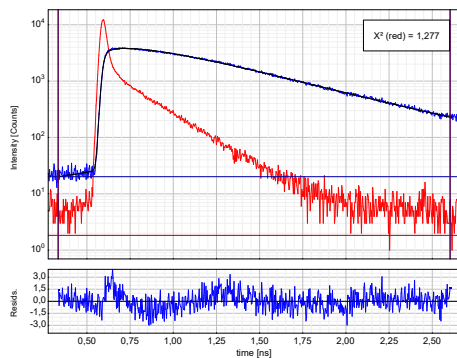
Plotted Data Set #0 Decay:

"\\._P_L_transient_MM313_exc730_OD5_40s_opt-1.sdt" (0)

Plotted Data Set #0 IRF: "\\._IRF_glass.sdt" (0)

X²(reduced): 1,2775 ; Fitted Data Points: 697

Main Plot



$$I(t) = \int_{-\infty}^t \text{IRF}(t') \sum_{m=1}^n A_m e^{-\frac{t-t'}{\tau_m}} dt'$$

Parameter	Value	Conf. Lower	Conf. Upper	Conf. Estimation
A ₁ [Cnts]	6216,1	-29,5	+29,5	Fitting
τ ₁ [ns]	0,54406	-0,00230	+0,00230	Fitting
Bkgr. dec. [Cnts]	20,13	-2,50	+2,50	Fitting
Bkgr. irr. [Cnts]	1,83	-1,33	+1,33	Fitting
Shift _{IRF} [ns]	0,005217	-0,000609	+0,000609	Fitting

PicoQuant FluorFit 14.12.2021

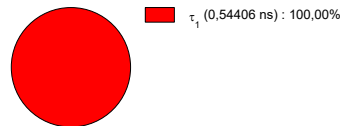


Average Lifetime:

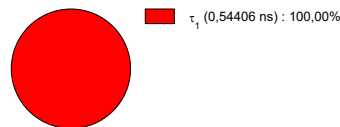
τ_{Av,1} = 0,54406 ns (intensity weighted)

τ_{Av,2} = 0,54406 ns (amplitude weighted)

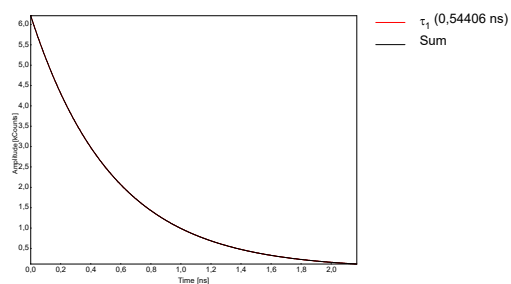
Fractional Intensities of the Positive Decay Components:



Fractional Amplitudes of the Positive Decay Components:



Fitted Decay and Exponential Components:



Note systematic error in the monoexponential residuals, that is also coherent with the TA conclusion of a non-monoexponential relaxation pathway.

Value shown in **Table 2** is taken from this fit, as it reflects the overall decay time.

E-AzCy5, lifetime ~ 386 ps

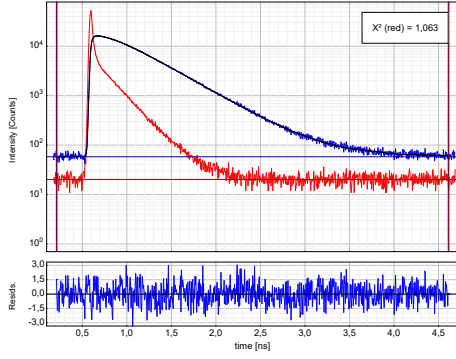
PicoQuant FluorFit 12.05.2023



E-AzCy5 bi-exponential fit

Model: Exp. [Reconv.] (Exponential)
 Plotted Data Set #0 Decay: ".\EazCy5_exc700_gain10.sdt" (0)
 Plotted Data Set #0 IRF: ".\IRF_glass_exc700_gain10.sdt" (0)
 χ^2 (reduced): 1,0632 ; Fitted Data Points: 901

Main Plot



$$I(t) = \int_{-\infty}^t \text{IRF}(t') \sum_{i=1}^n A_i e^{-\frac{t-t'}{\tau_i}} dt'$$

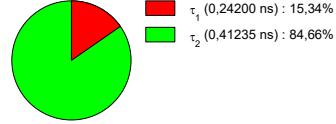
Parameter	Value	Conf. Lower	Conf. Upper	Conf. Estimation
A_1 [Cnts]	6874	-142	+142	Fitting
τ_1 [ns]	0,24200	-0,00486	+0,00486	Fitting
A_2 [Cnts]	22259,0	-88,1	+88,1	Fitting
τ_2 [ns]	0,41235	-0,00121	+0,00121	Fitting
Bkgr. dec. [Cnts]	57,95	-1,99	+1,99	Fitting
Bkgr. sp. [Cnts]	20,206	-0,641	+0,641	Fitting
Shift _{IRF} [ns]	0,005385	-0,000373	+0,000373	Fitting

PicoQuant FluorFit 12.05.2023

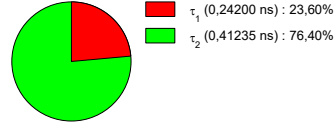


Average Lifetime:
 $\tau_{Av,1}$ = 0,38621 ns (intensity weighted)
 $\tau_{Av,2}$ = 0,37215 ns (amplitude weighted)

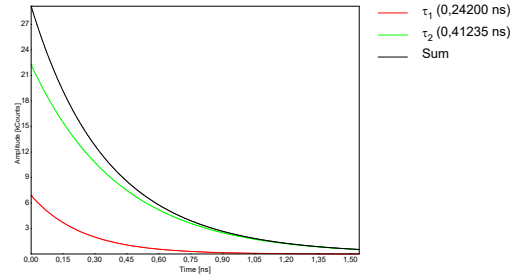
Fractional Intensities of the Positive Decay Components:



Fractional Amplitudes of the Positive Decay Components:



Fitted Decay and Exponential Components:



Value shown in **Table 2** is the intensity averaged decay time 386 ps.

E-AzCy7, lifetime ~ 363 ps

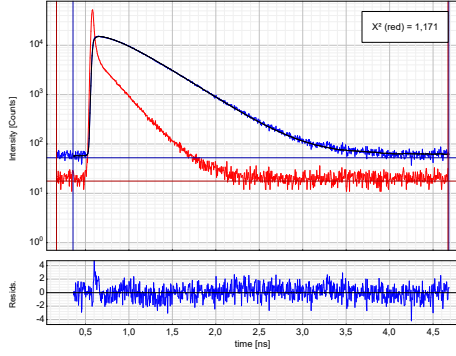
PicoQuant FluoFit 12.05.2023



E-AzCy7 mono-exponential fit

Model: Exp. [Reconv.] (Exponential)
 Plotted Data Set #0 Decay: ".\EazCy7_exc700_gain10.sd" (0)
 Plotted Data Set #0 IRF: ".\IRF_glass_exc700_gain10.sd" (0)
 X²(reduced): 1.1705 ; Fitted Data Points: 884

Main Plot



$$I(t) = \int_{-\infty}^t \text{IRF}(t') \sum_{i=1}^n A_i e^{-\frac{t-t'}{\tau_i}} dt'$$

Parameter	Value	Conf. Lower	Conf. Upper	Conf. Estimation
A ₁ [Cnts]	27098.6	-99.1	+99.1	Fitting
τ ₁ [ns]	0.36337	-0.00104	+0.00104	Fitting
Bkgf. dec. [Cnts]	52.52	-2.02	+2.02	Fitting
Bkgf. irf [Cnts]	17.669	-0.680	+0.680	Fitting
Shift irf [ns]	-0.008613	-0.000390	+0.000390	Fitting

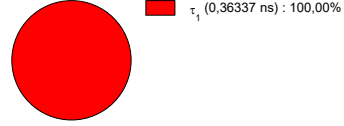
PicoQuant FluoFit 12.05.2023



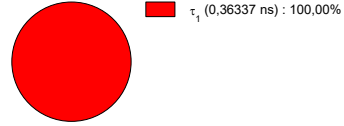
Average Lifetime:

τ_{av,1} = 0.36337 ns (intensity weighted)
 τ_{av,2} = 0.36337 ns (amplitude weighted)

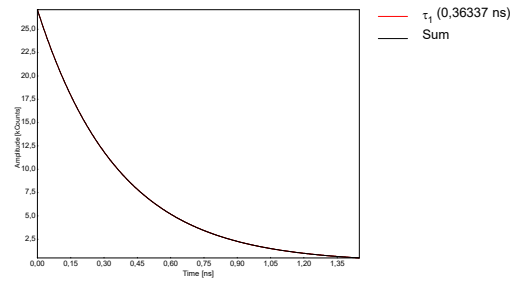
Fractional Intensities of the Positive Decay Components:



Fractional Amplitudes of the Positive Decay Components:



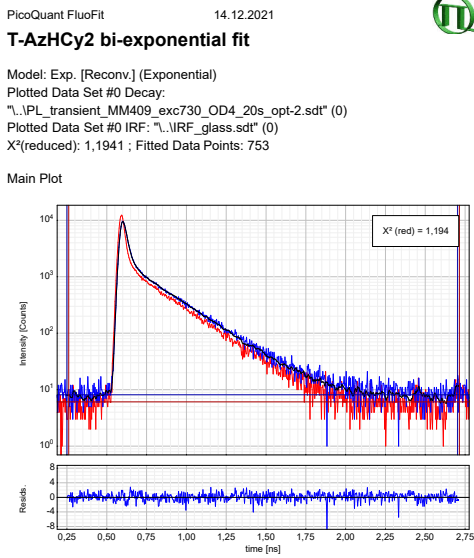
Fitted Decay and Exponential Components:



Value shown in **Table 2** is taken from this fit, as it reflects the overall decay time.

T-AzHCy2, lifetime ~ 13 ps

Ultrafast relaxation: since sample lifetime is on a smaller timescale than the IRF (red curve), its half-time cannot be read off the main plot but is found by the reconvolution fit (at right).



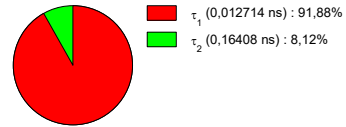
$$I(t) = \int_{-\infty}^t \text{IRF}(t') \sum_{i=1}^n A_i e^{-\frac{t-t'}{\tau_i}} dt'$$

PicoQuant FluoFit 14.12.2021

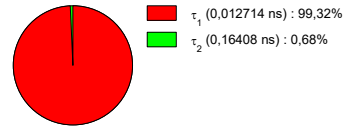
Parameter	Value	Conf. Lower	Conf. Upper	Conf. Estimation
A ₁ [Cnts]	70266	-717	+717	Fitting
τ ₁ [ns]	0,012714	-0,000111	+0,000111	Fitting
A ₂ [Cnts]	481,5	-38,1	+38,1	Fitting
τ ₂ [ns]	0,16408	-0,00953	+0,00953	Fitting
Bkgf. Dec. [Cnts]	8,127	-0,748	+0,748	Fitting
Bkgf. IRF [Cnts]	6,094	-0,750	+0,750	Fitting
Shift IRF [ns]	0,004113	-0,000284	+0,000284	Fitting

Average Lifetime:
 τ_{Av,1} = 0,025012 ns (intensity weighted)
 τ_{Av,2} = 0,013744 ns (amplitude weighted)

Fractional Intensities of the Positive Decay Components:



Fractional Amplitudes of the Positive Decay Components:



Value shown in **Table 2** is that of the major component of the biexponential fit. The small longer-lived contribution with negligible amplitude (0.7 %) results from uncertainties in detecting the instrument response function at the detection wavelength.

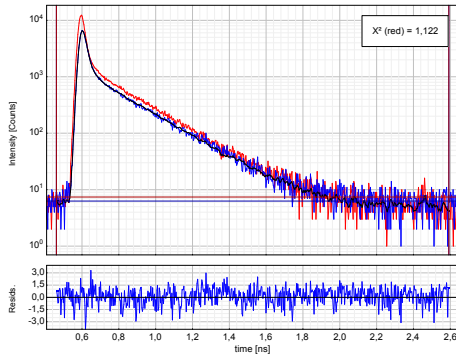
wsT-AzHCy, lifetime ~ 9 ps

Ultrafast relaxation: since sample lifetime is on a smaller timescale than the IRF (red curve), its half-time cannot be read off the main plot but is found by the reconvolution fit (at right).

PicoQuant FluoFit 14.12.2021
wsT-AzHCy bi-exponential fit

Model: Exp. [Reconv.] (Exponential)
 Plotted Data Set #0 Decay:
 "\.PL_transient_MM650_exc730_OD4_40s_opt-2.sdt" (0)
 Plotted Data Set #0 IRF: "\.IRF_glass.sdt" (0)
 X²(reduced): 1,1220 ; Fitted Data Points: 654

Main Plot



$$I(t) = \int_{-\infty}^t \text{IRF}(t') \sum_{i=1}^n A_i e^{-\frac{t-t'}{\tau_i}} dt'$$

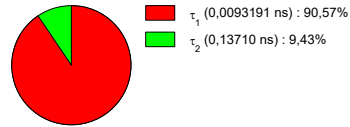
PicoQuant FluoFit 14.12.2021

Parameter	Value	Conf. Lower	Conf. Upper	Conf. Estimation
A ₁ [Cnts]	64392	-750	+750	Fitting
τ ₁ [ns]	0,0093191	-0,0000900	+0,0000900	Fitting
A ₂ [Cnts]	455,5	-34,2	+34,2	Fitting
τ ₂ [ns]	0,13710	-0,00792	+0,00792	Fitting
Bkgr. Dec. [Cnts]	6,294	-0,653	+0,653	Fitting
Bkgr. sep. [Cnts]	7,415	-0,992	+0,992	Fitting
Shift IRF [ns]	0,007525	-0,000301	+0,000301	Fitting

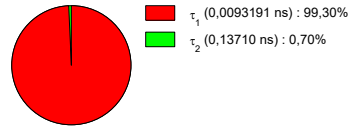
Average Lifetime:

τ_{Av,1} = 0,0213630 ns (intensity weighted)
 τ_{Av,2} = 0,0102167 ns (amplitude weighted)

Fractional Intensities of the Positive Decay Components:



Fractional Amplitudes of the Positive Decay Components:



Value shown in **Table 2** is that of the major component of the biexponential fit. The small longer-lived contribution with negligible amplitude (0.7 %) results from uncertainties in detecting the instrument response function at the detection wavelength.

QC-1 – lifetime ~ 2ps

Ultrafast relaxation: since sample lifetime is on a smaller timescale than the IRF (red curve), its halftime cannot be read off the main plot but is found by the reconvolution fit (at right).

PicoQuant FluorFit

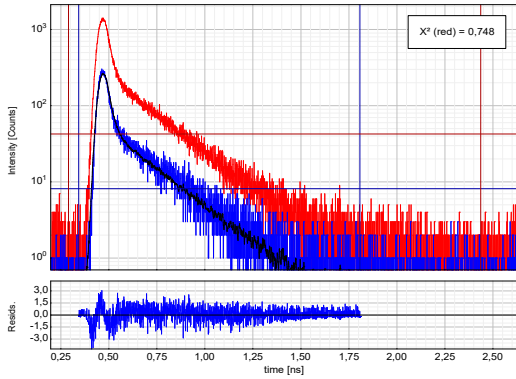
29.06.2023



QC1

Model: Exp. [Reconv.] (Exponential)
 Plotted Data Set #0 Decay: "\. \10.sdt" (0)
 Plotted Data Set #0 IRF: "\. \14.sdt" (0)
 X²(reduced): 0,7476 ; Fitted Data Points: 1799

Main Plot



$$I(t) = \int_{-\infty}^t \text{IRF}(t') \sum_{i=1}^n A_i e^{-\frac{t-t'}{\tau_i}} dt'$$

Parameter	Value	Conf. Lower	Conf. Upper	Conf. Estimation
A ₁ [Cnts]	13663	-374	+374	Fitting
τ ₁ [ns]	0,0023774	-0,0000550	+0,0000550	Fitting
Bkgr. Dec. [Cnts]	8,149	-0,266	+0,266	Fitting
Bkgr. IRF [Cnts]	42,55	-1,38	+1,38	Fitting
Shift IRF [ns]	0,006216	-0,000755	+0,000755	Fitting

PicoQuant FluorFit

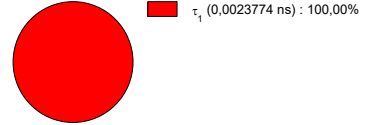
29.06.2023



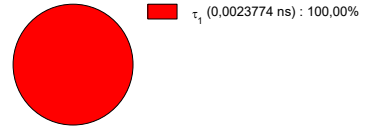
Average Lifetime:

τ_{AV,1} = 0,0023774 ns (intensity weighted)
 τ_{AV,2} = 0,0023774 ns (amplitude weighted)

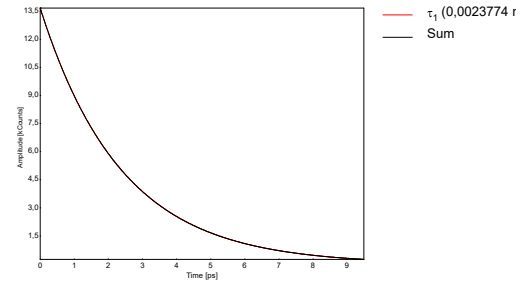
Fractional Intensities of the Positive Decay Components:



Fractional Amplitudes of the Positive Decay Components:

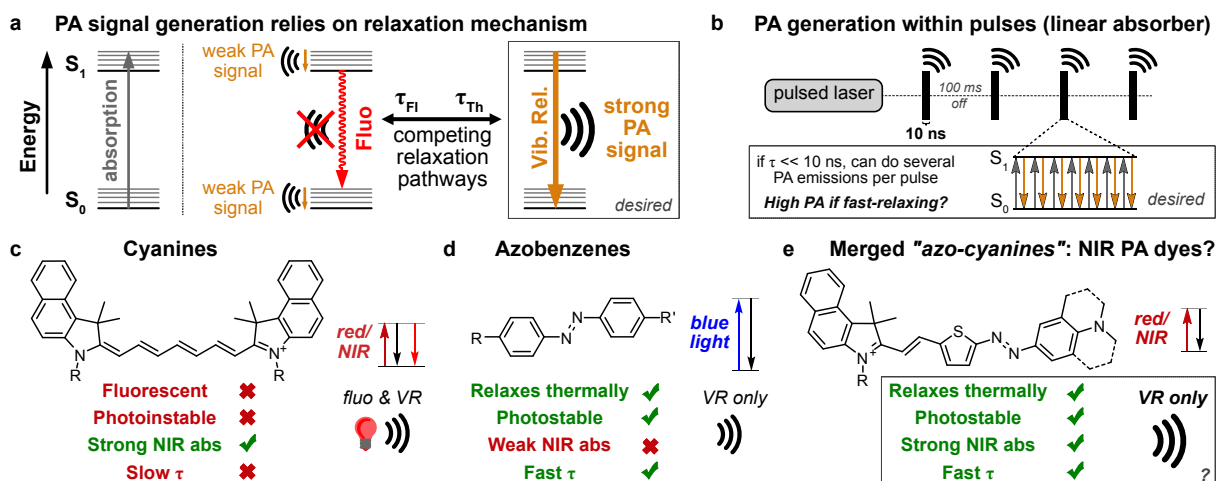


Fitted Decay and Exponential Components:

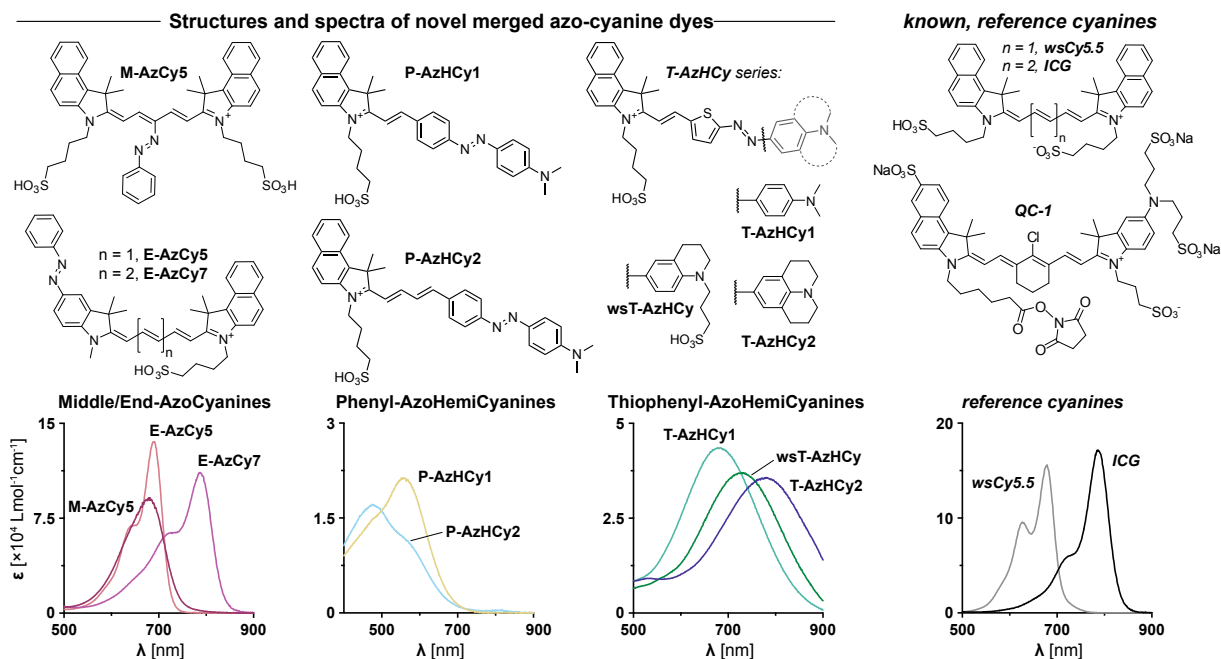


9.4 Vectorial copies of the images in the main text

As vectorial encoding is lost during the online generation of the main text PDF, all main figures are reproduced below so that an interested reader can zoom in, decompose them, etc.

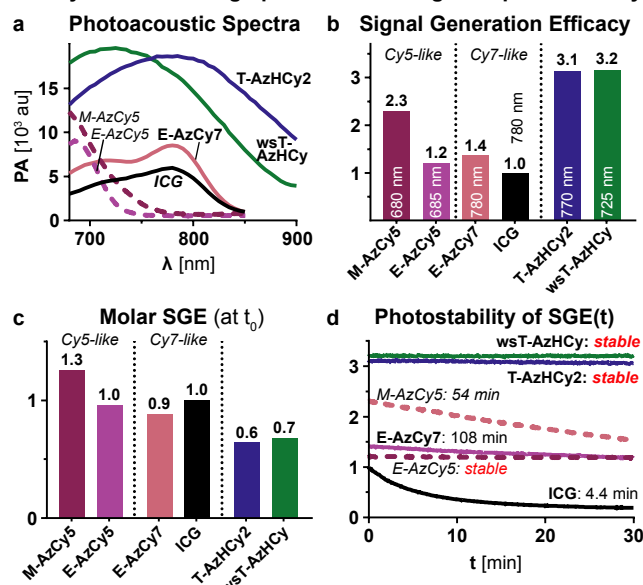


Main Figure 1. Design concept for molecular switch-based optoacoustic contrast agents. **(a)** Energy dissipated as heat contributes to PA signal (internal conversion then vibrational relaxation); fluorescence does not. **(b)** PA excitation is pulsed. For a linear absorber ($S_1 \rightarrow S_0$ relaxation half-life τ much shorter than the pulse), several $S_0 \rightarrow S_1 \rightarrow S_0$ excitation-relaxation cycles are possible within one pulse. **(c)** Cyanine dyes have strong NIR absorption, but are poor PA agents as they are slow-relaxing and non-photostable. **(d)** Azobenzenes have ultrafast nonradiative relaxation, but as UV/Vis-absorbers they are not useful for NIR PA. **(e)** **Hypothesis:** merging azobenzenes and cyanines should give strong, photostable NIR-absorbing PA emitters.



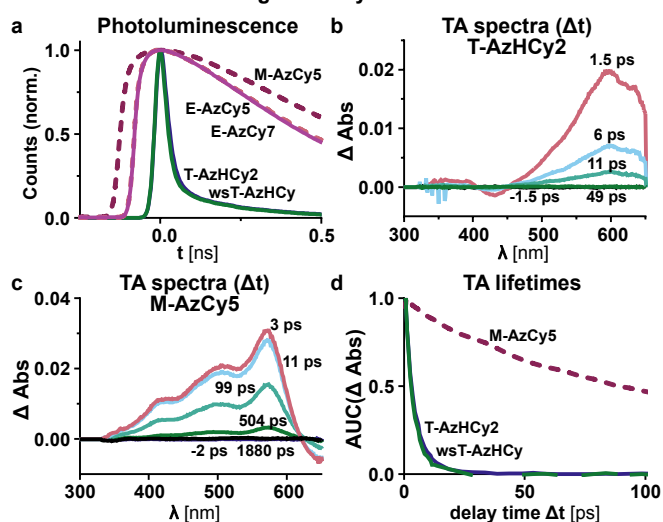
Main Figure 2. Structures and absorption spectra of azo-cyanines. (dyes in 1:1 EtOH:PBS at 10 μ M, except ICG at 5 μ M; further details at Fig S1).

Azo-cyanines have high photoacoustic signal & photostability

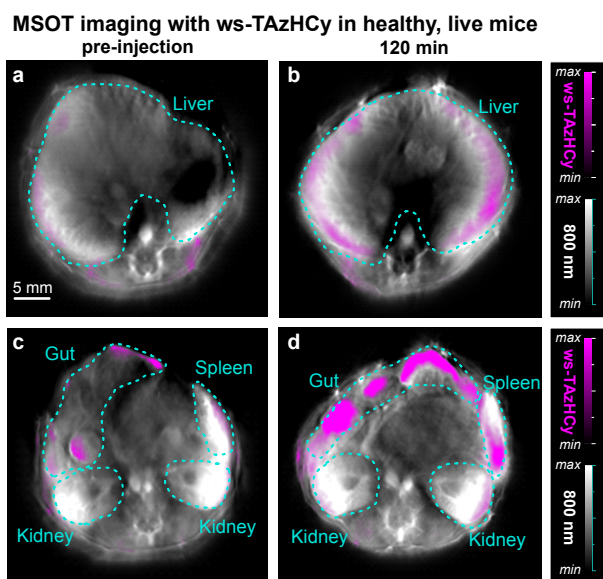


Main Figure 3. Optoacoustic properties. (a) Photoacoustic spectra at OD = 0.5 at λ_{\max} in 1:1 PBS:EtOH. (b) PA signal generation efficacy (SGE) at constant OD, showing relative dye "loudness". (c) SGE adjusted to constant molarity (ICG set to 1). (d) PA photostability determination.

Time-resolved data: merged azo-cyanines have ultrafast S1→S0



Main Figure 4. Time-resolved data. (a) Fluorescence shows decay rates of singlet excited states. (b-d) Transient absorption (TA) spectroscopy: T-AzHCy2 relaxes fully to S₀ with τ_{TAS} ~4 ps, but M-AzCy5 has τ_{TAS} ~180 ps. (d) TA Δ Abs decays (fitted lifetimes given in Table 2).



Main Figure 5. *In vivo* MSOT images. Transverse image sections of live, healthy mice, showing liver (top), kidney and spleen (bottom), before and 120 min after IV injection of **wsT-AzHCy** (100 μ L, 0.5 mM).

Supporting Information for:

Molecular rotors are loud, highly photostable, NIR/SWIR-active molecular optoacoustic contrast agents

Markus Müller^{a,b*}, Abha Valavalkar^{c,d}, Vipul Gujrati^{e,f}, Jan P. Prohaska^a, Divyesh Shelar^{e,f}, Michaela Kaltenecker^b, Benjamin Dietzek-Ivanšić^{c,d}, Vasilis Ntziachristos^{e,f}, Oliver Thorn-Seshold^{a,b*}

[a] Faculty of Chemistry and Food Chemistry, Technical University of Dresden, Bergstrasse 66, Dresden 01069, Germany.

[b] Department of Pharmacy, LMU Munich, Butenandtstrasse 7, Munich 81377, Germany.

[c] Leibniz Institute of Photonic Technology Jena, Research Department Functional Interfaces, Albert-Einstein-Straße 9, Jena 07745 Germany.

[d] Institute of Physical Chemistry, University of Jena, Lessingstraße 4, Jena 07743, Germany.

[e] Institute of Biological and Medical Imaging, Helmholtz Zentrum München, Ingolstädter Landstraße 1, Neuherberg 85764, Germany.

[f] Chair of Biological Imaging at the Central Institute for Translational Cancer Research (TranslaTUM), School of Medicine and Health, Technical University of Munich, Ismaninger Str. 22, Munich 81675, Germany.

Correspondence to: oliver.thorn-seshold@tu-dresden.de; markus.mueller2@tu-dresden.de.

Table of contents

1	Supporting Notes	1
1.1	Supporting Note 1: Design considerations for PA contrast agents.....	1
1.2	Supporting Note 2: pH-dependent absorption of TAM1H and TAM2H.....	1
1.3	Supporting Note 3: Photostability for Long-term Imaging.....	2
2	Photocharacterization	3
2.1	UV-VIS absorption spectroscopy.....	3
2.2	Fluorescence spectroscopy.....	3
3	Transient Absorption Spectroscopy (TAS)	4
4	Photoacoustics	5
4.1	MSOT set-up and data acquisition.....	5
5	Chemical Synthesis	7
5.1	Materials and Methods.....	7
5.2	Synthetic Procedures.....	7
6	References	12
7	NMR Spectra	13

1 Supporting Notes

1.1 Supporting Note 1: Design considerations for PA contrast agents

In PA, the electronic ground state S_0 is promoted by photon absorption typically into a vibrationally hot excited state S_1 (or S_n). Excited state relaxation is a multistep procedure that can usually be simplified to vibrational relaxation to the S_1 vibrational ground state, then either (i) **radiative** decay to a low-lying vibrationally excited S_0 state [fluorescence] followed by vibrational relaxation to the S_0 vibrational ground state (**Fig 1a**), or (ii) energetically horizontal internal conversion (IC) to a high vibrational energy S_0 state then **non-radiative** vibrational relaxation to S_0 ground state (**Fig 1b**). Vibrational relaxation typically takes place within fs-ps, hence IC is the rate limiting step for non-radiative decay, and accelerating IC is a specific molecular design task for PA contrast agents. IC-accelerating designs have e.g. been implemented into Nebraska Red (**NR**) by asymmetry induced vibronic coupling,^[1] into hemi-cyanines by large excited state geometry alterations (**PA-HD**),^[2,3] or into cyanine dyes by fusing them with molecular switches that allow ultrafast $S_1 \rightarrow T_1 \rightarrow S_0$ evolution due to conical intersections^[4] (**Fig 1c**). For more detail on the connection of molecular motion with non-radiative decay, we refer to an excellent recent review.^[5]

1.2 Supporting Note 2: pH-dependent absorption of TAM1H and TAM2H

UV-VIS spectroscopy for the first generation of TAMs (**TAM1H** and **TAM2H**) showed pH-dependent equilibria between a desired NIR-absorbing form and an undesired UV-absorbing form. The UV-form is assigned to a hydroxyl adduct at the central carbon, with interrupted π -system, since its absorption profile matches that for *N,N*-dimethyl-4-(thiophen-2-yl)aniline **S1**. The conjugated NIR-form predominates under acidic conditions, with a drop by ~50% for **TAM1H** and ~30% for **TAM2H** upon raising the pH to neutral (**Fig S1a,c**).

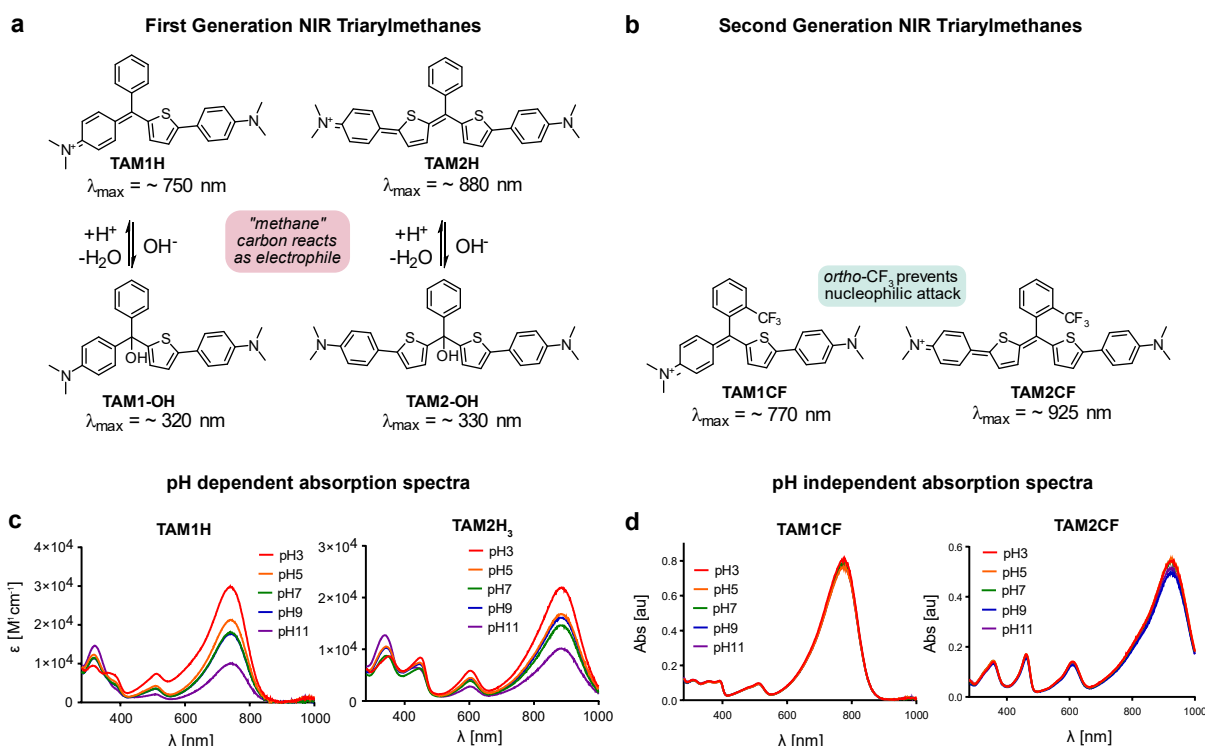


Figure S1. **a**) First-generation TAMs and their pH-dependent equilibria of NIR- and UV-absorbing forms. **b**) Second-generation TAMs bearing an *ortho* CF₃ group to prevent nucleophilic attack. **c-d**) UV-VIS absorption spectra of first and second generation TAMs (pH-dependent, and pH-independent, respectively) (dyes at 10 μ M, in 1:1 MeCN:Britton Robinson aqueous buffer 1:1).

To stabilize the NIR-absorbing form, a moderately bulky CF₃ group was introduced to the upper phenyl ring in *ortho*, which led to a strong and pH-independent NIR absorbance, as well as resistance to stronger nucleophiles such as GSH (**Fig S1b,d; S2**). We feel this is required for cellular measurements (intracellular [GSH] up to 10 mM). The TAM molar extinction coefficients (ϵ)

depend on the solvent and/or environment, with lowest ϵ in pure water and highest ϵ in apolar organic solvents (**Fig 2**), but intermediate values in solvent systems mimicking cellular or biological environments where partitioning and heterogeneity are important (**Fig S3**): highlighting that purely aqueous buffers are not always an appropriate choice for PA phantom imaging for such dyes.

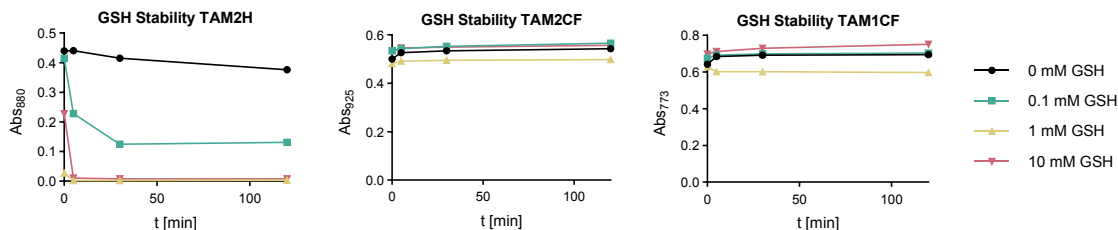


Figure S2. Evolution of the NIR absorption maxima of **TAM2H**, **TAM1CF**, and **TAM2CF** (10 μ M, 1:1 MeCN:PBS) when co-incubated with 0 mM, 0.1 mM, 1 mM, and 10 mM GSH.

This paper covers photophysical aspects of PA contrast agent development, and the design aspect of NIR molecular rotors, which this first-in-class report needed to demonstrate the potential of NIR molecular rotor systems as a concept for PA. The main text has argued for the importance of several key advantages that the TAMs bring as a molecular class, e.g. signal linearity (vs. excitation intensity) and signal photostability (for longitudinal imaging, **Supporting Note 3**). An obvious site for improvement for these initial TAMs, as compared to more developed PA agent classes, is their more moderate and environment-sensitive molar NIR absorbance (ϵ); since, for always-on PA agents, e.g. in anatomical imaging, raising the molar NIR absorbance (ϵ) is important for strong molar PA signal generation. However, we stress that for *conditionally-activated* PA agents, e.g. in molecular imaging, maximising the difference of the molar PA action spectra of the pre- and post-activation contrast agents is probably the far more crucial (and far more difficult) requirement: e.g., reaching baseline spectral separation to allow easily separating the signals of the pre- and post-activation chromophores. In that context, the remarkable switch from UV- to NIR-forms (>430 nm jump for **TAM1H**, 550 nm for **TAM2H**), leaping over the whole visible spectrum, should be noted as a rational structure-determined activation possibility (that is well preceded by decades of e.g. spirocycle-opening fluorogenic rhodamines) for future TAM generations.

1.3 Supporting Note 3: Photostability for Long-term Imaging

MSOT image slices ($[dye_n]$ per pixel) are generated by n -spectral deconvolution of sets of excitation-wavelength-dependent images, measured stepwise over a wide absorption spectrum range, typically averaging 10 frames per image wavelength: thus, under acceptable *in vivo* energy limits, a single MSOT slice needs 20 to 60 s of pulsed laser irradiation (200 nm range with 10 nm steps, to 300 nm range with 5 nm steps). Theoretically, pixel-dependent rates of dye bleaching could be crudely estimated based on the experimental setup, wavelength penetration, and their measured bleaching half-lives from phantom assays, to compensate for signal bleaching over time (even during single slice acquisition). However, this is vastly impractical in many ways, including that (1) for phantom photostability measurements, a sample is constantly irradiated at λ_{max} (rather than spectral stepping), so bleaching rates can be indicative at best; and (2) phantoms are usually cylindrical vessels (3 mm diameter) irradiated only at a specific transsection, such that the vast majority of the sample volume (non-irradiated) serves as a reservoir to resupply unbleached dye: so phantom bleaching half-times can vastly under-estimate true bleaching rates especially *in molecular PA imaging settings* (tissue-accumulation of contrast agent, rather than e.g. vascular anatomical imaging where the PA agent is continually replenished). The general result we argue is that PA dye photostability is *crucial* for reliable, repeated, long-term *in vivo* imaging especially in the context of molecular imaging.

2 Photocharacterization

2.1 UV-VIS absorption spectroscopy

UV-VIS. UV-VIS spectra were recorded on an Agilent Cary 60 UV-Vis spectrophotometer using 1 cm quartz or BRAND® UV-cuvette micro. All measurements were performed at room temperature in non-degassed solvents at a concentration of 10 μM , unless stated otherwise.

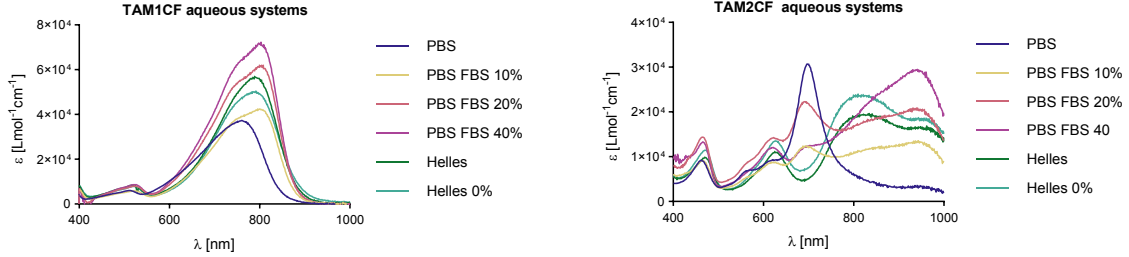


Figure S3. Absorption properties of **TAM1CF** and **TAM2CF** in biologically-mimicking solvents (at 10 μM).

Dye aggregation can be a problem for photoacoustic agents, as they can often π -stack even at low concentrations, giving major and irreproducible changes to molar SGE, spectra, bleaching rate, and even spatial distribution (see e.g. a re-evaluation of **QC-1**^[4]). We excluded aggregation effects with these TAMs under intended PA conditions (5-10 μM), since UV-Vis spectra were linear to concentration up to even 400 μM , and showed no evolution over time (60 min, 20°C) (**Figure S4**).

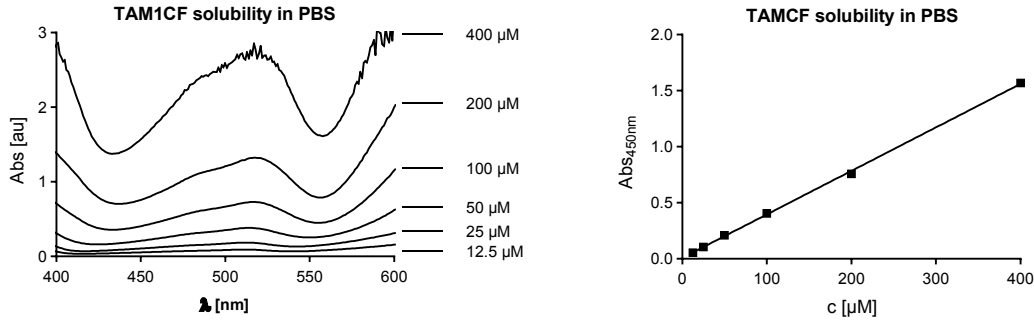


Figure S4. Lower bound for molecular solubility was 400 μM , based on linearity of UV-VIS spectroscopy.

2.2 Fluorescence spectroscopy

Fluorescence spectra were recorded on an Agilent Cary Eclipse 3500 fluorimeter using 1 cm quartz cuvettes, at room temperature, in non-degassed solvents, at absorbance < 0.1 . For **upper bounds for quantum yields (Table S1)**, samples (*i*) were measured against a fluorescence standard (*s*) with a known quantum yield Φ_F . For this purpose, absorbance and fluorescence were subsequently measured from the same sample. The fluorescence quantum yield is then calculated according to equation (1), with: $f_x(\lambda_{ex})$ = absorbance factor (derived from equation (2) and $A_x(\lambda_{ex})$ = measured absorbance), and $\int_{\lambda_{Em}} F_s(\lambda_{Em})$ = area under the curve of the fluorescence measurement.

$$\Phi_F^i = \Phi_F^s \frac{f_s(\lambda_{Ex}) \int_{\lambda_{Em}} F_i(\lambda_{Em})}{f_i(\lambda_{Ex}) \int_{\lambda_{Em}} F_s(\lambda_{Em})} \quad (1)$$

$$f_x(\lambda_{Ex}) = 1 - 10^{-A_x(\lambda_{Ex})} \quad (2)$$

Table S1: Fluorescence quantum yields of **TAM1CF**.

	PBS	PBS + 10% FBS	PBS + 20% FBS	PBS + 40% FBS
TAM1CF	< 0.1 %	< 1 %	< 1 %	< 1 %

3 Transient Absorption Spectroscopy (TAS)

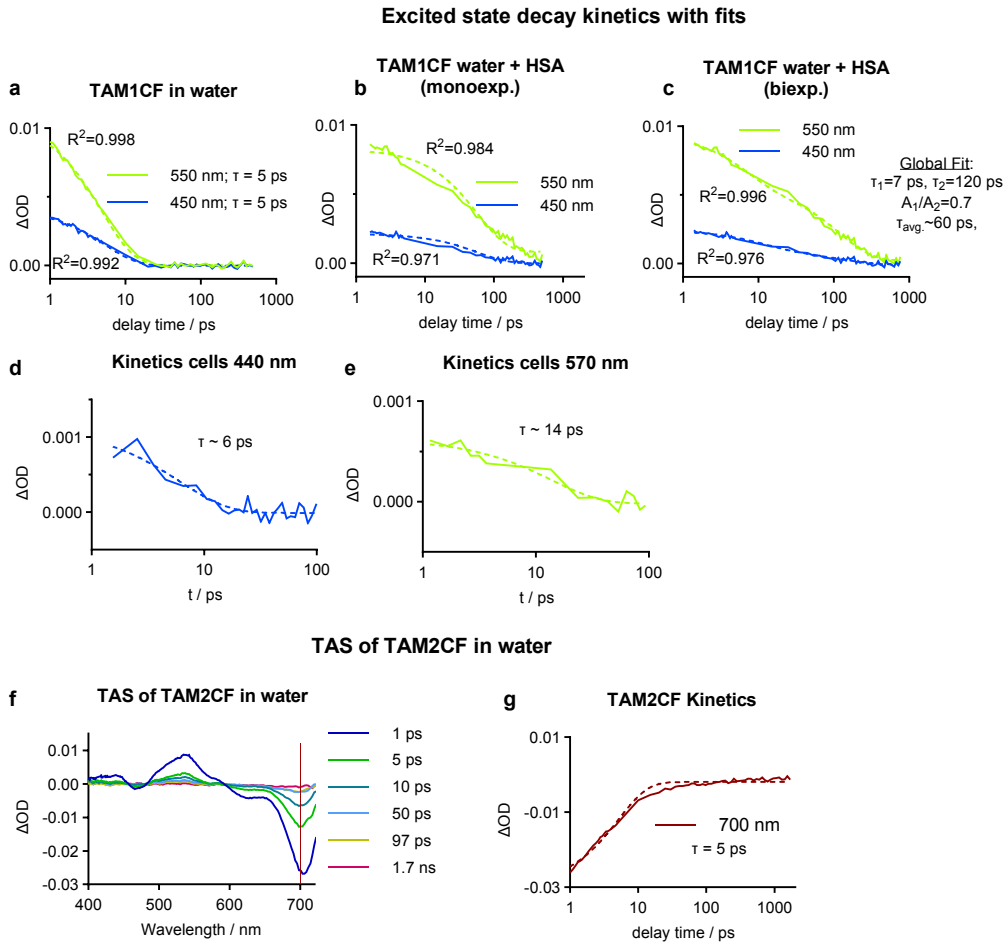


Figure S5. (a-f) Fits for excited state decay of **TAM1CF**: (a) monoexponentials (in water), (b) monoexponentials (in water with HSA), (c) biexponentials (in water + HSA), (d-e) monoexponentials (in cells). (f,g) Excited state decay of **TAM2CF** in water: (f) TAS spectra at selected delay times, (g) monoexponential fit. All fits as dotted lines.

The femtosecond-TA data were acquired on a custom-built setup. Briefly, a regenerative Ti:sapphire amplifier (Astrella, Coherent, USA) was used as the pump laser delivering pulses of 5 mJ pulse energy at 1 kHz pulse repetition rate. The output of the laser is divided by a beam splitter. The first part is focused into a rotating CaF_2 plate to generate a broadband white light supercontinuum beam covering 300 to 700 nm. This broadband pulse is subsequently split into two parts, which are used as reference and probe pulse. A second fraction of the Ti:Sa output is used to pump an optical parametric amplifier (TOPAS prime, Light conversion, Lithuania) for generating pump pulses of about 100 fs pulse duration (800 nm used). The output of the amplifier is tunable across the UV-Vis-NIR spectral range. The repetition rate of the pump pulses is then reduced to 500 Hz by a mechanical chopper. A Berek compensator and a polarizer are used to adjust the polarization difference of pump and the white light probe pulse to the magic angle of 54.7° . The probe pulse is focused into a quartz cuvette of 10 mm path length by a concave mirror of 500 mm focal length. The spectra of probe and reference pulses are acquired by a 150 mm focal length Czerny-Turner spectrograph (SP2150, Princeton Instruments) equipped with two CCD arrays (Pascher Instruments AB, Sweden). The TA data analysis was performed on data acquired after at least 150 fs delay time, and includes a spectral preprocessing to correct for the chirp of the broadband pulse. Solutions were acquired in a 1 mm cuvette at an OD between 0.1 and 0.2.

For the *in cellulo* experiments, single wavelength probes (440 nm and 570 nm) using a nonlinear optical parametric amplifier are employed instead of the white light probe. The cellular samples

(human breast cancer cell line MCF-7, pre-treated with 10 μM **TAM1CF** for 60 min in cell culture media) were measured in glass bottom μ -dishes (in 1 mL Hanks' balanced salt solution (HBSS)).

For white light measurements, data was corrected for the chirp using the Kimopack package.^[6]

All data was corrected by subtracting ΔAbs values measured before excitation ($\Delta t = -0.5$ ps). After spectral plotting for $\Delta\text{Abs}(t)$ (**Fig 3b,d; Fig S5**), we obtained the TA lifetimes by fitting single-wavelength-intercept data at $\lambda = 550$ nm (near the strong band maximum at 535 nm, well-formed region), and for plausibility comparing to data for 450 nm (saddle point between 535 and 430 nm bands, less well-formed) and occasionally also to data at 700 nm (within the ground state bleach band, but depending on the media it is close or occasionally overlapping with pump/probe spectral artifacts, therefore was not used). In cells, the corresponding wavelengths were 570 nm, compared to 450 nm, with 700 nm as a rough plausibility check only. Monoexponential fits were performed by default, except for **TAM1CF** in water + HSA where a biexponential was justified (see below). For consistency, we restricted all fits to the timespan 1 - 500 ps. This eliminates early ($t < 1$ ps) spectral evolutions that are not associated to the $S_1 \rightarrow S_0$ process that is of interest, and eliminates the late ($t > 500$ ps) time region in which noise dominates (since nearly all compound has relaxed to S_0). To check plausibility and robustness, we compared these to fit values obtained while additionally excluding 1-3 ps and/or 100-500 ps data.

For **TAM1CF** in water, monoexponential fits were excellent; forcing a global τ fit to both 550 nm and 450 nm data gives $\tau = 5$ ps, with $R^2 = 0.998$ & 0.992 respectively.

For **TAM1CF** in water + HSA, the monoexponential fits (550 nm: $\tau = 60$ ps, $R^2 = 0.984$; 450 nm: $\tau = 40$ ps, $R^2 = 0.971$; **global: $\tau = 60$ ps**, $R^2 = 0.984$ & 0.964) were not satisfactory, as it seemed that there were different systematic errors at shorter vs at longer times. Biexponentials fit the data better (550 nm: $\tau_1 = 7$ ps, $\tau_2 = 120$ ps, with pre-exponential factor ratio $A_1/A_2 = 0.7$; 450 nm: $\tau_1 = 12$ ps, $\tau_2 = 120$ ps, $A_1/A_2 = 1.3$; and **global fit to $\tau_1 = 7$ ps, $\tau_2 = 120$ ps, $A_1/A_2 = 0.7$** , with $R^2 = 0.996$ & 0.976) (**Fig S5c**). It seems reasonable that the fast τ corresponds to **TAM1CF** in free solution, and the slow τ to **TAM1CF** adsorbed on HSA (though for simplicity, **Fig 3** cites simply " $\tau_{\text{avg}} \sim 60$ ps").

Cell data was fitted monoexponentially. Its far greater noise level prevents higher-order fits from being justified, and also means that the cellular half-times (570 nm: 14 ps; 450 nm: 6 ps) should simply be taken as order of magnitude values: but these sufficed to indicate which environment the dye experiences in cells.

4 Photoacoustics

4.1 MSOT set-up and data acquisition

Phantom data were acquired^[7] using a commercially available MSOT scanner (MSOT256-TF, iThera Medical GmbH, Munich, Germany). Nanosecond-pulsed light was generated from a tunable optical parametric oscillator (OPO) laser and delivered to the sample through a ring-type fiber bundle. The wavelength range used for imaging was from 700 to 1050 nm, with a step size of 10 nm. The sample absorbs the light, generating an acoustic signal that propagates through the sample and is detected outside. In our experiments, we detected the acoustic signals using a cylindrically focused transducer consisting of 256 elements. The transducer array provided a coverage of 270° at multiple laser wavelengths. Optoacoustic images were reconstructed using a back-projection reconstruction method available in the viewMSOT software and subsequently analyzed using the same software.

To scan the dye samples,^[8,9] we used a cylindrical agar phantom equipped with 3 mm diameter holes for sample placement. The phantom was made up of 1.3% (w/w) agar (Sigma-Aldrich, St. Louis, MO, USA) to provide solidity, and 6% (v/v) intralipid emulsion (20%, Sigma-Aldrich) to ensure uniform illumination of the sample by light diffusion. The intralipid was added to decrease the scattering coefficient to 10 cm^{-1} , simulating scattering in biological tissue. To enable transversal

plane imaging at a single position, approximately in the middle of the phantom, MSOT data were acquired as described above and values plotted. Signal generation efficiency (SGE) was determined by linear regression (Fig S6).

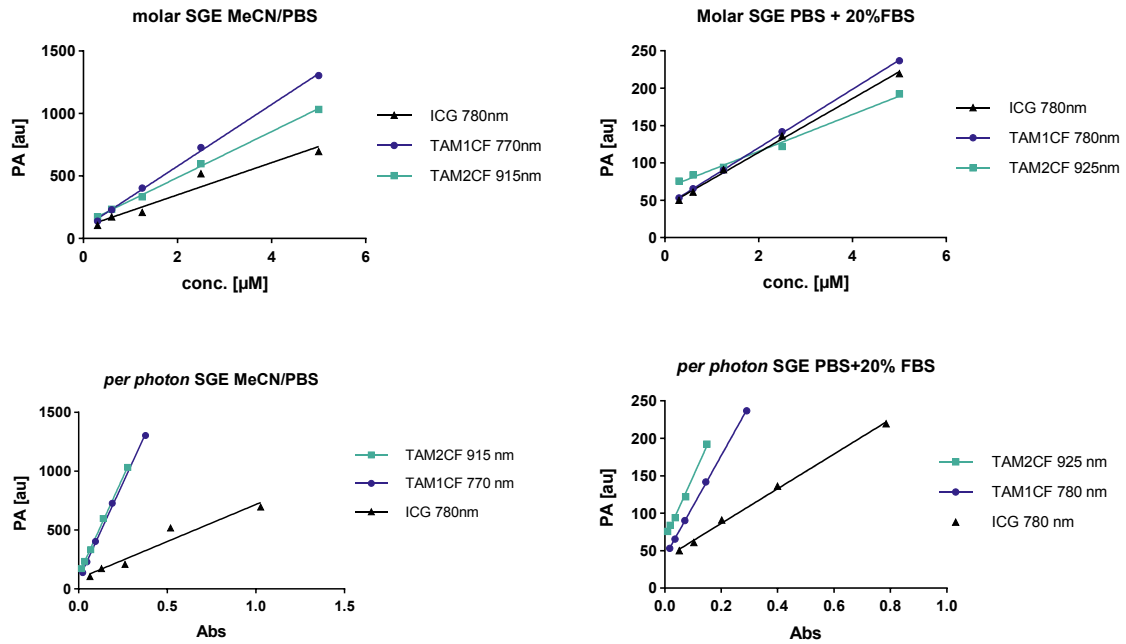


Figure S6. SGE determination by linear regression of PA signal plotted against concentration (molar SGE) or absorbance (per molecule SGE). Absorption spectra were measured for each sample before submitting to MSOT.

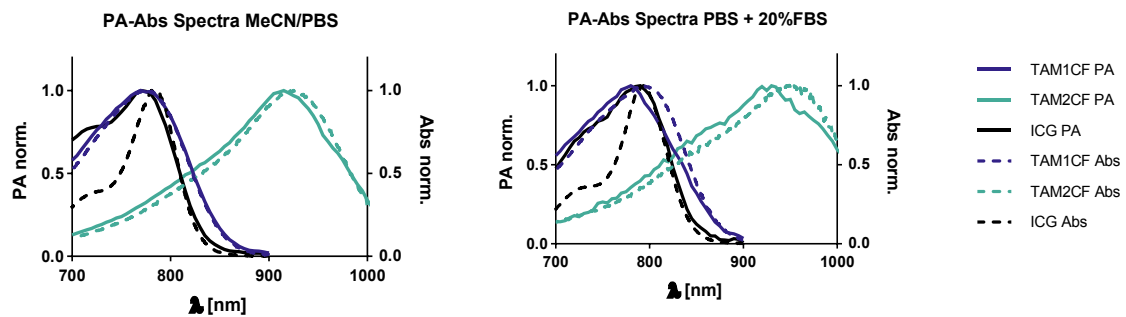


Figure S7. Overlay of absorption and PA spectra derived from 5 μM samples and normalized to the respective maximum.

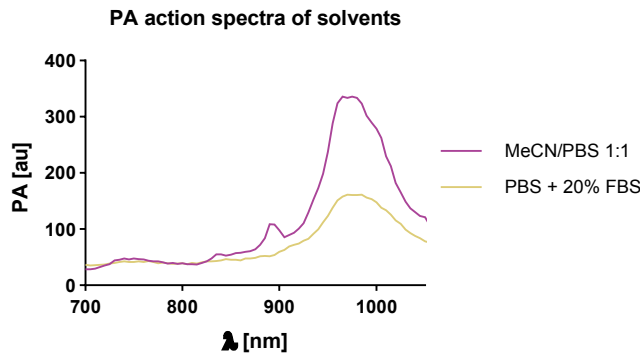


Figure S8. PA action spectra of solvents.

5 Chemical Synthesis

5.1 Materials and Methods

Reagents and conditions. Unless stated otherwise, (a) all reactions and characterisations were performed with unpurified, undried, non-degassed solvents and reagents, used as obtained, under closed air atmosphere without special precautions; (b) “hexane” used for chromatography was distilled from commercial crude isohexane fraction by rotary evaporation; (c) “flash column chromatography” refers to purification on a Biotage Selekt system, using prepacked silica or C18 cartridges purchased from Biotage or Phenomenex; (d) procedures and yields are unoptimized; (e) yields refer to isolated chromatographically and spectroscopically pure materials; (f) all eluent and solvent mixtures are given as volume ratios unless otherwise specified; (g) thin-layer chromatography (TLC) was run on 0.25 mm Merck silica gel plates (60, F-254) with UV light (254 nm) as a visualising agent.

Nuclear magnetic resonance (NMR) spectroscopy. Standard NMR characterisation was by ¹H- and ¹³C-NMR spectra on a Bruker Ascend 400, Bruker Ascend 500, Varian 600, Bruker Advance III HD 800. Chemical shifts (δ) are reported in ppm calibrated to residual non-perdeuterated solvent as an internal reference. Peak descriptions singlet (s), doublet (d), triplet (t), quartet (q), multiplet (m), and broad (br) are used. NMR spectra are given in the appendix at the end of this document.

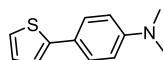
High resolution mass spectrometry (HRMS). HRMS used ESI ionisation on a Thermo Finnigan LTQ FT Ultra Fourier Transform Ion Cyclotron Resonance Spectrometer.

High performance liquid chromatography (HPLC) coupled to mass spectrometry (MS). Analytical HPLC-MS was performed on an Agilent 1100 SL with (a) a binary pump to deliver H₂O:MeCN eluent mixtures containing 0.1% formic acid at a 0.4 mL/min flow rate, (b) YMC-Triart C18 column (3.0 μm; 50 mm × 3 mm) maintained at 40 °C, (c) an Agilent 1100 series diode array detector, (d) an Agilent LC/MSD iQ mass spectrometer. Typical run conditions were: method A: a linear gradient of H₂O:MeCN from 90:10 to 0:100 (first 5 min), then 0:100 for 2 min for flushing; then the column was (re)equilibrated with 90:10 eluent mixture for 2 min; method B: a linear gradient of H₂O:MeCN from 50:50 to 0:100 (first 10 min), then 0:100 for 2 min for flushing; then the column was (re)equilibrated with 50:50 eluent mixture for 2 min.

Preparative HPLC. Preparative HPLC was performed on an Agilent 1200 SL with (a) a binary pump to deliver H₂O:MeCN eluent mixtures containing 0.1% TFA at 20 mL/min flow rate, (b) Agilent-Zorbax C18 column (10.0 μm; 250 mm × 30 mm) maintained at room temperature, (c) an Agilent 1200 series diode array detector, and (d) Agilent 1200 series fraction collector. Typical run conditions were a linear gradient of H₂O:MeCN from 90:10 to 0:100 within 25 minutes, then 0:100 for 5 min for flushing.

5.2 Synthetic Procedures

N,N-dimethyl-4-(thiophen-2-yl)aniline (S1) (known)^[10]



The compound was synthesized according to a modified literature procedure.^[10]

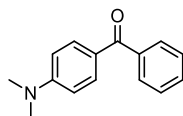
A pressure tube was charged with 2-bromothiophene (0.64 mL, 6.6 mmol, 1.0 eq), 4-(*N,N*-dimethylamino)phenylboronic acid (1.3 g, 7.9 mmol, 1.2 eq), Na₂CO₃ (1.09 g, 13.1 mmol, 2.0 eq), THF (27 mL), H₂O (3 mL) and purged with N₂. Tetrakis(triphenylphosphine)palladium (190 mg, 0.16 mmol, 0.025 eq) was added, the pressure tube was sealed, and the reaction mixture was stirred at 70 °C for 20 h. The reaction mixture was partitioned between EtOAc (200 mL) and brine

(200 mL), the organic layer washed with brine (2 × 200 mL) dried over Na₂SO₄, filtered and concentrated. The crude product was purified by flash chromatography (gradient: hexane/EtOAc, 1:0 to 9:1) to afford **S1** (1.13 g, 5.6 mmol, 85 %) as a colourless solid.

¹H NMR (400 MHz, CDCl₃) δ 7.49 (d, *J* = 8.9 Hz, 2H), 7.19 – 7.12 (m, 2H), 7.07 – 6.98 (m, 1H), 6.73 (d, *J* = 8.8 Hz, 2H), 2.98 (s, 6H).

Spectral data match literature data.^[10]

(4-(dimethylamino)phenyl)(phenyl)methanone (**S2**) (known)^[11]



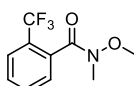
The compound was synthesized according to a modified literature procedure.^[11]

A flame dried flask was charged with 4-bromo-*N,N*-dimethylaniline (254 mg, 1.5 mmol, 1.0 eq) and THF (7 mL), then cooled to -78°C and *n*-butyllithium (0.60 mL, 2.5 M in hexanes, 1.0 eq) was added dropwise. The mixture was stirred at -78°C for 15 minutes and *N*-methoxy-*N*-methylbenzamide (248 mg, 1.5 mmol, 1.0 eq) was added as solution in THF (2 mL) and the reaction mixture was stirred at -78°C for 30 minutes, warmed up to rt and quenched with *st.* NH₄Cl solution. The mixture was extracted with EtOAc (2 × 20 mL), the organic layer washed with brine (20 mL), dried over Na₂SO₄, filtered and concentrated. The crude product was purified by flash chromatography (gradient: hexane/EtOAc, 95:5 to 75:25) to afford **S2** (251 mg, 1.1 mmol, 74 %) as a colourless solid.

¹H NMR (400 MHz, CDCl₃) δ 7.80 (d, *J* = 9.1 Hz, 2H), 7.76 – 7.69 (m, 2H), 7.56 – 7.50 (m, 1H), 7.48 – 7.41 (m, 2H), 6.68 (d, *J* = 9.1 Hz, 2H), 3.08 (s, 6H).

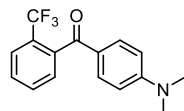
Spectral data match literature data.^[11]

N-methoxy-*N*-methyl-2-(trifluoromethyl)benzamide (**S3**) (known)^[12]



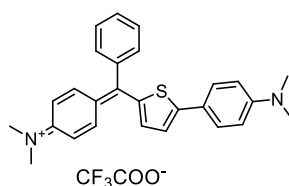
Oxalyl chloride (0.47 mL, 5.5 mmol, 1.1 eq) and one drop of DMF were added to a suspension of 2-(trifluoromethyl)benzoic acid in CH₂Cl₂ (25 mL) at 0°C. The mixture was stirred at room temperature for 2 h and the suspension became a clear solution. The reaction mixture was cooled in an ice bath to 0°C and *N,O*-dimethylhydroxylamine hydrochloride (0.54 g, 5.0 mmol, 1.0 eq) was added in one portion followed by dropwise addition of pyridine (0.89 mL, 11 mmol, 2.0 eq). The ice bath was removed, the reaction mixture stirred for 3 h and quenched with *st.* NH₄Cl solution. The mixture was extracted with CH₂Cl₂ (2 × 50 mL), the organic layer washed with brine (50 mL), dried over Na₂SO₄, filtered and concentrated. The crude product was purified by flash chromatography (gradient: hexane/EtOAc, 95:5 to 60:40) to afford **S3** (325 mg, 1.4 mmol, 28 %) as a colourless oil.

¹H NMR (400 MHz, CDCl₃) δ 7.68 (d, *J* = 7.8 Hz, 1H), 7.64 – 7.49 (m, 2H), 7.41 (dd, *J* = 7.4, 1.4 Hz, 1H), 3.88 (br, 0.6H), 3.41 (s, 2.4H), 3.36 (s, 2.4H), 3.04 (br, 0.6H). **¹³C NMR** (101 MHz, CDCl₃) δ 169.65, 134.05, 134.03, 131.54, 129.37, 127.87, 127.55, 127.37, 126.64, 126.60, 125.14, 122.42, 61.09, 32.73 (*observed complexity due to C-F coupling*). **¹⁹F NMR** (376 MHz, CDCl₃) δ -60.0. *Spectral data match literature data^[12] with slight differences for ¹³C spectrum due to a higher resolution spectrometer.*

(4-(dimethylamino)phenyl)(2-(trifluoromethyl)phenyl)methanone (S4)

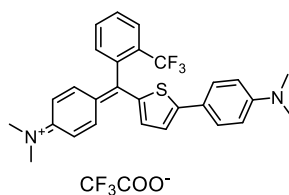
A flame dried flask was charged with 4-bromo-*N,N*-dimethylaniline (110 mg, 0.55 mmol, 1.1 eq) and THF (2 mL), then cooled to -78°C and *n*-butyllithium (0.22 mL, 2.5 M in hexanes, 0.55 mmol, 1.0 eq) was added dropwise. The mixture was stirred at -78°C for 15 minutes and **S3** (117 mg, 0.5 mmol, 1.0 eq) was added as solution in THF (1 mL) and the reaction mixture was stirred at -78°C for 30 minutes, warmed up to rt and quenched with *st.* NH_4Cl solution. The mixture was extracted with EtOAc (2×20 mL), the organic layer washed with brine (20 mL), dried over Na_2SO_4 , filtered and concentrated. The crude product was purified by flash chromatography (gradient: hexane/EtOAc, 90:10 to 60:40) to afford **S4** (58 mg, 0.20 mmol, 40 %) as a colourless solid.

^1H NMR (400 MHz, CDCl_3) δ 7.77 – 7.73 (m, 1H), 7.67 (d, $J = 9.0$ Hz, 2H), 7.62 – 7.52 (m, 2H), 7.39 – 7.34 (m, 1H), 6.67 (d, $J = 9.2$ Hz, 2H), 3.07 (s, 6H). **^{13}C NMR** (101 MHz, CDCl_3) δ 193.72, 153.74, 139.57, 132.72, 131.38, 129.19, 128.29, 128.24, 127.92, 126.63, 126.58, 125.25, 124.93, 122.53, 111.04, 40.38 (observed complexity due to C-F coupling). **^{19}F NMR** (376 MHz, CDCl_3) δ -58.28. **HRMS** for $\text{C}_{16}\text{H}_{14}\text{F}_3\text{NO}$ [MH^+] calc. 294.1101, found 294.1101.

TAM1H

A flame dried flask was charged with **S1** (35 mg, 0.17 mmol, 1.1 eq) and THF (1 mL), then cooled to -78°C and *n*-butyllithium (63 μL , 0.16 mmol, 2.5 M in hexanes, 1.0 eq) was added dropwise. The mixture was stirred at -78°C for 1 h and **S2** (35 mg, 0.16 mmol, 1.0 eq) was added as solution in THF (1mL) and the reaction mixture was stirred at -78°C for 30 minutes, warmed up to rt and quenched with *st.* NH_4Cl solution, and stirred 15 minutes. The mixture was extracted with CH_2Cl_2 (2×20 mL), the organic layer washed with brine (20 mL), dried over Na_2SO_4 , filtered and concentrated. The crude product was purified by reverse phase flash chromatography (gradient: $\text{H}_2\text{O}/\text{MeCN} + 0.05\%$ TFA, 95:5 to 75:25) to afford **TAM1H** (18 mg, 44 μmol , 28 %) as a blue solid.

^1H NMR (599 MHz, CD_3CN) δ 7.79 (d, $J = 4.7$ Hz, 1H), 7.78 – 7.75 (m, 2H), 7.75 – 7.72 (m, 1H), 7.70 (d, $J = 4.7$ Hz, 1H), 7.64 – 7.60 (m, 4H), 7.52 – 7.49 (m, 2H), 7.01 (d, $J = 9.5$ Hz, 2H), 6.82 (d, $J = 9.1$ Hz, 2H), 3.32 (s, 6H), 3.11 (s, 6H). **^{13}C NMR** (151 MHz, CD_3CN) δ 166.68, 158.20, 154.47, 147.11, 140.59, 140.56, 140.27, 134.44, 133.58, 130.15, 129.52, 129.48, 128.17, 127.77, 120.35, 115.49, 113.33, 41.53, 40.47. **HRMS** for $\text{C}_{27}\text{H}_{29}\text{N}_2\text{OS}$ [M^+] calc. 429.1995, found 429.1995.

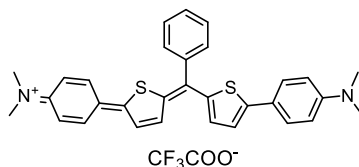
TAM1CF

A flame dried flask was charged with **S1** (52 mg, 0.27 mmol, 1.5 eq) and THF (2 mL), then cooled to 0°C and lithium diisopropylamide solution (0.13 mL, 0.27 mmol, 2.0 M in THF/heptane/ethylbenzene, 1.5 eq) was added dropwise. The mixture was stirred at 0°C for 30 min and then added dropwise to a solution of **S4** (55 mg, 0.17 mmol, 1.0 eq) in THF (1 mL) at 0°C. The reaction mixture was stirred at 0°C for 30 minutes, quenched with *st.* NH₄Cl solution, and stirred 15 minutes (deep blue colour formation). The mixture was extracted with CH₂Cl₂ (2 × 20 ml), the organic layer washed with brine (20 ml), dried over Na₂SO₄, filtered and concentrated. The crude product was purified by reverse phase flash chromatography (gradient: H₂O/MeCN + 0.05% TFA, 95:5 to 75:25) to afford **TAM1CF** (56 mg, 0.12 mmol, 69 %) as a blue solid.

¹H NMR (500 MHz, MeOD-*d*₄) δ 8.03 – 7.93 (m, 1H), 7.88 – 7.79 (m, 4H), 7.76 (d, *J* = 4.8 Hz, 1H), 7.67 (d, *J* = 9.2 Hz, 2H), 7.54 – 7.47 (m, 2H), 7.09 (d, *J* = 9.3 Hz, 2H), 6.87 (d, *J* = 9.0 Hz, 2H), 3.40 (s, 6H), 3.17 (s, 6H). **¹³C NMR** (126 MHz, MeOD-*d*₄) δ 171.50, 160.23, 158.64, 155.39, 147.38, 140.19, 139.47, 138.20, 133.65, 133.39, 132.04, 130.95, 130.69 (q, *J* = 30.6 Hz), 128.16 (q, *J* = 4.8 Hz), 127.78, 127.73, 125.11 (q, *J* = 273.9 Hz), 121.22, 116.27, 113.83, 41.41, 40.44. **¹⁹F NMR** (376 MHz, MeOD) δ -59.45. **HRMS** C₂₈H₂₆N₂F₃S₂ [M⁺] calc. 479.1764, found 479.1758.

Note on ¹³C spectrum: Assignments for CF₃ signals/coupling performed analogously to ref¹³¹.

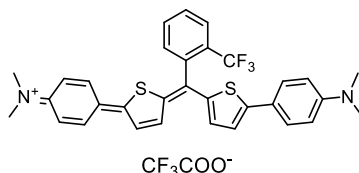
TAM2H



A flame dried flask was charged with **S1** (50 mg, 0.25 mmol, 2.5 eq) and THF (2 mL), then cooled to 0°C and lithium diisopropylamide solution (0.10 mL, 0.25 mmol, 2.0 M in THF/heptane/ethylbenzene, 2.5 eq) was added dropwise. The mixture was stirred at 0°C for 30 min and benzoyl chloride (11 μL, 0.10 mmol, 1.0 eq) dissolved in THF (1 mL) was added dropwise at 0°C. The reaction mixture was stirred at 0°C for 30 minutes, quenched with *st.* NH₄Cl solution, and stirred 15 minutes (deep green colour formation). The mixture was extracted with CH₂Cl₂ (2 × 20 mL), the organic layer washed with brine (20 mL), dried over Na₂SO₄, filtered and concentrated. The crude product was purified by reverse phase flash chromatography (gradient: H₂O/MeCN + 0.05% TFA, 95:5 to 75:25) to afford **TAM2H** (29 mg, 0.059 mmol, 60 %) as dark green solid.

¹H NMR (400 MHz, CDCl₃) δ 7.75 (d, *J* = 9.1 Hz, 4H), 7.68 – 7.63 (m, 1H), 7.61 – 7.59 (m, 2H), 7.58 – 7.55 (m, 2H), 7.54 – 7.50 (m, 2H), 7.48 – 7.44 (m, 2H), 6.83 (d, *J* = 9.1 Hz, 4H), 3.18 (s, 12H). **¹³C NMR** (101 MHz, CDCl₃) δ 169.45, 153.83, 152.69, 145.83, 139.41, 138.06, 131.74, 131.67, 130.45, 128.86, 127.24, 120.93, 113.44, 40.84. **HRMS** C₃₁H₂₉N₂S₂ [M⁺] calc. 493.1767, found 493.1760.

TAM2CF



A flame dried flask was charged with **S1** (45 mg, 0.22 mmol, 2.2 eq) and THF (2 mL), then cooled to 0°C and lithium diisopropylamide solution (0.13 mL, 0.25 mmol, 2.0 M in THF/heptane/ethylbenzene, 2.5 eq) was added dropwise. The mixture was stirred at 0°C for 30 min and methyl 2-(trifluoromethyl)benzoate (20 mg, 0.10 mmol, 1.0 eq) dissolved in THF (1 mL) was added dropwise at 0°C. The reaction mixture was stirred at 0°C for 30 minutes, quenched with *st.*

NH₄Cl solution, and stirred 15 minutes (deep green colour formation). The mixture was extracted with CH₂Cl₂ (2 × 20 mL), the organic layer washed with brine (20 mL), dried over Na₂SO₄, filtered and concentrated. The crude product was purified by reverse phase flash chromatography (gradient: H₂O/MeCN + 0.05% TFA, 95:5 to 75:25) to afford **TAM2CF** (35 mg, 0.062 mmol, 62 %) as dark green solid.

¹H NMR (599 MHz, MeOD-*d*₄) δ 8.02 – 7.96 (m, 1H), 7.91 – 7.82 (m, 6H), 7.69 (d, *J* = 4.9 Hz, 2H), 7.63 – 7.57 (m, 1H), 7.28 (d, *J* = 4.9 Hz, 2H), 6.93 (d, *J* = 9.2 Hz, 4H), 3.22 (s, 12H). **¹³C NMR** (151 MHz, MeOD-*d*₄) δ 170.52, 155.99, 147.64, 146.70, 139.81, 136.62, 133.62, 133.49, 131.90, 131.76, 130.51 (d, *J* = 30.5 Hz), 128.20 (q, *J* = 4.3 Hz), 127.94, 125.19 (d, *J* = 273.7 Hz), 121.72, 114.28, 40.61. **¹⁹F NMR** (376 MHz, MeOD) δ -59.83. **HRMS** C₃₂H₂₈F₃N₂S₂ [M⁺] calc. 561.1641, found 561.1634.

Note on ¹³C spectrum: Expected quartets from CF₃ coupling were observed as doublets because of low signal intensity. Assignments for CF₃ signals/coupling performed analogously to ref¹³.

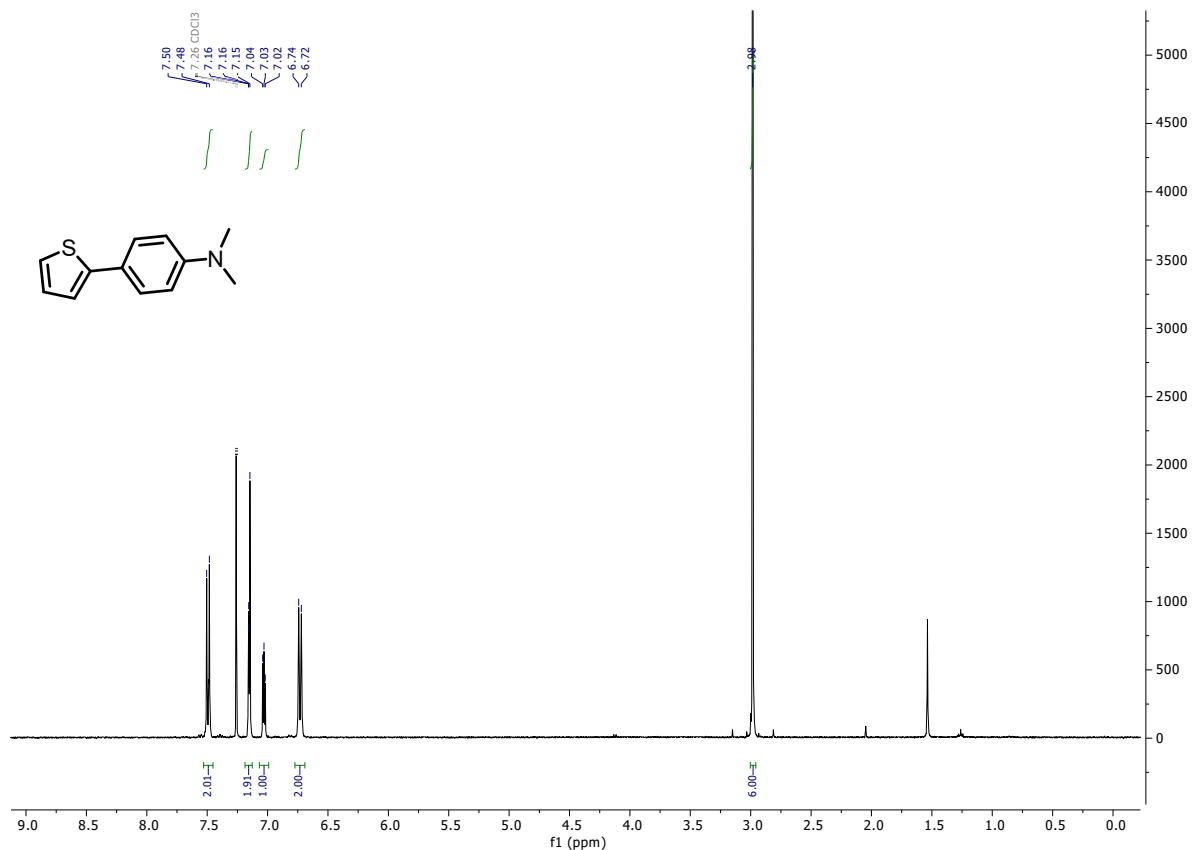
6 References

- [1] F. Brøndsted, H. Shield, J. Moore, X. Zhou, Y. Fang, C. Stains, **2024**, DOI 10.26434/chemrxiv-2024-7cbk2.
- [2] S. H. Gardner, C. J. Brady, C. Keeton, A. K. Yadav, S. C. Mallojjala, M. Y. Lucero, S. Su, Z. Yu, J. S. Hirschi, L. M. Mirica, J. Chan, *Angew. Chem. Int. Ed.* **2021**, *60*, 18860–18866.
- [3] S. Zhang, H. Chen, L. Wang, X. Qin, B.-P. Jiang, S.-C. Ji, X.-C. Shen, H. Liang, *Angew. Chem. Int. Ed.* **2021**, *61*, e202107076.
- [4] M. Müller, N. Liu, V. Gujrati, A. Valavalkar, S. Hartmann, P. Anzenhofer, U. Klemm, A. Telek, B. Dietzek-Ivanšić, A. Hartschuh, V. Ntziachristos, O. Thorn-Seshold, *Angew Chem Int Ed* **2024**, e202405636.
- [5] C. Xu, R. Ye, H. Shen, J. W. Y. Lam, Z. Zhao, B. Z. Tang, *Angew. Chem. Int. Ed.* **2022**, *61*, e202204604.
- [6] C. Müller, T. Pascher, A. Eriksson, P. Chabera, J. Uhlig, *J. Phys. Chem. A* **2022**, *126*, 4087–4099.
- [7] D. Razansky, A. Buehler, V. Ntziachristos, *Nat Protoc* **2011**, *6*, 1121–1129.
- [8] V. Gujrati, J. Prakash, J. Malekzadeh-Najafabadi, A. Stiel, U. Klemm, G. Mettenleiter, M. Aichler, A. Walch, V. Ntziachristos, *Nat Commun* **2019**, *10*, 1114.
- [9] N. Beziere, N. Lozano, A. Nunes, J. Salichs, D. Queiros, K. Kostarelos, V. Ntziachristos, *Biomaterials* **2015**, *37*, 415–424.
- [10] M. Zajac, P. Hrobárik, P. Magdolen, P. Foltínová, P. Zahradník, *Tetrahedron* **2008**, *64*, 10605–10618.
- [11] H. J. A. Dale, C. Nottingham, C. Poree, G. C. Lloyd-Jones, *J. Am. Chem. Soc.* **2021**, *143*, 2097–2107.
- [12] J. R. Martinelli, D. A. Watson, D. M. M. Freckmann, T. E. Barder, S. L. Buchwald, *J. Org. Chem.* **2008**, *73*, 7102–7107.
- [13] D. Doddrell, M. Barfield, W. Adcock, M. Aurangzeb, D. Jordan, *J. Chem. Soc., Perkin Trans. 2* **1976**, 402–412.

7 NMR Spectra

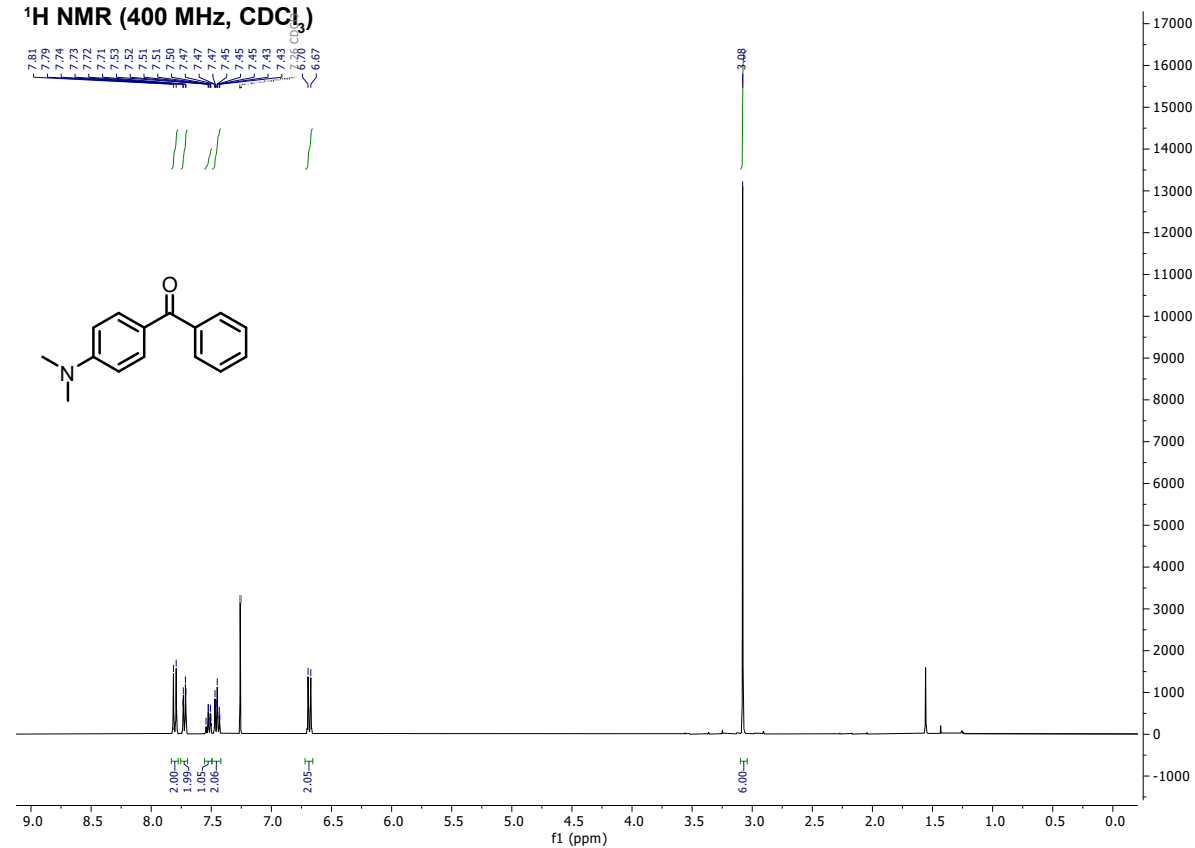
S1

¹H NMR (400 MHz, CDCl₃)



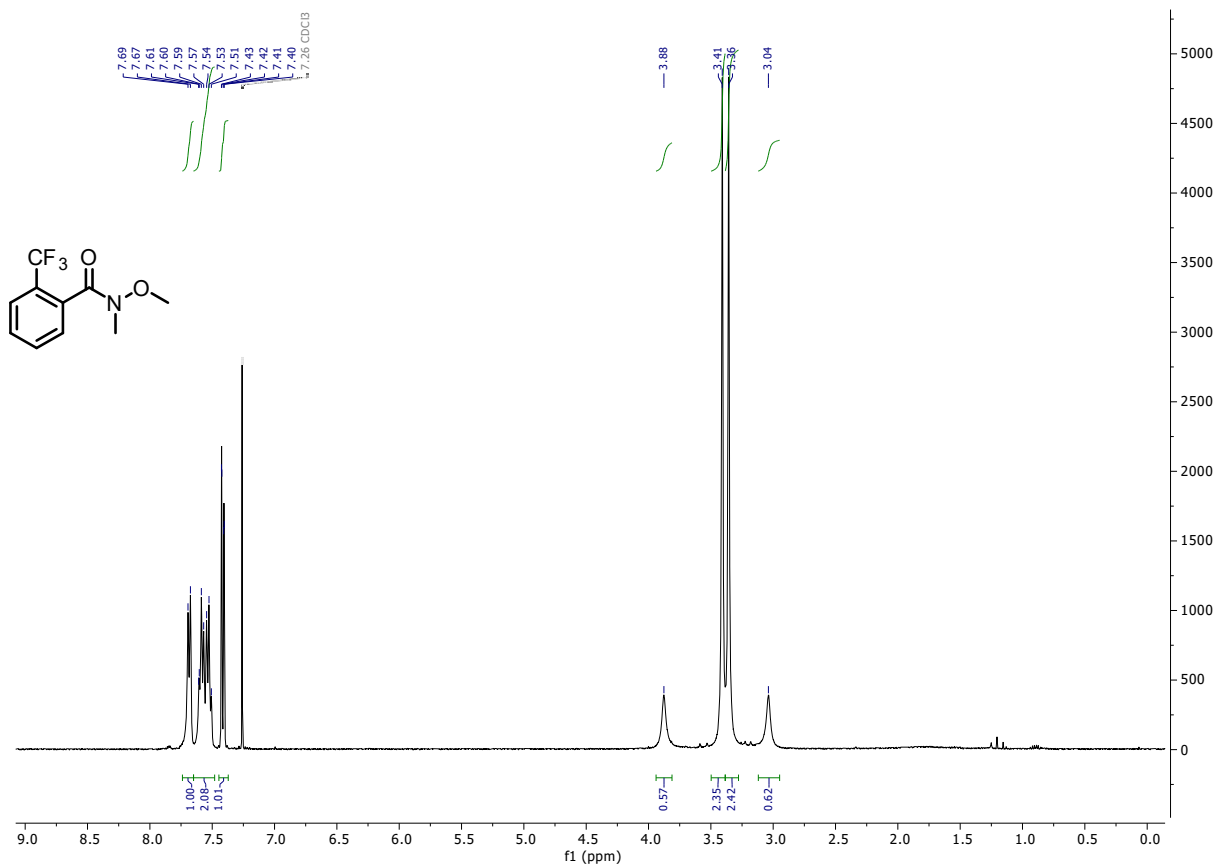
S2

¹H NMR (400 MHz, CDCl₃)

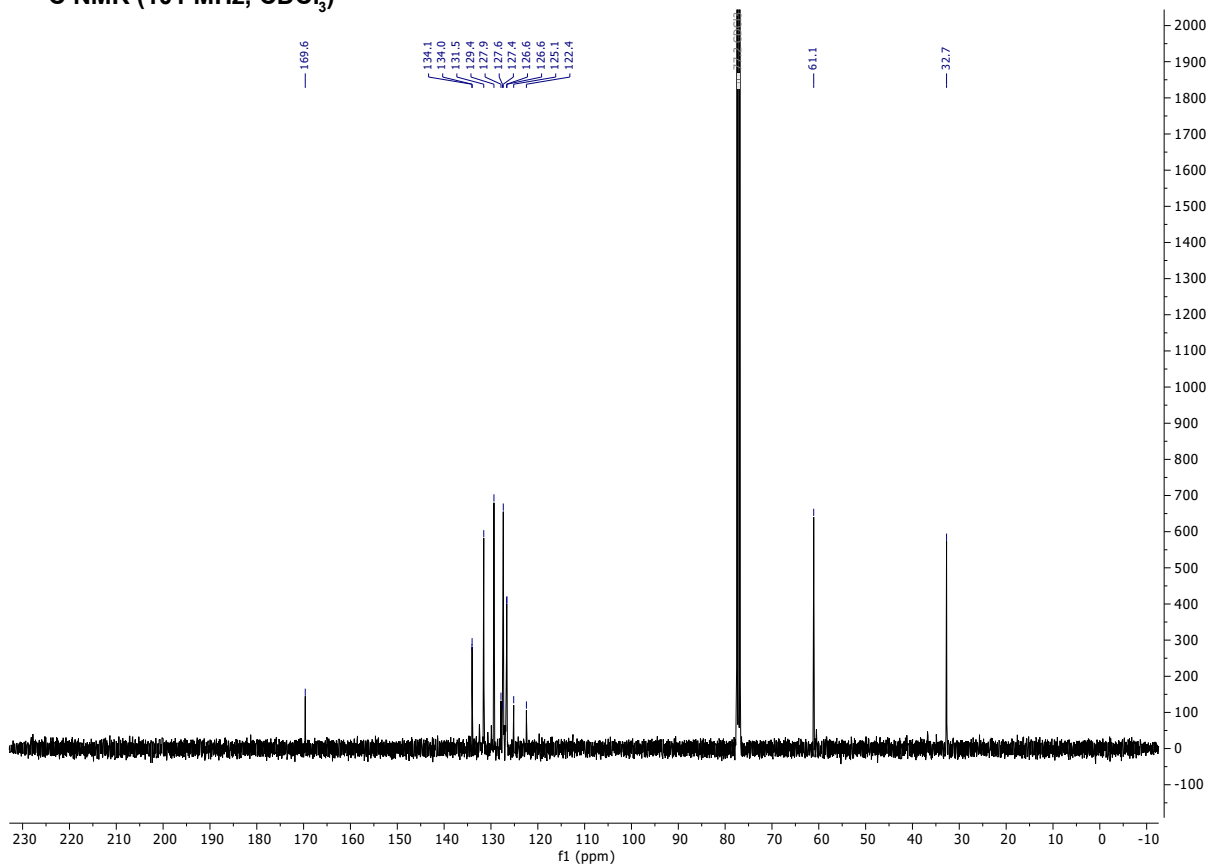


S3

¹H NMR (400 MHz, CDCl₃)

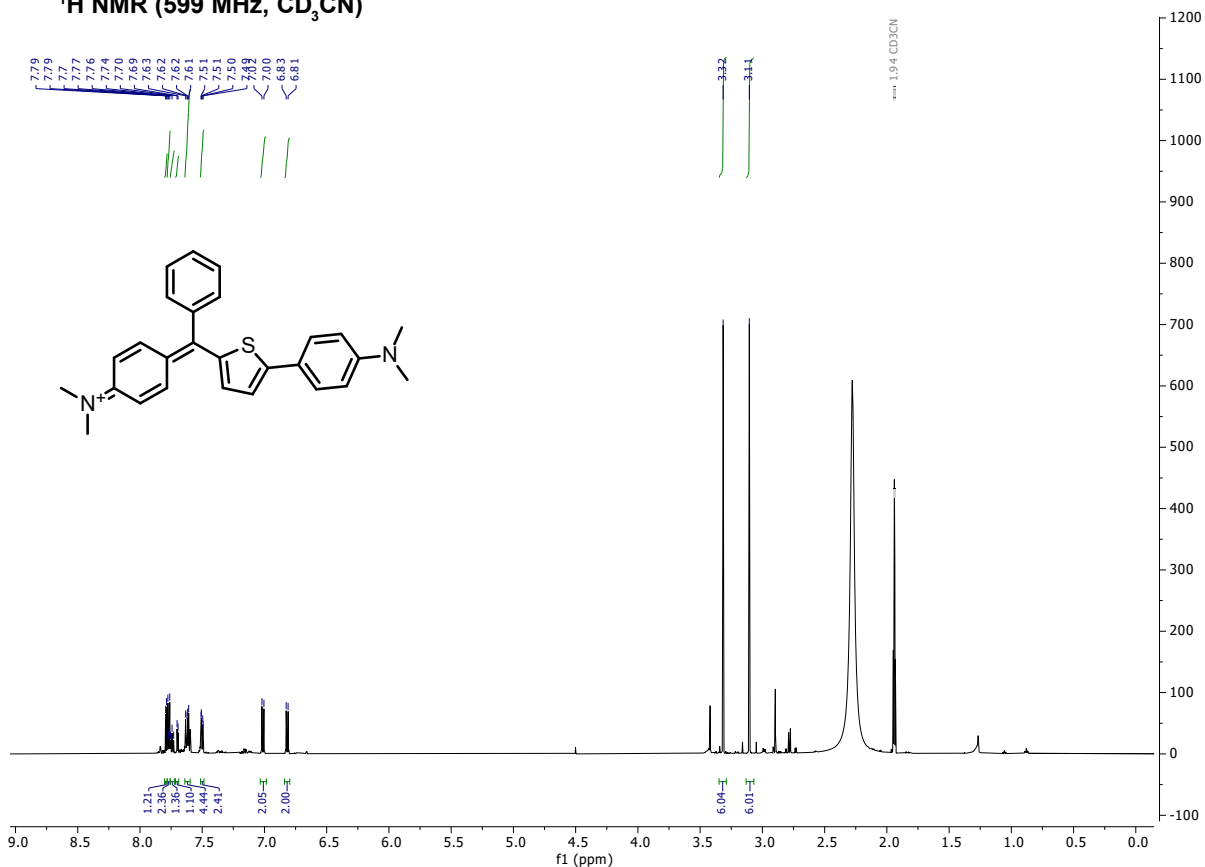


¹³C NMR (101 MHz, CDCl₃)

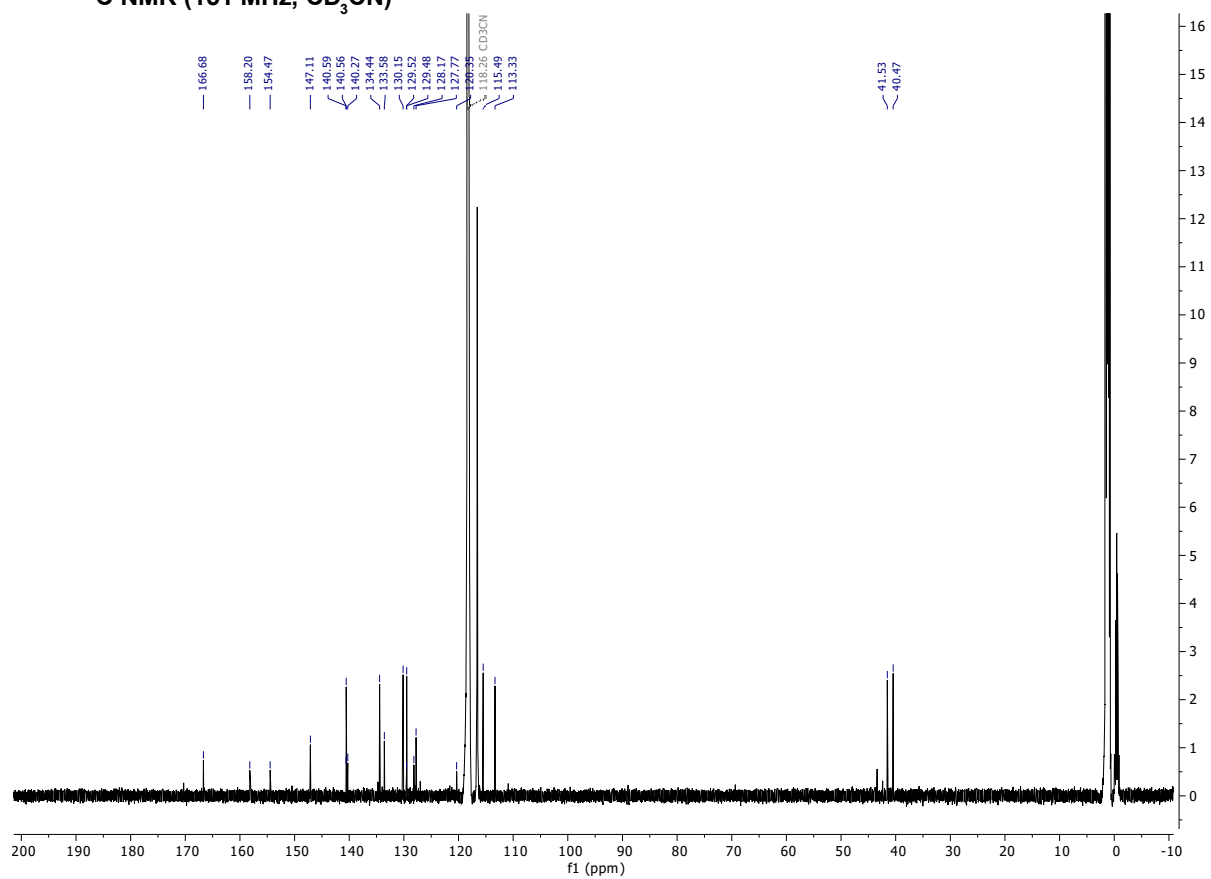


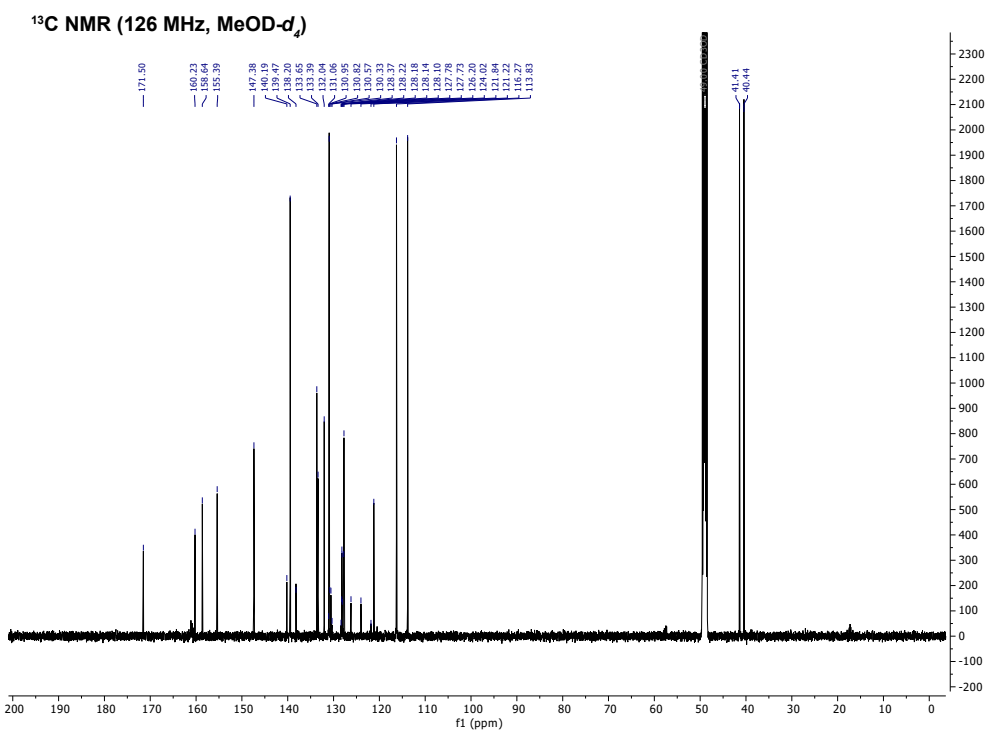
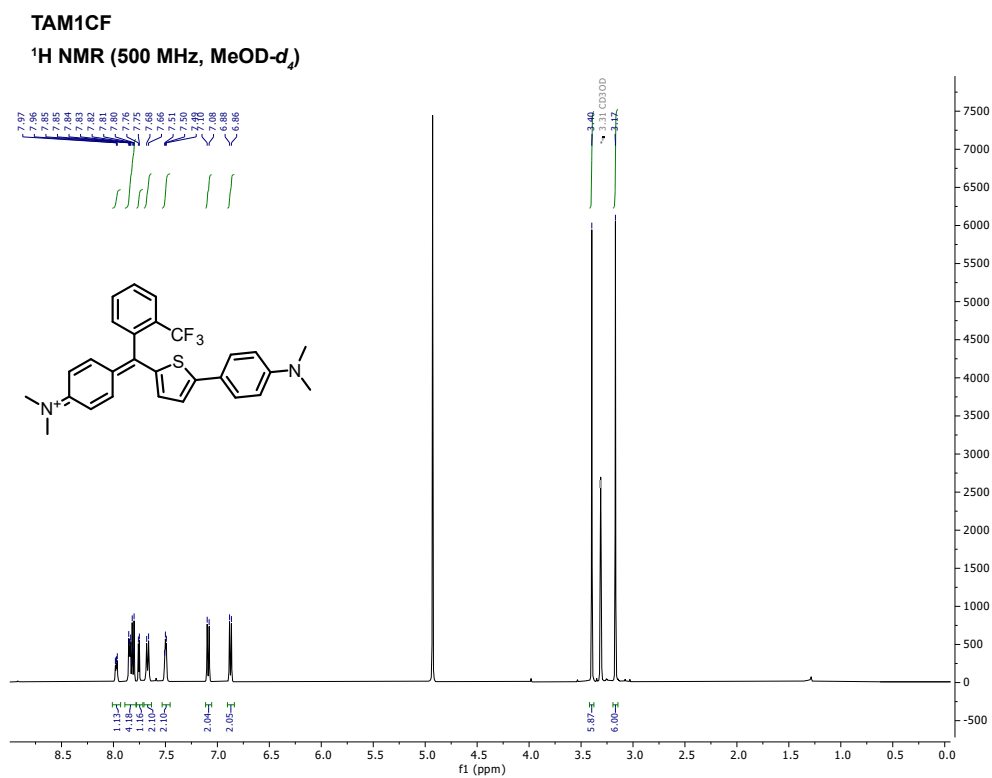
TAM1H

¹H NMR (599 MHz, CD₃CN)



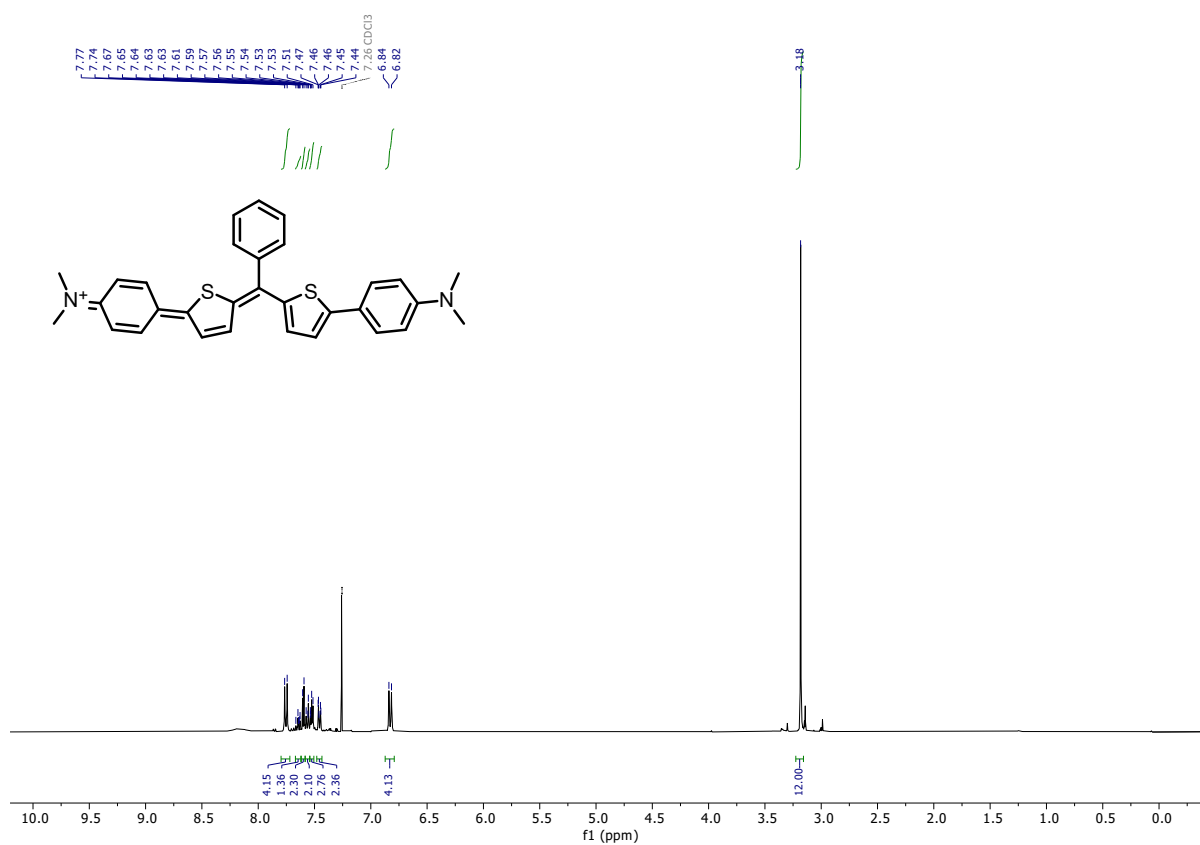
¹³C NMR (151 MHz, CD₃CN)



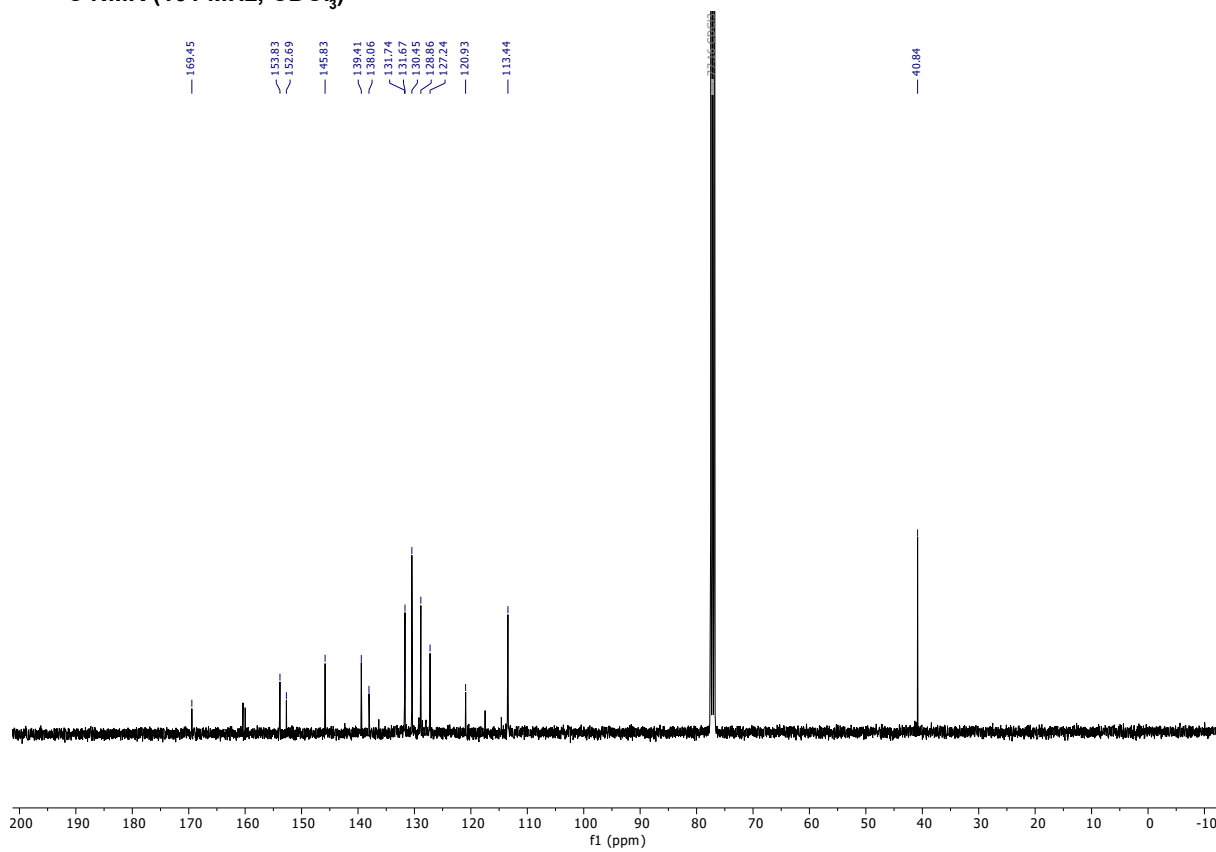


TAM2H

¹H NMR (400 MHz, CDCl₃)

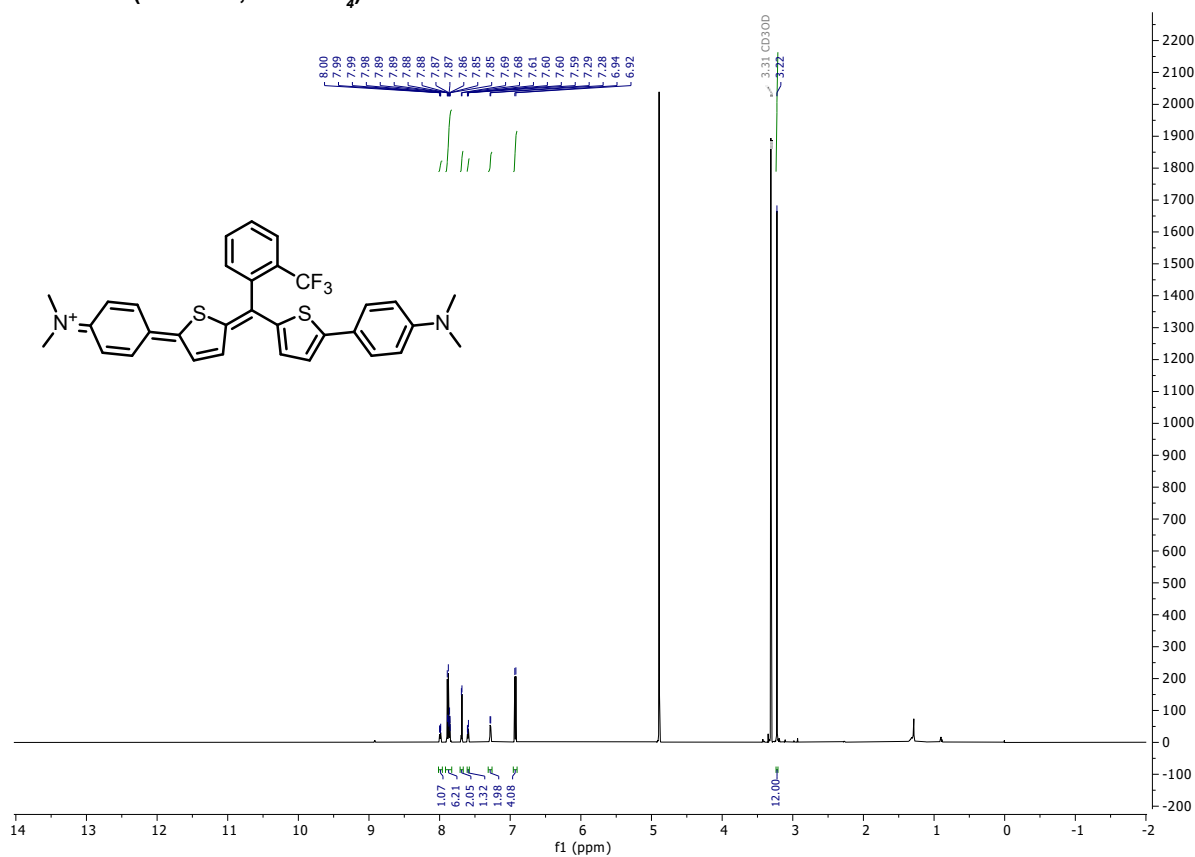


¹³C NMR (101 MHz, CDCl₃)



TAM2CF

¹H NMR (600 MHz, MeOD-d₄)



Supporting Information

BTDAzo: A Photoswitchable TRPC5 Channel Activator

*M. Müller, K. Niemeyer, N. Urban, N. K. Ojha, F. Zufall, T. Leinders-Zufall, M. Schaefer, O. Thorn-Seshold**

Supporting Information

Table of contents

Materials and Methods Chemistry	2
Synthetic procedures	4
Synthesis of Precursors	4
Synthesis of btda1-7	11
Photocharacterization	15
Solvent dependent photoisomerization of BTDAzo	16
Relaxation of BTDAzo.....	17
PSS spectra of btda1-7	18
Cell biology	20
FLIPR assays of btdas reveal good photoswitchability of Ca ²⁺ currents with btda3.....	22
Photoswitch-on and Photoswitch-off: extended characterisations	23
<i>E</i> -BTDAzo antagonises channel activation by BTD.....	25
btda compounds do not activate TRPC4.....	26
Mouse experiments	26
HPLC & NMR Spectra	32
References	54
High-Resolution Copies of all Main Text figures	55

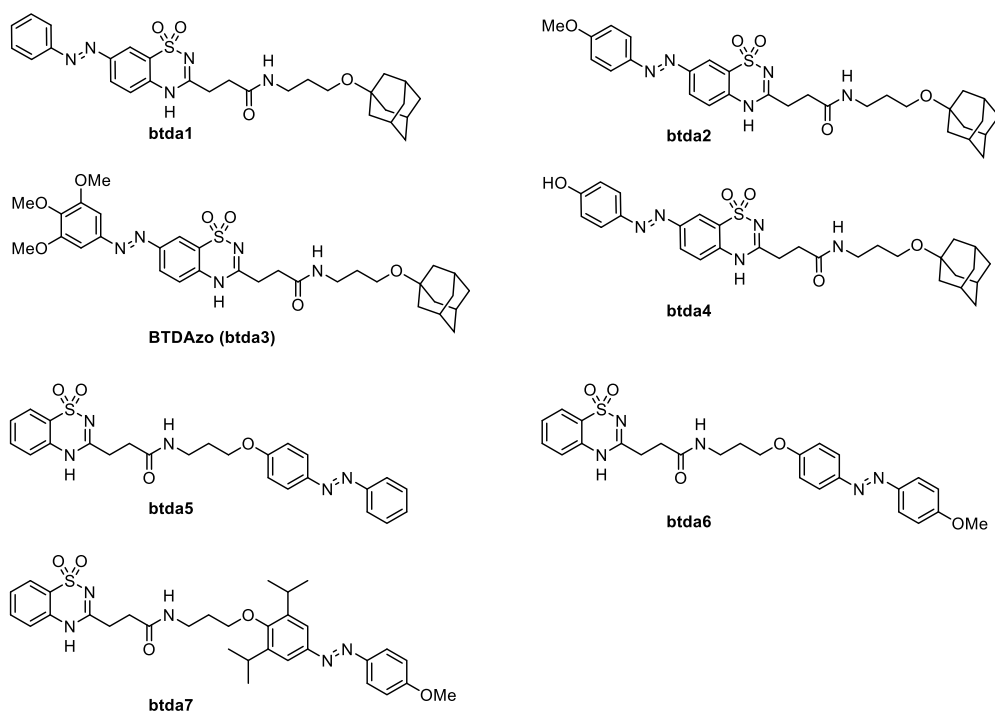


Figure S1. Structures of btda1-7.

Materials and Methods Chemistry

Reagents and Conditions. Unless stated otherwise, (a) all reactions and characterisations were performed with unpurified, undried, non-degassed solvents and reagents, used as obtained, under closed air atmosphere without special precautions; (b) "hexane" used for chromatography was distilled from commercial crude isohexane fraction by rotary evaporation; (c) "column" and "chromatography" refer to manual flash column chromatography on Merck silica gel Si-60 (40–63 μm); (d) "MPLC" refers to flash column chromatography purification on a Biotage Selekt system, using prepacked silica cartridges purchased from Biotage; (e) procedures and yields are unoptimized; (f) yields refer to isolated chromatographically and spectroscopically pure materials; (g) all eluent and solvent mixtures are given as volume ratios unless otherwise specified. (h) Thin-layer chromatography (TLC) was run on 0.25 mm Merck silica gel plates (60, F-254). UV light (254 nm) was used as a visualising agent. (i) "st" or "sat. aq." refer to saturated aqueous solutions of the given salt.

Nuclear magnetic resonance (NMR) spectroscopy. Standard NMR characterisation was by ^1H - and ^{13}C -NMR spectra on a Bruker Ascend 400 (400 MHz & 101 MHz for ^1H and ^{13}C respectively) and on a Bruker Ascend 500 (500 MHz & 126 MHz for ^1H and ^{13}C respectively). Chemical shifts (δ) are reported in ppm calibrated to residual non-perdeuterated solvent as an internal reference. Peak descriptions singlet (s), doublet (d), triplet (t), quartet (q), multiplet (m) and broad (br) are used. NMR spectra are given at the end of this document.

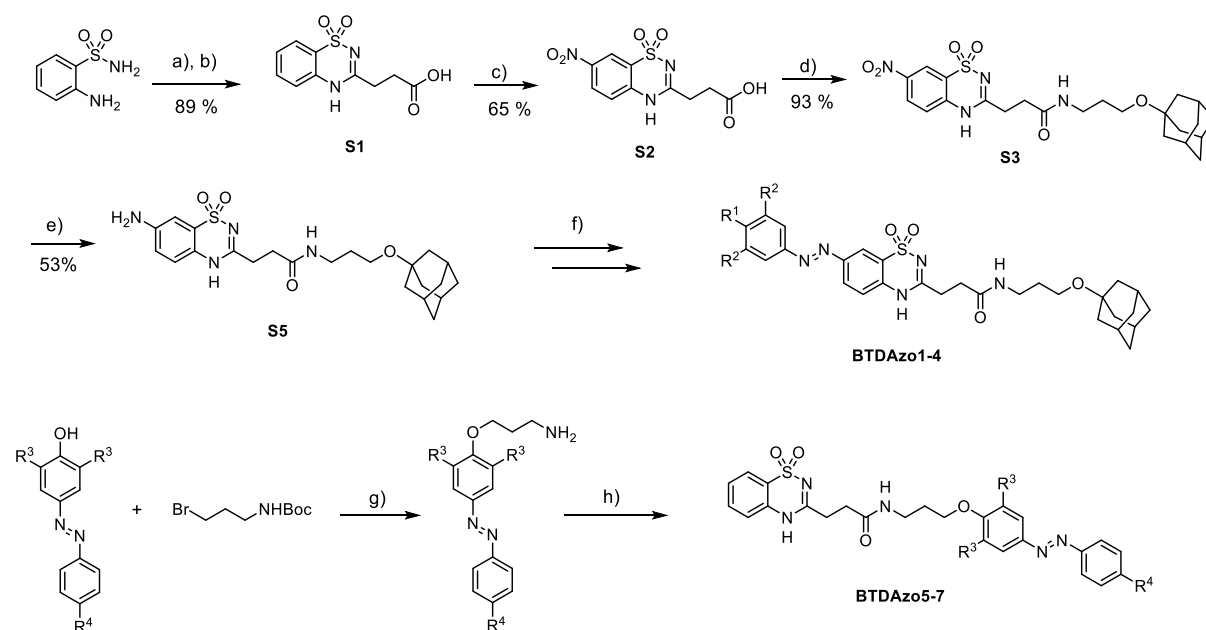
High resolution mass spectrometry (HRMS). HRMS was carried out by the Zentrale Analytik of the LMU Munich using ESI ionisation on a Thermo Finnigan LTQ FT Ultra Fourier Transform Ion Cyclotron Resonance Spectrometer.

High Performance liquid chromatography (HPLC) coupled with mass spectrometry (MS). Analytical HPLC-MS was performed on an Agilent 1100 SL with (a) a binary pump to deliver H₂O:MeCN eluent mixtures containing 0.1% formic acid at a 0.4 mL/min flow rate, (b) YMC-Triart C18 column (3.0 μm ; 50 mm \times 3 mm) maintained at 40 °C (c) an Agilent 1100 series diode array detector, (d) an Agilent LC/MSD iQ mass spectrometer. Typical run conditions were a linear gradient of H₂O:MeCN from 90:10 to 0:100 (first 5 min), then 0:100 for 2 min for flushing; then the column was (re)equilibrated with 90:10 eluent mixture for 2 min.

HPLC. Analytical HPLC was performed on an Agilent 1100 SL with (a) a binary pump to deliver H₂O:MeCN eluent mixtures containing 0.1% formic acid at a 0.4 mL/min flow rate, (b) Agilent-Zorbax C18 column (10 μm ; 250 mm \times 4.6 mm) maintained at 40 °C (c) an Agilent 1100 series diode array detector. Typical run conditions were a linear gradient of H₂O:MeCN from 75:25 to 2:98 (20 min), then 2:98 for 5 min for flushing; then the column was (re)equilibrated with 75:25 eluent mixture for 3 min.

Preparative HPLC. Preparative HPLC was performed on an Agilent 1200 SL with (a) a binary pump to deliver H₂O:MeCN eluent mixtures containing 0.1% formic acid at 20 mL/min flow rate, (b) Agilent-Zorbax C18 column (10.0 μm; 250 mm × 30 mm) maintained at room temperature, (c) an Agilent 1200 series diode array detector, (d) and Agilent 1200 series fraction collector.

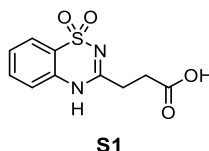
Synthetic procedures



Scheme S1. Synthetic overview on btda1-7. Conditions: a) succinic anhydride, AcOH; b) NaOH, reflux; c) HNO₃; d) **S4**, HBTU, DIPEA, DMF; e) SnCl₂, EtOH, 60 °C. f) i) Azo coupling/Mills reaction, ii) MeI, K₂CO₃, DMF, 40 °C; g) i) K₂CO₃, acetone, 60 °C; ii) HCl in Dioxane, CH₂Cl₂; h) HBTU, DIPEA, **S1**, DMF.

Synthesis of Precursors

3-(1,1-dioxido-4H-benzo[e][1,2,4]thiadiazin-3-yl)propanoic acid (**S1**)

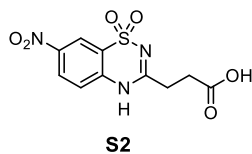


The synthesis was conducted according to a modified literature procedure.^[1]

2-Aminobenzenesulfonamide (1.0 g, 5.81 mmol, 1.0 eq) and succinic acid (872 mg, 8.71 mmol, 1.5 eq) were dissolved in AcOH (60 mL) and stirred at room temperature for 16 h. After removal of solvent under vacuum, the colourless residue was dissolved in 2 M NaOH (30 mL) and heated to 100 °C for 2 h. The reaction mixture was cooled down, neutralized with 2 M HCl and the precipitate was filtered and washed with water to afford **S1** as a colourless solid (1.31 g, 5.16 mmol, 89%). The compound is literature known but NMR spectra were not published.

¹H NMR (400 MHz, DMSO-*d*₆) δ: 12.09 (bs, 1H), 7.77 (dd, *J* = 8.0, 1.4 Hz, 1H), 7.71 – 7.62 (m, 1H), 7.47 – 7.39 (m, 1H), 7.32 (d, *J* = 8.3 Hz, 1H), 2.81 (t, *J* = 6.7 Hz, 2H), 2.66 (t, *J* = 6.7 Hz, 2H). **¹³C NMR** (126 MHz, DMSO-*d*₆) δ: 173.15, 159.34, 135.15, 133.12, 126.22, 123.53, 121.28, 117.28, 30.03, 29.28. **HRMS** (ESI, *m/z*): [M-H]⁻ calcd for C₁₀H₉N₂O₄S: 253.0289; found: 253.0289.

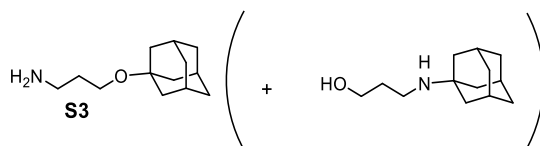
3-(7-nitro-1,1-dioxido-4H-benzo[e][1,2,4]thiadiazin-3-yl)propanoic acid (**S2**)



S1 (2.03 g, 8.00 mmol, 1 eq) was added in small portions to nitric acid (86%, 24 mL) at 0 °C and further stirred for 3 h at 0 °C. The reaction mixture was poured carefully on ice (60 g) and the resulting precipitate was collected by filtration and washed with water to afford **S2** as a colourless solid (1.55 g, 5.18 mmol, 65 %).

¹H NMR (400 MHz, DMSO-*d*6) δ: 12.64 (s, 1H), 8.70 – 8.30 (m, 2H), 7.54 (d, *J* = 9.0 Hz, 1H), 2.88 (t, *J* = 6.7 Hz, 2H), 2.68 (t, *J* = 6.7 Hz, 2H). **¹³C NMR** (101 MHz, DMSO- *d*6) δ: 173.06, 160.58, 144.25, 139.89, 128.02, 120.84, 120.16, 119.20, 30.20, 29.16. **HRMS** (ESI, *m/z*): [M-H]⁻ calcd for C₁₀H₈N₃O₆S: 298.0139; found: 298.0139.

3-((adamantan-1-yl)oxy)propan-1-amine (major product, **S3**)

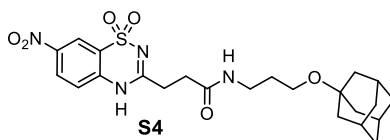


The synthesis was conducted according to a literature procedure.^[2]

A mixture of 1-bromoadamantane (4.35 g, 20 mmol, 1.0 eq), 3-amino-1-propanol (30.6 mL, 400 mmol, 20 eq), and triethylamine (5.62 mL, 40 mmol, 2 eq) was heated to 180 °C for 16 h. After cooling to room temperature, the mixture was diluted with CH₂Cl₂ (150 mL), washed with 0.1 M NaOH (5 x 100 mL) and with a mixture of brine/ 1 M NaOH (3:1, 100 mL). The organic layer was dried over anhydrous Na₂SO₄, filtered and concentrated to afford a crude reaction mixture containing **S3** and its minor regioisomer (overall 3.75 g, 17.9 mmol, 90 %; ¹H NMR analysis shows **major desired:minor undesired regioisomers in ratio 74:26** which is in accordance with the literature (~ 70:30)^[2].) The mixture was used without further purification as the minor isomer does not couple in the next step and so is removed in purification of **S4**.

¹H NMR of crude **S3** mixture: (400 MHz, CDCl₃) δ: 3.80 (t, *J* = 5.1 Hz, 2H, minor), 3.48 (t, *J* = 6.2 Hz, 2H, major), 2.87 (t, *J* = 5.6 Hz, 2H, minor), 2.78 (t, *J* = 6.7 Hz, 2H, major), 2.13 (br, 3H, major), 2.06 (br, 3H, minor), 1.76 – 1.54 (m, 14H major + 14H minor).

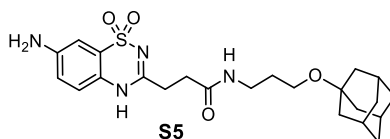
N-(3-((adamantan-1-yl)oxy)propyl)-3-(7-nitro-1,1-dioxido-4H-benzo[e]-[1,2,4]thiadiazin-3-yl)propanamide (**S4**)



HBTU (2.13 g, 5.62 mmol, 1.1 eq) was added to a solution of **S2** (1.53 g, 5.11 mmol, 1.0 eq) and DIPEA (2.70 ml, 15.3 mmol, 3.0 eq) in DMF (50 mL) and stirred for 10 min followed by addition of the crude mixture of **S3** (2.14 g, 10.2 mmol, 2.0 eq). After 2 h the reaction was quenched with st. NH₄Cl (100 mL) and st. NaHCO₃ (100 mL), the pH was set to 7 and the mixture was extracted with EtOAc (2 x 200 mL). The combined organic layers were washed with brine (5 x 100 mL), dried over anhydrous Na₂SO₄, filtered, and concentrated. The crude product was purified by flash chromatography (DCM/MeOH 100:0 to 95:5) to afford **S4** (2.30 g, 4.69 mmol, 93 %) as a slightly brown solid.

TLC (DCM/MeOH 95:5): R_f = 0.40. **¹H NMR** (400 MHz, DMSO-*d*₆) δ: 12.63 (br, 1H), 8.52 – 8.35 (m, 2H), 7.91 (t, *J* = 5.5 Hz, 1H), 7.54 (d, *J* = 8.9 Hz, 1H), 3.36 – 3.26 (m, 2H), 3.11 – 3.03 (m, 2H), 2.86 (t, *J* = 7.0 Hz, 2H), 2.55 (t, *J* = 7.0 Hz, 2H), 2.05 (br, 3H), 1.67 – 1.60 (m, 6H), 1.60 – 1.45 (m, 8H). **¹³C NMR** (101 MHz, DMSO-*d*₆) δ: 170.06, 160.97, 144.16, 139.94, 127.93, 120.82, 120.11, 119.18, 71.05, 56.73, 41.10, 36.13, 35.94, 30.78, 30.54, 30.15, 29.83. **HRMS** (ESI, *m/z*): [M-H]⁻ calcd for C₂₃H₂₉N₄O₆S: 489.1813; found: 489.1814.

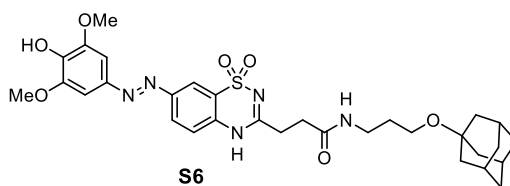
N-(3-((adamantan-1-yl)oxy)propyl)-3-(7-amino-1,1-dioxido-4H-benzo[e][1,2,4]thiadiazin-3-yl)propenamide (S5)



A flask was charged with **S4** (1.36 g, 2.77 mmol, 1.0 eq), tin(II)chloride (2.10 g, 11.1 mmol, 4 eq) and EtOH (30 mL). The reaction mixture was heated to 60 °C for 2 h and quenched by addition of water, st. aq. NaHCO₃ and st. aq. NH₄Cl. PH was set to 7 and the suspension was extracted with EA (6 x 100 mL). The combined organic layers were dried over anhydrous Na₂SO₄, filtered, and concentrated. The crude product was purified by flash chromatography (DCM/MeOH 100:0 to 90:10) to afford **S5** (670 mg, 1.45 mmol, 53 %) as a slightly brown solid.

TLC (DCM/MeOH 95:5): R_f = 0.29. **¹H NMR** (400 MHz, DMSO- *d*₆) δ: 11.67 (s, 1H), 7.86 (t, *J* = 5.5 Hz, 1H), 7.01 (dd, *J* = 8.8, 1.1 Hz, 1H), 6.89 – 6.81 (m, 2H), 5.54 (s, 2H), 3.33 – 3.30 (m, 2H), 3.07 (dd, *J* = 6.5 Hz, 2H), 2.69 (t, *J* = 7.3 Hz, 2H), 2.51 – 2.44 (m, 2H), 2.06 (br, 3H), 1.69 – 1.62 (m, 6H), 1.60 – 1.47 (m, 8H). **¹³C NMR** (101 MHz, DMSO-*d*₆) δ. 170.27, 157.65, 147.40, 124.64, 122.50, 119.46, 118.26, 104.51, 71.07, 56.75, 41.12, 36.12, 35.97, 31.05, 30.58, 30.15, 29.84. **HRMS** (ESI, *m/z*): [M+H]⁺ calcd for C₂₃H₃₃N₄O₄S: 461.2217; found: 461.2218.

N-(3-((adamantan-1-yl)oxy)propyl)-3-(7-((E)-(4-hydroxy-3,5-dimethoxyphenyl)diazenyl)-1,1-dioxido-4H-benzo[e][1,2,4]thiadiazin-3-yl)propanamide (S6)

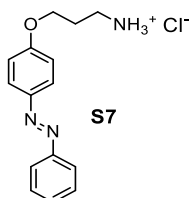


NaNO₂ (550 μ L, 2 M, 1.10 mmol, 1.1 eq) was added to a solution of **S5** (461 mg, 1.00 mmol, 1.0 eq) in Hydrochloric acid (4 mL, 2M) and MeOH (4 mL) at 0 °C. The reaction mixture was allowed to stir for 15 min at 0 °C and was subsequently added to a solution of 2,6-Dimethoxyphenol (185 mg, 1.2 mmol, 1.2 eq) in MeOH (3 mL) and Buffer (3 mL of 0.5 M K₂HPO₄ and 1 mL of 1 M KOH). The pH was adjusted to 9 - 11 and the reaction was stirred for 45 min at 0°C. The reaction was quenched by addition of st. NH₄Cl, pH was adjusted to 7 with st. NaHCO₃ and the mixture was extracted with EA (3 x 60 mL). The combined organic layers were dried over anhydrous Na₂SO₄, filtered, and concentrated. The crude product was purified by flash chromatography (DCM/MeOH 100:0 to 95:5) to afford **S6** (330 mg, 527 μ mol, 53 %) as a deep red oil which was used directly without further purification.

A representative sample was further purified by preparative HPLC (gradient: H₂O/ACN 75:25 \rightarrow 10:90 in 25 minutes) to obtain an analytical sample.

TLC (DCM/MeOH 95:5): R_f = 0.36. **¹H NMR** (500 MHz, DMSO-*d*6) δ : 8.17 – 8.12 (m, 2H), 7.90 (t, *J* = 5.5 Hz, 1H), 7.49 (d, *J* = 8.5 Hz, 1H), 7.32 (s, 2H), 3.88 (s, 6H), 3.37 – 3.28 (m, 2H), 3.11 – 3.03 (m, 2H), 2.82 (t, *J* = 7.2 Hz, 2H), 2.55 (t, *J* = 7.1 Hz, 2H), 2.05 (br, 3H), 1.65 – 1.59 (m, 6H), 1.60 – 1.48 (m, 8H). **¹³C NMR** (126 MHz, DMSO-*d*6) δ : 170.22, 160.15, 149.12, 148.25, 143.87, 140.14, 136.78, 127.56, 121.93, 119.01, 116.05, 101.11, 71.06, 56.73, 56.06, 41.11, 36.12, 35.95, 30.95, 30.83, 30.16, 29.82. **HRMS** (ESI, *m/z*): [M+H]⁺ calcd for C₃₁H₄₀N₅O₄S: 626.2643; found: 626.2650.

3-(4-(phenyldiazenyl)phenoxy)propan-1-amine (S7)



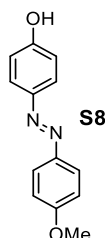
The synthesis was conducted according to a modified literature procedure.^[3]

A screw cap vial was charged with 4-Phenyldiazophenol (49 mg, 0.25 mmol, 1.0 eq), 3-(Boc-amino)propyl bromide (89 mg, 0.38 mmol, 1.5 eq), K₂CO₃ (69 mg, 0.50 mmol, 2 eq) and acetone (2.5 mL), locked and stirred at 50°C for 16 h. The mixture was diluted with EA (20 mL),

quenched with sat. NH_4Cl (10 mL), the layers separated, and the organic layer washed with brine (3 x 20 mL). The organic layers were dried over anhydrous Na_2SO_4 , filtered, and concentrated. The residue was filtered through a short silica column (iso-hexane/EA 90:10), concentrated, dissolved in abs DCM (5 mL) and HCl (4 M in dioxane, 625 μL , 2.5 mmol, 10 eq) was added dropwise to the solution. After 1 h stirring Et_2O was added, the product precipitated as hydrochloride, filtered off, washed with Et_2O and air-dried to afford **S7** (58 mg, 0.20 mmol, 80 %) as a yellow solid.

$^1\text{H NMR}$ (400 MHz, $\text{DMSO-}d_6$) δ 8.15 (br, 3H), 7.90 (d, $J = 9.0$ Hz, 2H), 7.87 – 7.81 (m, 2H), 7.62 – 7.47 (m, 3H), 7.15 (d, $J = 9.0$ Hz, 2H), 4.20 (t, $J = 6.1$ Hz, 2H), 3.04 – 2.92 (m, 2H), 2.15 – 2.03 (m, 2H). $^{13}\text{C NMR}$ (101 MHz, DMSO) δ 161.11, 151.98, 146.22, 130.87, 129.40, 124.56, 122.25, 115.12, 65.17, 36.10, 26.72.

4-((4-methoxyphenyl)diazonyl)phenol (**S8**)



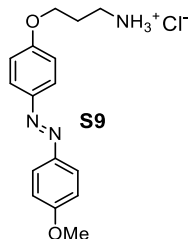
The synthesis was conducted according to a literature procedure.^[4]

NaNO_2 (1.10 mL, 2 M, 2.20 mmol, 1.1 eq) was added to a solution of *p*-anisidine (246 mg, 2.00 mmol, 1.0 eq) in hydrochloric acid (4 mL, 2M) and MeOH (6 mL) at 0 °C. The reaction mixture was allowed to stir for 15 min at 0 °C and was subsequently added to a solution of phenol (226 mg, 2.40 mmol, 1.2 eq) in MeOH (6 mL) and buffer (6 mL of 0.5 M K_2HPO_4 and 1 mL of 1 M KOH). The pH was adjusted to 9 - 11 and the reaction was stirred for 45 min at 0°C. The reaction was quenched by addition of sat. NH_4Cl , pH was adjusted to 7 with sat. NaHCO_3 and the mixture was extracted with EA (3 x 60 mL). The combined organic layers were dried over anhydrous Na_2SO_4 , filtered, and concentrated. The crude product was purified by flash chromatography (Isohexane/EA 80:20) to afford **S8** (248 mg, 1.09 mmol, 54 %) as a brown oil.

Spectral data are in accordance with the literature.^[4]

TLC (Hex/EtOAc 8:2): $R_f = 0.35$. $^1\text{H NMR}$ (400 MHz, CDCl_3) δ : 7.88 (d, $J = 9.0$ Hz, 2H), 7.83 (d, $J = 8.8$ Hz, 2H), 7.00 (d, $J = 9.0$ Hz, 2H), 6.93 (d, $J = 8.8$ Hz, 2H), 3.89 (s, 3H). $^{13}\text{C NMR}$ (101 MHz, CDCl_3) δ : 161.76, 157.87, 147.38, 147.15, 124.72, 124.53, 115.90, 114.34, 55.72.

3-(4-((4-methoxyphenyl)diazenyl)phenoxy)propan-1-amine (S9)



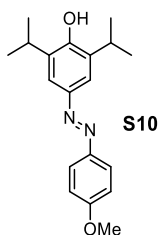
The synthesis was conducted according to a modified literature procedure.^[4]

A screw cap vial was charged with **S8** (57 mg, 0.25 mmol, 1.0 eq), 3-(Boc-amino)propyl bromide (89 mg, 0.38 mmol, 1.5 eq), K₂CO₃ (69 mg, 0.50 mmol, 2 eq) and acetone (2.5 mL), locked and stirred at 50°C for 16 h. The mixture was diluted with EA (20 mL), quenched with st. NH₄Cl (10 mL), the layers separated, and the organic layer washed with brine (3 x 20 mL). The organic layers were dried over anhydrous Na₂SO₄, filtered, and concentrated. The residue was filtered through a short silica column (Isohexane/EA 90:10), concentrated, dissolved in abs DCM (5 mL) and HCl (4 M in Dioxane, 625 μL, 2.5 mmol, 10 eq) was added dropwise to the solution. After 1 h stirring Et₂O was added, the product precipitated as hydrochloride, filtered off, washed with Et₂O and dried to afford **S9** (25 mg, 78 μmol, 31 %) as a yellow solid.

Spectral data are in accordance with the literature.^[4]

¹H NMR (400 MHz, DMSO-*d*₆) δ: 8.12 (br, 3H), 7.89 – 7.81 (m, 4H), 7.19 – 7.05 (m, 4H), 4.18 (t, *J* = 6.1 Hz, 2H), 3.85 (s, 3H), 3.05 – 2.90 (m, 2H), 2.17 – 2.01 (m, 2H). **¹³C NMR** (101 MHz, DMSO) δ 161.49, 160.52, 146.27, 146.17, 124.14, 124.10, 115.03, 114.54, 65.07, 55.60, 36.13, 26.75. **HRMS** (ESI, *m/z*): [M+H]⁺ calcd for C₁₆H₂₀O₂N₃: 286.1550; found: 286.1552.

2,6-diisopropyl-4-((4-methoxyphenyl)diazenyl)phenol (S10)



The synthesis was conducted according to a literature procedure.^[5]

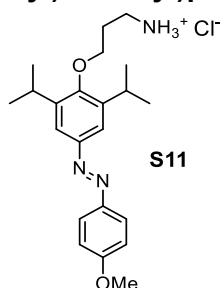
NaNO₂ solution (550 μL, 2 M, 1.10 mmol, 1.1 eq) was added to a solution of *p*-anisidine (123 mg, 1.00 mmol, 1.0 eq) in hydrochloric acid (2 mL, 2M) and MeOH (3 mL) at 0 °C. The reaction mixture was allowed to stir for 15 min at 0 °C and was subsequently added to a solution of 2,6-diisopropylphenol (123 mg, 1.2 mmol, 1.2 eq) in MeOH (3 mL) and buffer (3 mL of 0.5 M K₂HPO₄ and 1 mL of 1 M KOH). The pH was adjusted to 9 - 11 and the reaction was stirred for 45 min at 0°C. The reaction was quenched by addition of st. NH₄Cl, pH was adjusted to 7 with st. NaHCO₃ and the mixture was extracted with EA (3 x 60 mL). The combined organic layers

were dried over anhydrous Na₂SO₄, filtered, and concentrated. The crude product was purified by flash chromatography (Isohexane/EA 90:10 to 65:35) to afford **S10** (148 mg, 474 μmol, 47 %) as a deep red oil.

Spectral data are in accordance with the literature.^[5]

TLC (Hex/EtOAc 8:2): R_f = 0.45. **¹H NMR** (400 MHz, CDCl₃) δ: 7.94 – 7.83 (m, 2H), 7.69 (s, 2H), 7.04 – 6.96 (m, 2H), 5.13 (s, 1H), 3.89 (s, 3H), 3.20 (hept, *J* = 6.8 Hz, 2H), 1.34 (d, *J* = 6.8 Hz, 12H). **¹³C NMR** (101 MHz, CDCl₃) δ (ppm): 161.51, 152.61, 147.37, 147.14, 134.37, 124.35, 118.81, 114.27, 55.68, 27.54, 22.80.

3-(2,6-diisopropyl-4-((4-methoxyphenyl)diazenyl)phenoxy)propan-1-amine (**S11**)



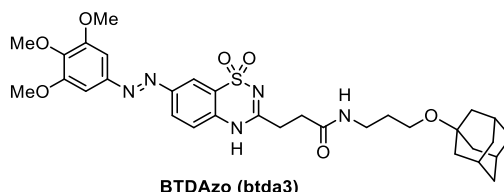
A screw cap vial was charged with **S10** (78 mg, 0.25 mmol, 1.0 eq), 3-(Boc-amino)propyl bromide (89 mg, 0.38 mmol, 1.5 eq), K₂CO₃ (69 mg, 0.50 mmol, 2 eq) and acetone (2.5 mL), locked and stirred at 50°C for 16 h. The mixture was diluted with EA (20 mL), quenched with sat. NH₄Cl (10 mL), the layers separated, and the organic layer washed with brine (3 x 20 mL). The organic layers were dried over anhydrous Na₂SO₄, filtered, and concentrated. The residue was filtered through a short silica column (hexane/EtOAc 90:10), concentrated, dissolved in abs DCM (5 mL) and HCl (4 M in dioxane, 625 μL, 2.5 mmol, 10 eq) was added dropwise to the solution. After 1 h stirring Et₂O was added, the product precipitated as hydrochloride, filtered off, washed with Et₂O and air-dried to afford **S11** (36 mg, 0.089 mmol, 36 %) as a yellow solid which was used without further purification.

A representative sample was further purified by reverse phase flash chromatography (Biotage Sfär C18, H₂O/MeCN +0.1% formic acid 90:10 to 5:95) to obtain spectroscopically pure material.

¹H NMR (500 MHz, DMSO-*d*₆) δ: 7.88 (d, *J* = 9.0 Hz, 2H), 7.63 (s, 2H), 7.12 (d, *J* = 9.0 Hz, 2H), 3.93 – 3.74 (m, 5H), 3.29 (p, *J* = 6.8 Hz, 2H), 2.97 (br, 2H), 2.05 (t, *J* = 7.2 Hz, 2H), 1.25 (d, *J* = 6.9 Hz, 12H). **¹³C NMR** (126 MHz, DMSO-*d*₆) δ 161.71, 155.24, 148.86, 146.21, 142.57, 124.38, 118.22, 114.54, 72.13, 55.63, 36.63, 29.61, 26.29, 23.77. **HRMS** (ESI, *m/z*): [M+H]⁺ calcd for C₂₂H₃₂O₂N₃: 370.2489; found: 370.2493.

Synthesis of btda1-7

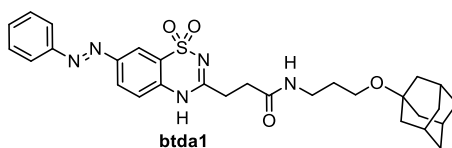
BTDAzo (btda3)



A screw cap vial was charged with **S6** (95 mg, 152 μmol , 1.0 eq), K_2CO_3 (42 mg, 304 μmol , 2.0 eq), DMF (1.5 mL) and iodomethane (10.4 μL , 167 μmol , 1.1 eq), locked and stirred 1 h at 40 $^\circ\text{C}$. The mixture was diluted with EA (30 mL), quenched with st. NH_4Cl (20 mL), the layers separated, the organic layer washed with brine (3 x 20 mL). The organic layers were dried over anhydrous Na_2SO_4 , filtered, and concentrated. The crude product was pre-purified by flash chromatography (DCM/MeOH 100:0 to 95:5) and further purified by recrystallization (EtOH/ H_2O 2:1) to afford **BTDAzo** (25 mg, 39 μmol , 26 %) as an orange solid. Recrystallization was necessary to separate the double methylated side product.

TLC (DCM/MeOH 95:5): R_f = 0.40. **$^1\text{H NMR}$** (400 MHz, $\text{DMSO-}d_6$) δ : 12.38 (s, 1H), 8.22 – 8.18 (m, 2H), 7.91 (t, J = 5.5 Hz, 1H), 7.52 (d, J = 9.4 Hz, 1H), 7.33 (s, 2H), 3.90 (s, 6H), 3.78 (s, 3H), 3.36 – 3.28 (m, 2H), 3.11 – 3.05 (m, 2H), 2.84 (t, J = 7.1 Hz, 2H), 2.56 (t, J = 7.1 Hz, 2H), 2.05 (br, 3H), 1.65 – 1.62 (m, 6H), 1.59 – 1.46 (m, 8H). **$^{13}\text{C NMR}$** (101 MHz, $\text{DMSO-}d_6$) δ : 170.17, 160.18, 153.38, 148.92, 147.55, 140.81, 137.09, 127.77, 121.86, 118.93, 116.81, 100.66, 71.05, 60.29, 56.72, 56.07, 41.10, 36.13, 35.94, 30.83, 30.73, 30.16, 29.82. **HRMS** (ESI, m/z): $[\text{M}+\text{H}]^+$ calcd for $\text{C}_{32}\text{H}_{42}\text{O}_7\text{N}_5\text{S}$: 640.2800; found: 640.2804.

btda1

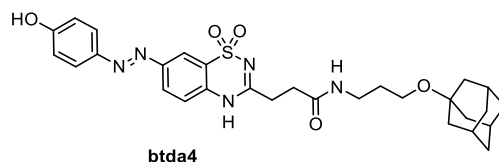


A screw cap vial was charged with **S4** (98 mg, 0.21 mmol, 1.0 eq), nitrosobenzene (25 mg, 0.23 mmol, 1.1 eq) and acetic acid (2 mL), locked and stirred for 16 h at room temperature. The resulting yellow suspension was diluted with EA, neutralized with st NaHCO_3 , the layers separated and the organic layer was washed with st NaHCO_3 (2 x 20 mL) and brine (20 mL). The organic layer was dried over anhydrous Na_2SO_4 , filtered, and concentrated. The crude product was purified by flash chromatography (DCM/MeOH 100:0 to 95:5) to afford **btda1** (32 mg, 67 μmol , 37 %) as a yellow solid.

TLC (DCM/MeOH 95:5): R_f = 0.47. **$^1\text{H NMR}$** (400 MHz, $\text{DMSO } d_6$) δ : 12.39 (br s, 1H), 8.25 – 8.19 (m, 2H), 7.98 – 7.87 (m, 3H), 7.66 – 7.58 (m, 3H), 7.56 – 7.51 (m, 1H), 3.38 – 3.28 (m, 2H), 3.08 (q, J = 6.5 Hz, 2H), 2.84 (t, J = 7.1 Hz, 2H), 2.56 (t, J = 7.1 Hz, 2H), 2.04 (br, 3H),

1.68 – 1.60 (m, 6H), 1.59 – 1.45 (m, 9H). **¹³C NMR** (101 MHz, DMSO *d*6) δ 170.14, 160.17, 151.69, 149.00, 137.26, 132.04, 129.57, 127.39, 122.80, 121.78, 118.96, 117.52, 71.04, 56.71, 41.09, 36.11, 35.93, 30.78, 30.71, 30.16, 29.81. **HRMS** (ESI, *m/z*): $[M+H]^+$ calcd for C₂₉H₃₆N₅O₄S: 550.2483; found: 550.2483.

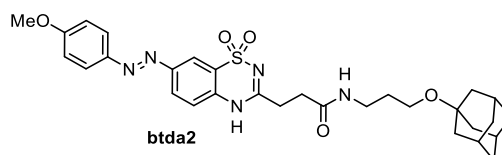
bt da4



NaNO₂ (113 μ L, 2 M, 0.227 mmol, 1.1 eq) was added to a solution of **S4** (95 mg, 0.206 mmol, 1.0 eq) in hydrochloric acid (413 μ L, 2M) and MeOH (0.4 mL) at 0 °C. The reaction mixture was allowed to stir for 15 min at 0 °C and was subsequently added to a solution of phenol (23.3 mg, 0.248 mmol, 1.2 eq) in MeOH (0.4 mL) and buffer (0.4 mL of 0.5 M K₂HPO₄ and 0.1 mL of 1 M KOH). The pH was adjusted to 9 - 11 and the reaction was stirred for 45 min at 0°C. The reaction was quenched by addition of st. NH₄Cl, pH was adjusted to 7 with st. NaHCO₃ and the mixture was extracted with EA (3 x 20 mL). The combined organic layers were dried over anhydrous Na₂SO₄, filtered, and concentrated. The crude product was purified by flash chromatography (DCM/MeOH 100:0 to 90:10) to afford **bt da4** (34 mg, 60.1 μ mol, 34 %) as a yellow solid.

TLC (DCM/MeOH 95:5): R_f = 0.34. **¹H NMR** (400 MHz, DMSO *d*6) δ : 12.33 (br s, 1H), 10.42 (br s, 1H), 8.13 (dd, *J* = 8.7, 2.2 Hz, 1H), 8.10 (d, *J* = 2.2 Hz, 1H), 7.90 (t, *J* = 5.6 Hz, 1H), 7.85 (d, *J* = 8.9 Hz, 2H), 7.49 (d, *J* = 8.7 Hz, 1H), 6.96 (d, *J* = 8.9 Hz, 2H), 3.34 – 3.28 (m, 2H), 3.08 (q, *J* = 6.5 Hz, 2H), 2.83 (t, *J* = 7.1 Hz, 2H), 2.55 (t, *J* = 7.1 Hz, 2H), 2.04 (br, 3H), 1.67 – 1.59 (m, 6H), 1.59 – 1.47 (m, 9H). **¹³C NMR** (101 MHz, DMSO *d*6) δ : 170.17, 161.51, 160.01, 149.33, 145.04, 136.43, 127.23, 125.25, 121.81, 118.84, 116.43, 116.09, 71.06, 56.72, 41.10, 36.12, 35.95, 30.78, 30.75, 30.16, 29.82. **HRMS** (ESI, *m/z*): $[M+H]^+$ calcd for C₂₉H₃₆N₅O₅S: 566.2432; found: 566.2432.

bt da2



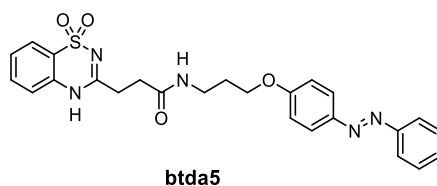
A screw cap vial was charged with **bt da4** (27 mg, 48 μ mol, 1.0 eq), K₂CO₃ (13 mg, 96 μ mol, 2.0 eq), DMF (0.5 mL) and iodomethane (3.3 μ L, 53 μ mol, 1.1 eq), locked and stirred 1 h at 40 °C. The mixture was diluted with EA (20 mL), quenched with st. NH₄Cl (10 mL), the layers separated, the organic layer washed with brine (3 x 20 mL). The organic layers were dried over

anhydrous Na₂SO₄, filtered, and concentrated. The crude product was pre-purified by flash chromatography (DCM/MeOH 100:0 to 95:5) and further purified by preparative HPLC (gradient: H₂O/ACN 75:25 → 10:90 in 25 minutes) to afford **btda2** (7 mg, 12 μmol, 25 %) as a yellow solid.

¹H NMR (400 MHz, DMSO-*d*6) δ: 12.29 (br, 1H), 8.20 – 8.10 (m, 2H), 7.98 – 7.85 (m, 3H), 7.50 (d, *J* = 8.6 Hz, 1H), 7.20 – 7.09 (m, 2H), 3.88 (s, 3H), 3.33 – 3.27 (m, 2H), 3.11 – 3.05 (m, 2H), 2.83 (t, *J* = 7.1 Hz, 2H), 2.55 (t, *J* = 7.3 Hz, 2H), 2.04 (br, 3H), 1.68 – 1.59 (m, 6H), 1.60 – 1.46 (m, 9H). **¹³C NMR** (101 MHz, DMSO-*d*6) δ: 170.23, 162.46, 160.20, 149.14, 145.99, 137.03, 127.22, 124.93, 121.85, 119.08, 116.77, 114.77, 71.06, 56.73, 55.74, 41.11, 36.13, 35.95, 30.93, 30.82, 30.17, 29.83. **1D NOE** (400 MHz, DMSO *d*6, pulse at 3.89 ppm) δ: 7.17, 7.14. **HRMS** (ESI, *m/z*): [M+H]⁺ calcd for C₃₀H₃₈O₅N₅S: 580.2588; found: 580.2588.

Note: The exchangeable NH-proton on the benzothiadiazine core at 12.29 ppm is only a very faint signal in the NMR.

btda5

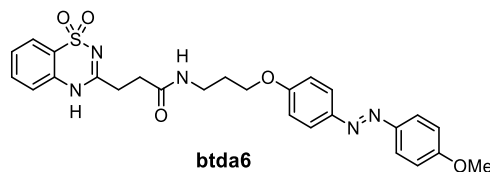


HBTU (42. mg, 0.11 mmol, 1.1 eq) was added to a solution of **S1** (28 mg, 0.11 mmol, 1.1 eq) and DIPEA (73 μL, 0.40 mmol, 4.0 eq) in DMF (1 mL) and stirred for 10 min followed by addition of **S7** (29 mg, 0.10 mmol, 1.0 eq). After 1 h the reaction was quenched with st. NH₄Cl (10 mL) and the mixture was extracted with EtOAc (2 x 20 mL). The combined organic layers were washed with brine (5 x 10 mL), dried over anhydrous Na₂SO₄, filtered, and concentrated. The crude product was purified by flash chromatography (DCM/MeOH 100:0 to 95:5) to afford **btda5** (32 mg, 65 μmol, 65 %) as a yellow solid.

¹H NMR (400 MHz, DMSO-*d*6) δ: 12.05 (br, 1H), 8.10 (t, *J* = 5.7 Hz, 1H), 7.88 – 7.82 (m, 4H), 7.78 (dd, *J* = 7.9, 1.4 Hz, 1H), 7.66 (ddd, *J* = 8.5, 7.3, 1.4 Hz, 1H), 7.61 – 7.55 (m, 2H), 7.54 – 7.50 (m, 1H), 7.43 (ddd, *J* = 8.2, 7.3, 1.1 Hz, 1H), 7.31 (dd, *J* = 8.3, 1.1 Hz, 1H), 7.10 (d, *J* = 9.0 Hz, 2H), 4.08 (t, *J* = 6.2 Hz, 2H), 3.28 – 3.19 (m, 2H), 2.81 (t, *J* = 7.1 Hz, 2H), 2.55 (t, *J* = 7.1 Hz, 2H), 1.88 (t, *J* = 6.4 Hz, 2H). **¹³C NMR** (101 MHz, DMSO-*d*6) δ: 170.54, 161.48, 159.72, 152.04, 146.09, 135.18, 133.08, 130.85, 129.43, 126.19, 124.58, 123.52, 122.27, 121.27, 117.30, 115.08, 65.73, 35.46, 30.71, 30.60, 28.82.

HRMS (ESI, *m/z*): [M+H]⁺ calcd for C₂₅H₂₆O₄N₅S: 492.1700; found: 492.1700.

btda6

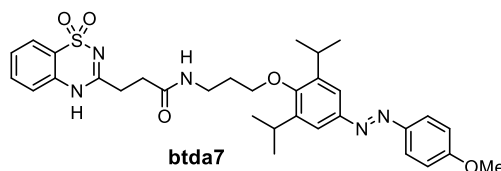


HBTU (26 mg, 69 μ mol, 1.1 eq) was added to a solution of **S1** (18 mg, 69 μ mol, 1.1 eq) and DIPEA (44 μ L, 0.25 mmol, 4.0 eq) in DMF (0.6 mL) and stirred for 10 min followed by addition of **S9** (29 mg, 0.10 mmol, 1.0 eq). After 1 h the reaction was quenched with sat. NH₄Cl (10 mL) and the mixture was extracted with EtOAc (2 x 20 mL). The combined organic layers were washed with brine (5 x 10 mL), dried over anhydrous Na₂SO₄, filtered, and concentrated. The crude product was purified by flash chromatography (DCM/MeOH 100:0 to 95:5) to afford **btda6** (30 mg, 58 μ mol, 55 %) as a yellow solid.

¹H NMR (400 MHz, DMSO-*d*₆) δ : 12.04 (br, 1H), 8.09 (t, *J* = 5.7 Hz, 1H), 7.84 (d, *J* = 8.9 Hz, 2H), 7.81 – 7.76 (m, 3H), 7.66 (ddd, *J* = 8.7, 7.3, 1.5 Hz, 1H), 7.43 (t, *J* = 7.7 Hz, 1H), 7.31 (d, *J* = 8.2 Hz, 1H), 7.15 – 7.00 (m, 4H), 4.06 (t, *J* = 6.2 Hz, 2H), 3.85 (s, 3H), 3.27 – 3.19 (m, 2H), 2.81 (t, *J* = 7.1 Hz, 2H), 2.55 (t, *J* = 7.1 Hz, 2H), 1.93 – 1.82 (m, 2H). **¹³C NMR** (101 MHz, DMSO-*d*₆) δ : 170.50, 161.46, 160.87, 159.69, 146.22, 146.11, 135.16, 133.05, 126.16, 124.14, 124.10, 123.50, 121.25, 117.28, 114.97, 114.55, 65.63, 55.61, 35.45, 30.70, 30.59, 28.82.

HRMS (ESI, *m/z*): [M+H]⁺ calcd for C₂₆H₂₈O₅N₅S: 522.1806; found: 522.1807.

btda7



HBTU (37 mg, 98 μ mol, 1.1 eq) was added to a solution of **S1** (25 mg, 98 μ mol, 1.1 eq) and DIPEA (64 μ L, 0.36 mmol, 4.0 eq) in DMF (1 mL) and stirred for 10 min followed by addition of **S9** (36 mg, 89 μ mol, 1.0 eq). After 1 h the reaction was quenched with sat. NH₄Cl (10 mL) and the mixture was extracted with EtOAc (2 x 20 mL). The combined organic layers were washed with brine (5 x 10 mL), dried over anhydrous Na₂SO₄, filtered, and concentrated. The crude product was purified by flash chromatography (DCM/MeOH 100:0 to 95:5) to afford **btda7** (42 mg, 69 μ mol, 78 %) as a yellow solid.

¹H NMR (400 MHz, DMSO-*d*₆) δ : 12.05 (br, 1H), 8.06 (t, *J* = 5.5 Hz, 1H), 7.92 – 7.86 (m, 2H), 7.77 (dd, *J* = 8.0, 1.4 Hz, 1H), 7.71 – 7.62 (m, 1H), 7.62 (s, 2H), 7.47 – 7.38 (m, 1H), 7.32 (d, *J* = 8.2 Hz, 1H), 7.16 – 7.09 (m, 2H), 3.86 (s, 3H), 3.78 (t, *J* = 6.3 Hz, 2H), 3.32 – 3.23 (m, 4H), 2.82 (t, *J* = 7.2 Hz, 2H), 2.57 (t, *J* = 7.2 Hz, 2H), 2.01 – 1.85 (m, 2H), 1.23 (d, *J* = 6.8 Hz, 12H).

¹³C NMR (101 MHz, DMSO) δ : 170.42, 161.68, 159.66, 155.36, 148.81, 146.22, 142.61, 135.18, 133.01, 126.12, 124.36, 123.47, 121.26, 118.21, 117.28, 114.53, 72.46, 55.62, 35.74, 30.72, 30.63, 29.98, 26.23, 23.79. **HRMS** (ESI, m/z): [M+H]⁺ calcd for C₃₂H₄₀O₅N₅S: 606.2745; found: 606.2747.

Photocharacterization

UV-VIS. UV-Vis spectra were recorded on an Agilent Cary 60 UV-Vis spectrophotometer using 1 cm quartz or PMMA cuvettes. All photoisomerisations and relaxation rate measurements were performed at room temperature in non-degassed solvents unless stated differently. Samples were irradiated with a Polycon V monochromator (TILL Photonics, Gräfelfing, Germany) by shining from the top of the cuvette, until the spectra did not change further (photoequilibrium). Unless stated differently, all measurements were performed at a default concentration of 25 μ M. *Dark state* refers to stocks in DMSO kept at 60 °C for >14 h prior to measurements (*all-trans*).

PSS as Ratio of Z/E. Samples were irradiated until PSS was reached; (a) for BTDAzo in different solvents PSS was calculated from the UV-Vis spectrum under the assumption that the absorbance of the Z isomer at 378-384 nm is effectively zero compared to that of the E isomer, so that the absorbance at this wavelength gives the fractional content of E isomer, which is then used to back-calculate the fraction of Z as (1 - E). In the important solvents for this paper, which are aprotic apolar (e.g. EtOAc/hexanes), the Z-absorbance is ca. 3% of the E-isomer's at this wavelength: so results at 100% E isomer are ~100% accurate, while results at 100% Z isomer would be calculated as 3% E therefore 97% Z, ie. a maximal error of 3%, which we considered entirely acceptable. (b) PSS determined from HPLC: analysis by integrating the signal at the respective isosbestic point derived from UV/VIS and calculating the ratio from the integrals.

Solvent dependent photoisomerization of BTDAzo

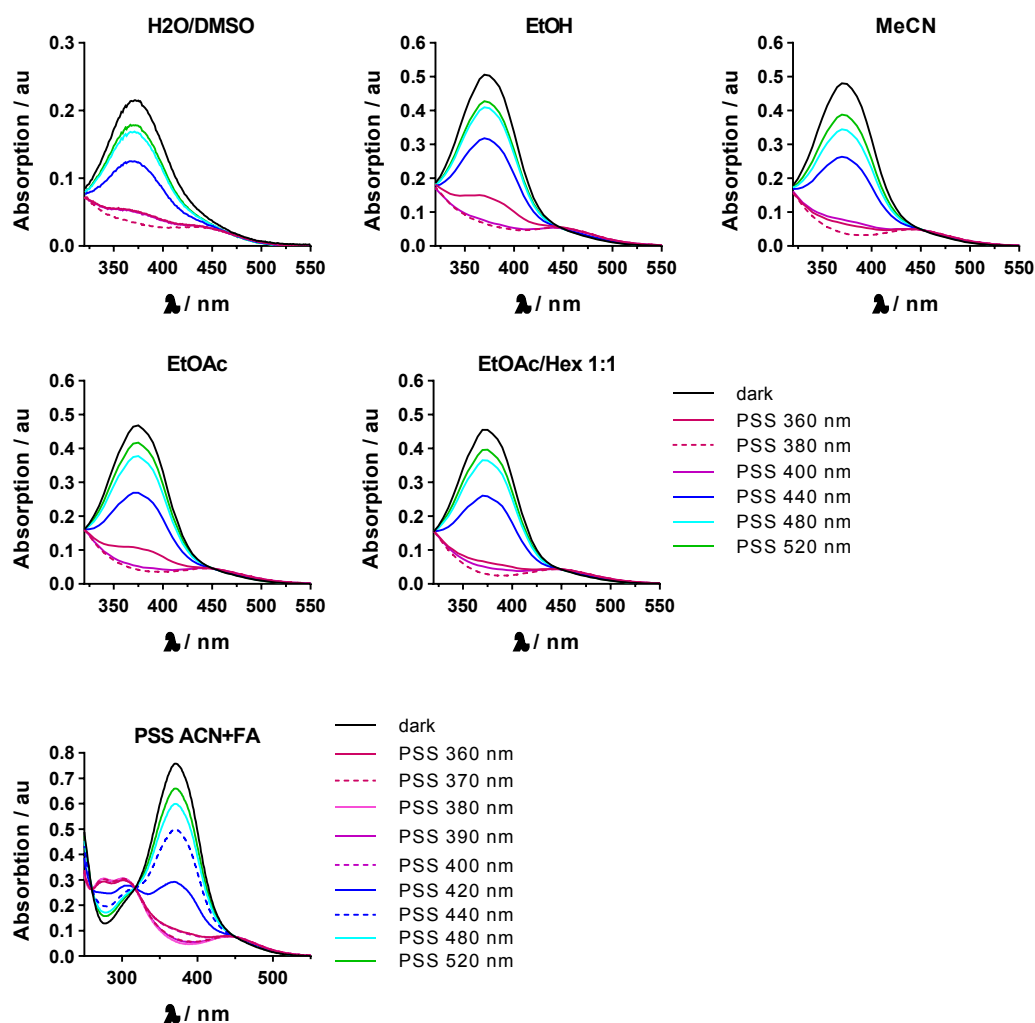


Figure S2. PSS spectra of **BTDAzo** in different solvents. ACN+FA is acetonitrile with 0.1% formic acid, useful in calibrating the spectra obtained from the HPLC DAD. H₂O/DMSO is a 90/10 mixture with a reduced concentration of 10 μ M.

Table S1. Ratios of Z/E at PSS in different solvents calculated from UV/VIS spectra.

λ [nm]	90% H ₂ O 10% DMSO	50% EtOAc 50% Hexane	MeCN	EtOH	EtOAc
360	77:23	86:14	87:13	72:28	78:22
380	85:15	94:6	93:7	88:12	92:8
400	77:23	90:10	84:16	86:14	89:11
440	42:58	43:57	46:54	38:62	43:57
480	23:77	20:80	29:71	19:81	20:80
520	18:82	13:87	20:80	16:84	11:89

Relaxation of BTDAzo

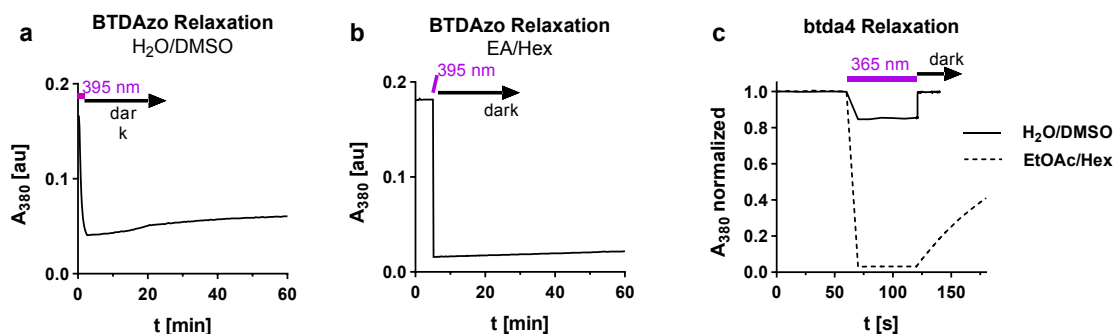


Fig S3. Spontaneous thermal relaxation a) of **BTDAzo** in polar protic solvent, b) of **BTDAzo** in apolar aprotic solvent, c) and of **btda4** in polar protic/apolar aprotic solvent, at 25°C.

Relaxation of Z-BTDAzo

The thermal relaxation of **Z-BTDAzo** to **E-BTDAzo** was determined in a) polar protic environment and b) apolar solvent mixture to mimic cellular lipid environment. In both cases spontaneous relaxation ($t_{1/2} \gg 4$ h; **Fig S3a-b**) is negligible on the time scale of biological experiments (seconds-scale switching, minutes-scale experiments).

Relaxation of Z-btda4

In contrast to **BTDAzo**, *para*-hydroxy **btda4** can relax "quickly" on the biological timescale depending on the solvent environment. In polar protic media the thermal relaxation from **Z-btda4** to **E-btda4** takes place in the ms time scale (**Fig. S3c**). Therefore, a "real" photostationary state is not obtained in our cuvette switching experiments because the rate of thermal back-reaction to **E-btda4** ($\tau=44$ ms) is much faster than the photon encounter rate. However, in aprotic apolar, membrane-mimicking environment (hexane/ethyl acetate 1:1) the thermal relaxation from **Z-btda4** to **E-btda4** at room temperature is slowed to $\tau=134$ s; therefore, a photostationary state is obtained. We believed that this would allow us to estimate the effective cellular environment that **btda4** (and hence also **BTDAzo**) is located in:

In cellular FLIPR studies **btda4** was found to reversibly activate TRPC5 under the same illumination conditions as **BTDAzo** (Fig. S5). With an EC_{50} of 45 μ M under 365 nm illumination **btda4** is only a weak photoswitchable agonist, but we suggest that the photoswitch behaviour enables useful conclusions on the environment. In a polar protic environment, >90% relaxation should occur within 150 ms: but instead we observed similar on-and-off kinetics of cellular current responses as with slow-relaxing **BTDAzo**. We believe this indicates that the **Z-to-E** "off-switching" of **btda4** is likewise majorly under photocontrol, not thermal relaxation: therefore, the environment relevant for action of **btda4** is lipophilic. A similar solvent dependent behaviour for azobenzene-based photoswitches in membranes has been observed elsewhere,

e.g. in Lanzani's studies;^[6] further experimental discussions of microscopic localisation and inhomogenous environment effects^[7,8] are given in the section **Comment on Action Spectra** below; and although an alternative explanation could be that (very) slow off-rates could combine with suppression of thermal relaxation in the bound state to reproduce similar effects, and although conclusive investigations would require much further work beyond the scope of this paper, we note recent work showing that simply binding to a protein does not impede (photo)isomerisation of photoswitches^[9] and we believe that for compounds where both *E* and *Z* isomers are capable of binding (certainly this is the case with the sterically larger **BTDAzo**, revealed through the competition experiment use of *E*-**BTDAzo** as well as the channel activation use of *Z*-**BTDAzo**), it is likely that the isomerisation process is at least not sterically forbidden in the protein.

PSS spectra of btda1-7

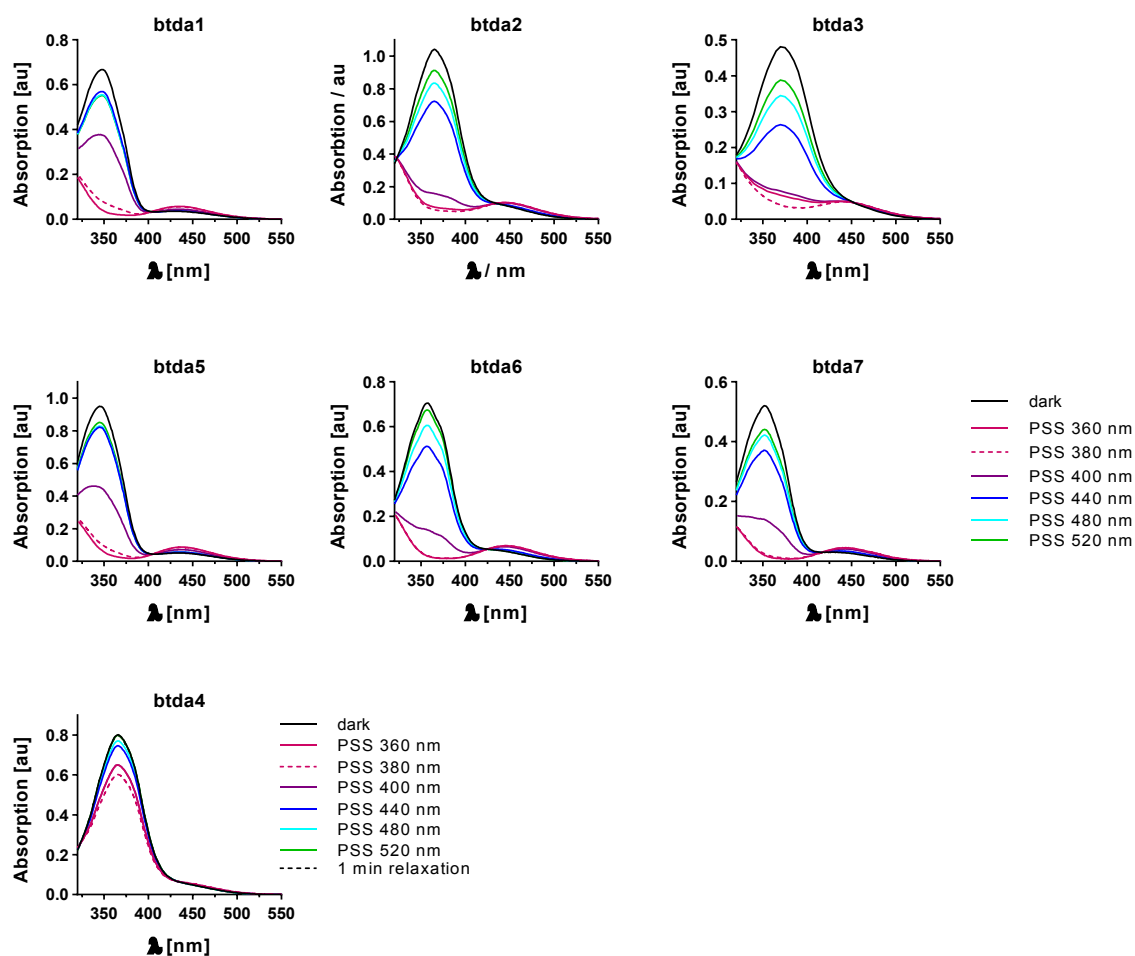


Figure S4 PSS spectra of btda1-7 (in MeCN).

Table S2. Ratios of Z/E at relevant PSSs in ACN determined by HPLC at the isosbestic point.

	Isosbestic point [nm]	PSS at 365 nm	PSS at 440 nm
btDa1	403	92:8	28:72
btDa2	434	86:14	6:94
btDa3	450	89:11	44:56
btDa5	405	96:4	26:74
btDa6	424	87:13	28:72
btDa7	417	96:4	30:70

btDa4 was not determined because its fast relaxation.

Cell biology

Ca²⁺ influx assays in cell suspensions. The initial characterisation of biological activity of **btda1-7** on TRPC5 was performed in a stably transfected HEK293 cell line that expresses TRPC5 after induction with 1 μ M tetracycline (HEK_{TRPC5-CFP}). Cells were induced to express TRPC5, harvested and loaded with the Ca²⁺ indicator dye as described earlier.^[10] The fluorescence imaging plate reader was modified with an additional high-power light-emitting diode (LED) to allow for an even illumination of the microplate at 365 nm. The original BTDA compound and newly synthesised **btda1-7** compounds were serially diluted and applied to the microplate during fluorescence imaging by a liquid handling device equipped with a 384-well multichannel head (Fluent 480 with MCA384, Tecan, Männedorf, Switzerland). Fluorescence emission was continuously recorded with an Andor Zyla 5.5 camera (Andor, Belfast, UK) under the control of a μ Manager 2.0 gamma imaging software.^[11] Data were averaged over single wells, and background signals were subtracted prior to export to MS Excel (Microsoft, Redmond, WA, U.S.A.). Graphs and concentration response curves were generated by fitting a four-parameter Hill equation to the experimental data (MS Excel Solver function).

Microfluorometric Ca²⁺ influx assays in single cells. To obtain action spectra and illumination-dependencies of on- and off-switching of functional responses in HEK_{TRPC5-CFP} cells, we applied single-cell imaging of fluo-4-loaded adherent cells in an inverted microscope (Zeiss Axio, Zeiss AG, Jena, Germany) equipped with a 10x/0.5 Fluar objective (Zeiss AG) monochromator (Polychrome V)-assisted imaging system (TILL Photonics, Gräfelfing, Germany). The monochromator switching protocols were programmed as illustrated in Figure 3, and data were collected and processed in TILLVision 4.2 and MS Excel. After background subtraction, fluorescence intensity data were corrected for partial photobleaching of the single-wavelength Ca²⁺ indicator dye. Correction factors were derived from imaging untreated, fluo-4-loaded cells with the identical illumination protocols. The wavelength dependence of on- and off-switching was sampled in 10-nm-steps, and data from single cells as well as averaged data of all cells within a single experiment were obtained and displayed. To obtain the off-switching action spectrum, cells were exposed to a defined on-switching step (500 ms exposure to 360 nm light) followed by 200 ms of either no illumination, or illumination at the indicated wavelengths. The following rise in fluo-4-fluorescence imaged at short pulses of 480-nm light showed the functional response to the remaining fraction of active BTDAzo compound, and subsequent longer exposure (1.5 s) to 440 nm light served to switch the compound off again before repeating the cycle with another off-switching wavelength. The Xe lamp in the Polychrome V monochromator has no tunable intensity, therefore, the light power was not adjusted between the different wavelengths. Further discussion in section: Photoswitch-on and Photoswitch-off: extended characterisations.

Characterisation of BTDAzo-induced ionic currents. Electrophysiological recordings of TRPC5 currents were performed on adherent HEK_{TRPC5-CFP} cells with an Axopatch 200B amplifier connected to a Digidata 1440A digitizer (Axon Instruments, Molecular Devices, San Jose, CA, U.S.A.). Borosilicate filaments, pipette and bath solutions were prepared as described^[10] and supplemented with 10 μ M **BTDAzo** for subsequent photoswitching during the recording of whole cell currents at -80 mV. A Polychrome II monochromator (TILL Photonics) was coupled to the inverted microscope (Zeiss Axiovert 100 with α Plan-Fluar 100x/1.45 objective) and controlled by the analog output of the Digidata 1440A device to apply 360 nm and 440 nm light in a timely fashion during the recording sweeps. Current voltage relationships were measured by applying slow (200 ms/100 mV) voltage ramps to the cells after illumination with 360 nm or 440 nm as illustrated. Holding currents were filtered at 1 kHz (four-pole Bessel filter) and sampled at 5 kHz. To characterize currents through heteromeric TRPC1:TRPC5 channel complexes, a stably transfected HEK_{TRPC5-CFP:TRPC1-YFP} cell line was generated by transfecting the HEK_{TRPC5-CFP} cell line with an expression plasmid encoding TRPC1-YFP, and isolating transfected colonies after selection with G418 (1 μ g/ml). All results are expressed as current densities (pA/pF), the cell capacitance in the experiments shown was 10-12 pF.

FLIPR assays of *btdas* reveal good photoswitchability of Ca²⁺ currents with *btda3*

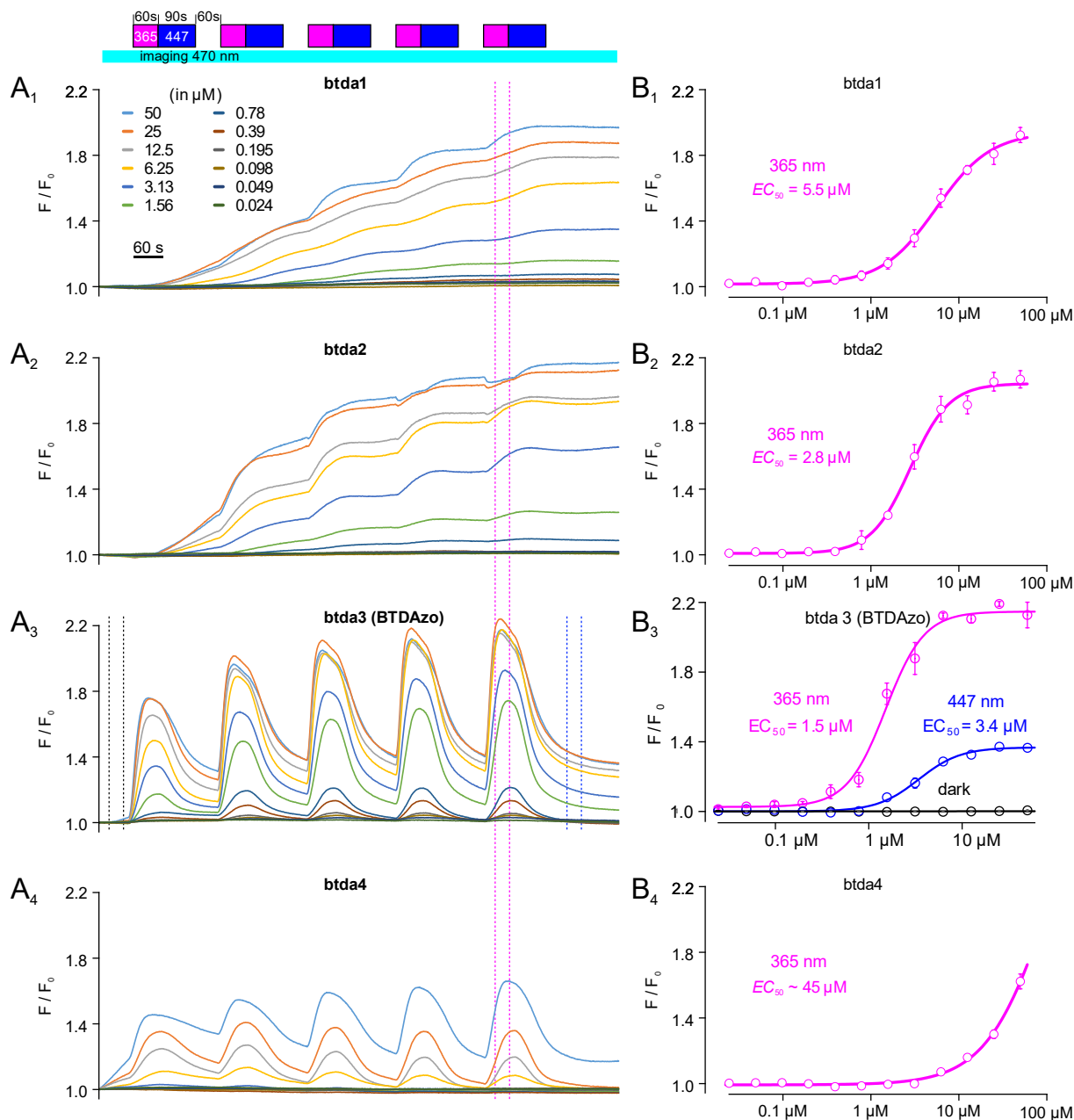


Figure S5 Comparative analysis of biological activity of *btd1*-*btd7* (FLIPR). The *btdas* were serially diluted and applied to fluo-4-loaded HEK_mTRPC5-CFP cell suspensions in a fluorescence imaging plate reader device built into a robotic liquid handling system (Tecan Fluent 480). **(a)** Fluorescence intensities (readout at 480 nm excitation) were continuously recorded during application of the indicated concentrations of the compounds and subsequent alternating illumination with 365 nm and 447 nm light. Results for *btda5*-*btda7* are not shown since they had **no** activity in TRPC5-expressing cells. **(b)** Concentration response curves were constructed from peak responses during the 5th illumination cycle (indicated by the dotted bracketing lines in panels **(a)**). All experiments conducted as minimum of 3 independent experiments with each experiment averaging data in technical duplicates.

Photoswitch-on and Photoswitch-off: extended characterisations

Setup: with the Polychrome V monochromator, the maximum intensity (Xenon light source) is at 470 nm with a maximum intensity drop at 400 nm of only 25% and power (as measured by output from a coupled fibre) is constant to within a factor of 2 over the full range of interest (370-480 nm), which should translate to fairly similar intensities also on the stage. Thus, the action spectra are so slightly biased towards longer wavelengths, that to best approximation the optimal wavelengths at identical intensities are indeed returned by our data.

Off-switching assay (Fig 3e-f): The off-switching response assay measures how completely and how photon-efficiently a given switchoff wavelength (200 ms) counteracts the $E \rightarrow Z$ isomerisation in an immediately preceding 360 nm phase (500 ms). The 360 nm part establishes a fixed Z/E ratio, which by itself would cause strong channel activation (see first cycle in Fig 3e, "none"). But if the switchoff pulse efficiently performs $Z \rightarrow E$ isomerisation, this Z/E ratio is reduced and so is channel activation as revealed during the next 20 seconds of imaging, seen as the peak height reached in each cycle: more peak suppression = better switchoff. After this 20 s imaging that reaches the peak plateau, the cells are reset towards a non-activated basal level to enable the next test round by the 1.5 seconds of 440 nm in the middle of the cycle does (validated in Fig S6); the 60 s imaging after that confirms that we are nearing or have reached a plateau. Thus each cycle tells us about the efficiency of the tested switchoff wavelength.

On-switching assay (Fig 3c-d): Conceptually similar to the off-switching assay, but somewhat simpler, here an activation wavelength is tested against a bracketing background of 440 nm switchoff phases, to see which activation wavelength most efficiently causes $E \rightarrow Z$ isomerisation and channel activation in these flux settings.

Practical Photoswitching: these tests are designed to operate with minimal flux, identifying effective wavelengths that will later allow a maximum of photoswitching cycles before bleaching and photodamage. Effective wavelengths (360/440 nm) are therefore identified, rather than theoretically more complete wavelengths that would however require prohibitively high light fluxes to be used, rendering them suboptimal in practice (370/480-520 nm).

Dark Delay in Imaging Experiments: Any excitation wavelength for imaging Fluo-4 intensities will cause at least a partial change of E/Z ratios. Dark periods were therefore included to allow Ca^{2+} signals in TRPC5-expressing cells to develop for some time towards their plateau without such interference that would depress peak signals (there is a much slower response of the Ca^{2+} -imaging agent, on a seconds scale, than electrophysiology readouts that are on the millisecond scale). The data points used to construct the action spectrum were collected from

the very first images after the dark phase, reflecting the Ca^{2+} influx induced by the applied on-switching wavelength during a defined dark time interval.

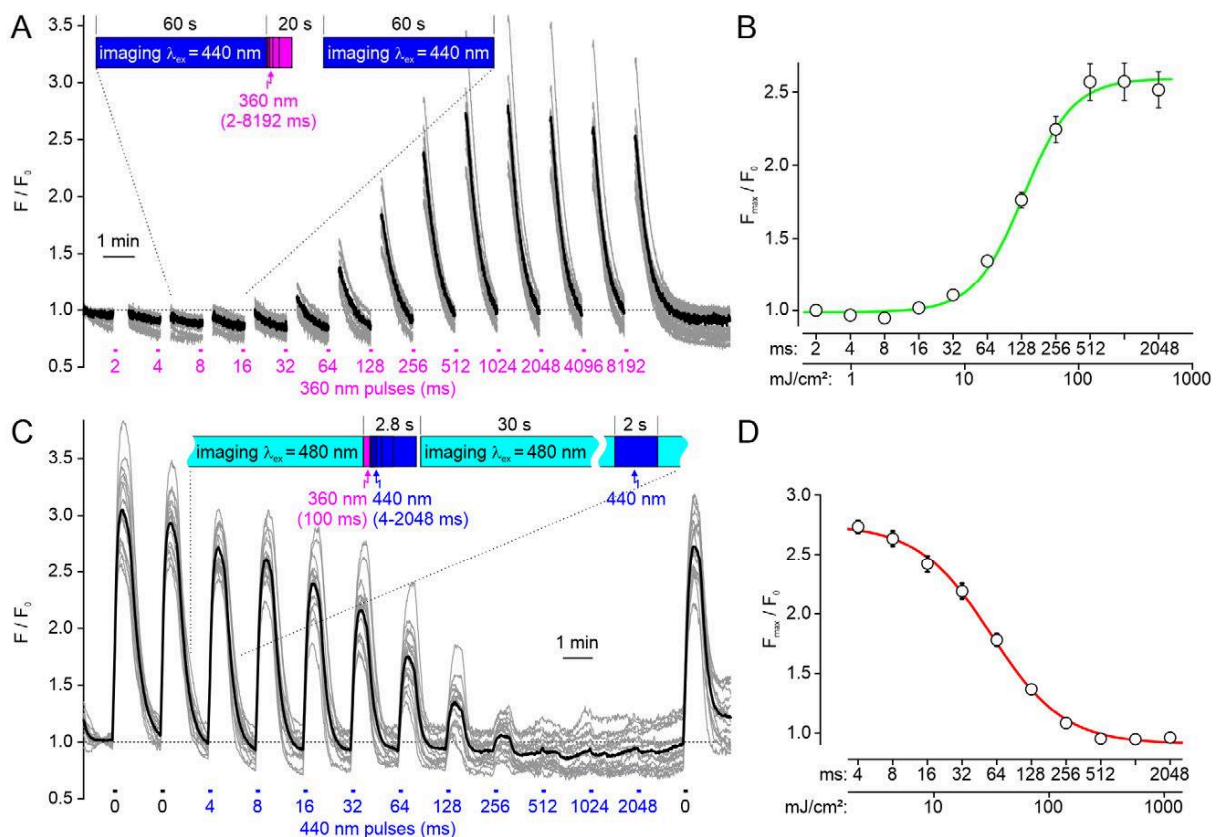


Figure S6 Light energy dependence (power spectra) of BTDAzo-induced Ca^{2+} influx responses in single HEK_{TRPC5-CFP} cells, reflecting $E \rightarrow Z$ and $Z \rightarrow E$ photoisomerisation in cells. Fluo-4-loaded adherent HEK_{TRPC5-CFP} cells were imaged through a 10x/0.5 Fluor objective (Zeiss) in a monochromator (Polychrome V, TILL Photonics)-equipped imaging system built around an inverted microscope. Based on the action spectra shown in Fig. 3 of the main manuscript, the on- and off-photoswitching efficiency was assayed at optimal illumination wavelengths of 360 nm and 440 nm, respectively. **(a)** On-photoswitching responses in TRPC5-expressing cells in the presence of 1 μM BTDAzo. The on-photoswitching was induced by illuminating the visual field with 360 nm light for the indicated times. Imaging of fluo-4 fluorescence intensities was initiated 20 s after the onset of the on-switching illumination pulse. Shown are background- and photobleaching-corrected fluorescence intensities F after normalisation to the respective initial intensities F_0 determined in regions of interest that covered single cells, each (grey lines). Black line: averaged response of all cells measured in the experiment. **(b)** Semilogarithmic plot of on-switching illumination times and resulting peak fluorescence intensities in first images following the on-photoswitching illumination derived from data shown in **(a)**. The second x axis depicts the energy of applied 360 nm light as calculated from the excitation power density of the imaging system and the respective illumination times. **(c)** Similar experiment as in **(a)**, but with 10 μM BTDAzo in the bath solution and with a constant on-switching illumination time of 100 ms, immediately followed by illumination at 440 nm for the indicated times. Imaging of fluo-4 fluorescence intensities was done by applying short (40 ms) pulses of 480 nm excitation to minimize off-switching by the imaging procedure. After 30 s of imaging, 440 nm light was applied for 2 s to intentionally switch the compound back to its off-state. **(d)** Semilogarithmic plot of off-switching illumination times and resulting attenuation of Ca^{2+} influx signals in TRPC5-expressing HEK cells.

Comment on action spectra: The $E \rightarrow Z$ action spectrum scan (Fig 3d) used 100 ms pulses, which we know from the 360 nm $E \rightarrow Z$ power spectrum does *not* deliver PSS at this wavelength, or any other (as they do not have significantly greater bulk photoconversion rates). Therefore Fig 3d presents photon-flux-limited results that depend not only on the final PSS values that *would* eventually be reached after saturating illumination, but also on the rapidity

of bulk $E \rightarrow Z$ isomerisation, which is a practical parameter of great interest for biological use (to minimise sample bleaching etc). We believe that the PSS spectra and values that were measured in homogenous media (e.g. **Fig 2d**) do not sufficiently predict the narrowness of this action spectrum peak. Noting that bulk $E \rightarrow Z$ isomerisation rates depend on the relative magnitudes of the E and Z extinction coefficients, so that this ratio can be strongly affected by environment-dependency of absorption band breadth particularly in the Z isomer, we believe the narrowed action spectrum reflects narrowed bands in the cellular setting, due to concentration of this lipophilic photoswitch into water-excluded cellular environments. Though measurements to study this appropriately would be outside the scope of this paper, we refer the interested reader to other examples of photoswitch performance being dependent on microscopic localisation and inhomogenous environment effects^[7,8].

***E*-BTDAzo antagonises channel activation by BTD**

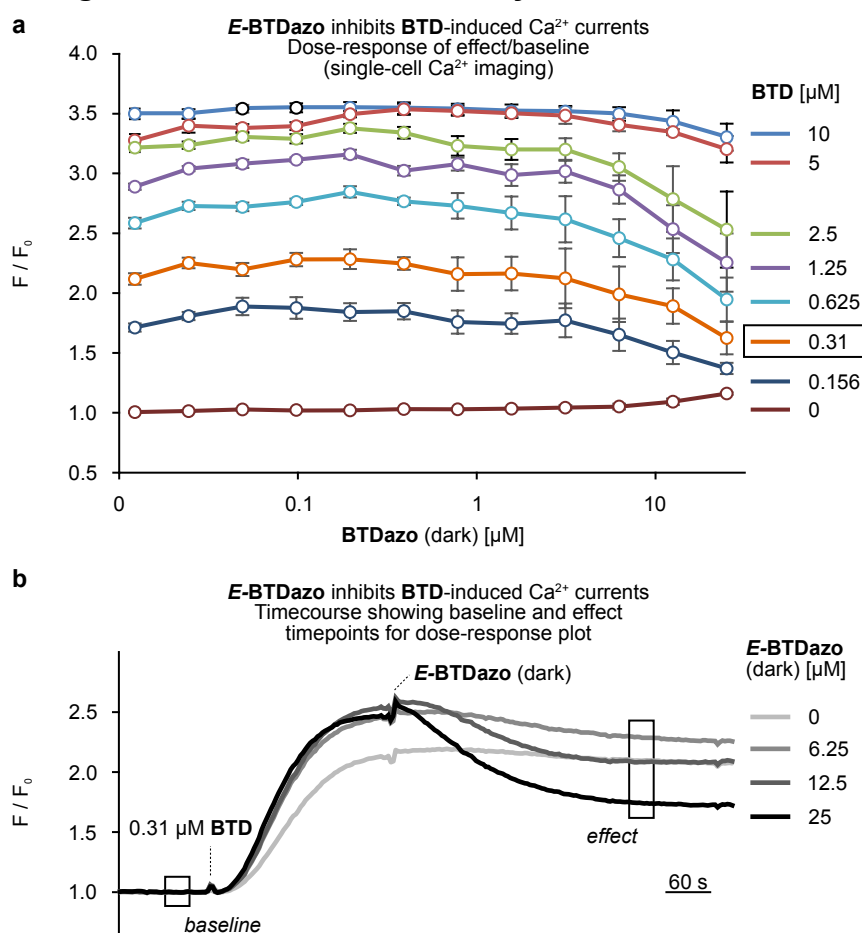


Figure S7 *E*-BTDAzo dose-dependently inhibits BTD-induced Ca^{2+} currents. (Zero-concentration curve in panel **b** measured at edge of plate, magnitude of effect ca. 20% lower than other curves which are from interior wells)

btda compounds do not activate TRPC4

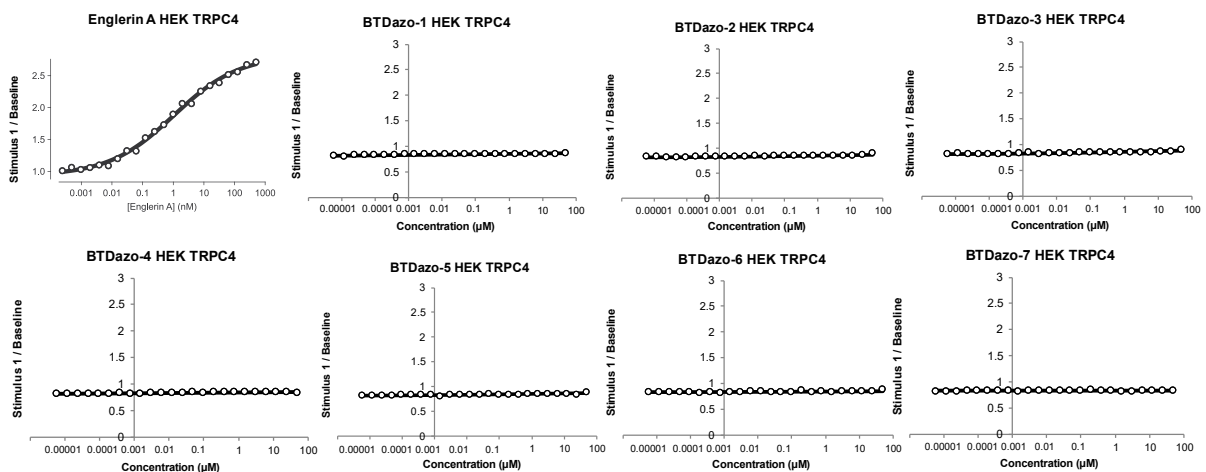


Figure S8 Lack of biological activity of btda1-btada7 compounds on TRPC4. The selectivity of btda1-btada7 was assessed by FLIPR in fluo-4-loaded HEK cell suspensions stably overexpressing mouse TRPC4 β C-terminally fused to cyan fluorescent protein (HEK_{TRPC4-CFP}). TRPC4 is the closest relative of TRPC5 and capable of forming functionally active homotetrameric channel complexes.^[12] The experimental procedure followed that described in Fig. 3a,b of the main manuscript.

Mouse experiments

Mice. Adult female mice (7 - 20 weeks old) were kept under standard light/dark cycle (12:12; lights on 0600; lights off 1800) with food (Ssniff feed containing 9% fat, 24% protein, and 67% carbohydrate) and water ad libitum. Mice were maintained in IVC housing containing enrichment (nesting, bedding and other material). We used the following mouse strains: B6.Cg-7630403G23RikTg(Th-cre)1Tmd/J (RRID:IMSR_JAX:008601, referred to as Th-Cre mice)^[13] B6;129S-Gt(ROSA)26Sortm95.1(CAG-GCaMP6f)Hze/J (RRID:IMSR_JAX:024105, referred to as R26-GCaMP6f or Ai95D mice)^[14] and Trpc5tm1.1Lbi (RRID:IMSR_JAX:024535; MMRRC Stock No: 37349-JAX, referred to as Trpc5-E5 $-/-$ mice.^[15,16] We crossed Th-Cre mice with R26-GCaMP6f reporter mice resulting in a strain in which all Th⁺ cells are identifiable through their green fluorescence (referred to as Th-GCaMP6f mice). These mice were also crossed with Trpc5-E5 $-/-$ mice, resulting in a strain in which all Th⁺ cells, identifiable through their green fluorescence, are deficient for Trpc5-E5 (referred to as Th-GCaMP6f- Δ Trpc5). Th-GCaMP6f and Th-GCaMP6f- Δ Trpc5 mice were heterozygous for Cre and GCaMP6f.

Animal care and experimental procedures were performed in accordance with the guidelines established by the German Animal Welfare Act, European Communities Council Directive

2010/63/EU, the institutional ethical and animal welfare guidelines of the Saarland University (approval number of the Institutional Animal Care and Use Committee: H-2.2.4.1.1). The number of animals used is a minimum necessary to provide adequate data to test the hypotheses of this project. We minimized the number of animals required by the animal welfare committees wherever possible.

Solutions and Chemicals. Oxygenated extracellular solution aCSF (95% O₂/5% CO₂) contained (in mM): 120 NaCl (Guëssing, Germany), 25 NaHCO₃ (Merck, Darmstadt, Germany), 5 KCl (Guëssing, Germany), 5 N,N-bis(2-hydroxyethyl)-2-aminoethanesulfonic acid (BES), 1 MgSO₄, 1 CaCl₂ (Guëssing), 10 glucose (Merck). Prolactin stock solutions were prepared in distilled water (1 mg/ml), diluted in aCSF and stored at -20 °C. **BTDAzo** (Bio-Techne GmbH, Germany) stock solution was prepared in dimethyl sulfoxide (DMSO; 5 mM) and stored at -20 °C. The **BTDAzo** stock solution was then diluted in aCSF to make final working concentrations of 1, 5, and 10 µM on the day of the experiment. **BTDAzo** (**btada3**) was prepared in DMSO (20 mM) and diluted in aCSF to 100 µM. Warming the solution to 40 °C combined with a short sonication yielded a clear yellowish solution of the BTDAzo. The BTDAzo stock was further diluted in aCSF to yield 10 µM BTDAzo at the day of the experiment. DMSO concentrations were ≤ 0.05 % (vol/vol) in the final working solution. Unless stated otherwise, all chemicals were purchased from Sigma (Munich, Germany). Chemicals were of analytical or higher grade.

Preparation of Hypothalamic Brain Tissue Slices. All experiments were performed on coronal brain slices (Bregma -1.6 and -2.2 mm) freshly prepared from female mice adapting previously described methods.^[16,17] Mice were anesthetized with isoflurane, followed by decapitation. Brains were removed quickly, submerged in ice-cold extracellular aCSF solution, and sliced (275 µm thick) using a vibrating-blade microtome (Leica, Germany). Slices were

kept in oxygenated aCSF (95% O₂/5% CO₂) at 31.5 °C for 15 min and then at RT for 30 min before starting an experiment.

Ca²⁺ Imaging and Combined Laser Scanning-controlled Photoswitching. We used an upright scanning confocal microscope (Zeiss LSM 880 Indimo) equipped with a standard Argon laser for excitation at a wavelength of 488 nm and a UV laser (Coherent) emitting 355 nm.^[18–20] Emitted fluorescence was collected between 500 and 560 nm. All scanning head settings were kept constant during each experiment. Images were acquired at 1.7 Hz and analysed using a combination of Zen (Zeiss), ImageJ (NIH), Igor (Wavemetrics) and OriginLab (OriginLab Corporation) software.

For laser scanning-controlled photoswitching of **BTDAzo**, the UV laser light coupled to the confocal microscope was focused onto the image plane through a 20 x 1.0 NA Plan-Apochromat water immersion objective (Zeiss). The depth of focus was 16 µm which ensured, together with the region of interest (ROI) diameter, illumination of individual cells. Before photoswitching, UV laser light was optimally focused using 18 µm thick brain tissue sections loaded with Hoechst 33342 (1:10000; ThermoFisher) and the semi-automated correction tool of the Zen software (Zeiss). **BTDAzo** (10 µM) was added to the bath chamber containing the brain slice and subsequently incubated for about 15 min in the dark. GCaMP6f fluorescence was then measured in the presence of **BTDAzo** using the 488 nm Argon laser (2% 25 mW). Photoswitching was achieved by directing UV laser light (6, 10 or 15 mW) on preselected ROIs using the Zen software (Zeiss), followed by exposure to the Argon laser light to resume monitoring of GCaMP6f fluorescence and switching **BTDAzo** back into the inactive state. For a typical single Th⁺ neuron with a size of approximately 154 µm², a UV stimulation consisted of 10 individual scans of this ROI (647 pixels with a pixel size of 0.238 µm²). Given a laser dwell time of 2.05 µs/pixel, the total UV exposure (= number of scans x area x dwell time/pixel) was thus 13.3 ms in this example. Due to slight changes in individual neuron size, UV exposure

ranged from 10 to 20 ms in the experiments shown in **Fig 4**. Depending on the depth of a given cell within the tissue slice, UV laser power was set to either 6, 10 or 15 mW.

Additional experiments analyzed the response delay as a function of total UV exposure time (**Fig S9d-e**). Here, the UV stimulation (6 mW or 10 mW 355 nm) consisted of either (i) 300 individual scans across the cell soma with a pixel dwell time of 0.82 μ s or 1.02 μ s, or (ii) 100 individual scans with a pixel dwell time of 2.05 μ s.

To protect the ultrasensitive GaAsP photomultiplier tubes from the 355 nm light, high-speed shutters closed and opened at the beginning and end of the UV exposure. Hence, GCaMP6f fluorescence could not be collected during this time (see example **Fig S9d**). The response delay was calculated from the end of the UV stimulation protocol until the time when the GCaMP6f fluorescence baseline or peak values increased their previous values (i.e. before UV stimulation) by 2 x SD.

Changes in GCaMP6f fluorescence were expressed as relative fluorescence changes, i.e. $\Delta F/F_0$ (F_0 was the average of the fluorescence values of 30 frames before stimulation). Fluorescence (F) data were normalized to the $Peak_{max}$ obtained during control measurements and plotted as a function of time (t). To quantify the changes in the dynamics of individual Ca^{2+} responses, we calculated the area under the curve (AUC) as a measure for the increase in intracellular Ca^{2+} . A control AUC was taken at the beginning of each recording for 3 min. The AUCs of **BTD** and **BTD_{Azo}** were calculated from the last 3 min of the recording. The duration of the recordings was 9 min. Duration of the Ca^{2+} recordings after prolactin treatment lasted 15 min because more time is needed to induce an increase in calcium fluorescence. Therefore, control AUCs in these recordings were taken for 5 min at the beginning of the recording. Prolactin-induced AUCs were taken from the last 5 min of the recording.

Quantification and Statistical Analysis. Statistical analyses were performed using Origin Pro 2017G (OriginLab Corporation, Northampton, MA, USA). Assumptions of normality and

homogeneity of variance were tested before conducting the following statistical approaches. A paired two-tailed Student's t-test was used to measure the significance of the differences between two distributions (treatments) of the same Th⁺ neuron. Multiple groups were compared using a two-way analysis of variance (ANOVA) with Tukey's multiple comparison test as a posthoc comparison. In case the results failed the test of normality, the Kruskal-Wallis ANOVA in combination with the Dunn's test were performed. The probability of error level (alpha) was chosen to be 0.05. Unless otherwise stated, data are expressed as means \pm SD. Legends of the figures indicate the number of independent measurements. We used at least 3 mice per genotype, as required by the animal welfare committee.

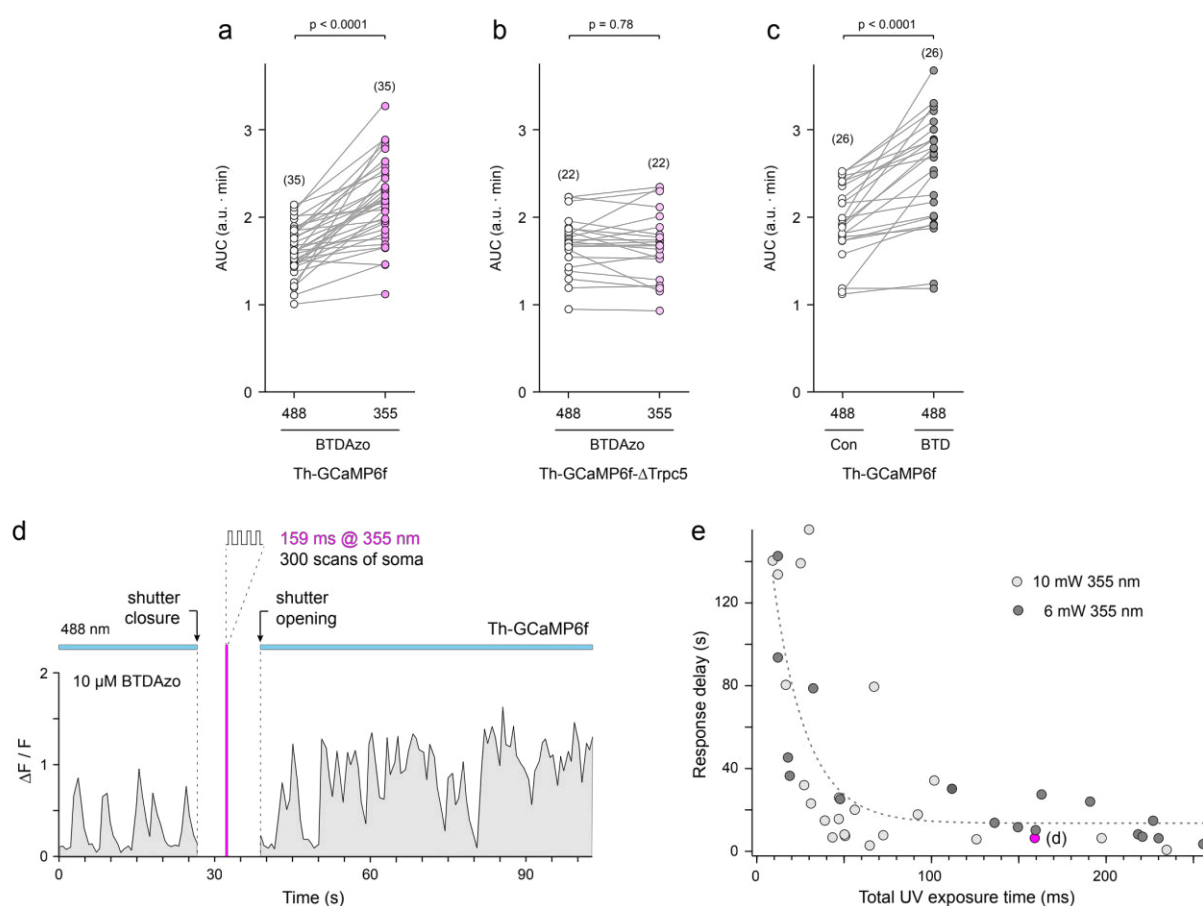
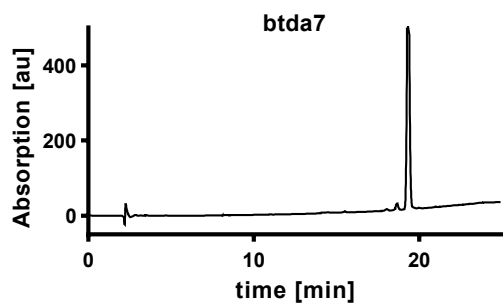
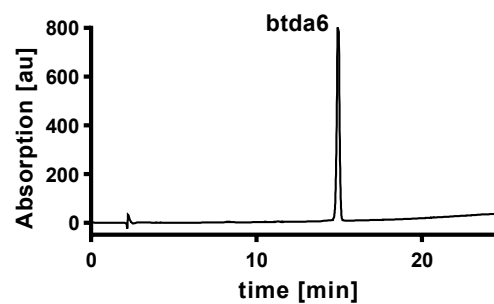
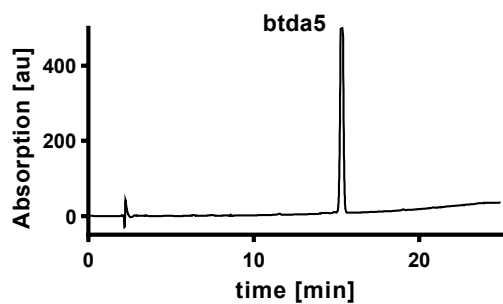
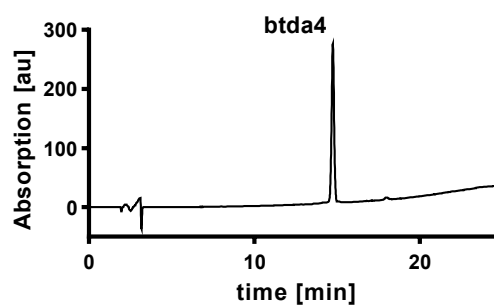
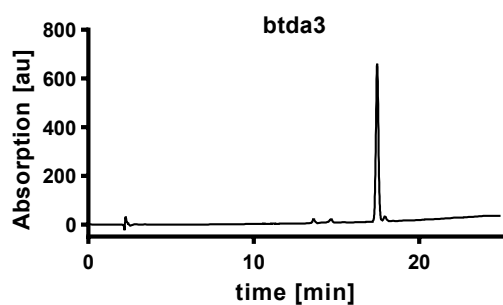
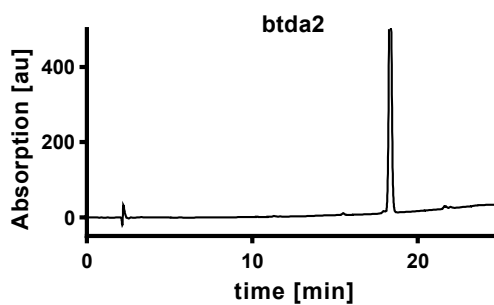
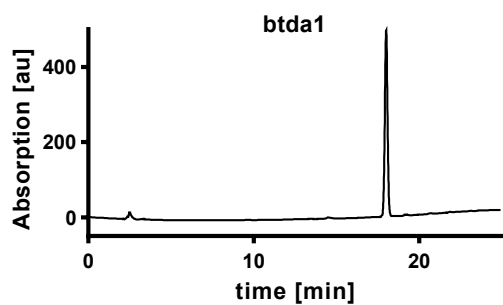


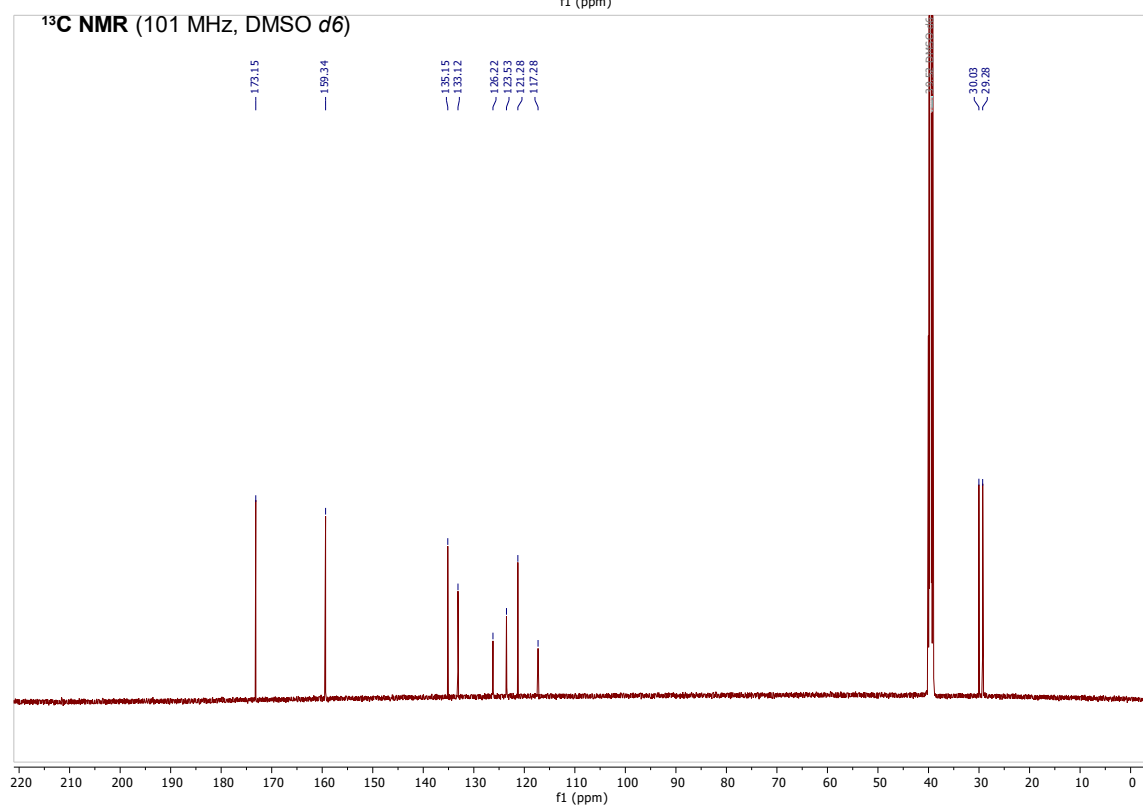
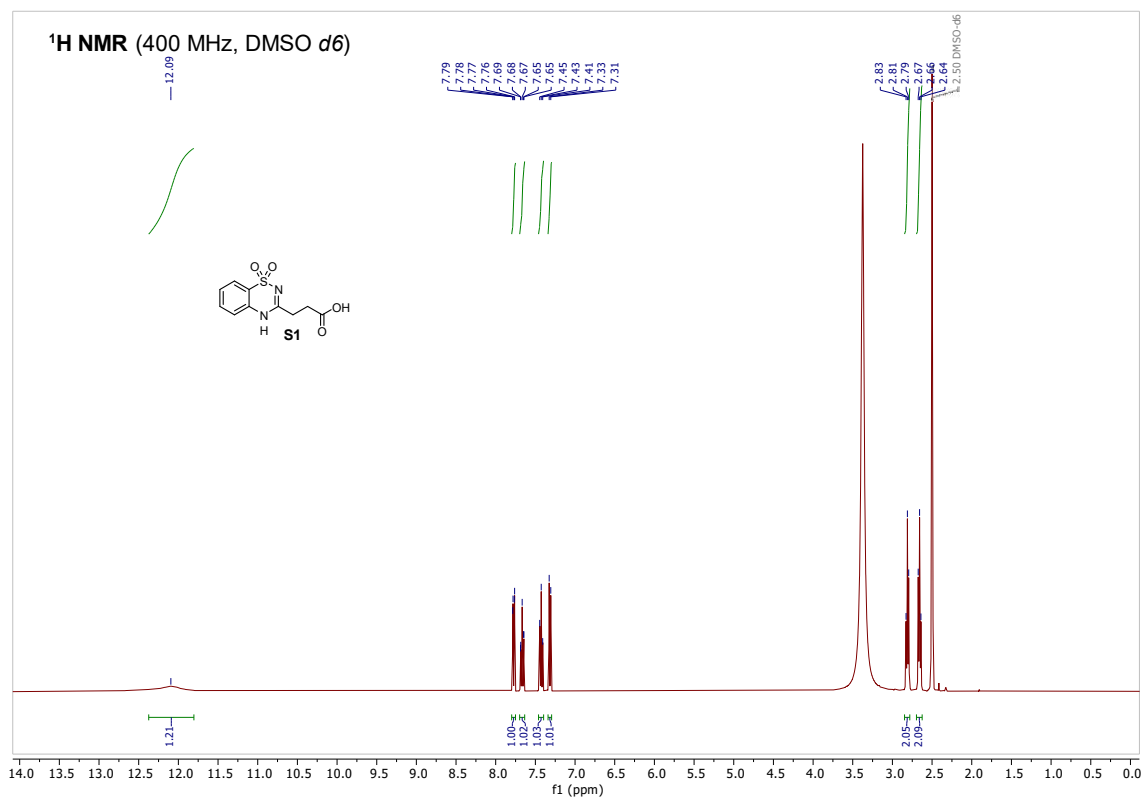
Figure S9: (a) AUC (area under the curve) plots from individual Th⁺ neurons shown in Fig. 4h. In the presence of 10 μ M BTDAzo, AUC values increased after 355 nm UV light illumination in Th⁺ neurons of Th-GCaMP6f mice (n = 5). Paired t-test: $t(34) = 8.183$, $p < 0.0001$. (b) TRPC5 channel knockout prevented the UV light-induced increase in AUC in Th⁺ neurons of Th-GCaMP6f- Δ Trpc5 mice (n = 3). Paired t-test: $t(21) = 0.289$, $p = 0.78$. (c) Application of 10 μ M BTD produced very similar results as UV stimulation of BTDAzo in Th⁺ neurons of Th-GCaMP6f mice (n = 4). Paired t-test: $t(25) = 5.530$, $p < 0.0001$. Number of individual cells is indicated in parentheses above each bar. (d) Example showing BTDAzo stimulation with a longer total UV exposure time resulting in a much shorter delay (6.2 s) of the TRPC5-dependent Ca²⁺ response. The UV stimulation (6 mW 355 nm) consisted of 300 individual scans of the cell soma with a pixel dwell time of 0.82 μ s which resulted in a total UV exposure time of 159 ms.

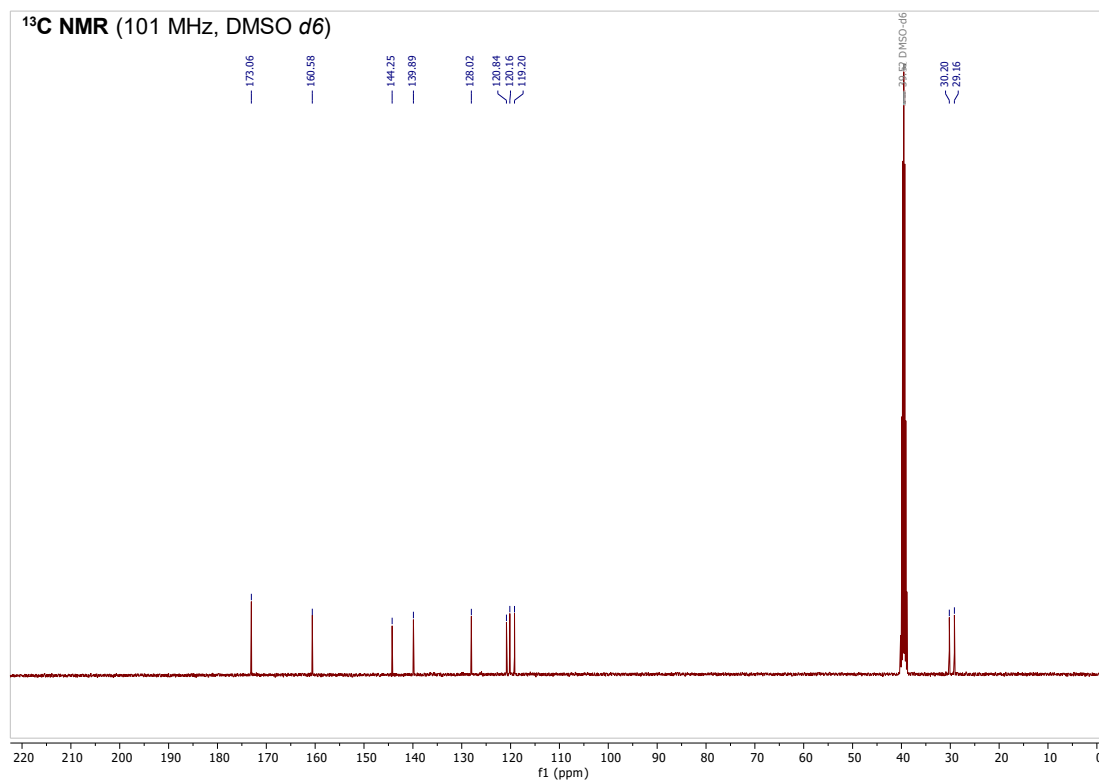
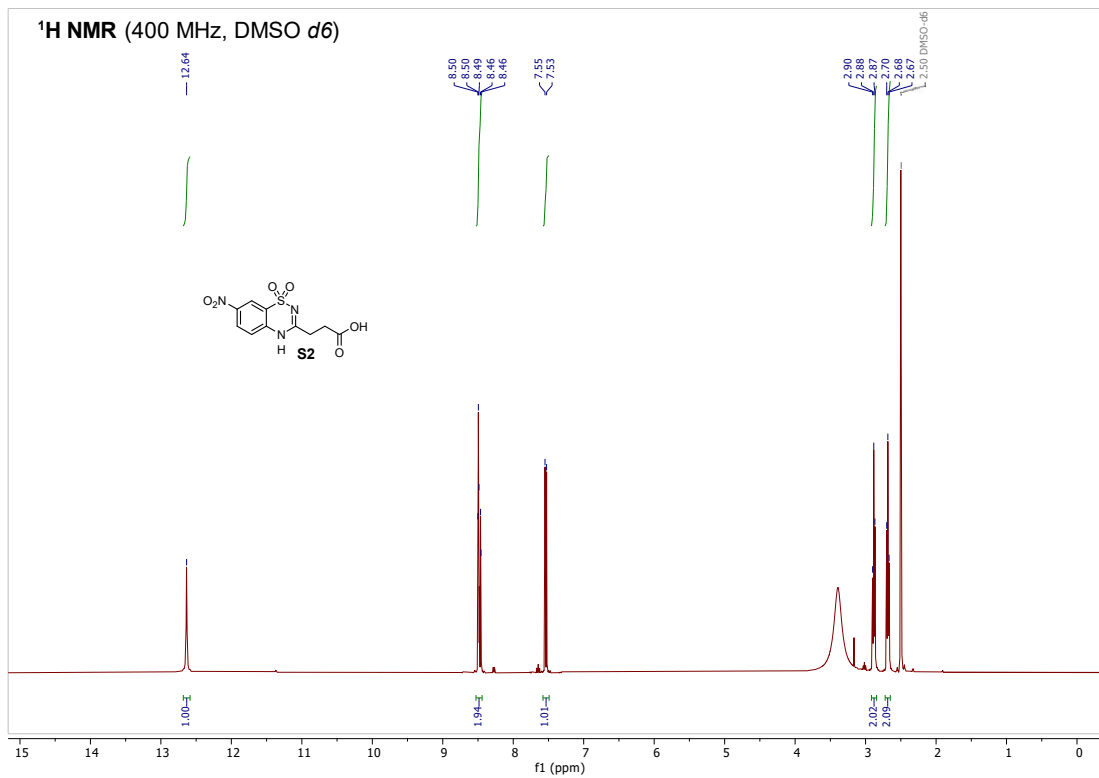
The time required for the repeated UV laser stimulation protocol and the opening/closing of the laser shutter was 11.5 s. **(e)** Group data showing a plot of response delay vs. total UV exposure time. With exposure times > 120 ms, the delays ranged between 0.7 - 27.5 s (mean \pm SD: 10.6 ± 7.5 s, n = 14). Dashed line is an exponential fit of the datapoints to determine the horizontal asymptote reflecting the mean response delay. The pink data point labelled (d) represents the example shown in **(d)**.

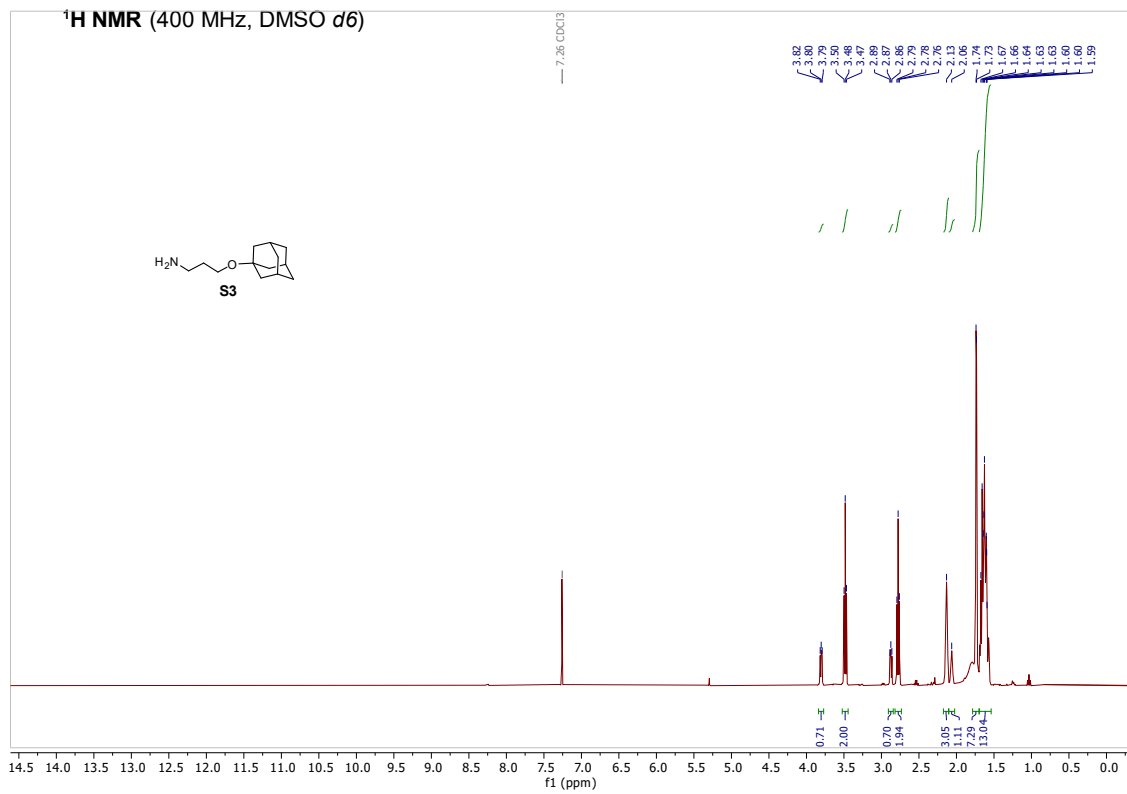
HPLC & NMR Spectra

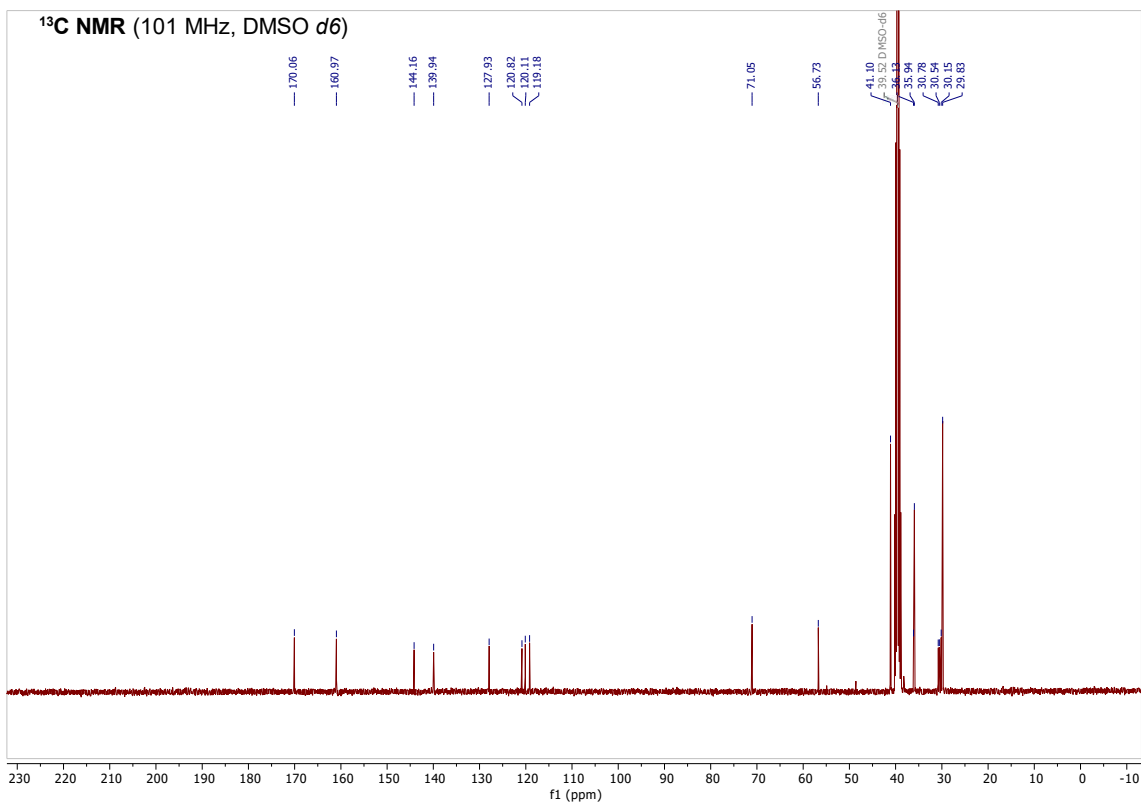
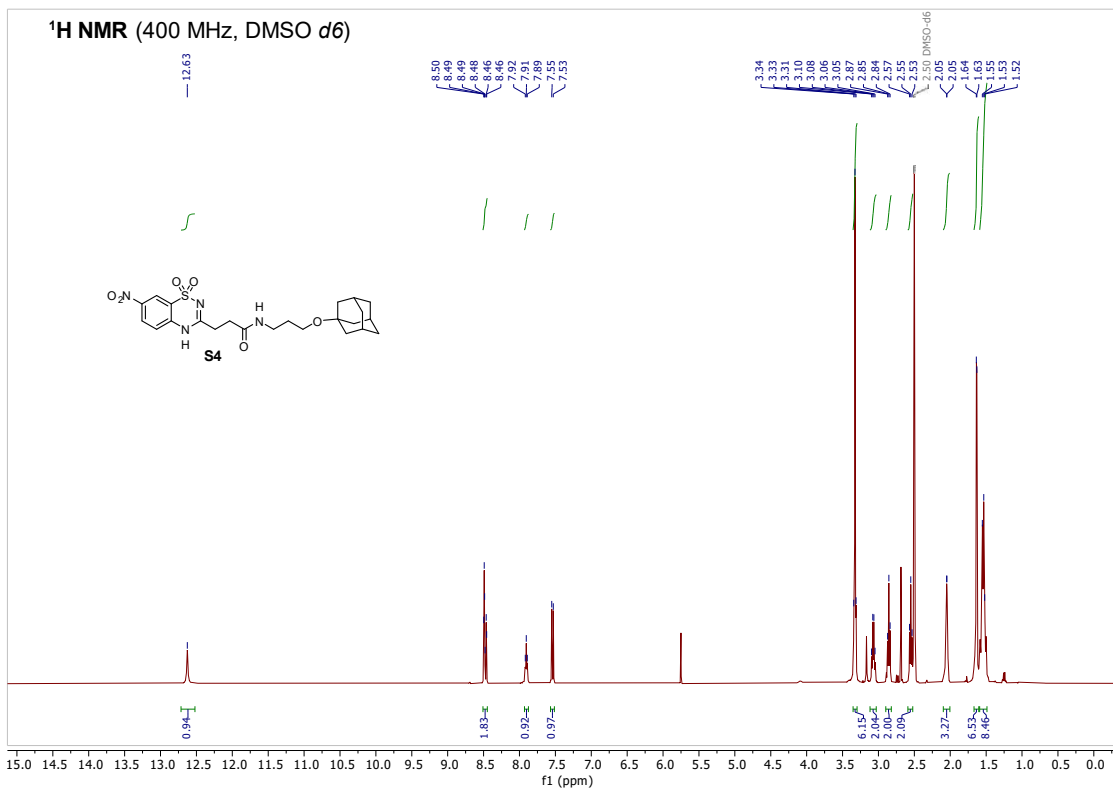


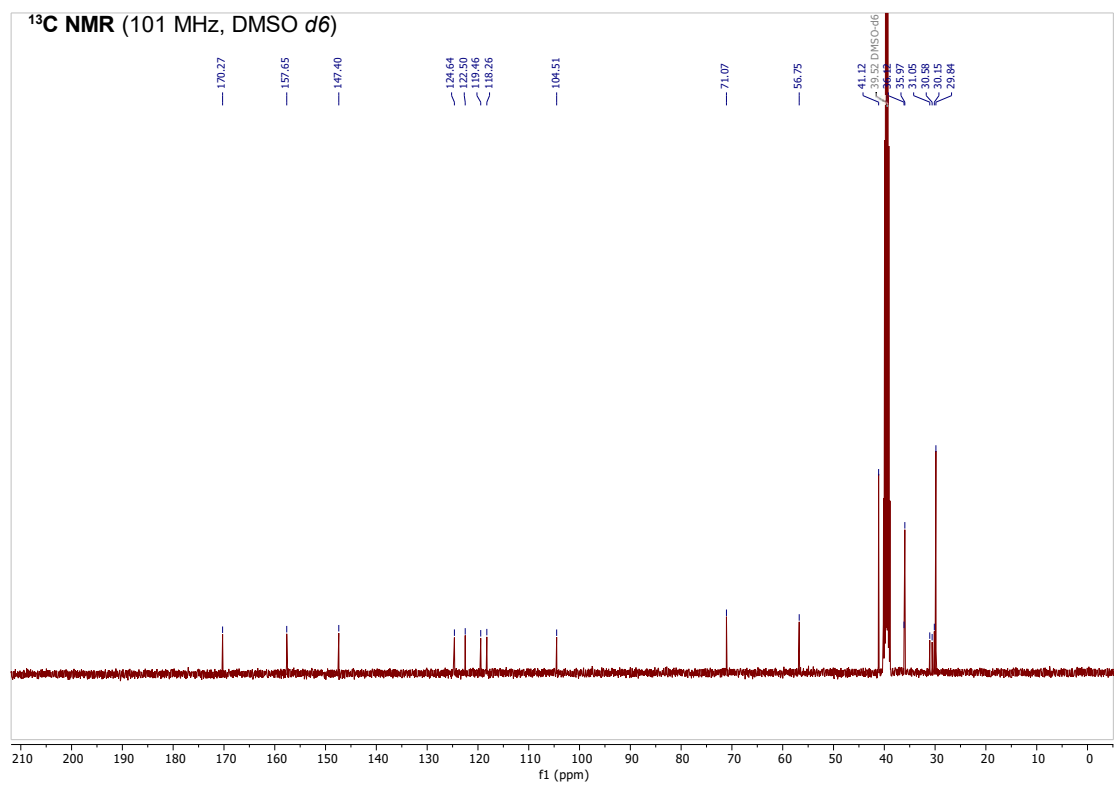
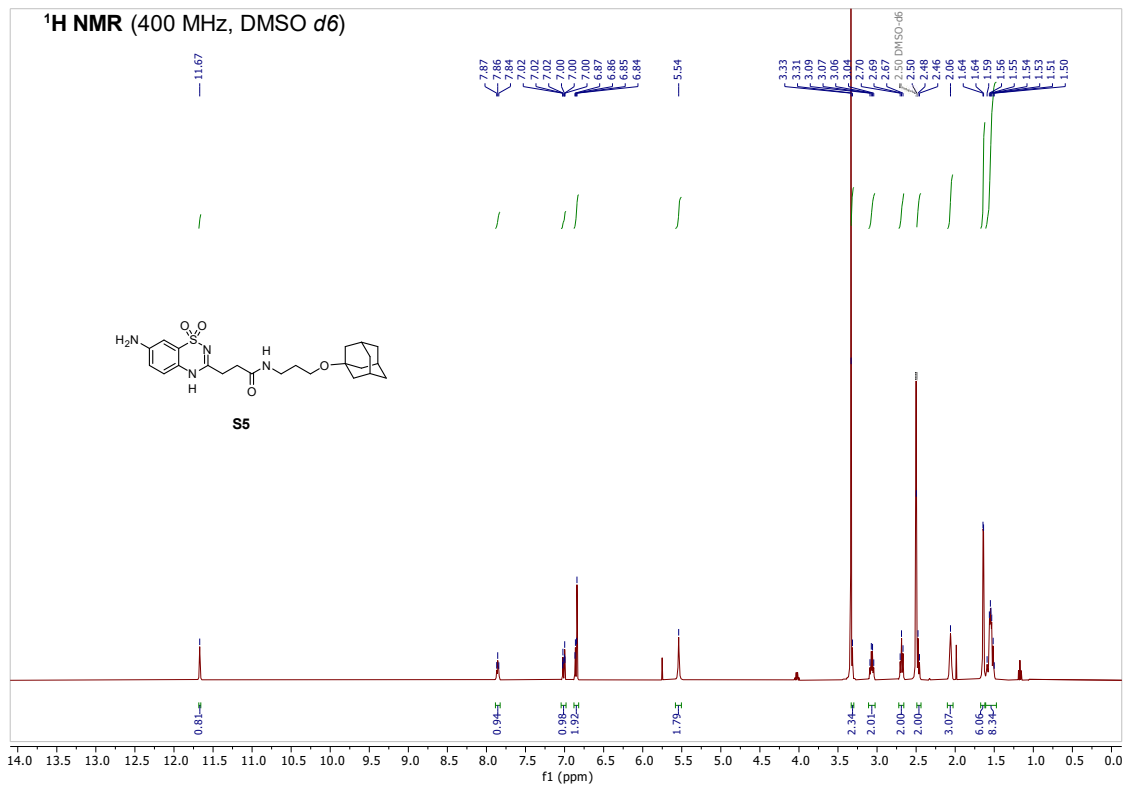
HPLC traces of *E*-btda1-7 with absorption at 254 nm.

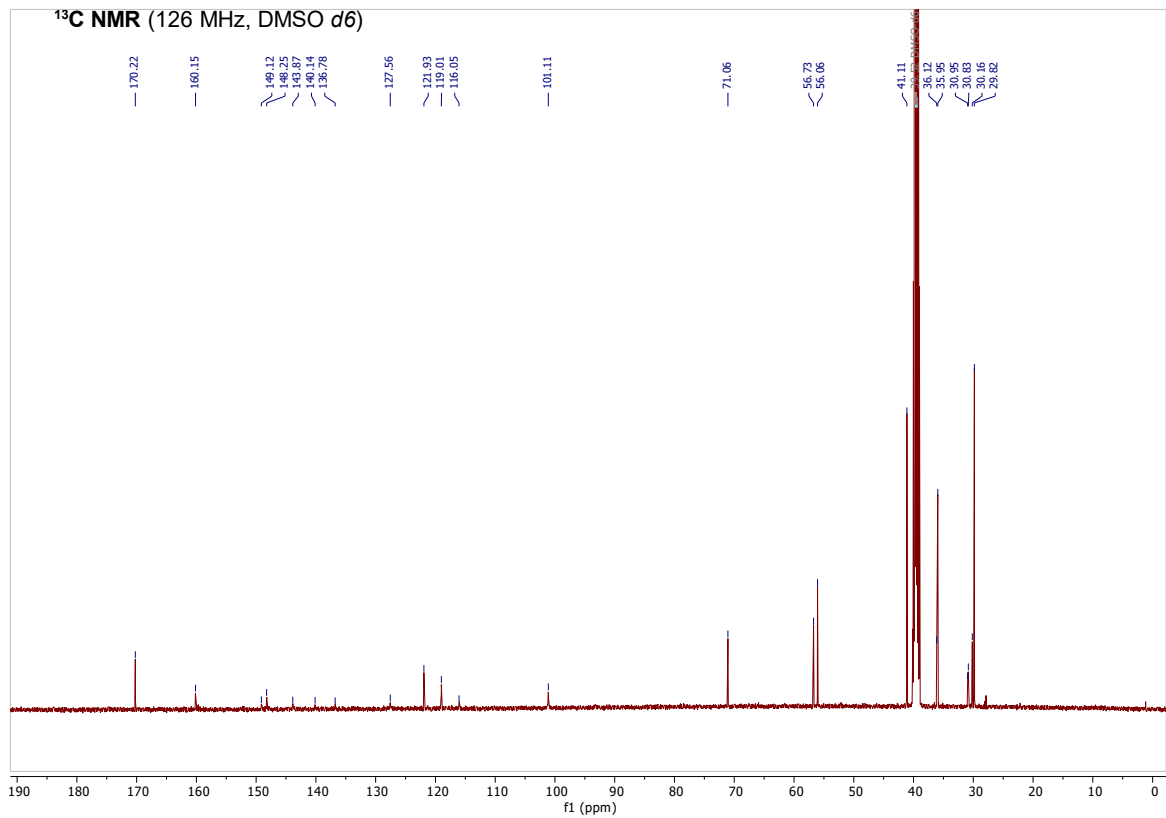
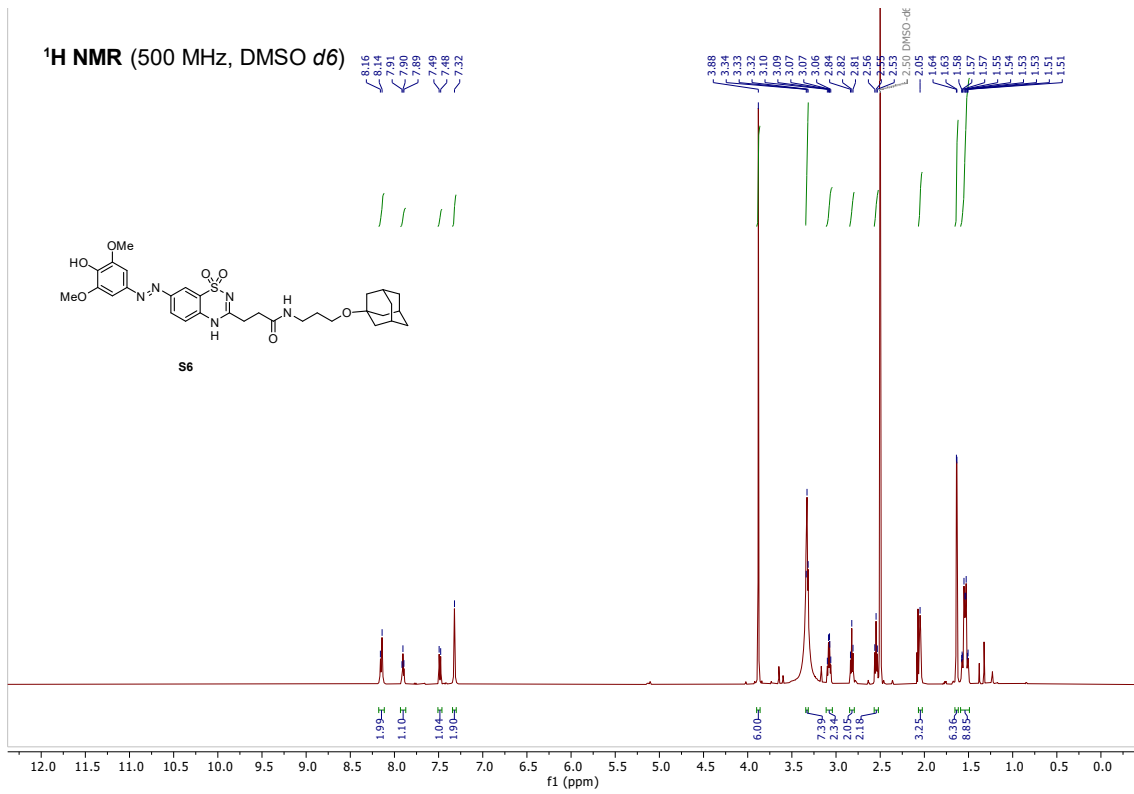


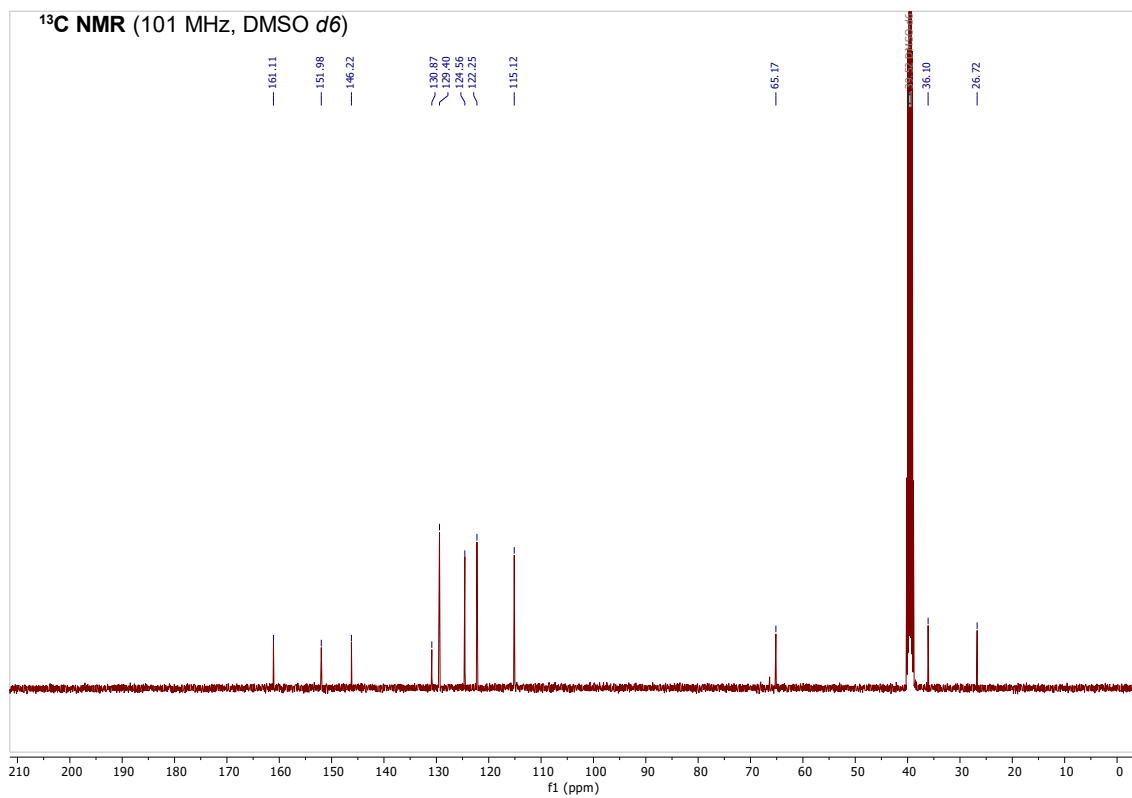
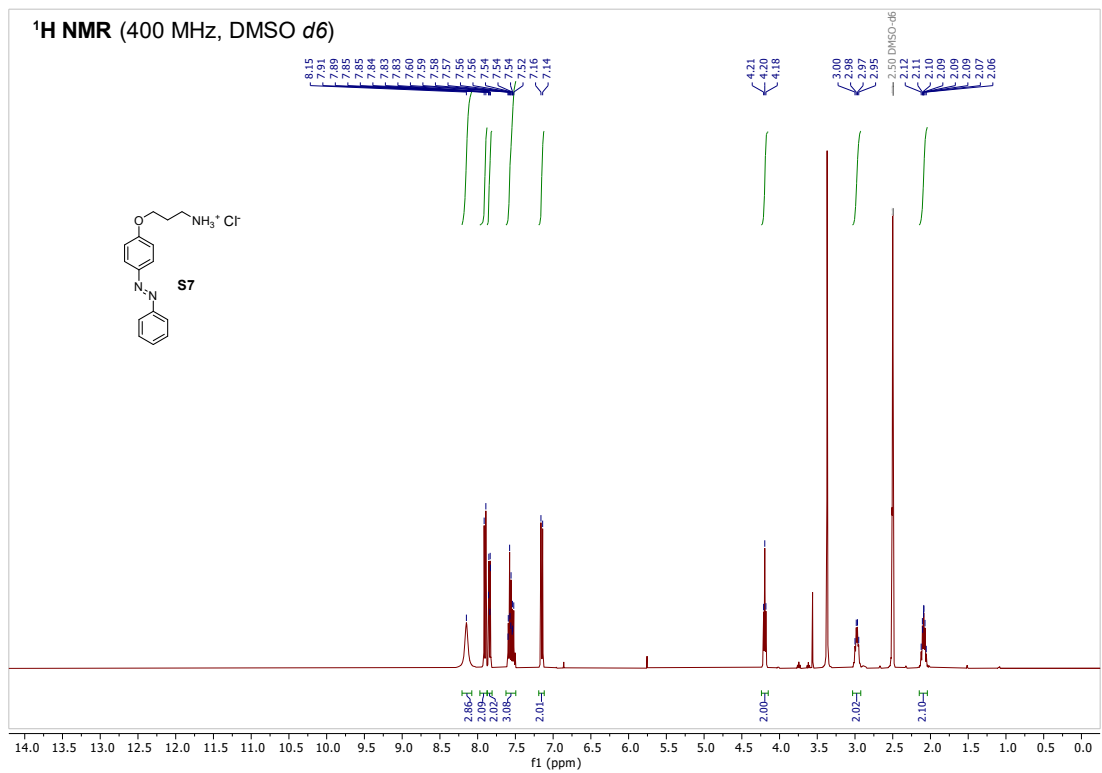


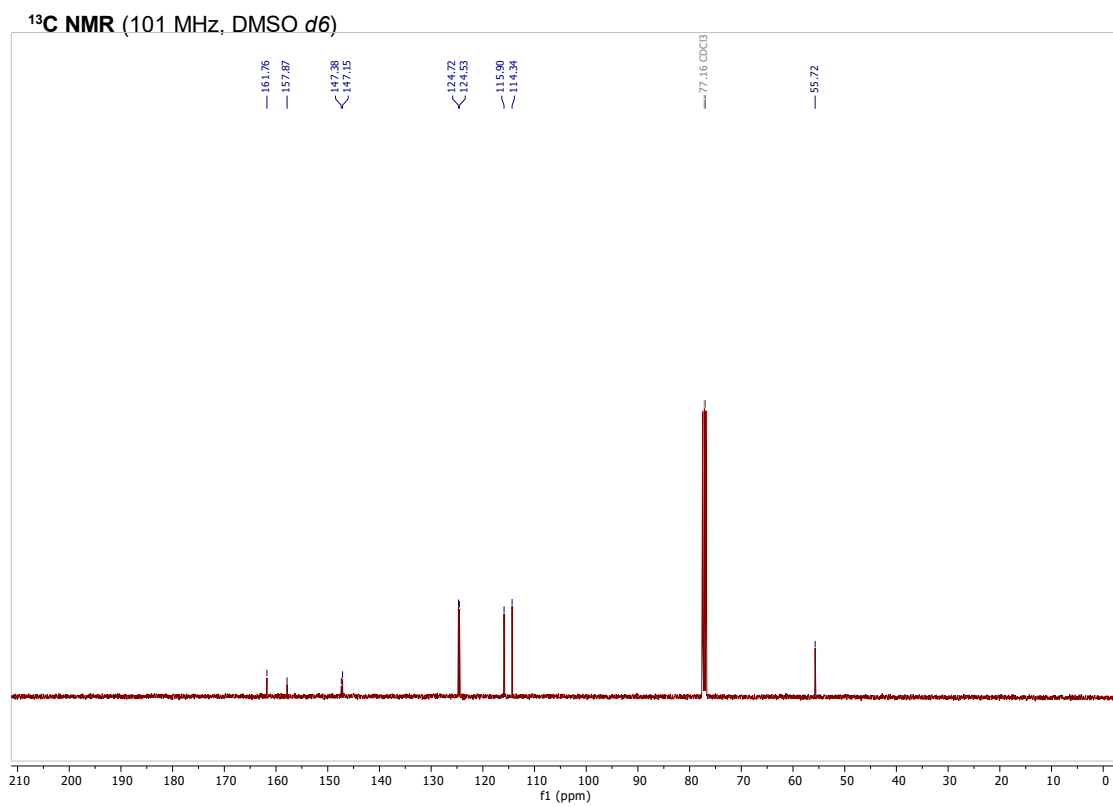
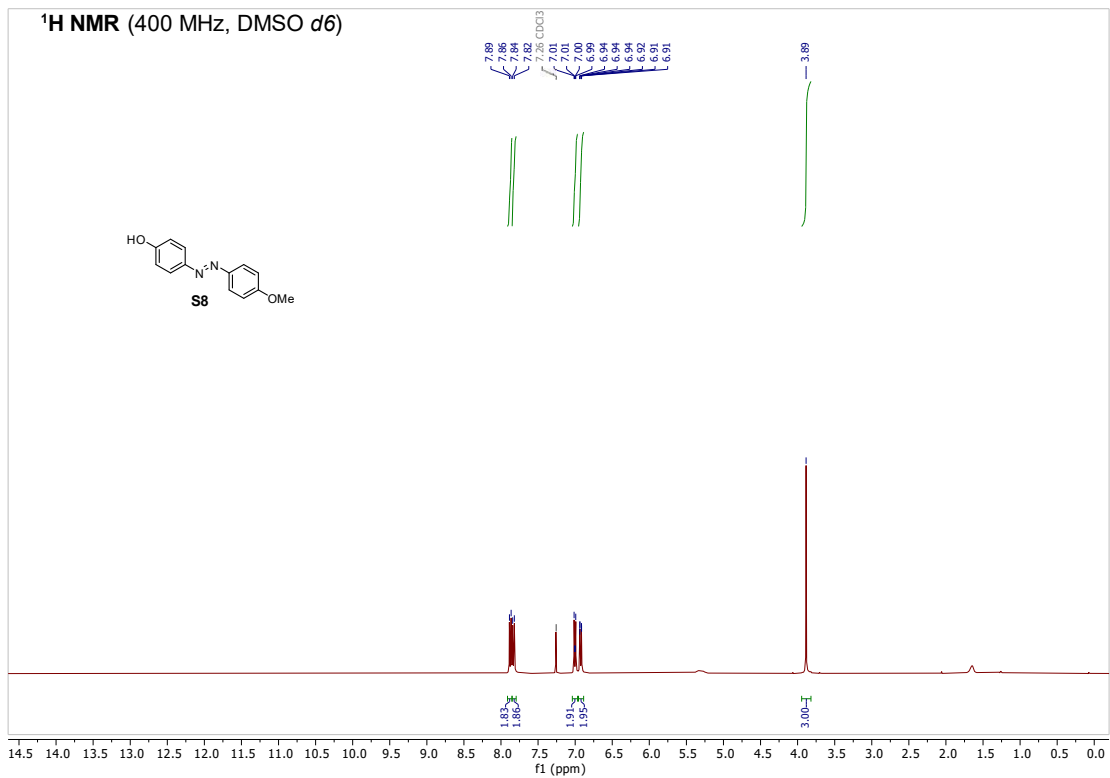


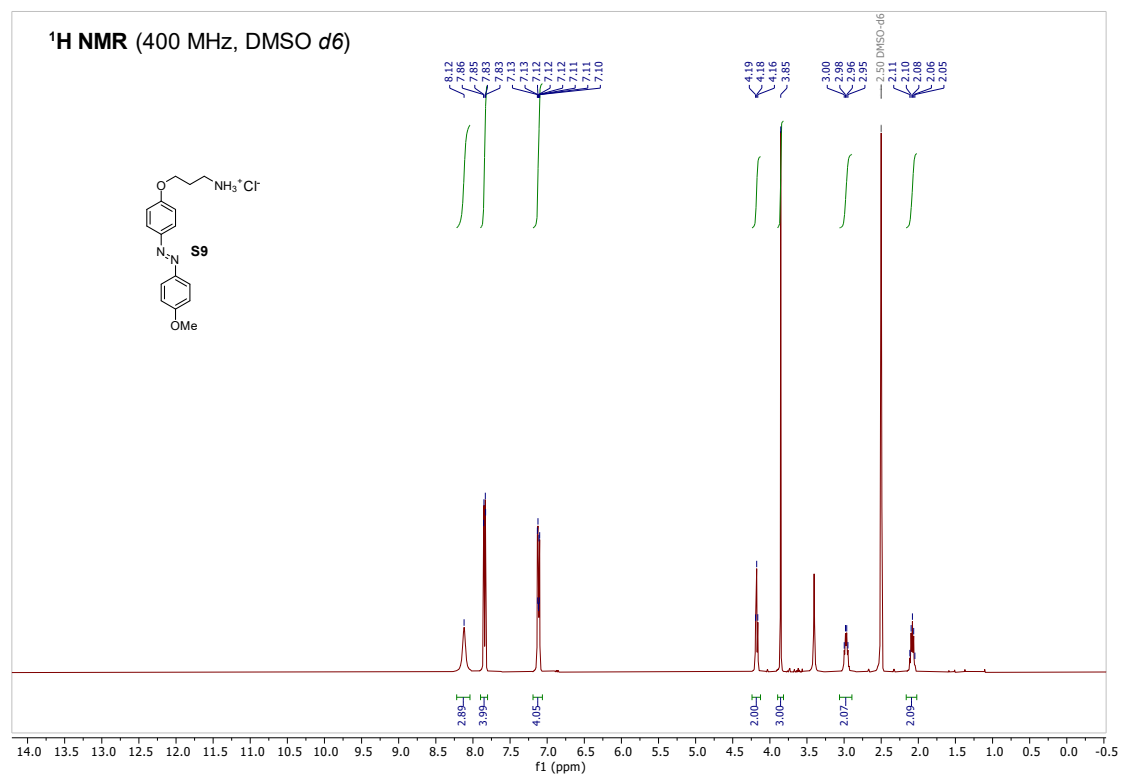




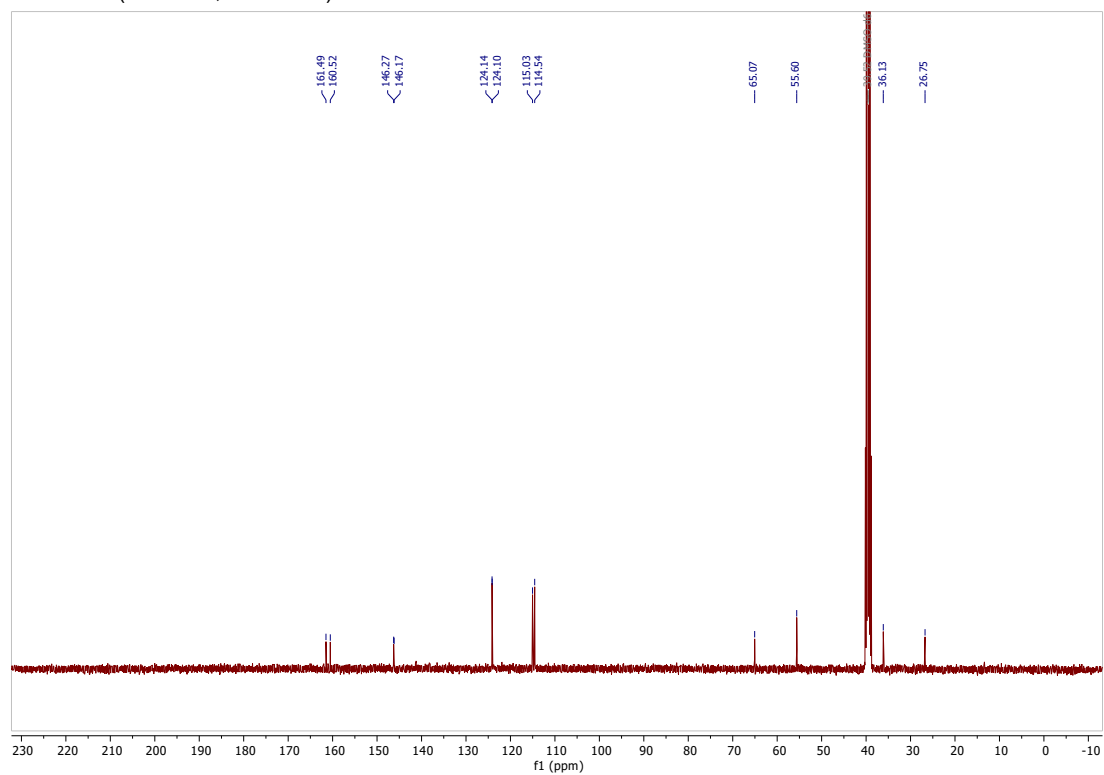


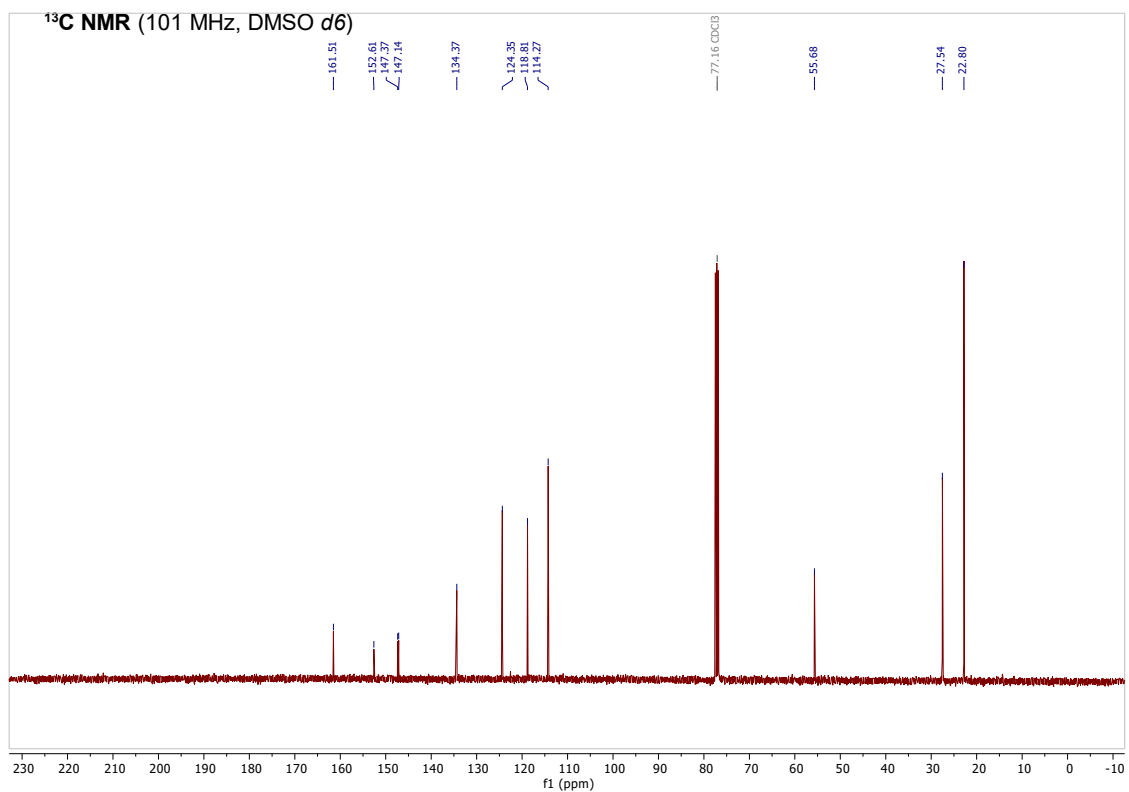
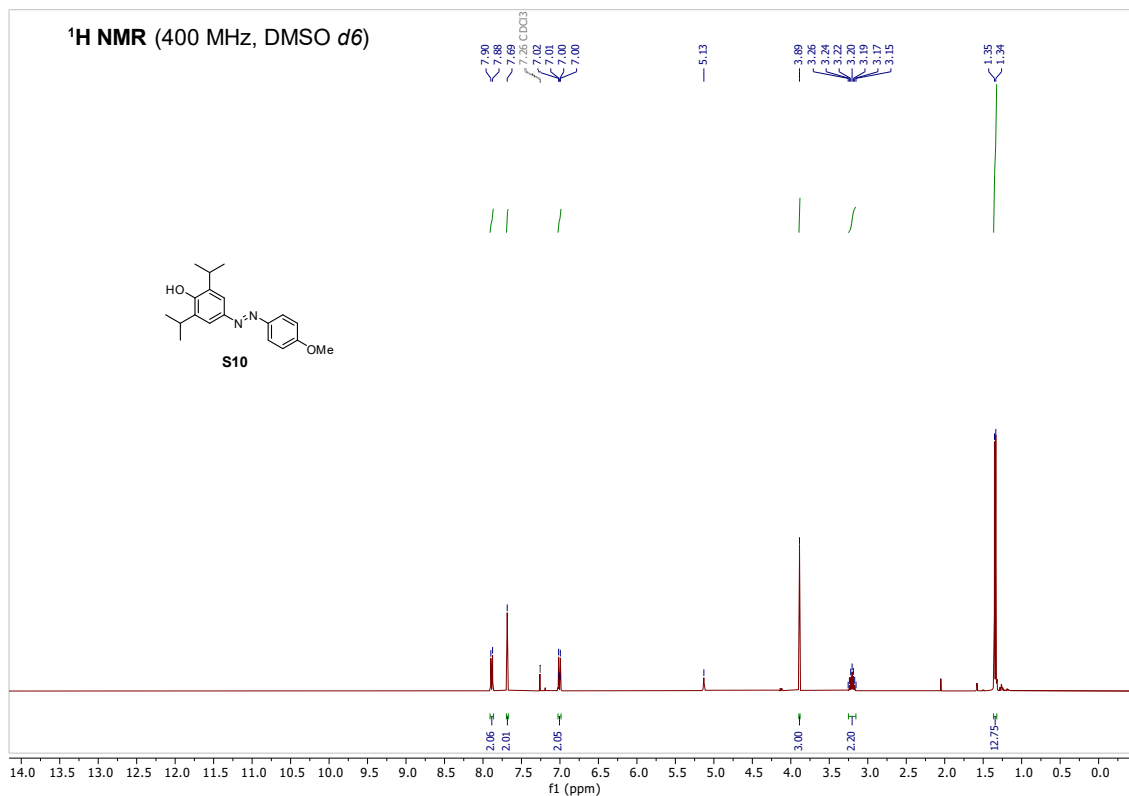


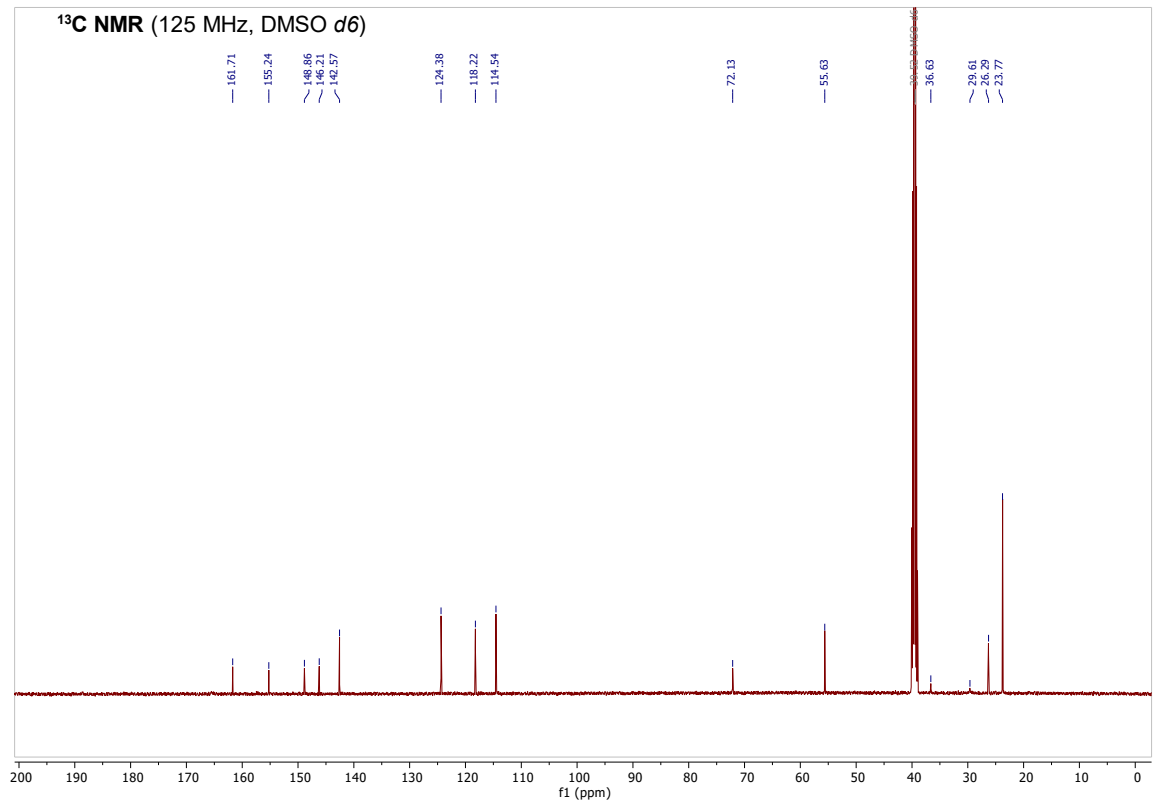
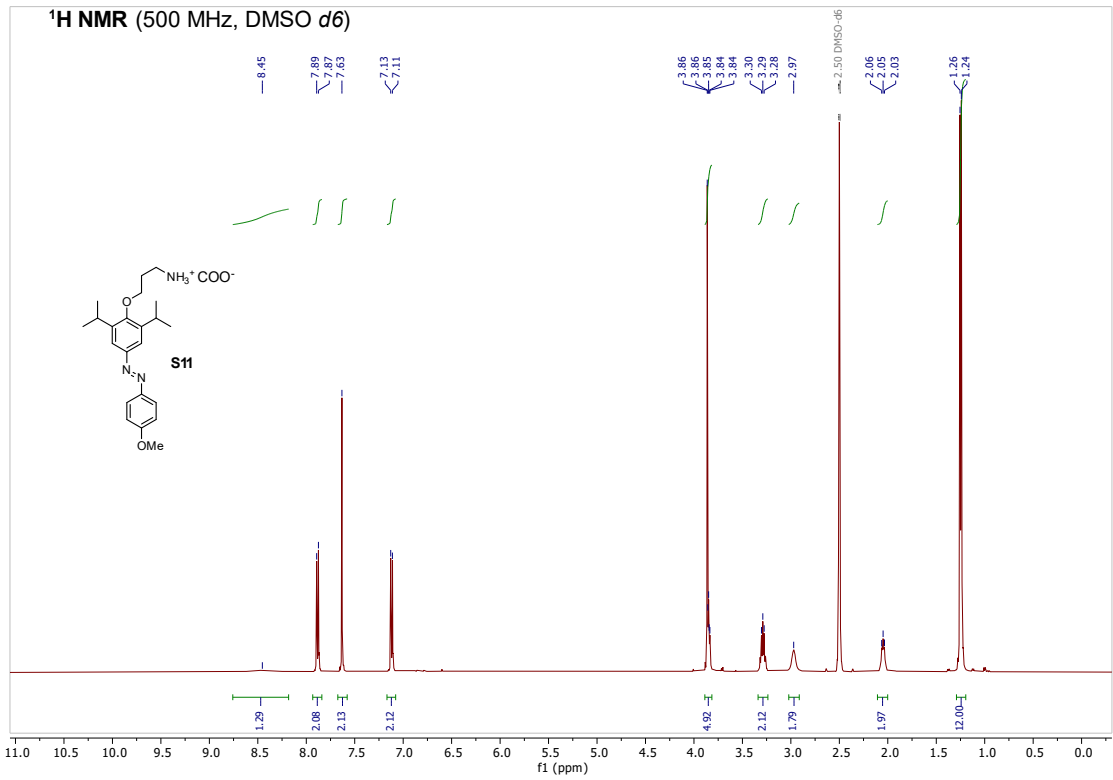


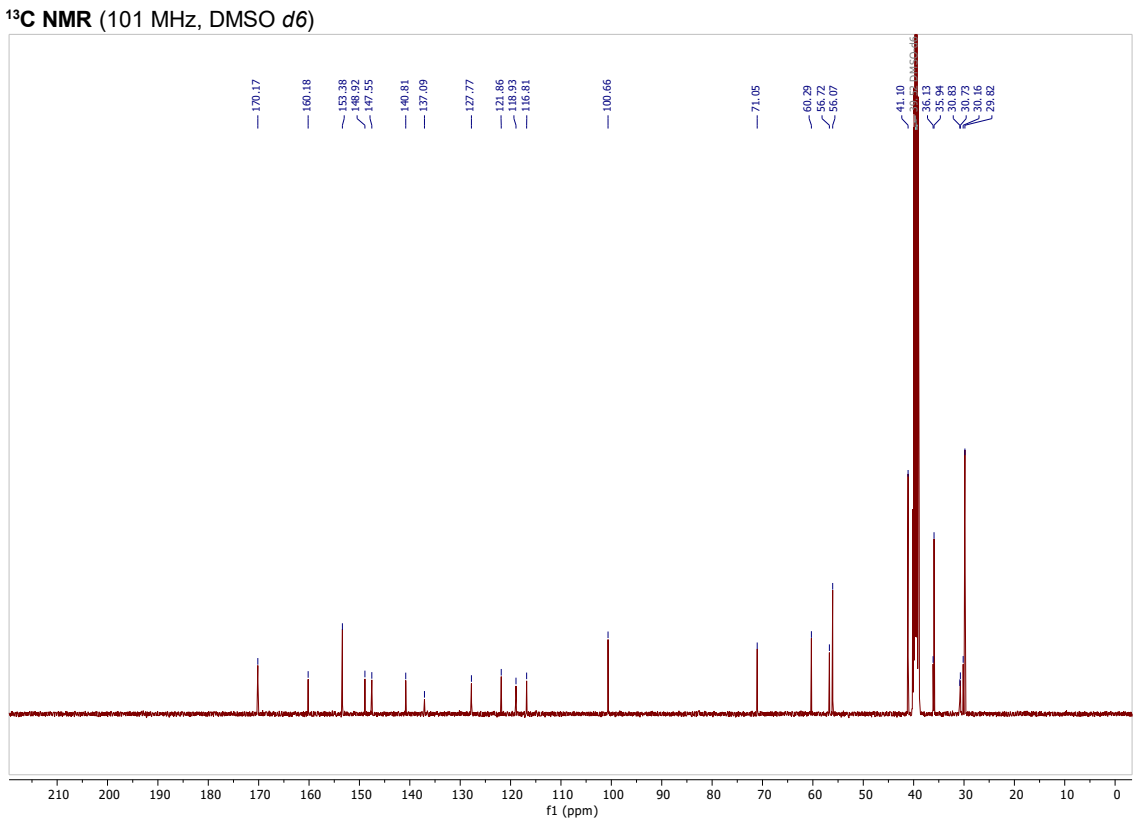
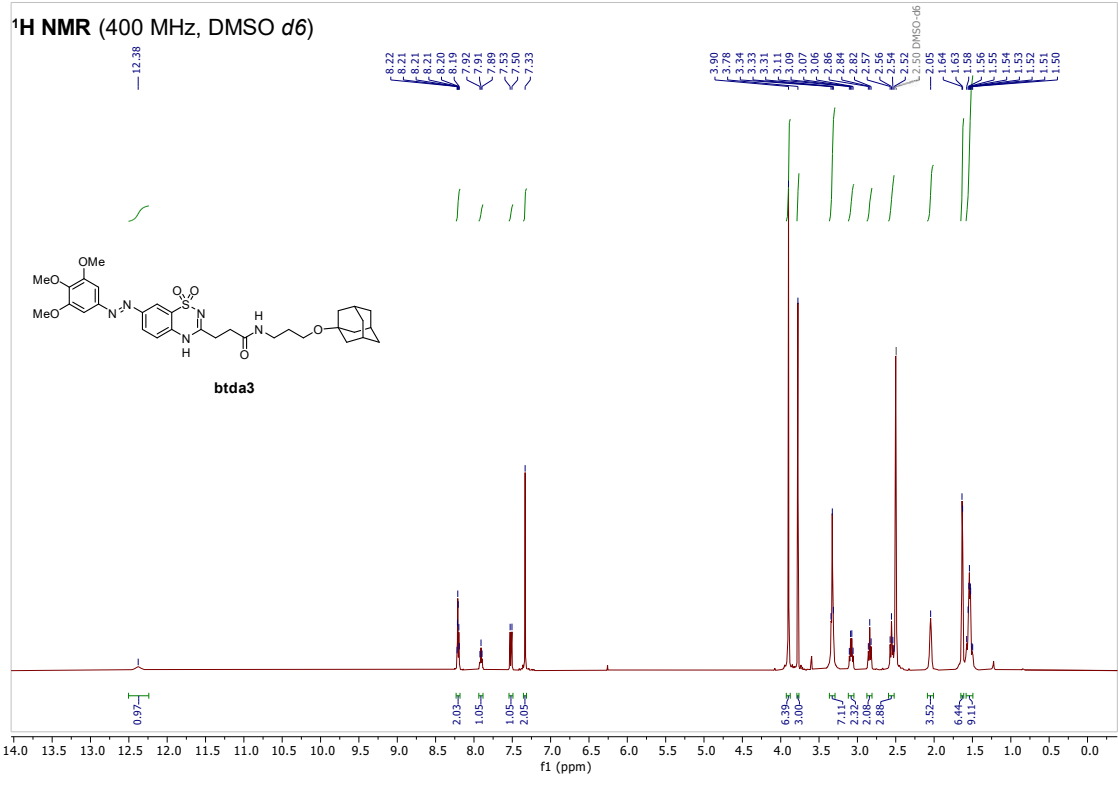


¹³C NMR (101 MHz, DMSO *d*₆)

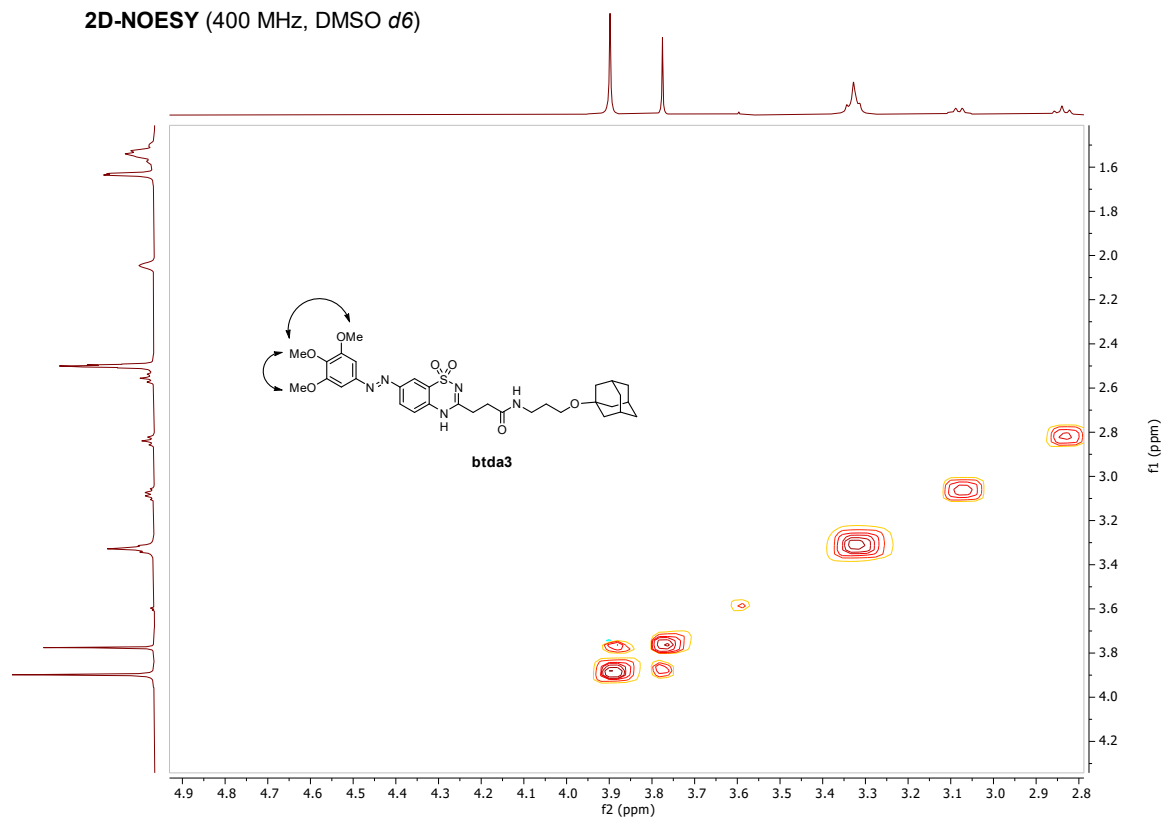




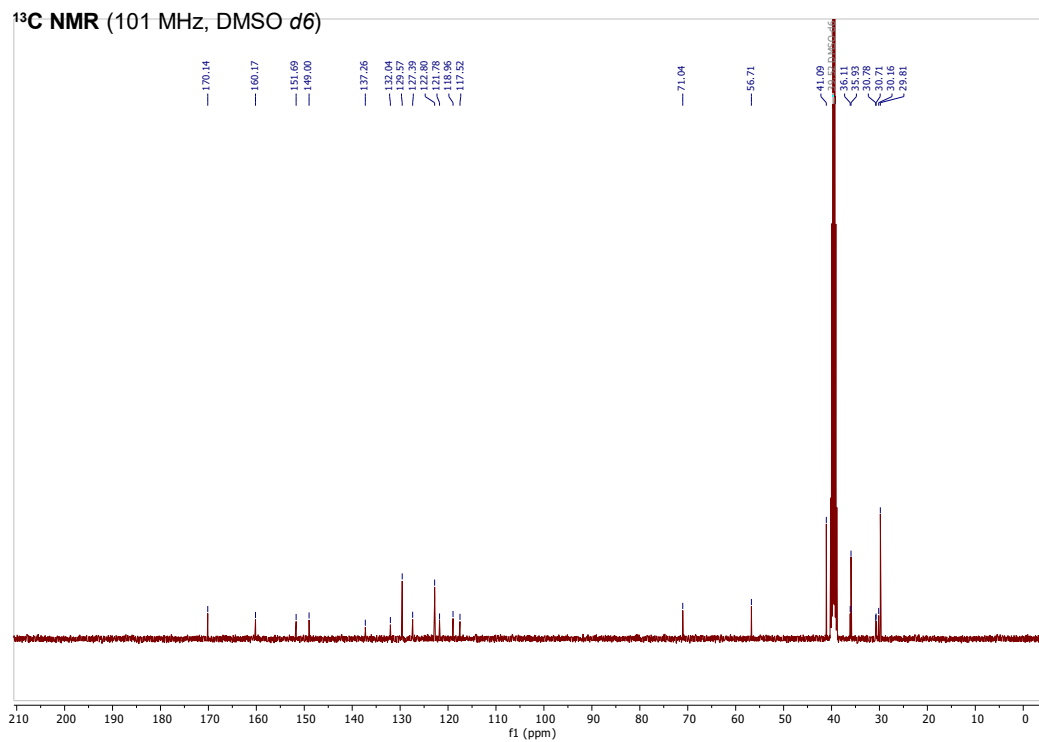
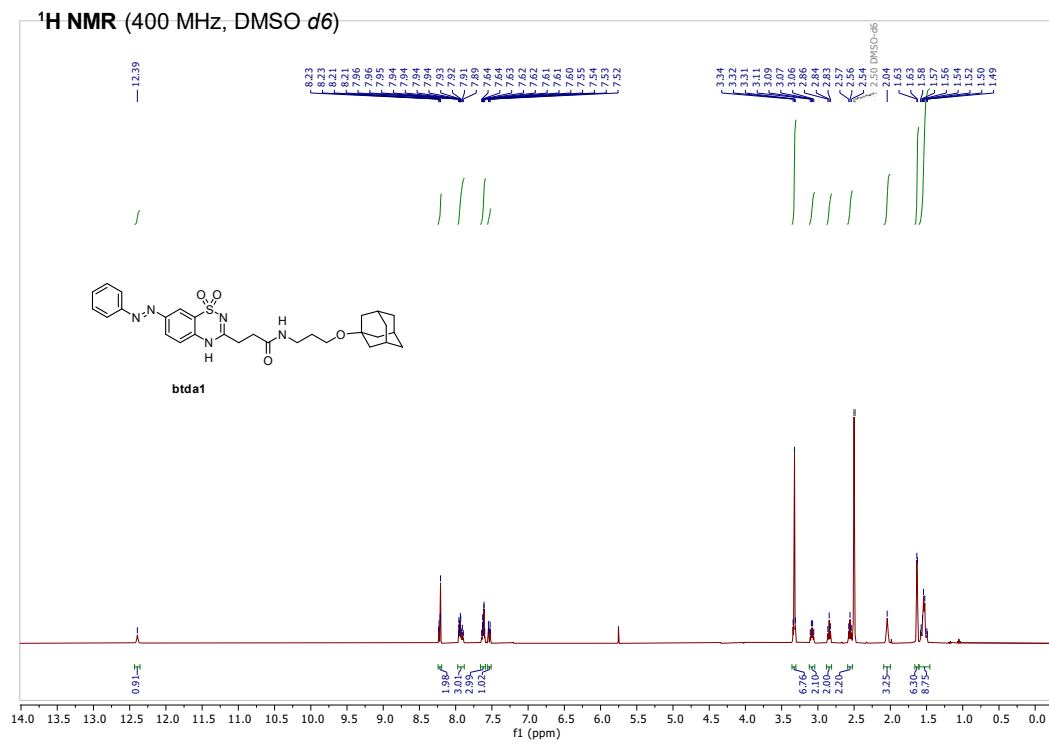


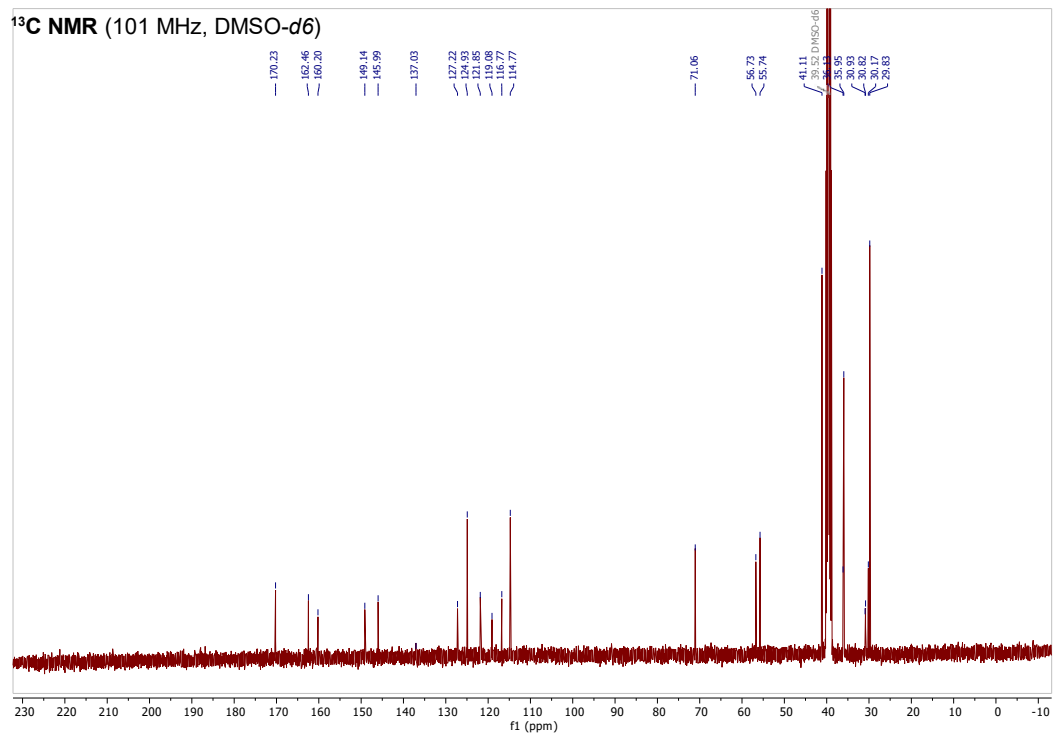
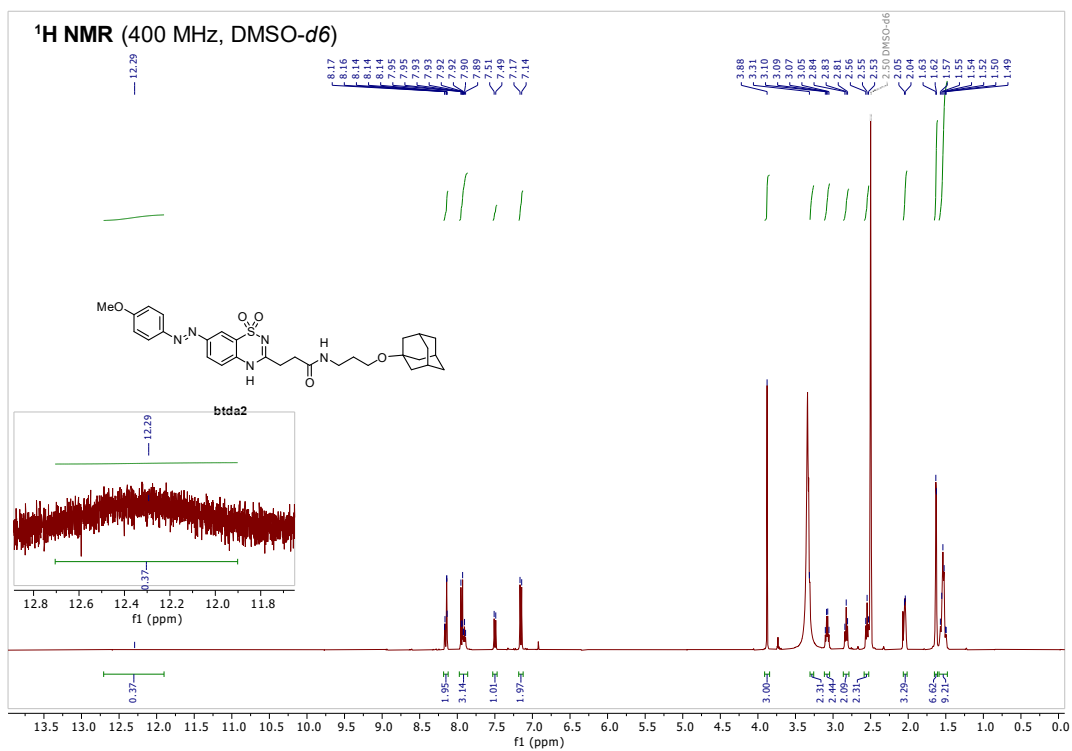


2D-NOESY (400 MHz, DMSO *d*₆)

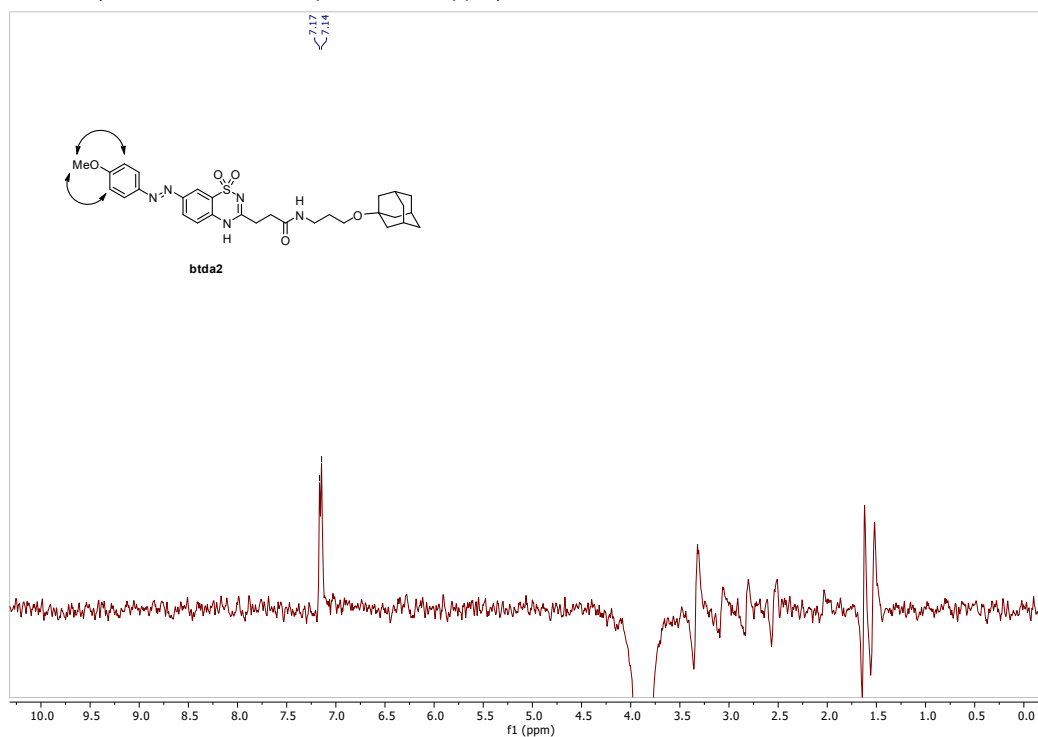


2D NOE spectrum of BTDAzo (btdda3): NOE cross peak between methoxy groups at 3.90 ppm and 3.78 ppm indicating the desired O-alkylated product.

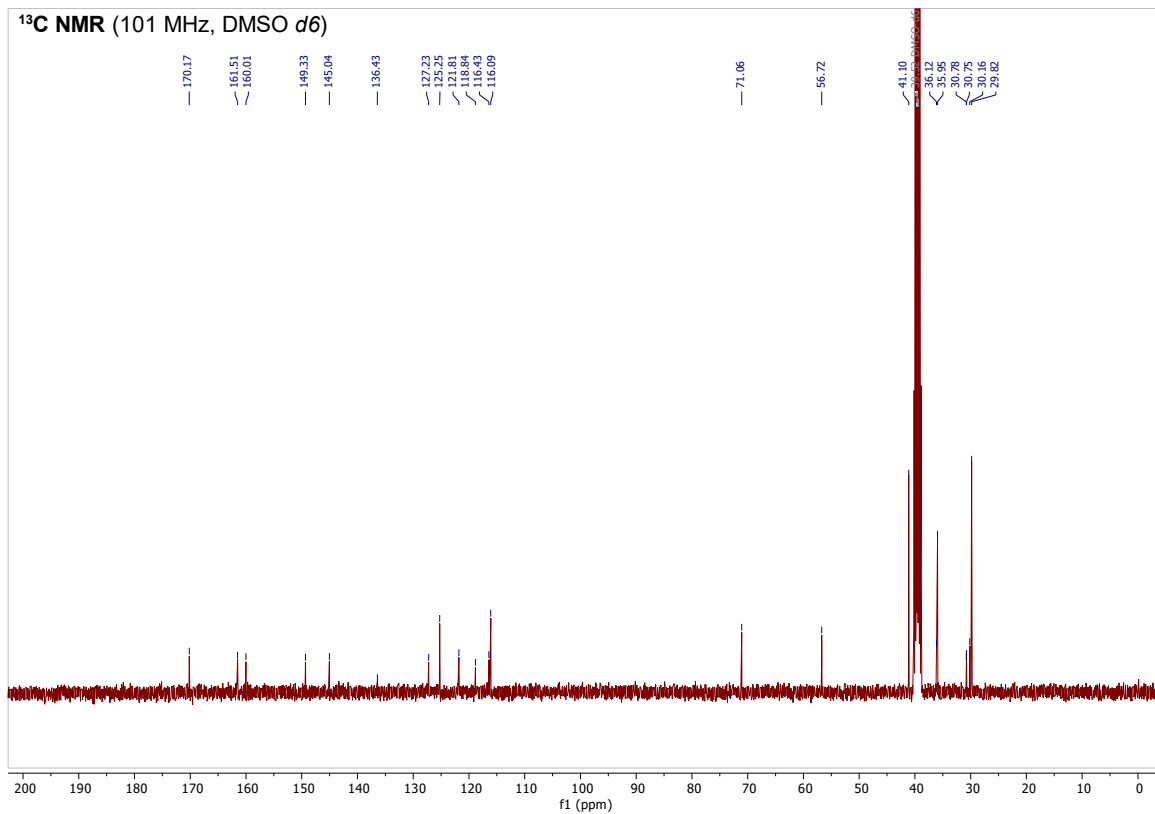
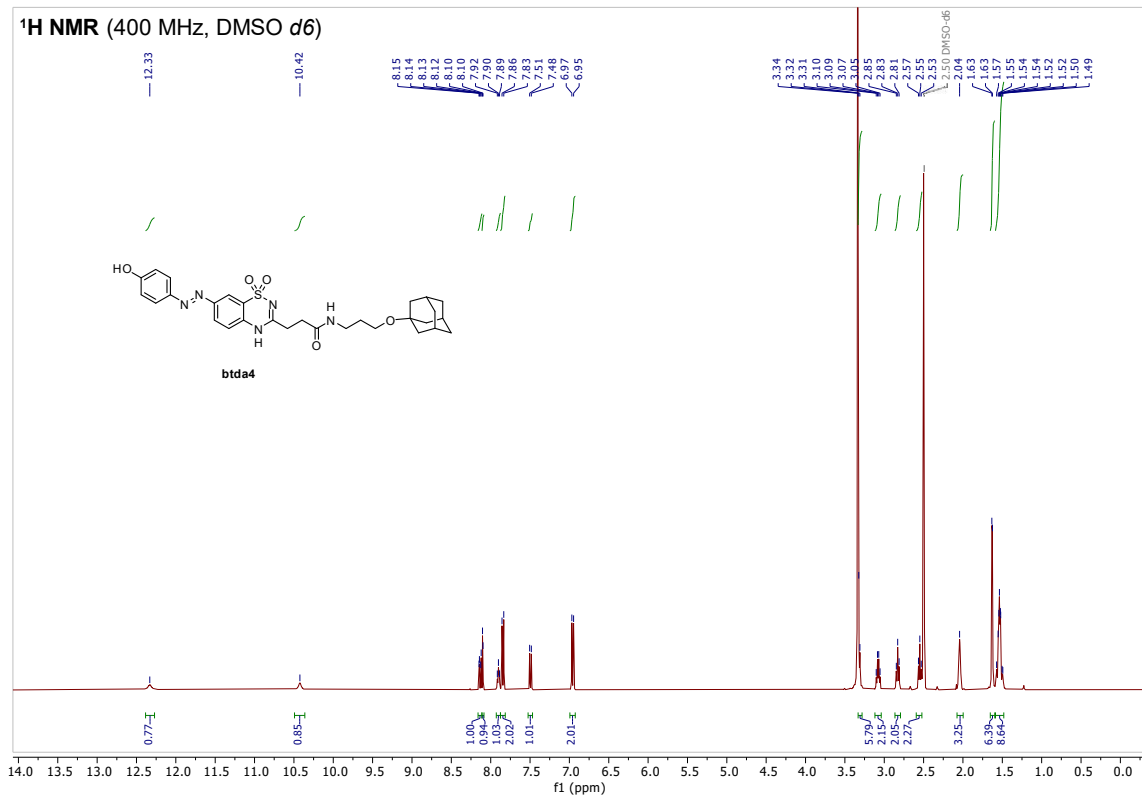




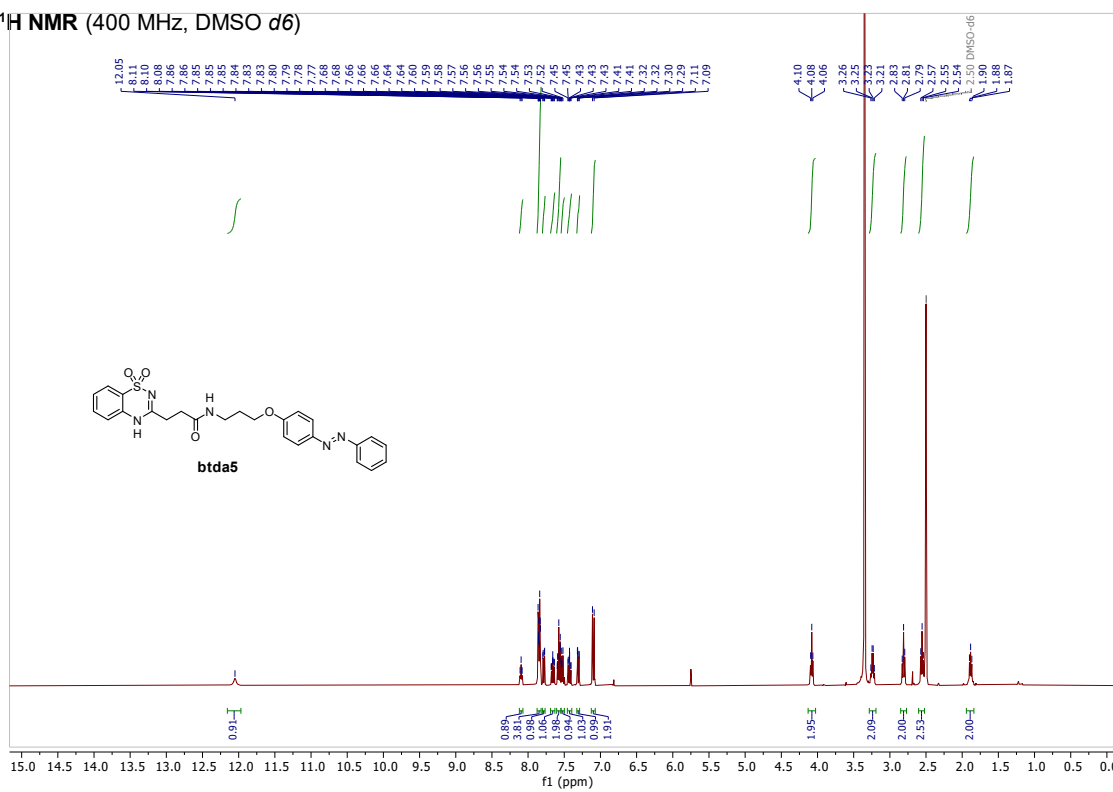
1D NOE (400 MHz, DMSO *d*₆, pulse at 3.89 ppm)



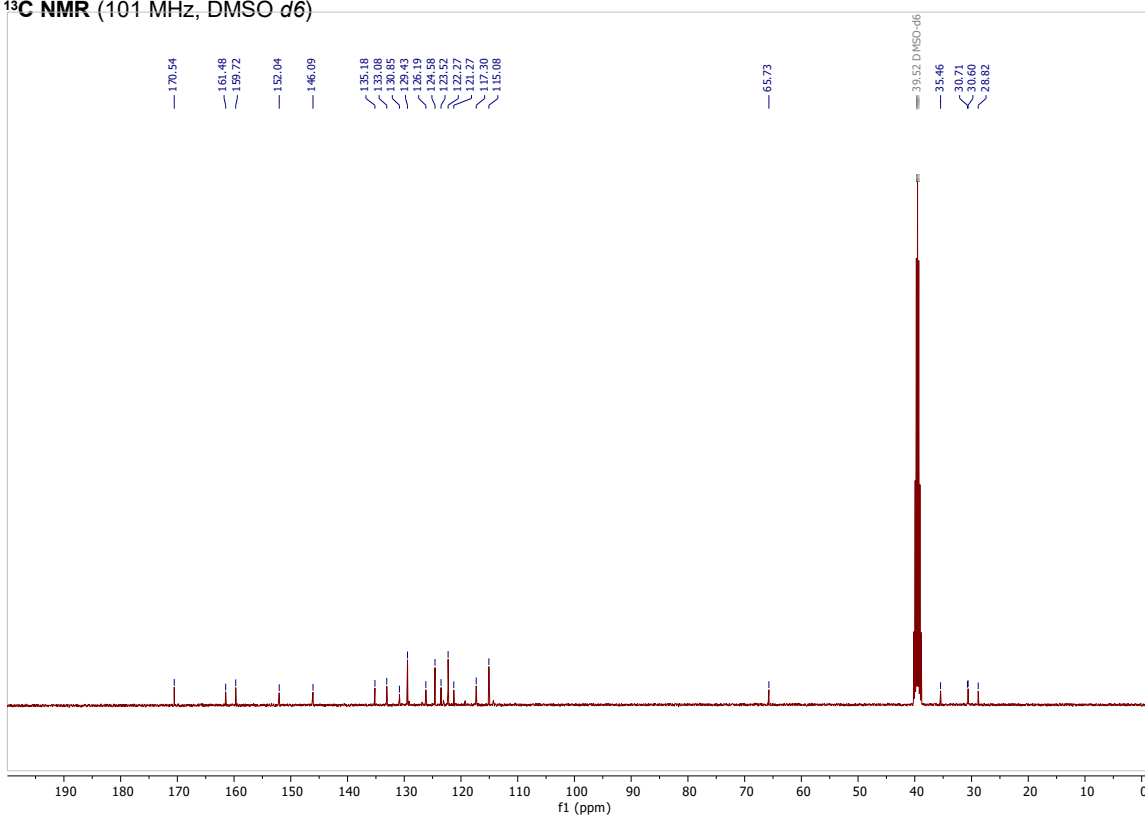
1D NOE spectrum of **btda2**: pulse at 3.89 ppm on the methoxy group and NOE cross peak at 7.17 and 7.14 ppm with *ortho* protons indicating the desired O-alkylated product.

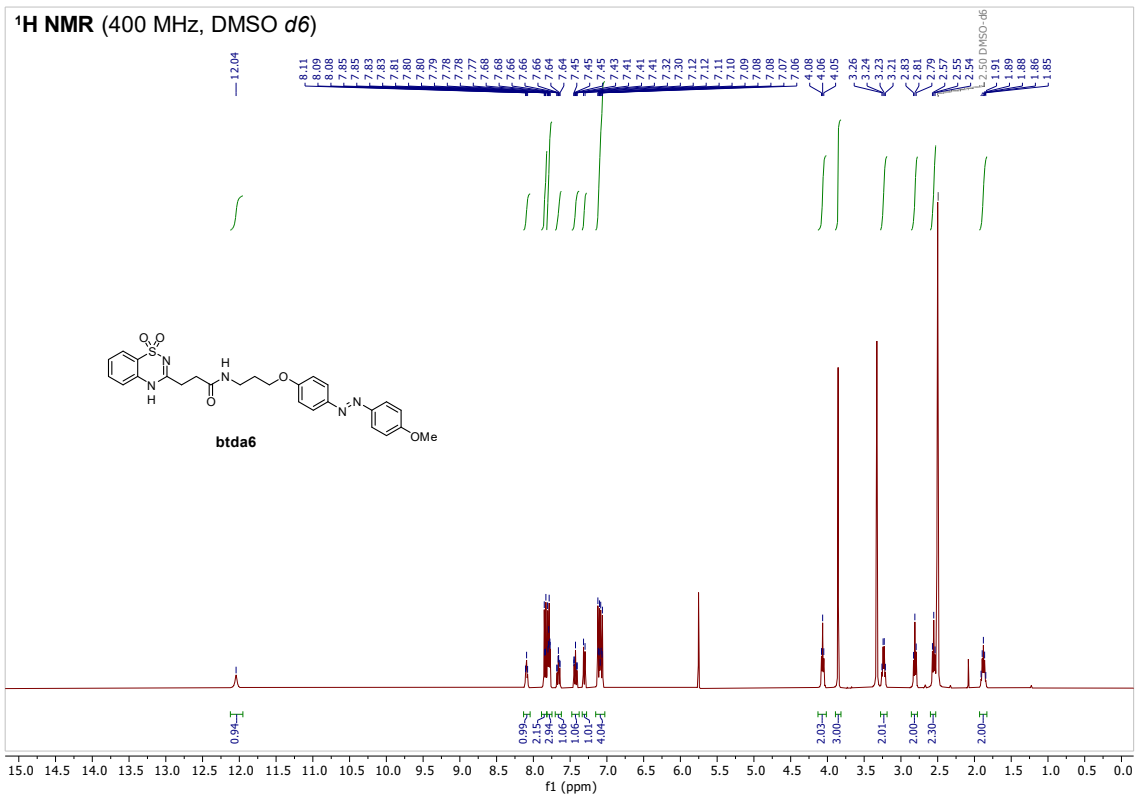


¹H NMR (400 MHz, DMSO d6)

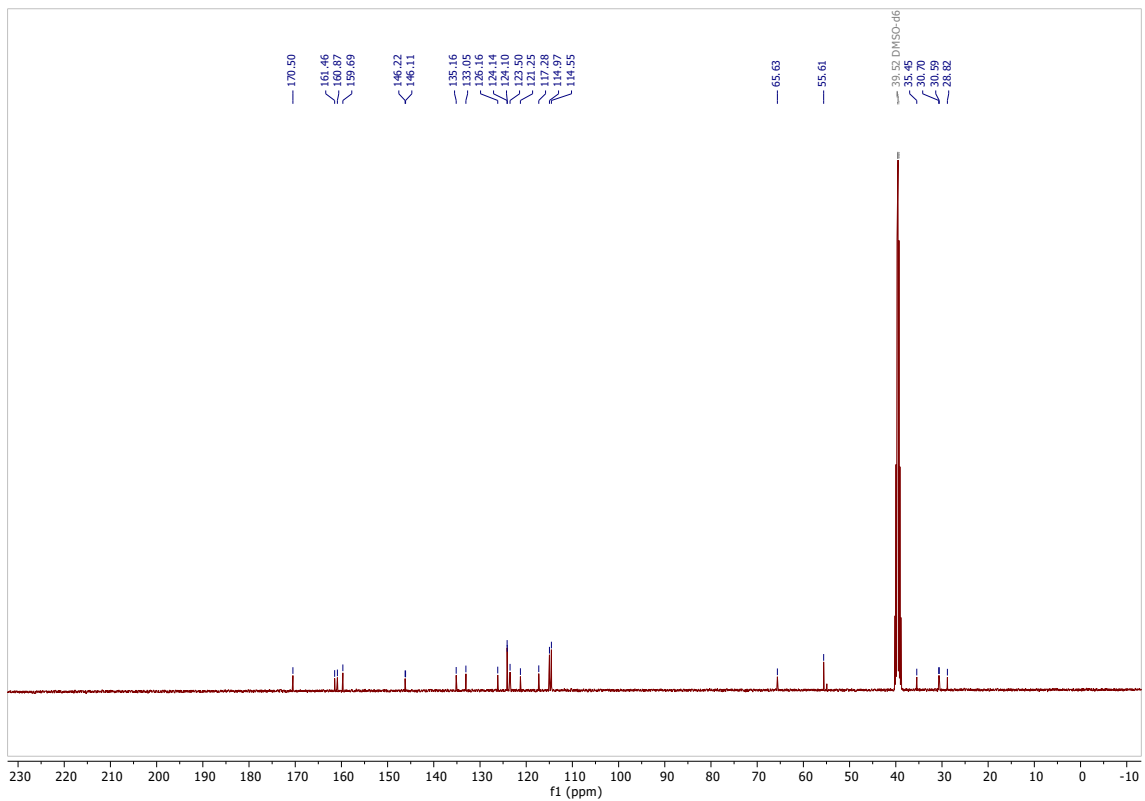


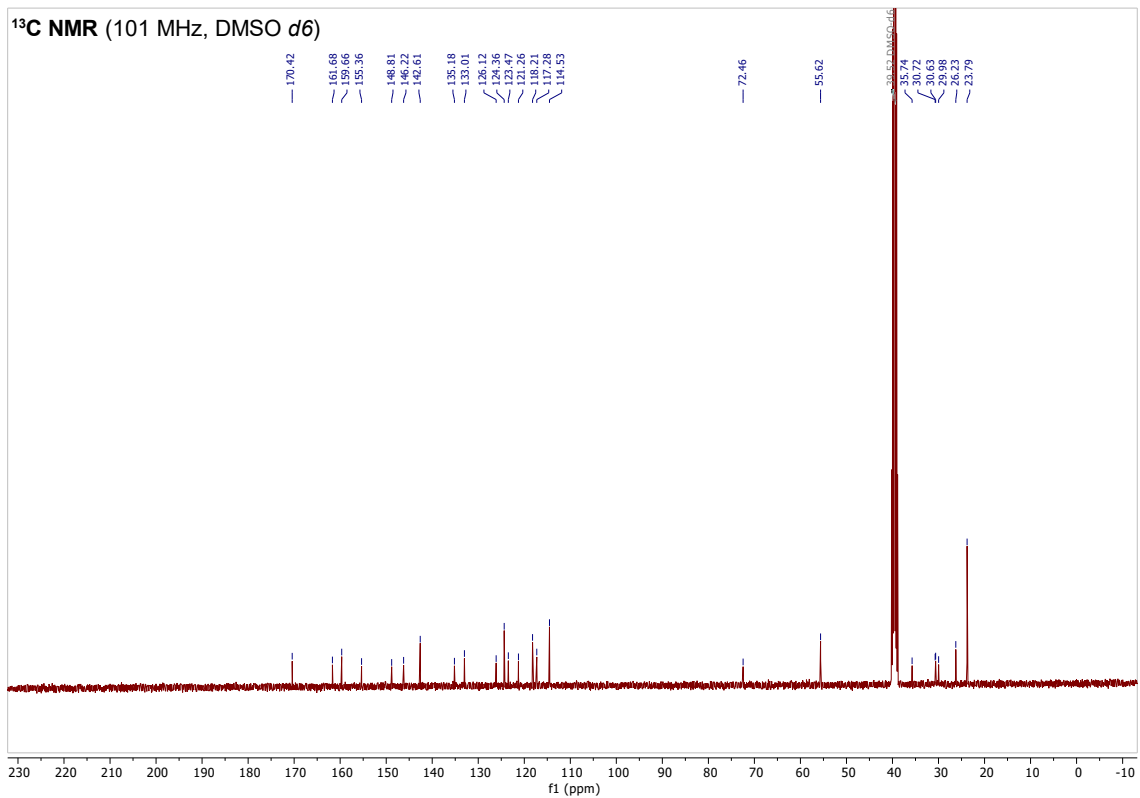
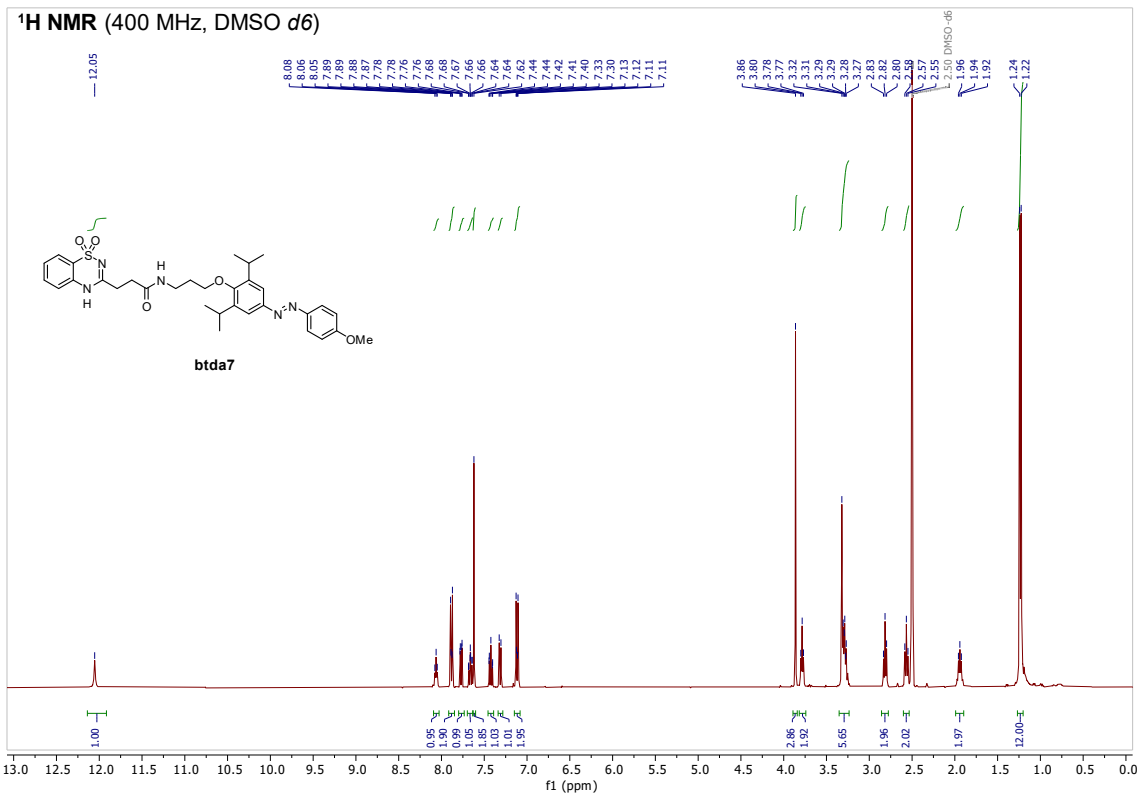
¹³C NMR (101 MHz, DMSO d6)

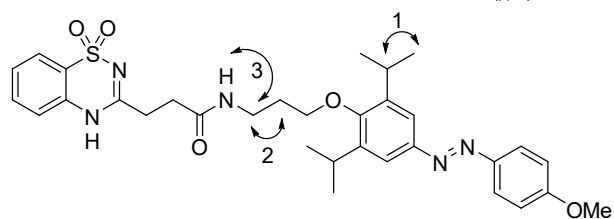
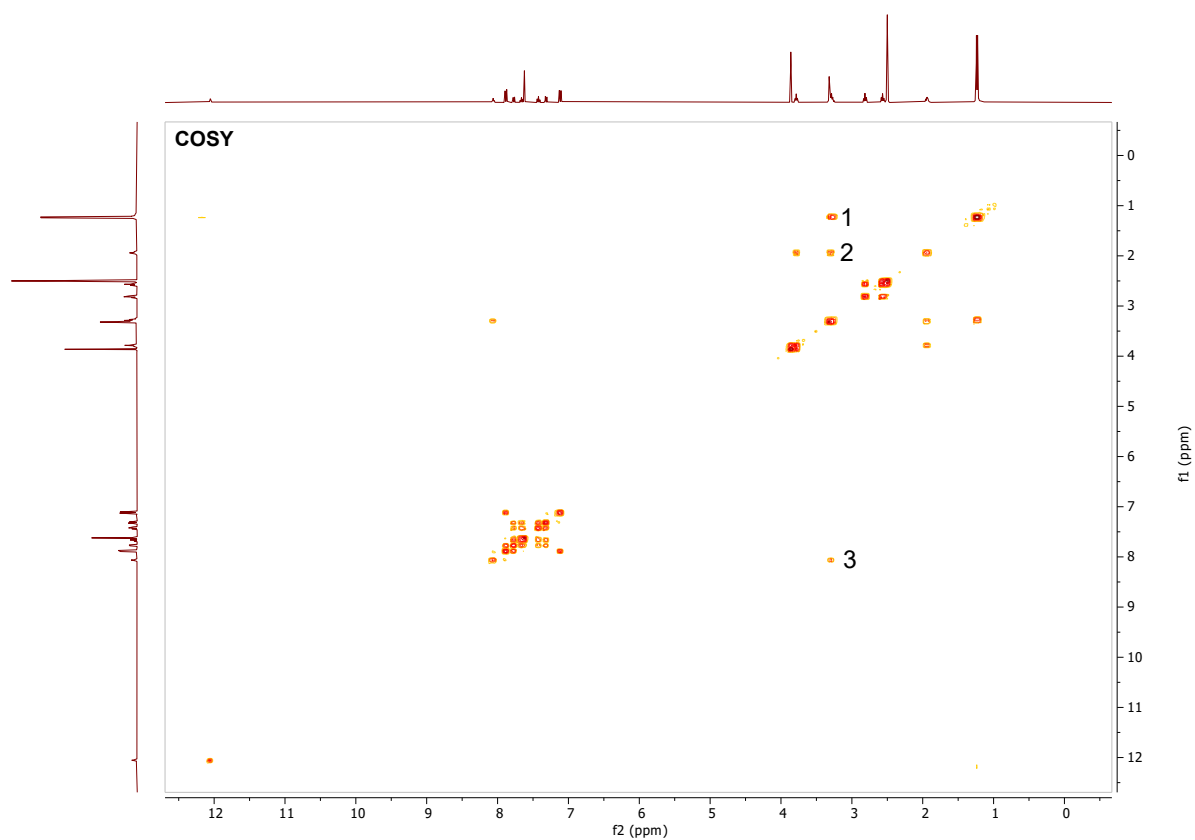




¹³C NMR (101 MHz, DMSO *d*₆)







1-H,1H COSY of **btda7** to resolve the CH group of the isopropyl and the CH₂ group connected to the amide from the overlaying water solvent peak.

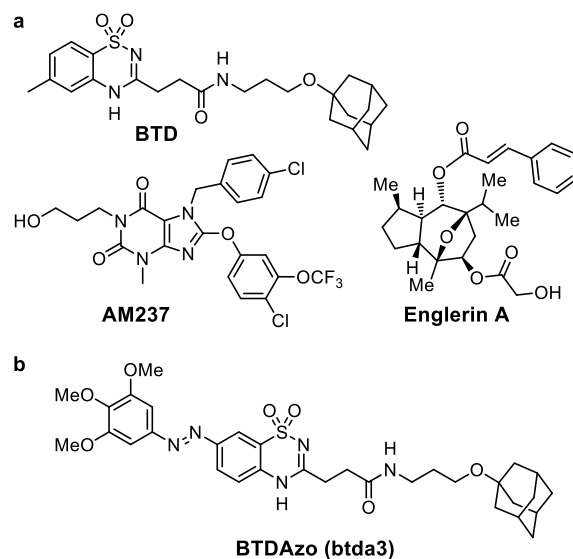
References

- [1] C. Parenti, L. Costantino, M. D. Bella, L. Raffa, G. G. Baggio, P. Zanoli, *Arch. Pharm.* **1985**, *318*, 903–911.
- [2] K. J. C. van Bommel, M. R. de Jong, G. A. Metselaar, W. Verboom, J. Huskens, R. Hulst, H. Kooijman, A. L. Spek, D. N. Reinhoudt, *Chem. Eur. J* **2001**, *7*, 3603–3615.
- [3] G. Xie, P. Li, Z. Zhao, X.-Y. Kong, Z. Zhang, K. Xiao, H. Wang, L. Wen, L. Jiang, *Angew. Chem. Int. Ed.* **2018**, *57*, 16708–16712.
- [4] K. Kreger, P. Wolfer, H. Audorff, L. Kador, N. Stingelin-Stutzmann, P. Smith, H.-W. Schmidt, *J. Am. Chem. Soc.* **2010**, *132*, 509–516.
- [5] M. Stein, S. J. Middendorp, V. Carta, E. Pejo, D. E. Raines, S. A. Forman, E. Sigel, D. Trauner, *Angew. Chem. Int. Ed.* **2012**, *51*, 10500–10504.
- [6] M. L. DiFrancesco, F. Lodola, E. Colombo, L. Maragliano, M. Bramini, G. M. Paternò, P. Baldelli, M. D. Serra, L. Lunelli, M. Marchioretto, G. Grasselli, S. Cimò, L. Colella, D. Fazzi, F. Ortica, V. Vurro, C. G. Eleftheriou, D. Shmal, J. F. Maya-Vetencourt, C. Bertarelli, G. Lanzani, F. Benfenati, *Nat. Nanotechnol.* **2020**, *15*, 296–306.
- [9] A. Sailer, J. C. M. Meiring, C. Heise, L. N. Pettersson, A. Akhmanova, J. Thorn-Seshold, O. Thorn-Seshold, *Angew. Chem. Int. Ed.* **2021**, *60*, 23695–23704.
- [8] P. Urban, S. D. Pritzl, D. B. Konrad, J. A. Frank, C. Pernpeintner, C. R. Roeske, D. Trauner, T. Lohmüller, *Langmuir* **2018**, *34*, 13368–13374.
- [9] M. Wranik, T. Weinert, C. Slavov, T. Masini, A. Furrer, N. Gaillard, D. Gioia, M. Ferrarotti, D. James, H. Glover, M. Carrillo, D. Kekilli, R. Stipp, P. Skopintsev, S. Brünle, T. Mühlethaler, J. Beale, D. Gashi, K. Nass, D. Ozerov, P. J. M. Johnson, C. Cirelli, C. Bacellar, M. Braun, M. Wang, F. Dworkowski, C. Milne, A. Cavalli, J. Wachtveitl, M. O. Steinmetz, J. Standfuss, *bioRxiv* **2022**, DOI 10.1101/2022.02.17.480857
- [10] J. M. Richter, M. Schaefer, K. Hill, *Br. J. Pharmacol.* **2014**, *171*, 158–170.
- [11] A. D. Edelstein, M. A. Tsuchida, N. Amodaj, H. Pinkard, R. D. Vale, N. Stuurman, *J. Biol. Methods* **2014**, *1*, e10–e10.
- [12] M. Schaefer, T. D. Plant, N. Stresow, N. Albrecht, G. Schultz, *J. Biol. Chem.* **2002**, *277*, 3752–3759.
- [13] J. M. Savitt, S. S. Jang, M. Wu, V. L. Dawson, T. M. Dawson, *Journal of Neuroscience* **2005**, *25*, 6721–6728.
- [14] L. Madisen, A. R. Garner, D. Shimaoka, A. S. Chuong, N. C. Klapoetke, L. Li, A. van der Bourg, Y. Niino, L. Ego, C. Monetti, H. Gu, M. Mills, A. Cheng, B. Tasic, T. N. Nguyen, S. M. Sunkin, A. Benucci, A. Nagy, A. Miyawaki, F. Helmchen, R. M. Empson, T. Knöpfel, E. S. Boyden, R. C. Reid, M. Carandini, H. Zeng, *Neuron* **2015**, *85*, 942–958.
- [15] K. D. Phelan, U. T. Shwe, J. Abramowitz, H. Wu, S. W. Rhee, M. D. Howell, P. E. Gottschall, M. Freichel, V. Flockerzi, L. Birnbaumer, F. Zheng, *Mol. Pharmacol.* **2013**, *83*, 429–438.
- [16] T. Blum, A. Moreno-Pérez, M. Pyrski, B. Bufe, A. Arifovic, P. Weissgerber, M. Freichel, F. Zufall, T. Leinders-Zufall, *Proc. Natl. Acad. Sci. USA* **2019**, *116*, 15236–15243.
- [17] C. Schauer, T. Tong, H. Petitjean, T. Blum, S. Peron, O. Mai, F. Schmitz, U. Boehm, T. Leinders-Zufall, *J. Neurophysiol.* **2015**, *114*, 1008–1021.
- [18] P. Chamero, J. Weiss, M. T. Alonso, M. Rodríguez-Prados, C. Hisatsune, K. Mikoshiba, T. Leinders-Zufall, F. Zufall, *Sci Rep* **2017**, *7*, 10260.
- [19] T. Leinders-Zufall, U. Storch, K. Bleyemehl, M. Mederos y Schnitzler, J. A. Frank, D. B. Konrad, D. Trauner, T. Gudermann, F. Zufall, *Cell Chem. Bio.* **2018**, *25*, 215–223.e3.
- [20] T. Leinders-Zufall, U. Storch, M. Mederos y Schnitzler, N. K. Ojha, K. Koike, T. Gudermann, F. Zufall, *STAR Protocols* **2021**, *2*, 100527.

High-Resolution Copies of all Main Text figures

For readers accessing the main text in a medium that has removed information content by image compression, the main-text figures are reproduced here vectorially.

Figure 1



Scheme 1

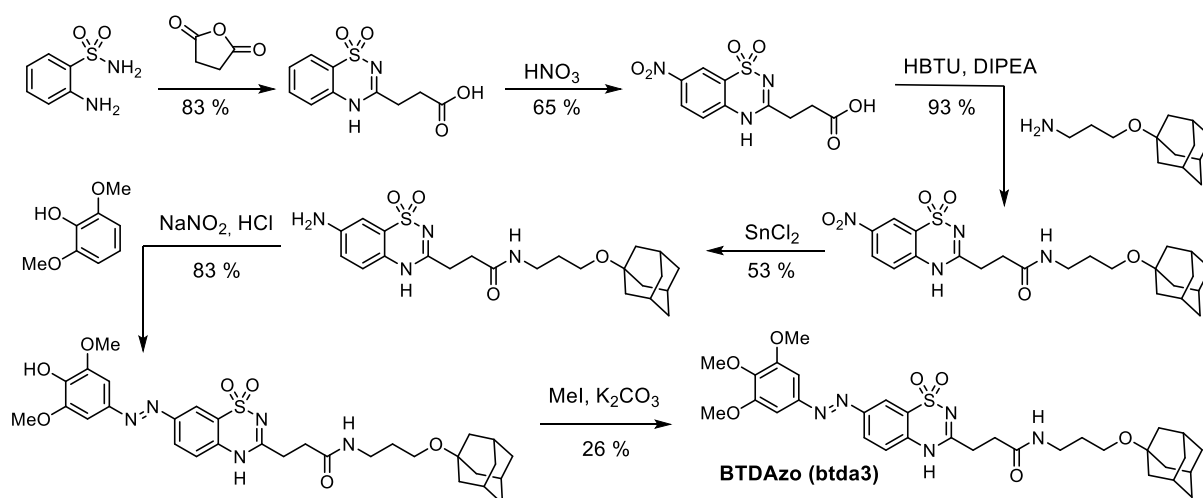


Figure 2

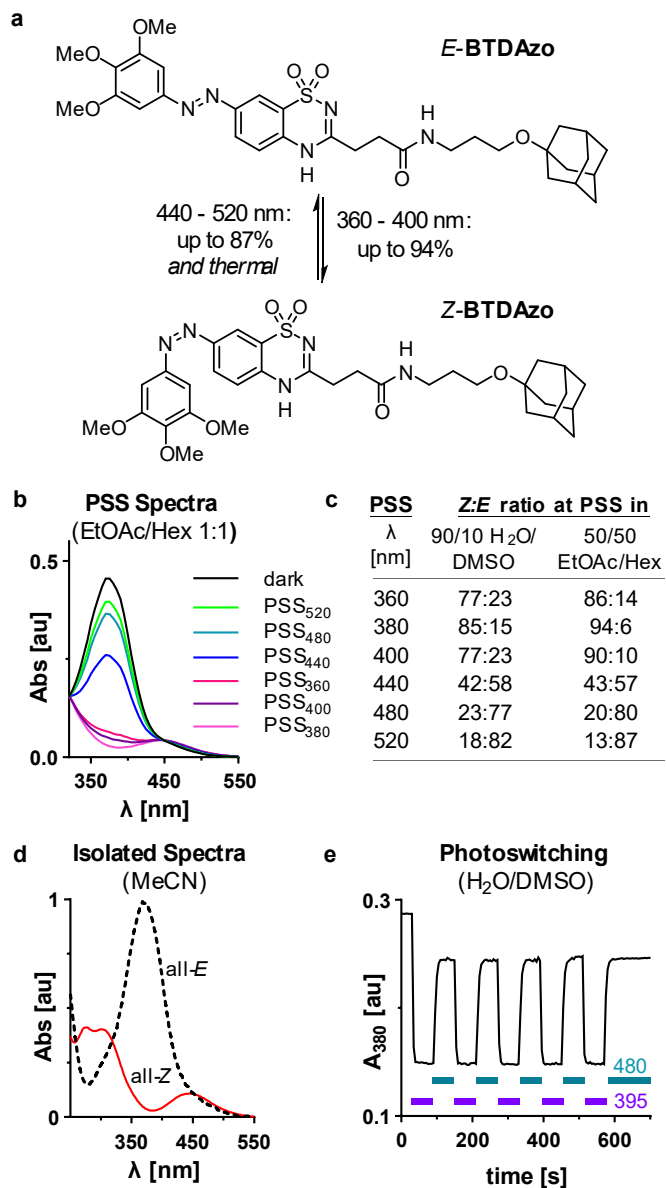


Figure 3

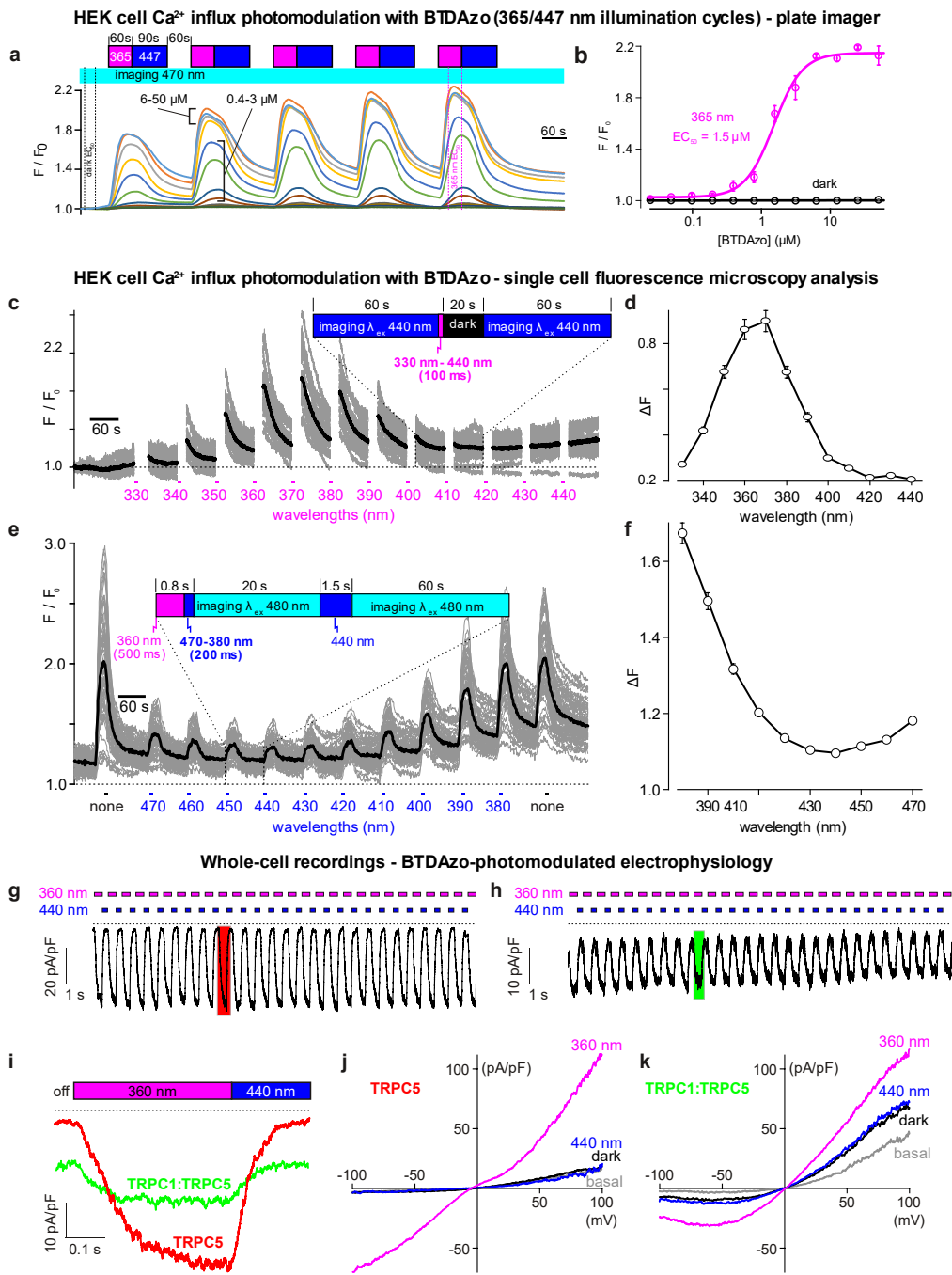
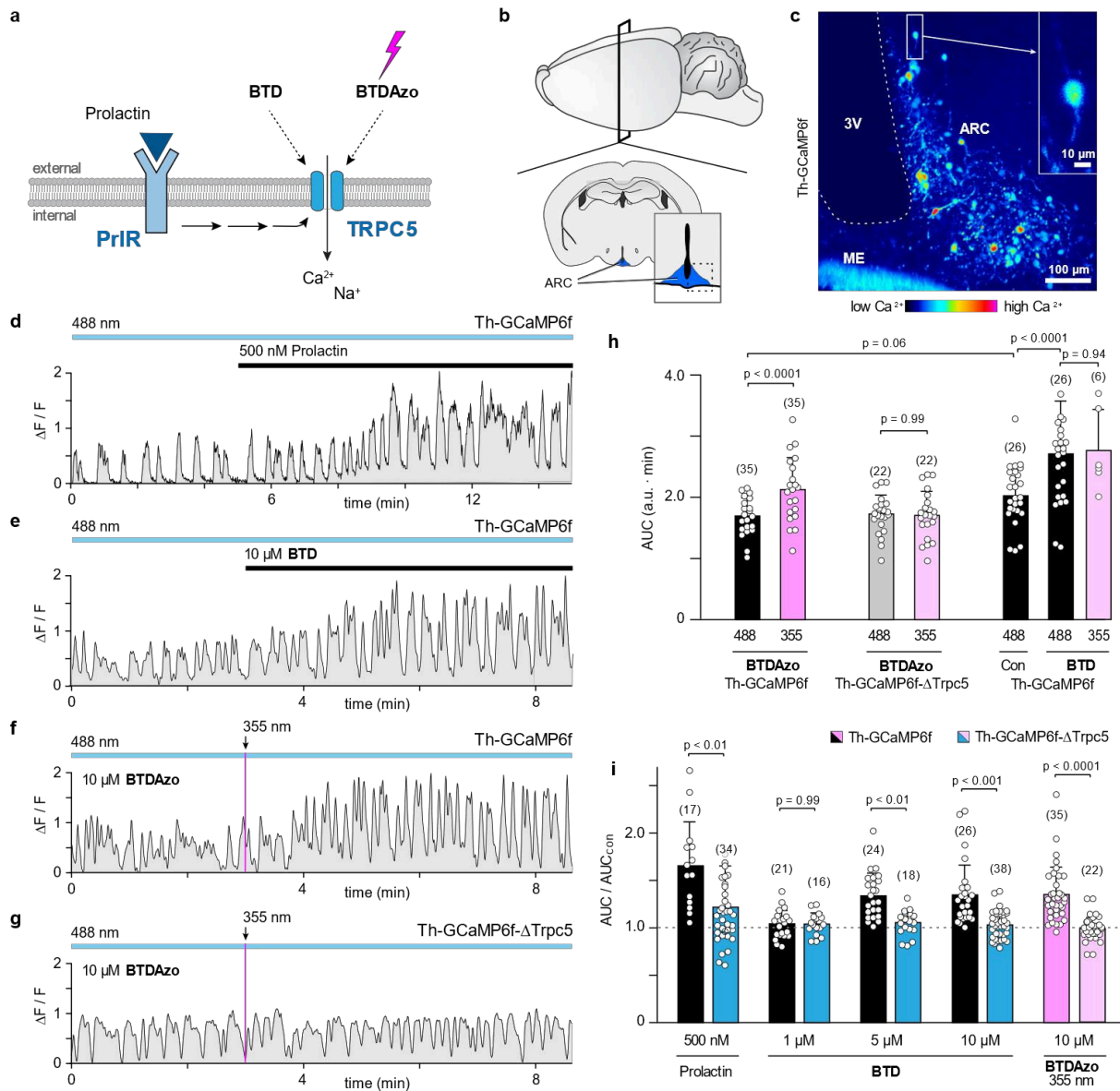


Figure 4



Ideal efficacy photoswitches for TRPC4/5 channels harness high potency for spatiotemporally-resolved control of TRPC function in live tissues

Markus Müller^{1‡}, Konstantin Niemeyer^{2‡}, Navin K. Ojha³, Sebastian A. Porav^{4,5}, Deivanayagabharathy Vinayagam,⁶ Nicole Urban², Fanny Büchau², Katharina Oleinikov³, Mazen Makke³, Claudia C. Bauer^{4,5}, Aidan V. Johnson^{4,5}, Stephen P. Muench^{5,7}, Frank Zufall³, Dieter Bruns³, Yvonne Schwarz³, Stefan Raunser⁶, Trese Leinders-Zufall³, Robin S. Bon^{4,5}, Michael Schaefer^{2,*}, Oliver Thorn-Seshold^{1,*}

Table of Contents

1	Supporting Notes	2
1.1	Supporting Note 1: Pharmacology for Efficacy Switching	2
1.1.1	<i>From always-active antagonists and agonists towards efficacy photoswitches</i>	3
1.1.2	<i>Mechanistic test for efficacy photoswitching</i>	3
1.2	Supporting Note 2: Prior Art in Efficacy Photoswitching	5
1.2.1	<i>Reported Prior Art in Efficacy Photoswitching</i>	5
1.2.2	<i>Unsuspected Prior Art in (Ideal) Efficacy Photoswitching</i>	5
1.2.3	<i>Tangential Remarks & Outlook for Efficacy Photoswitches</i>	6
	Supporting Note 3: Results from Other Compounds in our Panel	7
1.3	Supporting Note 4: Structural Biology and TRP Selectivity	8
1.3.1	<i>Detailed Commentary: hTRPC5:E/Z-AzHC</i>	8
1.3.2	<i>Detailed Commentary: TRPC4_{DR}:E/Z-AzPico</i>	10
1.3.3	<i>Note on TRPC4 / TRPC5 Sequence Alignment</i>	11
1.3.4	<i>Differences and selectivity between TRPC5 and TRPC4?</i>	11
1.4	Supporting Note 5: AzHC & TRPC5-dependent Ca ²⁺ in mouse hypothalamus.....	13
2	Photocharacterization	14
3	Cultured Cell Lines (primarily for Figure 1 and Figure 2)	15
3.1	FLIPR Ca ²⁺ influx assay in cell suspensions.	16
3.2	Ephys Characterisation of Photocontrolled Induced Ionic Currents	18
3.3	Pharmacology of TRPC4 and TRPC5 variants (Figure S8)	18
4	Structural biology (Figure 3)	20
4.1	Structural biology of TRPC5:AzHC.....	20
4.2	Structural biology of TRPC4:AzPico.....	26
5	Cultured neurons and chromaffin cells (Figure 4)	29
6	Mouse experiments – brain tissue slices (Figure 5)	30
7	Spontaneous motility and isometric contractility (Figure 6)	34
7.1	Tissue Switching Reveals the Power of the Ideal Efficacy Switch Paradigm	34
7.1.1	<i>First Saturate with Ligand, Then Dial the Wavelength</i>	34
7.1.2	<i>Ideal Efficacy Switches That Also Have High Affinity</i>	35
7.2	Minor Remarks on Additional Experiments (Figure S22) and Prior Art	35
7.3	Why is AzPico/AzHC-like efficacy photoswitching useful <i>in vivo</i> in practice?	37
8	Chemistry	38
8.1	Materials and Methods - Chemistry	38
8.2	Chemical Synthesis Overview	39
8.3	Standard Synthetic Procedures.....	39
8.4	Synthesis of Building Blocks.....	40
8.5	Synthesis of AzPicos & AzHCs	45
9	Supporting References	49
10	NMR Spectra	54
11	Copies of Main Figures With Full Legends	72

1 Supporting Notes

1.1 Supporting Note 1: Pharmacology for Efficacy Switching

Xanthines **Pico145** and **HC-070**¹ are low nanomolar/picomolar potency inhibitors of homomeric and heteromeric TRPC1/4/5 channels.^{2,3} The very similar **AM237**¹ (single-atom replacement from **Pico145**: chlorine instead of hydrogen at C'4) is instead a nanomolar partial *agonist* of homomeric TRPC5, despite being a nanomolar *inhibitor* of the full agonist (-)-englerin A (**EA**) in the context of homomeric TRPC4 and heteromeric TRPC1/5 and TRPC1/4 (structures: **Figure S1**; potencies: **Table S1**).⁴ Structures of TRPC5 in complex with **Pico145** and **HC-070** were recently obtained, showing their conserved binding site at the transmembrane domain between two monomers.^{5,6} A docking study of **AM237** into the structure of **Pico145** bound to TRPC5 indicated that avoiding a steric clash of the chlorine with a single amino acid residue of the protein requires rearranging the structure (either the protein or the ligand) resulting in a plausible mechanism for the switch from inhibitory **Pico145** to agonistic **AM237**. A similarly dramatic efficacy change resulting from a tiny structural modification was also observed for **E54**, formally a deoxygenated ether derivative of **EA**, which also antagonises **EA**'s activation of homomeric TRPC4 (weakly), and homomeric TRPC5 and heteromeric TRPC1:4 (strongly), presumably by competitive binding with suppressed channel activation⁴.

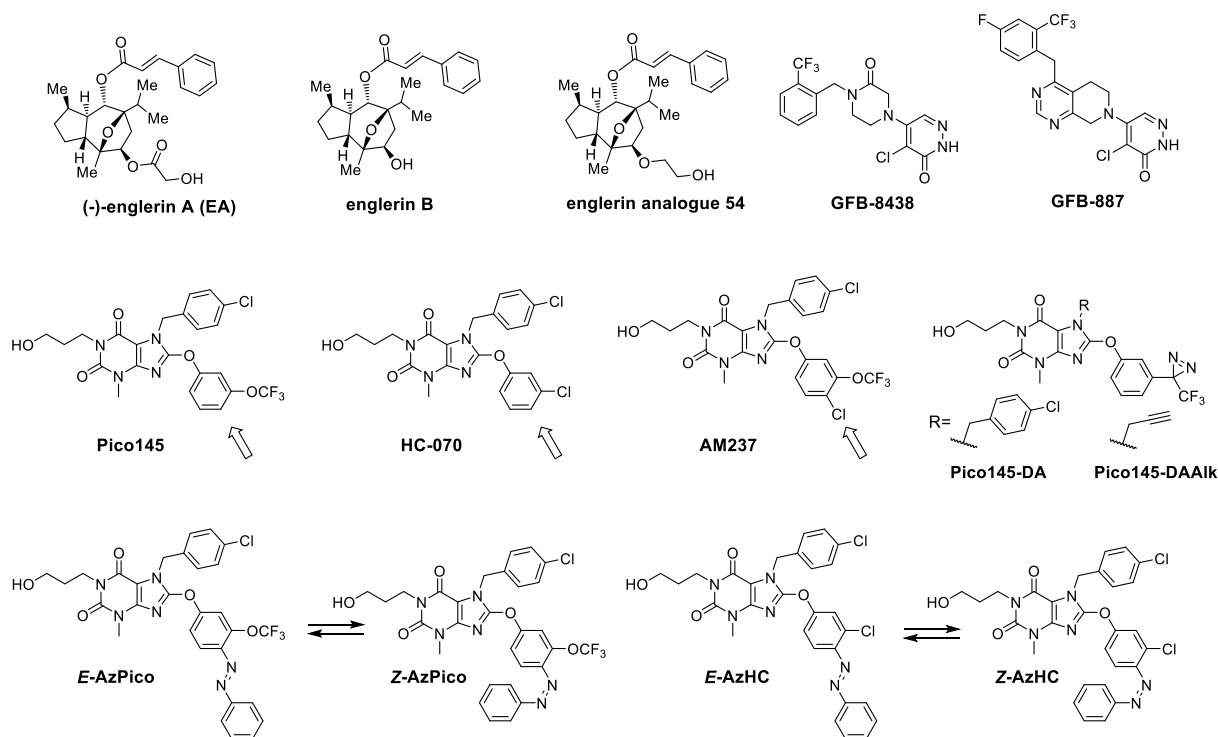


Figure S1. Structures of lead compounds incl. **Pico145**, **HC-070**, **AM237** (xanthines), xanthine derived photoaffinity probes **Pico145-DA** and **Pico145-DAalk**, and (-)-englerin A and **E54** (englerins supposedly share the same binding site with xanthines), as well as pyridazinones **GFB-8438** and **GFB887** (different binding site); alongside this work's star photoswitchable modulators **AzPico** and **AzHC**.

For interpreting the EC_{50} s reported in **Fig 1n** and **Table S1**, two notes should be kept in mind: (1) **comparing EC_{50}/IC_{50} s for agonist Z and antagonist E does not deliver any information about relative binding affinity**, since (a) the experiment types are so different in nature (agonists: sole-ligand assay; antagonists: out-competing 10-30 nM of the high-affinity **EA**), and (b) there are many additional unknown (and complicating) factors related to the multiple binding sites per channel, including potential binding cooperativities. A discussion of these effects is beyond the scope of this paper; but it is plausible that the binding affinity of **E-AzHC** and **E-AzPico** isomers is similar to that of the ca. 1 nM potent **EA**, given that their EC_{50} s for antagonism in the competition

assay are only ca. 3-5 times the applied concentration of **EA**. This is a handwaving explanation, but it can justify why the affinity of the *E/Z*-isomers may be similar.

(2) The EC₅₀ values are reported as the midpoints of *unconstrained* sigmoidal fits to the FLIPR data (**Fig 11** and **Figure S2**): with different levels of channel activation / blocking and very different Hill slopes across different compounds, isomers, and the two channels. This argues that **the midpoint values only capture one of the several important factors describing the compounds' activity**.

We believe that it is possible to derive indicative relative values for binding affinity comparing the *E* and *Z* isomers of the same compound using only the combination of FLIPR and ephys data as reported in this paper; this analysis is being developed in a separate paper (see also below).

Table S1. Potencies on TRPC4/5 depicted as either simple agonistic potency (blue) or else inhibitory potency against activation by 10-30 nM **EA** (orange). *Z**-values refer to mostly-*Z*-isomer reached at PSS at 365 nm, *E**-values refer to experiments that initially applied 100% *E*-isomer (thermally relaxed), though in both cases the Ca²⁺ imaging in FLIPR with Fluo4-AM uses 470 nm excitation, which may over time promote photoswitching towards a PSS that is intermediate between those of pure-365 nm and all-*E*; this is controlled for in the more reliable ephys measurements). (Table indices: a, data from ref¹; b, data from ref²; c, data from ref³; d, data from ref⁴.)

	EC ₅₀ [nM] (for simple agonism or EA-competitive inhibition)	
	TRPC4	TRPC5
EA	11 ag. ^a	7.6 ag. ^a
Pico145	0.35 (vs 10 nM EA) ^b	1.3 (vs 10 nM EA) ^b
HC-070	0.5 (vs 10 μM carbachol) ^c	2.0 (vs 20 μM carbachol) ^c
AM237	7 (vs 30 nM EA) ^d	20 ag. ^d 13 (vs 30 nM EA) ^d
<i>E</i> -AzPico	90 (vs 30 nM EA)	67 (vs 30 nM EA)
<i>Z*</i> -AzPico	3.0 ag.	4.0 ag.
<i>E</i> -AzHC	110 (vs 30 nM EA)	149 (vs 30 nM EA)
<i>Z*</i> -AzHC	>1000	6.4 ag.
	orange: inhibitory effect	ag.: agonistic effect

1.1.1 From always-active antagonists and agonists towards efficacy photoswitches

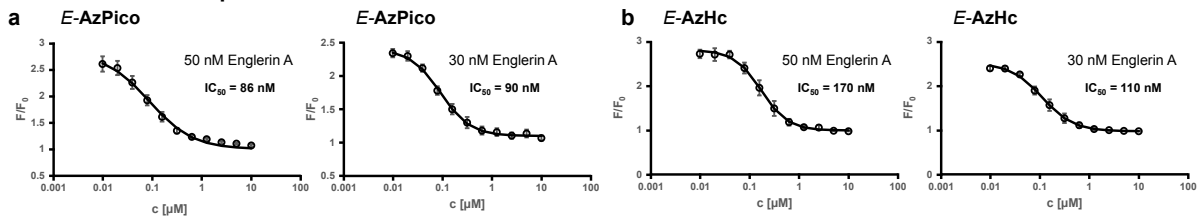
In this paper, we will show that this “chemical efficacy switch” behaviour can be mimicked by photoisomerising an azobenzene that is merged in at the C’4 position yielding the compounds **AzPico** and **AzHC** which show a strong lit active agonistic effect for the *Z*-isomers and a strong inhibitory effect for the *E*-isomers (**Table S1**). Essentially, the effects of **Pico145** and **AM237** are latent within a single (two-state reversibly photoswitchable) molecule. This combination is what we call an *efficacy switch* (also see main text **Figure 1e-j**).

1.1.2 Mechanistic test for efficacy photoswitching

The concentration-independent-but-PSS-determined channel activation that **AzHC** and **AzPico** deliver (**Figures 1-2**) is a powerful support for an efficacy switch interpretation. To indirectly support this further, we also measured the effects of *E*-AzPico and *E*-AzHC against EA-activated TRPC4/5. Both *E*-isomers bind to TRPC4/5 and inhibit EA-evoked currents with nanomolar potencies (**Figure S2, Table S2**). This supports the hypothesis that *E*-AzHC/AzPico are EA-competitive tight binders on both channels (much as **Pico145** was proposed to be an EA-competitive binder^{5,9,10}), so their efficacy as single agent photoswitches results from *E/Z*-competitive binding that is determined by their PSS.

Inhibitory effect of *E*-AzPico and *E*-AzHC on EA-activated TRPC4 and TRPC5

HEK293-mTRPC4 β -YFP



HEK293-mTRPC5-YFP

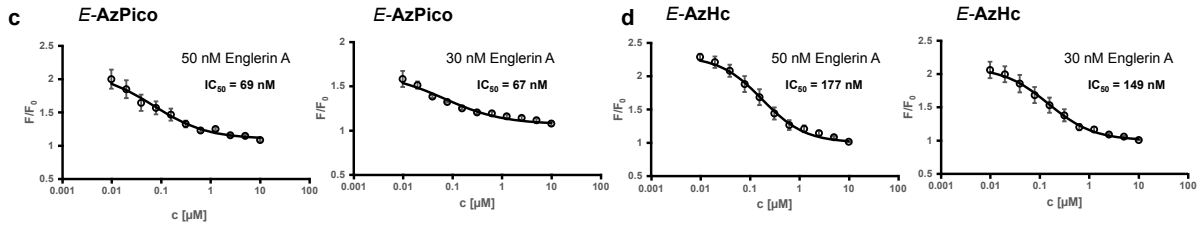


Figure S2. Dose response curves for *E*-AzPico and *E*-AzHC silencing the activation of TRPC4 and TRPC5 that is driven by 30-50 nM of EA. **(a-b)** 3 μ M Fluo-4-loaded HEK293-mTRPC4 β -YFP; **(c-d)** 3 μ M Fluo-4-loaded HEK293-mTRPC5-YFP. **(a)** *E*-AzPico TRPC4 activated by 30 nM or 50 nM EA. **(b)** *E*-AzHC TRPC4 activated by 30 nM or 50 nM EA. **(c)** *E*-AzPico TRPC5 activated by 30 nM or 50 nM EA. **(d)** *E*-AzHC TRPC5 activated by 30 nM or 50 nM EA.

Table S2. Potencies on TRPC4/5 depicted as inhibitory against EA activation. (^a Inhibitory effect measured against 30 nM EA; ^b Inhibitory effect measured against 50 nM EA).

	IC ₅₀ TRPC4 [nM]	IC ₅₀ TRPC5 [nM]
<i>E</i> -AzPico	90 ^a / 86 ^b	110 ^a / 170 ^b
<i>E</i> -AzHC	67 ^a / 69 ^b	149 ^a / 177 ^b

1.2 Supporting Note 2: Prior Art in Efficacy Photoswitching

1.2.1 Reported Prior Art in Efficacy Photoswitching

In general, ligand development with confirmed efficacy switching has been rather thinly represented in the literature; and there are several examples of claimed efficacy switches that do not hold up to scrutiny, or which are not as useful as might be hoped (small relative changes in activity without a change in the sign of activity; and/or low potency; and/or were not photoisomerised or perhaps not usefully photoisomerisable *in situ*; etc). We recommend Leurs' 2018 *Angewandte*¹¹ and particularly Leurs' 2019 *Beilstein JOC*¹² as being the clearest demonstrations and discussions of efficacy switches that were well-characterised and were used as photoswitches. Leurs' later review article¹³ also explicitly contains some literature statistics on efficacy switches (see that paper's Figure 7f), and Szymanski and Feringa's review¹⁴ collected and commented the references to the efficacy switches that we have also cited in this work.^{12,15–23}

While these preceding cases have been published, we believe that our discussion goes beyond those reports in the sense of interpreting efficacy switching as a systematic feature that is fundamentally different and advantageous for photopharmacology: hence our explicit call to develop high-potency, high-affinity, self-competitive-binding efficacy photoswitches *as a means to succeed in reproducible photoswitching despite variable biodistribution* (expected *in vivo* and in deep tissue) *by fixing selected wavelengths to drive fixed activity profiles by fixed PSS ratios* (the opposite of typical "chromodosing" wherein both wavelength and applied concentration are tuned to drive fixed activity profiles by fixed concentration of an active photoisomer).

1.2.2 Unsuspected Prior Art in (Ideal) Efficacy Photoswitching

Probably very many more compounds that have been reported without explicit commentary, or even reported implicitly as though they were affinity switches, actually *are* efficacy photoswitches, just that they have not been tested or proven to act as such; and of these, we believe a significant number are "ideal" in the sense of near-identical *E/Z*-affinities. One hallmark we expect in such cases is that the wavelength-dose-response profiles should plateau, at different heights, under different wavelengths: as depicted in **Figure 1i** for non-ideal-readouts/light conditions (or similarly, for non-ideal-efficacy-switches); or **Figure 1g** for ideal wavelengths on an ideal efficacy switch.

Such plot shapes *can* however be confused with drugs whose solubility reaches a limit beyond which no further increase in concentration-dependent bioactivity is possible (plateau), if only two wavelengths are used for activity determination.

Our suggestion for unambiguous identification and interpretation of efficacy switches is thus to plot action spectrum based data instead, at multiple concentrations if needed (**Figure 2h-j**). Form fitting to $\log([Z])$ or $\log([E])$ traces derived from PSS values (in an appropriate solvent!) will identify affinity switches (**Figure 2ij**), whereas form fitting to $\log([Z/E])$ traces marks efficacy switches (**Figure 2h**).

We have re-parsed some of our favourite photopharmacology literature to search for unsuspected ~ideal efficacy switching. A more comprehensive theoretical treatment that traces the target-based and pharmacology-based *drivers* of efficacy switching is in preparation as a separate paper; below we list just some of the reported examples that to us seem very likely to have been ideal efficacy switches. We note that several of these were translated from cell culture into complex settings and even *in vivo* photoswitching (e.g. Trauner 2019²⁴, Fuchter 2020²⁵) with success that would have been unexplainable for an affinity switch. For the photopharmacology field beyond TRP channels, this is probably the key message of our paper: the rewards and importance of designing and recognising ideal efficacy switches, in order to optimise and exploit them as such.

Five of the more recent examples are:

(1) Trauner *et al.*, **PhotoS1P** for sphingosine-1-phosphate receptors (S1P_n): in *Optical control of sphingosine-1-phosphate formation and function* (Nat Chem Biol 2019²⁴). Efficacy-switch-like profile in Fig 3a, HTC4 S1P₃; and efficacy *in vivo* is shown in mouse in Fig 4.

(2) Fuchter *et al.*, **TRPswitch-A** for the TRPA1 channel: in *TRPswitch—A Step-Function Chemo-optogenetic Ligand for the Vertebrate TRPA1 Channel* (JACS 2020²⁵). Photoswitching with green light (est. ca. 71%*E*) returns channel activity completely to baseline, even though photoswitching with violet light (21%*E*) gives high activation (Fig 1de, Table S2); and, green/violet switching is effective at controlling TRPA1 *in vivo* in zebrafish.

(3) Groschner *et al.*, **OptoBI-1** for the TRPC3 channel: in *Lipid-independent control of endothelial and neuronal TRPC3 channels by light* (Chem Sci 2019²⁶). Not an unsuspected case as such, since the efficacy-switch-like profiles in Fig 2d and Fig S5 are discussed as indicating a *trans*-weak, *cis*-strong agonist; but we conjecture that *cis/trans*-competitive binding with similar affinities is required to explain why bioactivity photoswitching is essentially complete and constant over a 100-fold concentration range, despite only 75%-complete *Z*→*E* photoswitching.

(4) Pepperberg *et al.*, **MPC088** for GABA_A receptor: in *Robust photoregulation of GABA_A receptors by allosteric modulation with a propofol analogue* (Nat Comm 2012²⁷). Eff.-switch profile, Fig 2b.

(5) Trauner *et al.*, **AzoLPA** for lysophosphatidic acid receptors (LPA_n): in *Optical Control of Lysophosphatidic Acid Signaling* (JACS 2020²⁸). Dramatic efficacy switch profile in Fig 3a, LPA₁.

1.2.3 Tangential Remarks & Outlook for Efficacy Photoswitches

(1) In the main text, we argued that the major reason why affinity switches' applicability for bidirectional photocontrol has been mainly limited to highly controlled cell culture settings is that the bioactivity applied by an affinity switch is so sensitive to its concentration (**Figure 1j**), yet linearly-reproducible dose-fixing is problematic or impossible for deep tissue or *in vivo* work. We note though, that if only unidirectional photo-turn-on is used ("one-shot"), this limitation diminishes somewhat since light dose can be titrated at a fixed wavelength. Then again, such cases also do not require a *photoswitch* per se, and can be (probably better) achieved by photocages.

(2) In addition to the features outlined in the main text, we suggest that another special feature of a high-potency efficacy photoswitch with near-equal-affinity isomers is that, when binding site saturation is ensured, the PSS dependence of activity can give insights into cooperativity that would not otherwise be accessible with always-active ligand/s. For example, at 400 nm the PSS *E*:*Z* ratio is ca. 3:1 (**Table S1**), and there is no detectable channel activation (**Figure 2eg**). Of course, even at full saturation, there will always be a statistical distribution of E_n/Z_{4-n} -TRP complexes (and even that C2-symmetric E_2/Z_2 -TRP may have a different activity profile than its C1-symmetric E_2/Z_2 -TRP isomer): nonetheless, this finding is quite suggestive that occupying just one of the four TRPC4/5 binding sites with the xanthine agonist (*Z*-**AzPico**) is insufficient for channel activity, if the other three sites are occupied by an antagonist (*E*-**AzPico**; further discussion at **Figure S14**).

(3) As hinted in several locations, it seems clear to us that there are many levels of target-based features which can be used to pre-select potential targets for developing efficacy photoswitches even when no ligand SAR data is known that would predict an efficacy cliff. The most significant level, in our opinion, is that "**poised targets**" that natively must be able to swap back and forth between (at least) two metastable states to balance and deliver their physiological function, such as ligand-gated channels and receptors, seem ideal candidates for efficacy photoswitch operation in general.²⁹ This as well as the other levels of target selection, as well as the general features and consequences of efficacy photoswitching for chemists and for biologists, will be addressed in more detail in our upcoming conceptual Perspective article that accompanies and comments on this paper's experimental results.

Supporting Note 3: Results from Other Compounds in our Panel

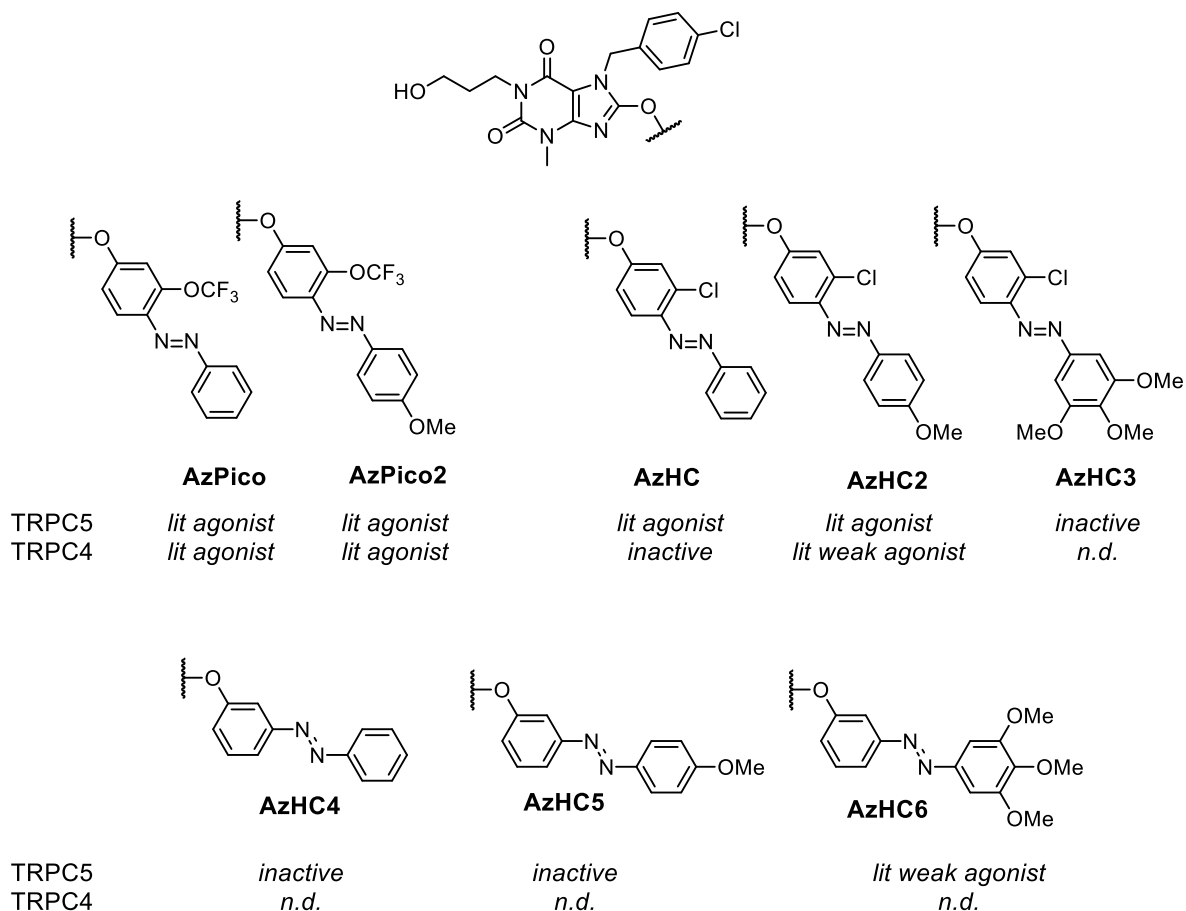


Figure S3. structures of all the compounds made and tested in this work; and short summary of biological activity that guided the selection of **AzHC** and **AzPico** as the best candidates to progress.

The initial FLIPR screening was carried out with all compounds shown in **Figure S3** on TRPC5; only hits **AzPico**, **AzPico2**, **AzHC** and **AzHC2** were further analysed on TRPC4. It is interesting to note that the structural changes which ruined agonistic potency in the abandoned compounds are comparatively small, e.g. 3,4,5-trimethoxy for **AzHC3**, a motif that tends to improve photoswitching completion and replacement of the C'3 residue with a photoswitch did not result in any biological relevant photoswitching performance and those compounds were not elucidated further. Among the hit compounds, **AzPico2** and **AzHC2** were discontinued even though their para-methoxy increases $E \rightarrow Z$ photoswitching completion (**Figure S9**), because their $Z \rightarrow E$ switching was less complete, their solubility was worse, and their total Ca^{2+} signal was lower, as compared to **AzPico** and **AzHC** respectively. We thus chose to investigate both **AzPico** and **AzHC** because of their different selectivity profile on TRPC4/5 (continued in **Supporting Note 4**).

1.3 Supporting Note 4: Structural Biology and TRP Selectivity

We prepared and acquired TRPC5:*E/Z*-AzHC samples in one lab, and TRPC4:*E/Z*-AzPico independently in another, which was useful for several plausibility checks. (1) There are additional lipid densities in the pockets that are present in both TRPC4 and TRPC5, and the changes to the lipid densities in the EM maps between *E* and *Z* isomers are similar in TRPC4 and TRPC5 as well: so these changes are not dependent on protein, nature of amphipol used, or lab in which the data were obtained/processed, but are rather inherent features of the system. (2) The positions of the distal rings which are much less-well-resolved than the rest of the ligand, were independently best aligned for the *E* and *Z* isomers, and in each case found to be *Z*-buried vs. *E*-projected, which gives more confidence in this structure-based analysis. (3) Identical deleterious effects of DTT were found in each lab, and removing it removed those problems.

1.3.1 Detailed Commentary: hTRPC5:*E/Z*-AzHC

To start, we note that although no channel-open structures are known, and all reported ligand structures are with inhibitors, there has been docking work done on xanthine-based TRPC5 *activators* such as **AM237**, **Pico145-DA**, and **Pico145-DAAIk**, (**Figures S1**). Docking suggested that a slight twist of their C-8 aryloxy substituents, compared to those of the inhibitors **Pico145** and **HC-070**, is needed to avoid potential clashes with nearby residues V610, V579 and L521.^{8,30} Because the functional data suggest **AzHC** is a TRPC5 efficacy switch (*E*-antagonist / *Z*-agonist), it would be expected that the *E/Z*-isomers both bind to TRPC5 but in different ways. To study TRPC5 complexes with both **AzHC** isomers by cryo-EM, we made several changes to our previously published cryo-EM pipeline³¹ (see **Supporting Section 4**). In brief, **AzHC** samples were irradiated with blue light (440 nm; to access (**E**)-AzHC) or UV-A light (365 nm; to access (**Z**)-AzHC) prior to incubation with purified MBP-hTRPC5 $\Delta_{766-975}$ and during grid preparation; at all other times, samples were handled under red light (650 nm) to minimise photoisomerisation. We found that **AzHC** degrades in DTT-containing buffers, as confirmed by HPLC analysis; and solving initial "*E/Z*-AzHC:TRPC5" cryo-EM structures obtained with DTT-containing buffers either did not locate the terminal phenyl ring of the azobenzene and could have been assigned to reductive N=N bond cleavage, or else indicated an unusual ca. 120° CNNC torsion angle that could have been assigned to the diphenylhydrazine; we therefore discontinued analysis of these data sets and DTT was omitted from buffers used to prepare all remaining **TRPC5:AzHC** (and TRPC4:AzPico) samples.

We determined high-resolution structures of hTRPC5:(**E**)-AzHC (2.60 Å) and hTRPC5:(**Z**)-AzHC (2.90 Å) without applying symmetry (**Figure 3**; **Figures S4-S5** and **S15-S18**; **Table S4**).

In **Figure 3ab**, TRPC5 is bound to *E*-AzHC (resolved to 2.60 Å in C1 symmetry); 4 **AzHC** molecules are bound and the best-resolved binding site is shown. There is high confidence in the binding pose (there are slightly different solutions for the *E*-azobenzene in the 4 sites but no major differences); and there is some lipid density still present in the map (likely: displaced phospholipid). In **Figure 3cd**, TRPC5 is bound to *Z*-AzHC (resolved to 2.90 Å in C1 symmetry); 4 **AzHC** molecules are bound, the best resolved is shown; EM map suggests flexibility of the *Z*-azobenzene as multiple poses could be docked by Glide-EM; lipid density is still present in map, but overlaps partly with the compound density (probably due to multiple conformations in the binding pocket in data set). Applying C4 symmetry led to higher overall resolution, but less well-defined densities for the azobenzene, potentially because of incomplete photoswitching of **AzHC** during sample preparation and/or incomplete displacement of the resident lipid from the binding sites. The **AzHC** *E* and *Z* isomers could be built into the lipid/xanthine binding site, with near-identical positions to **Pico145**³¹ for the xanthine core, the 3-hydroxypropyl on *N*-1, and the 4-chlorobenzyl on *N*-7 (**Figure 3**). Clear differences between the **AzHC** *E* and *Z* isomers were seen for the azobenzene distal ring: in (**E**)-**AzHC** it makes a π - π interaction with Phe522, while in (**Z**)-**AzHC**, it makes a π - π interaction instead with Tyr524 (**Figure 3**; **Figure S4a**). Considering the protein, most residues in the ligand binding site are in similar positions in both structures, except for Phe520, which flips strongly when the

agonistic **Z-AzHC** is bound (**Figure S4b**). These data further support the finding that **AzHC** acts as an efficacy switch and provide the first structural insights into how closely related xanthenes can have opposite effects on TRPC5 function (i.e. inhibition vs. activation).

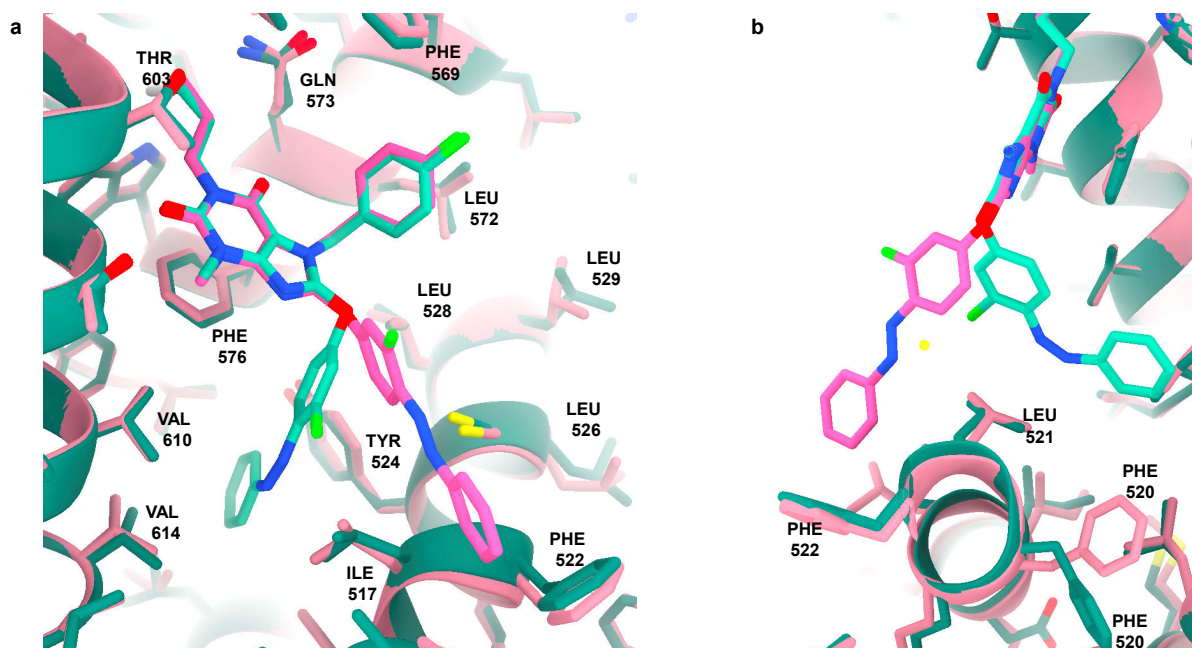


Figure S4. Comparison of hTRPC5 binding modes of the AzHC isomers. (a) The azobenzene distal phenyl ring interacts with Phe522 for (*E*)-AzHC (magenta ligand and protein), but with Tyr524 for (*Z*)-AzHC (teal ligand and protein). (b) *E/Z*-Photoisomers of AzHC feature a major difference in the conformation of Phe520 (at lower right).

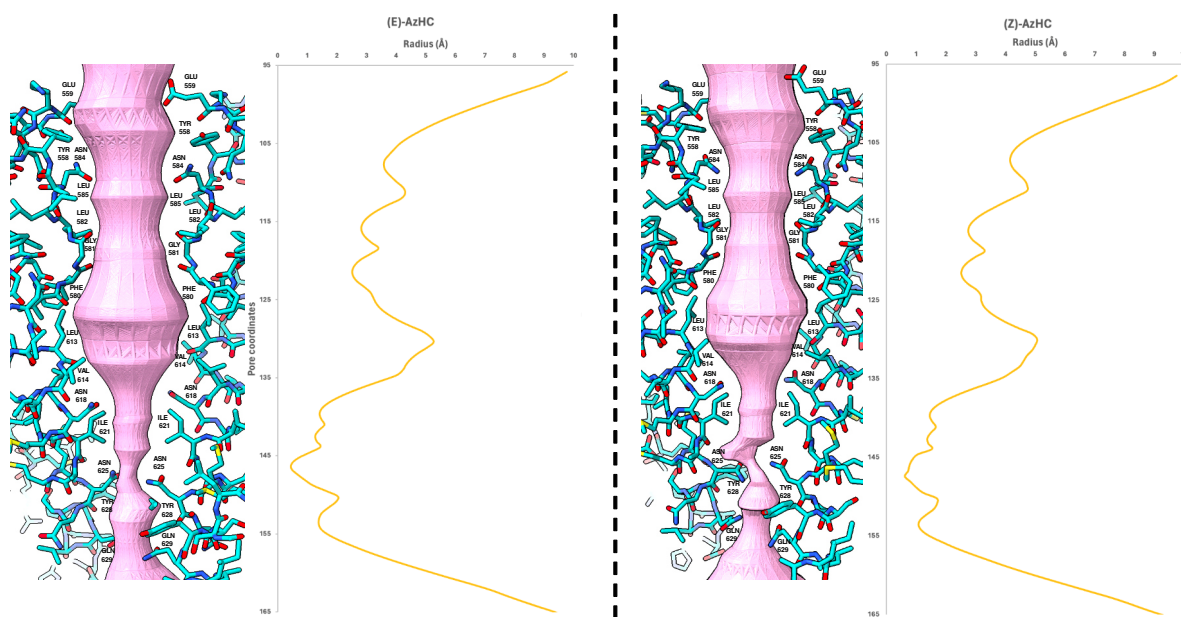


Figure S5. Pore analysis of TRPC5 structures. Asymmetric pore analysis of TRPC5:(*E*)-AzHC and TRPC5:(*Z*)-AzHC structures with PoreAnalyser³² (default settings) suggests that both structures are in a closed state.

Acquiring open-pore TRP channel structures is highly challenging. PoreAnalyser³² analysis suggests that both *E* and *Z* structures are channel-closed (**Figure S5**), which we believe is due to the channel's restraint in the amphipol stabiliser though it could also be due to low open state probability (especially without membrane potential), or the absence of cellular factors needed for opening (e.g., the membrane environment, Ca²⁺, bound lipids, post-translational modifications, protein-protein interactions); incomplete switching in all binding sites or incomplete displacement of lipid might also contribute. Still, while needing cautious interpretation, the structural rearrangements upon binding of agonist **Z-AzHC** in the closed form may still be usefully indicative.

1.3.2 Detailed Commentary: TRPC4_{DR}:*E/Z*-AzPico

We likewise determined the structure of DR-TRPC4:(*E*)-**AzPico** (3.0 Å) and DR-TRPC4:(*Z*)-**AzPico** (3.1 Å) without applying symmetry. The high-resolution structures enabled us to model the ligand into the density that was distinct from the annular lipid density reported from our earlier studies.^{33,34} We could model the ligand xanthine core with high confidence which is similar to the previously reported structure of Pico145 bound with TRPC5.⁵

The difference in the *cis* (*Z*) and *trans* (*E*) isomers of the **AzPico** could be modelled after processing the data with C1 symmetry that gave a slightly better density for the less-resolved terminal benzene ring. The relative displacement of the stabilising residues Leu517, Leu520 and Phe521 was visible when comparing the *E*-**AzPico** and *Z*-**AzPico** densities, boosting our confidence in ligand modelling (**Figure S6**). The terminal benzene ring makes a π - π interaction with Phe521 in *E*-**AzPico** while in *Z*-**AzPico** the terminal ring flips to make a π - π interaction with Tyr523.

Surprisingly, the *Z*-**AzPico** that activates the channel, yielded a closed state (**Figure S7**) which could be attributed to the low open state probability of the channel or the absence of other cellular factors required for opening the channel as mimicked by TRPC5. Nevertheless, the *Z*-bound structure gives a plausible explanation for channel activation, in that the terminal benzene ring of *Z*-**AzPico** interacts with S6 helix residues closer to channel gating residues that might influence opening, whereas in the *E* isomer the terminal ring interacts with the S5 helix (**Figures S6-7**).

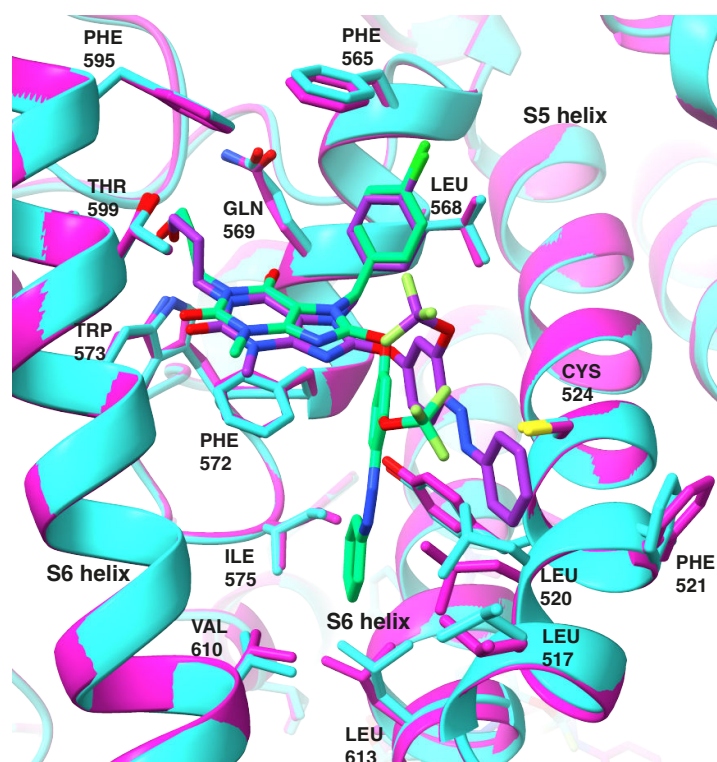


Figure S6. Comparison of the binding modes of *E/Z*-**AzPico** isomers to TRPC4. *Z*-**AzPico** bound TRPC4 is shown in cyan with the ligand in green. *E*-**AzPico** bound TRPC4 is shown in magenta with the ligand in dark purple. The residues interacting with the ligand are shown with sticks and labelled. The residues interacting with the xanthine core of the ligand show less relative displacement between *E* and *Z* structures than those interacting with the terminal benzene ring. The S6 helix involved in channel gating is labelled.

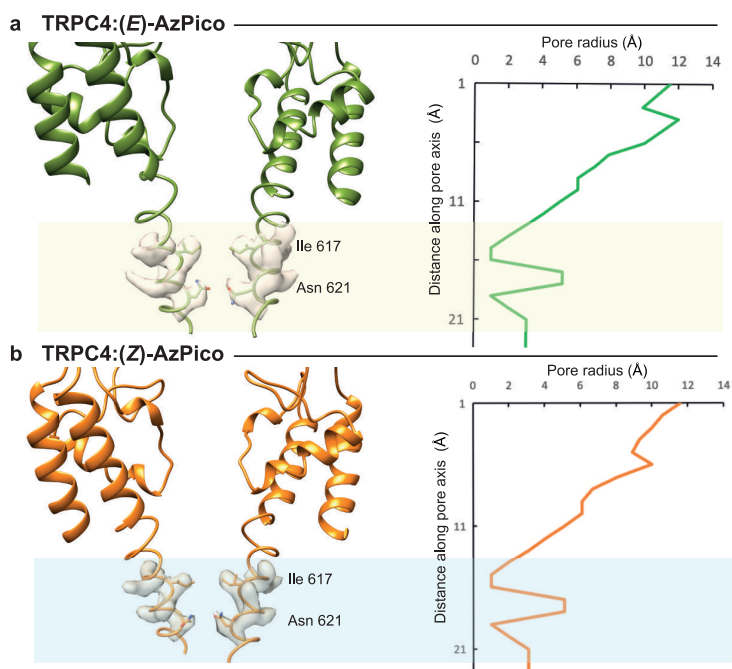


Figure S7. Pore analysis of TRPC4_{DR} structures with bound *E/Z*-AzPico. Asymmetric pore radius calculation of the (a) TRPC4:(*E*)-AzPico and (b) TRPC4:(*Z*)-AzPico structures with PoreWalker³⁵ indicates the tight constriction at the lower gating residues Ile617 and Asn621 (transparent shaded region), indicating that both structures are in a closed state.

1.3.3 Note on TRPC4 / TRPC5 Sequence Alignment

The key contact residues of interest in the ligand binding site are highly conserved between TRPC4 and TRPC5. The relevant sequences in the site are:

TRPC4_{DR}, 501 - 529:

HLGPLQISL GRMLLDILKF LFIYCLVLLA

hTRPC5, residues 502 - 530:

HLGPLQISL GRMLLDILKF LFIYCLVLLA

1.3.4 Differences and selectivity between TRPC5 and TRPC4?

AM237 activates TRPC5 but inhibits **EA** mediated activation of TRPC4; **Pico145** inhibits both TRPC4 and TRPC5. Thus, somewhat naively, it could be argued that it is the *para* substituent here which affects both the efficacy mode and the selectivity for TRPC4 and/or TRPC5.

Intriguingly, **Z-AzPico** activates TRPC4 and TRPC5 with low nanomolar potency whereas **Z-AzHC** only activates TRPC5 but not TRPC4. Therefore, the *meta* substituent is now responsible for the selectivity in this case. The cryo-EM structures of **Pico145** and **HC-070** in complex with TRPC5 indicated the same binding site but the southern phenyl ring bearing the OCF₃/Cl group is flipped and pointing in opposite directions. Our structural data with **AzHC:TRPC5** and **AzPico:TRPC4** does not reproduce the ring flip but shows the same orientation shift for the diazene motif for *E* and *Z* isomers, i.e. *Z*-buried vs. *E*-projected. Additionally, both **E-AzPico** and **E-AzHC** inhibit **EA** mediated activation on TRPC4 and TRPC5, hence both scaffolds can bind to either protein but the *efficacy switch* does not occur for **AzHC** on TRPC4.

It is not surprising that both ligands bind to either protein because there is a high sequence similarity among the TRPC family in the identified binding pocket for **Pico145 /HC-070**, and in the binding region, human TRPC4/5 differ only by a single amino acid (TRPC5: V579, TRPC4: I579). We hypothesised that the selective activation of TRPC5 vs TRPC4 by **AzHC** (and **AM237**⁸) could be the result of differences in this residue. To test this hypothesis, we used [Ca²⁺]_i recordings to study

the effect of **AzHC** and **AM237** on the variant TRPC5-V579I (in which V579, the only residue in the **AzHC** binding site that is different between TRPC4/5, is mutated to its TRPC4 counterpart), and the reverse variant TRPC4 β -I575V (residues correspond exactly; the sequence numbering differs between the channels). These point mutations do not switch the effect of **AM237** and **AzHC** (**Figure S8**), suggesting that the molecular basis for **AzHC**'s TRPC5-selective activation is more complex than the immediate residues it contacts, and perhaps is regulated allosterically by other TRPC4/5 domains instead of direct binding within this pocket.

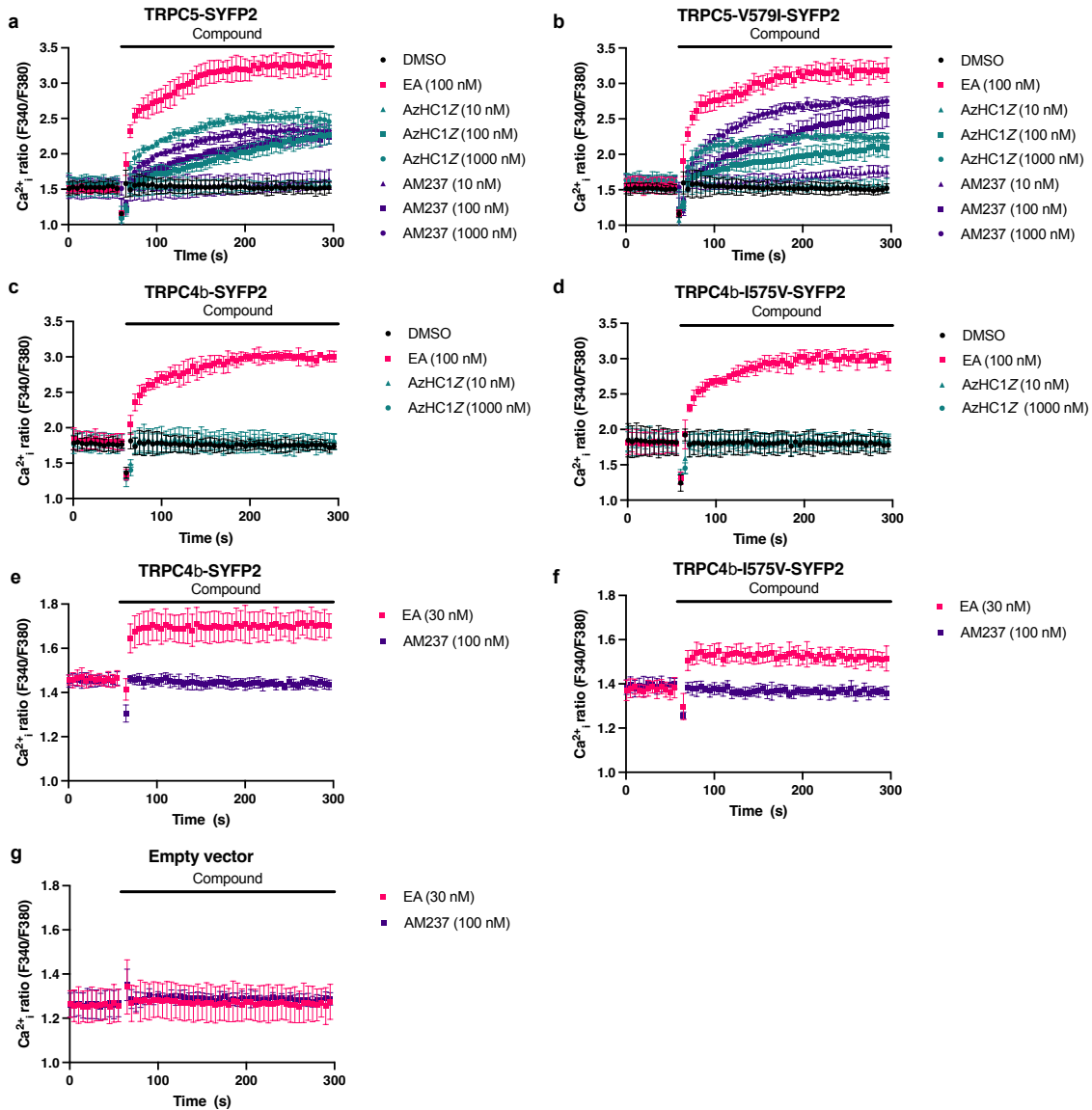


Figure S8. Selective TRPC5 activation by **AM237** and **AzHC** is not the result of differences in residues lining the AzHC binding site. $[Ca^{2+}]_i$ measurements were made from HEK 293 cells transiently expressing the indicated plasmid. Each panel displays data from a single 96-well plate ($N = 6$; mean \pm SD over technical replicates) showing the baseline recording (0-60 s) followed by the effect of addition of the indicated compound (61-300 s). TRPC1/4/5 activator (-)-englerin A (**EA**) was used as a positive control to determine the maximum $[Ca^{2+}]_i$ response. **(a-b)** **AM237** and (Z)-**AzHC** are partial agonists of TRPC5 as well as TRPC5_{V579I}. **(c-f)** **AM237** and (Z)-**AzHC** do not activate TRPC4, nor TRPC4_{I575V}. **(g)** This control experiment shows that transfection with TRPC4/5 is necessary for detection of a $[Ca^{2+}]_i$ response to **EA** or **AM237**.

1.4 Supporting Note 5: AzHC & TRPC5-dependent Ca²⁺ in mouse hypothalamus

Expanded from main text:

TRPC5 is expressed in dopamine (i.e., tyrosine hydroxylase-positive, Th⁺) neurons of the dorsomedial aspect of the hypothalamic arcuate nucleus (ARC) (**Fig. 5a**), which has been confirmed by molecular biology and electrophysiological techniques.³⁶ The channel contributes to both spontaneous oscillatory activity and sustained activation following stimulation with the hormone prolactin, which is essential for normal prolactin homeostasis in the body.^{36,37} Using brain slices through the ARC of mice expressing the Ca²⁺ indicator GCaMP6f in Th⁺ neurons (Fig. 4), we investigated (1) whether Ca²⁺ responses at endogenous TRPC5 expression levels can be photoswitched by UV illumination of **AzHC** or **AzPico**, (2) whether Ca²⁺ responses depend on TRPC5 expression using TRPC5-deficient brain slices, (3) whether a dose dependence could be detected, and (4) whether there are properties in channel activity that can be distinguished between photoswitchable small TRPC modulators.

Th⁺ neurons are known for their spontaneous oscillatory burst-firing activity,³⁶ which is also evident in their spontaneous Ca²⁺ responses (**Fig. 5b**). These spontaneous rhythmic Ca²⁺ activities are characterized by periods of high and low Ca²⁺ fluorescence.³⁷ Th⁺ neurons treated with 500 nM **AzHC** and stimulated with a 355 nm UV laser for ~60 ms inducing an E→Z isomerization (**Z-AzHC**) induced a sustained high Ca²⁺ fluorescence that lasted up to 3 min (14 of 33 cells, 42%). Genetic deletion of the TRPC5 channel in the Th-GCaMP6f-ΔTrpc5 mouse, prevented the increase in **Z-AzHC** induced Ca²⁺ activity in Th⁺ neurons (**Fig. 5c**), indicating channel selectivity of **AzHC**. The area under the curve (AUC) of Ca²⁺ signals quantifies that **AzHC** does not induce changes under 488-nm illumination alone, but requires both isomerization with 355-nm light ($p < 0.0001$) and TRPC5 expression to produce Ca²⁺ increases ($p < 0.001$) (**Figure S21ab**).

To determine the sensitivity of **Z-AzHC** induced Ca²⁺ responses in Th⁺ neurons, we performed concentration-response measurements (**Fig. 5d**). These results showed a dose dependence with a Hill coefficient of 1.95 and an EC₅₀ of $0.13 \pm 0.10 \mu\text{M}$. At **AzHC** concentrations of 1 μM , no change in spontaneous Ca²⁺ activity was observed in TRPC5-deficient Th⁺ neurons compared with before UV stimulation (**Fig. 5e**).

In wildtype slices, **AzPico** also induced long-lasting high Ca²⁺ signals after 355 nm pulsing (13 out of 31 cells), with overall Ca²⁺ signal properties that are not distinguishable from **Z-AzHC**. A comparison of both **Z-AzHC** and **Z-AzPico** illustrates that both photoswitchable modulators similarly prolonged the mean Ca²⁺ burst duration and consequently lowered the mean Ca²⁺ burst frequencies, as well as increased the mean amplitude of the Ca²⁺ responses (**Fig. 5g,h; Figure S21d-l**).

The total duration of the Ca²⁺ fluorescence increase after 355 nm UV illumination indicates that **Z-AzHC**, **Z-AzPico** and the photoswitchable agonist **Z-BTDazo**³⁷ are very effective in elevating the Ca²⁺ response in Th⁺ neurons ($p < 0.001$; **Figure S21g**). Comparing the properties of the TRPC5-dependent **Z-AzHC** and **Z-BTDazo** the main difference is the higher frequency of the **Z-BTDazo** Ca²⁺ signals ($p < 0.0001$; **Fig. 5h**). Consequently, **BTDazo** had mainly shorter lasting Ca²⁺ burst durations (29 out of 35 cells, 83 %) and only few mean Ca²⁺ durations up to 3 min (6 out of 35 cells, 17 %). These results can suggest a different binding site or interaction sites in the same binding pocket for **AzHC** and **BTDazo** in the TRPC5 channel.

2 Photocharacterization

UV-VIS. UV-Vis spectra were recorded on an Agilent Cary 60 UV-Vis spectrophotometer using 1 cm quartz or PMMA cuvettes. All photoisomerisations were performed at room temperature in non-degassed solvents unless stated differently. Samples were irradiated with either a CoolLED pE-4000 or Polycon V monochromator (TILL Photonics, Gräfelfing, Germany) by shining from the top of the cuvette, until the spectra did not change further (photoequilibrium). Unless stated differently, all measurements were performed at a default concentration of 20 μM . Dark state refers to stocks in DMSO kept at 60 °C for >14 h prior to measurements (*all-trans*). All other measurement methods have been detailed elsewhere (refs ^{37–39}). *All-E* and PSS spectra are shown in **Figure S9**.

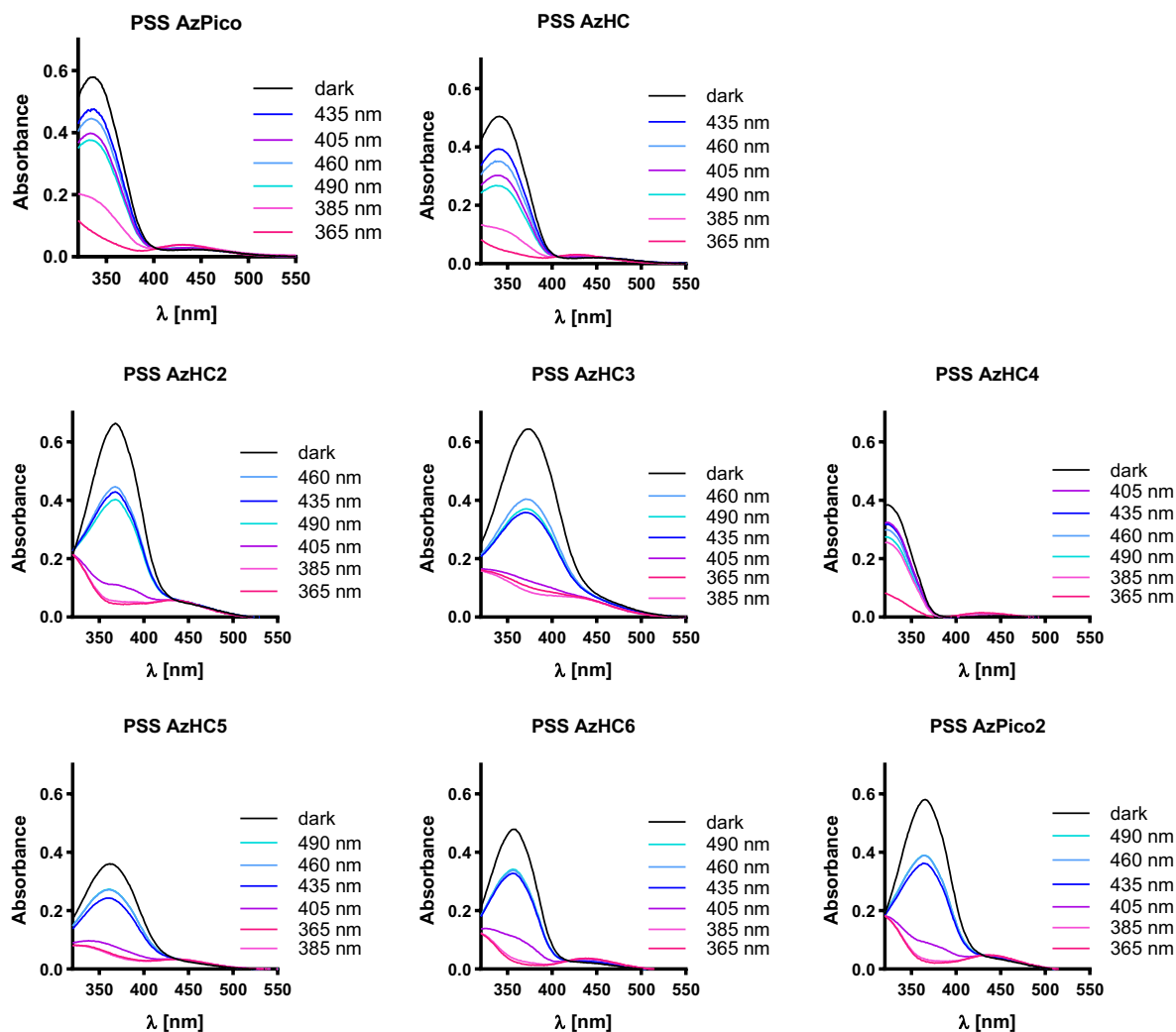


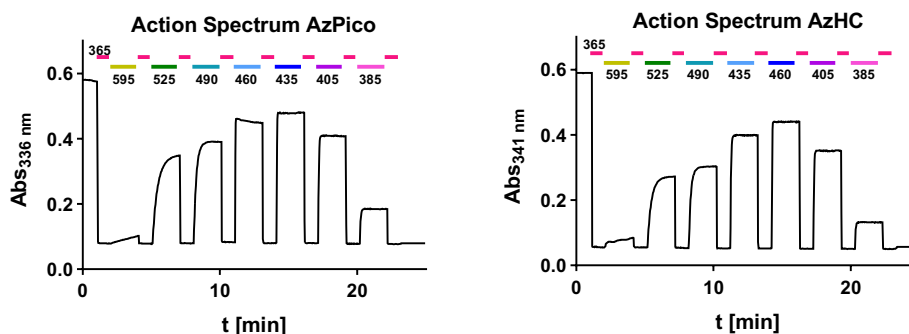
Figure S9: PSS spectra of **AzPico1-2** & **AzHC1-6** at different wavelengths. Measured at 20 μM in DMSO/H₂O 9:1 (volumetric ratio). Illumination with CoolLED pE-4000. (**AzHC1** == **AzHC**, **AzPico1** == **AzPico**).

HPLC for PSS *E/Z* ratios. Analytical HPLC was performed on an Agilent 1200 SL with (a) a binary pump able to deliver H₂O:MeCN eluent mixtures containing 0.1% formic acid at a 1 mL/min flow rate [for PSS measurements of final compounds, only MeCN was used], (b) YMC Carotenoid 5 μm , 4.6 \times 150 mm, maintained at 40 °C, (c) an Agilent 1200 series diode array detector. Samples (100 μM , MeCN) in HPLC vials were irradiated for at least 6 min from top with the monochromator light source (slit opening set to maximum of 15 nm) until PSS was reached, then injected (*E* and *Z* separate well); PSS ratio was then determined by integrating the signal at an isosbestic region found by UV/VIS in pure MeCN, and calculating the ratio from the integrals (**Table S3**).

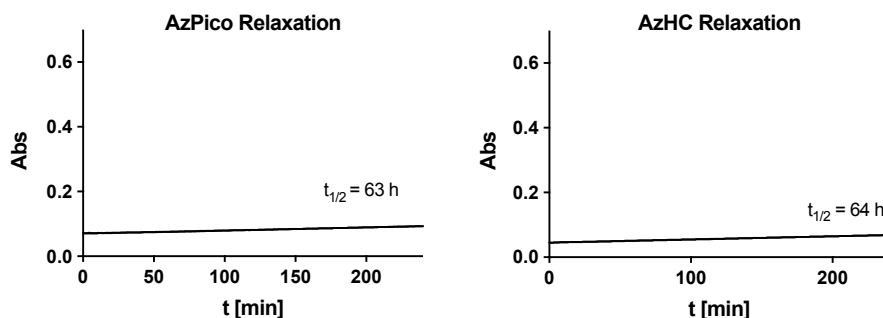
Table S3. PSS %E & %Z for **AzPico** & **AzHC** at different wavelengths (monochromator, narrow-bandwidth), determined with HPLC integration (296 nm).

λ [nm]	AzPico		AzHC	
	% E	% Z	% E	% Z
330	16	84	21	79
340	8	92	6	94
350	5	95	4	96
360	5	95	4	96
370	11	89	7	93
380	23	77	23	78
390	38	62	52	48
400	79	21	74	26
410	84	16	81	19
420	84	16	80	20
430	82	18	79	21
440	80	20	76	24
450	77	23	72	28
460	74	27	68	32
470	70	30	63	37
480	67	33	59	41
490	64	36	55	45
500	61	39	52	48

Action Spectra, Cell-Free. Samples were measured by UV-Vis with CoolLED pE-4000 illumination (most LEDs are relatively narrow-band) during an initial 1 min dark (*E*) followed by alternating illumination cycles of 1 min at 365 nm (50 mW/mm²) then 2 min of each indicated wavelength (10 mW/mm²), to gain an impression of the relative rates per-photon of approaching PSS at the indicated wavelengths (**Figure S10**).

**Figure S10.** Action spectra for **AzPico** & **AzHC** (LED illuminations, moderate-bandwidth).

Spontaneous Z→E Relaxation, Cell-Free. Samples were monitored by UV-Vis to confirm that spontaneous *Z*→*E* relaxation is orders of magnitude slower than assay timescales, i.e. active bidirectional photoswitching is needed to modulate the activity of **AzPico** and **AzHC** (**Figure S11**).

**Figure S11.** Very slow thermal *Z*→*E* relaxation of **AzPico** and **AzHC** at 37°C at 20 μM in DMSO:H₂O 9:1. Data was force-fitted as exponential decay to obtain *lower limits* to the relaxation half times.

3 Cultured Cell Lines (primarily for Figure 1 and Figure 2)

3.1 FLIPR Ca²⁺ influx assay in cell suspensions.

We initially screened for photoswitchability of activity in cells, using a fluorometric imaging plate reader (**FLIPR**) calcium flux assay, with human embryonic kidney cell line HEK293 stably transfected to express mouse TRPC4 β - or TRPC5-CFP fusion protein (HEK_mTRPC4 β -CFP / HEK_mTRPC5-CFP). The FLIPR setup provides high-content data, but it is limited to photocontrol LED wavelengths of 365 nm (best-Z) and 447 nm (suboptimal-E), while imaging at 470 nm excitation (Fluo-4 AM as Ca²⁺ indicator; this imaging light counteracts both PSSs). Therefore, we expected the FLIPR results to under-estimate the true photocontrol power accessible to the reagents.

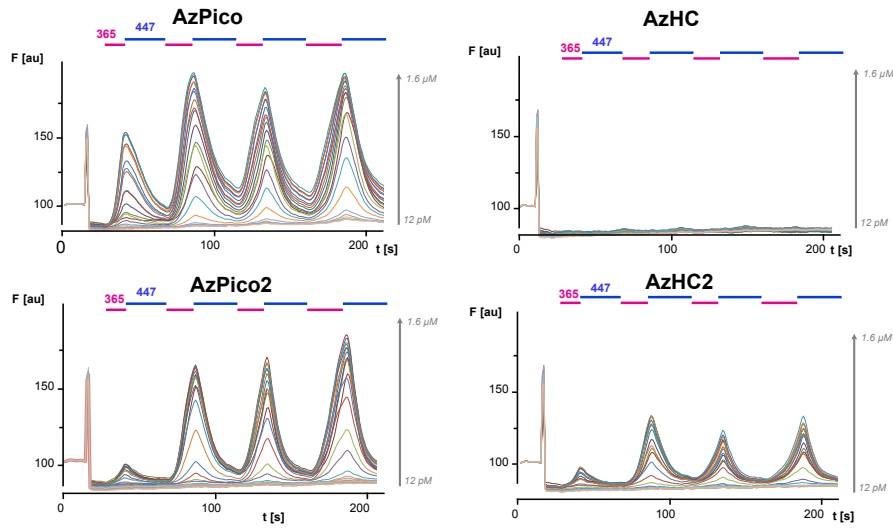
Cells were grown to 70%-90% confluency in a 75-cm² culture flask, trypsinised, washed and resuspended in BSA-containing (0.1%) HBS, and supplemented with 3 μ M Fluo-4/AM. As described earlier, stably TRPC-transfected cells were induced with tetracycline 24 h prior to the experiments.^{40,41} After incubation at 37°C for 30 min [Fluo-4 loading], cells were again washed, resuspended, and dispensed (40 μ l/well) into black pigmented, clear-bottom 384-well plates (Greiner μ -clear). To image the Fluo-4 fluorescence during the application and photoswitching of test compounds, these plates were first mounted to a Tecan Fluent 480 (Tecan, Männedorf, Switzerland) liquid handling device, equipped with a 384-tip multichannel arm and a gripper arm. A custom-made plate-imaging device was used for photoswitching during fluorescence imaging, which features LED-based excitation modules (365 nm and 447 nm used here for photoswitching, and 470 nm used here for Fluo-4 readout) projected onto the bottom of the microwell plate, with a cooled scientific complementary metal oxide sensor (sCMOS) camera (Zyla 5.5, Andor, Belfast, UK) equipped with a Nokton 42.5 mm f/0.95 (Voigtlaender, Fürth, Germany) for detection. The LEDs were controlled with an Arduino device and constant current drivers (1 A for 365 and 470 nm LEDs; 3 A for 447 nm LED); detection was under the control of Micromanager 2.0 software. Compounds were serially diluted and applied to the Fluo-4-loaded cell suspensions inside this custom plate-imaging device, then fluorescence intensities (under 470 nm excitation) were continuously recorded during programmed illuminations e.g. with alternating 365 nm and 447 nm phases.

AzPico, **AzPico2**, **AzHC**, and **AzHC2** all showed photoswitchable activity on TRPC5 and were tested also on TRPC4 (**Figure S12**); the other tested compounds (**AzHC3-6**) did not show activity on TRPC5 and were not tested on TRPC4.

Concentration-response curves for the Z-isomers (channel activation) were then constructed from the maximal signals during 365 nm phases, after a suitable number of "priming" cycles to allow the system to reach stable performance (**Figure S13**).

All experiments were conducted as a minimum of 3 independent experiments with each experiment averaging data in technical duplicates.

Cellular TRPC4 photoswitching: HEK cell Ca^{2+} influx photomodulation with AzPico or AzHC (365/447 nm illumination cycles) - plate imager



Cellular TRPC5 photoswitching: HEK cell Ca^{2+} influx photomodulation with AzPico or AzHC (365/447 nm illumination cycles) - plate imager

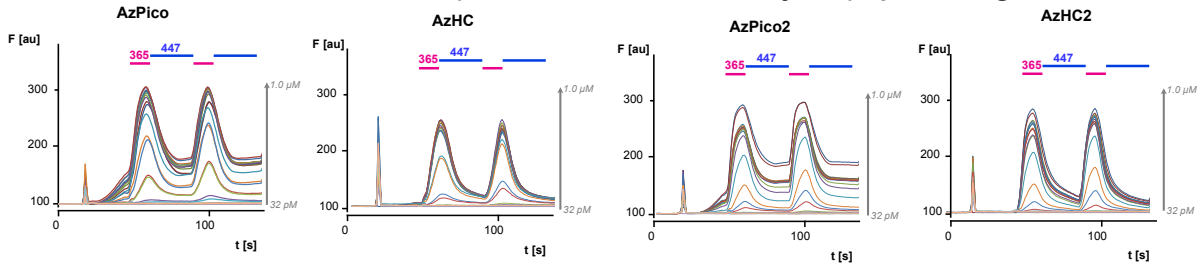


Figure S12. Activity of AzPico, AzPico2, AzHC, AzHC2 on TRPC5 and TRPC4 (FLIPR assay).

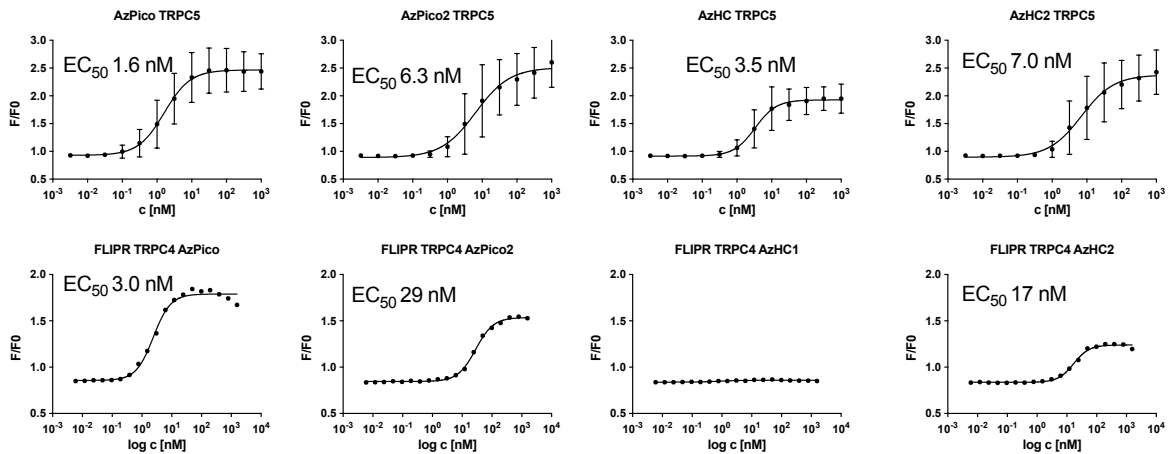


Figure S13. Dose response curves of Z-AzPico, Z-AzPico2, Z-AzHC, and Z-AzHC2 on TRPC5 and TRPC4 (FLIPR assay).

3.2 Ephys Characterisation of Photocontrolled Induced Ionic Currents

Expanded from main text: We recorded full wavelength-dependent action spectra of **AzPico** and **AzHC** under fast photoswitching in ephys in TRPC4 and/or TRPC5-expressing cells (**Figure 2**, **Figure S14**). The advantage of the ephys setup is that freely chosen monochromated wavelengths can be used for photoswitching, while in parallel there is no optical imaging light to counteract these optimal wavelengths: and this allows for optimising the photoswitchability. They now performed to the full potential of ideal efficacy switches. For example, **AzPico** reversibly photomodulated TRPC4 currents over >60 consecutive cycles with a fully constant activation profile, without fatigue (**Figure 2a,b**). Current/voltage (*I/V*) curves show a strong activation of ion flux at best-Z (360 nm) PSS; yet, only at nonphysiological voltages (<-80 mV or >+60 mV) could any small differences between basal activity and good-E (440 nm) PSS be detected (**Figure 2c**). The repeatability of on/off photocycling allowed us to extract action spectra for both (1) photoactivation (**Figure 2d,e**) and (2) photodeactivation (**Figure 2f,g**) *in situ* in live cells. To obtain the activation action spectrum we used an irradiation protocol with varying wavelengths from 330-505 nm for 500 ms followed by 200 ms of 440 nm to set the channel activity back to a constant baseline value. For the deactivation action spectrum we first activated with 300 ms of 360 nm and then applied varying wavelengths from 330-505 nm for 200 ms followed by a baselining step with 360 nm and 440 nm. Optimal on-responses were elicited in the range of 350-365 nm, whereas a broader wavelength range of 400-480 nm can be applied for effective off-photoswitching.

A special feature of a high-potency efficacy photoswitch with similar-affinity isomers is that, if binding site saturation is ensured, the PSS dependence of activity should give insights into the stoichiometry of target activity modulation that would not be accessible or reliable when simply titrating always-active ligand/s. For example, at 400 nm the PSS *E:Z* ratio is ca. 3:1 (**Table S3**), and there is no channel activation detectable (**Figure 2e,g**): giving the expectation that occupying one of the four TRPC4/5 binding sites with the low nanomolar xanthine agonist **Z-AzPico** is still insufficient for channel activity, if the other three sites are occupied by the inverse agonist **E-AzPico**. As a corollary, the observed complete shutdown of channel currents at 25% *Z*-occupancy is a dramatic reflection of the power of efficacy switching: a potency switch with only 75%-complete *Z*→*E*-switching away from such a potent *Z* isomer could not deliver such a functional ON-OFF switch when its biological response, at the quasi-linear dose-response region of a sigmoid curve, is given by the logarithm of the *Z*-concentration.

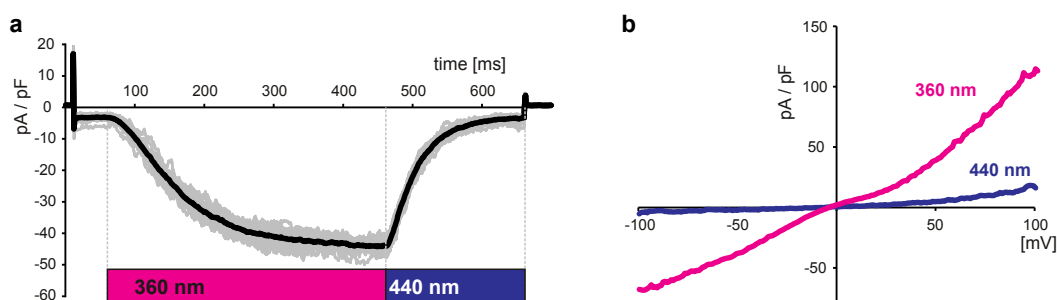


Figure S14. (a) Electrophysiological whole-cell recordings of TRPC5 currents in voltage clamp ($V_h = -80$ mV) mode. Overlay of ionic currents in a TRPC5-expressing HEK293 cell during >60 consecutive cycles of 360/440 nm illumination in the presence of 10 nM **AzPico**. (b) *I/V* curves of whole cell currents in voltage-clamped TRPC5-expressing cells exposed to 360 nm and 440 nm light with 10 nM **AzPico** in the bath solution.

3.3 Pharmacology of TRPC4 and TRPC5 variants (Figure S8)

3.3.1 Plasmids

Generation of TRPC5-SYFP2 and TRPC4 β -SYFP2 has been reported previously.⁸ TRPC5-V579I-SYFP2 and TRPC4 β -I575V-SYFP2 were generated using the Q5[®] Site-Directed Mutagenesis Kit

(New England Biolabs) using back-to-back primers to insert the desired mutations. Primers were designed using NEBaseChanger® (<https://nebasechanger.neb.com/>) and purchased desalted from Integrated DNA Technologies.

TRPC5-V579I-SYFP2 forward primer: 5' CTTCTGGTCTataTTTGGCCTTTTAAATC 3'; reverse primer 5' AGTGAAGTGAAGAGTCTCAAAG 3'

TRPC4β-I575V-SYFP2 forward primer: 5' GTTTTGGTCAgtaTTTGGGCTCATC 3'; reverse primer: 5' AGGGACTGCAGTGTCTCA 3'.

All constructs were sequenced to verify identity (Azenta).

3.3.2 Chemicals

AM237 was prepared according to previously reported procedures.⁸ (-)-englerin A (**EA**) was obtained from PhytoLab (Vestenbergsgreuth, Germany). **AM237**, **EA** and **AzHC** were made up as 10 mM stocks in 100% DMSO, aliquots of which were stored at -20 °C (**AM237** and **AzHC**) or -80 °C (**EA**). Further dilutions of compounds were made in DMSO and these were dissolved 1:1000 in a compound buffer (SBS + 0.01% pluronic acid) before being added to cells. Fura-2 AM (Invitrogen UK) was dissolved at 1 mM in DMSO and stored at -20 °C.

3.3.3 Intracellular calcium recordings

Intracellular calcium ($[Ca^{2+}]_i$) was measured using the ratiometric Ca^{2+} dye Fura-2. Experiments with TRPC5-SYFP2, TRPC5-V579I-SYFP2, TRPC4β-SYFP2, and TRPC4β-I575V-SYFP2 were carried out in HEK 293 cells (ATCC, Teddington, UK) transiently transfected with the relevant plasmid.

HEK293 cells were maintained in Dulbecco's Modified Eagle Medium, high glucose, GlutaMAX, + pyruvate (ThermoFisher Scientific), supplemented with foetal bovine serum (FBS (Merck); 10%), penicillin–streptomycin (ThermoFisher Scientific) (100 units per ml; 100 μgml^{-1}). Cells were kept in a humidified incubator at 37 °C at 5% CO_2 . Passage of the cells was carried out twice weekly.

Cells were transfected with the relevant plasmid using jetPRIME transfection reagent (VWR). Assays were performed 48 h after transfection. 24 h before experiments, transfected cells were plated onto black, clear bottom poly-D-lysine coated 96-well plates (ThermoFisher Scientific) at a density of 60,000 cells/well. To load cells with the Fura-2 dye, media was removed, and cells were incubated with standard bath solution (SBS; composition, in mM, NaCl 130, KCl 5, glucose 8, HEPES 10, $MgCl_2$ 1.2, and $CaCl_2$ 1.5) containing 2 μM Fura-2 acetoxymethyl ester (Fura-2 AM (Invitrogen UK)) and 0.01% pluronic acid (Merck) for 1 h at 37 °C. Dye-containing media was removed and the cells washed twice briefly with SBS. SBS was then changed to recording buffer (SBS with 0.1% BSA (Sigma Life Science) and 0.5% DMSO for **Figure S8ab**; SBS with 0.01% pluronic acid and 0.1% DMSO for **Figure S8c-g**) immediately prior to experimentation. Inclusion of BSA and a higher concentration of DMSO in **Figure S8ab** was to improve the solubility of **AzHC**. However, these additions did not affect the responses: recordings without BSA and with 0.1% DMSO gave near-identical data (not shown).

For **Figure S8a-d**, loaded compound buffer on a clear round-bottom 96-well plate (Sarstedt, Germany) was illuminated at 380 nm by the DISCO system⁴² for a minimum of 20 min. Ambient light was excluded from this plate between DISCO illumination and Ca^{2+} measurement. The level of activation seen to be produced by **EA** and **AM237** indicated these compounds were not degraded by illumination at 380 nm.

$[Ca^{2+}]_i$ was measured in the FlexStation3 (Molecular Devices, Wokingham, UK), by alternating excitation at 340 nm and 380 nm, with an emission at 510 nm. Measurements were performed at rt for 300 s at 5 s intervals. **EA**, **AzHC**, and **AM237** were dissolved at 2× final concentration in compound buffer (see above for composition) and added to cells after recording for 60 s.

4 Structural biology (Figure 3)

4.1 Structural biology of TRPC5:AzHC

4.1.1 Plasmid

Structural studies of TRPC5:AzHC were conducted using the previously described construct MBP-hTRPC5 $_{\Delta 766-975}$,³¹ which contains human TRPC5 in C-terminally truncated form ($\Delta 766-975$) with an N-terminal maltose-binding protein tag followed by a PreScission protease cleavage site. Bacmids and baculoviruses were produced according to the Bac-to-Bac protocol (Invitrogen). The BacMam vector was a kind gift from Professor Eric Gouaux (Vollum Institute).⁴³

4.1.2 Protein expression and purification

P2 virus was added to 2.0 million per ml of Freestyle™ 293-F Cells (ThermoFisher Scientific) in Gibco FreeStyle 293 Expression Medium (Invitrogen) at a final volume of 7.5% at 37 °C and 5% CO₂. After 8-12 h, 5 mM sodium butyrate (Sigma Aldrich) was added, and the temperature was lowered to 30 °C. After a further 40 h, cells were harvested by centrifugation and then frozen. The protein purification protocol was adapted from Duan *et al.*⁴⁴ Unless stated otherwise, all detergents (and amphipol PMAL-C8) were supplied by Generon and Anatrace. For a typical purification, a 200 ml cell pellet was thawed and resuspended with 20 ml of 1% DDM, 0.1% CHS, 150 mM NaCl (Sigma Aldrich), 30 mM HEPES (Sigma Aldrich) pH 7.4, 1 mM DTT (Fisher Scientific Ltd) and protease inhibitor cocktail (Sigma Aldrich), and incubated by rotating at 4 °C for 1 h. The insoluble material was removed by centrifugation at 10,000×g for 1 h at 4 °C. The soluble fraction was incubated with 500 µl bed volume of pre-washed amylose resin (New England Biolabs) for 12-16 h, rotating at 4 °C. The resin was washed with 30 ml of 0.1% DDM and 0.01% CHS, 150 mM NaCl, 30 mM HEPES pH 7.4, 1 mM DTT. The resin was resuspended in 8 ml of 0.2% PMAL-C8, 150 mM NaCl, 30 mM HEPES pH 7.4, 1 mM DTT and rotated for 6 h at 4 °C. The detergent was removed by addition of Biobeads (Bio-rad) at a ratio of 10 mg/ml, followed by incubation for 16-20 h. The resin was washed with 20 ml of buffer without detergent (150 mM NaCl, 30 mM HEPES pH 7.4, 1 mM DTT). To avoid denaturation of **AzHC** by DTT, we further washed the resin with 4 ml of the same buffer *without* DTT before elution. The sample was eluted in 2 ml of the same buffer (without DTT) plus 50 mM maltose (Sigma Aldrich). The eluate was subjected to centrifugation at 20,000×g for 15 min at 4 °C to remove any precipitated material. The supernatant was concentrated step-wise to the required concentration with 100 kDa cut off Vivaspin 500 concentrators (Sigma Aldrich). In a typical purification protocol, ~200 µg of purified TRPC5 was produced from 200 ml of cell suspension.

4.1.3 Sample preparation and data collection

To access the required isomer of **AzHC**, the compound samples were illuminated with blue light (440 nm, 3W LED) for (**E**)-**AzHC** or UV-A light (365 nm, 3W LED) for (**Z**)-**AzHC**. Following this illumination, to minimise the risk of photoswitching, the compounds were manipulated only under red light (650 nm LED) or under the light source used to access the required isomer. For cryoEM studies, 1 mg of purified TRPC5 in PMAL-C8 at 1.0 mg/ml was incubated with 100 µM of the relevant **AzHC** isomer (taken from a 10 mM DMSO stock, never exceeding 1% DMSO final concentration in protein samples). A 3.5 µl aliquot of the sample was applied to an UltrAuFoil Holey Au R1.2/1.3, 300 mesh grid (Quantifoil), which had been glow-discharged twice for 45 s using a Pelco easyGlow glow discharge unit. An FEI Vitrobot, retrofitted with the light source used to access the relevant **AzHC** isomer, was used to blot the grids for 6 s (blot force 1) at 100% humidity and 4 °C before plunging into liquid ethane. The grids were loaded into an FEI Titan Krios transmission electron microscope (Astbury Biostructure Laboratory, University of Leeds) operating at 300 kV, fitted with a Falcon 4i direct electron detector. Automated data collection was carried out using EPU software, with fringe-free imaging in counting mode, using a defocus range between -0.7 to -3 µm in 0.3 µm increments. We collected a total of 3,000 EER movies for the (**E**)-**AzHC** sample and

3,504 EER movies for the **(Z)-AzHC** sample. In both cases, the movies were collected with a pixel size of 0.74 Å and a total dose of 35.72 e⁻/Å². The fractions were combined into 27 frames resulting an exposure dose of 1 e⁻/Å² per frame.

4.1.4 Image processing

An overview of the image processing protocol is shown in **Figure S11** and **Figure S12**. All processing was completed in Cryosparc-v4.1 and v4.4⁴⁵ unless stated otherwise. The initial drift and beam-induced motions were corrected for using *Patch Motion Correction* while CTF estimation was performed using *Patch CTF Estimation*, both with default settings. For particle picking we used a TRPC5 map previously obtained in-house, down-filtered to 20 Å to generate 50 templates using *Create templates* tool in Cryosparc. The obtained templates were used for template picking, resulting - after filtering the picks based on the NCC score (>0.26) - in 565k particles for the **(E)-AzHC** sample, and 702k particles for the **(Z)-AzHC** sample. After several rounds of 2D classification, particle stacks of 134k and 105k for **(E)-AzHC** and **(Z)-AzHC**, respectively, were produced. Further, *Ab-initio* was used to generate five initial models, from which at least one had the expected shape. The five models were used to sort particles further using *Heterogeneous refinement*, resulting in particle stacks of 87k for **(E)-AzHC** and 60k **(Z)-AzHC**. A further round of heterogeneous refinement with the fully extracted particle set, using as input the best model and three bad models to pull out bad particles was then performed. Using this approach, we observed that our final stack of good particles increased by roughly 20% while also improving particle orientation by either increasing the number of exotic orientation or by increasing the particle number in low-populated 2D classes. After the last heterogeneous refinement, we ended up with 161k particles for **(E)-AzHC** and 125k particles for **(Z)-AzHC**. A final round of 2D classification was used to remove bad particles or classes that did not show high resolution features. The final particle stack comprised 89k and 69k particles for **(E)-AzHC** and **(Z)-AzHC**, respectively. These particle stacks were taken forward and refined using non-uniform refinement with 5 extra passes, and having defocus refinement, CTF refinement (all option true) and EWS correction active. In both cases the structures were refined without imposing symmetry to a global resolution of 2.60 Å for **TRPC5:(E)-AzHC** and 2.90 Å for **TRPC5:(Z)-AzHC**, as estimated based on the gold standard FSC = 0.143 criterion. We used ResolveCryoEM⁴⁶ features of Phenix⁴⁷ to improve the interpretability of the map.

4.1.5 Model building

The models of **TRPC5:(E)-AzHC** and **TRPC5:(Z)-AzHC** were built using ModelAngelo⁴⁸. The models obtained were inspected and manually completed in Coot⁴⁹. Several rounds of real-space refinement were performed in Phenix before fitting the corresponding ligand. For ligand fitting, we used LigandFit⁵⁰ in Phenix with small molecule constraints generated by eLBOW⁵¹ function within Phenix, using AM1 geometry optimisation starting from a SMILE string. After automated fitting of the ligand, we manually checked the structures in Coot and performed addition real-space refinement in Phenix. Protein-ligand interactions were visualised with PoseEdit⁵² (<https://proteins.plus>) and ChimeraX^{53,54}. All structural images were produced using ChimeraX, Coot or one of the softwares used for protein-ligand visualisation.

4.1.6 Additional TRPC5:AzHC Data and Figures

Supporting Note 4 contains the figures and discussion that are key to the paper; this section contains figures and data on workflows (**Figures S15-S16**), statistics (**Table S4**), and data quality (**Figures S17-18**).

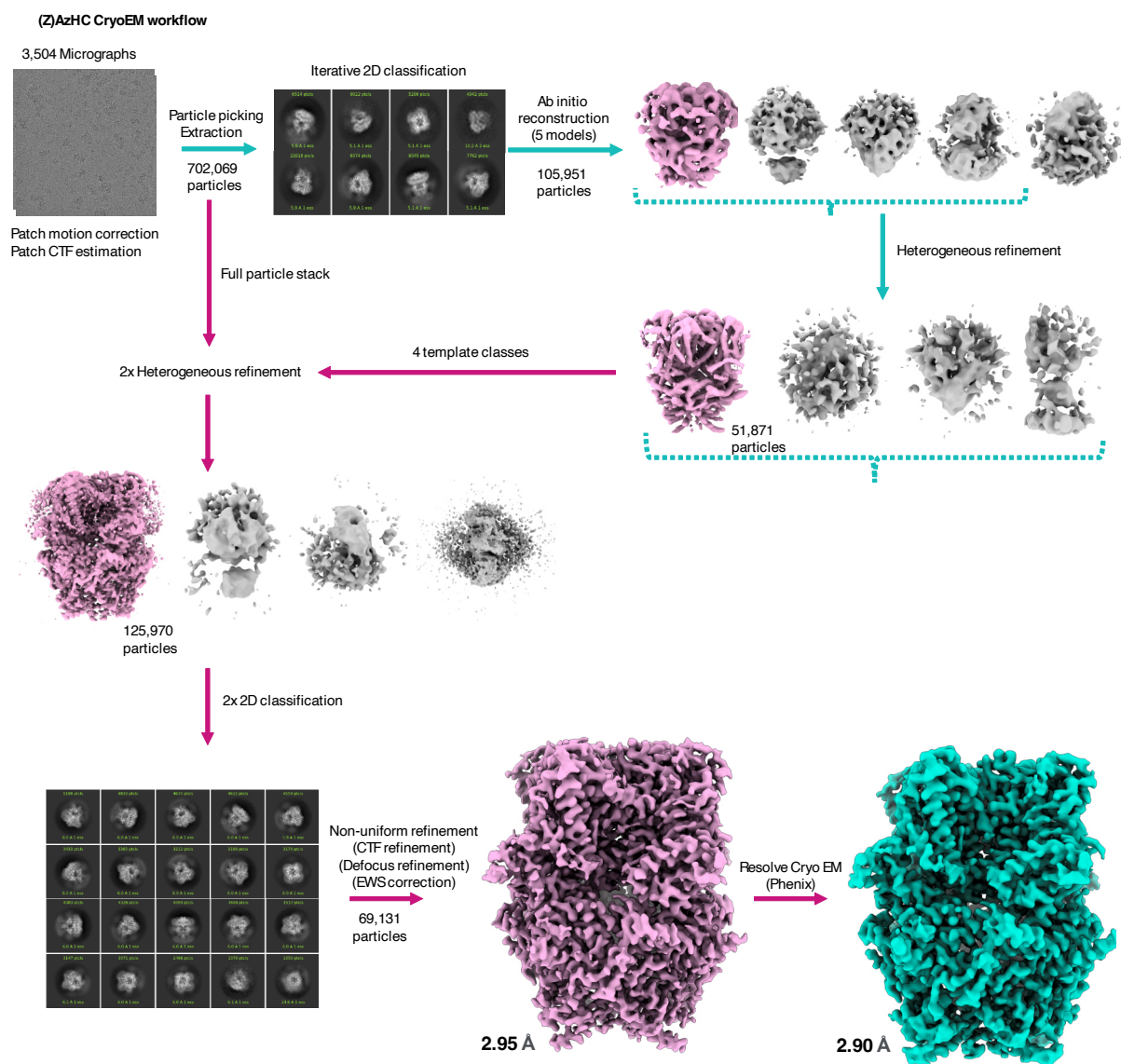


Figure S15. CryoEM workflow for TRPC5 in complex with (Z)-AzHC.

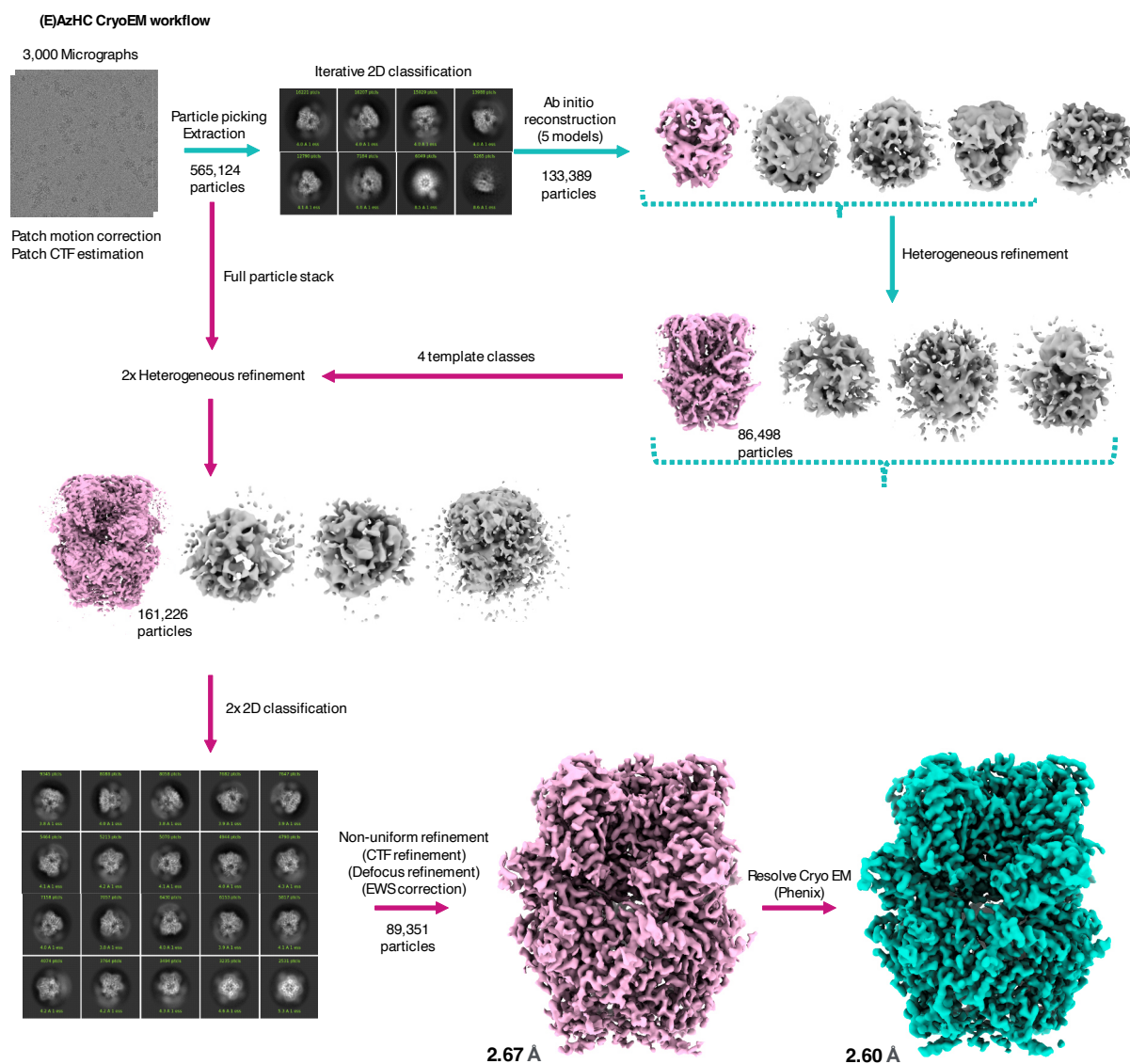


Figure S16. CryoEM workflow for TRPC5 in complex with (E)-AzHC.

Table S4. Cryo-EM data collection, refinement, and validation statistics.

	(E)-AzHC	(Z)-AzHC
Data collection and processing		
Magnification	165k	165k
Voltage (kV)	300	300
Electron exposure ($e^-/\text{Å}^2$)	35.72	35.72
Defocus range (μm)	-0.7 to -3.00	-0.7 to -3.00
Pixel size (Å)	0.74	
Symmetry imposed	C1	
Final particle images (no.)	89,351	69,131
Map resolution range (Å)	2.6	2.9
FSC threshold	0.143	0.143
Refinement		
Initial model	ModelAngelo	ModelAngelo
Map sharpening B factor (Å^2)	66.4	72.1
Model composition		
Non-hydrogen atoms	22307	22211
Protein residues	2705	2705
Ligands	4	4

<i>Bonds (RMSD)</i>		
Length (Å) (# > 4σ)	0.003 (0)	0.003 (0)
Angles (°) (# > 4σ)	0.368 (0)	0.595 (8)
Validation		
MolProbity score	2.35	1.33
EMRinger score*	3.25	2.66
Clash score	18.52	6.10
<i>Ramachandran plot (%)</i>		
Outliers	0.00	0.00
Allowed	2.14	1.54
Favored	97.86	98.46
<i>Ramachandran Z-score</i>		
whole	1.60 (0.16)	1.06 (0.16)
helix	1.58 (0.12)	1.04 (0.12)
sheet	--- (---)	--- (---)
loop	-0.06 (0.21)	0.17 (0.22)
Rotamer outliers (%)	5.33	0.62
Cβ outliers (%)	NA	NA
<i>Peptide plane (%)</i>		
Cis proline/general	0.0/0.0	0.0/0.0
Twisted proline/general	0.0/0.0	0.0/0.0
CaBLAM outliers (%)	0.11	0.19
<i>ADP (B-factors)</i>		
Iso/Aniso (#)	22211/0	22211/0
B factors (Å ²)	(min/max/mean)	(min/max/mean)
Protein	6.68/176.88/76.94	34.19/220.63/112.90
Ligand	13.55/105.99/46.90	44.59/149.06/86.47
<i>Occupancy</i>		
Mean	1.00	1.00
occ = 1 (%)	100.00	100.00
0 < occ < 1 (%)	0.00	0.00
occ > 1 (%)	0.00	0.00
Resolve CryoEM		
<i>Box</i>		
Lengths (Å)	119.88, 120.62, 141.34	111.74, 111.00, 137.64
Angles (°)	90.00, 90.00, 90.00	90.00, 90.00, 90.00
Supplied Resolution (Å)	2.6	2.9
Resolution Estimates (Å)	Masked/Unmasked	Masked/Unmasked
d FSC (half maps; 0.143)	---/---	---/---
d 99 (full/half1/half2)	(2.8/---/---) / (2.8/---/---)	(3.3/---/---) / (3.3/---/---)
d model	2.8/2.8	3.2/3.2
d FSC model (0/0.143/0.5)	(2.3/2.4/2.6) / (2.4/2.4/2.6)	(2.3/2.3/2.9) / (2.3/2.3/2.9)
Map min/max/mean	-8.10/12.26/0.00	-5.71/10.04/0.00
Model vs. Data		
CC (mask)	0.89	0.88
CC (box)	0.64	0.64
CC (peaks)	0.68	0.65
CC (volume)	0.87	0.87
Mean CC for ligands	0.88	0.83

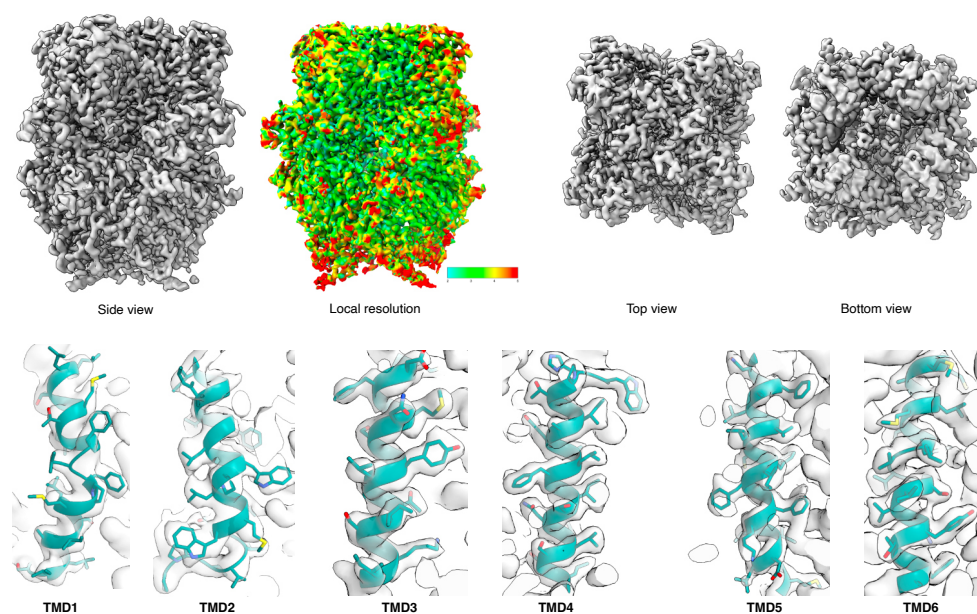


Figure S17. CryoEM data quality 1. Top: CryoEM map for TRPC5 in complex with (E)-AzHC (different views and local resolution shown). Bottom: Fit of the 6 trans-membrane domains of TRPC5 (teal) in the cryoEM map (grey mesh).

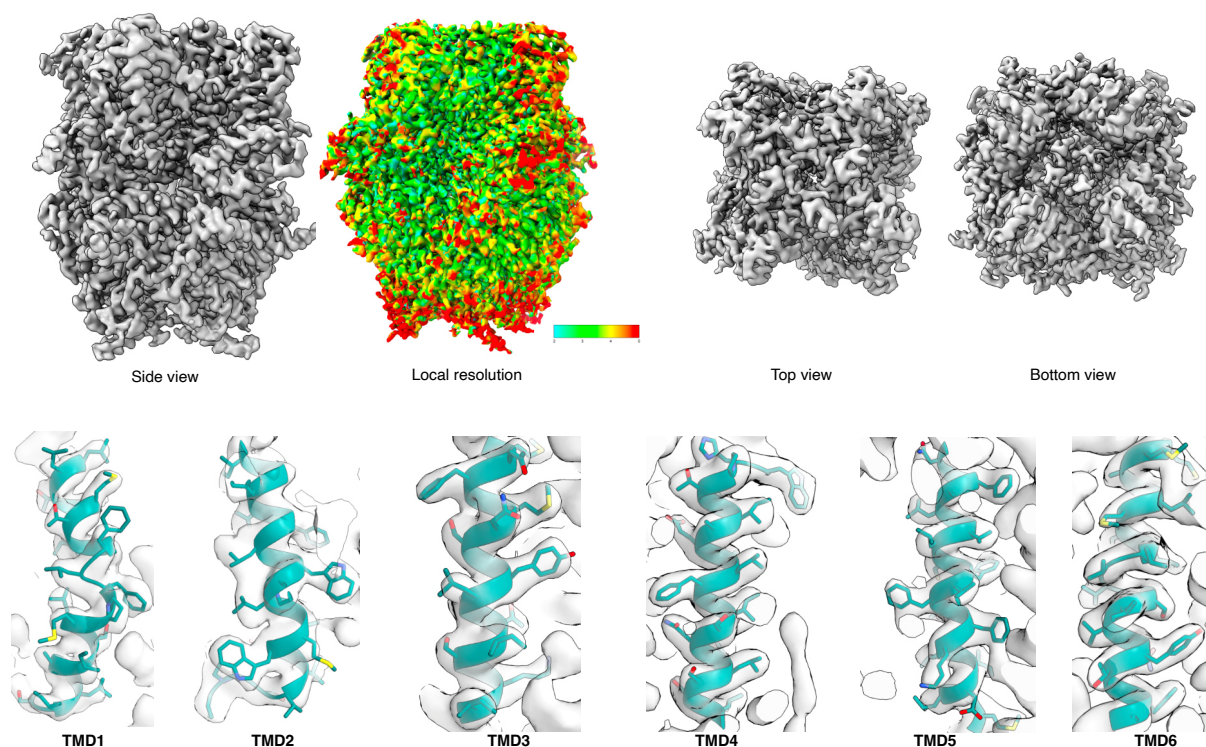


Figure S18. CryoEM data quality 2. Top: CryoEM map for TRPC5 in complex with (Z)-AzHC (different views and local resolution shown). Bottom: Fit of the 6 trans-membrane domains of TRPC5 (teal) in the cryoEM map (grey mesh).

4.2 Structural biology of TRPC4:AzPico

4.2.1 Cryo-EM grid preparation and screening

TRPC4_{DR} from zebrafish was expressed and purified for cryo-EM as described previously.³³ For cryo-EM **AzPico** dissolved in DMSO was added to TRPC4 (final concentration of 100 µM, and 1% DMSO). The detergent was then exchanged with amphipols and incubated overnight before plunging using a Vitrobot cryo-plunger (FEI Thermo Fisher).

For the dark state (**E-AzPico**), sample preparation was performed under red light illumination and residual light was minimized to prevent isomerization. In case of the bright state (**Z-AzPico**), the molecule was activated for ~ 1 min using LEDs with a wavelength of 365 nm.

2.5 µl of TRPC4_{DR} at a concentration of 0.45 mg ml⁻¹ were applied onto freshly glow-discharged holey carbon grids (C-Flat (1.2/1.3) 400 mesh) blotted using 3.0 s blotting time, 0 blotting force with 100% humidity at 4°C and vitrified in liquid ethane cooled by liquid nitrogen.

4.2.2 Cryo-EM data acquisition and image processing

Data sets were collected using EPU software on Titan Krios microscopes (FEI Thermo Fisher) operated at 300 kV and equipped with an X-FEG. All the datasets were collected using the aberration-free image shift (AFIS) feature of EPU to speed up the data-collection process. Equally dosed frames were collected on K3 (Gatan) direct electron detectors in super-resolution mode in combination with a GIF quantum-energy filter set to a filter width of 20 eV. The dataset was collected with a pixel size of 0.455 in super resolution mode. Typically, 60 frames were collected with a total dose of ~60 e⁻Å⁻². Data collection was monitored live using TranSPHIRE,⁵⁵ allowing for direct adjustments of data acquisition settings when necessary, i.e. defocus range or astigmatism. Preprocessing included drift correction with MotionCor2,⁵⁶ creating aligned full-dose and dose-weighted micrographs. The super-resolution images were binned twice after motion correction. CTF estimation was also performed within TranSPHIRE using CTFFIND 4.1.13⁵⁷ on non-dose-weighted aligned micrographs. Unaligned frame averages were manually inspected and removed based on ice and image quality, resulting in a removal of 5–20% of the data sets. Following processing steps were performed using motion-corrected dose-weighted sums in the SPHIRE software package unless otherwise indicated.⁵⁸

Single particles were picked automatically with crYOLO using the general model.⁵⁹ The particles were then windowed to a final box size of 300 × 300 pixels. Reference-free 2-D classification and cleaning of the data set was performed with the iterative stable alignment and clustering approach ISAC⁶⁰ in SPHIRE. A subset of particles producing 2-D class averages and reconstructions with high-resolution features were then selected for further structure refinement in Relion 3.0.⁶¹ 3D classification was performed with C1 symmetry to classify the subpopulation. The classes having high-resolution features bound with ligands were selected and further polished and CTF-refined. Finally, the polished particles were exported to CryoSPARC⁴⁵ to improve the resolution with non-uniform refinement.

The previously reported model of TRPC4³³ was initially docked into the density and fitted into the map as rigid body using UCSF Chimera.⁵³ The model was further adjusted to fit in the density using Coot⁶² with an iterative process of real space refinement in Phenix⁶³ and model adjustment in Coot until convergence as evaluated by model-to-map fit with valid geometrical parameters. For the ligand molecules, cif files were generated using eLBOW tool in Phenix and used as geometrical restraints in Coot and Phenix during modelling and refinement respectively.

4.2.3 Additional TRPC4:AzPico Data and Figures

Supporting Note 4 contains the figures and discussion that are key to the paper; this section contains figures and data on workflows (**Figure S19**), refinement and statistics (**Tables S5-S7**).

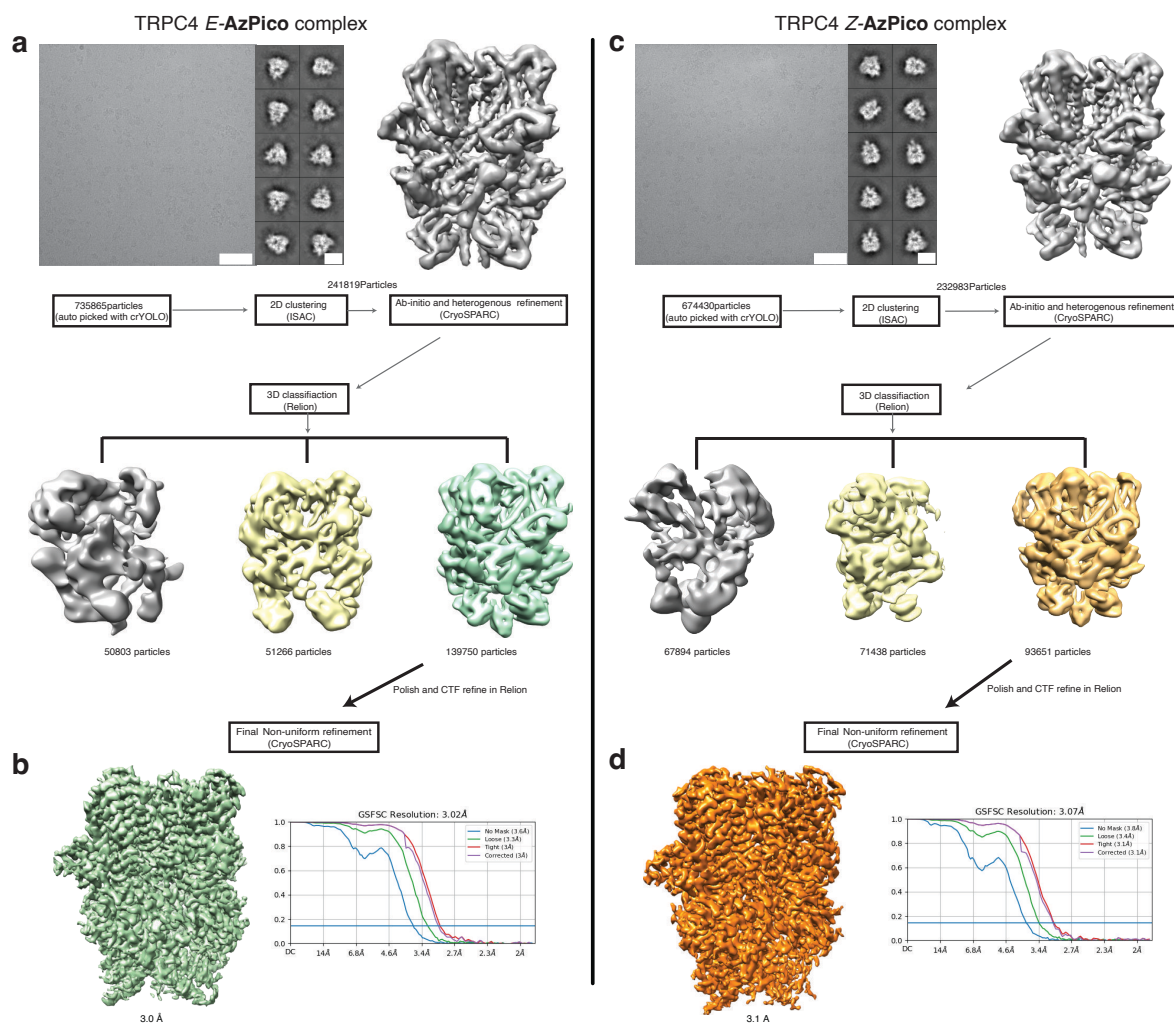


Figure S19. Cryo-EM data processing of TRPC4 in complex with AzPico (*E* and *Z* isomers). (a) Representative digital micrograph (scale bar, 50 nm) and selected 2D class averages (scale bar, 10 nm) of TRPC4 in complex with *E*-AzPico. The initial density obtained after *ab initio* and heterogeneous refinement is shown next to the 2D class averages. (b) Density obtained after 3D classification and a final round of non-uniform refinement. The Fourier shell correlation curves (FSC) corresponding to two independently refined particle subsets are shown. The horizontal light blue line indicates the FSC=0.143 criterion used for resolution estimation. (c,d) Same as in a,b, respectively, for the TRPC4 in complex with *Z*-AzPico. Scale bars: 50 nm and 10 nm, respectively.

Table S5. Data Collection details

Sample	TRPC4- <i>E</i> -AzPico	TRPC4- <i>Z</i> -AzPico
Voltage [kV]	300	300
Defocus range [μ m]	0.48- 4.04	0.49- 3.07
Camera	K3 Super resolution	K3 Super resolution
Pixel size [\AA]	0.455 /0.91 ^a	0.455 /0.91 ^a
Exposure time [s]	3.0	3.5
Total electron dose [$e^-/\text{\AA}^2$]	52.47	56.34
Frames per movie	60	60
Number of images	2,598	3,311

Table S6. Refinement and model validation statistics

Sample	TRPC4- <i>E-AzPico</i>	TRPC4- <i>Z-AzPico</i>
Number of particles used in refinement	139750	93651
Final resolution [Å]	3.0	3.1
Map sharpening factor [Å ²]	111.7	101.9
Electron dose particles final refinement [e ⁻ /Å ²]	Polished particles	Polished particles

Table S7. Model geometry and Refinement statistics

	Atomic model composition	
Non-hydrogen atoms		
	Refinement (Phenix)	
RMSD bond	0.002	0.002
RMSD angle	0.506	0.589
Model to map fit, CC mask	0.79	0.76
Ramachandran plot (%)	Validation	
outliers	0.12	0.12
allowed	4.14	4.62
favoured	95.74	95.26
Rotamer outliers (%)	2.95	4.25
Molprobrity score	1.93	1.99
EMRinger score	1.86	2.46

5 Cultured neurons and chromaffin cells (Figure 4)

5.1.1 Animals

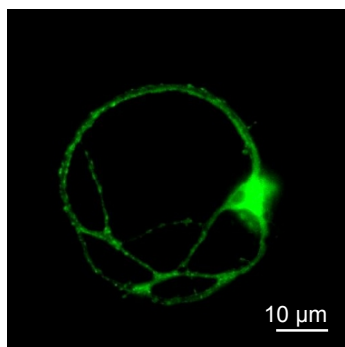
All mice were kept according European Animal Welfare regulations and ethical guidelines from the local governing body (approval number of the Institutional Animal Care and Use Committee: **Az. 2.4.1.3/Bruns**). TRPC1/C4/C5 triple knockout (**145tko**), TRPC5 single knockout (**5ko**), and TRPC5 IC eR26 τ GFP mice (i.e. TRPC5 knock-in, **5ki**) were generated as described previously;^{64–66} C57BL/6N mice from Charles River, housed under the same conditions, were used as the wildtype (**wt**) controls.

5.1.2 Primary Cell culture

Primary hippocampal autaptic neurons (i.e. neurons cultured under conditions where single neurons grow in isolation and make synapses only back onto themselves) were prepared as described⁶⁵. Briefly, neurons were prepared from age matched **145tko**,⁶⁴ **5ko**, **wt** and **5ki**⁶⁵ P0-P1 mice (all C57Bl/6N strain) and cultured on pre-seeded astrocytic microislands. Neurons were grown for 10-17 days in NBA medium containing 2% B-27, 1% Glutamax and 1% penicillin/streptomycin at 5% CO₂ and 37°C. Only max. ca. 50% of **wt** cells express Trpc5,⁶⁵ while their results set expectations for the ability of **AzPico** to *directly* photostimulate wt hippocampal neurons, the **5ki** cells can be considered an appropriate control for the **5ko** and **145tko** cells in terms of determining the relevance of Trpc5 to the direct photocontrol of endogenous neuronal activity. Fluorescence imaging was used to confirm the knock-in efficiency in **5ki** cells before recording (**Figure S20**).

Adrenal chromaffin cells were prepared as described previously.⁶⁷ Briefly, chromaffin glands from adult wt and TRPC tko mice (10-12 weeks old) were digested in an enzyme solution containing 20-25 U/ml papain (Worthington). After inactivation, cells were washed with pre-warmed DMEM growth medium, supplemented with 0.4% PenStrep, and 1% ITSX (Thermo Fisher Scientific). After trituration, cells were plated onto coverslips and incubated for two days at 37 °C / 11 % CO₂. Electrophysiological recordings were carried out at DIC2.

Patch clamp electrophysiology



Dunn's multiple comparisons test	Significant?	Adjusted P Value
TRPC5 τ GFP vs. wt	No	>0.9999
TRPC5 τ GFP vs. TRPC tko	Yes	0.0024
TRPC5 τ GFP vs. TRPC5 ko	No	0.1092
wt vs. TRPC tko	Yes	0.0437
wt vs. TRPC5 ko	No	0.709
TRPC tko vs. TRPC5 ko	No	>0.9999

Figure S20 (related to **Figure 4**). **left**: fluorescence image of autaptic **5ki** neuron (GFP imaging), used to confirm the presence of TRPC5. **right**: expanded statistics for the data shown in **Figure 4ab** (one-way ANOVA post-hoc Kruskal Wallis and Dunn's multiple comparison test). Note that values listed in **Figure 4d** were mean \pm SEM with Student's two-tailed t-test used instead for statistics.

For photoswitching **AzPico** (30 nM), cells were transiently illuminated on the stage of an inverted microscope (Axiovert 200, Zeiss, Germany) with light from a Polychrome 4 monochromator (Till Photonics, Germany) at the indicated wavelengths, with default slit width 10 nm.

Ephys of autaptic hippocampal neurons: Recording pipettes had a resistance of 4-5 M Ω . Inward currents were measured in the voltage-clamp mode at -70 mV in extracellular solution containing (in mM): 120 NaCl, 2.6 KCl, 1-2 CaCl₂, 2 MgCl₂, 20 HEPES, 30 glucose, pH 7.3, 290-300 mOsm. The intracellular patch pipette solution contained (in mM): 140 K-gluconate, 11 NaCl, 2 Mg-ATP, 0.2 Na₂-GTP, 1.1 EGTA, 11 HEPES, 11 glucose, 280 mOsm (pH 7.3 with NaOH). Recordings were

performed with an EPC10 amplifier (HEKA Electronic, Germany) controlled by Pulse 8.5 program (HEKA Electronic, Germany). Only cells with an access resistance of 5-15 M Ω , 60-80 % resistance compensation and a leak current of <300 pA were analysed. Ephys measurements were recorded at the digitalization rate of 20 kHz and analysed using customized routine in IgorPro (Wavemetrics, USA). Data were analysed using Igor Pro 5.0. The maximal current amplitudes were determined at the phase's plateau devoid of any spontaneous activity (thus the "460 nm" values would typically reflect a value from between 3-5 seconds into the followup 460 nm phase, while the "UV" values would typically reflect a value from the five seconds before switching back to 460 nm). Each cell's photoswitch-based current differential $\Delta I_{C\lambda}$ [pA] was determined as the absolute value of its 365 nm plateau current minus its followup 460 nm plateau current. **Figure 4ab** lists mean \pm SEM values; one-way ANOVA post-hoc Kruskal Wallis used for statistics (**Figure S20**).

Ephys of cultured chromaffin cells: Current recordings were performed at room temperature in voltage clamp mode using the whole cell patch clamp technique (holding potential – 70 mV). The extracellular Ringer's solution used for all electrophysiological recordings contained (in mM): 130 NaCl, 4 KCl, 2 CaCl₂, 1 MgCl₂, 30 glucose, 10 HEPES-NaOH (pH 7.3, 310 mOsm). Thick-walled borosilicate pipettes (pipette resistance 4-5 M Ω) were filled with intracellular solution containing (in mM): 75 K-glutamate, 10 HEPES, 10 NaCl, 121 glucose, 0.1 EGTA (300 mOsm, pH = 7.3 with KOH). 360 nm light was used for activation, flanked by illuminations at 470 nm which silenced the channel activity. Cell membrane capacitance (CM) was determined before and after UV activation (360 nm). Current signals were filtered at 2.9 kHz and digitized gap-free at 20 kHz prior to analysis. Data were acquired with the Pulse software (HEKA, Lambrecht, Germany) and capacitance measurements were performed by the Lindau–Neher technique (sine wave stimulus: 1000 Hz, 35 mV peak-to-peak amplitude, DC-holding potential -70 mV). To avoid misinterpretation, current values in sine wave stimulus phases used for CM determination are not displayed in **Figure 4c**.

6 Mouse experiments – brain tissue slices (Figure 5)

Mice. Adult female mice (7 - 20 weeks old) were kept under standard light/dark cycle (12:12; lights on 0600; lights off 1800) with food (Ssniff feed containing 9% fat, 24% protein, and 67% carbohydrate) and water ad libitum. Mice were maintained in IVC housing containing enrichment (nesting, bedding and other material). We used the following mouse strains: B6.Cg-7630403G23RikTg(Th-cre)1Tmd/J (RRID:IMSR_JAX:008601, referred to as Th-Cre mice)⁶⁸, B6;129S-Gt(ROSA)26Sortm95.1(CAG-GCaMP6f)Hze/J (RRID:IMSR_JAX:024105, referred to as R26-GCaMP6f or Ai95D mice)⁶⁹, B6.Cg-Gt(ROSA)26Sortm14(CAG-tdTomato)Hze/J (JR # 007914, referred to as R26-tdTomato mice)⁷⁰ and Trpc5tm1.1Lbi (RRID:IMSR_JAX:024535; MMRRC Stock No: 37349-JAX, referred to as Trpc5-E5-/- mice.^{36,71} We crossed Th-Cre mice with either R26-tdTomato or R26-GCaMP6f reporter mice resulting in a strain in which all Th+ cells are identifiable either through their red fluorescence (referred to as Th-tdTomato) or through their green fluorescence (referred to as Th-GCaMP6f mice). Th-tdTomato mice were heterozygous for Cre and tdTomato. The Th-GCaMP6f mice were also crossed with Trpc5-E5-/- mice, resulting in a strain in which all Th+ cells, identifiable through their green fluorescence, are deficient for Trpc5-E5 (referred to as Th-GCaMP6f- Δ Trpc5). Th-GCaMP6f and Th-GCaMP6f- Δ Trpc5 mice were heterozygous for Cre and GCaMP6f.

Animal care and experimental procedures were performed in accordance with the guidelines established by the German Animal Welfare Act, European Communities Council Directive 2010/63/EU, the institutional ethical and animal welfare guidelines of the Saarland University (approval number of the Institutional Animal Care and Use Committee: **CIPMM-2.2.4.1.1, 2.4.1.1.-Leinders-Zufall**). The number of animals used is a minimum necessary to provide adequate data to test the hypotheses of this project. We minimized the number of animals required by the animal welfare committees wherever possible.

Solutions and Chemicals for hypothalamic brain slices. Oxygenated extracellular bath solution (95% O₂/5% CO₂) was prepared in ultrapure water (>18.2 MΩ-cm resistivity at 25 °C, low ppt in divalent cations) and contained (in mM): 120 NaCl (Guëssing, Germany), 25 NaHCO₃ (Merck, Darmstadt, Germany), 5 KCl (Guëssing, Germany), 5 *N,N*-bis(2-hydroxyethyl)-2-aminoethanesulfonic acid (BES), 1 MgSO₄, 1 CaCl₂ (Guëssing), 10 glucose (Merck); osmolarity: ~300 mOsm/kg and pH: 7.3. The **AzPico** and **AzHC** stock solutions (10 mM or 1 mM) were prepared in anhydrous DMSO. To dissolve **AzPico** and **AzHC** the solution was heated to 60 °C followed by a short period of sonication. The stock solutions of **AzPico** and **AzHC** were further diluted in the extracellular bath solution to make the final working solution. DMSO concentrations were ≤ 0.05 % (vol/vol) except for 1 μM **AzHC**. Here the DMSO concentration was ≤ 0.2 % (vol/vol). Unless stated otherwise, all chemicals were purchased from Sigma (Munich, Germany). Chemicals were of analytical or higher grade.

Preparation of Hypothalamic Brain Tissue Slices. All experiments were performed on coronal brain slices (Bregma -1.6 and -2.2 mm) freshly prepared from female mice adapting previously described methods.^{36,72} Mice were anesthetized with 20% isoflurane (vol/vol) in propylene glycol using the open-drop method followed by decapitation. Brains were removed quickly, submerged in ice-cold extracellular bath solution, and sliced (275 μm thick) using a vibrating-blade microtome (Leica, Germany). Slices were kept at 31.5 °C for 15 min and then brought back at RT for 30 min before starting an experiment. We minimized the amount of mice wherever possible as requested by the animal welfare committee, but used at least 3 mice per genotype in independent experiments.

Ca²⁺ Imaging and Combined Laser Scanning-controlled Photoswitching. We used an upright scanning confocal microscope (Zeiss LSM 880 Indimo) equipped with a standard Argon laser for GCaMP6f excitation at a wavelength of 488 nm and a UV laser (Coherent) emitting 355 nm for photoswitching **AzHC** and **AzPico**.^{73–75} Emitted fluorescence was collected between 500 and 560 nm. All scanning head settings, e.g., frame size (512 x 256), pinhole size (16.1 μm section), pixel size (1.04 μm), and pixel dwell (2.05 μs), were kept constant during each experiment. Images were acquired at 1.7 Hz and analysed using a combination of Zen (Zeiss), ImageJ (NIH), Igor (Wavemetrics) and OriginLab (OriginLab Corporation) software.

For laser scanning-controlled photoswitching of **AzHC** or **AzPico**, the UV laser light (355 nm) coupled to the confocal microscope was focused onto the image plane through a 20 x 1.0 NA Plan-Apochromat water immersion objective (Zeiss). The depth of focus was 16 μm which ensured, together with the region of interest (ROI) diameter, illumination of individual cells. Before photoswitching, UV laser light was optimally focused using 18 μm thick brain tissue sections loaded with Hoechst 33342 (1:10000; ThermoFisher) and the semi-automated correction tool of the Zen software (Zeiss). **AzHC** or **AzPico** was added to the bath chamber containing the brain slice and subsequently incubated for about 10 min in the dark. GCaMP6f fluorescence was then measured in the presence of the photoswitchable compound using the 488 nm Argon laser (2% 25 mW). Photoswitching was achieved by directing UV laser light (10 mW) on preselected ROIs using the Zen software (Zeiss), followed by exposure to the Argon laser light to resume monitoring of GCaMP6f fluorescence and switching the **AzHC** or **AzPico** back into the inactive state. The UV exposure time of the Th⁺ neurons in tissue slices ranged between 23 - 133 ms for **AzHC** and 7 - 156 ms for **AzPico**, which could be contingent on the depth of the neurons within the brain slice. The overall mean exposure time was either 68 ms with 500 nM **AzHC** or 58 ms with 500 nM **AzPico**. To protect the ultrasensitive GaAsP photomultiplier tubes from the 355 nm light, high-speed shutters closed and opened at the beginning and end of the UV exposure. Hence, GCaMP6f fluorescence could not be collected during this time. Similar photoswitching experiments were performed in absence of photoswitchable compounds to ensure that UV laser light (10 mW) and 488 nm light (2 % 25 mW) do not directly alter cell health or produce artefacts^{37,76}.

Data were analyzed using a combination of Zen (Zeiss), Igor (Wavemetrics) and OriginLab (OriginLab Corporation) software. The change in GCaMP6f fluorescence was expressed as relative fluorescence changes, i.e. $\Delta F/F_0$ (F_0 was the average of the fluorescence values of 30 frames before stimulation). Fluorescence (F) data were normalized with the $Peak_{max}$ obtained during control measurements and plotted as the function of time (t). The Ca^{2+} dynamics were quantified by calculating the area under the curve (AUC). A control AUC was taken at the beginning of each recording for 3 min (AUC_{488}). The AUCs after photoswitching of **AzPico** and **AzHC** were calculated from the last 3 min of the recording (AUC_{355}). The total duration of the recordings was 9 min. AUC data were plotted either as box or as violin plots to show the distribution and density probability of the data. The violin plots were created using Igor Pro (Wavemetrics) with a bandwidth following Scott's rules and a Gaussian kernel. The response index (RI) of **AzPico** and **AzHC** were deduced by normalizing the estimated change in AUC after photoswitching with the mean of control AUCs, and is a measure used to calculate whether a compound is stimulatory (RI >1), ineffective (RI = 0), or inhibitory (RI <0). The mean and total burst duration along with the mean frequency of Ca^{2+} waves were calculated at the level of 20% of the signal amplitude of the normalized Ca^{2+} waveform measured for 3 minutes under control conditions, and later compared with Ca^{2+} signals measured in the last 3 minutes of recordings after the UV illumination. The mean amplitude was calculated by taking account of all the F_{max} of Ca^{2+} waveforms measured within 3 minutes under control conditions and after UV illumination. The change in the area under the curve (ΔAUC) is the AUC_{355} minus AUC_{488} . Through the Igor Pro software package, user-defined functions in combination with an iterative Levenberg-Marquardt nonlinear, least-squares fitting routine were applied to the data. Dose-response curves were fitted by the equation:

$$f(x) = E_{min} + (E_{max} - E_{min}) / \{1 + [EC50/x]^n\}$$

where x is the drug concentration, E_{min} the baseline response, E_{max} the maximal response at saturating concentrations, and EC50 the drug concentration that produces 50% of the maximal response, with slope n being the Hill coefficient of the sigmoid curve.

Quantification and Statistical Analysis. Statistical analyses were performed using Origin Pro 2017G (OriginLab Corporation, Northampton, MA, USA). Assumptions of normality and homogeneity of variance were tested before conducting the following statistical approaches. A paired two-tailed Student's t-test was used to measure the significance of the differences between two distributions of the same Th+ neuron. Multiple groups were compared using the Kruskal-Wallis ANOVA in combination with the Dunn's test. The probability of error level (alpha) was chosen to be 0.05. Box plots display the interquartile ranges, median (line) and mean (black rhombus) values with whiskers indicating SD values. Additional data and representations relevant to **Figure 5** are given in **Figure S21** and detailed in its caption:

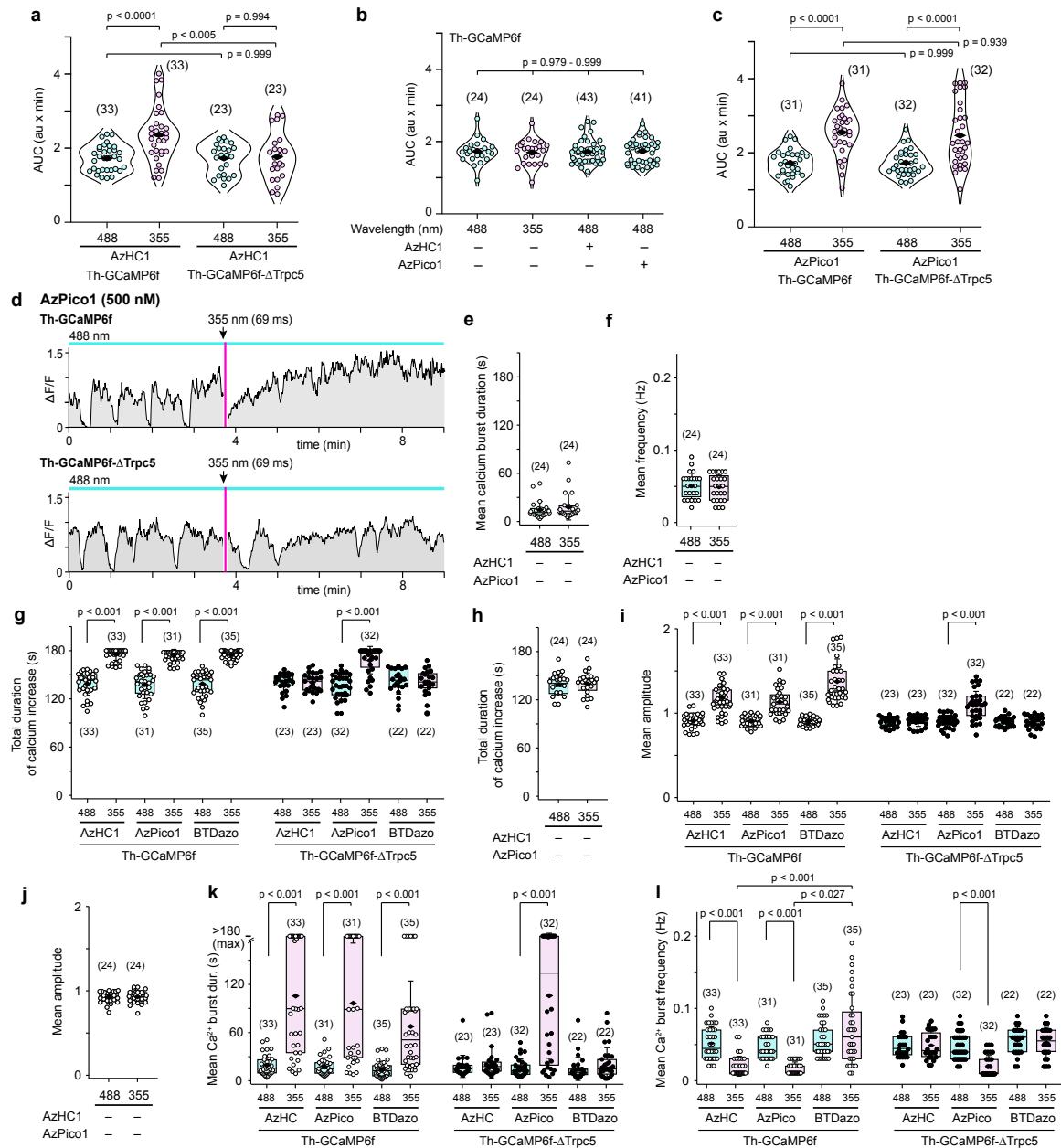


Figure S21 (related to **Figure 5**; note: for expanded legend to **Figure 5**, see **Figure S27**). (a) Area under the curve (AUC) from Ca²⁺ signals before (488 nm) and after 355 nm UV illumination of Th⁺ neurons treated with AzHC (500 nM) in arcuate hypothalamic brain slices of Th-GCaMP6f and Th-GCaMP6f-ΔTrpc5 mice. (b) AUC from Ca²⁺ signals before (488 nm) and after 355 nm UV illumination of Th⁺ neurons in absence of AzHC and AzPico as well as at 488 nm illumination in presence of either AzHC (500 nM) or AzPico (500 nM). (c) AUC from Ca²⁺ signals before (488 nm) and after 355 nm UV illumination of Th⁺ neurons treated with AzPico (500 nM) in arcuate hypothalamic brain slices of Th-GCaMP6f and Th-GCaMP6f-ΔTrpc5 mice. (d) Original traces of spontaneous Ca²⁺ responses in Th⁺ neurons of a Th-GCaMP6f and a Th-GCaMP6f-ΔTrpc5 mouse treated with AzPico (500 nM) stimulated by E→Z isomerization of AzPico using a 355 nm UV laser pulse for 69 ms. (e, f) The mean Ca²⁺ burst duration (e) and mean frequency (f) of Th⁺ neurons before (488 nm) and after 355 nm UV laser without photoswitchable modulators. (g-j) The total duration of Ca²⁺ increase (g,h) and the mean amplitude of the Ca²⁺ fluorescence signal (i,j) in Th⁺ neurons in Th-GCaMP6f and Th-GCaMP6f-ΔTrpc5 mice before (488 nm) and after 355 nm UV laser using (g,i) AzHC (500 nM), AzPico (500 nM) and BTDazo (10 μM) or (h,j) without photoswitchable modulators. (k,l) Replotting main **Figure 5** panels g,h with linear rather than logarithmic vertical scaling. **Additional detail related to both Figure 5 and Figure S21:** Th⁺ neurons treated with 500 nM E-AzHC are unaffected by 488 nm imaging (**Fig S19b**), but a ≥23 ms exposure (mean = 68 ± 29 ms, range: 22.3 - 133.2 ms) to 355 nm light (E→Z) induced a sustained (low frequency) high-Ca²⁺ signal lasting up to ≥3 min (14 of 33 cells; **Figure 5bd**). In wildtype slices, AzPico also induced long-lasting high Ca²⁺ signals after 355 nm pulsing (13 out of 31 cells), with overall Ca²⁺ signal properties that are not distinguishable from Z-AzHC (**Figure 5gh**). **Figure 5** and its supplementary data are deposited in Figshare (doi:10.6084/m9.figshare.26232254).

7 Spontaneous motility and isometric contractility (Figure 6)

After sacrificing mice in accordance to the European (Council Directive 2010/63/EU) and German guidelines for the welfare of experimental animals, the abdomen was opened, and intestinal loops were mobilised. Ileal segments were obtained starting 10 mm from the ileocecal junction. Ileal segments with a length of 3 mm for myography experiments or with a length of 8-12 mm for observation of spontaneous movement were cut out and flushed with carbogen-equilibrated KBRS. The adventitial layer was carefully peeled off, using a pair of forceps. The remaining intestinal segments, comprising mucosal, submucosal and muscular layers were placed in carbogen-saturated KBRS and immediately used for the experiments. Throughout these experiments, "wild-type" mice have the same genetic background as the knockout mice.

Spontaneous motility: for macroscopic observation, ileal segments were placed in KBRS-filled 24-well plates, and treated with 300 nM atropine (which has long been known to override the inherent oscillatory bias of the gut nerve system to paralyse digestion) or its solvent. The multiwell plate was mounted onto the FLIPR device used in cell culture studies (**Figures 1-2**) with a transmitted light source (dim white light from a fluorescent bulb) applied from the top through a diffusing sheet of white paper. A time-lapse movie was recorded, and 365 nm or 447 nm LED were electronically switched to induce photoswitching. The recorded image stack was cut into substacks, covering a single well, each. The temporal variance of the shadow cast by the segments was calculated for consecutive 1 s bins and taken as a measure to obtain the temporal signature of the motility. Gross movements of the observed ileal segments most likely indicate activity of the longitudinal muscular layer (**Figure 6bc**, **Figure S22b**, **Movie S1**).

Myographic isometric contractility: The contractile forces exerted by the circular layer of intestinal segments were quantitatively assessed by measurement in a 4-channel calibrated multi myograph device (DMT 620M, Danish Myo Technology, Hinnerup, Denmark), with digital data acquisition controlled by Labchart software (Version v8; ADINSTRUMENTS). Heated (37°C) bath chambers were filled with carbogen-equilibrated KBRS, and typically 3-mm ileal segments were manoeuvred over custom-made u-shaped hooks that prevented the mucosal layer from prolapsing on the edges. A pre-tension of typically 1.5-2 mN/mm was applied, and ileal segments were allowed to equilibrate to the conditions for at least 10 min in the presence of typically 1-30 nM **AzPico** or its solvent (0.5% DMSO). After renewing the pre-tension, the recording of isometric contractions was started, while applying alternating illuminations typically at 365 nm and 447 nm, or else at 385 nm and 470 nm, (typically 10 s exposure each) over typically 9-11 cycles, with no additional illumination afterwards. Data were sampled at 1 kHz, and displayed after normalisation to the length of the segments (N/m) (**Figure 6d-h**, **Figure S22c-g**).

7.1 Tissue Switching Reveals the Power of the Ideal Efficacy Switch Paradigm

7.1.1 First Saturate with Ligand, Then Dial the Wavelength

Even in the usually tricky situation that a targeted biological effect only occurs when a protein target is *partially but not fully stimulated* (here: physiology-like contractility as in **Figure 6e**, with the overlay of the normal oscillatory frequency), ideal efficacy switches are *still* perfectly capable of addressing them robustly. What is possible in the rare case that only fixed operating wavelengths may be available [e.g. in **Figure 6ef**, if only 365 nm and 447 nm would be available], would be to use a sub-saturating concentration of the switch (i.e. titrating it in, just like all affinity switch approaches): this could compensate for the fixed wavelength/s being "too complete" in their switching and thus overstimulating the target to drive unwanted activity. As an example, in **Figure S22c**, the 365 nm photogenerated Z-rich PSS is "too efficient" at target activation when (presumably saturating) 30 nM **AzPico** is used, resulting in a rictus-like freezing of the muscle with suppression of the desired oscillatory frequency. However, we highlight that titrating an ideal efficacy switch's concentration is no more logical than "driving a Ferrari in reverse, just to reduce

its maximum speed". The more reliable approach would be to install e.g. 385 nm or 395 nm LEDs, that drive higher *E/Z* ratios under UV light (c.f. **Figure 1c**), and thus be able to exploit the reproducibility of a saturating concentration of switch without over-stimulating the channel. Indeed, when multiplying the **AzPico** concentration by 10 (to 300 nM), simply altering the LED source to 385 nm allowed to avoid the over-stimulated rictus and instead capture the repeatable, physiological-like oscillatory overlay (**Figure S22f**) even under this saturating concentration.

7.1.2 Ideal Efficacy Switches That Also Have High Affinity

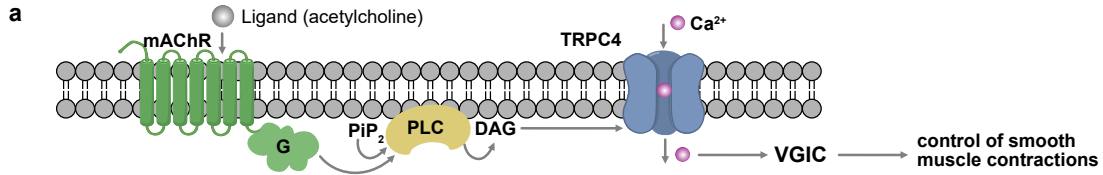
The "ideal" efficacy switch by our definition (includes: high affinity) may benefit from the intensely practical benefit that compound wash-in can be *complete, and long-lasting*, yet tissue-level photocontrol may still be *entirely reproducible even hours later*: as long as saturation is achieved. We demonstrated this by exploiting the high affinity and presumably also hydrophobicity of **AzPico**, first exposing tissues, then exchanging for fresh medium (no **AzPico** content) for 2 hours: and the tissues remained perfectly photoreversibly operable (**Figure S22g**). The exact performance we show there may be assisted by the facts that (a) likely, far more **AzPico** is sequestered in tissues than the concentration of TRPC4/[5] channels (e.g. hydrophobicity-driven partitioning into lipid environments in cells and tissues that act as reservoirs); but potentially also (b) not every TRPC4 channel must be activated in order to obtain the desired physiological-like readout, therefore some more loss over time may be tolerated than for targets where 100% saturation must be ensured. Nonetheless, we note that the persistence time is excellently long; and that even if the degree of activation under 385 nm had reduced, one could still imagine to *dial* in a slightly shorter wavelength with higher *Z*-content PSS, even down to 365 nm, in order to reach maximum possible activation.

7.2 Minor Remarks on Additional Experiments (Figure S22) and Prior Art

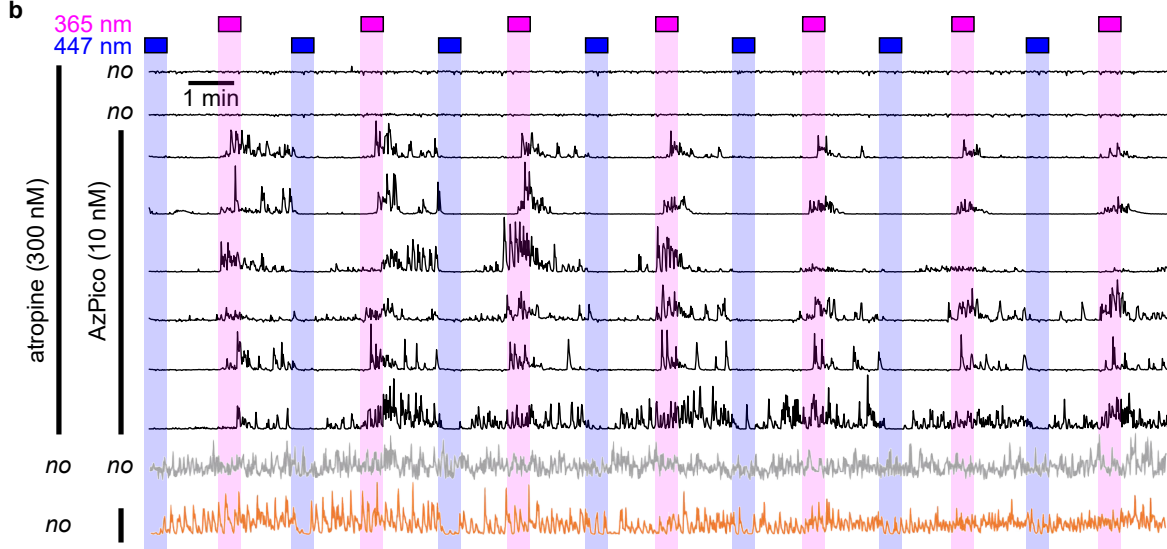
When returning to basal tension under blue light, we note that there is some temporary suppression of spontaneous oscillations under blue light and even when it is switched off; this is visible both in gross motility and in myography. Most prosaically, one could imagine a temporary desensitisation and ionic balance reset. If only the motility data were considered, one might suggest that the block lifts after the broadband fluorescent bulb spectrum used for imaging shifts the population *E:Z* equilibrium ratio slightly towards a lower *E* proportion that is less inhibitory to intestinal motions; or, e.g., that a dynamic and TRPC4-dependent effect such as in-pocket switching is in action: but, the same effect is evident *after* 447 nm switchoff in the myography (where bulb illumination is not applied) and it seems an unnecessarily complicated hypothesis. We also note that unless the binding affinities of the *E/Z* isomers are truly (almost) identical across all bound stoichiometries, such **AzPico**-derived effects ought also to depend on the dosage applied. Since they were instead robust and context-independent at photoequilibrium, we suggest that the affinities are equal. An obvious suggestion is to report the separately-experimentally-measured affinities, but, due to the special circumstances of the transmembrane tetramer and its lipophilic ligands, we were not able to design a satisfactory, direct practical protocol for this: so we rely on these indirect indications.

Related to the issues discussed in section 7.1 above, we note that under 365 nm, when lowering or raising the **AzPico** concentration vs the typically 3 nM+365 nm that works photoreversibly as desired, divergent effects on the tonic and oscillatory forces were seen (e.g. **Figure S22c** for 30 nM+365 nm). This confirms that just 3 nM **AzPico** in the bath solution did not saturate the channel in deep tissue. However, under 447 nm, even at 30 nM which drove the rictus-like state under 365 nm, the tonic tension always dropped to baseline and oscillatory contractions always recovered within 10-30 s (**Figure S22c**, cf **Figure S22d**). This extremely fast switch-off of muscle tension under 447 nm is as notable as the robust and repeatable activation of tension under UV.

• Intestinal contractions, molecular mechanism model through TRPC4



• Photoswitching intestinal *movements* with AzPico (readout: translight pixel intensity change)



• Photoswitching intestinal *contractility* with AzPico (readout: force measurement of ring muscle contraction)

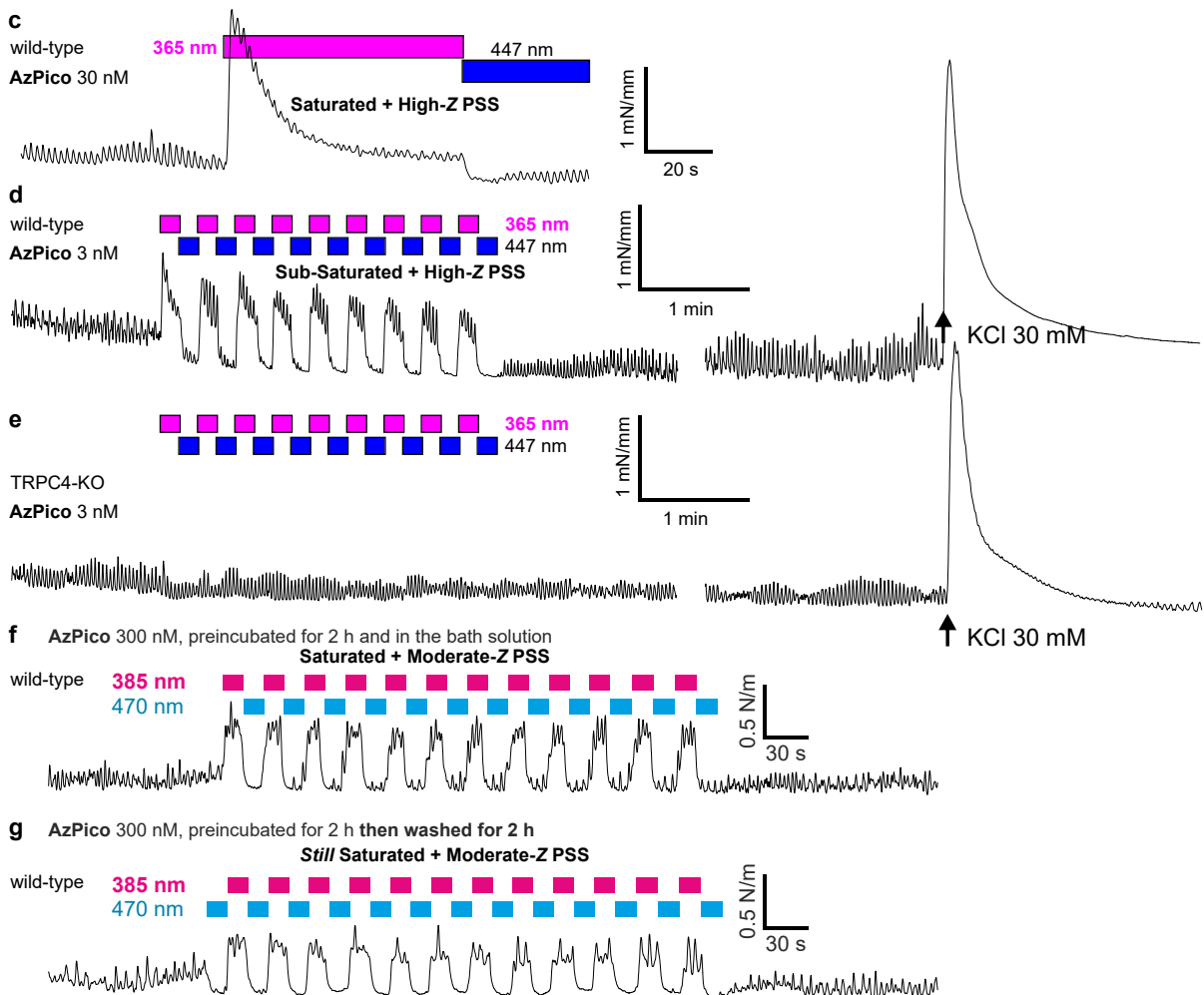


Figure S22 (related to **Figure 6**). **(a) Molecular mechanism** advanced for TRPC4-dependent intestinal contractility (overlaps in content with **Figure 6a**, reproduced for reference). Physiological intestinal contractions are

macroscopically coordinated, oscillatory motions. Intestinal segments have a "tonic" resting contractile force (baseline); they also propagate an inherent, slow oscillatory electrical pacemaker potential, that is amplified by classical signaling routes (e.g. via acetylcholine ACh > mAChR > phospholipase C > diacylglycerols > TRPC4 cation influx > membrane depolarisation) until it surpasses a threshold that triggers the oscillatory contractility of peristalsis. (b; expands on traces shown in **Figure 6c**) Additional **macroscopic motility** imaging traces (vertical axis: average change of pixel intensity for transmitted light image at time t compared to the previous frame, arbitrary units on a common scale (for details see **Figure S28**). The photoreproducibility and photoreversibility of the macroscopic motions triggered despite atropine blockade by **AzPico** $E \rightarrow Z$ switching (UV light) are striking. There is no photoresponse in the absence of **AzPico** (top traces and second-from-bottom trace). In the absence of atropine blockade, tonic motility is significant (second trace from bottom); and **AzPico** $E \rightarrow Z$ photoswitching has no apparent additional effect, however, especially initial $Z \rightarrow E$ phases seem to induce a temporary block on intestinal motility during the time of active 447 nm light application (bottom trace) however, we believe this is better understood as the typical time window for E -suppression of spontaneous oscillations (see section 7.2). (c-e; expands on data shown in **Figure 6d-f**) **Myography traces** of ring muscle contraction. (c) At high **AzPico** concentration (presumed saturating), under 365 nm the tonic tension increase is larger, and the amplitude of the oscillations is somewhat decreased. (d) At low **AzPico** concentrations (3 nM), under 365 nm the *amplitude* of the contractile oscillations increases but their tonic tension does not change; the KCl spike establishes a reference for muscle contractility, and tension drop over time. (e) Segments from TRPC4-deficient mice never responded to E/Z -**AzPico**. (f) Similar experiments as in panels c-d, but with vast excess of **AzPico**, can deliver fully photoreversible physiological-type contractility when avoiding the Z-maximised PSS of 365 nm (c) in favour of a Z-moderated PSS at 385 nm: a consequence of the ideal efficacy switch paradigm. (g) The high affinity and presumably also hydrophobicity of **AzPico** meant that tissues could be exposed, then the medium replaced (no **AzPico** content), but tissues remain perfectly photoreversibly operable for long times afterwards (here, 2 h).

Bon and Zholos⁷⁷ published the conclusion of TRPC4-dependent intestinal contractility on the basis of indirect experiments with the classical drug Pico145, with onset of effect taking minutes, and being irreversible after application (no un-blocking of motility or cycles of effect). While they could use **EA** and carbachol (target: mAChR) to record currents in isolated myocytes, for whole tissue experiments only carbachol was used to activate the intestine segments, with optional **Pico145** to block them: which, essentially, pharmacologically reproduces the effects of TRPC4 genetic knockout⁷⁸. TRPC4 was however never *directly* activated in tissues before, and its effective and reproducible demonstration in this paper may thus have novelty as well as practical value.

7.3 Why is AzPico/AzHC-like efficacy photoswitching useful *in vivo* in practice?

We conclude by briefly recalling the main **end-user** advantages of **AzPico** and **AzHC**, noting also that these ought to also apply to any other high-potency ideal efficacy switches, for other targets, created according to the paradigm in **Figure 1**. Their paradigm allows easy spatiotemporal targeting, through reversible, rapid, non-invasive modulation using light; they can fully reproducibly apply the same levels of applied bioactivity (c.f. baseline, physiologically stimulated, or overstimulated, as shown in **Figure 6e-g**) regardless of local or inter-assay concentration variations (that are otherwise significant and arise from a mixture of ADME-PK, technical handling, inter-animal differences, different distances of target cells from a reservoir or blood vessel, or assay timescales, etc: see section 7.1.1) as long as appropriate fixed wavelength/s are dialled in (i.e. it is convenient to apply); unlike slow wash-in/wash-out rates, their photoswitch mechanism acts much faster than tissue desensitisation, thus allowing multiple cycles of on-/off- switching in tissues (e.g. in each segment of the intestine), for statistics and reproducibility; and photoswitching also acts as an effective internal control e.g. in neighbouring cells in the same tissue slice, or by considering UV-vs-blue activity.

8 Chemistry

8.1 Materials and Methods - Chemistry

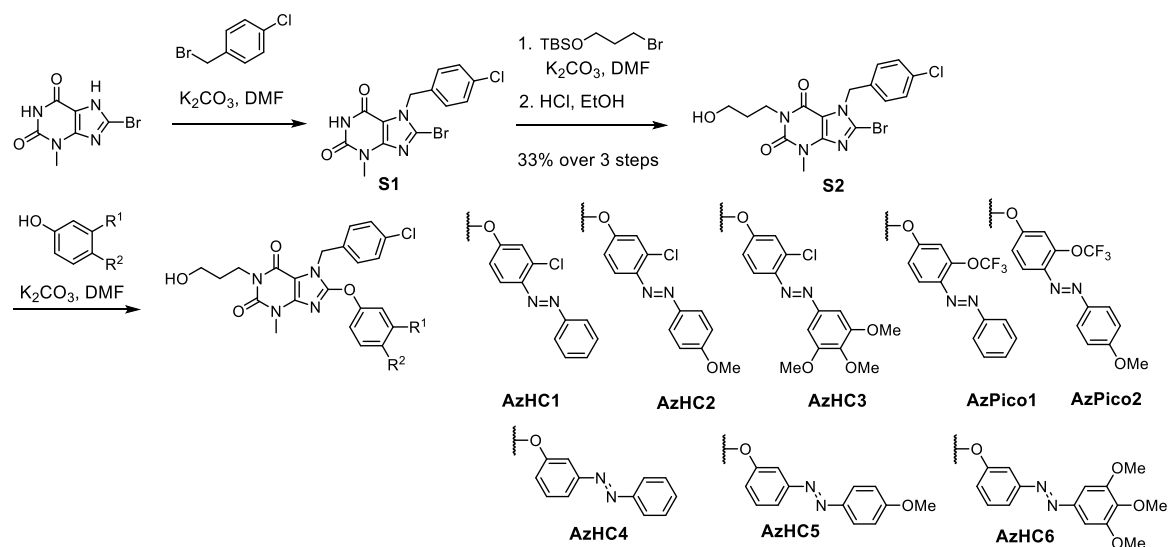
Reagents and Conditions. Unless stated otherwise, (1) all reactions and characterisations were performed with unpurified, undried, non-degassed solvents and reagents, used as obtained, under closed air atmosphere without special precautions; (2) “hexane” used for chromatography was distilled from commercial crude isohexane fraction by rotary evaporation; (3) “column” and “chromatography” refer to manual column chromatography on Merck silica gel Si-60 (40–63 μm); (4) flash column chromatography refers to purification on a Biotage Selekt system, using prepacked silica cartridges purchased from Biotage; (5) procedures and yields are unoptimized; (6) yields refer to isolated chromatographically and spectroscopically pure materials; (7) all eluent and solvent mixtures are given as volume ratios unless otherwise specified. (8) Thin-layer chromatography (TLC) was run on 0.25 mm Merck silica gel plates (60, F-254). UV light (254 nm) was used as a visualising agent. (9) *st.* refers to a saturated aqueous solution in deionised water. (10) For early-stage reactions, particularly if run with one reagent in excess, liquid reagents measured by volume as e.g. “92 μL ” were pipetted by adjustable mechanical pipette without calibration.

Nuclear magnetic resonance (NMR) spectroscopy. Standard NMR characterisation was by ^1H - and ^{13}C -NMR spectra on a Bruker Ascend 400 (400 MHz & 101 MHz for ^1H and ^{13}C respectively) and on a Bruker Ascend 500 (500 MHz & 126 MHz for ^1H and ^{13}C respectively). Chemical shifts (δ) are reported in ppm calibrated to residual non-perdeuterated solvent as an internal reference. Peak descriptions singlet (s), doublet (d), triplet (t), quartet (q), multiplet (m) and broad (br) are used. NMR spectra are given in **Part 10**.

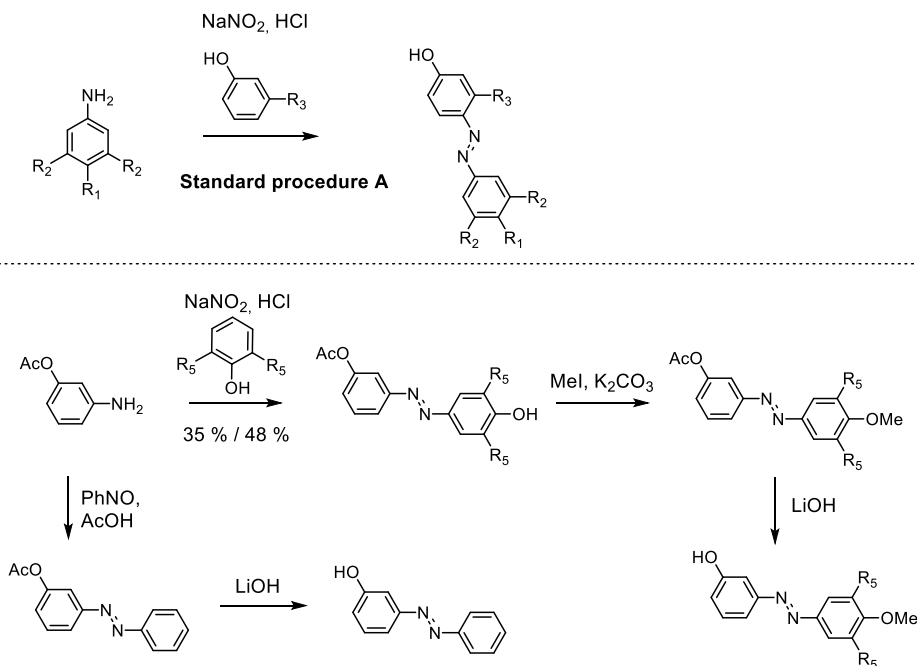
High resolution mass spectrometry (HRMS). HRMS was carried out by the Zentrale Analytik of the LMU Munich using ESI ionisation on a Thermo Finnigan LTQ FT Ultra Fourier Transform Ion Cyclotron Resonance Spectrometer.

High Performance liquid chromatography (HPLC) coupled with mass spectrometry (MS). Analytical HPLC-MS was performed on an Agilent 1100 SL with (a) a binary pump to deliver $\text{H}_2\text{O}:\text{MeCN}$ eluent mixtures containing 0.1% formic acid at a 0.4 mL/min flow rate, (b) YMC-Triart C18 column (3.0 μm ; 50 mm \times 3 mm) maintained at 40 $^\circ\text{C}$ (c) an Agilent 1100 series diode array detector, (d) an Agilent LC/MSD iQ mass spectrometer. Typical run conditions were a linear gradient of $\text{H}_2\text{O}:\text{MeCN}$ from 90:10 to 0:100 (first 5 min), then 0:100 for 2 min for flushing; then the column was (re)equilibrated with 90:10 eluent mixture for 2 min.

8.2 Chemical Synthesis Overview



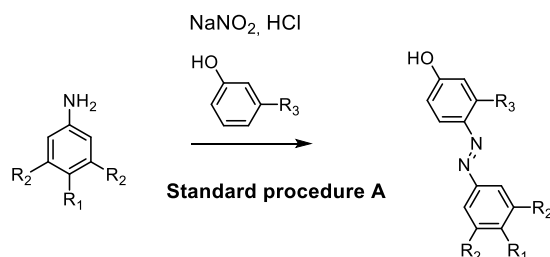
Scheme S1: Synthetic overview of AzPicos & AzHCs



Scheme S2: Synthesis of *p*-hydroxy-azobenzene building blocks.

8.3 Standard Synthetic Procedures

General Procedure A

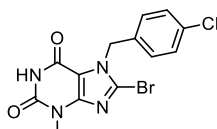


NaNO_2 (1.10 mL, 2 M, 2.20 mmol, 1.1 eq) was added to a solution of the corresponding aniline (2.00 mmol, 1.0 eq) in hydrochloric acid (4 mL, 2M) and MeOH (4 mL) at 0 °C. The reaction mixture was allowed to stir for 15 min at 0 °C and was subsequently added to a solution of the phenol

(2.0 mmol, 1.0 eq) in MeOH (6 mL) and buffer (6 mL of 0.5 M K₂HPO₄ and 2 mL of 1 M KOH). The pH was adjusted to 9 - 11 and the reaction was stirred for 45 min at 0°C. The reaction was quenched by addition of *st.* NH₄Cl, and the mixture was extracted with EA (3 x 100 mL). The combined organic layers were dried over anhydrous Na₂SO₄, filtered, and concentrated. The crude product was purified by flash chromatography. If not stated otherwise the reaction was carried out in 2 mmol scale.

8.4 Synthesis of Building Blocks

8-bromo-7-(4-chlorobenzyl)-3-methyl-3,7-dihydro-1H-purine-2,6-dione (S1)

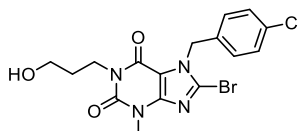


Compound is *lit.* known but no NMR spectra were provided.^{1,9}

The compound was prepared according to a literature procedure:⁹ A flask was charged with 8-bromo-3-methylxanthine (1.23 g, 5 mmol, 1.0 eq), 4-chlorobenzyl bromide (1.03 g, 5 mmol, 1.0 eq), potassium carbonate (1.04 g, 7.5 mmol, 1.5 eq) and DMF (50 mL) and the mixture was stirred at 45°C for 90 min. The mixture was cooled down, partitioned between brine (200 mL) and EtOAc (200 mL), the organic layer was washed with brine (2 x 100 mL), dried over Na₂SO₄, filtered and concentrated. The crude product was purified by flash chromatography (gradient: Hexane/EtOAc, 8:2 to 1:1) to afford **S1** (1.37 g, 3.71 mmol, 74 %) as a colourless solid.

¹H NMR (400 MHz, DMSO-*d*₆) δ [ppm]: 7.42 (d, *J* = 8.5 Hz, 2H), 7.28 (d, *J* = 8.4 Hz, 2H), 5.49 (s, 2H), 3.29 (s, 3H). ¹³C NMR (101 MHz, DMSO-*d*₆) δ [ppm]: 157.0, 152.9, 149.2, 135.1, 132.4, 129.1, 128.7, 126.1, 109.4, 48.3, 28.5. HPLC-MS *rt* = 5.55 min; ESI (*m/z*): [M+H]⁺ = 368.8 and 370.9.

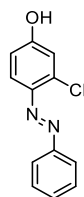
8-bromo-7-(4-chlorobenzyl)-1-(3-hydroxypropyl)-3-methyl-3,7-dihydro-1H-purine-2,6-dione (S2)



Compound is *lit.* known but no NMR spectra were provided.^{1,9}

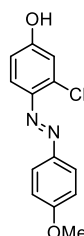
A flask was charged with **S1** (350 mg, 0.95 mmol, 1.0 eq), (3-bromopropoxy)(*tert*-butyl)dimethylsilane (218 μL, 0.95 mmol, 1.0 eq), potassium carbonate (196 mg, 1.42 mmol, 1.5 eq) and DMF (5 mL) and the mixture was stirred at 90°C for 5 h. The mixture was cooled down, 6M HCl (3.16 mL, 18.9 mmol, 20 eq) was added carefully and the mixture was stirred for further 90 min at 90°C. The mixture was cooled down again, neutralized with *st.* NaHCO₃ and partitioned between H₂O (50 mL) and EtOAc (50 mL), the organic layer was washed with brine (2x 500 mL), dried over Na₂SO₄, filtered and concentrated. The crude product was purified by flash chromatography (gradient: Hexane/EtOAc, 1:1 to 100 % EtOAc) to afford **S2** (234 mg, 0.56 mmol, 59 %) as a colourless solid.

¹H NMR (400 MHz, DMSO-*d*₆) δ [ppm]: 7.43 (d, *J* = 8.5 Hz, 2H), 7.28 (d, *J* = 8.5 Hz, 2H), 5.51 (s, 2H), 4.45 (t, *J* = 5.2 Hz, 1H), 3.98 – 3.85 (m, 2H), 3.50 – 3.38 (m, 5H), 1.74 – 1.60 (m, 2H). ¹³C NMR (101 MHz, DMSO-*d*₆) δ [ppm]: 153.6, 150.4, 148.0, 134.3, 132.6, 129.0, 128.8, 128.3, 108.3, 58.8, 48.7, 38.6, 30.9, 29.5. HPLC-MS *rt* = 5.79 min; ESI (*m/z*): [M+H]⁺ = 426.8 and 428.9.

3-chloro-4-(phenyldiazenyl)phenol (S3)

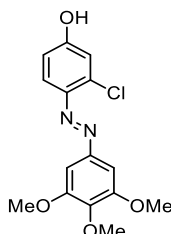
Prepared according to **General Procedure A** using aniline (184 μ L, 2 mmol) and 3-chlorophenol (211 μ L, 2 mmol). Purification: hexane/EtOAc, 5:95 to 65:35; **S3** (382 mg, 1.64 mmol, 82 %) was obtained as a red solid.

Rf = 0.36 hexane/EtOAc, 8:2. **¹H NMR** (400 MHz, CDCl₃) δ [ppm]: 7.96 – 7.90 (m, 2H), 7.74 (d, J = 8.9 Hz, 1H), 7.56 – 7.43 (m, 3H), 7.04 (d, J = 2.7 Hz, 1H), 6.80 (dd, J = 8.9, 2.7 Hz, 1H), 5.40 (s, 1H). **¹³C NMR** (101 MHz, CDCl₃) δ [ppm]: 158.5, 152.9, 143.2, 137.5, 131.1, 129.2, 123.2, 119.0, 118.2, 114.9. **HPLC-MS** r_t = 6.34 min; ESI (m/z): [M+H]⁺ = 233.0.

3-chloro-4-((4-methoxyphenyl)diazenyl)phenol (S4)

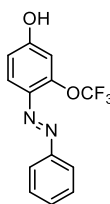
Prepared according to **General Procedure A** using p-anisidine (246 mg, 2 mmol) and 3-chlorophenol (232 μ L, 2.2 mmol). Purification: hexane/EtOAc, 5:95 to 65:35. **S4** (218 mg, 0.83 mmol, 42 %) was obtained as a brown solid.

Rf = 0.40 hexane/EtOAc, 8:2. **¹H NMR** (400 MHz, CDCl₃) δ [ppm]: 7.92 (d, J = 9.0 Hz, 2H), 7.69 (d, J = 8.8 Hz, 1H), 7.06 – 6.94 (m, 3H), 6.78 (dd, J = 8.9, 2.7 Hz, 1H), 3.89 (s, 3H). **¹³C NMR** (101 MHz, CDCl₃) δ [ppm]: 162.1, 158.1, 147.4, 143.2, 136.7, 125.1, 118.8, 117.1, 114.9, 114.4, 55.7. **HPLC-MS** r_t = 7.16 min; ESI (m/z): [M+H]⁺ = 322.9.

3-chloro-4-((3,4,5-trimethoxyphenyl)diazenyl)phenol (S5)

Prepared according to **General Procedure A** using 3,4,5-trimethoxyaniline (183 mg, 1 mmol) and 3-chlorophenol (116 μ L, 1.1 mmol). Purification: hexane/EtOAc, 5:95 to 65:35. **S5** (260 mg, 0.81 mmol, 81 %) was obtained as an orange solid.

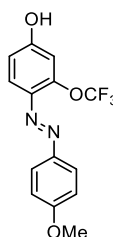
Rf = 0.45 hexane/EtOAc, 8:2. **¹H NMR** (400 MHz, DMSO-*d*₆) δ 7.67 (d, J = 9.0 Hz, 1H), 7.21 (s, 2H), 7.04 (d, J = 2.5 Hz, 1H), 6.86 (dd, J = 9.0, 2.6 Hz, 1H), 3.87 (s, 6H), 3.75 (s, 3H). **HPLC-MS** r_t = 7.43 min; ESI (m/z): [M+H]⁺ = 262.9.

4-(phenyldiazenyl)-3-(trifluoromethoxy)phenol (S6)

Prepared according to **General Procedure A** using aniline (92 μ L, 1 mmol) and 3-(trifluoromethoxy)phenol (117 μ L, 0.9 mmol). Purification: hexane/EtOAc, 10:90 to 60:40. **S6** (183 mg, 0.65 mmol, 65 %) was obtained as an orange solid.

Rf = 0.38 hexane/EtOAc, 8:2. **$^1\text{H NMR}$** (500 MHz, CDCl_3) δ [ppm]: 7.95 – 7.89 (m, 2H), 7.81 (d, J = 8.9 Hz, 1H), 7.54 – 7.44 (m, 3H), 6.93 – 6.91 (m, 1H), 6.86 (dd, J = 8.9, 2.6 Hz, 1H). **$^{13}\text{C NMR}$** (126 MHz, CDCl_3) δ [ppm]: 159.1, 152.8, 148.5, 139.3, 131.3, 129.3, 123.2, 120.7 (d, J = 258.3 Hz), 118.9, 114.9, 109.9. **$^{19}\text{F NMR}$** (471 MHz, CDCl_3) δ [ppm]: -57.40. **HPLC-MS** r_t = 6.78 min; ESI (m/z): $[\text{M}+\text{H}]^+$ = 283.1.

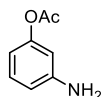
Note on ^{13}C spectrum: CF_3 quartet was detected as doublet.

4-((4-methoxyphenyl)diazenyl)-3-(trifluoromethoxy)phenol (S7)

Prepared according to **General Procedure A** using p-anisidine (246 mg, 2 mmol) and 3-(trifluoromethoxy)phenol (286 μ L, 2.2 mmol). Purification: hexane/EtOAc, 10:90 to 60:40. **S6** (225 mg, 0.72 mmol, 36 %) was obtained as a brown solid.

Rf = 0.42 hexane/EtOAc, 8:2. **$^1\text{H NMR}$** (400 MHz, CDCl_3) δ [ppm]: 7.95 – 7.88 (m, 2H), 7.76 (d, J = 8.9 Hz, 1H), 7.04 – 6.98 (m, 2H), 6.89 (dd, J = 2.7, 1.3 Hz, 1H), 6.83 (dd, J = 8.9, 2.6 Hz, 1H), 3.89 (s, 3H). **$^{13}\text{C NMR}$** (101 MHz, CDCl_3) δ [ppm]: 162.2, 158.5, 147.9, 147.4, 139.4, 125.0, 120.7 (d, J = 257.9 Hz), 118.7, 114.8, 114.4, 109.9, 55.7. **HPLC-MS** r_t = 6.80 min; ESI (m/z): $[\text{M}+\text{H}]^+$ = 313.1.

Note on ^{13}C spectrum: CF_3 quartet was detected as doublet.

3-aminophenyl acetate (S8)

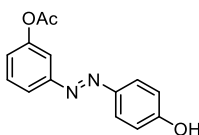
Prepared according to a literature procedure.⁷⁹

Acetic anhydride (0.47 mL, 5.0 mmol, 1.0 eq) and Et_3N (0.75 mL, 5.5 mmol, 1.1 eq) were added to a solution of 3-aminophenol (546 mg, 5.0 mmol, 1.0 eq) in CH_2Cl_2 (50 mL) and stirred for 20 h at room temperature. The mixture was partitioned between EtOAc (200 mL) and *st.* Na_2CO_3 (200 mL) solution, the organic layer washed with *st.* NH_4Cl (200 mL) and brine (200 mL) then dried over Na_2SO_4 , filtered and concentrated to obtain **S8** (695 mg, 4.6 mmol, 92%) as a brown oil.

$^1\text{H NMR}$ (400 MHz, CDCl_3) δ [ppm]: 7.13 (dd, J = 8.0 Hz, 1H), 6.55 (ddd, J = 8.1, 2.2, 0.9 Hz, 1H), 6.48 (ddd, J = 8.0, 2.2, 0.9 Hz, 1H), 6.43 (dd, J = 2.2 Hz, 1H), 3.89 (br, 2H), 2.27 (s, 3H). **HPLC-MS** r_t = 2.42 min; ESI (m/z): $[\text{M}+\text{H}]^+$ = 152.1.

Spectroscopic data match literature data.⁷⁹

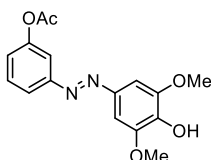
3-((4-hydroxyphenyl)diazenyl)phenyl acetate (**S9**)



Prepared according to **General Procedure A** using aniline **S8** (130 mg, 0.86 mmol, 1.0 eq) and phenol (81 mg, 0.86 mmol, 1.0 eq). Purification: hexane/EtOAc, 10:90 to 60:40. **S9** (106 mg, 0.41 mmol, 48 %) was obtained as an orange solid that was carried over without detailed analysis.

¹H NMR (400 MHz, CDCl₃) δ 7.87 – 7.80 (m, 2H), 7.78 (ddd, *J* = 7.9, 1.8, 1.0 Hz, 1H), 7.60 (t, *J* = 2.1 Hz, 1H), 7.51 (t, *J* = 8.0 Hz, 1H), 7.17 (ddd, *J* = 8.0, 2.4, 1.0 Hz, 1H), 6.90 (d, *J* = 8.8 Hz, 2H), 5.56 (br, 1H), 2.35 (s, 3H). **HPLC-MS** *rt* = 6.88 min; ESI (*m/z*): [M+H]⁺ = 256.9.

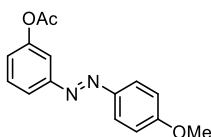
3-((4-hydroxy-3,5-dimethoxyphenyl)diazenyl)phenyl acetate (**S10**)



Prepared according to **General Procedure A** using aniline **S8** (130 mg, 0.86 mmol, 1.0 eq) and 2,6-dimethoxyphenol (133 mg, 0.86 mmol, 1.0 eq). Purification: hexane/EtOAc, 10:90 to 60:40. **S9** (96 mg, 0.30 mmol, 35 %) was obtained as a red oil that was carried over without detailed analysis.

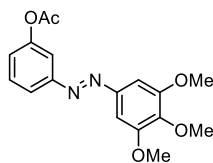
¹H NMR (400 MHz, CDCl₃) δ 7.79 (ddd, *J* = 8.0, 1.9, 1.0 Hz, 1H), 7.64 (t, *J* = 2.1 Hz, 1H), 7.51 (t, *J* = 8.0 Hz, 1H), 7.29 (s, 2H), 7.17 (ddd, *J* = 8.1, 2.3, 1.0 Hz, 1H), 3.98 (s, 6H), 2.33 (s, 3H). **HPLC-MS** *rt* = 6.96 min; ESI (*m/z*): [M+H]⁺ = 317.0.

3-((4-methoxyphenyl)diazenyl)phenyl acetate (**S11**)



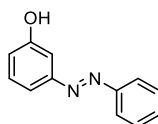
A vial was charged with **S9** (80 mg, 0.31 mmol, 1.0 eq), K₂CO₃ (65 mg, 0.47 mmol, 1.5 eq), acetone (3 mL) and iodomethane (20 μL, 0.33 mmol, 1.05 eq), sealed and stirred for 16h at room temperature. The mixture was partitioned between water (25 mL) and EtOAc (25 mL), the organic layer was washed with brine (2x 25 mL), dried over Na₂SO₄, filtered and concentrated. The crude product was purified by flash chromatography (gradient: hexane 100% to hexane/EtOAc, 3:7) to afford **S11** (47 mg, 0.17 mmol, 56 %) as a red solid that was carried over without further analysis.

HPLC-MS *rt* = 7.71 min; ESI (*m/z*): [M+H]⁺ = 271.0.

3-((3,4,5-trimethoxyphenyl)diazenyl)phenyl acetate (S12)

A vial was charged with **S10** (80 mg, 0.25 mmol, 1.0 eq), K_2CO_3 (52 mg, 0.38 mmol, 1.5 eq), acetone (3 mL) and iodomethane (17 μ L, 0.27 mmol, 1.05 eq), sealed and stirred for 16h at room temperature. HPLC-MS monitoring revealed incomplete conversion and further K_2CO_3 (52 mg, 0.38 mmol, 1.5 eq), and iodomethane (17 μ L, 0.27 mmol, 1.05 eq) were added to the reaction, and the mixture was stirred for further 8h. The mixture was partitioned between water (25 mL) and EtOAc (25 mL), the organic layer was washed with brine (2x 25 mL), dried over Na_2SO_4 , filtered and concentrated. The crude product was purified by flash chromatography (gradient: hexane/EtOAc, 1:0 to 3:7) to afford **S12** (63 mg, 0.19 mmol, 75 %) as a red solid that was carried over without further analysis.

HPLC-MS rt = 7.58 min; ESI (m/z): $[M+H]^+ = 331.0$.

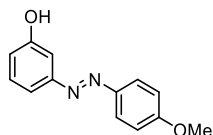
3-(phenyldiazenyl)phenol (S13) (known⁸⁰)

The procedure was conducted according to a literature procedure.⁸⁰

A mixture of 3-aminophenol (109 mg, 1.0 mmol, 1.0 eq), nitrosobenzene (107 mg, 1.0 mmol, 1.0 eq) and acetic acid (5 mL) was stirred at room temperature. After 16 h the mixture was neutralized with *st.* $NaHCO_3$, extracted with EtOAc (50 mL) and the organic layer was washed with brine (2x 50 mL), dried over Na_2SO_4 , filtered and concentrated. The crude product was purified by flash chromatography (gradient: hexane 100% to hexane/EtOAc, 4:6) to afford **S13** (22 mg, 0.11 mmol, 11 %) as a brown oil.

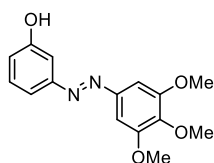
¹H NMR (400 MHz, $CDCl_3$) δ [ppm]: 7.97 – 7.78 (m, 2H), 7.59 – 7.44 (m, 4H), 7.42 – 7.29 (m, 2H), 7.10 – 6.84 (m, 1H), 5.15 (s, 1H). **HPLC-MS** rt = 7.10 min; ESI (m/z): $[M+H]^+ = 198.9$.

Spectral data match literature data.⁸⁰

3-((4-methoxyphenyl)diazenyl)phenol (S14)

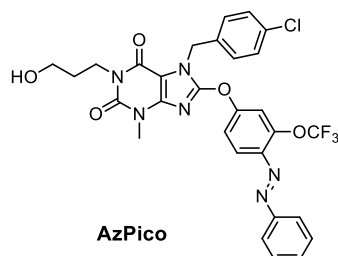
KOH (146 mg, 2.6 mmol, 15 eq) was added to a solution of **S11** (47 mg, 0.17 mmol, 1.0 eq) in MeOH (2 mL) and water (0.2 mL). The reaction mixture was stirred for 14 h, quenched by addition of *st.* NH_4Cl (20 mL), extracted with EtOAc (20 mL), the organic layer was washed with brine (2x 20 mL), dried over Na_2SO_4 , filtered and concentrated. The crude product was used immediately without further purification.

HPLC-MS rt = 7.10 min; ESI (m/z): $[M+H]^+ = 229.0$.

3-((3,4,5-trimethoxyphenyl)diazenyl)phenol (S15)

KOH (161 mg, 2.9 mmol, 15 eq) was added to a solution of **S12** (63 mg, 0.19 mmol, 1.0 eq) in MeOH (2 mL) and water (0.2 mL). The reaction mixture was stirred for 14 h, quenched by addition of *st.* NHCl₄ (20 mL), extracted with EtOAc (20 mL), the organic layer was washed with brine (2x 20 mL), dried over Na₂SO₄, filtered and concentrated. The crude product was used immediately without further purification.

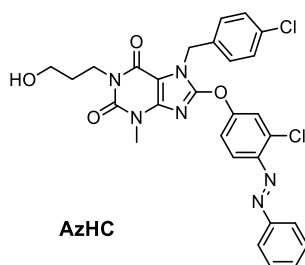
HPLC-MS *rt* = 6.88 min; ESI (*m/z*): [M+H]⁺ = 289.0.

8.5 Synthesis of AzPicos & AzHCs**AzPico**

A vial was charged with **S2** (51 mg, 0.12 mmol, 1.0 eq), **S6** (34 mg, 0.12 mmol, 1.0 eq), K₂CO₃ (33 mg, 0.24 mmol, 2.0 eq) and DMF (1.2 mL), sealed and the reaction was stirred at 80°C. After 5 h the reaction was cooled to room temperature, H₂O (2.4 mL) was added, and after 30 min the precipitate was collected by filtration. The crude product was recrystallized from EtOH to afford **AzPico** (25 mg, 0.040 mmol, 33 %) as a yellow solid.

¹H NMR (500 MHz, DMSO-*d*6) δ [ppm]: 7.96 – 7.82 (m, 4H), 7.73 – 7.56 (m, 4H), 7.49 – 7.40 (m, 4H), 5.47 (s, 2H), 4.46 (t, *J* = 5.2 Hz, 1H), 4.00 – 3.85 (m, 2H), 3.54 – 3.38 (m, 2H), 3.34 (s, 3H), 1.84 – 1.63 (m, 2H). **¹³C NMR** (126 MHz, DMSO-*d*6) δ [ppm]: 155.4, 153.9, 152.0, 151.6, 150.6, 146.0, 145.4, 141.7, 135.2, 132.7, 132.4, 129.7, 129.6, 129.6, 128.8, 122.8, 120.1 (d, *J* = 257.8 Hz), 119.8, 118.7, 115.1, 102.8, 58.8, 46.0, 38.4, 31.0, 29.5. **¹⁹F NMR** (471 MHz, DMSO-*d*6) δ [ppm]: -56.75. **HRMS** (ESI, *m/z*): [M+H]⁺ calcd for C₂₉H₂₅ClF₃N₆O₅: 629.1522; found: 629.1517.

Note on ¹³C spectrum: CF₃ quartet was detected as doublet.

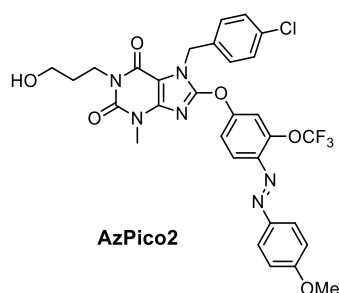
AzHC

A vial was charged with **S2** (50 mg, 0.12 mmol, 1.0 eq), **S3** (27 mg, 0.12 mmol, 1.0 eq), K₂CO₃ (32 mg, 0.23 mmol, 2.0 eq) and DMF (1 mL), sealed and the reaction was stirred at 80°C. After 5 h

the reaction was cooled to room temperature, H₂O (2 mL) was added, and after 30 min the precipitate was collected by filtration. The crude product was recrystallized from EtOH to afford **AzHC** (36 mg, 0.062 mmol, 53 %) as an orange solid.

¹H NMR (400 MHz, DMSO-*d*₆) δ [ppm]: 7.97 – 7.90 (m, 2H), 7.83 (d, *J* = 2.6 Hz, 1H), 7.79 (d, *J* = 9.0 Hz, 1H), 7.66 – 7.59 (m, 3H), 7.52 (dd, *J* = 9.0, 2.6 Hz, 1H), 7.47 – 7.40 (m, 4H), 5.46 (s, 2H), 4.46 (t, *J* = 5.2 Hz, 1H), 4.02 – 3.86 (m, 2H), 3.50 – 3.39 (m, 2H), 3.32 (s, 3H), 1.76 – 1.66 (m, 2H). ¹³C NMR (126 MHz, DMSO) δ [ppm]: 155.3, 153.9, 152.0, 151.7, 150.6, 145.5, 145.4, 135.2, 135.0, 132.7, 132.3, 129.7, 129.6, 128.8, 122.9, 121.5, 119.4, 118.8, 102.8, 58.8, 46.0, 38.4, 31.0, 29.6. HRMS (ESI, *m/z*): [M+H]⁺ calcd for C₂₈H₂₅Cl₂N₆O₄: 579.1309; found: 579.1302.

AzPico2

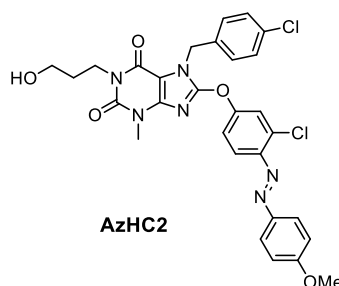


A vial was charged with **S2** (50 mg, 0.12 mmol, 1.0 eq), **S7** (37 mg, 0.12 mmol, 1.0 eq), K₂CO₃ (32 mg, 0.23 mmol, 2.0 eq) and DMF (1.2 mL), sealed and the reaction was stirred at 80°C. After 5 h the reaction was cooled to room temperature, H₂O (2.4 mL) was added, and after 30 min the precipitate was collected by filtration. The crude product was recrystallized from EtOH to afford **AzPico2** (32 mg, 0.048 mmol, 49 %) as a yellow solid.

¹H NMR (500 MHz, DMSO-*d*₆) δ [ppm]: 7.91 (d, *J* = 9.0 Hz, 2H), 7.85 (d, *J* = 9.0 Hz, 1H), 7.82 – 7.79 (m, 1H), 7.58 (dd, *J* = 9.0, 2.6 Hz, 1H), 7.47 – 7.41 (m, 4H), 7.18 (d, *J* = 9.0 Hz, 2H), 5.46 (s, 2H), 4.46 (t, *J* = 5.2 Hz, 1H), 3.97 – 3.92 (m, 2H), 3.49 – 3.41 (m, 2H), 3.32 (s, 3H), 1.76 – 1.65 (m, 2H). ¹³C NMR (126 MHz, DMSO-*d*₆) δ [ppm]: 162.8, 154.7, 153.9, 151.8, 150.6, 146.4, 145.6, 145.4, 141.9, 135.2, 132.7, 129.6, 128.8, 125.0, 120.1 (d, *J* = 258.2 Hz), 119.8, 118.6, 115.0, 114.9, 102.8, 58.8, 55.8, 46.0, 38.4, 31.0, 29.5. HRMS (ESI, *m/z*): [M+H]⁺ calcd for C₃₀H₂₇ClF₃N₆O₆: 659.1627; found: 659.1613.

Note on ¹³C spectrum: CF₃ quartet was detected as doublet.

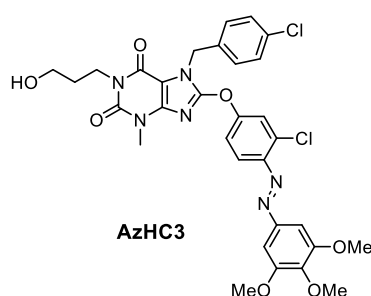
AzHC2



A vial was charged with **S2** (50 mg, 0.12 mmol, 1.0 eq), **S4** (27 mg, 0.12 mmol, 1.0 eq), K₂CO₃ (32 mg, 0.23 mmol, 2.0 eq) and DMF (1 mL), sealed and the reaction was stirred at 80°C. After 5 h the reaction was cooled to room temperature, H₂O (2 mL) was added, and after 30 min the precipitate was collected by filtration. The crude product was recrystallized from EtOH to afford **AzHC2** (61 mg, 0.10 mmol, 86 %) as a yellow solid.

¹H NMR (500 MHz, DMSO-*d*6) δ [ppm]: 7.96 – 7.91 (m, 2H), 7.79 (d, *J* = 2.6 Hz, 1H), 7.75 (d, *J* = 8.9 Hz, 1H), 7.49 (dd, *J* = 9.0, 2.6 Hz, 1H), 7.44 (s, 4H), 7.17 (d, *J* = 9.0 Hz, 2H), 5.45 (s, 2H), 4.46 (s, 1H), 3.97 – 3.91 (m, 2H), 3.47 – 3.41 (m, 2H), 3.32 (s, 3H), 1.74 – 1.66 (m, 2H). **¹³C NMR** (126 MHz, DMSO-*d*6) δ [ppm]: 162.7, 154.6, 153.9, 151.9, 150.6, 146.4, 145.5, 145.5, 135.2, 134.3, 132.7, 129.7, 128.8, 125.2, 121.4, 119.4, 118.6, 114.8, 102.7, 58.8, 55.8, 46.0, 38.4, 31.0, 29.6. **HRMS** (ESI, *m/z*): [M+H]⁺ calcd for C₂₉H₂₇Cl₂N₆O₅: 609.1414; found: 609.1408.

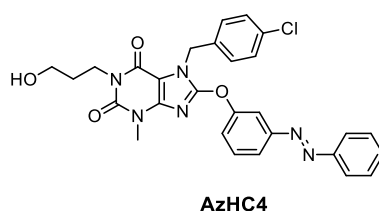
AzHC3



A vial was charged with **S2** (43 mg, 0.10 mmol, 1.0 eq), **S5** (32 mg, 0.10 mmol, 1.0 eq), K₂CO₃ (28 mg, 0.20 mmol, 2.0 eq) and DMF (1 mL), sealed and the reaction was stirred at 80°C. After 5 h the reaction was cooled to room temperature, H₂O (2 mL) was added, and after 30 min the precipitate was collected by filtration. The crude product was recrystallized from DMSO/H₂O (volumetric ratio 9:1) and the filter cake washed with cold MeOH to afford **AzHC3** (15 mg, 0.022 mmol, 22 %) as an orange solid.

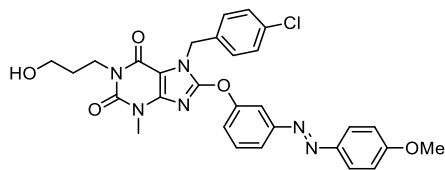
¹H NMR (400 MHz, DMSO-*d*6) δ [ppm]: 7.82 (d, *J* = 2.6 Hz, 1H), 7.76 (d, *J* = 9.0 Hz, 1H), 7.50 (dd, *J* = 9.0, 2.6 Hz, 1H), 7.45 – 7.42 (m, 4H), 7.30 (s, 2H), 5.45 (s, 2H), 4.46 (t, *J* = 5.2 Hz, 1H), 3.97 – 3.90 (m, 2H), 3.89 (s, 6H), 3.78 (s, 3H), 3.49 – 3.41 (m, 2H), 3.32 (s, 3H), 1.75 – 1.65 (m, 2H). **¹³C NMR** (101 MHz, DMSO-*d*6) δ [ppm]: 155.0, 154.0, 153.4, 151.8, 150.56, 147.9, 145.5, 145.3, 141.1, 135.2, 134.7, 132.7, 129.7, 128.8, 121.4, 119.4, 118.7, 102.8, 100.8, 60.3, 58.8, 56.0, 46.2, 38.4, 31.0, 29.6. **HRMS** (ESI, *m/z*): [M+H]⁺ calcd for C₃₁H₃₁Cl₂N₆O₇: 669.1626; found: 669.1616.

AzHC4



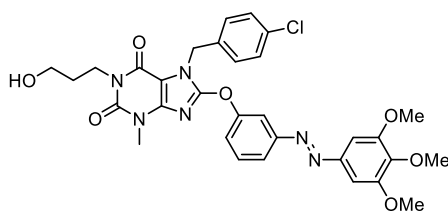
A vial was charged with **S2** (30 mg, 71 μ mol, 1.0 eq), **S13** (14 mg, 71 μ mol, 1.0 eq), K₂CO₃ (20 mg, 141 μ mol, 2.0 eq) and DMF (1 mL), sealed and the reaction was stirred at 80°C. After 5 h the reaction was cooled to room temperature, H₂O (2 mL) was added, and after 30 min the precipitate was collected by filtration. The crude product was recrystallized from DMSO/H₂O (volumetric ratio 9:1) and the filter cake washed with cold MeOH to afford **AzHC4** (9 mg, 17 μ mol, 23 %) as a yellow solid.

¹H NMR (400 MHz, DMSO-*d*6) δ [ppm]: 7.94 – 7.89 (m, 2H), 7.88 – 7.83 (m, 1H), 7.79 – 7.77 (m, 1H), 7.70 (t, *J* = 8.0 Hz, 1H), 7.65 – 7.53 (m, 4H), 7.47 – 7.42 (m, 4H), 5.47 (s, 2H), 4.45 (t, *J* = 5.2 Hz, 1H), 3.98 – 3.86 (m, 2H), 3.49 – 3.40 (m, 2H), 3.29 (s, 3H), 1.75 – 1.65 (m, 2H). **¹³C NMR** (101 MHz, DMSO-*d*6) δ [ppm]: 153.9, 153.9, 153.0, 152.7, 151.7, 150.6, 145.6, 135.3, 132.6, 132.1, 130.9, 129.6, 129.6, 128.8, 122.7, 122.6, 121.4, 112.3, 102.6, 58.8, 45.9, 38.3, 31.0, 29.6. **HRMS** (ESI, *m/z*): [M+H]⁺ calcd for C₂₈H₂₆ClN₆O₄: 545.1699; found: 545.1693.

AzHC5**AzHC5**

A vial was charged with **S2** (73 mg, 0.17 mmol, 1.0 eq), **S14** (39 mg, 0.17 mmol, 1.0 eq), K₂CO₃ (39 mg, 0.17 mmol, 2.0 eq) and DMF (1.7 mL), sealed and the reaction was stirred at 80°C. After 5 h the reaction was cooled to room temperature, H₂O (3.4 mL) was added, and after 30 min the precipitate was collected by filtration. The crude product was recrystallized from DMSO/H₂O (volumetric ratio 9:1) and the filter cake washed with cold MeOH to afford **AzHC5** (22 mg, 0.038 mmol, 23 %) as a brown solid.

¹H NMR (400 MHz, DMSO-*d*₆) δ [ppm]: 7.91 (d, *J* = 9.0 Hz, 2H), 7.83 – 7.78 (m, 1H), 7.73 – 7.70 (m, 1H), 7.66 (t, *J* = 8.1 Hz, 1H), 7.53 – 7.47 (m, 1H), 7.46 – 7.42 (m, 4H), 7.15 (d, *J* = 9.0 Hz, 2H), 5.46 (s, 2H), 4.45 (t, *J* = 5.2 Hz, 1H), 3.98 – 3.90 (m, 2H), 3.88 (s, 3H), 3.49 – 3.40 (m, 2H), 3.28 (s, 3H), 1.74 – 1.64 (m, 2H). **¹³C NMR** (101 MHz, DMSO-*d*₆) δ [ppm]: 162.5, 153.9, 153.9, 153.2, 152.7, 150.6, 145.9, 145.6, 135.3, 132.6, 130.8, 129.6, 128.8, 124.9, 121.9, 121.1, 114.7, 112.0, 102.6, 58.8, 55.7, 45.9, 38.3, 31.0, 29.6. **HRMS** (ESI, *m/z*): [M+H]⁺ calcd for C₂₉H₂₈ClN₆O: 575.1804; found: 575.1799.

AzHC6**AzHC6**

A vial was charged with **S2** (81 mg, 0.19 mmol, 1.0 eq), **S15** (55 mg, 0.19 mmol, 1.0 eq), K₂CO₃ (53 mg, 0.38 mmol, 2.0 eq) and DMF (2 mL), sealed and the reaction was stirred at 80°C. After 5 h the reaction was cooled to room temperature, H₂O (4 mL) was added, and after 30 min the precipitate was collected by filtration. The crude product was recrystallized from DMSO/H₂O (volumetric ratio 9:1) and the filter cake washed with cold MeOH to afford **AzHC5** (17 mg, 0.027 mmol, 14 %) as an orange solid.

¹H NMR (400 MHz, DMSO-*d*₆) δ [ppm]: 7.89 – 7.80 (m, 1H), 7.75 (t, *J* = 2.2 Hz, 1H), 7.69 (t, *J* = 8.1 Hz, 1H), 7.59 – 7.52 (m, 1H), 7.48 – 7.42 (m, 4H), 7.28 (s, 2H), 5.47 (s, 2H), 4.45 (t, *J* = 5.2 Hz, 1H), 4.02 – 3.90 (m, 2H), 3.89 (s, 6H), 3.77 (s, 3H), 3.49 – 3.40 (m, 2H), 3.28 (s, 3H), 1.75 – 1.63 (m, 2H). **¹³C NMR** (101 MHz, DMSO-*d*₆) δ [ppm]: 153.9, 153.9, 153.4, 152.9, 152.7, 150.6, 147.5, 145.6, 140.8, 135.3, 132.6, 130.9, 129.6, 128.8, 122.3, 121.3, 112.3, 102.6, 100.6, 60.3, 58.8, 56.0, 45.9, 38.3, 31.0, 29.6. **HRMS** (ESI, *m/z*): [M+H]⁺ calcd for C₃₁H₃₂ClN₆O₇: 635.2016; found: 635.2007.

9 Supporting References

- (1) Chenard, B.; Gallaschun, R. Substituted Xanthenes and Methods of Use Thereof. WO2014143799A2, September 18, 2014. <https://patents.google.com/patent/WO2014143799A2/en> (accessed 2024-03-08).
- (2) Rubaiy, H. N.; Ludlow, M. J.; Henrot, M.; Gaunt, H. J.; Miteva, K.; Cheung, S. Y.; Tanahashi, Y.; Hamzah, N.; Musialowski, K. E.; Blythe, N. M.; Appleby, H. L.; Bailey, M. A.; McKeown, L.; Taylor, R.; Foster, R.; Waldmann, H.; Nussbaumer, P.; Christmann, M.; Bon, R. S.; Muraki, K.; Beech, D. J. Picomolar, Selective, and Subtype-Specific Small-Molecule Inhibition of TRPC1/4/5 Channels. *J. Biol. Chem* **2017**, *292* (20), 8158–8173. <https://doi.org/10.1074/jbc.M116.773556>.
- (3) Just, S.; Chenard, B. L.; Ceci, A.; Strassmaier, T.; Chong, J. A.; Blair, N. T.; Gallaschun, R. J.; del Camino, D.; Cantin, S.; D'Amours, M.; Eickmeier, C.; Fanger, C. M.; Hecker, C.; Hessler, D. P.; Hengerer, B.; Kroker, K. S.; Malekiani, S.; Mihalek, R.; McLaughlin, J.; Rast, G.; Witek, J.; Sauer, A.; Pryce, C. R.; Moran, M. M. Treatment with HC-070, a Potent Inhibitor of TRPC4 and TRPC5, Leads to Anxiolytic and Antidepressant Effects in Mice. *PLoS ONE* **2018**, *13* (1), e0191225. <https://doi.org/10.1371/journal.pone.0191225>.
- (4) Rubaiy, H. N.; Seitz, T.; Hahn, S.; Choidas, A.; Habenberger, P.; Klebl, B.; Dinkel, K.; Nussbaumer, P.; Waldmann, H.; Christmann, M.; Beech, D. J. Identification of an (–)-Englerin A Analogue, Which Antagonizes (–)-Englerin A at TRPC1/4/5 Channels. *British Journal of Pharmacology* **2018**, *175* (5), 830–839. <https://doi.org/10.1111/bph.14128>.
- (5) Wright, D. J.; Simmons, K. J.; Johnson, R. M.; Beech, D. J.; Muench, S. P.; Bon, R. S. Human TRPC5 Structures Reveal Interaction of a Xanthine-Based TRPC1/4/5 Inhibitor with a Conserved Lipid Binding Site. *Commun. Biol.* **2020**, *3* (1), 704. <https://doi.org/10.1038/s42003-020-01437-8>.
- (6) Song, K.; Wei, M.; Guo, W.; Quan, L.; Kang, Y.; Wu, J.-X.; Chen, L. Structural Basis for Human TRPC5 Channel Inhibition by Two Distinct Inhibitors. *eLife* **2021**, *10*, e63429. <https://doi.org/10.7554/eLife.63429>.
- (7) Akbulut, Y.; Gaunt, H. J.; Muraki, K.; Ludlow, M. J.; Amer, M. S.; Bruns, A.; Vasudev, N. S.; Radtke, L.; Willot, M.; Hahn, S.; Seitz, T.; Ziegler, S.; Christmann, M.; Beech, D. J.; Waldmann, H. (–)-Englerin A Is a Potent and Selective Activator of TRPC4 and TRPC5 Calcium Channels. *Angew. Chem. Int. Ed.* **2015**, *54* (12), 3787–3791. <https://doi.org/10.1002/anie.201411511>.
- (8) Minard, A.; Bauer, C. C.; Chuntharpursat-Bon, E.; Pickles, I. B.; Wright, D. J.; Ludlow, M. J.; Burnham, M. P.; Warriner, S. L.; Beech, D. J.; Muraki, K.; Bon, R. S. Potent, Selective, and Subunit-Dependent Activation of TRPC5 Channels by a Xanthine Derivative. *British journal of pharmacology* **2019**, *176* (20), 3924–3938. <https://doi.org/10.1111/bph.14791>.
- (9) Rubaiy, H. N.; Ludlow, M. J.; Henrot, M.; Gaunt, H. J.; Miteva, K.; Cheung, S. Y.; Tanahashi, Y.; Hamzah, N.; Musialowski, K. E.; Blythe, N. M.; Appleby, H. L.; Bailey, M. A.; McKeown, L.; Taylor, R.; Foster, R.; Waldmann, H.; Nussbaumer, P.; Christmann, M.; Bon, R. S.; Muraki, K.; Beech, D. J. Picomolar, Selective, and Subtype-Specific Small-Molecule Inhibition of TRPC1/4/5 Channels. *J. Biol. Chem* **2017**, *292* (20), 8158–8173. <https://doi.org/10.1074/jbc.M116.773556>.
- (10) Dryn, D. O.; Melnyk, M. I.; Bon, R. S.; Beech, D. J.; Zholos, A. V. Pico145 Inhibits TRPC4-Mediated mICAT and Postprandial Small Intestinal Motility. *Biomedicine & Pharmacotherapy* **2023**, *168*, 115672. <https://doi.org/10.1016/j.biopha.2023.115672>.
- (11) Gómez-Santacana, X.; de Munnik, S. M.; Vijayachandran, P.; Da Costa Pereira, D.; Bebelman, J. P. M.; de Esch, I. J. P.; Vischer, H. F.; Wijtmans, M.; Leurs, R. Photoswitching the Efficacy of a Small-Molecule Ligand for a Peptidergic GPCR: From Antagonism to Agonism. *Angewandte Chemie International Edition* **2018**, *57* (36), 11608–11612. <https://doi.org/10.1002/anie.201804875>.
- (12) Gómez-Santacana, X.; Munnik, S. M. de; Mocking, T. A. M.; Hauwert, N. J.; Sun, S.; Vijayachandran, P.; Esch, I. J. P. de; Vischer, H. F.; Wijtmans, M.; Leurs, R. A Toolbox of Molecular Photoswitches to Modulate the CXCR3 Chemokine Receptor with Light. *Beilstein J. Org. Chem.* **2019**, *15* (1), 2509–2523. <https://doi.org/10.3762/bjoc.15.244>.
- (13) Wijtmans, M.; Josimovic, I.; Vischer, H. F.; Leurs, R. Optical Control of Class A G Protein-Coupled Receptors with Photoswitchable Ligands. *Current Opinion in Pharmacology* **2022**, *63*, 102192. <https://doi.org/10.1016/j.coph.2022.102192>.
- (14) Kobauri, P.; Dekker, F. J.; Szymanski, W.; Feringa, B. L. Rational Design in Photopharmacology with Molecular Photoswitches. *Angewandte Chemie International Edition* **2023**, *62* (30), e202300681. <https://doi.org/10.1002/anie.202300681>.
- (15) Bahamonde, M. I.; Taura, J.; Paoletta, S.; Gakh, A. A.; Chakraborty, S.; Hernando, J.; Fernández-Dueñas, V.; Jacobson, K. A.; Gorostiza, P.; Ciruela, F. Photomodulation of G Protein-Coupled Adenosine Receptors by a Novel Light-Switchable Ligand. *Bioconjugate Chem.* **2014**, *25* (10), 1847–1854. <https://doi.org/10.1021/bc5003373>.

- (16) Agnetta, L.; Kauk, M.; Canizal, M. C. A.; Messerer, R.; Holzgrabe, U.; Hoffmann, C.; Decker, M. A. Photoswitchable Dualsteric Ligand Controlling Receptor Efficacy. *Angewandte Chemie International Edition* **2017**, *56* (25), 7282–7287. <https://doi.org/10.1002/anie.201701524>.
- (17) Steinmüller, S. A. M.; Tutov, A.; Hislop, J. N.; Decker, M. Bridging the Binding Sites 2.0: Photoswitchable Dualsteric Ligands for the Cannabinoid 2 Receptor. *ACS Chem. Neurosci.* **2023**, *14* (20), 3737–3744. <https://doi.org/10.1021/acscchemneuro.3c00509>.
- (18) Hansen, M. J.; Hille, J. I. C.; Szymanski, W.; Driessen, A. J. M.; Feringa, B. L. Easily Accessible, Highly Potent, Photocontrolled Modulators of Bacterial Communication. *Chem* **2019**, *5* (5), 1293–1301. <https://doi.org/10.1016/j.chempr.2019.03.005>.
- (19) Gerwe, H.; He, F.; Pottie, E.; Stove, C.; Decker, M. Enlightening the “Spirit Molecule”: Photomodulation of the 5-HT_{2A} Receptor by a Light-Controllable N,N-Dimethyltryptamine Derivative. *Angewandte Chemie International Edition* **2022**, *61* (26), e202203034. <https://doi.org/10.1002/anie.202203034>.
- (20) Riefolo, F.; Matera, C.; Garrido-Charles, A.; Gomila, A. M. J.; Sortino, R.; Agnetta, L.; Claro, E.; Masgrau, R.; Holzgrabe, U.; Batlle, M.; Decker, M.; Guasch, E.; Gorostiza, P. Optical Control of Cardiac Function with a Photoswitchable Muscarinic Agonist. *J. Am. Chem. Soc.* **2019**, *141* (18), 7628–7636. <https://doi.org/10.1021/jacs.9b03505>.
- (21) Gómez-Santacana, X.; de Munnik, S. M.; Vijayachandran, P.; Da Costa Pereira, D.; Bebelman, J. P. M.; de Esch, I. J. P.; Vischer, H. F.; Wijtmans, M.; Leurs, R. Photoswitching the Efficacy of a Small-Molecule Ligand for a Peptidergic GPCR: From Antagonism to Agonism. *Angewandte Chemie International Edition* **2018**, *57* (36), 11608–11612. <https://doi.org/10.1002/anie.201804875>.
- (22) Arkhipova, V.; Fu, H.; Hoorens, M. W. H.; Trinco, G.; Lameijer, L. N.; Marin, E.; Feringa, B. L.; Poelarends, G. J.; Szymanski, W.; Slotboom, D. J.; Guskov, A. Structural Aspects of Photopharmacology: Insight into the Binding of Photoswitchable and Photocaged Inhibitors to the Glutamate Transporter Homologue. *J. Am. Chem. Soc.* **2021**, *143* (3), 1513–1520. <https://doi.org/10.1021/jacs.0c11336>.
- (23) Westphal, M. V.; Schafrath, M. A.; Sarott, R. C.; Imhof, M. A.; Bold, C. P.; Leippe, P.; Dhopeswarkar, A.; Grandner, J. M.; Katritch, V.; Mackie, K.; Trauner, D.; Carreira, E. M.; Frank, J. A. Synthesis of Photoswitchable Δ^9 -Tetrahydrocannabinol Derivatives Enables Optical Control of Cannabinoid Receptor 1 Signaling. *J. Am. Chem. Soc.* **2017**, *139* (50), 18206–18212. <https://doi.org/10.1021/jacs.7b06456>.
- (24) Morstein, J.; Hill, R. Z.; Novak, A. J. E.; Feng, S.; Norman, D. D.; Donthamsetti, P. C.; Frank, J. A.; Harayama, T.; Williams, B. M.; Parrill, A. L.; Tigyi, G. J.; Riezman, H.; Isacoff, E. Y.; Bautista, D. M.; Trauner, D. Optical Control of Sphingosine-1-Phosphate Formation and Function. *Nature Chemical Biology* **2019**, *15* (6), 623–631. <https://doi.org/10.1038/s41589-019-0269-7>.
- (25) Lam, P.-Y.; Thawani, A. R.; Balderas, E.; White, A. J. P.; Chaudhuri, D.; Fuchter, M. J.; Peterson, R. T. TRPswitch—A Step-Function Chemo-Optogenetic Ligand for the Vertebrate TRPA1 Channel. *J. Am. Chem. Soc.* **2020**, *142* (41), 17457–17468. <https://doi.org/10.1021/jacs.0c06811>.
- (26) Tiapko, O.; Shrestha, N.; Lindinger, S.; Cruz, G. G. de la; Graziani, A.; Klec, C.; Butorac, C.; Graier, W. F.; Kubista, H.; Freichel, M.; Birnbaumer, L.; Romanin, C.; Glasnov, T.; Groschner, K. Lipid-Independent Control of Endothelial and Neuronal TRPC3 Channels by Light. *Chem. Sci.* **2019**, *10* (9), 2837–2842. <https://doi.org/10.1039/C8SC05536J>.
- (27) Yue, L.; Pawlowski, M.; Dellal, S. S.; Xie, A.; Feng, F.; Otis, T. S.; Bruzik, K. S.; Qian, H.; Pepperberg, D. R. Robust Photoregulation of GABA_A Receptors by Allosteric Modulation with a Propofol Analogue. *Nature Communications* **2012**, *3* (1), 1095. <https://doi.org/10.1038/ncomms2094>.
- (28) Morstein, J.; Dacheux, M. A.; Norman, D. D.; Shemet, A.; Donthamsetti, P. C.; Citir, M.; Frank, J. A.; Schultz, C.; Isacoff, E. Y.; Parrill, A. L.; Tigyi, G. J.; Trauner, D. Optical Control of Lysophosphatidic Acid Signaling. *J. Am. Chem. Soc.* **2020**, *142* (24), 10612–10616. <https://doi.org/10.1021/jacs.0c02154>.
- (29) Photoswitching in 2030: What Concepts Do We Need To Reach Impactful Photopharmacology? *article in preparation*.
- (30) Bauer, C. C.; Minard, A.; Pickles, I. B.; Simmons, K. J.; Chuntharpursat-Bon, E.; Burnham, M. P.; Kapur, N.; Beech, D. J.; Muench, S. P.; Wright, M. H.; Warriner, S. L.; Bon, R. S. Xanthine-Based Photoaffinity Probes Allow Assessment of Ligand Engagement by TRPC5 Channels. *RSC Chem. Biol.* **2020**, 10.1039/D0CB00126K. <https://doi.org/10.1039/D0CB00126K>.
- (31) Wright, D. J.; Simmons, K. J.; Johnson, R. M.; Beech, D. J.; Muench, S. P.; Bon, R. S. Human TRPC5 Structures Reveal Interaction of a Xanthine-Based TRPC1/4/5 Inhibitor with a Conserved Lipid Binding Site. *Communications Biology* **2020**, *3* (1), 704. <https://doi.org/10.1038/s42003-020-01437-8>.

- (32) Seiferth, D.; Biggin, P. C. Exploring the Influence of Pore Shape on Conductance and Permeation. *bioRxiv* April 21, 2024, p 2024.04.18.589791. <https://doi.org/10.1101/2024.04.18.589791>.
- (33) Vinayagam, D.; Mager, T.; Apelbaum, A.; Bothe, A.; Merino, F.; Hofnagel, O.; Gatsogiannis, C.; Raunser, S. Electron Cryo-Microscopy Structure of the Canonical TRPC4 Ion Channel. *eLife* **2018**, *7*, e36615. <https://doi.org/10.7554/eLife.36615>.
- (34) Vinayagam, D.; Quentin, D.; Yu-Strzelczyk, J.; Sitsel, O.; Merino, F.; Stabrin, M.; Hofnagel, O.; Yu, M.; Ledebroer, M. W.; Nagel, G.; Malojcic, G.; Raunser, S. Structural Basis of TRPC4 Regulation by Calmodulin and Pharmacological Agents. *eLife* **2020**, *9*, e60603. <https://doi.org/10.7554/eLife.60603>.
- (35) Pellegrini-Calace, M.; Maiwald, T.; Thornton, J. M. PoreWalker: A Novel Tool for the Identification and Characterization of Channels in Transmembrane Proteins from Their Three-Dimensional Structure. *PLOS Computational Biology* **2009**, *5* (7), e1000440. <https://doi.org/10.1371/journal.pcbi.1000440>.
- (36) Blum, T.; Moreno-Pérez, A.; Pyrski, M.; Bufo, B.; Arifovic, A.; Weissgerber, P.; Freichel, M.; Zufall, F.; Leinders-Zufall, T. Trpc5 Deficiency Causes Hypoprolactinemia and Altered Function of Oscillatory Dopamine Neurons in the Arcuate Nucleus. *Proc. Natl. Acad. Sci. USA* **2019**, *116* (30), 15236–15243. <https://doi.org/10.1073/pnas.1905705116>.
- (37) Müller, M.; Niemeyer, K.; Urban, N.; Ojha, N. K.; Zufall, F.; Leinders-Zufall, T.; Schaefer, M.; Thorn-Seshold, O. BTDAzo: A Photoswitchable TRPC5 Channel Activator**. *Angew Chem Int Ed* **2022**, *61* (36). <https://doi.org/10.1002/anie.202201565>.
- (38) Baumgartner, B.; Glembockyte, V.; Mayer, R.; Gonzalez-Hernandez, A.; Kindler, R.; Valavalkar, A.; Wiegand, A.; Müller-Deku, A.; Grubert, L.; Steiner, F.; Gross, C.; Reynders, M.; Grenier, V.; Broichhagen, J.; Hecht, S.; Tinnefeld, P.; Ofial, A.; Dietzek-Ivansic, B.; Levitz, J.; Thorn-Seshold, O. Azobenzenes Can Achieve Near-Infrared Photocontrol in Biological Systems, with Quantitative Z→E Photoisomerization, via Singlet Manifold Photoredox. *ChemRxiv* **2023**. <https://doi.org/10.26434/chemrxiv-2023-37sv4>.
- (39) Baumgartner, B.; Glembockyte, V.; Gonzalez-Hernandez, A.; Valavalkar, A.; Mayer, R.; Fillbrook, L.; Müller-Deku, A.; Zhang, J.; Steiner, F.; Wiegand, A.; Gross, C.; Reynders, M.; Munguba, H.; Arefin, A.; Ofial, A.; Beves, J.; Lohmüller, T.; Dietzek-Ivansic, B.; Broichhagen, J.; Tinnefeld, P.; Levitz, J.; Thorn-Seshold, O. A General Method for Near-Infrared Photoswitching in Biology, Demonstrated by the >700 Nm Photocontrol of GPCR Activity in Brain Slices. *ChemRxiv* **2024**. <https://doi.org/10.26434/chemrxiv-2024-vm4n3>.
- (40) Richter, J. M.; Schaefer, M.; Hill, K. Clemizole Hydrochloride Is a Novel and Potent Inhibitor of Transient Receptor Potential Channel TRPC5. *Mol Pharmacol* **2014**, *86* (5), 514–521. <https://doi.org/10.1124/mol.114.093229>.
- (41) Richter, J. M.; Schaefer, M.; Hill, K. Riluzole Activates TRPC5 Channels Independently of PLC Activity. *Br. J. Pharmacol.* **2014**, *171* (1), 158–170. <https://doi.org/10.1111/bph.12436>.
- (42) Borowiak, M.; Nahaboo, W.; Reynders, M.; Nekolla, K.; Jalinot, P.; Hasserodt, J.; Rehberg, M.; Delattre, M.; Zahler, S.; Vollmar, A.; Trauner, D.; Thorn-Seshold, O. Photoswitchable Inhibitors of Microtubule Dynamics Optically Control Mitosis and Cell Death. *Cell* **2015**, *162* (2), 403–411. <https://doi.org/10.1016/j.cell.2015.06.049>.
- (43) Goehring, A.; Lee, C. H.; Wang, K. H.; Michel, J. C.; Claxton, D. P.; Bacongus, I.; Althoff, T.; Fischer, S.; Garcia, K. C.; Gouaux, E. Screening and Large-Scale Expression of Membrane Proteins in Mammalian Cells for Structural Studies. *Nature Protocols* **2014**, *9* (11), 2574–2585. <https://doi.org/10.1038/nprot.2014.173>.
- (44) Duan, J.; Li, J.; Chen, G.-L.; Ge, Y.; Liu, J.; Xie, K.; Peng, X.; Zhou, W.; Zhong, J.; Zhang, Y.; Xu, J.; Xue, C.; Liang, B.; Zhu, L.; Liu, W.; Zhang, C.; Tian, X.-L.; Wang, J.; Clapham, D. E.; Zeng, B.; Li, Z.; Zhang, J. Cryo-EM Structure of TRPC5 at 2.8-Å Resolution Reveals Unique and Conserved Structural Elements Essential for Channel Function. *Science advances* **2019**, *5* (7), eaaw7935. <https://doi.org/10.1126/sciadv.aaw7935>.
- (45) Punjani, A.; Rubinstein, J. L.; Fleet, D. J.; Brubaker, M. A. cryoSPARC: Algorithms for Rapid Unsupervised Cryo-EM Structure Determination. *Nat Methods* **2017**, *14* (3), 290–296. <https://doi.org/10.1038/nmeth.4169>.
- (46) Terwilliger, T. C.; Ludtke, S. J.; Read, R. J.; Adams, P. D.; Afonine, P. V. Improvement of Cryo-EM Maps by Density Modification. *Nat Methods* **2020**, *17* (9), 923–927. <https://doi.org/10.1038/s41592-020-0914-9>.
- (47) Liebschner, D.; Afonine, P. V.; Baker, M. L.; Bunkóczi, G.; Chen, V. B.; Croll, T. I.; Hintze, B.; Hung, L.-W.; Jain, S.; McCoy, A. J.; Moriarty, N. W.; Oeffner, R. D.; Poon, B. K.; Prisant, M. G.; Read, R. J.; Richardson, J. S.; Richardson, D. C.; Sammito, M. D.; Sobolev, O. V.; Stockwell, D. H.; Terwilliger, T. C.; Urzhumtsev, A. G.; Videau, L. L.; Williams, C. J.; Adams, P. D. Macromolecular Structure Determination Using X-Rays, Neutrons and Electrons: Recent

- Developments in *Phenix*. *Acta Crystallogr D Struct Biol* **2019**, *75* (10), 861–877. <https://doi.org/10.1107/S2059798319011471>.
- (48) Jamali, K.; Käll, L.; Zhang, R.; Brown, A.; Kimanius, D.; Scheres, S. H. W. Automated Model Building and Protein Identification in Cryo-EM Maps. *Nature* **2024**, *628* (8007), 450–457. <https://doi.org/10.1038/s41586-024-07215-4>.
- (49) Emsley, P.; Lohkamp, B.; Scott, W. G.; Cowtan, K. Features and Development of *Coot*. *Acta Crystallogr D Biol Crystallogr* **2010**, *66* (4), 486–501. <https://doi.org/10.1107/S0907444910007493>.
- (50) Terwilliger, T. C.; Adams, P. D.; Moriarty, N. W.; Cohn, J. D. Ligand Identification Using Electron-Density Map Correlations. *Acta Crystallogr D Biol Crystallogr* **2007**, *63* (1), 101–107. <https://doi.org/10.1107/S0907444906046233>.
- (51) Moriarty, N. W.; Grosse-Kunstleve, R. W.; Adams, P. D. *Electronic Ligand Builder and Optimization Workbench (eLBOW)*: A Tool for Ligand Coordinate and Restraint Generation. *Acta Crystallogr D Biol Crystallogr* **2009**, *65* (10), 1074–1080. <https://doi.org/10.1107/S0907444909029436>.
- (52) Diedrich, K.; Krause, B.; Berg, O.; Rarey, M. PoseEdit: Enhanced Ligand Binding Mode Communication by Interactive 2D Diagrams. *J Comput Aided Mol Des* **2023**, *37* (10), 491–503. <https://doi.org/10.1007/s10822-023-00522-4>.
- (53) Goddard, T. D.; Huang, C. C.; Meng, E. C.; Pettersen, E. F.; Couch, G. S.; Morris, J. H.; Ferrin, T. E. UCSF ChimeraX: Meeting Modern Challenges in Visualization and Analysis. *Protein Science* **2018**, *27* (1), 14–25. <https://doi.org/10.1002/pro.3235>.
- (54) Meng, E. C.; Goddard, T. D.; Pettersen, E. F.; Couch, G. S.; Pearson, Z. J.; Morris, J. H.; Ferrin, T. E. UCSF CHIMERAX: Tools for Structure Building and Analysis. *Protein Science* **2023**, *32* (11), e4792. <https://doi.org/10.1002/pro.4792>.
- (55) Stabrin, M.; Schoenfeld, F.; Wagner, T.; Pospich, S.; Gatsogiannis, C.; Raunser, S. TransPHIRE: Automated and Feedback-Optimized on-the-Fly Processing for Cryo-EM. *Nat Commun* **2020**, *11* (1), 5716. <https://doi.org/10.1038/s41467-020-19513-2>.
- (56) Zheng, S. Q.; Palovcak, E.; Armache, J.-P.; Verba, K. A.; Cheng, Y.; Agard, D. A. MotionCor2: Anisotropic Correction of Beam-Induced Motion for Improved Cryo-Electron Microscopy. *Nat Methods* **2017**, *14* (4), 331–332. <https://doi.org/10.1038/nmeth.4193>.
- (57) Rohou, A.; Grigorieff, N. CTFFIND4: Fast and Accurate Defocus Estimation from Electron Micrographs. *Journal of Structural Biology* **2015**, *192* (2), 216–221. <https://doi.org/10.1016/j.jsb.2015.08.008>.
- (58) Moriya, T.; Saur, M.; Stabrin, M.; Merino, F.; Voicu, H.; Huang, Z.; Penczek, P. A.; Raunser, S.; Gatsogiannis, C. High-resolution Single Particle Analysis from Electron Cryo-microscopy Images Using SPHIRE. *JoVE (Journal of Visualized Experiments)* **2017**, No. 123, e55448. <https://doi.org/10.3791/55448>.
- (59) Wagner, T.; Merino, F.; Stabrin, M.; Moriya, T.; Antoni, C.; Apelbaum, A.; Hagel, P.; Sitsel, O.; Raisch, T.; Prumbaum, D.; Quentin, D.; Roderer, D.; Tacke, S.; Siebolds, B.; Schubert, E.; Shaikh, T. R.; Lill, P.; Gatsogiannis, C.; Raunser, S. SPHIRE-crYOLO Is a Fast and Accurate Fully Automated Particle Picker for Cryo-EM. *Commun Biol* **2019**, *2* (1), 1–13. <https://doi.org/10.1038/s42003-019-0437-z>.
- (60) Yang, Z.; Fang, J.; Chittuluru, J.; Asturias, F. J.; Penczek, P. A. Iterative Stable Alignment and Clustering of 2D Transmission Electron Microscope Images. *Structure* **2012**, *20* (2), 237–247. <https://doi.org/10.1016/j.str.2011.12.007>.
- (61) Zivanov, J.; Nakane, T.; Forsberg, B. O.; Kimanius, D.; Hagen, W. J.; Lindahl, E.; Scheres, S. H. New Tools for Automated High-Resolution Cryo-EM Structure Determination in RELION-3. *eLife* **2018**, *7*, e42166. <https://doi.org/10.7554/eLife.42166>.
- (62) Emsley, P.; Lohkamp, B.; Scott, W. G.; Cowtan, K. Features and Development of *Coot*. *Acta Cryst D* **2010**, *66* (4), 486–501. <https://doi.org/10.1107/S0907444910007493>.
- (63) Adams, P. D.; Afonine, P. V.; Bunkóczi, G.; Chen, V. B.; Davis, I. W.; Echols, N.; Headd, J. J.; Hung, L.-W.; Kapral, G. J.; Grosse-Kunstleve, R. W.; McCoy, A. J.; Moriarty, N. W.; Oeffner, R.; Read, R. J.; Richardson, D. C.; Richardson, J. S.; Terwilliger, T. C.; Zwart, P. H. PHENIX: A Comprehensive Python-Based System for Macromolecular Structure Solution. *Acta Cryst D* **2010**, *66* (2), 213–221. <https://doi.org/10.1107/S0907444909052925>.
- (64) Bröker-Lai, J.; Kollewe, A.; Schindeldecker, B.; Pohle, J.; Nguyen Chi, V.; Mathar, I.; Guzman, R.; Schwarz, Y.; Lai, A.; Weißgerber, P.; Schwegler, H.; Dietrich, A.; Both, M.; Sprengel, R.; Draguhn, A.; Köhr, G.; Fakler, B.; Flockerzi, V.; Bruns, D.; Freichel, M. Heteromeric Channels Formed by TRPC1, TRPC4 and TRPC5 Define Hippocampal Synaptic Transmission and Working Memory. *The EMBO Journal* **2017**, *36* (18), 2770–2789. <https://doi.org/10.15252/embj.201696369>.
- (65) Schwarz, Y.; Oleinikov, K.; Schindeldecker, B.; Wyatt, A.; Weißgerber, P.; Flockerzi, V.; Boehm, U.; Freichel, M.; Bruns, D. TRPC Channels Regulate Ca²⁺-Signaling and Short-Term Plasticity of

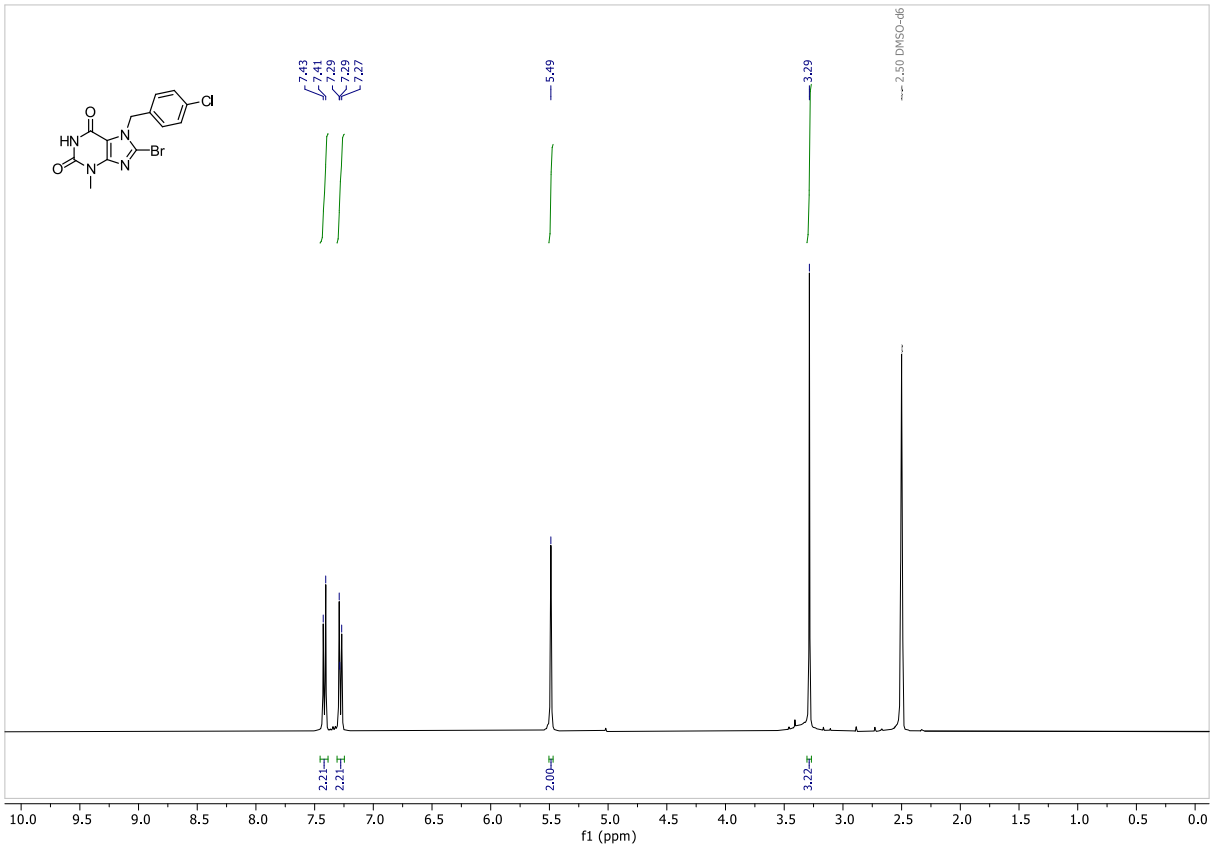
- Fast Glutamatergic Synapses. *PLOS Biology* **2019**, *17* (9), e3000445. <https://doi.org/10.1371/journal.pbio.3000445>.
- (66) Kollewe, A.; Schwarz, Y.; Oleinikov, K.; Raza, A.; Haupt, A.; Wartenberg, P.; Wyatt, A.; Boehm, U.; Ectors, F.; Bildl, W.; Zolles, G.; Schulte, U.; Bruns, D.; Flockerzi, V.; Fakler, B. Subunit Composition, Molecular Environment, and Activation of Native TRPC Channels Encoded by Their *Interactomes*. *Neuron* **2022**, *110* (24), 4162–4175.e7. <https://doi.org/10.1016/j.neuron.2022.09.029>.
- (67) Borisovska, M.; Zhao, Y.; Tsytsyura, Y.; Glyvuk, N.; Takamori, S.; Matti, U.; Rettig, J.; Südhof, T.; Bruns, D. v-SNAREs Control Exocytosis of Vesicles from Priming to Fusion. *The EMBO Journal* **2005**, *24* (12), 2114–2126. <https://doi.org/10.1038/sj.emboj.7600696>.
- (68) Savitt, J. M.; Jang, S. S.; Wu, M.; Dawson, V. L.; Dawson, T. M. Bcl-x Is Required for Proper Development of the Mouse Substantia Nigra. *Journal of Neuroscience* **2005**, *25* (29), 6721–6728. <https://doi.org/10.1523/JNEUROSCI.0760-05.2005>.
- (69) Madisen, L.; Garner, A. R.; Shimaoka, D.; Chuong, A. S.; Klapoetke, N. C.; Li, L.; van der Bourg, A.; Niino, Y.; Egolf, L.; Monetti, C.; Gu, H.; Mills, M.; Cheng, A.; Tasic, B.; Nguyen, T. N.; Sunkin, S. M.; Benucci, A.; Nagy, A.; Miyawaki, A.; Helmchen, F.; Empson, R. M.; Knöpfel, T.; Boyden, E. S.; Reid, R. C.; Carandini, M.; Zeng, H. Transgenic Mice for Intersectional Targeting of Neural Sensors and Effectors with High Specificity and Performance. *Neuron* **2015**, *85* (5), 942–958. <https://doi.org/10.1016/j.neuron.2015.02.022>.
- (70) Madisen, L.; Zwingman, T. A.; Sunkin, S. M.; Oh, S. W.; Zariwala, H. A.; Gu, H.; Ng, L. L.; Palmiter, R. D.; Hawrylycz, M. J.; Jones, A. R.; Lein, E. S.; Zeng, H. A Robust and High-Throughput Cre Reporting and Characterization System for the Whole Mouse Brain. *Nat Neurosci* **2010**, *13* (1), 133–140. <https://doi.org/10.1038/nn.2467>.
- (71) Phelan, K. D.; Shwe, U. T.; Abramowitz, J.; Wu, H.; Rhee, S. W.; Howell, M. D.; Gottschall, P. E.; Freichel, M.; Flockerzi, V.; Birnbaumer, L.; Zheng, F. Canonical Transient Receptor Channel 5 (TRPC5) and TRPC1/4 Contribute to Seizure and Excitotoxicity by Distinct Cellular Mechanisms. *Mol. Pharmacol.* **2013**, *83* (2), 429–438. <https://doi.org/10.1124/mol.112.082271>.
- (72) Schauer, C.; Tong, T.; Petitjean, H.; Blum, T.; Peron, S.; Mai, O.; Schmitz, F.; Boehm, U.; Leinders-Zufall, T. Hypothalamic Gonadotropin-Releasing Hormone (GnRH) Receptor Neurons Fire in Synchrony with the Female Reproductive Cycle. *J. Neurophysiol.* **2015**, *114* (2), 1008–1021. <https://doi.org/10.1152/jn.00357.2015>.
- (73) Chamero, P.; Weiss, J.; Alonso, M. T.; Rodríguez-Prados, M.; Hisatsune, C.; Mikoshiba, K.; Leinders-Zufall, T.; Zufall, F. Type 3 Inositol 1,4,5-Trisphosphate Receptor Is Dispensable for Sensory Activation of the Mammalian Vomeronasal Organ. *Sci Rep* **2017**, *7* (1), 10260. <https://doi.org/10.1038/s41598-017-09638-8>.
- (74) Leinders-Zufall, T.; Storch, U.; Bleyemehl, K.; Mederos y Schnitzler, M.; Frank, J. A.; Konrad, D. B.; Trauner, D.; Gudermann, T.; Zufall, F. PhoDAGs Enable Optical Control of Diacylglycerol-Sensitive Transient Receptor Potential Channels. *Cell Chem. Bio.* **2018**, *25* (2), 215–223.e3. <https://doi.org/10.1016/j.chembiol.2017.11.008>.
- (75) Leinders-Zufall, T.; Storch, U.; Mederos y Schnitzler, M.; Ojha, N. K.; Koike, K.; Gudermann, T.; Zufall, F. A Diacylglycerol Photoswitching Protocol for Studying TRPC Channel Functions in Mammalian Cells and Tissue Slices. *STAR Protocols* **2021**, *2* (2), 100527. <https://doi.org/10.1016/j.xpro.2021.100527>.
- (76) Ojha, A.; Ojha, N. K. Excitation Light-Induced Phototoxicity during Fluorescence Imaging. *Journal of Biosciences* **2021**, *46* (3), 78. <https://doi.org/10.1007/s12038-021-00193-z>.
- (77) Dryn, D. O.; Melnyk, M. I.; Bon, R. S.; Beech, D. J.; Zholos, A. V. Pico145 Inhibits TRPC4-Mediated mICAT and Postprandial Small Intestinal Motility. *Biomedicine & Pharmacotherapy* **2023**, *168*, 115672. <https://doi.org/10.1016/j.biopha.2023.115672>.
- (78) Tsvilovskyy, V. V.; Zholos, A. V.; Aberle, T.; Philipp, S. E.; Dietrich, A.; Zhu, M. X.; Birnbaumer, L.; Freichel, M.; Flockerzi, V. Deletion of TRPC4 and TRPC6 in Mice Impairs Smooth Muscle Contraction and Intestinal Motility In Vivo. *Gastroenterology* **2009**, *137* (4), 1415–1424. <https://doi.org/10.1053/j.gastro.2009.06.046>.
- (79) Norcott, P.; McErlean, C. S. P. Synthesis of Carbazoloquinone Natural Products ‘on-Water.’ *Org. Biomol. Chem.* **2015**, *13* (24), 6866–6878. <https://doi.org/10.1039/C5OB00852B>.
- (80) Steinwand, S.; Halbritter, T.; Rastädter, D.; Ortiz-Sánchez, J. M.; Burghardt, I.; Heckel, A.; Wachtveitl, J. Ultrafast Spectroscopy of Hydroxy-Substituted Azobenzenes in Water. *Chemistry – A European Journal* **2015**, *21* (44), 15720–15731. <https://doi.org/10.1002/chem.201501863>.
- (81) Zholos, A. V.; Melnyk, M. I.; Dryn, D. O. Molecular Mechanisms of Cholinergic Neurotransmission in Visceral Smooth Muscles with a Focus on Receptor-Operated TRPC4 Channel and Impairment of Gastrointestinal Motility by General Anaesthetics and Anxiolytics. *Neuropharmacology* **2024**, *242*, 109776. <https://doi.org/10.1016/j.neuropharm.2023.109776>.

10 NMR Spectra

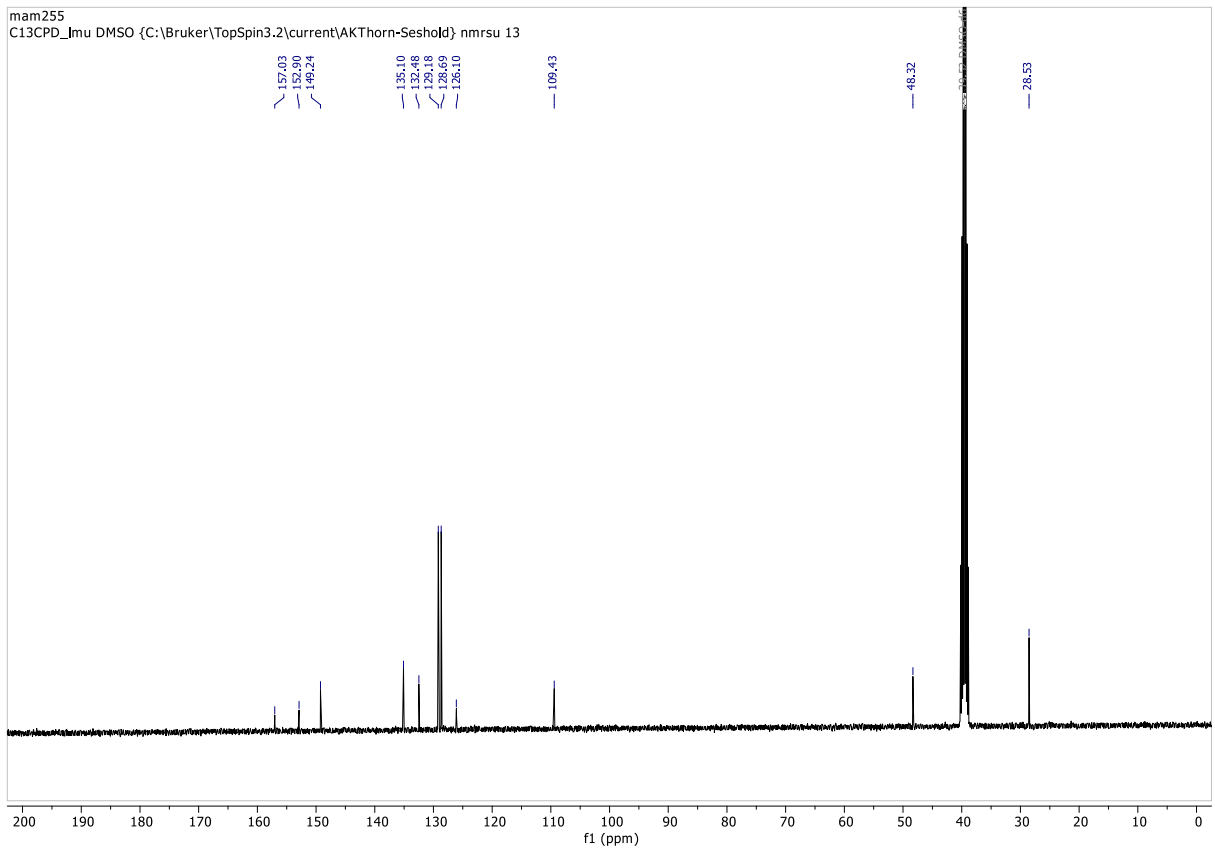
S1	S55
S2	S56
S3	S57
S4	S58
S5	S59
S6	S60
S7	S61
S8	S62
S9	S62
S10	S63
S13	S63
AzPico	S64
AzHC	S65
AzPico2	S66
AzHC2	S67
AzHC3	S68
AzHC4	S69
AzHC5	S70
AzHC6	S71

S1

¹H NMR (400 MHz, DMSO-*d*₆)

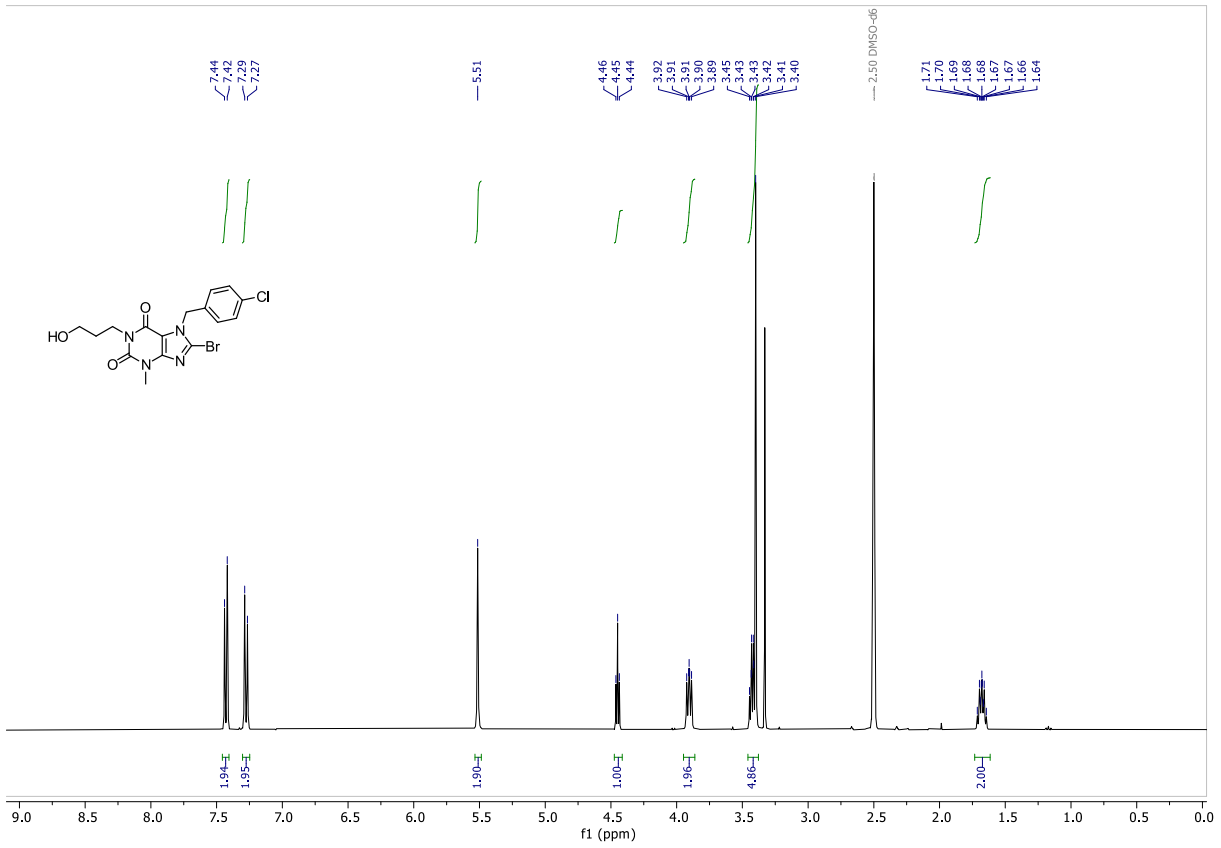


¹³C NMR (101 MHz, DMSO-*d*₆)

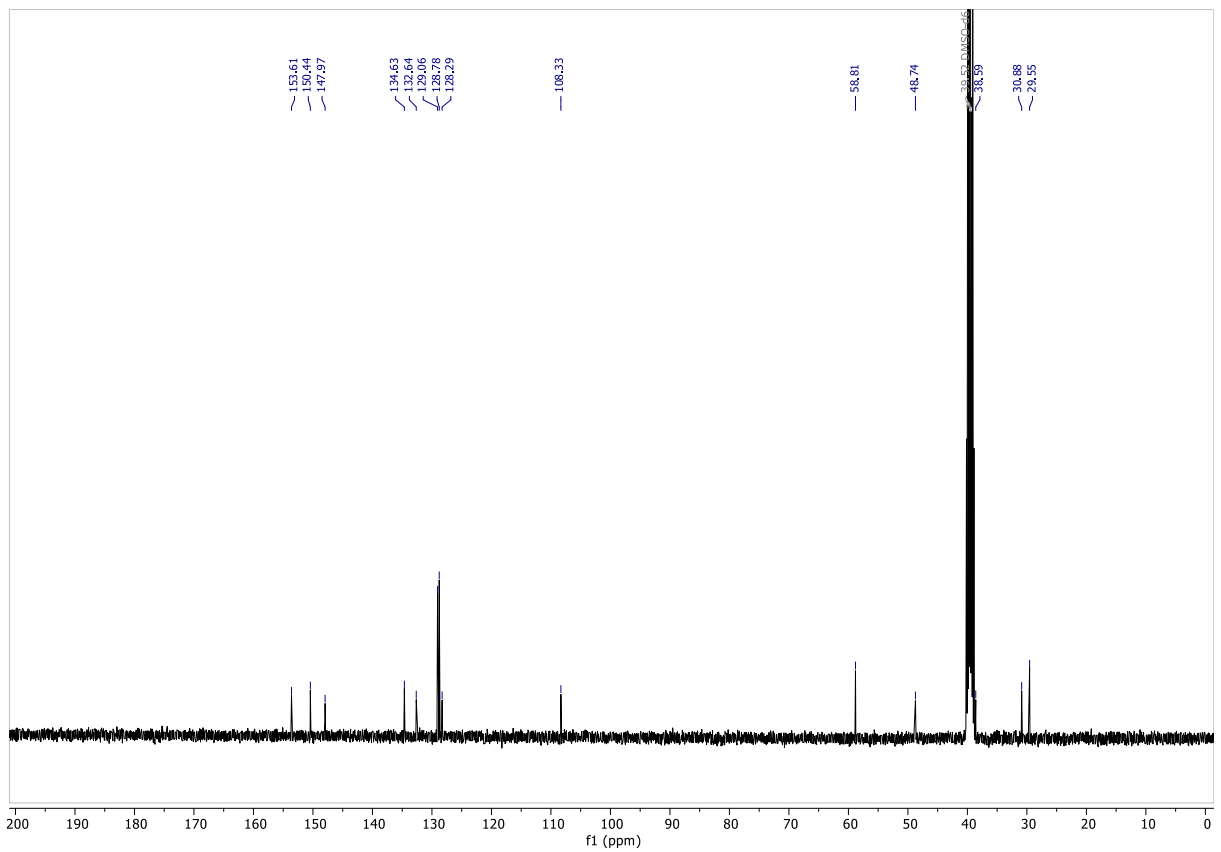


S2

¹H NMR (400 MHz, DMSO-*d*₆)

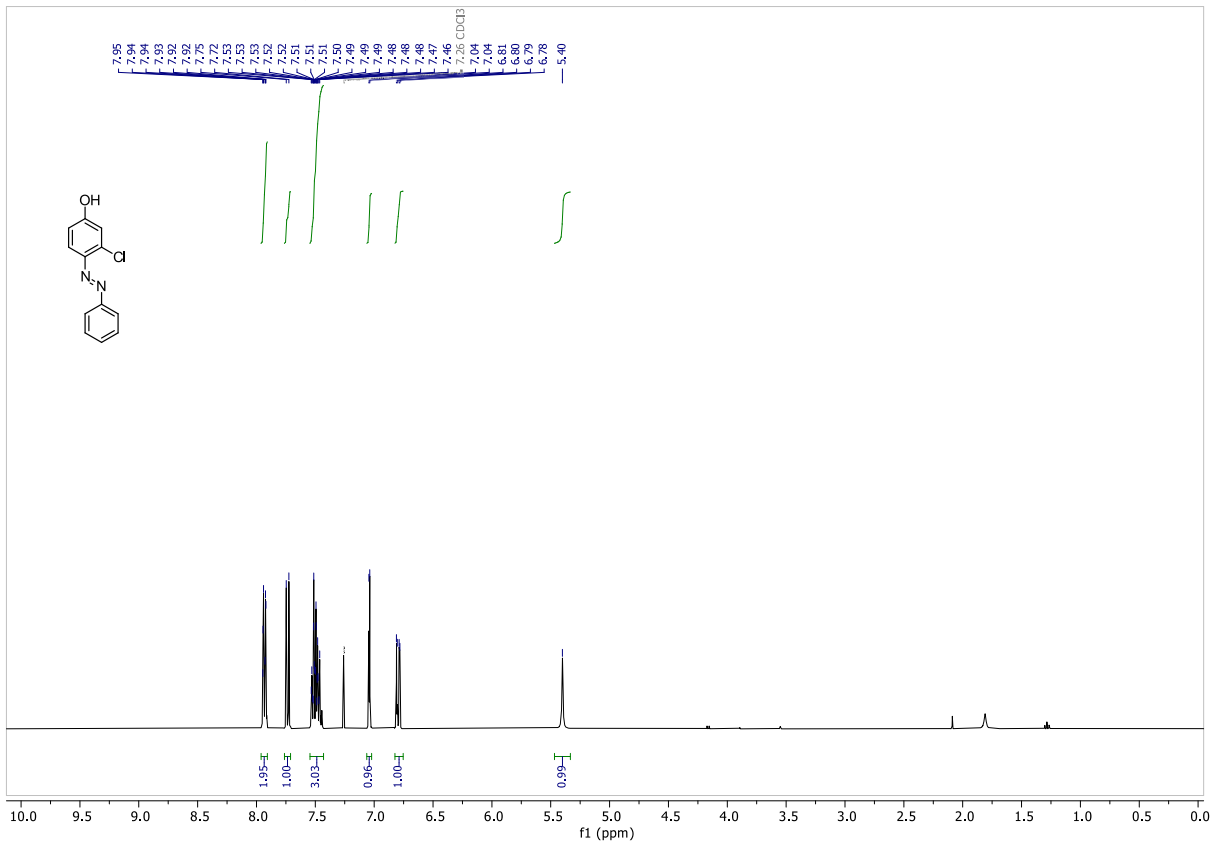


¹³C NMR (101 MHz, DMSO-*d*₆)

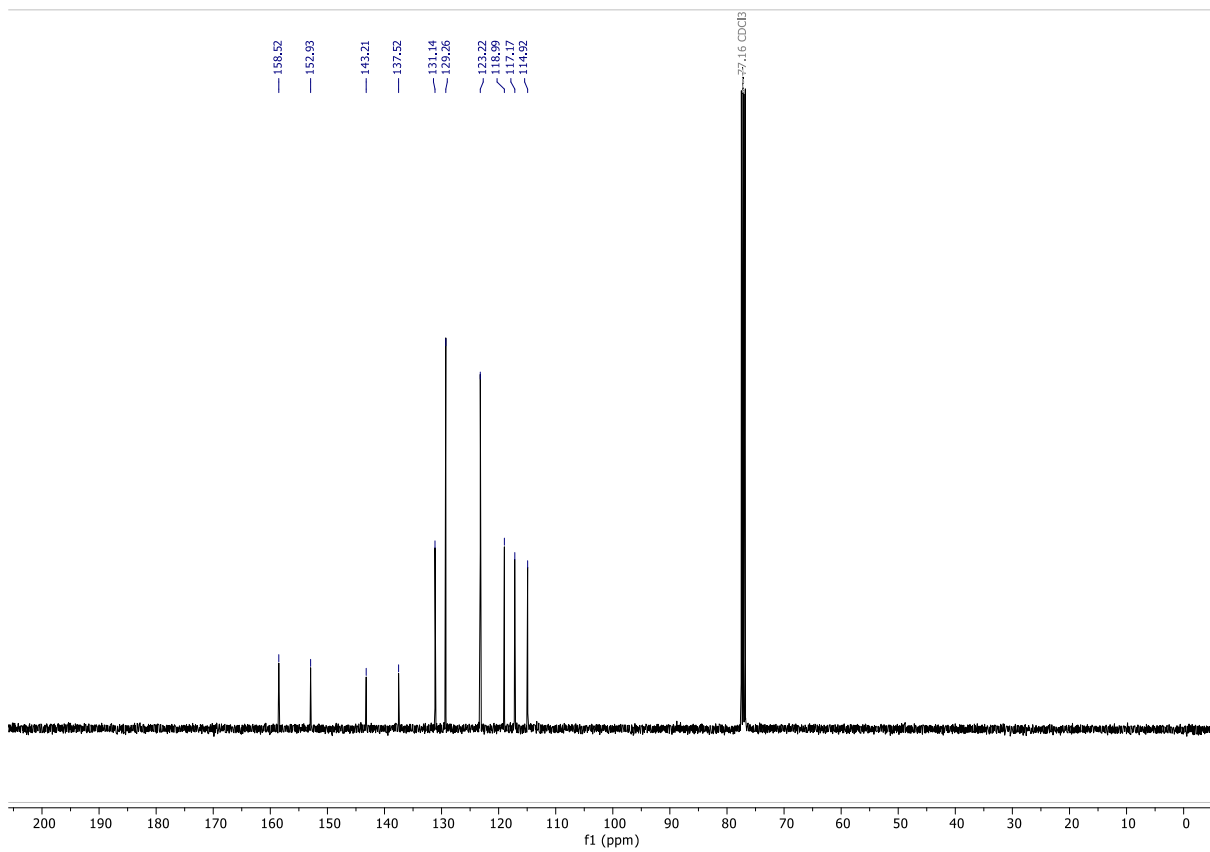


S3

¹H NMR (400 MHz, CDCl₃)

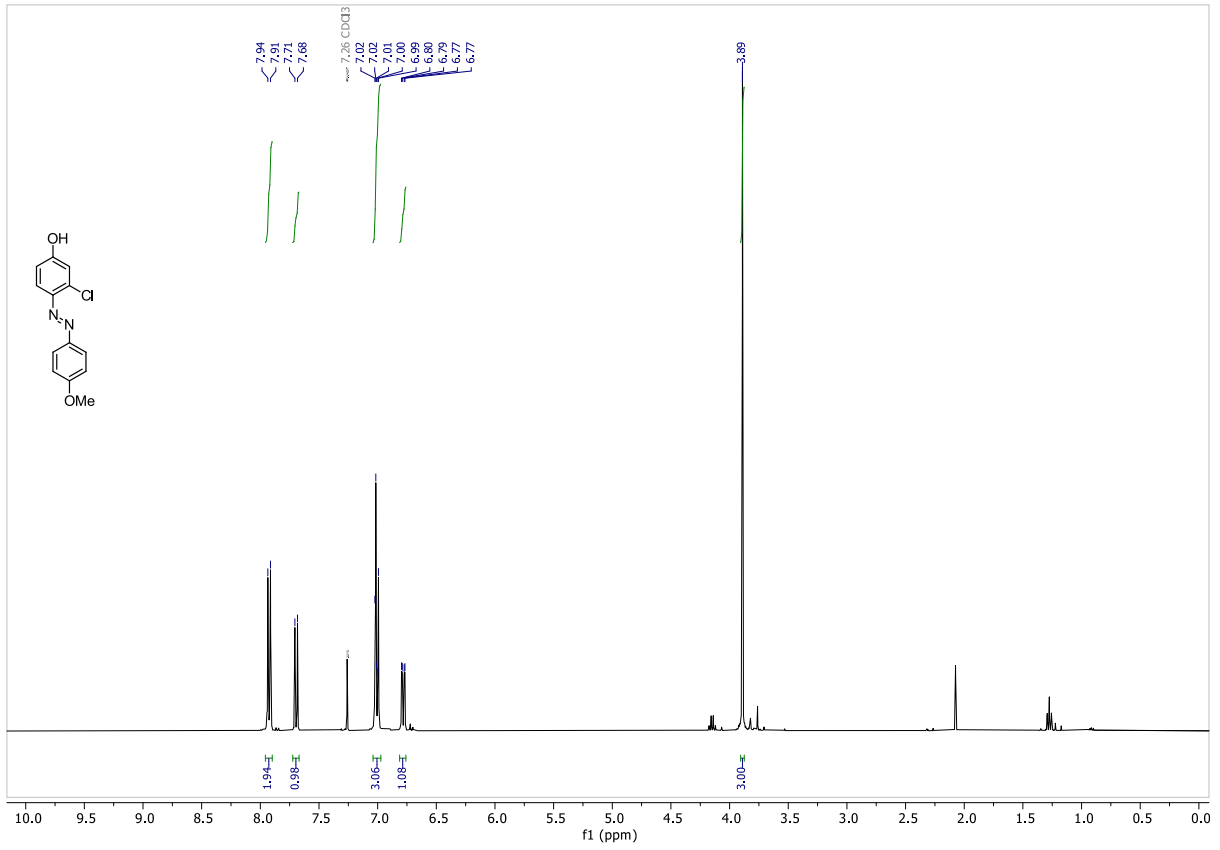


¹³C NMR (101 MHz, CDCl₃)

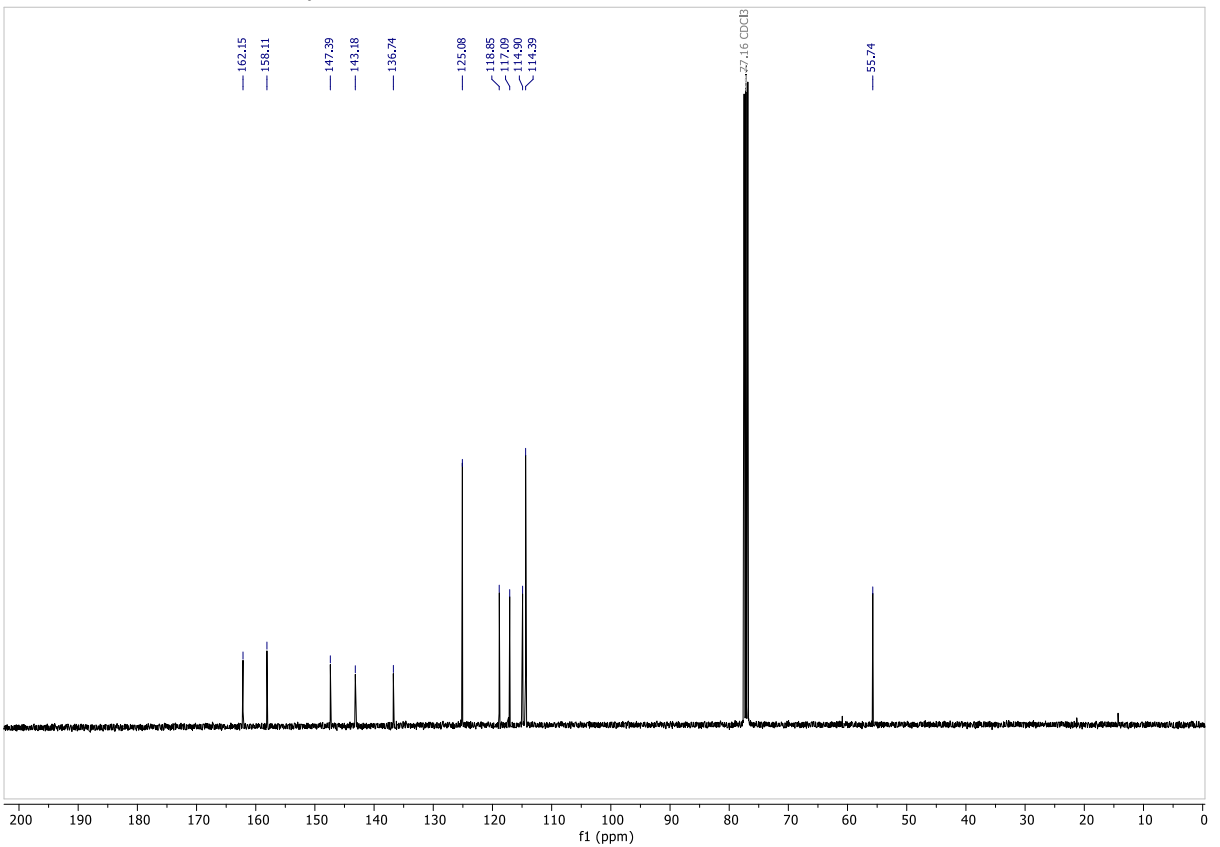


S4

¹H NMR (400 MHz, CDCl₃)

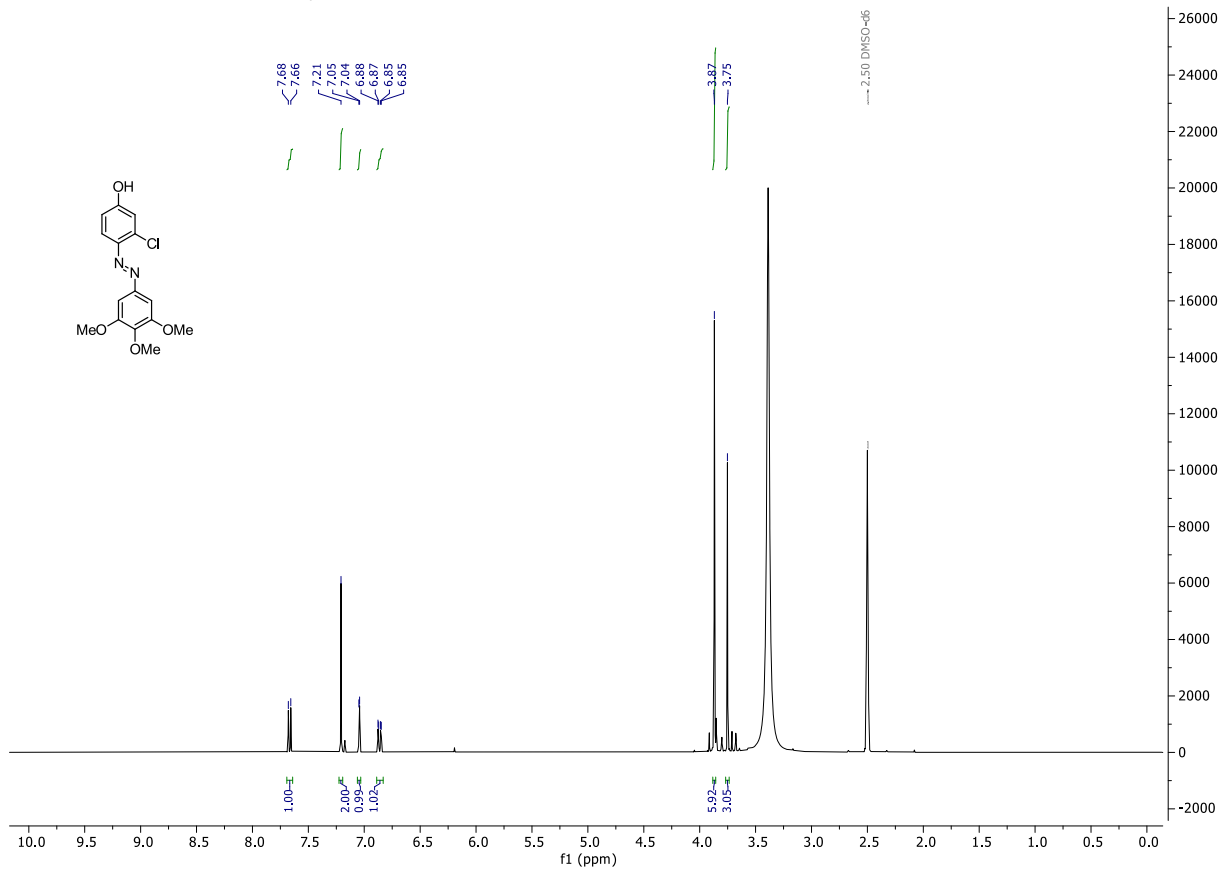


¹³C NMR (101 MHz, CDCl₃)



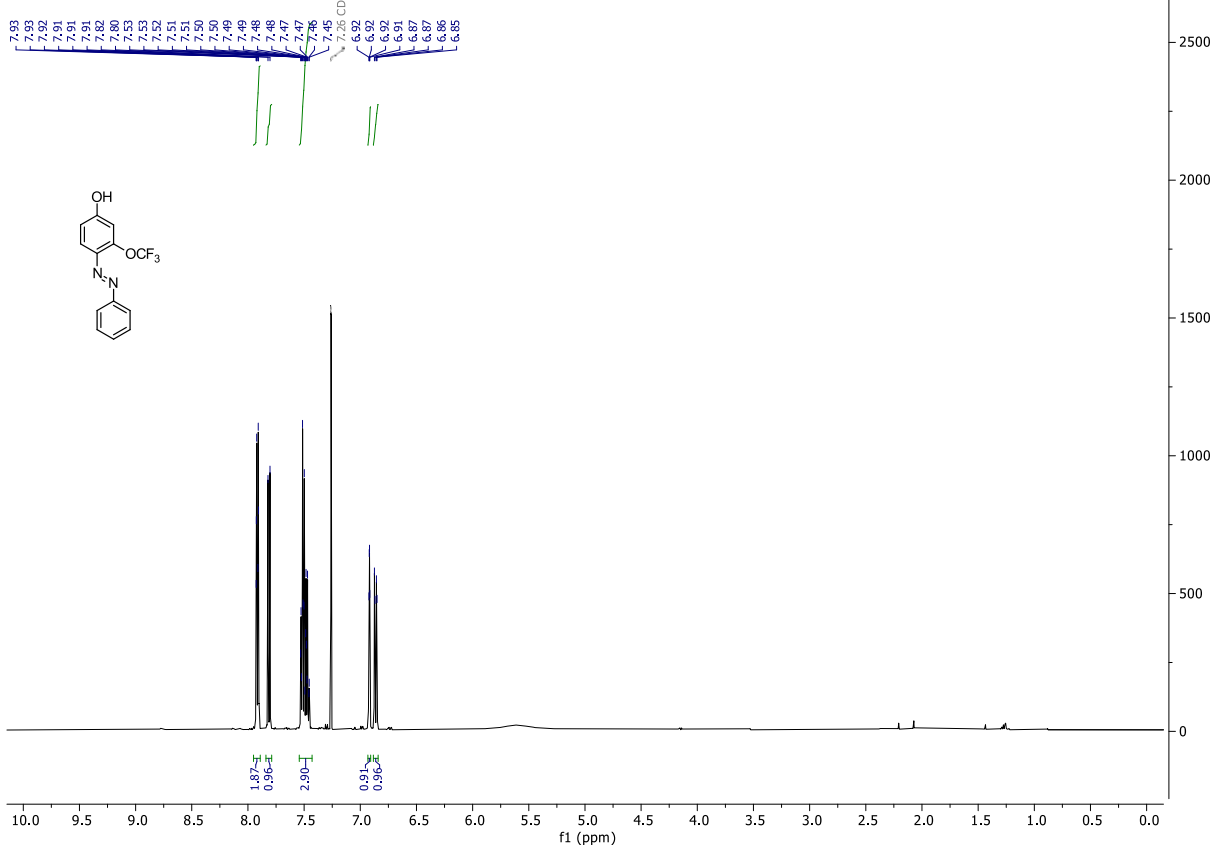
S5

¹H NMR (400 MHz, CDCl₃)

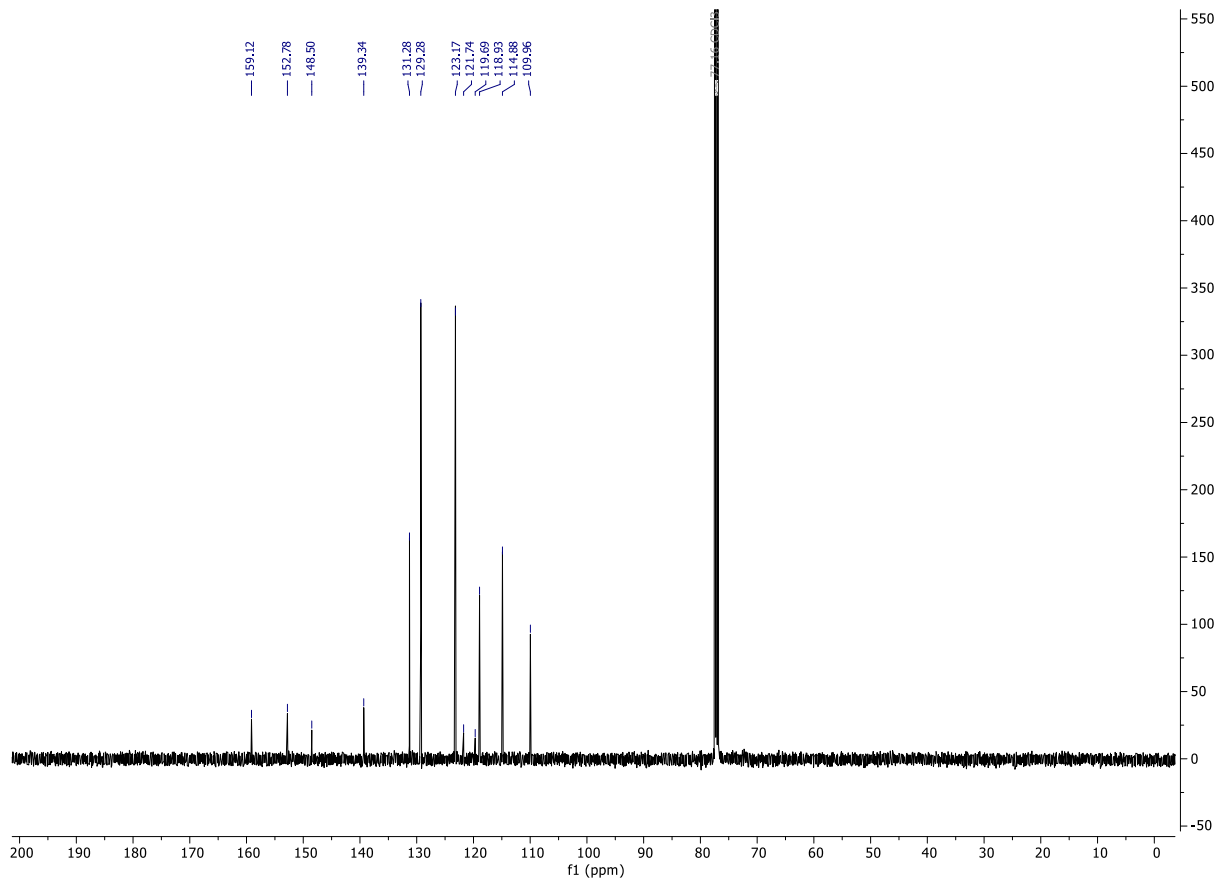


S6

¹H NMR (500 MHz, CDCl₃)

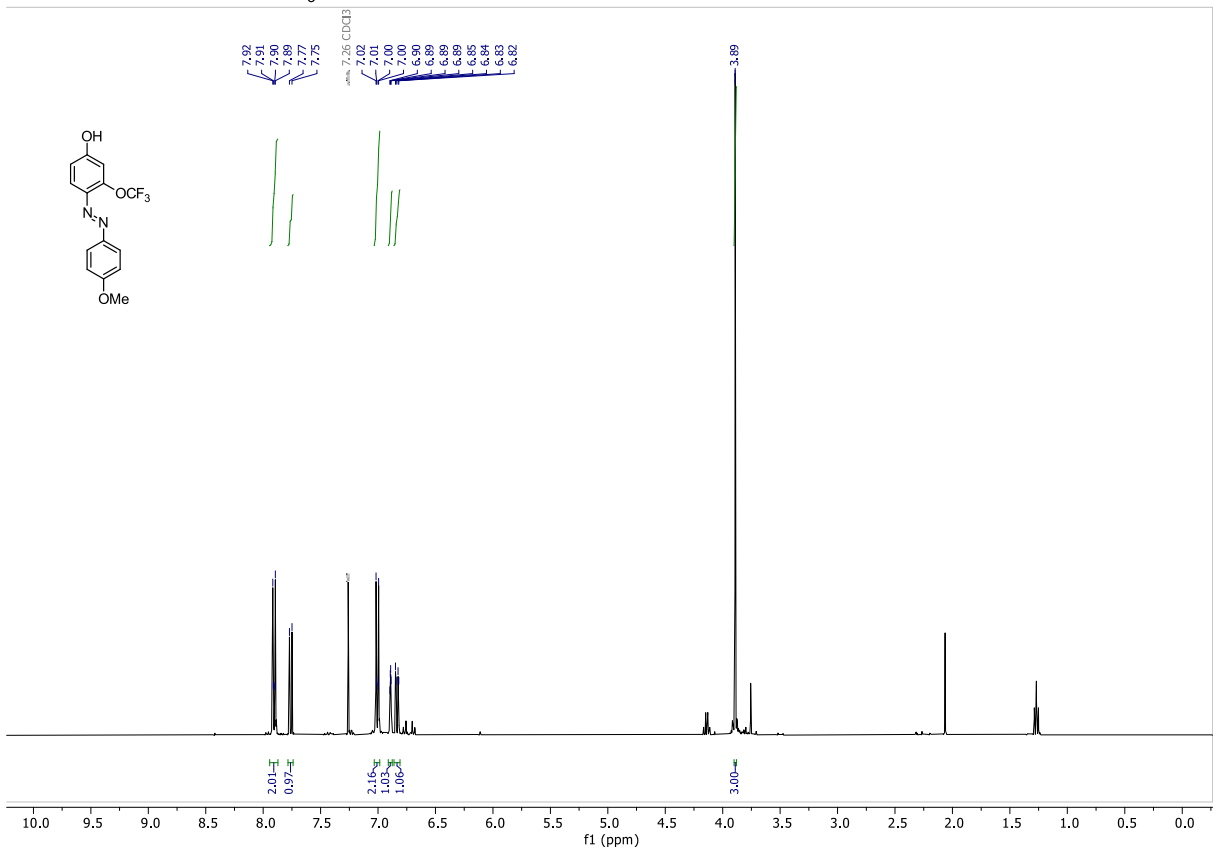


¹³C NMR (126 MHz, CDCl₃)

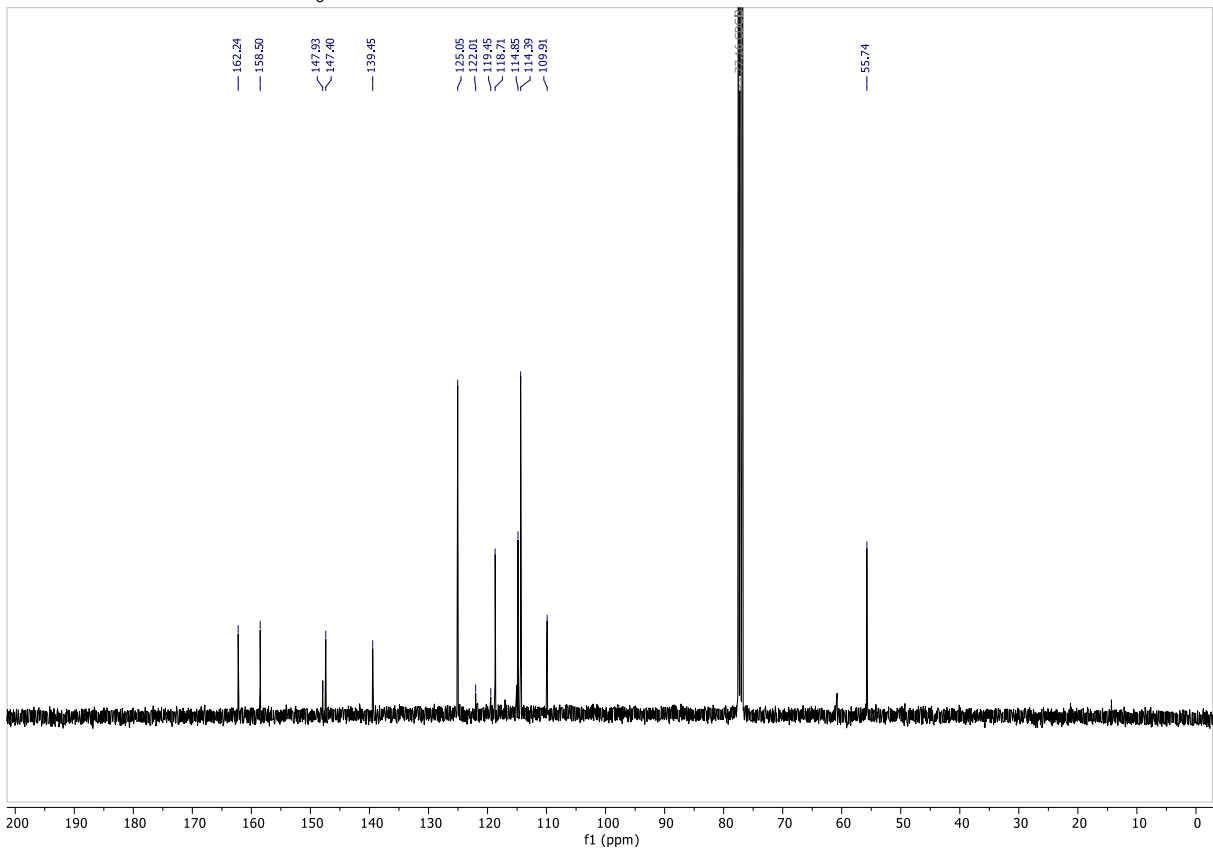


S7

¹H NMR (400 MHz, CDCl₃)

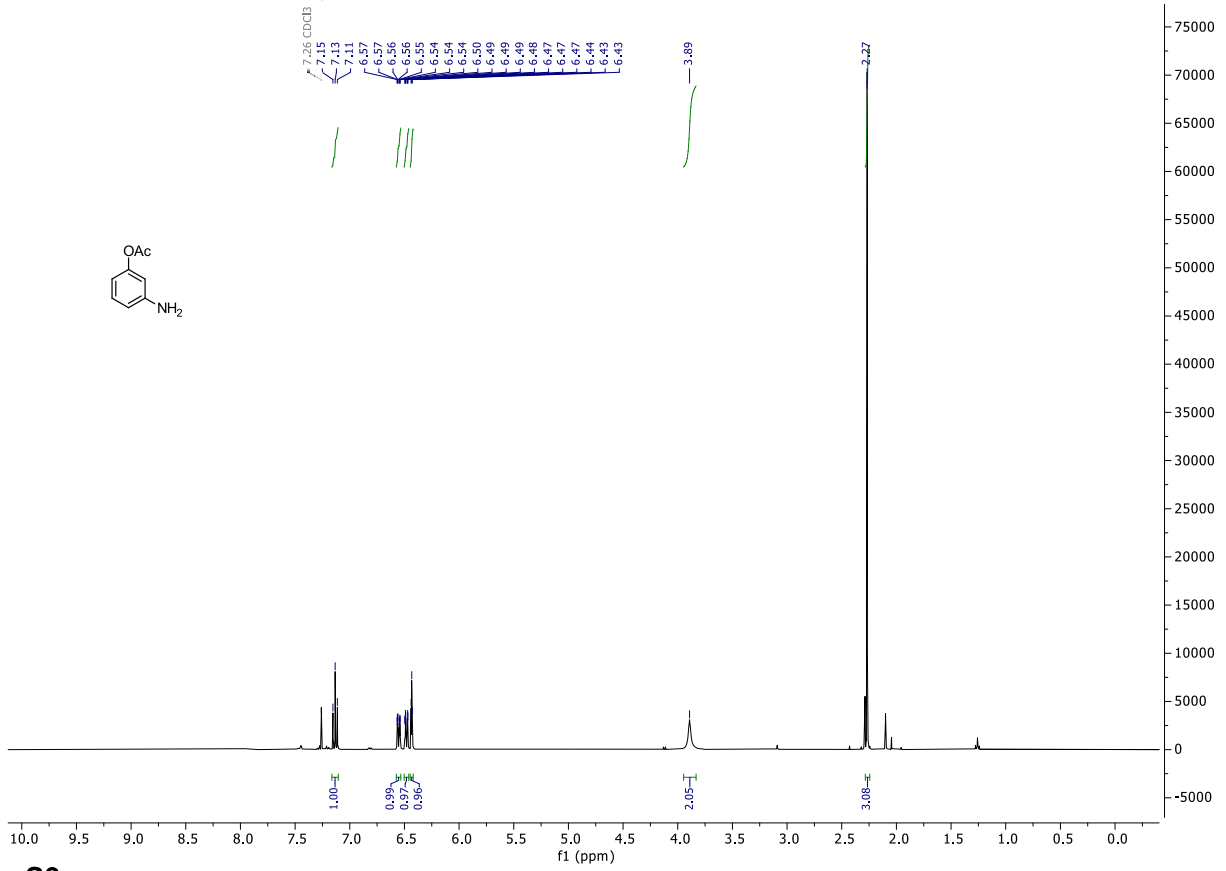


¹³C NMR (101 MHz, CDCl₃)



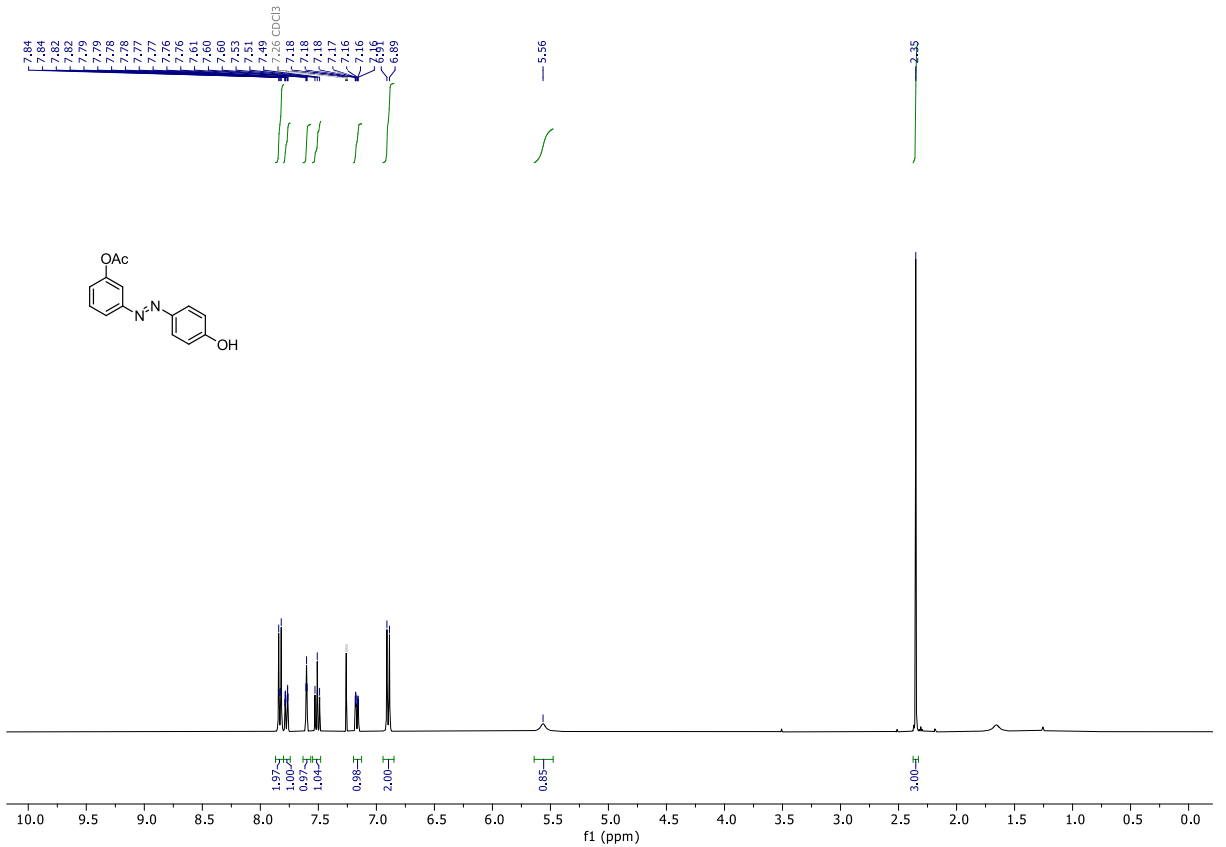
S8

¹H NMR (400 MHz, CDCl₃)



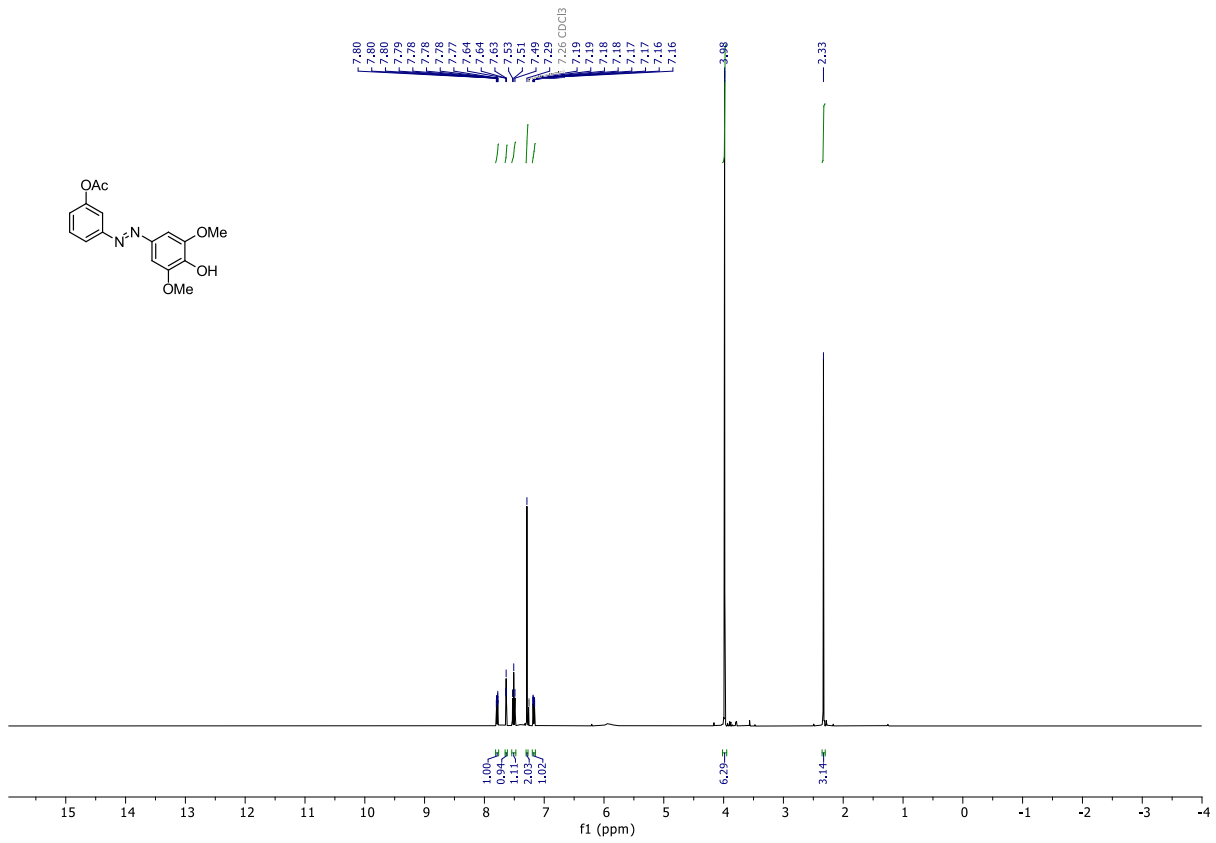
S9

¹H NMR (400 MHz, CDCl₃)



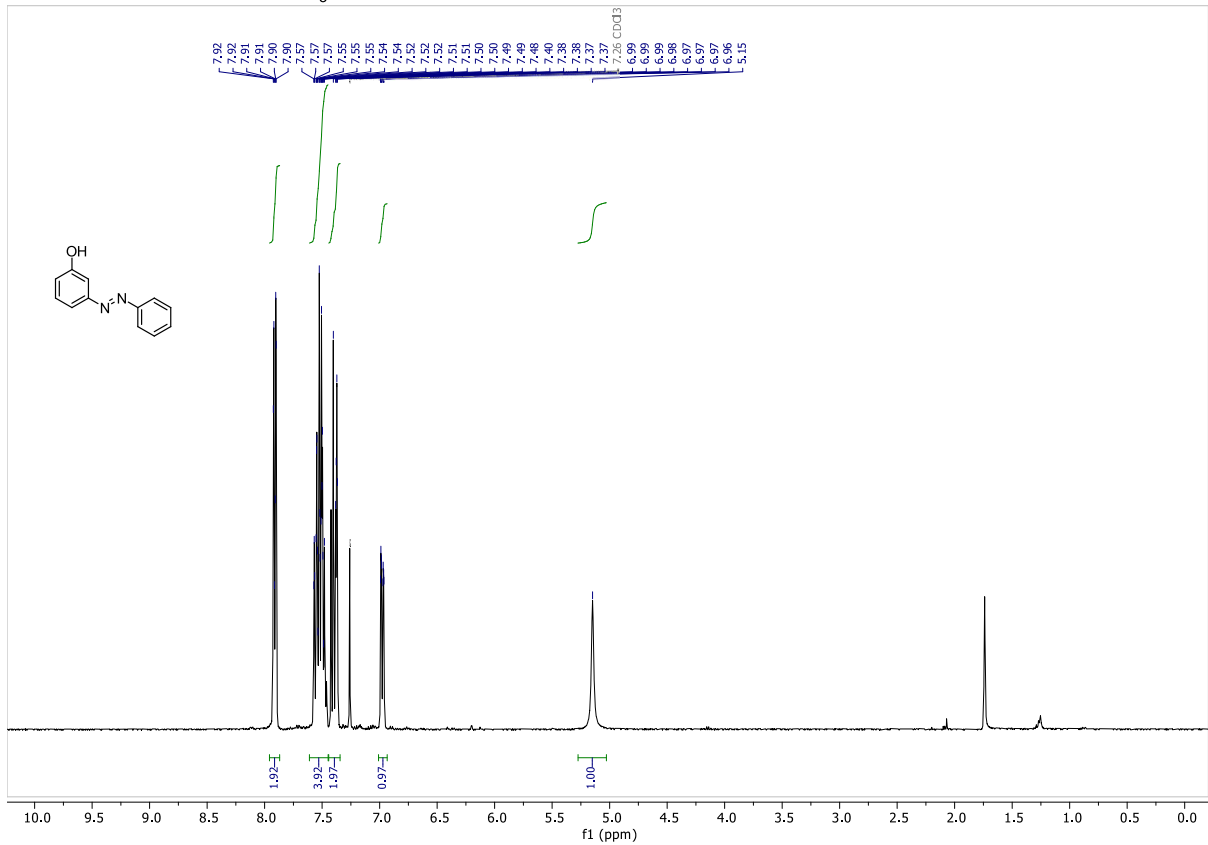
S10

$^1\text{H NMR}$ (400 MHz, CDCl_3)



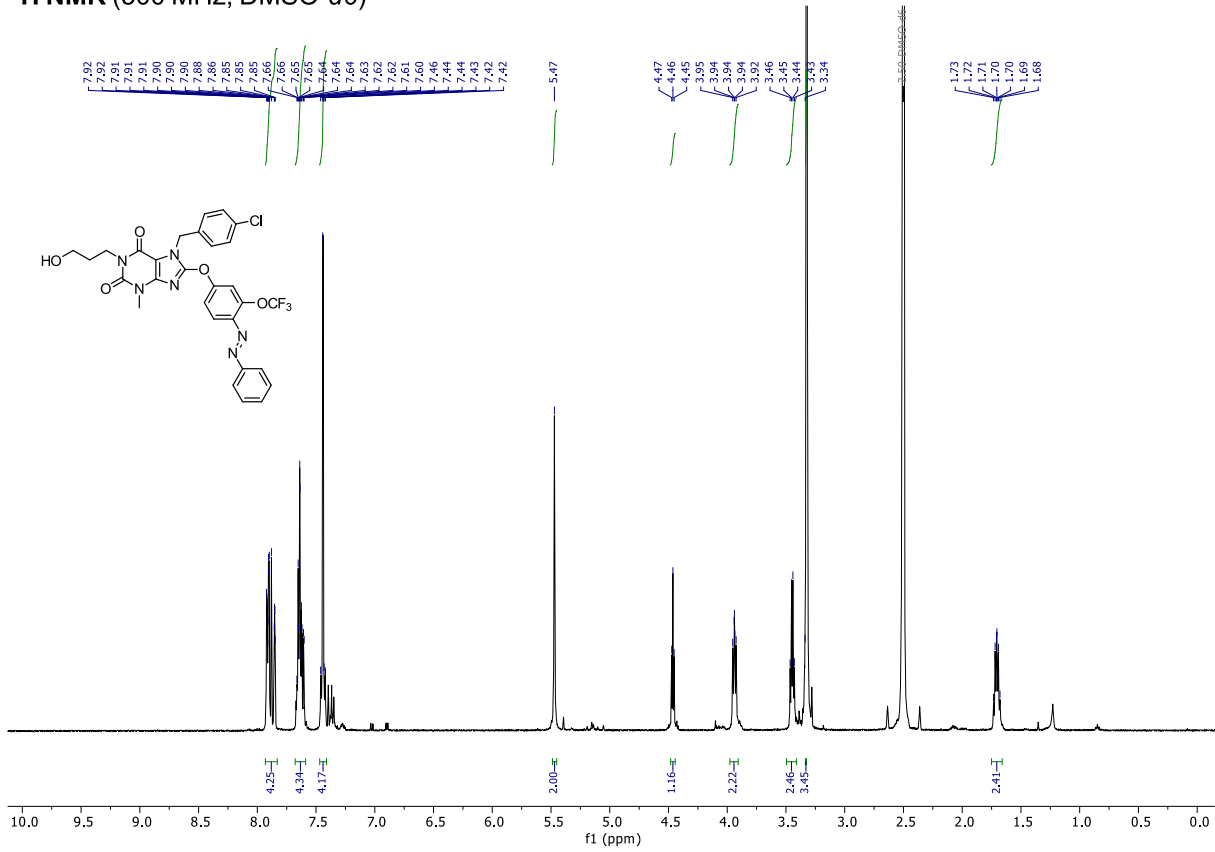
S13

$^1\text{H NMR}$ (400 MHz, CDCl_3)

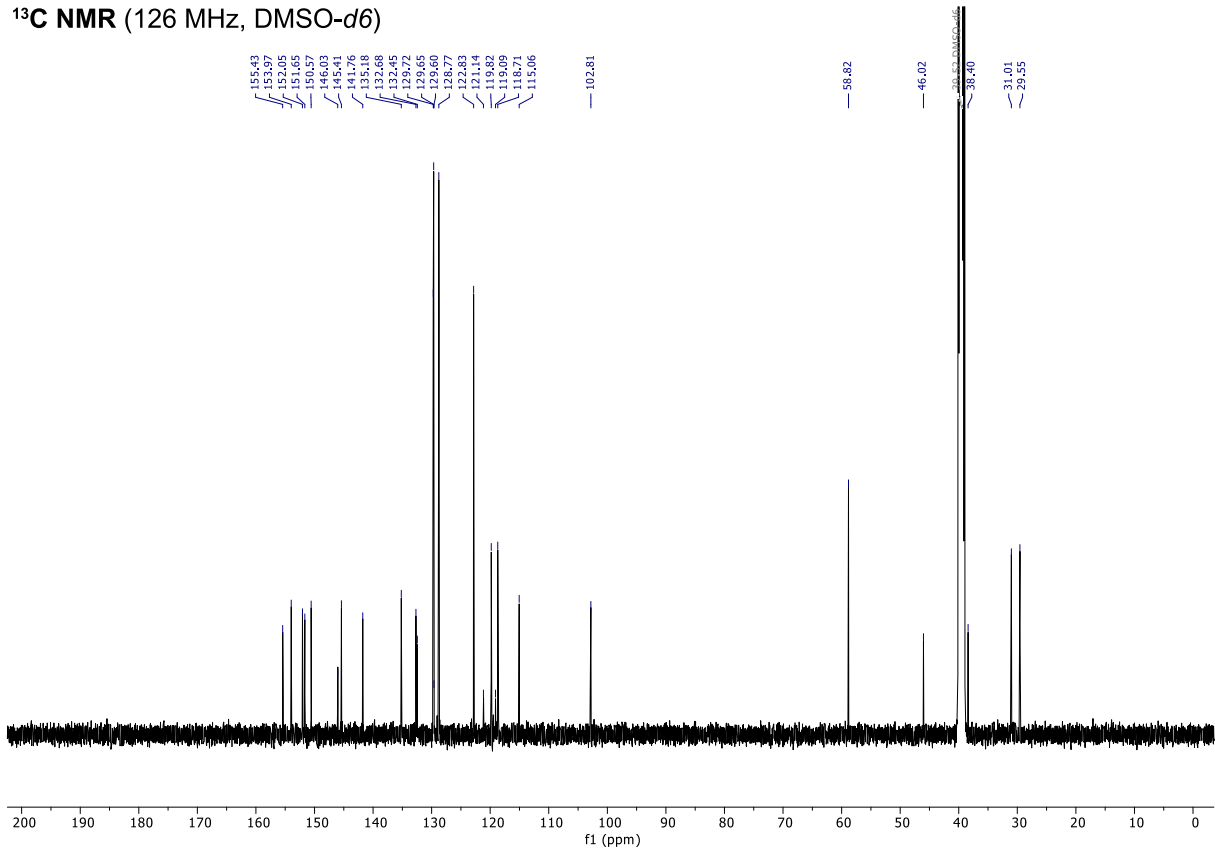


AzPico

¹H NMR (500 MHz, DMSO-d₆)

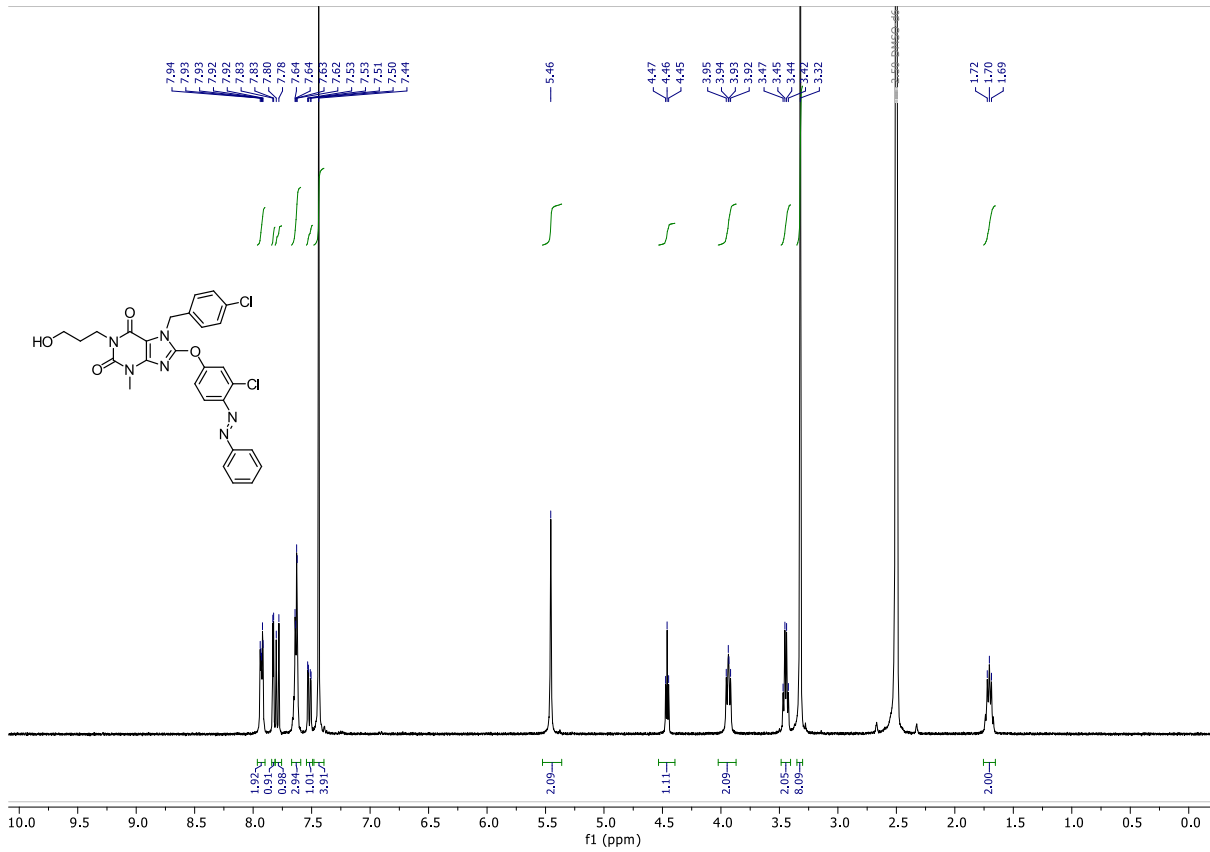


¹³C NMR (126 MHz, DMSO-d₆)

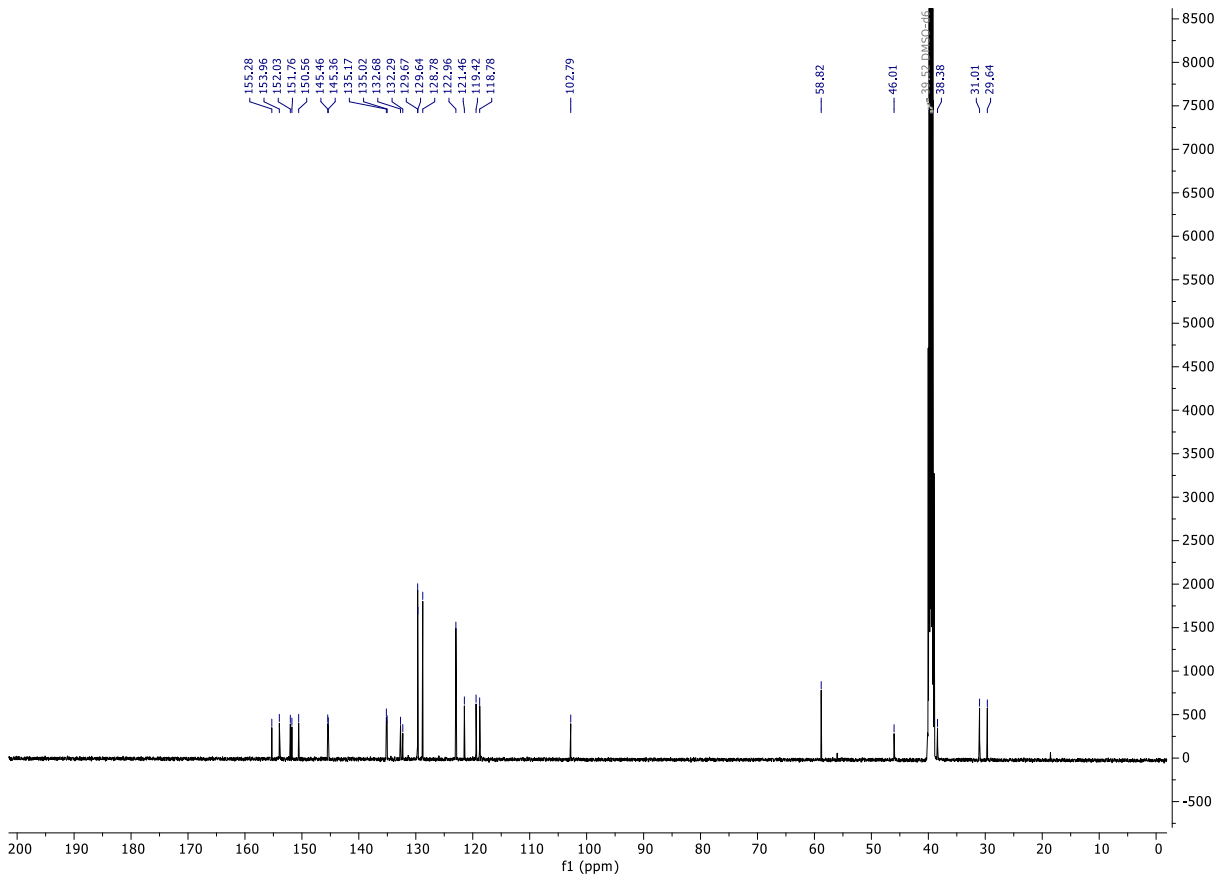


AzHC

¹H NMR (400 MHz, DMSO-d₆)

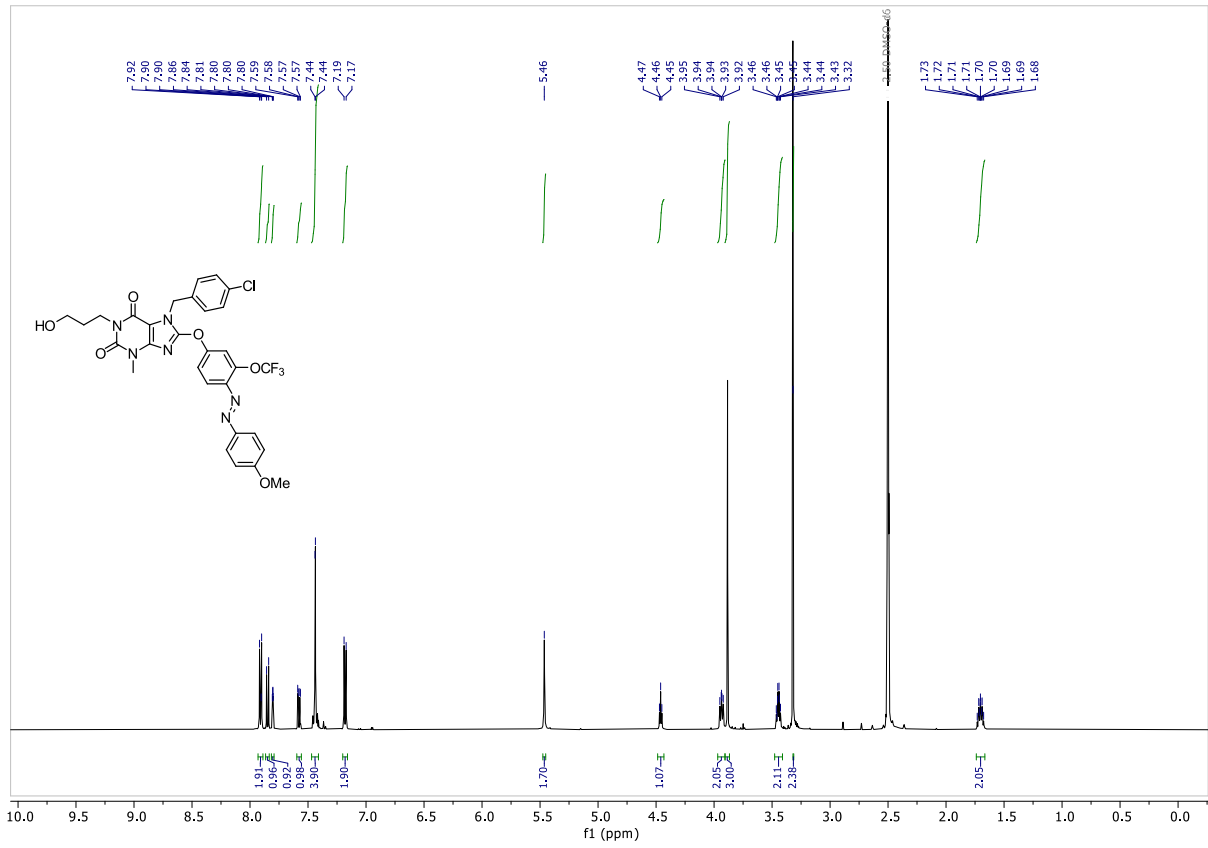


¹³C NMR (126 MHz, DMSO-d₆)

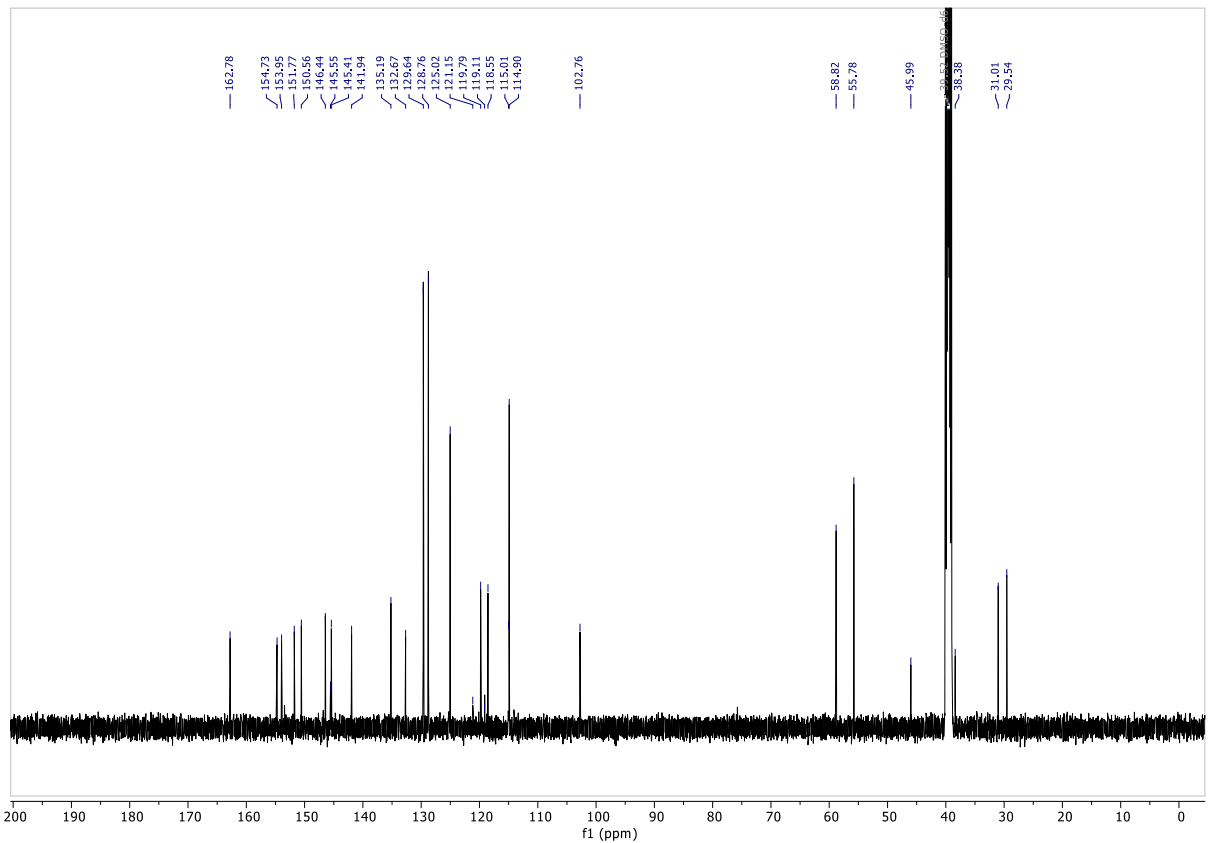


AzPico2

¹H NMR (500 MHz, DMSO-*d*₆)

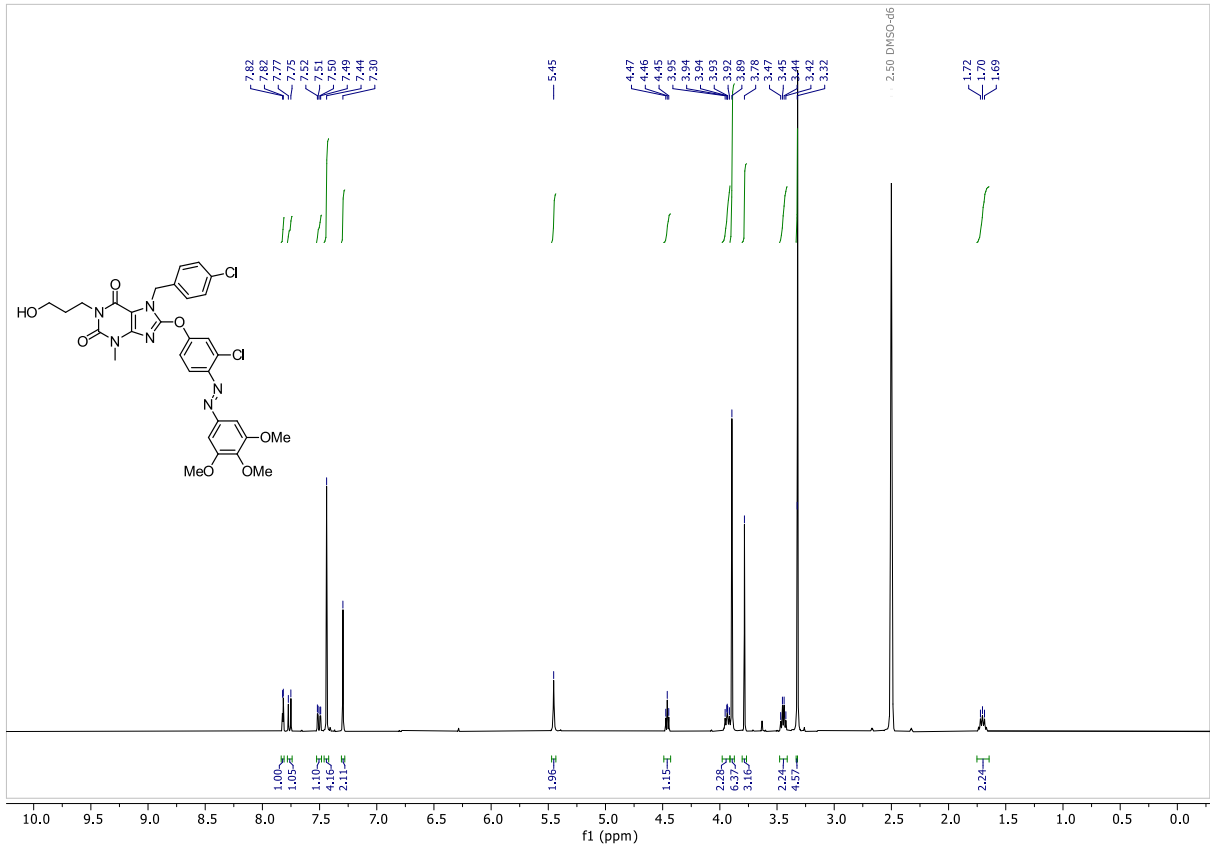


¹³C NMR (126 MHz, DMSO-*d*₆)

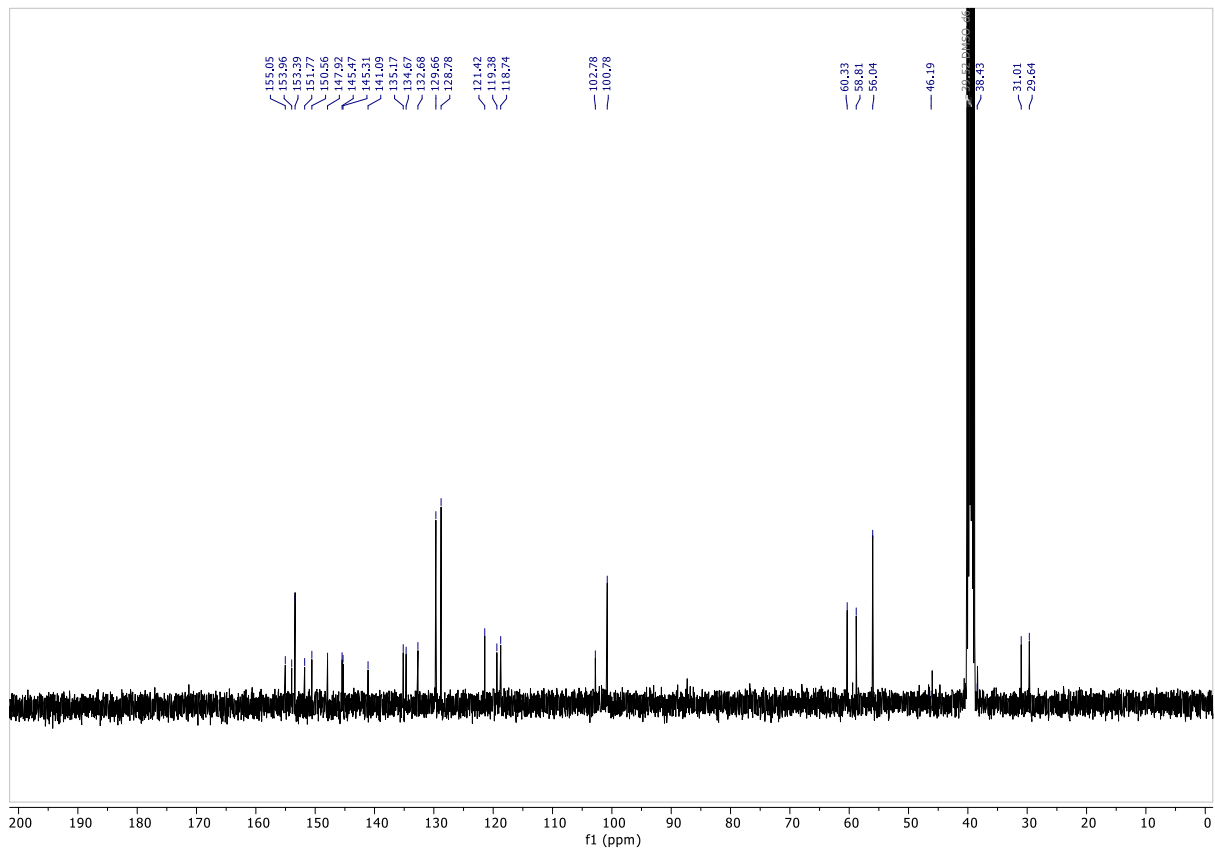


AzHC3

¹H NMR (400 MHz, DMSO-*d*₆)

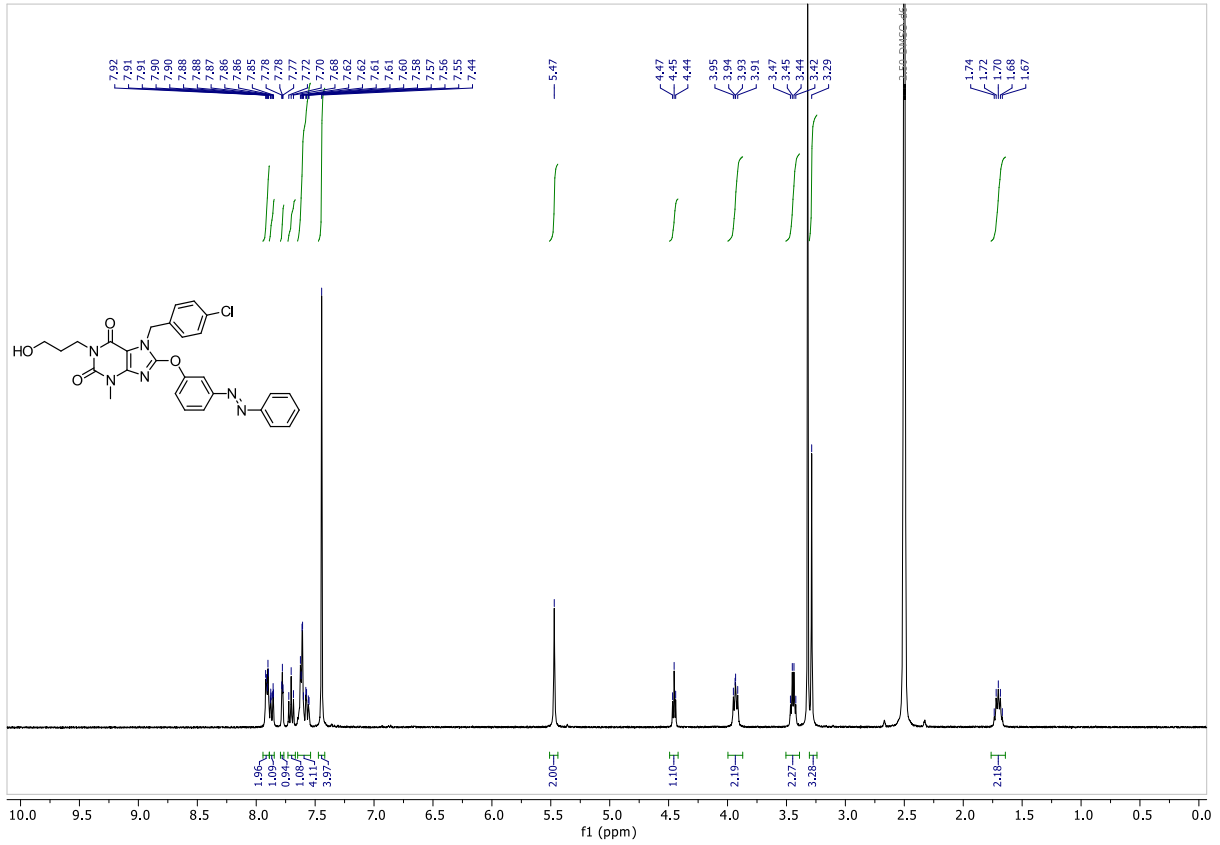


¹³C NMR (101 MHz, DMSO-*d*₆)

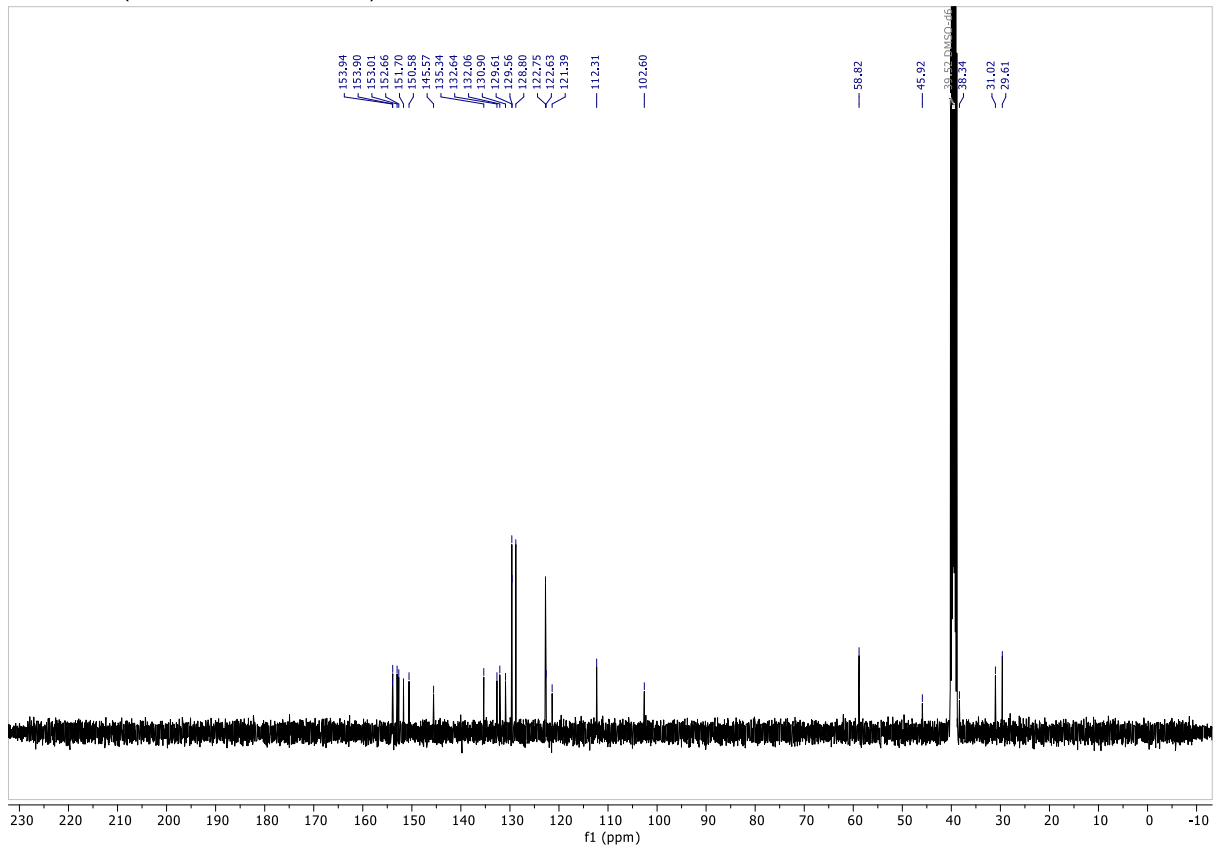


AzHC4

¹H NMR (400 MHz, DMSO-d₆)

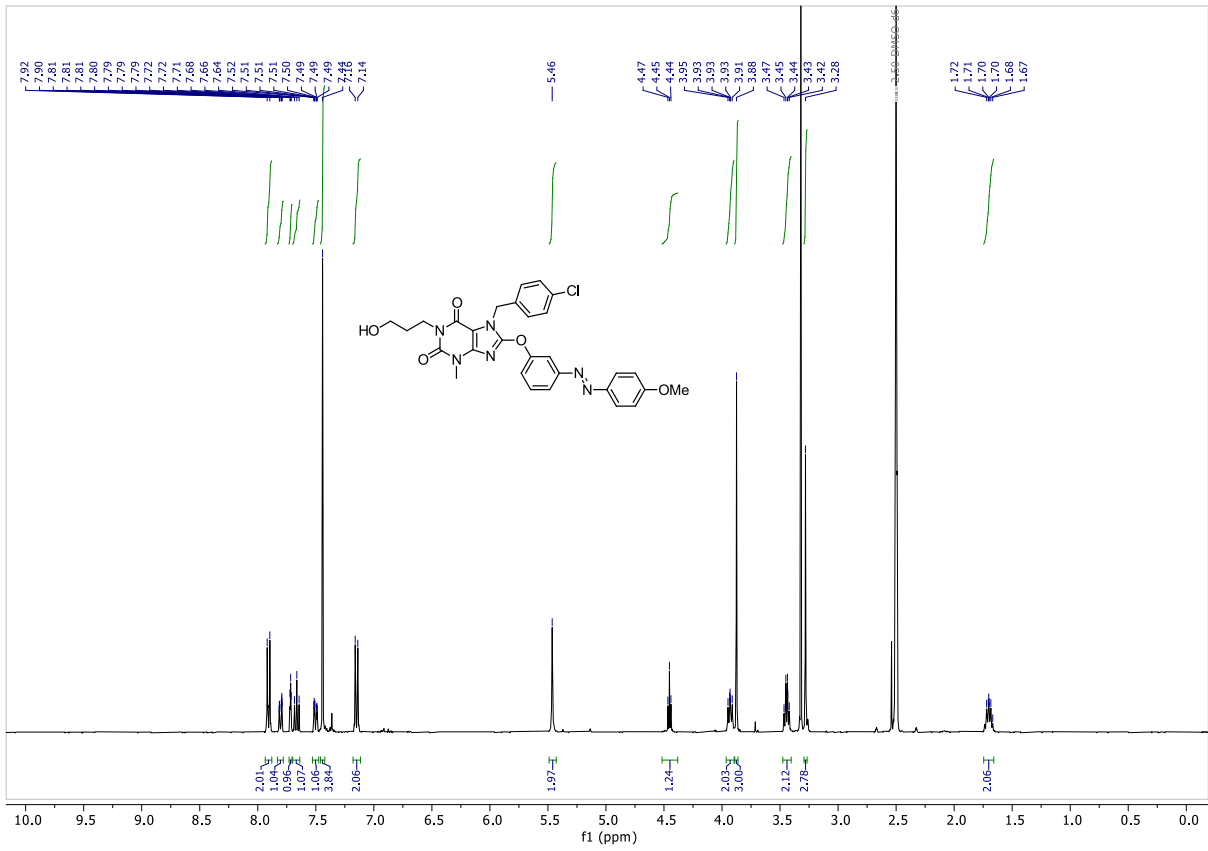


¹³C NMR (101 MHz, DMSO-d₆)

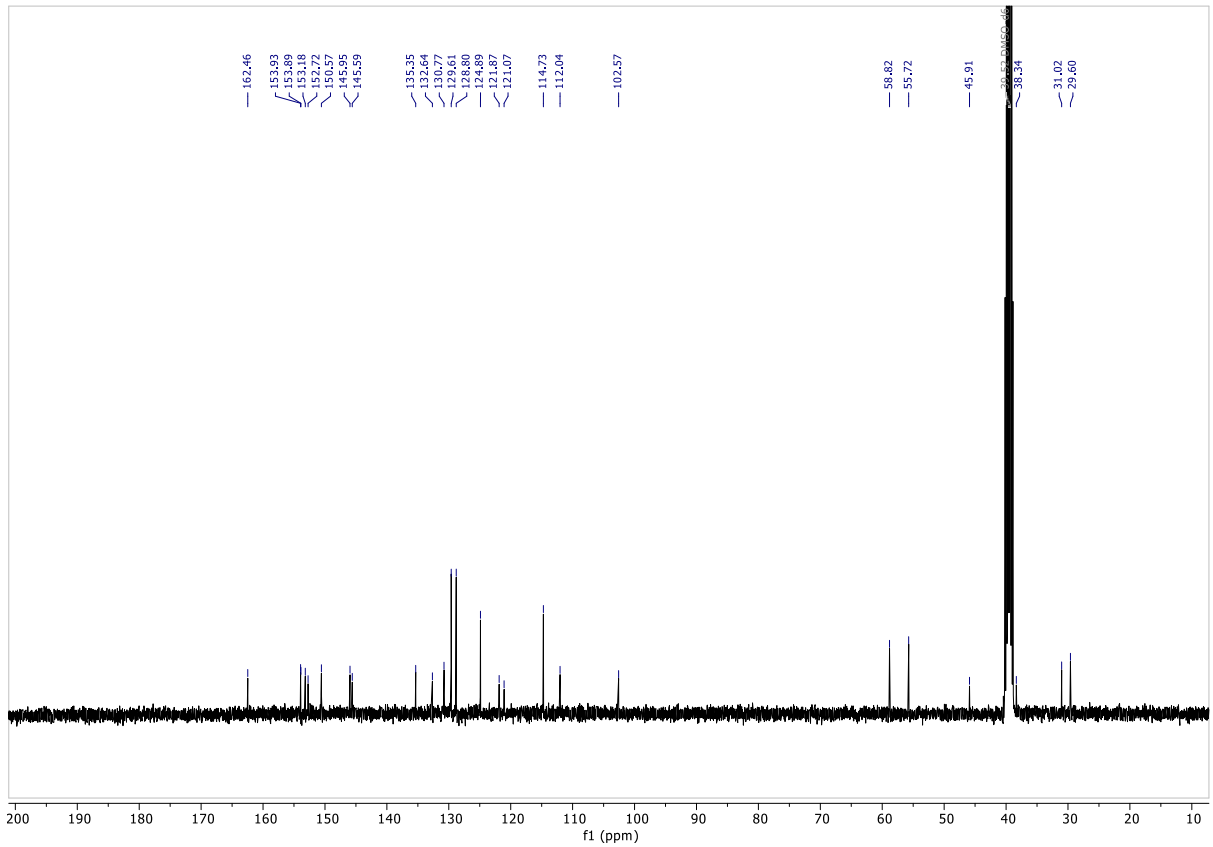


AzHC5

¹H NMR (400 MHz, DMSO-*d*₆)

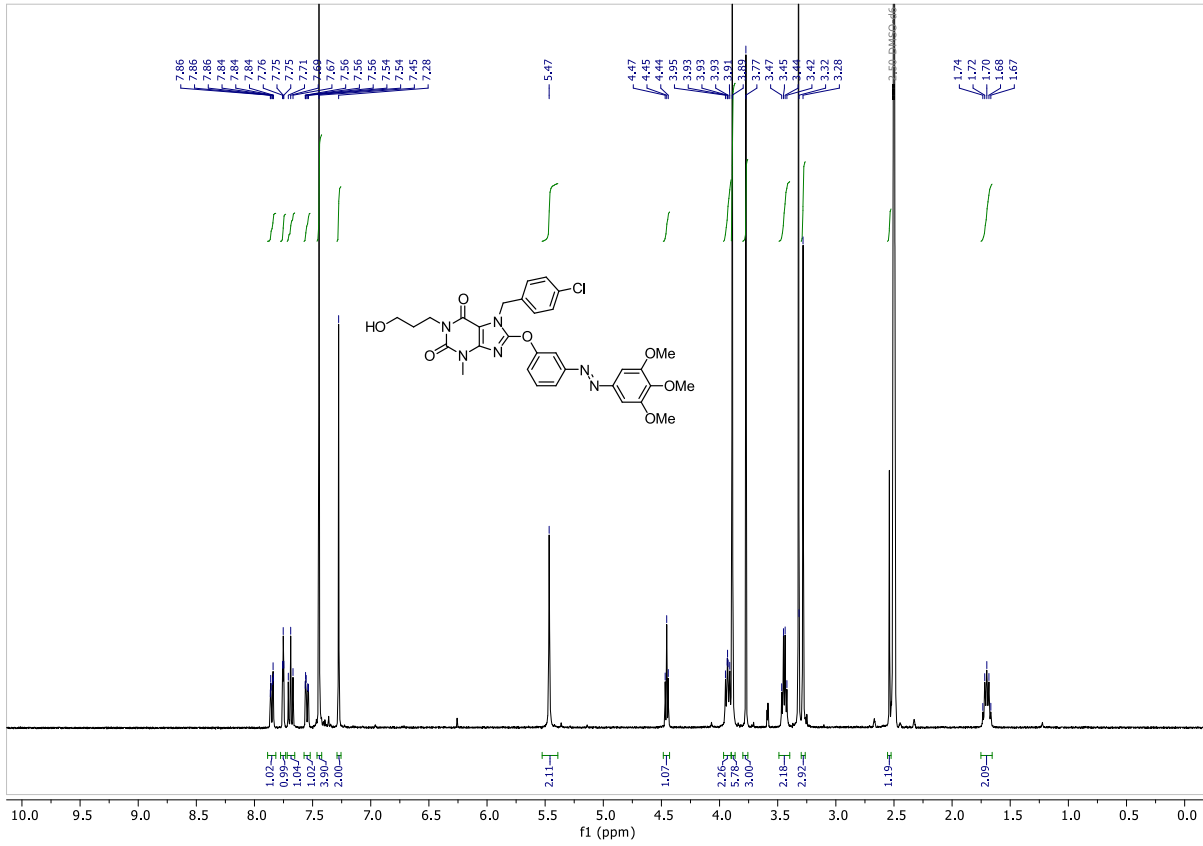


¹³C NMR (101 MHz, DMSO-*d*₆)

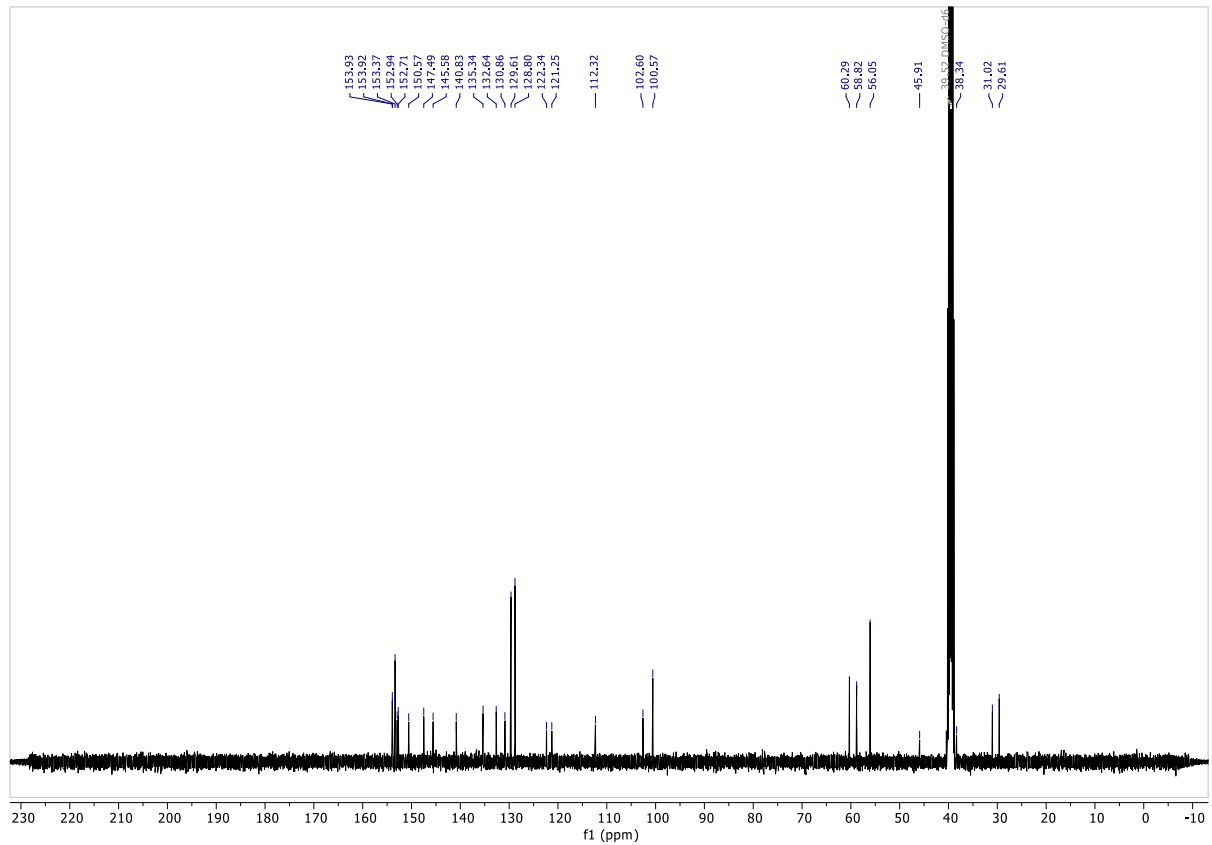


AzHC6

¹H NMR (400 MHz, DMSO-*d*₆)



¹³C NMR (101 MHz, DMSO-*d*₆)



11 Copies of Main Figures With Full Legends

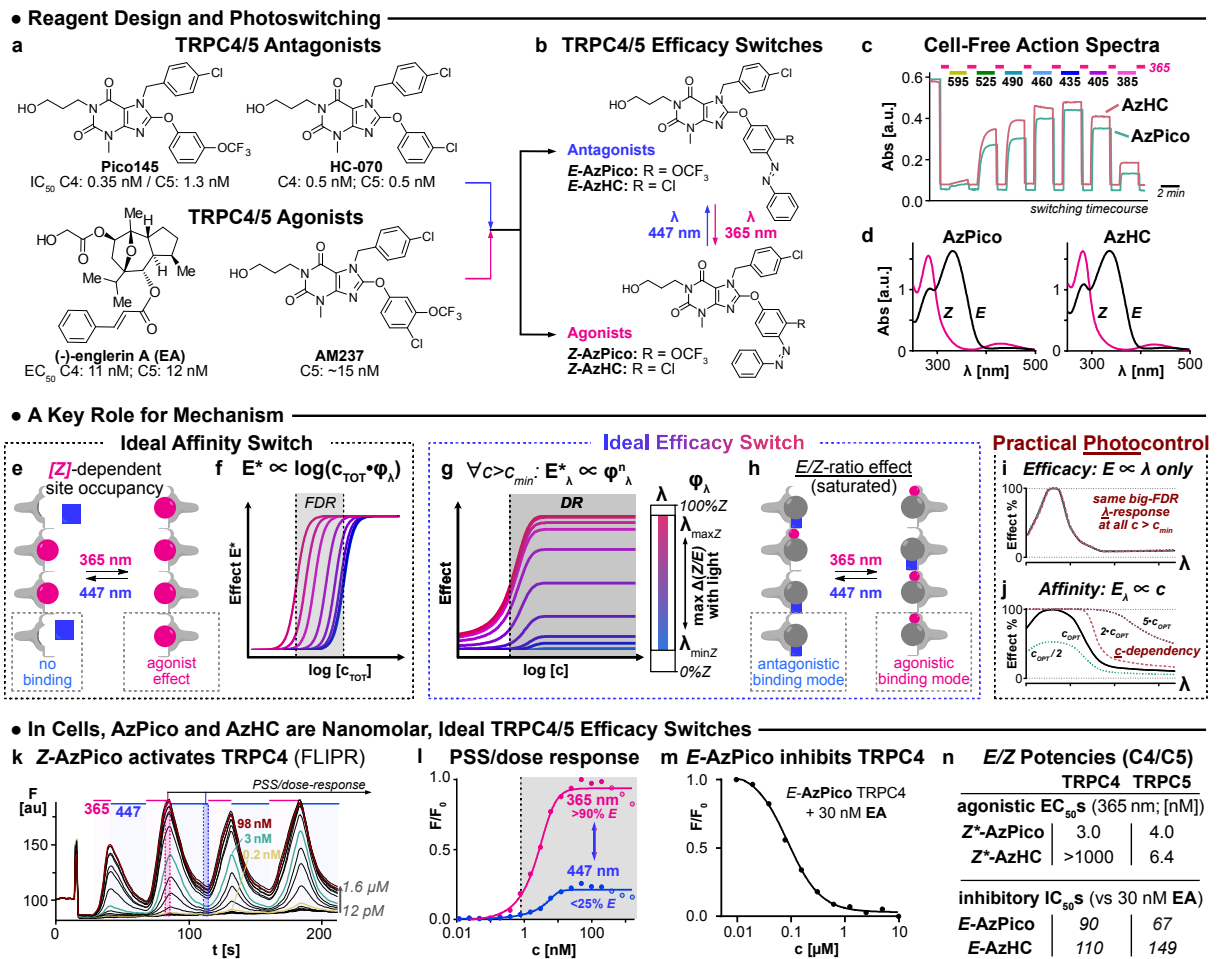


Figure S23 (copy of main figure 1): Efficacy photoswitches for TRPC4/5. **a**, Known TRPC4/5 modulators. **b**, Photoswitchable TRPC4/5 modulators **AzPico** and **AzHC**. **c-d**, Photoisomerisation action spectra and *E/Z* isomer absorption spectra of **AzPico** and **AzHC**. **e-f**, For an ideal affinity switch, only one isomer binds the target. Within the FDR window, binding site occupancy and thus biological effect E^* depend on the total switch concentration c_{TOT} and the PSS fraction of active isomer ϕ_λ . **g,h**, For an ideal efficacy switch, both isomers bind, with similar affinities, but with different efficacies. The dynamic range (DR) where the biological effect E^*_λ is PSS-dependent but concentration-independent covers all $c > c_{min}$. **i,j**, Photocontrol in practice: for an efficacy switch, small variations in PSS(λ) sensitively control performance (whereas in affinity switches they are unimportant); but even large variations in concentration, which would ruin the performance of an affinity switch, are irrelevant. **k,l**, Reversible Ca²⁺ influx modulation with **AzPico** under 365/447 nm cycles, as timecourse and peak amplitudes. **m**, **E-AzPico** binds competitively to **EA**. **n**, EC_{50} and IC_{50} values of *E/Z-AzPico* & **AzHC** on TRPC4 and TRPC5. (**k-n**, Fluo-4-loaded HEK_mTRPC4 β cells).

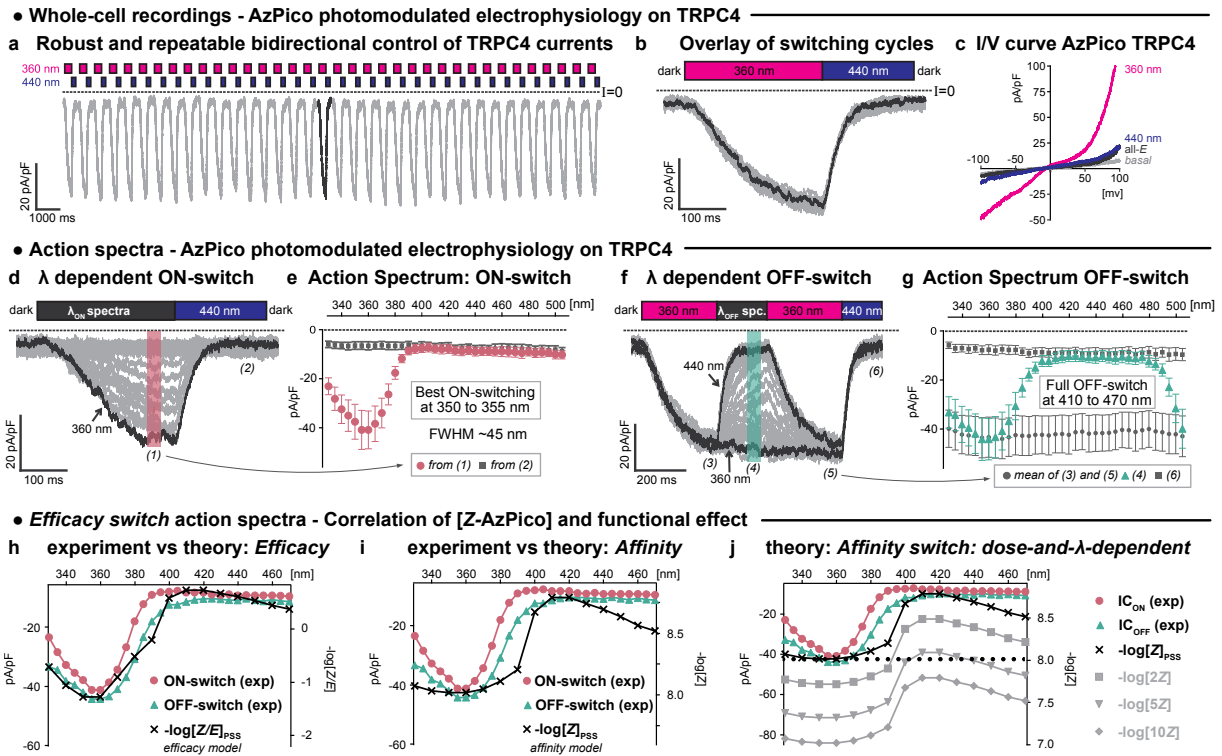
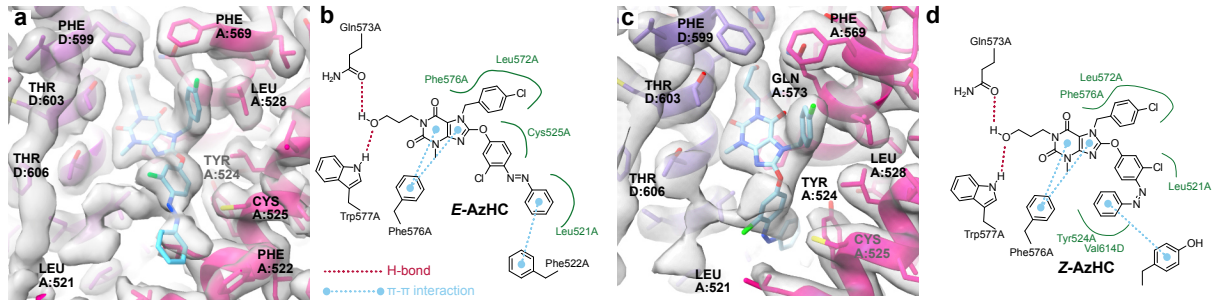


Figure S24 (copy of main figure 2 with extended legend): AzPico-photocontrolled electrophysiology of TRPC4. **a-g**, Electrophysiological whole-cell recordings of TRPC4 currents in voltage clamp mode (**a,b,d-g**: $V_h = -80$ mV; **c**: V_h scan) in HEK293 cells with 10 nM **AzPico** during photoswitching. **a-b**, Reproducibility of 36 consecutive photoswitching cycles of 360/440 nm (**a**: time-course; **b**: overlay of all cycles). **c**, I/V curves show that 440 nm drives almost full return to baseline currents throughout the applied voltage range. **d-g**, Spectral scans to extract the wavelength dependency of channel current photoswitch-on (**d-e**, cycles of $\lambda_{ON}/440$ nm) and photoswitch-off (**f-g**, 360 nm/ λ_{OFF}). Panel **e** shows action spectra derived from **d** (plotted: inward currents at timepoints (1) for λ_{ON} , (2) for 440 nm); panel **g** shows action spectra derived from **f** (plotted: at timepoints (2) for λ_{OFF} , means of (1) and (3) for 360 nm, and (4) for 440 nm). In panel **f**, the reference cycle at 360/440 nm after each 360 nm/ λ_{OFF} scan cycle was incorporated so as to be able to exclude that artifacts from e.g. run-down or prolonged channel opening might be present. **h-j**: Ephys action spectra of **AzPico** match PSS-informed expectations for an efficacy switch (**h**), not an affinity switch (**i**). This is important, since an affinity switch would have severe concentration dependency (**j**).

• Cryo-EM structures of *E/Z*-AzHC in complex with TRPC5



• Cryo-EM structures of *E/Z*-AzPico in complex with TRPC4

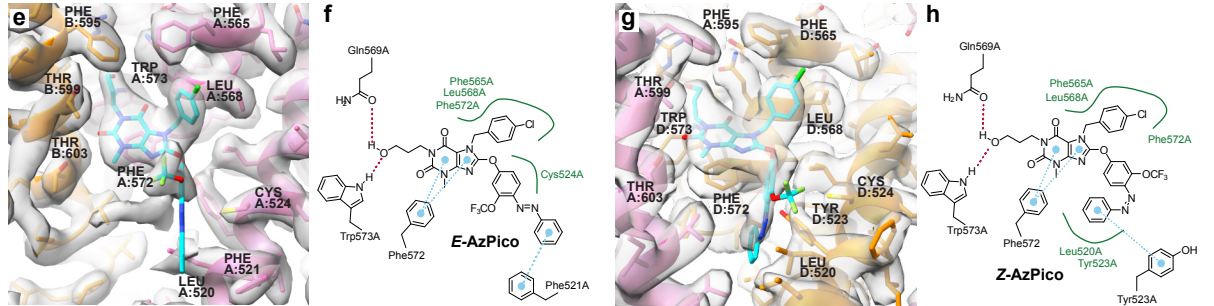
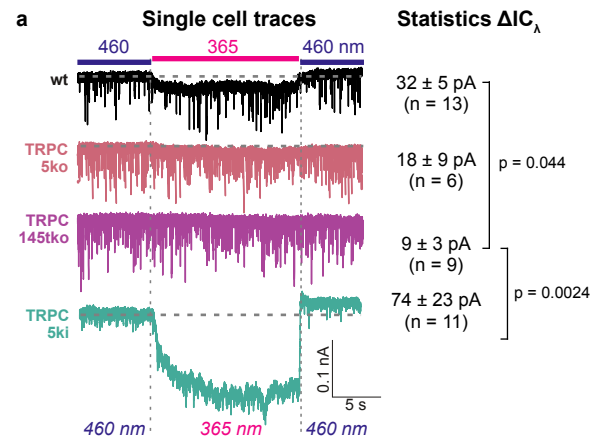


Figure S25 (copy of main figure 3): Structures of TRPC4/5 in complex with *E/Z*-isomers of efficacy photoswitches. **a-d**, hTRPC5:*E/Z*-AzHC complexes (*E*: 2.6 Å, PDB: 9G4Y, EMDB: 51074; *Z*: 2.9 Å, PDB: 9G50, EMD: 51076; C1 symmetry). Note the flip of the distal azobenzene ring. **e-g**, TRPC4_{DR}:*E/Z*-AzPico complexes (*E*: 3.0 Å, PDB 9FXL, EMDB 50850; *Z*: 3.1 Å, PDB 9FXM, EMDB: 50851; C1 symmetry). Each complex's best-resolved xanthine binding site is highlighted; 2D maps of ligand-protein interactions are shown.

• Photocontrol of primary hippocampal neurons (AzPico)



• Photocontrol of primary chromaffin cells (AzPico)

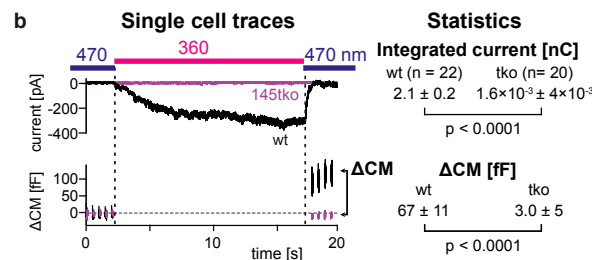


Figure S26 (copy of main figure 4): AzPico (30 nM) photoswitchably evokes currents in primary neuronal and neuroendocrine cells with endogenous TRPC levels (single cell traces at left, group statistics at right). **a**, photoswitching-based current differentials ΔIC_{λ} in hippocampal neurons (currents at 365 nm relative to 460 nm). **b**, photoswitch-based currents and net charge transfer (top) correlate to membrane capacitance changes ΔCM (bottom), indicating that phototriggering of TRPC[1]/4/5 leads to exocytosis (details at **Figure S20**).

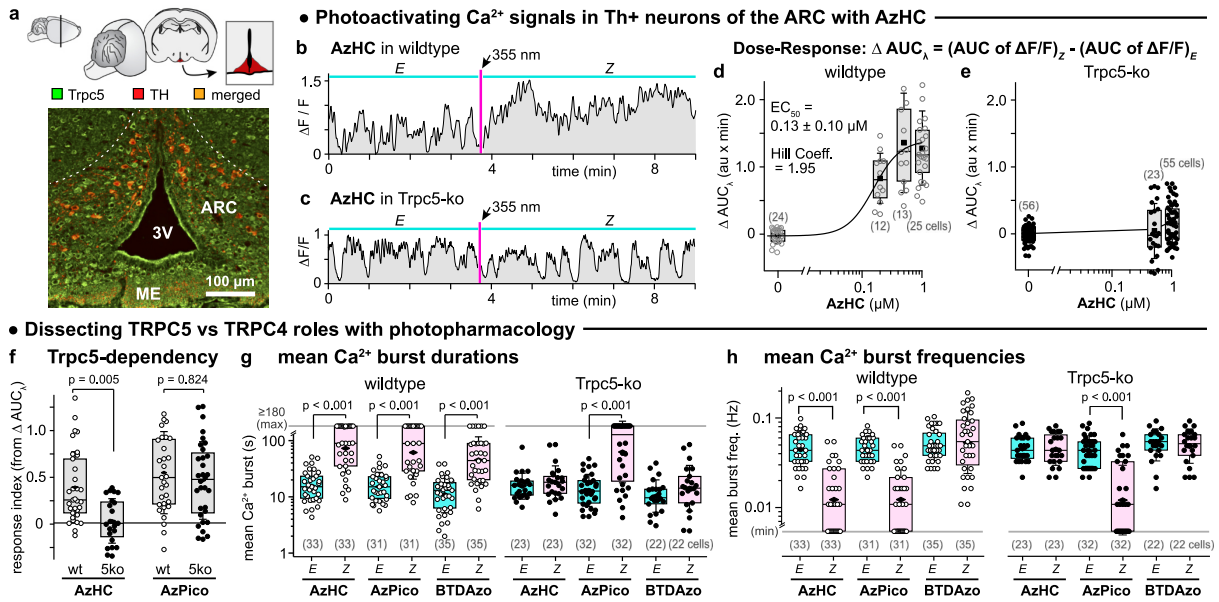


Figure S27 (copy of main figure 5 with extended legend): AzHC and AzPico are potent photoswitchable activators of TRPC-dependent Ca²⁺ responses in mouse hypothalamus. **a**, immunohistochemical (IHC) image of TRPC5 (green) and Th⁺ neurons (red, tdTomato) in a brain slice of a Th-tdTomato mouse. 3V, third ventricle; ME, median eminence. Th⁺ neurons of the dorsomedial ARC express TRPC5 (yellow, merged). Cartoon of the coronal brain slice and region of the ARC (red) are indicated above the IHC image. **b-h**, Ca²⁺ responses in Th⁺ neurons of Th-GCaMP6f (wildtype or wt) or Th-GCaMP6f- Δ Trpc5 (Trpc5-ko or 5ko) mice. **b,c**, Single-cell Ca²⁺ traces before ("E") and after ("Z") a 355 nm pulse (default 67 ms long). **d,e**, ΔAUC_{λ} : light-dependency of the area under the curves as acquired in (**b,c**). **f**, **AzHC** only photocontrols TRPC5-dependent Ca²⁺ responses; **AzPico** can photocontrol Ca²⁺ responses by another route (likely TRPC4) (the numbers of cells in each group are 33 & 23 (**AzHC** wt & 5ko), 31 & 32 (**AzPico** wt & 5ko)). **g,h**, mean Ca²⁺ burst durations and frequencies in wt and 5ko upon E→Z photoswitching. The maximum measurement time window of 180 s results in **boundary values** e.g. when a cell has high signal throughout, its burst duration is capped at 180 s (frequency 0.006 Hz). For the sake of statistics, these values are taken literally in the calculation of the mean, median, SD, and statistical significance. Since boundary values only arise for Z-switches but not the E-switches to which their statistical significance is calculated, the p-values presented are true upper bound p-values (higher statistical significance would be found if measurement were continued longer). Since the absolute size as well as the statistical significance of the EZ differentials in the results are clear (and since these are the goal of the entire paper), we are satisfied with the very conservative underestimate that this data and analysis convey, about the power of the reagents' photocontrol in biology. Other significant p-values are: (i) Z-BTDAzo vs Z-AzHC, p < 0.001; (ii) Z-BTDAzo vs Z-AzPico, p < 0.027. (Default settings: **AzHC/AzPico** at 500 nM except in dose-response; **BTDAzo** at 10 μ M; **d-h**: each point is 1 cell, (n) cells per group; box plots show interquartile ranges, median (line), mean (black rhombus), and SD whiskers; **f-h**: Kruskal-Wallis ANOVA, Dunn's p values; for min/max values and other details, see **Figure S21**).

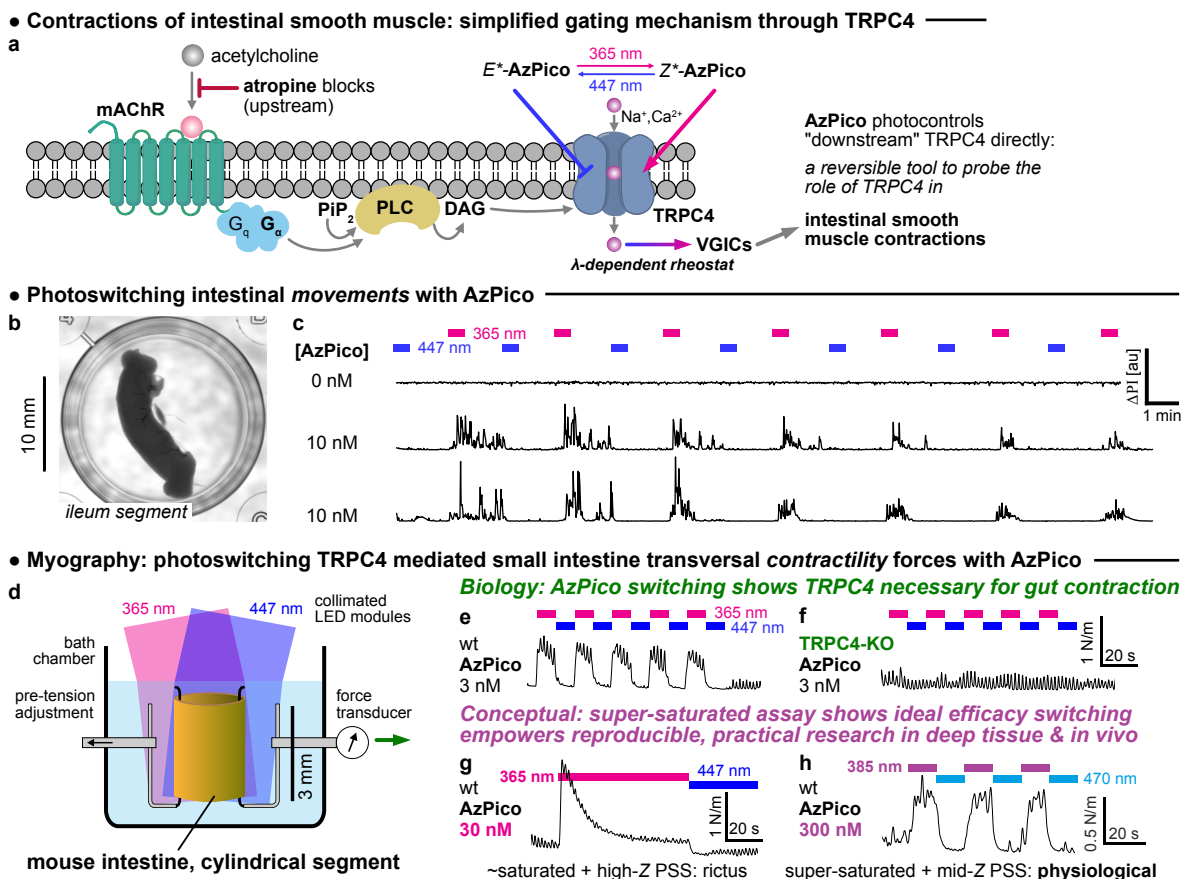


Figure S28 (copy of main figure 6 with extended legend): **AzPico** photocontrol of macroscopic movements and coordinated contractility in intestine shows the key role of TRPC4 and the power of ideal efficacy switching. **a**, simplified molecular mechanism for TRPC4-dependent intestinal contractility⁸¹, that was now directly testable using **AzPico** (E^*/Z^* indicate E/Z -rich-PSSs). **b,c** (see also **Movie S1**), sizeable intestinal segments (mouse ileum) whose motility was blocked by atropine (300 nM) but were treated with **AzPico** were driven into phases of fast macroscopic motions by 365 nm UV photoswitching (with longitudinal as well as ring muscle contractility), then returned to immobility by 447 nm blue light, reversibly over many cycles (narrow-band LED sources used, bandwidth FWHM ca. 30 nm). The metric used for assessment here is " Δ PI" i.e. the absolute value of the well-average instantaneous change of Pixel Intensity in the transmitted light image at time t compared to the previous frame (i.e. $|I(t) - I(t-1)|$, arbitrary units) which serves as a bias-free measure of gross displacement motion (an underestimate of total motion, since only covering or uncovering new pixels leads to large values). In the absence of **AzPico**, no photoresponse is detected. **Figure S22** shows additional traces and controls. **d-f**, physiological-like ring contractility is reversibly stimulated and suppressed by alternating 365 nm / blue illumination of segments treated with sub-saturating **AzPico**, in a TRPC4-dependent manner (knockout not photoresponsive). **g,h**, the ideal efficacy switch paradigm allows fully reproducible control of deep tissue bioactivity, by leveraging the *saturation* of dose-and-photon-flux (hard to titrate) but the *selection* of wavelength (easy to choose). Whereas roughly saturating concentrations of **AzPico** lead to over-stimulation under optimal-Z illumination at 365 nm, highly saturated **AzPico** can instead be used without overstimulation just by dialling in a PSS with slightly lower Z content (385 nm).

5.1.5 Experimental sections for unpublished preliminary results

5.1.5.1 Materials and methods

Reagents and conditions. Unless stated otherwise, (a) all reactions and characterisations were performed with unpurified, undried, non-degassed solvents and reagents, used as obtained, under closed air atmosphere without special precautions; (b) “flash column chromatography” refers to purification on a Biotage Selekt system, using prepacked silica or C18 cartridges purchased from Biotage or Phenomenex; (c) procedures and yields are unoptimized; (d) all eluent and solvent mixtures are given as volume ratios unless otherwise specified.

Nuclear magnetic resonance (NMR) spectroscopy. Standard NMR characterisation was by ^1H - and ^{13}C -NMR spectra on a Bruker Ascend 400, Bruker Ascend 500, Varian 600, Bruker Advance III HD 800. Chemical shifts (δ) are reported in ppm calibrated to residual non-perdeuterated solvent as an internal reference. Peak descriptions singlet (s), doublet (d), triplet (t), quartet (q), multiplet (m), and broad (br) are used.

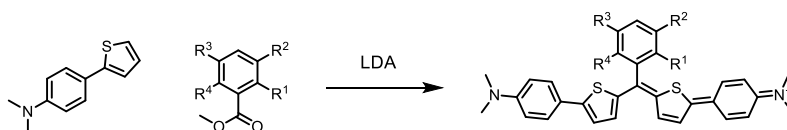
High resolution mass spectrometry (HRMS). HRMS was carried out by the Zentrale Analytik of the LMU Munich using ESI ionisation on a Thermo Finnigan LTQ FT Ultra Fourier Transform Ion Cyclotron Resonance Spectrometer.

High performance liquid chromatography (HPLC) coupled to mass spectrometry (MS). Analytical HPLC-MS was performed on an Agilent 1100 SL with (a) a binary pump to deliver $\text{H}_2\text{O}:\text{MeCN}$ eluent mixtures containing 0.1% formic acid at a 0.4 mL/min flow rate, (b) YMC-Triart C18 column (3.0 μm ; 50 mm \times 3 mm) maintained at 40 $^\circ\text{C}$, (c) an Agilent 1100 series diode array detector, (d) an Agilent LC/MSD iQ mass spectrometer. Typical run conditions were either method A: a linear gradient of $\text{H}_2\text{O}:\text{MeCN}$ from 90:10 to 0:100 (first 5 min), then 0:100 for 2 min for flushing; then the column was (re)equilibrated with 90:10 eluent mixture for 2 min; or method B: a linear gradient of $\text{H}_2\text{O}:\text{MeCN}$ from 50:50 to 0:100 (first 5 min), then 0:100 for 2 min for flushing; then the column was (re)equilibrated with 50:50 eluent mixture for 2 min.

Preparative HPLC. Preparative HPLC was performed on an Agilent 1200 SL with (a) a binary pump to deliver $\text{H}_2\text{O}:\text{MeCN}$ eluent mixtures containing 0.1% trifluoroacetic acid at 20 mL/min flow rate, (b) Agilent-Zorbax C18 column (10.0 μm ; 250 mm \times 30 mm) maintained at room temperature, (c) an Agilent 1200 series diode array detector, and (d) Agilent 1200 series fraction collector. Typical run condition were a gradient of $\text{H}_2\text{O}:\text{MeCN}$ from 90:10 to 0:100 over 30 minutes.

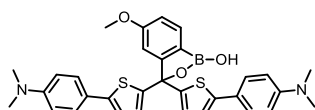
5.1.5.2 Synthetic procedures

General procedure A: One pot synthesis of TAMs type TAM2



A flame dried flask was charged with N,N-dimethyl-4-(thiophen-2-yl)aniline (50 mg, 0.25 mmol, 2.5 eq) and THF (2 mL), then cooled to 0 $^\circ\text{C}$ and lithium diisopropylamide solution (0.20 mL, 0.40 mmol, 2.0 M in THF/heptane/ethylbenzene, 4 eq) was added dropwise. The mixture was stirred at 0 $^\circ\text{C}$ for 30 min and the respective methyl benzoate (0.10 mmol, 1.0 eq) dissolved in THF (1mL) was added dropwise at 0 $^\circ\text{C}$. The reaction mixture was stirred at 0 $^\circ\text{C}$ for 30 minutes, quenched with *sat.* NH_4Cl solution, and stirred 15 minutes (usually a deep green colour formation is formed at this step). The mixture was extracted with CH_2Cl_2 (2 \times 20 mL), the organic layer washed with brine (20 mL), dried over Na_2SO_4 , filtered and concentrated. The crude product was then purified by reverse phase flash chromatography or preparative HPLC. The reaction was carried out at 0.1 mmol scale unless stated otherwise.

TAM2-B-(2)



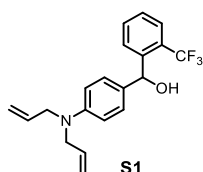
The reaction was conducted according to a modified version of general procedure A.

A flame dried flask was charged with N,N-dimethyl-4-(thiophen-2-yl)aniline (90 mg, 0.44 mmol, 2.2 eq) and THF (4 mL), then cooled to 0°C and *n*-butyllithium (0.18 mL, 0.44 mmol, 2.5 M in hexane, 2.2 eq) was added dropwise. The mixture was stirred at 0°C for 30 min and methyl 2-bromo-5-methoxybenzoate (50 mg, 0.20 mmol, 1.0 eq) dissolved in THF (2mL) was added dropwise at 0°C. The reaction mixture was stirred at 0°C for 30 minutes, then cooled to -78°C and *n*-butyllithium (0.09 mL, 0.22 mmol, 2.5 M in hexane, 1.1 eq) was added dropwise. The mixture was stirred 15 min at -78°C and triisopropylborate (0.23 mL, 1 mmol, 5 eq) was added, the mixture stirred 15 min at -78° and then allowed to warm to rt. The reaction mixture was quenched with sat. NH₄Cl solution and stirred 15 minutes. The mixture was extracted with CH₂Cl₂ (2 × 20 mL), the organic layer washed with brine (20 mL), dried over Na₂SO₄, filtered and concentrated. The crude product was then purified by preparative HPLC and **TAM(II)-B-(2)** was obtained as a colourless solid (2.0 mg, 3.5 μmol, 2 %).

HPLC-MS method B: rt = 9.71 min; ESI (m/z): [M+H]²⁺ = 284.1.

Synthesis of TAM1-NH-LAP

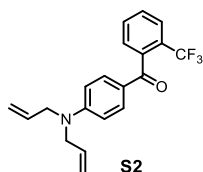
(4-(diallylamino)phenyl)(2-(trifluoromethyl)phenyl)methanol (**S1**)



A flame dried flask was charged with 2-bromobenzotrifluoride (0.28 mL, 2 mmol, 1.0 eq) and THF (10 mL), then cooled to 0°C and isopropylmagnesium chloride (0.62 mL, 0.8 mmol, 1.3 mol/L in THF, 0.4 eq) followed by *n*-butyllithium (0.64 mL, 1.6 mmol, 2.5 M in hexane, 0.8 eq) were added dropwise. The reaction mixture was stirred 30 min and 4-(diallylamino)benzaldehyde (443 mg, 2.2 mmol, 1.1 eq) dissolved in THF (5 mL) was added dropwise and stirred for further 30 minutes. The reaction mixture was quenched with sat. NH₄Cl solution and stirred 15 minutes. The mixture was extracted with CH₂Cl₂ (2 × 20 mL), the organic layer washed with brine (20 mL), dried over Na₂SO₄, filtered and concentrated and **S1** (410 mg, 1.2 mmol, 59%) was obtained as a colourless oil and used directly without further purification.

HPLC-MS method A: rt = 7.41 min; ESI (m/z): [M+H]⁺ = 348.2.

(4-(diallylamino)phenyl)(2-(trifluoromethyl)phenyl)methanone (**S2**)

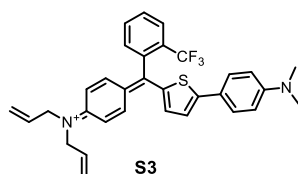


2,3-Dichloro-5,6-dicyano-1,4-benzoquinone (0.27 g, 1.2 mmol, 1.0 eq) was added to a solution of **S2** (0.41 g, 1.2 mmol, 59%) in CH₂Cl₂ (5 mL) and stirred for 30 min at rt. The mixture was directly purified via flash chromatography (gradient: hexane/EtOAc, 90:10 to 60:40) and **S2** (0.24 g, 0.70 mmol, 59 %) was obtained as a colourless oil.

¹H NMR (400 MHz, CDCl₃) δ 7.78 – 7.69 (m, 1H), 7.66 – 7.60 (m, 2H), 7.59 – 7.49 (m, 2H), 7.40 – 7.31 (m, 1H), 6.72 – 6.61 (m, 2H), 5.92 – 5.74 (m, 2H), 5.24 – 5.12 (m, 4H), 4.04 – 3.94 (m, 4H). **¹³C NMR** (101 MHz, CDCl₃) δ 193.57, 152.79, 139.55, 132.78, 132.40, 131.32, 129.16, 128.32, 128.26, 127.94, 126.61 (q, *J* = 4.7 Hz), 125.07, 123.89 (d, *J* = 274.2 Hz), 117.00, 111.23, 52.91. **¹⁹F NMR** (376 MHz, CDCl₃) δ -58.26. **HPLC-MS** method A: rt = 7.41 min; ESI (m/z): [M+H]⁺ = 346.2.

Note: Expected quartets from CF₃ coupling were observed as doublets because of low signal intensity.

N-allyl-N-(4-((5-(4-(dimethylamino)phenyl)thiophen-2-yl)(2-(trifluoromethyl)phenyl)methylene)cyclohexa-2,5-dien-1-ylidene)prop-2-en-1-aminium (**S3**)



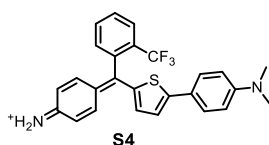
The reaction was conducted according to a modified version of general procedure A.

A flame dried flask was charged with N,N-dimethyl-4-(thiophen-2-yl)aniline (69 mg, 0.34 mmol, 1.0 eq) and THF (2 mL), then cooled to 0°C and lithium diisopropylamide solution (0.26 mL, 0.51 mmol, 2.0 M in THF/heptane/ethylbenzene, 1.5 eq) was added dropwise. The mixture was stirred at 0°C for 30 min and **S2** (0.12 g, 0.34 mmol, 1.0 eq) dissolved in THF (2 mL) was added dropwise. The reaction mixture was stirred 1 h at rt, then quenched with sat. NH₄Cl solution and stirred 15 minutes (deep blue colour formation). The mixture was extracted with CH₂Cl₂ (2 × 20 mL), the organic layer washed with brine (20 mL), dried over Na₂SO₄, filtered and concentrated. The crude product was then purified by reverse phase flash chromatography (gradient H₂O/MeCN + 0.05% TFA, 90:10 to 10:90) and **S3** (0.12 g, 0.19 mmol, 57 % as TFA salt) was obtained as a dark blue solid.

HRMS for C₃₂H₃₀F₃N₂S [M⁺] calc. 531.2076, found 531.2069. **HPLC-MS** method A: rt = 5.50 min; ESI (m/z): [M+H]²⁺ = 266.2.

Note: Using formic acid as modifier in reverse phase solvents results in undesired reduction of the compound!

4-((5-(4-(dimethylamino)phenyl)thiophen-2-yl)(2-(trifluoromethyl)phenyl)methylene)cyclohexa-2,5-dien-1-iminium (**S4**)

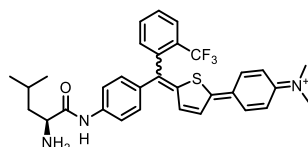


A screw cap vial was charged with **S3** (0.12 g, 0.19 mmol, 1.0 eq), 1,3-dimethylbarbituric acid (66 mg, 0.42 mmol, 2.2 eq), tetrakis(triphenylphosphine)palladium(0) (22 mg, 0.019 mmol, 0.1 eq) and THF (3 mL), purged with N₂. The vial was sealed and the reaction mixture stirred at 60°C for 3 h, cooled to rt and concentrated. The crude mixture was directly purified by reverse phase flash chromatography (gradient H₂O/MeCN + 0.05% TFA, 90:10 to 10:90) and **S4** (0.10 g, 0.18 mmol, 94 %, as TFA salt) was obtained as a dark green solid.

¹H NMR (500 MHz, MeOD-*d*₄) δ 7.98 – 7.93 (m, 1H), 7.87 – 7.78 (m, 4H), 7.74 (d, *J* = 4.8 Hz, 1H), 7.68 – 7.58 (m, 3H), 7.52 – 7.47 (m, 2H), 6.86 (d, *J* = 8.9 Hz, 4H), 3.16 (s, 6H). **¹³C NMR** (126 MHz, MeOD-*d*₄) δ 171.78, 155.47, 147.54, 140.72, 139.98, 138.21, 138.20, 133.80, 133.78, 133.65, 133.34, 133.13, 133.04, 132.08, 130.97, 130.83, 130.59, 130.03, 129.94, 128.21, 128.17, 128.14, 128.10, 127.96, 127.72, 126.18, 124.00, 121.12, 118.09, 113.79, 40.40. **¹⁹F NMR** (471 MHz, MeOD-*d*₄) δ -59.41. **HRMS** for C₂₆H₂₂F₃N₂S [M⁺] calc. 451.1450, found 451.1445. **HPLC-MS** method A: rt = 5.90 min; ESI (m/z): [M+H]²⁺ = 323.7.

Observed complexity for ¹³C because of CF₃ coupling.

TAM1-NH-LAP

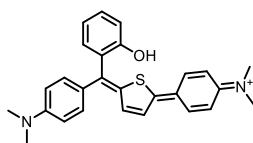


FMOC-Leu-OH (24 mg, 0.066 mmol, 1.5 eq), HBTU (25 mg, 0.066 mmol, 1.5 eq) and DIPEA (39 μL, 0.22 mmol, 5 eq) were dissolved in DMF (1 mL), stirred for 15 min before **S4** (20 mg, 0.44 mmol, 1.0 eq) was added to the mixture and stirred for 60 minutes at rt (the reaction turned from deep green into a deep blue). Methylpiperazine (98 mg, 0.89 mmol, 20 eq) was added and the reaction stirred for 30 min, then H₂O (2 mL) was added, the mixture acidified with TFA and directly purified by preparative HPLC to obtain **TAM(I)-NH-LAP** (13 mg, 0.020 mmol, 45 %, as TFA salt) as a dark blue solid.

¹H NMR (500 MHz, MeOD-*d*₄) δ 8.20 (q, *J* = 5.8 Hz, 1H), 8.10 (br, 1.4H), 8.03 (d, *J* = 5.7 Hz, 0.8H), 7.93 (t, *J* = 7.6 Hz, 1.1H), 7.88 (d, *J* = 7.9 Hz, 0.8H), 7.86 – 7.76 (m, 3.8H), 7.71 (d, *J* = 7.5 Hz, 0.5H), 7.58 (d, *J* = 8.5 Hz, 1.2H), 7.54 (d, *J* = 7.5 Hz, 0.5H), 7.41 (d, *J* = 8.6 Hz, 1H), 7.35 (d, *J* = 5.6 Hz, 0.5H), 7.15 (br, 1H), 7.10 (d, *J* = 9.3 Hz, 1.1H), 4.07 (td, *J* = 7.1, 3.0 Hz, 1H), 3.45 (s, 3.3H), 3.42 (s, 2.6H), 1.86 – 1.79 (m, 2H), 1.79 – 1.72 (m, 1H), 1.05 (s, 3H), 1.04 (s, 3H). **¹³C NMR** (151 MHz, MeOD-*d*₄) δ 180.32, 178.28, 169.72, 169.66, 159.93, 159.79, 153.49, 152.49, 148.56, 147.48, 145.93, 143.81, 142.85, 142.80, 138.67, 137.68, 135.74, 135.34, 135.10, 134.17, 134.16, 133.96, 133.80, 133.62, 133.44, 133.32, 132.89, 132.20, 131.79, 130.59, 130.38, 130.18, 128.58, 128.54, 128.50, 128.47, 126.04, 125.90, 124.22, 124.08, 123.71, 123.04, 121.07, 121.05, 121.01, 120.99, 115.11, 111.44, 53.84, 41.78, 41.71, 41.62, 25.50, 23.28, 21.83. **¹⁹F NMR** (471 MHz, MeOD-*d*₄) δ -59.51, -59.88. **HRMS** for C₃₂H₃₃F₃N₃OS [M⁺] calc. 564.2291, found 564.2284. **HPLC-MS** method A: rt = 5.49 min; ESI (m/z): [M]⁺ = 564.2.

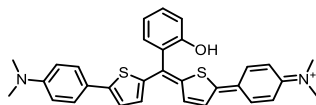
Note: two isomers in relative intensities of 0.56 and 0.44 were found, either E-Z about the double bond or atropisomers. Observed complexity for ¹³C because of CF₃ coupling.

TAM1-OH



HPLC-MS method B: rt = 4.14 min; ESI (m/z): [M+H]²⁺ = 214.2.

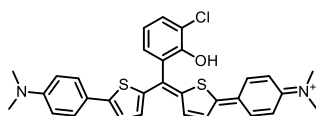
TAM2-OH



Prepared according to general procedure A with methyl salicylate (13 μL, 0.1 mmol, 1.0 eq). Purification was carried out by preparative HPLC and **TAM(II)-2-OH** (1.3 mg, 2.6 μmol, 3 %) was obtained as a dark green solid.

HPLC-MS method B: rt = 6.05 min; ESI (m/z): [M+H]²⁺ = 255.1.

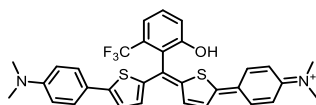
TAM2-OH,3-Cl



Prepared according to general procedure A with methyl 3-chloro-2-hydroxybenzoate (19 mg, 0.1 mmol, 1.0 eq). Purification was carried out by preparative HPLC and **TAM(II)-2-OH,3-Cl** (3 mg, 6 μmol, 6 %) was obtained as a dark green solid.

HPLC-MS method B: rt = 6.12 min; ESI (m/z): [M+H]²⁺ = 273.1.

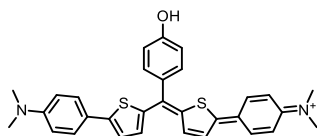
TAM2-OH,6-F



Prepared according to general procedure A with methyl 2-fluoro-6-hydroxybenzoate (17 mg, 0.1 mmol, 1.0 eq). Purification was carried out by preparative HPLC and **TAM(II)-2-OH,6-CF₃** (20 mg, 38 μmol, 38 %) was obtained as a dark green solid.

HPLC-MS method B: rt = 5.74 min; ESI (m/z): [M+H]²⁺ = 264.2.

TAM2H-4-OH



Prepared according to general procedure A with methyl 2-fluoro-6-hydroxybenzoate (17 mg, 0.1 mmol, 1.0 eq). Purification was carried out by preparative HPLC and **TAM(II)-4-OH** (20 mg, 38 μ mol, 38 %) was obtained as a dark green solid.

HPLC-MS method B: t_r = 6.07 min; ESI (m/z): $[M+H]^{2+}$ = 255.2.

5.1.5.3 UV/VIS Spectroscopy

UV-VIS. UV-VIS spectra were recorded on an Agilent Cary 60 UV-Vis spectrophotometer using 1 cm quartz or plastic cuvettes (BRAND, UV micro). All measurements were performed at room temperature in non-degassed solvents at a concentration of 10 μ M, unless stated otherwise. Britton Robinson buffer was used to adjust pH.

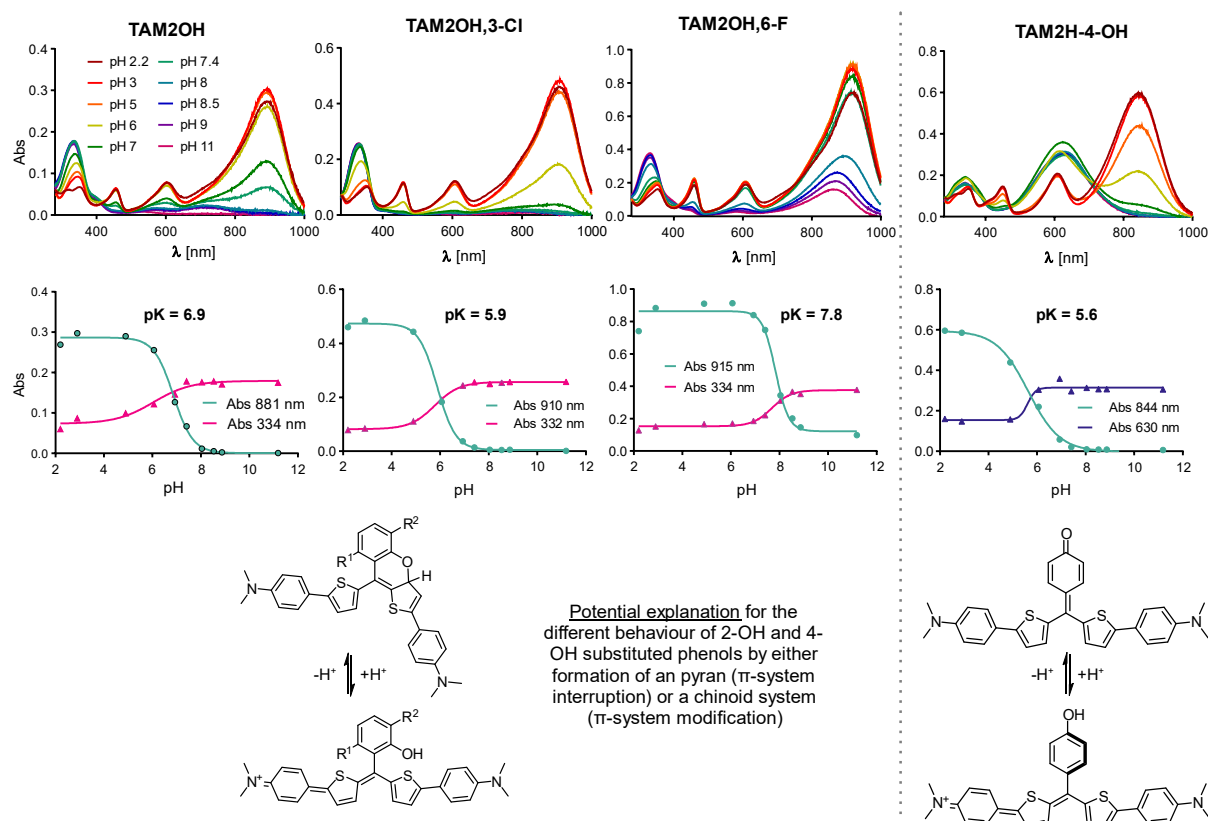


Figure S1. pH dependent absorption of **TAM2OH**, **TAM2OH,3-Cl**, **TAM2OH,6-F**, **TAM2H-4-OH** and plotted pH function with calculated pK value.

Supporting Note to "pH dependent absorption spectra": Introduction of an *ortho*-phenolic group at the upper ring results in a pH dependent equilibrium of UV or NIR absorbing forms. The equilibrium forms immediately and the UV absorption indicates formation of a sp^3 carbon which interrupts the π -system. Decreasing the pK_a of the phenol also decreases pK_{cycle} which indicates that the nucleophilic phenolate forms the ring, and additionally the equilibrium can be modulated by introduction of a second

ortho substituent that sterically blocks the ring formation (higher pK_{cycle}). The dynamic modulation of pK_{cycle} is the basis for the envisioned enzyme activatable probes built on this scaffold.

A control compound was synthesized to exclude other mechanisms that facilitate nucleophilic attack at the central carbon. Therefore, the phenol was introduced in *para* position and an equilibrium between an orange/red absorbing and a NIR absorbing form which indicates formation of a quinoid form as a weaker push pull system with a shorter π -system. Due to this result and preliminary LCMS and ^1H NMR studies, I assigned the UV absorbing form tentatively to the pyran.

5.2 List of Abbreviations

a.u.	Arbitrary units	IC	Internal conversion
Ac	Acetyl	IC	Inward current
ALF	Acoustic loudness factor	IC ₅₀	Half maximum inhibitory concentration
Ar	Aryl	ICG	Indocyanine green
ATP	Adenosine triphosphate	<i>i</i> pr	Isopropyl
AzCy	Azocyanine	k _B	Boltzmann constant
AzHCy	Azohemicyanine	ki	Knockin
BBQ	Blackberry quencher	ko	Knockout
BHQ	Black hole quencher	LA	Linear absorber
BODIPY	4,4-Difluor-4-bora-3a,4a-diaza-s-indacene	LAP	Leucin aminopeptidase
BSA	Bovine serum albumin	LDA	Lithium diisopropylamide
CBR	Cannabinoid receptor	LUMO	Lowest unoccupied molecular orbital
CMZ	Clemizole	Me	Methyl
CNS	Central nervous system	MeCN	Acetonitril
Cryo-EM	Cryogenic electron microscopy	MFP	Mean free path
CT	Computer tomography	MPE	Maximum permissible exposure
CYP450	Cytochrome P450	mRNA	messenger ribonucleic acid
DAG	Diacylglycerol	MRT	Magnetic resonance tomography
DIPEA	<i>N,N</i> -Diisopropylamine	MS	Mass spectrometry
DkTx	Double knot toxin (spider toxin)	MSOT	Multispectral optoacoustic tomography
DMSO	Dimethylsulfoxide	nBuLi	<i>n</i> -butyllithium
DNA	Deoxyribonucleic acid	NHERF	Na ⁺ /H ⁺ exchanger regulatory factor
DR	Dynamic range	NIR	Near infrared
DTT	Dithiothreitol	NMR	Nucleic magnetic resonance
EA	Englerin A	OA	Optoacoustic
EC50	Half-maximal effective concentration	OD	Optical density
EDG	Electron donating group	PA	Photoacoustic
eq	Equivalent	PAINS	Pan-assay interference compounds
ESI	Electron spray ionization	PET	Positron emission tomography
Et	Ethyl	PeT	Photoinduced electron transfer
EtOAc	Ethylacetate	Ph	Phenyl
EWG	Electron withdrawing group	pK	Logarithmic value of the equilibrium constant
FA	Formic acid	POI	Protein of interest
FBS	Fetal bovine serum	PSS	Photostationary state
FDA	Food and drug administration	ROCE	Receptor operated calcium entry
FDR	Functional dynamic range	RSA	Reverse saturable absorber
FRET	Fluorescence resonance energy transfer	rt	Room temperature
FSGS	Focal segmental glomerulosclerosis	SA	Saturable absorber
GPCR	G-protein coupled receptor	SAR	Structure activity relationship
GSH	Glutathione	SGE	Signal generation efficiency
HD	Hemicyanine dye	SOCE	Store operated calcium entry
HMBC	Heteronuclear multibond coherence	SWIR	Short wave infrared
hNQO1	Human- NAD(P)H quinone oxidoreductase 1	TAS	Transient absorption spectroscopy
HOMO	Highest occupied molecular orbital	<i>t</i> bu	Tert-butyl
HPLC	High performance liquid chromatography	TFA	Trifluoroacetic acid
HRMS	High resolution mass spectroscopy	TICT	Twisted intramolecular charge transfer
HSA	Human serum albumin	TRP	Transient receptor potential
HSQC	Heteronuclear single quantum coherence	TRPA	Transient receptor potential ankyrin
IBP	Inhibitor binding pocket	TRPC	Transient receptor potential canonical

TRPM	Transient receptor potential melastatin
TRPML	Transient receptor potential mucopolipins
TRPP	Transient receptor potential polycystins
TRPV	Transient receptor potential vanilloid
TRX	Thioredoxin
UV	Ultraviolet
VIS	Visible
VLSD	Voltage sensing-like domain
w/o	Without
wt	Wildtype

6 Bibliography

- Bell, A. G. The Production of Sound by Radiant Energy. *Science* **1881**, os-2 (48), 242–253. <https://doi.org/10.1126/science.os-2.48.242>.
- Rosencwaig, A. *Photoacoustics and Photoacoustic Spectroscopy*; Chemical analysis; Wiley: New York, 1980.
- Ntziachristos, V. Going Deeper than Microscopy: The Optical Imaging Frontier in Biology. *Nat. Methods* **2010**, 7 (8), 603–614. <https://doi.org/10.1038/nmeth.1483>.
- Rosencwaig, A. Photoacoustic Spectroscopy of Biological Materials. *Science* **1973**, 181 (4100), 657–658. <https://doi.org/10.1126/science.181.4100.657>.
- Bowen, T.; Nasoni, R. L.; Pifer, A. E. Thermoacoustic Imaging Induced by Deeply Penetrating Radiation. In *Acoustical Imaging*; Kaveh, M., Mueller, R. K., Greenleaf, J. F., Eds.; Springer US: Boston, MA, 1984; pp 409–427. https://doi.org/10.1007/978-1-4613-2779-0_32.
- Oraevsky, A. A.; Jacques, S. L.; Esenaliev, R. O.; Tittel, F. K. Laser-Based Photoacoustic Imaging in Biological Tissues. In *Laser-Tissue Interaction V; and Ultraviolet Radiation Hazards*; SPIE, 1994; Vol. 2134, pp 122–128. <https://doi.org/10.1117/12.182927>.
- Wang, L. V.; Hu, S. Photoacoustic Tomography: In Vivo Imaging from Organelles to Organs. *Science* **2012**, 335 (6075), 1458–1462. <https://doi.org/10.1126/science.1216210>.
- Wang, X.; Pang, Y.; Ku, G.; Xie, X.; Stoica, G.; Wang, L. V. Noninvasive Laser-Induced Photoacoustic Tomography for Structural and Functional in Vivo Imaging of the Brain. *Nat Biotechnol* **2003**, 21 (7), 803–806. <https://doi.org/10.1038/nbt839>.
- Ntziachristos, V.; Ripoll, J.; Wang, L. V.; Weissleder, R. Looking and Listening to Light: The Evolution of Whole-Body Photonic Imaging. *Nat Biotechnol* **2005**, 23 (3), 313–320. <https://doi.org/10.1038/nbt1074>.
- Kim, C.; Favazza, C.; Wang, L. V. In Vivo Photoacoustic Tomography of Chemicals: High-Resolution Functional and Molecular Optical Imaging at New Depths. *Chem. Rev.* **2010**, 110 (5), 2756–2782. <https://doi.org/10.1021/cr900266s>.
- Weissleder, R.; Ntziachristos, V. Shedding Light onto Live Molecular Targets. *Nat Med* **2003**, 9 (1), 123–128. <https://doi.org/10.1038/nm0103-123>.
- Oliinik, O. S.; Ma, C.; Pletnev, S.; Baloban, M.; Taboada, C.; Sheng, H.; Yao, J.; Verkhusha, V. V. Deep-Tissue SWIR Imaging Using Rationally Designed Small Red-Shifted near-Infrared Fluorescent Protein. *Nat Methods* **2023**, 20 (1), 70–74. <https://doi.org/10.1038/s41592-022-01683-0>.
- Sandell, J. L.; Zhu, T. C. A Review of In-Vivo Optical Properties of Human Tissues and Its Impact on PDT. *Journal of Biophotonics* **2011**, 4 (11–12), 773–787. <https://doi.org/10.1002/jbpo.201100062>.
- Bruns, O. T.; Bischof, T. S.; Harris, D. K.; Franke, D.; Shi, Y.; Riedemann, L.; Bartelt, A.; Jaworski, F. B.; Carr, J. A.; Rowlands, C. J.; Wilson, M. W. B.; Chen, O.; Wei, H.; Hwang, G. W.; Montana, D. M.; Coropceanu, I.; Achorn, O. B.; Kloepper, J.; Heeren, J.; So, P. T. C.; Fukumura, D.; Jensen, K. F.; Jain, R. K.; Bawendi, M. G. Next-Generation in Vivo Optical Imaging with Short-Wave Infrared Quantum Dots. *Nat Biomed Eng* **2017**, 1 (4), 1–11. <https://doi.org/10.1038/s41551-017-0056>.
- Carr, J. A.; Franke, D.; Caram, J. R.; Perkinson, C. F.; Saif, M.; Askoxylakis, V.; Datta, M.; Fukumura, D.; Jain, R. K.; Bawendi, M. G.; Bruns, O. T. Shortwave Infrared Fluorescence Imaging with the Clinically Approved Near-Infrared Dye Indocyanine Green. *PNAS* **2018**, 115 (17), 4465–4470. <https://doi.org/10.1073/pnas.1718917115>.
- Cosco, E. D.; Caram, J. R.; Bruns, O. T.; Franke, D.; Day, R. A.; Farr, E. P.; Bawendi, M. G.; Sletten, E. M. Flavylum Polymethine Fluorophores for Near- and Shortwave Infrared Imaging. *Angew. Chem. Int. Ed.* **2017**, 56 (42), 13126–13129. <https://doi.org/10.1002/anie.201706974>.
- Wong, K. C. Y.; Sletten, E. M. Extending Optical Chemical Tools and Technologies to Mice by Shifting to the Shortwave Infrared Region. *Curr. Opin. Chem. Bio.* **2022**, 68, 102131. <https://doi.org/10.1016/j.cbpa.2022.102131>.
- Razansky, D.; Vinegoni, C.; Ntziachristos, V. Multispectral Photoacoustic Imaging of Fluorochromes in Small Animals. *Opt. Lett.*, **OL** **2007**, 32 (19), 2891–2893. <https://doi.org/10.1364/OL.32.002891>.
- Ntziachristos, V.; Razansky, D. Molecular Imaging by Means of Multispectral Photoacoustic Tomography (MSOT). *Chem. Rev.* **2010**, 110 (5), 2783–2794. <https://doi.org/10.1021/cr9002566>.
- Razansky, D.; Buehler, A.; Ntziachristos, V. Volumetric Real-Time Multispectral Photoacoustic Tomography of Biomarkers. *Nat Protoc* **2011**, 6 (8), 1121–1129. <https://doi.org/10.1038/nprot.2011.351>.
- Weber, J.; Beard, P. C.; Bohndiek, S. E. Contrast Agents for Molecular Photoacoustic Imaging. *Nat. Methods* **2016**, 13 (8), 639–650. <https://doi.org/10.1038/nmeth.3929>.
- Karlas, A.; Kallmayer, M.; Fasoula, N.-A.; Liapis, E.; Bariotakis, M.; Krönke, M.; Anastasopoulou, M.; Reber, J.; Eckstein, H.-H.; Ntziachristos, V. Multispectral Photoacoustic Tomography of Muscle Perfusion and Oxygenation under Arterial and Venous Occlusion: A Human Pilot Study. *Journal of Biophotonics* **2020**, 13 (6), e201960169. <https://doi.org/10.1002/jbpo.201960169>.

- (23) Razansky, D.; Klohs, J.; Ni, R. Multi-Scale Optoacoustic Molecular Imaging of Brain Diseases. *Eur J Nucl Med Mol Imaging* **2021**, *48* (13), 4152–4170. <https://doi.org/10.1007/s00259-021-05207-4>.
- (24) Dima, A.; Ntziachristos, V. Non-Invasive Carotid Imaging Using Optoacoustic Tomography. *Opt. Express, OE* **2012**, *20* (22), 25044–25057. <https://doi.org/10.1364/OE.20.025044>.
- (25) Neuschmelting, V.; Burton, N. C.; Lockau, H.; Ulrich, A.; Harmsen, S.; Ntziachristos, V.; Kircher, M. F. Performance of a Multispectral Optoacoustic Tomography (MSOT) System Equipped with 2D vs. 3D Handheld Probes for Potential Clinical Translation. *Photoacoustics* **2016**, *4* (1), 1–10. <https://doi.org/10.1016/j.pacs.2015.12.001>.
- (26) Taruttis, A.; Ntziachristos, V. Advances in Real-Time Multispectral Optoacoustic Imaging and Its Applications. *Nat. Photon* **2015**, *9* (4), 219–227. <https://doi.org/10.1038/nphoton.2015.29>.
- (27) Attia, A. B. E.; Balasundaram, G.; Moothanchery, M.; Dinish, U. S.; Bi, R.; Ntziachristos, V.; Olivo, M. A Review of Clinical Photoacoustic Imaging: Current and Future Trends. *Photoacoustics* **2019**, *16*, 100144. <https://doi.org/10.1016/j.pacs.2019.100144>.
- (28) Giepmans, B. N. G.; Adams, S. R.; Ellisman, M. H.; Tsien, R. Y. The Fluorescent Toolbox for Assessing Protein Location and Function. *Science* **2006**, *312* (5771), 217–224. <https://doi.org/10.1126/science.1124618>.
- (29) Shu, X.; Royant, A.; Lin, M. Z.; Aguilera, T. A.; Lev-Ram, V.; Steinbach, P. A.; Tsien, R. Y. Mammalian Expression of Infrared Fluorescent Proteins Engineered from a Bacterial Phytochrome. *Science* **2009**, *324* (5928), 804–807. <https://doi.org/10.1126/science.1168683>.
- (30) Grimm, J. B.; Lavis, L. D. Caveat Fluorophore: An Insiders' Guide to Small-Molecule Fluorescent Labels. *Nat Methods* **2022**, *19* (2), 149–158. <https://doi.org/10.1038/s41592-021-01338-6>.
- (31) Grimm, J. B.; Muthusamy, A. K.; Liang, Y.; Brown, T. A.; Lemon, W. C.; Patel, R.; Lu, R.; Macklin, J. J.; Keller, P. J.; Ji, N.; Lavis, L. D. A General Method to Fine-Tune Fluorophores for Live-Cell and in Vivo Imaging. *Nat Methods* **2017**, *14* (10), 987–994. <https://doi.org/10.1038/nmeth.4403>.
- (32) Lavis, L. D.; Raines, R. T. Bright Ideas for Chemical Biology. *ACS Chem. Biol.* **2008**, *3* (3), 142–155. <https://doi.org/10.1021/cb700248m>.
- (33) Kobayashi, H.; Ogawa, M.; Alford, R.; Choyke, P. L.; Urano, Y. New Strategies for Fluorescent Probe Design in Medical Diagnostic Imaging. *Chem. Rev.* **2010**, *110* (5), 2620–2640. <https://doi.org/10.1021/cr900263j>.
- (34) Chi, K. R. Super-Resolution Microscopy: Breaking the Limits. *Nature Methods* **2009**, *6* (1), 15–18. <https://doi.org/10.1038/nmeth.f.234>.
- (35) Balzarotti, F.; Eilers, Y.; Gwosch, K. C.; Gynnà, A. H.; Westphal, V.; Stefani, F. D.; Elf, J.; Hell, S. W. Nanometer Resolution Imaging and Tracking of Fluorescent Molecules with Minimal Photon Fluxes. *Science* **2017**, *355* (6325), 606–612. <https://doi.org/10.1126/science.aak9913>.
- (36) Scheiderer, L.; von der Emde, H.; Hesselink, M.; Weber, M.; Hell, S. W. MINSTED Tracking of Single Biomolecules. *Nat Methods* **2024**, *21* (4), 569–573. <https://doi.org/10.1038/s41592-024-02209-6>.
- (37) Reinhardt, S. C. M.; Masullo, L. A.; Baudrexel, I.; Steen, P. R.; Kowalewski, R.; Eklund, A. S.; Strauss, S.; Unterauer, E. M.; Schlichthaerle, T.; Strauss, M. T.; Klein, C.; Jungmann, R. Ångström-Resolution Fluorescence Microscopy. *Nature* **2023**, *617* (7962), 711–716. <https://doi.org/10.1038/s41586-023-05925-9>.
- (38) Berezin, M. Y.; Achilefu, S. Fluorescence Lifetime Measurements and Biological Imaging. *Chem. Rev.* **2010**, *110* (5), 2641–2684. <https://doi.org/10.1021/cr900343z>.
- (39) Ofori, L. O.; Withana, N. P.; Prestwood, T. R.; Verdoes, M.; Brady, J. J.; Winslow, M. M.; Sorger, J.; Bogoyo, M. Design of Protease Activated Optical Contrast Agents That Exploit a Latent Lysosomotropic Effect for Use in Fluorescence-Guided Surgery. *ACS Chem. Biol.* **2015**, *10* (9), 1977–1988. <https://doi.org/10.1021/acscchembio.5b00205>.
- (40) Ito, R.; Kamiya, M.; Urano, Y. Molecular Probes for Fluorescence Image-Guided Cancer Surgery. *Current Opinion in Chemical Biology* **2022**, *67*, 102112. <https://doi.org/10.1016/j.cbpa.2021.102112>.
- (41) Van Keulen, S.; Hom, M.; White, H.; Rosenthal, E. L.; Baik, F. M. The Evolution of Fluorescence-Guided Surgery. *Mol Imaging Biol* **2023**, *25* (1), 36–45. <https://doi.org/10.1007/s11307-022-01772-8>.
- (42) Fujita, K.; Kamiya, M.; Yoshioka, T.; Ogasawara, A.; Hino, R.; Kojima, R.; Ueo, H.; Urano, Y. Rapid and Accurate Visualization of Breast Tumors with a Fluorescent Probe Targeting α -Mannosidase 2C1. *ACS Cent. Sci.* **2020**, *6* (12), 2217–2227. <https://doi.org/10.1021/acscentsci.0c01189>.
- (43) Widen, J. C.; Tholen, M.; Yim, J. J.; Antaris, A.; Casey, K. M.; Rogalla, S.; Klaassen, A.; Sorger, J.; Bogoyo, M. AND-Gate Contrast Agents for Enhanced Fluorescence-Guided Surgery. *Nat Biomed Eng* **2021**, *5* (3), 264–277. <https://doi.org/10.1038/s41551-020-00616-6>.
- (44) Faucher, F. F.; Liu, K. J.; Cosco, E. D.; Widen, J. C.; Sorger, J.; Guerra, M.; Bogoyo, M. Protease Activated Probes for Real-Time Ratiometric Imaging of Solid Tumors. *ACS Cent. Sci.* **2023**, *9* (5), 1059–1069. <https://doi.org/10.1021/acscentsci.3c00261>.
- (45) Wu, Y.; Zhang, F. Exploiting Molecular Probes to Perform Near-Infrared Fluorescence-Guided Surgery. *VIEW* **2020**, *1* (4), 20200068. <https://doi.org/10.1002/VIW.20200068>.
- (46) Cherry, S. R. MULTIMODALITY IN VIVO IMAGING SYSTEMS: Twice the Power or Double the Trouble? *Annual Review of Biomedical Engineering* **2006**, *8* (Volume 8, 2006), 35–62. <https://doi.org/10.1146/annurev.bioeng.8.061505.095728>.
- (47) Yang, X.; Wang, L. V. Monkey Brain Cortex Imaging by Photoacoustic Tomography. *JBO* **2008**, *13* (4), 044009. <https://doi.org/10.1117/1.2967907>.
- (48) Nyayapathi, N.; Xia, J. Photoacoustic Imaging of Breast Cancer: A Mini Review of System Design and Image Features. *JBO* **2019**, *24* (12), 121911. <https://doi.org/10.1117/1.JBO.24.12.121911>.
- (49) Ermilov, S. A.; Khamapirad, T.; Conjuteau, A.; Leonard, M. H.; Laceywell, R.; Mehta, K.; Miller, T.; Oraevsky, A. A. Laser Optoacoustic Imaging System for Detection of Breast Cancer. *JBO* **2009**, *14* (2), 024007. <https://doi.org/10.1117/1.3086616>.
- (50) Borg, R. E.; Rochford, J. Molecular Photoacoustic Contrast Agents: Design Principles & Applications. *Photochem. Photobiol.* **2018**, *94* (6), 1175–1209. <https://doi.org/10.1111/php.12967>.
- (51) Knopoff, L.; Shapiro, J. N. Pseudo-Grüneisen Parameter for Liquids. *Phys. Rev. B* **1970**, *1* (10), 3893–3895. <https://doi.org/10.1103/PhysRevB.1.3893>.
- (52) Li, M.; Xu, Y.; Peng, X.; Kim, J. S. From Low to No O₂-Dependent Hypoxia Photodynamic Therapy (hPDT): A New Perspective. *Acc. Chem. Res.* **2022**, *55* (22), 3253–3264. <https://doi.org/10.1021/acsc.accounts.2c00531>.
- (53) Zhang, X.; Wang, Z.; Hou, Y.; Yan, Y.; Zhao, J.; Dick, B. Recent Development of Heavy-Atom-Free Triplet Photosensitizers: Molecular Structure Design, Photophysics and Application. *J. Mater. Chem. C* **2021**, *9* (36), 11944–11973. <https://doi.org/10.1039/D1TC02535J>.
- (54) Glembockyte, V.; Lincoln, R.; Cosa, G. Cy3 Photoprotection Mediated by Ni²⁺ for Extended Single-Molecule Imaging: Old Tricks for New Techniques. *J. Am. Chem. Soc.* **2015**, *137* (3), 1116–1122. <https://doi.org/10.1021/ja509923e>.

- (55) Vogelsang, J.; Kasper, R.; Steinhauer, C.; Person, B.; Heilemann, M.; Sauer, M.; Tinnefeld, P. A Reducing and Oxidizing System Minimizes Photobleaching and Blinking of Fluorescent Dyes. *Angewandte Chemie International Edition* **2008**, *47* (29), 5465–5469. <https://doi.org/10.1002/anie.200801518>.
- (56) Wang, S.; Zhang, X. Design Strategies of Photoacoustic Molecular Probes. *ChemBioChem* **2021**, *22* (2), 308–316. <https://doi.org/10.1002/cbic.202000514>.
- (57) Hatamimoslehabadi, M.; Bellinger, S.; La, J.; Ahmad, E.; Frenette, M.; Yelleswarapu, C.; Rochford, J. Correlation of Photophysical Properties with the Photoacoustic Emission for a Selection of Established Chromophores. *J. Phys. Chem. C* **2017**, *121* (43), 24168–24178. <https://doi.org/10.1021/acs.jpcc.7b07598>.
- (58) Sissaoui, J.; Budkina, D. S.; Vauthey, E. Torsional Disorder, Symmetry Breaking, and the Crystal Violet Shoulder Controversy. *J. Phys. Chem. Lett.* **2023**, *14* (24), 5602–5606. <https://doi.org/10.1021/acs.jpcclett.3c01038>.
- (59) Brøndsted, F.; Shield, H.; Moore, J.; Zhou, X.; Fang, Y.; Stains, C. Acoustic Loudness Factor: An Experimental Parameter for Benchmarking Small Molecule Photoacoustic Probes. **2024**. <https://doi.org/10.26434/chemrxiv-2024-7cbk2>.
- (60) Zhao, Z.; Swartzchick, C. B.; Chan, J. Targeted Contrast Agents and Activatable Probes for Photoacoustic Imaging of Cancer. *Chem. Soc. Rev.* **2022**. <https://doi.org/10.1039/D0CS00771D>.
- (61) Gujrati, V.; Mishra, A.; Ntziachristos, V. Molecular Imaging Probes for Multi-Spectral Optoacoustic Tomography. *Chem. Commun.* **2017**, *53* (34), 4653–4672. <https://doi.org/10.1039/C6CC09421J>.
- (62) Mishra, K.; Fuenzalida-Werner, J. P.; Pennacchietti, F.; Janowski, R.; Chmyrov, A.; Huang, Y.; Zakian, C.; Klemm, U.; Testa, I.; Niessing, D.; Ntziachristos, V.; Stiel, A. C. Genetically Encoded Photo-Switchable Molecular Sensors for Optoacoustic and Super-Resolution Imaging. *Nat. Biotechnol.* **2022**, *40* (4), 598–605. <https://doi.org/10.1038/s41587-021-01100-5>.
- (63) Vigdeman, L.; Khanal, B. P.; Zubarev, E. R. Functional Gold Nanorods: Synthesis, Self-Assembly, and Sensing Applications. *Advanced Materials* **2012**, *24* (36), 4811–4841. <https://doi.org/10.1002/adma.201201690>.
- (64) Lavis, L. D. Teaching Old Dyes New Tricks: Biological Probes Built from Fluoresceins and Rhodamines. *Annual Review of Biochemistry* **2017**, *86* (Volume 86, 2017), 825–843. <https://doi.org/10.1146/annurev-biochem-061516-044839>.
- (65) Schnermann, M. J.; Lavis, L. D. Rejuvenating Old Fluorophores with New Chemistry. *Current Opinion in Chemical Biology* **2023**, *75*, 102335. <https://doi.org/10.1016/j.cbpa.2023.102335>.
- (66) Beziere, N.; Lozano, N.; Nunes, A.; Salichs, J.; Queiros, D.; Kostarelos, K.; Ntziachristos, V. Dynamic Imaging of PEGylated Indocyanine Green (ICG) Liposomes within the Tumor Microenvironment Using Multi-Spectral Optoacoustic Tomography (MSOT). *Biomaterials* **2015**, *37*, 415–424. <https://doi.org/10.1016/j.biomaterials.2014.10.014>.
- (67) Zhong, J.; Yang, S.; Zheng, X.; Zhou, T.; Xing, D. In Vivo Photoacoustic Therapy with Cancer-Targeted Indocyanine Green-Containing Nanoparticles. *Nanomedicine* **2013**, *8* (6), 903–919. <https://doi.org/10.2217/nnm.12.123>.
- (68) Fuenzalida Werner, J. P.; Huang, Y.; Mishra, K.; Janowski, R.; Vetschera, P.; Heichler, C.; Chmyrov, A.; Neufert, C.; Niessing, D.; Ntziachristos, V.; Stiel, A. C. Challenging a Preconception: Optoacoustic Spectrum Differs from the Optical Absorption Spectrum of Proteins and Dyes for Molecular Imaging. *Anal. Chem.* **2020**, *92* (15), 10717–10724. <https://doi.org/10.1021/acs.analchem.0c01902>.
- (69) Keiding, S.; Ott, P.; Bass, L. Enhancement of Unbound Clearance of ICG by Plasma Proteins, Demonstrated in Human Subjects and Interpreted without Assumption of Facilitating Structures. *Journal of Hepatology* **1993**, *19* (3), 327–344. [https://doi.org/10.1016/S0168-8278\(05\)80541-0](https://doi.org/10.1016/S0168-8278(05)80541-0).
- (70) Philip, R.; Penzkofer, A.; Bäuml, W.; Szeimies, R. M.; Abels, C. Absorption and Fluorescence Spectroscopic Investigation of Indocyanine Green. *Journal of Photochemistry and Photobiology A: Chemistry* **1996**, *96* (1), 137–148. [https://doi.org/10.1016/1010-6030\(95\)04292-X](https://doi.org/10.1016/1010-6030(95)04292-X).
- (71) Xu, C.; Ye, R.; Shen, H.; Lam, J. W. Y.; Zhao, Z.; Tang, B. Z. Molecular Motion and Nonradiative Decay: Towards Efficient Photothermal and Photoacoustic Systems. *Angew. Chem. Int. Ed.* **2022**, *61* (30), e202204604. <https://doi.org/10.1002/anie.202204604>.
- (72) Linder, K. E.; Metcalfe, E.; Nanjappan, P.; Arunachalam, T.; Ramos, K.; Skedzielewski, T. M.; Marinelli, E. R.; Tweedle, M. F.; Nunn, A. D.; Swenson, R. E. Synthesis, In Vitro Evaluation, and In Vivo Metabolism of Fluor/Quencher Compounds Containing IRDye 800CW and Black Hole Quencher-3 (BHQ-3). *Bioconjugate Chem.* **2011**, *22* (7), 1287–1297. <https://doi.org/10.1021/bc100457s>.
- (73) Ikeno, T.; Hanaoka, K.; Iwaki, S.; Myochin, T.; Murayama, Y.; Ohde, H.; Komatsu, T.; Ueno, T.; Nagano, T.; Urano, Y. Design and Synthesis of an Activatable Photoacoustic Probe for Hypochlorous Acid. *Anal. Chem.* **2019**, *91* (14), 9086–9092. <https://doi.org/10.1021/acs.analchem.9b01529>.
- (74) Myochin, T.; Hanaoka, K.; Iwaki, S.; Ueno, T.; Komatsu, T.; Terai, T.; Nagano, T.; Urano, Y. Development of a Series of Near-Infrared Dark Quenchers Based on Si-Rhodamines and Their Application to Fluorescent Probes. *J. Am. Chem. Soc.* **2015**, *137* (14), 4759–4765. <https://doi.org/10.1021/jacs.5b00246>.
- (75) Merkes, J. M.; Lammers, T.; Kancherla, R.; Rueping, M.; Kiessling, F.; Banala, S. Tuning Optical Properties of BODIPY Dyes by Pyrrole Conjugation for Photoacoustic Imaging. *Advanced Optical Materials* **2020**, *8* (11), 1902115. <https://doi.org/10.1002/adom.201902115>.
- (76) Frenette, M.; Hatamimoslehabadi, M.; Bellinger-Buckley, S.; Laoui, S.; La, J.; Bag, S.; Mallidi, S.; Hasan, T.; Bouma, B.; Yelleswarapu, C.; Rochford, J. Shining Light on the Dark Side of Imaging: Excited State Absorption Enhancement of a Bis-Styryl BODIPY Photoacoustic Contrast Agent. *J. Am. Chem. Soc.* **2014**, *136* (45), 15853–15856. <https://doi.org/10.1021/ja508600x>.
- (77) Levi, J.; Kothapalli, S. R.; Ma, T.-J.; Hartman, K.; Khuri-Yakub, B. T.; Gambhir, S. S. Design, Synthesis, and Imaging of an Activatable Photoacoustic Probe. *J. Am. Chem. Soc.* **2010**, *132* (32), 11264–11269. <https://doi.org/10.1021/ja104000a>.
- (78) Knox, H. J.; Chan, J. Acoustogenic Probes: A New Frontier in Photoacoustic Imaging. *Acc. Chem. Res.* **2018**, *51* (11), 2897–2905. <https://doi.org/10.1021/acs.accounts.8b00351>.
- (79) Yuan, L.; Lin, W.; Yang, Y.; Chen, H. A Unique Class of Near-Infrared Functional Fluorescent Dyes with Carboxylic-Acid-Modulated Fluorescence ON/OFF Switching: Rational Design, Synthesis, Optical Properties, Theoretical Calculations, and Applications for Fluorescence Imaging in Living Animals. *J. Am. Chem. Soc.* **2012**, *134* (2), 1200–1211. <https://doi.org/10.1021/ja209292b>.
- (80) Zeng, Z.; Liew, S. S.; Wei, X.; Pu, K. Hemicyanine-Based Near-Infrared Activatable Probes for Imaging and Diagnosis of Diseases. *Angewandte Chemie International Edition* **2021**, *n/a* (n/a). <https://doi.org/10.1002/anie.202107877>.
- (81) Lucero, M. Y.; Chan, J. Photoacoustic Imaging of Elevated Glutathione in Models of Lung Cancer for Companion Diagnostic Applications. *Nat. Chem.* **2021**, *13* (12), 1248–1256. <https://doi.org/10.1038/s41557-021-00804-0>.
- (82) Wu, Y.; Huang, S.; Wang, J.; Sun, L.; Zeng, F.; Wu, S. Activatable Probes for Diagnosing and Positioning Liver Injury and Metastatic Tumors by Multispectral Optoacoustic Tomography. *Nat. Commun.* **2018**, *9* (1), 3983. <https://doi.org/10.1038/s41467-018-06499-1>.

- (83) Zhen, X.; Zhang, J.; Huang, J.; Xie, C.; Miao, Q.; Pu, K. Macrotheranostic Probe with Disease-Activated Near-Infrared Fluorescence, Photoacoustic, and Photothermal Signals for Imaging-Guided Therapy. *Angew. Chem. Int. Ed.* **2018**, *57* (26), 7804–7808. <https://doi.org/10.1002/anie.201803321>.
- (84) Huang, J.; Wu, Y.; Zeng, F.; Wu, S. An Activatable Near-Infrared Chromophore for Multispectral Optoacoustic Imaging of Tumor Hypoxia and for Tumor Inhibition. *Theranostics* **2019**, *9* (24), 7313–7324. <https://doi.org/10.7150/thno.36755>.
- (85) Zhang, J.; Zhen, X.; Zeng, J.; Pu, K. A Dual-Modal Molecular Probe for Near-Infrared Fluorescence and Photoacoustic Imaging of Peroxynitrite. *Anal. Chem.* **2018**, *90* (15), 9301–9307. <https://doi.org/10.1021/acs.analchem.8b01879>.
- (86) Chen, J.; Fang, Y.; Sun, L.; Zeng, F.; Wu, S. An Activatable Probe for Detecting Alcoholic Liver Injury via Multispectral Optoacoustic Tomography and Fluorescence Imaging. *Chem. Commun.* **2020**, *56* (75), 11102–11105. <https://doi.org/10.1039/D0CC04635C>.
- (87) Gardner, S. H.; Brady, C. J.; Keeton, C.; Yadav, A. K.; Mallojjala, S. C.; Lucero, M. Y.; Su, S.; Yu, Z.; Hirschi, J. S.; Mirica, L. M.; Chan, J. A General Approach to Convert Hemicyanine Dyes into Highly Optimized Photoacoustic Scaffolds for Analyte Sensing**. *Angew. Chem. Int. Ed.* **2021**, *60* (34), 18860–18866. <https://doi.org/10.1002/anie.202105905>.
- (88) Zhang, S.; Chen, H.; Wang, L.; Qin, X.; Jiang, B.-P.; Ji, S.-C.; Shen, X.-C.; Liang, H. A General Approach to Design Dual Ratiometric Fluorescent and Photoacoustic Probe for Quantitatively Visualizing Tumor Hypoxia Levels in Vivo. *Angew. Chem. Int. Ed.* **2021**, *61*, e202107076. <https://doi.org/10.1002/ange.202107076>.
- (89) Liu, F.; Shi, X.; Liu, X.; Wang, F.; Yi, H.-B.; Jiang, J.-H. Engineering an NIR Rhodol Derivative with Spirocyclic Ring-Opening Activation for High-Contrast Photoacoustic Imaging. *Chem. Sci.* **2019**, *10* (40), 9257–9264. <https://doi.org/10.1039/C9SC02764E>.
- (90) Mauker, P.; Beckmann, D.; Kitowski, A.; Heise, C.; Wientjens, C.; Davidson, A. J.; Wanderoy, S.; Fabre, G.; Harbauer, A. B.; Wood, W.; Wilhelm, C.; Thorn-Seshold, J.; Misgeld, T.; Kerschensteiner, M.; Thorn-Seshold, O. Fluorogenic Chemical Probes for Wash-Free Imaging of Cell Membrane Damage in Ferroptosis, Necrosis, and Axon Injury. *J. Am. Chem. Soc.* **2024**, *146* (16), 11072–11082. <https://doi.org/10.1021/jacs.3c07662>.
- (91) Lardon, N.; Wang, L.; Tschanz, A.; Hoess, P.; Tran, M.; D'Este, E.; Ries, J.; Johnsson, K. Systematic Tuning of Rhodamine Spirocyclization for Super-Resolution Microscopy. *J. Am. Chem. Soc.* **2021**, *143* (36), 14592–14600. <https://doi.org/10.1021/jacs.1c05004>.
- (92) Grimm, J. B.; Tkachuk, A. N.; Xie, L.; Choi, H.; Mohar, B.; Falco, N.; Schaefer, K.; Patel, R.; Zheng, Q.; Liu, Z.; Lippincott-Schwartz, J.; Brown, T. A.; Lavis, L. D. A General Method to Optimize and Functionalize Red-Shifted Rhodamine Dyes. *Nat Methods* **2020**, *17* (8), 815–821. <https://doi.org/10.1038/s41592-020-0909-6>.
- (93) Brøndsted, F.; Fang, Y.; Li, L.; Zhou, X.; Grant, S.; Stains, C. I. Single Atom Stabilization of Phosphinate Ester-Containing Rhodamines Yields Cell Permeable Probes for Turn-On Photoacoustic Imaging**. *Chem. Eur. J* **2024**, *30* (1), e202303038. <https://doi.org/10.1002/chem.202303038>.
- (94) Knox, H. J.; Hedhli, J.; Kim, T. W.; Khalili, K.; Dobrucki, L. W.; Chan, J. A Bioreducible N-Oxide-Based Probe for Photoacoustic Imaging of Hypoxia. *Nat Commun* **2017**, *8* (1), 1794. <https://doi.org/10.1038/s41467-017-01951-0>.
- (95) Zhou, E. Y.; Knox, H. J.; Liu, C.; Zhao, W.; Chan, J. A Conformationally Restricted Aza-BODIPY Platform for Stimulus-Responsive Probes with Enhanced Photoacoustic Properties. *J. Am. Chem. Soc.* **2019**, *141* (44), 17601–17609. <https://doi.org/10.1021/jacs.9b06694>.
- (96) Chan, J.; Dodani, S. C.; Chang, C. J. Reaction-Based Small-Molecule Fluorescent Probes for Chemoselective Bioimaging. *Nat. Chem.* **2012**, *4* (12), 973–984. <https://doi.org/10.1038/nchem.1500>.
- (97) Li, H.; Zhang, P.; Smaga, L. P.; Hoffman, R. A.; Chan, J. Photoacoustic Probes for Ratiometric Imaging of Copper(II). *J. Am. Chem. Soc.* **2015**, *137* (50), 15628–15631. <https://doi.org/10.1021/jacs.5b10504>.
- (98) Zeng, L.; Ma, G.; Xu, H.; Mu, J.; Li, F.; Gao, X.; Deng, Z.; Qu, J.; Huang, P.; Lin, J. In Vivo Chemoselective Photoacoustic Imaging of Copper(II) in Plant and Animal Subjects. *Small* **2019**, *15* (6), 1803866. <https://doi.org/10.1002/sml.201803866>.
- (99) Dürr, H.; Bouas-Laurent, H. *Photochromism: Molecules and Systems*, Rev. ed.; Elsevier: Amsterdam Boston, 2003.
- (100) *Molecular Photoswitches: Chemistry, Properties, and Applications*; Pianowski, Z. L., Ed.; Wiley-VCH: Weinheim, 2022.
- (101) Demselben, Ueber Das Stickstoffbenzid. *Ann. Pharm.* **1834**, *12* (2–3), 311–314. <https://doi.org/10.1002/jlac.18340120282>.
- (102) Griffiths, J. II. Photochemistry of Azobenzene and Its Derivatives. *Chem. Soc. Rev.* **1972**, *1* (4), 481–493. <https://doi.org/10.1039/CS9720100481>.
- (103) Hartley, G. S. The Cis-Form of Azobenzene. *Nature* **1937**, *140* (3537), 281–281. <https://doi.org/10.1038/140281a0>.
- (104) Fiegl, H.; Köhn, A.; Hättig, C.; Ahlrichs, R. Ab Initio Calculation of the Vibrational and Electronic Spectra of Trans- and Cis-Azobenzene. *J. Am. Chem. Soc.* **2003**, *125* (32), 9821–9827. <https://doi.org/10.1021/ja034433o>.
- (105) Beharry, A. A.; Woolley, G. A. Azobenzene Photoswitches for Biomolecules. *Chem. Soc. Rev.* **2011**, *40* (8), 4422–4437. <https://doi.org/10.1039/C1CS15023E>.
- (106) Bandara, H. M. D.; Burdette, S. C. Photoisomerization in Different Classes of Azobenzene. *Chem. Soc. Rev.* **2012**, *41* (5), 1809–1825. <https://doi.org/10.1039/C1CS15179G>.
- (107) *Fakultät für Chemie und Pharmazie | Molekülvisualisierungen | Home*. <https://molvis.cup.uni-muenchen.de/> (accessed 2024-07-04).
- (108) Chang, C.-W.; Lu, Y.-C.; Wang, T.-T.; Diau, E. W.-G. Photoisomerization Dynamics of Azobenzene in Solution with S1 Excitation: A Femtosecond Fluorescence Anisotropy Study. *J. Am. Chem. Soc.* **2004**, *126* (32), 10109–10118. <https://doi.org/10.1021/ja049215p>.
- (109) Fujino, T.; Arzhantsev, S. Yu.; Tahara, T. Femtosecond Time-Resolved Fluorescence Study of Photoisomerization of Trans-Azobenzene. *J. Phys. Chem. A* **2001**, *105* (35), 8123–8129. <https://doi.org/10.1021/jp0110713>.
- (110) Lednev, I. K.; Ye, T.-Q.; Matousek, P.; Towrie, M.; Foggi, P.; Neuwahl, F. V. R.; Umaphathy, S.; Hester, R. E.; Moore, J. N. Femtosecond Time-Resolved UV-Visible Absorption Spectroscopy of Trans-Azobenzene: Dependence on Excitation Wavelength. *Chemical Physics Letters* **1998**, *290* (1), 68–74. [https://doi.org/10.1016/S0009-2614\(98\)00490-4](https://doi.org/10.1016/S0009-2614(98)00490-4).
- (111) Bléger, D.; Schwarz, J.; Brouwer, A. M.; Hecht, S. O-Fluoroazobenzenes as Readily Synthesized Photoswitches Offering Nearly Quantitative Two-Way Isomerization with Visible Light. *J. Am. Chem. Soc.* **2012**, *134* (51), 20597–20600. <https://doi.org/10.1021/ja310323y>.
- (112) Garcia-Amorós, J.; Maerz, B.; Reig, M.; Cuadrado, A.; Blancafort, L.; Samoylova, E.; Velasco, D. Picosecond Switchable Azo Dyes. *Chem. Eur. J* **2019**, *25* (32), 7726–7732. <https://doi.org/10.1002/chem.201900796>.
- (113) Dong, M.; Babalhavaeji, A.; Samanta, S.; Beharry, A. A.; Woolley, G. A. Red-Shifting Azobenzene Photoswitches for in Vivo Use. *Acc. Chem. Res.* **2015**, *48* (10), 2662–2670. <https://doi.org/10.1021/acs.accounts.5b00270>.
- (114) Qian, G.; Wang, Z. Y. Near-Infrared Organic Compounds and Emerging Applications. *Chemistry – An Asian Journal* **2010**, *5* (5), 1006–1029. <https://doi.org/10.1002/asia.200900596>.
- (115) Kinnibrugh, T. L.; Salman, S.; Getmanenko, Y. A.; Coropceanu, V.; Porter, W. W. I.; Timofeeva, T. V.; Matzger, A. J.; Brédas, J.-L.; Marder, S. R.; Barlow, S. Dipolar Second-Order Nonlinear Optical Chromophores Containing Ferrocene,

- Octamethylferrocene, and Ruthenocene Donors and Strong π -Acceptors: Crystal Structures and Comparison of π -Donor Strengths. *Organometallics* **2009**, *28* (5), 1350–1357. <https://doi.org/10.1021/om800986s>.
- (116) Bléger, D.; Hecht, S. Visible-Light-Activated Molecular Switches. *Angewandte Chemie International Edition* **2015**, *54* (39), 11338–11349. <https://doi.org/10.1002/anie.201500628>.
- (117) Siewertsen, R.; Neumann, H.; Buchheim-Stehn, B.; Herges, R.; Näther, C.; Renth, F.; Temps, F. Highly Efficient Reversible Z–E Photoisomerization of a Bridged Azobenzene with Visible Light through Resolved S1($N\pi^*$) Absorption Bands. *J. Am. Chem. Soc.* **2009**, *131* (43), 15594–15595. <https://doi.org/10.1021/ja906547d>.
- (118) Yang, Y.; Hughes, R. P.; Aprahamian, I. Near-Infrared Light Activated Azo-BF₂ Switches. *J. Am. Chem. Soc.* **2014**, *136* (38), 13190–13193. <https://doi.org/10.1021/ja508125n>.
- (119) Sadovski, O.; Beharry, A. A.; Zhang, F.; Woolley, G. A. Spectral Tuning of Azobenzene Photoswitches for Biological Applications. *Angewandte Chemie International Edition* **2009**, *48* (8), 1484–1486. <https://doi.org/10.1002/anie.200805013>.
- (120) Beharry, A. A.; Sadovski, O.; Woolley, G. A. Azobenzene Photoswitching without Ultraviolet Light. *J. Am. Chem. Soc.* **2011**, *133* (49), 19684–19687. <https://doi.org/10.1021/ja209239m>.
- (121) Dong, M.; Babalhavaeji, A.; Collins, C. V.; Jarrah, K.; Sadovski, O.; Dai, Q.; Woolley, G. A. Near-Infrared Photoswitching of Azobenzenes under Physiological Conditions. *J. Am. Chem. Soc.* **2017**, *139* (38), 13483–13486. <https://doi.org/10.1021/jacs.7b06471>.
- (122) Goulet-Hanssens, A.; Rietze, C.; Titov, E.; Abdullahu, L.; Grubert, L.; Saalfrank, P.; Hecht, S. Hole Catalysis as a General Mechanism for Efficient and Wavelength-Independent Z \rightarrow E Azobenzene Isomerization. *Chem* **2018**, *4* (7), 1740–1755. <https://doi.org/10.1016/j.chempr.2018.06.002>.
- (123) Gemen, J.; Church, J. R.; Ruoko, T.-P.; Durandin, N.; Biatek, M. J.; Weißenfels, M.; Feller, M.; Kazes, M.; Odaybat, M.; Borin, V. A.; Kalepu, R.; Diskin-Posner, Y.; Oron, D.; Fuchter, M. J.; Priimagi, A.; Schapiro, I.; Klajn, R. Disequilibrating Azobenzenes by Visible-Light Sensitization under Confinement. *Science* **2023**, *381* (6664), 1357–1363. <https://doi.org/10.1126/science.adh9059>.
- (124) Isokuortti, J.; Kuntze, K.; Virkki, M.; Ahmed, Z.; Vuorimaa-Laukkanen, E.; Filatov, M. A.; Turshatov, A.; Laaksonen, T.; Priimagi, A.; Durandin, N. A. Expanding Excitation Wavelengths for Azobenzene Photoswitching into the Near-Infrared Range via Endothermic Triplet Energy Transfer. *Chem. Sci.* **2021**, *12* (21), 7504–7509. <https://doi.org/10.1039/D1SC01717A>.
- (125) Baumgartner, B.; Glembockyte, V.; Gonzalez-Hernandez, A. J.; Valavalkar, A.; Mayer, R. J.; Fillbrook, L. L.; Müller-Deku, A.; Zhang, J.; Steiner, F.; Gross, C.; Reynders, M.; Munguba, H.; Arefin, A.; Ofial, A.; Beves, J. E.; Lohmueller, T.; Dietzek-Ivanšić, B.; Broichhagen, J.; Tinnefeld, P.; Levitz, J.; Thorn-Seshold, O. A General Method for Near-Infrared Photoswitching in Biology, Demonstrated by the >700 Nm Photocontrol of GPCR Activity in Brain Slices. *ChemRxiv* April 30, 2024. <https://doi.org/10.26434/chemrxiv-2024-vm4n3>.
- (126) Baumgartner, B.; Glembockyte, V.; Mayer, R.; Gonzalez-Hernandez, A.; Kindler, R.; Valavalkar, A.; Wiegand, A.; Müller-Deku, A.; Grubert, L.; Steiner, F.; Gross, C.; Reynders, M.; Grenier, V.; Broichhagen, J.; Hecht, S.; Tinnefeld, P.; Ofial, A.; Dietzek-Ivanšić, B.; Levitz, J.; Thorn-Seshold, O. Azobenzenes Can Achieve Near-Infrared Photocontrol in Biological Systems, with Quantitative Z \rightarrow E Photoisomerization, via Singlet Manifold Photoredox. *ChemRxiv* September 14, 2023. <https://doi.org/10.26434/chemrxiv-2023-37sv4>.
- (127) Chevalier, A.; Renard, P.-Y.; Romieu, A. Straightforward Synthesis of Bioconjugatable Azo Dyes. Part 1: Black Hole Quencher-1 (BHQ-1) Scaffold. *Tetrahedron Letters* **2014**, *55* (50), 6759–6763. <https://doi.org/10.1016/j.tetlet.2014.10.053>.
- (128) Chevalier, A.; Renard, P.-Y.; Romieu, A. Straightforward Synthesis of Bioconjugatable Azo Dyes. Part 2: Black Hole Quencher-2 (BHQ-2) and BlackBerry Quencher 650 (BBQ-650) Scaffolds. *Tetrahedron Letters* **2014**, *55* (50), 6764–6768. <https://doi.org/10.1016/j.tetlet.2014.10.054>.
- (129) Kupferschmidt, K. *Blau: Wie Die Schönheit in Die Welt Kommt*, 3. Auflage.; Hoffmann und Campe: Hamburg, 2020.
- (130) Fleet, M. E.; Liu, X. X-Ray Absorption Spectroscopy of Ultramarine Pigments: A New Analytical Method for the Polysulfide Radical Anion S₃⁻ Chromophore. *Spectrochimica Acta Part B: Atomic Spectroscopy* **2010**, *65* (1), 75–79. <https://doi.org/10.1016/j.sab.2009.11.008>.
- (131) Kato, S.; Matsui, T.; Gatsogiannis, C.; Tanaka, Y. Molluscan Hemocyanin: Structure, Evolution, and Physiology. *Biophys Rev* **2018**, *10* (2), 191–202. <https://doi.org/10.1007/s12551-017-0349-4>.
- (132) Pennisi, E. How a Blue Protein Turns Tree Frogs Bright Green. *Science* **2020**. <https://doi.org/10.1126/science.abd8020>.
- (133) Halepas, S.; Hamchand, R.; Lindeyer, S. E. D.; Brückner, C. Isolation of Biliverdin IX α , as Its Dimethyl Ester, from Emu Eggshells. *J. Chem. Educ.* **2017**, *94* (10), 1533–1537. <https://doi.org/10.1021/acs.jchemed.7b00449>.
- (134) Shiono, M.; Matsugaki, N.; Takeda, K. Structure of the Blue Cornflower Pigment. *Nature* **2005**, *436* (7052), 791–791. <https://doi.org/10.1038/436791a>.
- (135) Kupferschmidt, K. *Blue: In Search of Nature's Rarest Color*, The Experiment: New York, 2021.
- (136) Huang, C.-Y. (Dennis); Hecht, S. A Blueprint for Transforming Indigos to Photoresponsive Molecular Tools. *Chemistry – A European Journal* **2023**, *29* (43), e202300981. <https://doi.org/10.1002/chem.202300981>.
- (137) de Melo, J. S. S.; Rondão, R.; Burrows, H. D.; Melo, M. J.; Navaratnam, S.; Edge, R.; Voss, G. Spectral and Photophysical Studies of Substituted Indigo Derivatives in Their Keto Forms. *ChemPhysChem* **2006**, *7* (11), 2303–2311. <https://doi.org/10.1002/cphc.200600203>.
- (138) Clapham, D. E. TRP Channels as Cellular Sensors. *Nature* **2003**, *426* (6966), 517–524. <https://doi.org/10.1038/nature02196>.
- (139) Montell, C. Drosophila Sensory Receptors—a Set of Molecular Swiss Army Knives. *Genetics* **2021**, *217* (1), 1–34. <https://doi.org/10.1093/genetics/iyaa011>.
- (140) Cosens, D. J.; Manning, A. Abnormal Electroretinogram from a Drosophila Mutant. *Nature* **1969**, *224* (5216), 285–287. <https://doi.org/10.1038/224285a0>.
- (141) Minke, B.; Wu, C.-F.; Pak, W. L. Induction of Photoreceptor Voltage Noise in the Dark in Drosophila Mutant. *Nature* **1975**, *258* (5530), 84–87. <https://doi.org/10.1038/258084a0>.
- (142) Montell, C.; Rubin, G. M. Molecular Characterization of the Drosophila Trp Locus: A Putative Integral Membrane Protein Required for Phototransduction. *Neuron* **1989**, *2* (4), 1313–1323. [https://doi.org/10.1016/0896-6273\(89\)90069-X](https://doi.org/10.1016/0896-6273(89)90069-X).
- (143) Suss-Toby, E.; Selinger, Z.; Minke, B. Lanthanum Reduces the Excitation Efficiency in Fly Photoreceptors. *J. Gen. Physiol* **1991**, *98* (4), 849–868. <https://doi.org/10.1085/jgp.98.4.849>.
- (144) Hardie, R. C.; Minke, B. The Trp Gene Is Essential for a Light-Activated Ca²⁺ Channel in Drosophila Photoreceptors. *Neuron* **1992**, *8* (4), 643–651. [https://doi.org/10.1016/0896-6273\(92\)90086-S](https://doi.org/10.1016/0896-6273(92)90086-S).
- (145) Phillips, A. M.; Bull, A.; Kelly, L. E. Identification of a Drosophila Gene Encoding a Calmodulin-Binding Protein with Homology to the Trp Phototransduction Gene. *Neuron* **1992**, *8* (4), 631–642. [https://doi.org/10.1016/0896-6273\(92\)90085-R](https://doi.org/10.1016/0896-6273(92)90085-R).

- (146) Zhu, X.; Chu, P. B.; Peyton, M.; Birnbaumer, L. Molecular Cloning of a Widely Expressed Human Homologue for the Drosophila Trp Gene. *FEBS Letters* **1995**, *373* (3), 193–198. [https://doi.org/10.1016/0014-5793\(95\)01038-G](https://doi.org/10.1016/0014-5793(95)01038-G).
- (147) Wes, P. D.; Chevesich, J.; Jeromin, A.; Rosenberg, C.; Stetten, G.; Montell, C. TRPC1, a Human Homolog of a Drosophila Store-Operated Channel. *Proceedings of the National Academy of Sciences* **1995**, *92* (21), 9652–9656. <https://doi.org/10.1073/pnas.92.21.9652>.
- (148) Nilius, B.; Owsianik, G. The Transient Receptor Potential Family of Ion Channels. *Genome Biol* **2011**, *12* (3), 1–11. <https://doi.org/10.1186/gb-2011-12-3-218>.
- (149) Clapham, D. E.; Montell, C.; Schultz, G.; Julius, D. International Union of Pharmacology. XLIII. Compendium of Voltage-Gated Ion Channels: Transient Receptor Potential Channels. *Pharmacol Rev* **2003**, *55* (4), 591–596. <https://doi.org/10.1124/pr.55.4.6>.
- (150) Caterina, M. J.; Schumacher, M. A.; Tominaga, M.; Rosen, T. A.; Levine, J. D.; Julius, D. The Capsaicin Receptor: A Heat-Activated Ion Channel in the Pain Pathway. *Nature* **1997**, *389* (6653), 816–824. <https://doi.org/10.1038/39807>.
- (151) Patapoutian, A.; Peier, A. M.; Story, G. M.; Viswanath, V. ThermoTRP Channels and beyond: Mechanisms of Temperature Sensation. *Nat Rev Neurosci* **2003**, *4* (7), 529–539. <https://doi.org/10.1038/nrn1141>.
- (152) Dhaka, A.; Viswanath, V.; Patapoutian, A. TRP ION CHANNELS AND TEMPERATURE SENSATION. *Annual Review of Neuroscience* **2006**, *29* (Volume 29, 2006), 135–161. <https://doi.org/10.1146/annurev.neuro.29.051605.112958>.
- (153) McKemy, D. D.; Neuhauser, W. M.; Julius, D. Identification of a Cold Receptor Reveals a General Role for TRP Channels in Thermosensation. *Nature* **2002**, *416* (6876), 52–58. <https://doi.org/10.1038/nature719>.
- (154) Peier, A. M.; Moqrich, A.; Hergarden, A. C.; Reeve, A. J.; Andersson, D. A.; Story, G. M.; Earley, T. J.; Dragoni, I.; McIntyre, P.; Bevan, S.; Patapoutian, A. A TRP Channel That Senses Cold Stimuli and Menthol. *Cell* **2002**, *108* (5), 705–715. [https://doi.org/10.1016/S0092-8674\(02\)00652-9](https://doi.org/10.1016/S0092-8674(02)00652-9).
- (155) Ranade, S. S.; Woo, S.-H.; Dubin, A. E.; Moshourab, R. A.; Wetzel, C.; Petrus, M.; Mathur, J.; Bégay, V.; Coste, B.; Mainquist, J.; Wilson, A. J.; Francisco, A. G.; Reddy, K.; Qiu, Z.; Wood, J. N.; Lewin, G. R.; Patapoutian, A. Piezo2 Is the Major Transducer of Mechanical Forces for Touch Sensation in Mice. *Nature* **2014**, *516* (7529), 121–125. <https://doi.org/10.1038/nature13980>.
- (156) Szallasi, A.; Blumberg, P. M. Resiniferatoxin, a Phorbol-Related Diterpene, Acts as an Ultrapotent Analog of Capsaicin, the Irritant Constituent in Red Pepper. *Neuroscience* **1989**, *30* (2), 515–520. [https://doi.org/10.1016/0306-4522\(89\)90269-8](https://doi.org/10.1016/0306-4522(89)90269-8).
- (157) Hinman, A.; Chuang, H.; Bautista, D. M.; Julius, D. TRP Channel Activation by Reversible Covalent Modification. *Proceedings of the National Academy of Sciences* **2006**, *103* (51), 19564–19568. <https://doi.org/10.1073/pnas.0609598103>.
- (158) Koivisto, A.-P.; Belvisi, M. G.; Gaudet, R.; Szallasi, A. Advances in TRP Channel Drug Discovery: From Target Validation to Clinical Studies. *Nat Rev Drug Discov* **2022**, *21* (1), 41–59. <https://doi.org/10.1038/s41573-021-00268-4>.
- (159) Song, K.; Wang, H.; Kamm, G. B.; Pohle, J.; Reis, F. de C.; Heppenstall, P.; Wende, H.; Siemens, J. The TRPM2 Channel Is a Hypothalamic Heat Sensor That Limits Fever and Can Drive Hypothermia. *Science* **2016**. <https://doi.org/10.1126/science.aaf7537>.
- (160) Clapham, D. E.; Runnels, L. W.; Strübing, C. The Trp Ion Channel Family. *Nature Reviews Neuroscience* **2001**, *2* (6), 387–396. <https://doi.org/10.1038/35077544>.
- (161) Cao, E. Structural Mechanisms of Transient Receptor Potential Ion Channels. *J Gen Physiol* **2020**, *152* (3). <https://doi.org/10.1085/jgp.201811998>.
- (162) Structural Pharmacology of TRP Channels. *Journal of Molecular Biology* **2021**, *433* (17), 166914. <https://doi.org/10.1016/j.jmb.2021.166914>.
- (163) Madej, M. G.; Ziegler, C. M. Dawning of a New Era in TRP Channel Structural Biology by Cryo-Electron Microscopy. *Pflügers Arch - Eur J Physiol* **2018**, *470* (2), 213–225. <https://doi.org/10.1007/s00424-018-2107-2>.
- (164) Gaudet, R. TRP Channels Entering the Structural Era. *The Journal of Physiology* **2008**, *586* (15), 3565–3575. <https://doi.org/10.1113/jphysiol.2008.155812>.
- (165) Lishko, P. V.; Procko, E.; Jin, X.; Phelps, C. B.; Gaudet, R. The Ankyrin Repeats of TRPV1 Bind Multiple Ligands and Modulate Channel Sensitivity. *Neuron* **2007**, *54* (6), 905–918. <https://doi.org/10.1016/j.neuron.2007.05.027>.
- (166) Lau, S.-Y.; Procko, E.; Gaudet, R. Distinct Properties of Ca²⁺-Calmodulin Binding to N- and C-Terminal Regulatory Regions of the TRPV1 Channel. *J Gen Physiol* **2012**, *140* (5), 541–555. <https://doi.org/10.1085/jgp.201210810>.
- (167) Moiseenkova-Bell, V. Y.; Stanciu, L. A.; Serysheva, I. I.; Tobe, B. J.; Wensel, T. G. Structure of TRPV1 Channel Revealed by Electron Cryomicroscopy. *Proceedings of the National Academy of Sciences* **2008**, *105* (21), 7451–7455. <https://doi.org/10.1073/pnas.0711835105>.
- (168) Li, X.; Mooney, P.; Zheng, S.; Booth, C. R.; Braunfeld, M. B.; Gubbens, S.; Agard, D. A.; Cheng, Y. Electron Counting and Beam-Induced Motion Correction Enable near-Atomic-Resolution Single-Particle Cryo-EM. *Nat Methods* **2013**, *10* (6), 584–590. <https://doi.org/10.1038/nmeth.2472>.
- (169) Liao, M.; Cao, E.; Julius, D.; Cheng, Y. Structure of the TRPV1 Ion Channel Determined by Electron Cryo-Microscopy. *Nature* **2013**, *504* (7478), 107–112. <https://doi.org/10.1038/nature12822>.
- (170) Cao, E.; Liao, M.; Cheng, Y.; Julius, D. TRPV1 Structures in Distinct Conformations Reveal Activation Mechanisms. *Nature* **2013**, *504* (7478), 113–118. <https://doi.org/10.1038/nature12823>.
- (171) Patapoutian, A.; Tate, S.; Woolf, C. J. Transient Receptor Potential Channels: Targeting Pain at the Source. *Nat Rev Drug Discov* **2009**, *8* (1), 55–68. <https://doi.org/10.1038/nrd2757>.
- (172) Molecular Basis for Species-Specific Sensitivity to “Hot” Chili Peppers. *Cell* **2002**, *108* (3), 421–430. [https://doi.org/10.1016/S0092-8674\(02\)00637-2](https://doi.org/10.1016/S0092-8674(02)00637-2).
- (173) Chu, Y.; Cohen, B. E.; Chuang, H. A Single TRPV1 Amino Acid Controls Species Sensitivity to Capsaicin. *Sci Rep* **2020**, *10* (1), 1–12. <https://doi.org/10.1038/s41598-020-64584-2>.
- (174) Laursen, W. J.; Schneider, E. R.; Merriman, D. K.; Bagriantsev, S. N.; Gracheva, E. O. Low-Cost Functional Plasticity of TRPV1 Supports Heat Tolerance in Squirrels and Camels. *Proceedings of the National Academy of Sciences* **2016**, *113* (40), 11342–11347. <https://doi.org/10.1073/pnas.1604269113>.
- (175) Wang, H.; Cheng, X.; Tian, J.; Xiao, Y.; Tian, T.; Xu, F.; Hong, X.; Zhu, M. X. TRPC Channels: Structure, Function, Regulation and Recent Advances in Small Molecular Probes. *Pharmacology & Therapeutics* **2020**, *209*, 107497. <https://doi.org/10.1016/j.pharmthera.2020.107497>.
- (176) Baron, J.; Groschner, K.; Tiapko, O. Calcium Transport and Sensing in TRPC Channels – New Insights into a Complex Feedback Regulation. *Cell Calcium* **2023**, *116*, 102816. <https://doi.org/10.1016/j.ceca.2023.102816>.
- (177) Dietrich, A.; Fahlbusch, M.; Gudermann, T. Classical Transient Receptor Potential 1 (TRPC1): Channel or Channel Regulator? *Cells* **2014**, *3* (4), 939–962. <https://doi.org/10.3390/cells3040939>.

- (178) Zhang, S. L.; Yu, Y.; Roos, J.; Kozak, J. A.; Deerinck, T. J.; Ellisman, M. H.; Stauderman, K. A.; Cahalan, M. D. STIM1 Is a Ca²⁺ Sensor That Activates CRAC Channels and Migrates from the Ca²⁺ Store to the Plasma Membrane. *Nature* **2005**, *437* (7060), 902–905. <https://doi.org/10.1038/nature04147>.
- (179) Vig, M.; Peinelt, C.; Beck, A.; Koormo, D. L.; Rabah, D.; Koblan-Huberson, M.; Kraft, S.; Turner, H.; Fleig, A.; Penner, R.; Kinet, J.-P. CRACM1 Is a Plasma Membrane Protein Essential for Store-Operated Ca²⁺ Entry. *Science* **2006**. <https://doi.org/10.1126/science.1127883>.
- (180) Feske, S.; Gwack, Y.; Prakriya, M.; Srikanth, S.; Puppel, S.-H.; Tanasa, B.; Hogan, P. G.; Lewis, R. S.; Daly, M.; Rao, A. A Mutation in Orai1 Causes Immune Deficiency by Abrogating CRAC Channel Function. *Nature* **2006**, *441* (7090), 179–185. <https://doi.org/10.1038/nature04702>.
- (181) Hofmann, T.; Obukhov, A. G.; Schaefer, M.; Harteneck, C.; Gudermann, T.; Schultz, G. Direct Activation of Human TRPC6 and TRPC3 Channels by Diacylglycerol. *Nature* **1999**, *397* (6716), 259–263. <https://doi.org/10.1038/16711>.
- (182) Storch, U.; Forst, A.-L.; Pardatscher, F.; Erdogmus, S.; Philipp, M.; Gregoritz, M.; Mederos y Schnitzler, M.; Gudermann, T. Dynamic NHERF Interaction with TRPC4/5 Proteins Is Required for Channel Gating by Diacylglycerol. *Proceedings of the National Academy of Sciences* **2017**, *114* (1), E37–E46. <https://doi.org/10.1073/pnas.1612263114>.
- (183) Xu, S.-Z.; Sukumar, P.; Zeng, F.; Li, J.; Jairaman, A.; English, A.; Naylor, J.; Ciurtin, C.; Majeed, Y.; Milligan, C. J.; Bahnasi, Y. M.; Al-Shawaf, E.; Porter, K. E.; Jiang, L.-H.; Emery, P.; Sivaprasadarao, A.; Beech, D. J. TRPC Channel Activation by Extracellular Thioredoxin. *Nature* **2008**, *451* (7174), 69–72. <https://doi.org/10.1038/nature06414>.
- (184) Callaway, E. Revolutionary Cryo-EM Is Taking over Structural Biology. *Nature* **2020**, *578* (7794), 201–201. <https://doi.org/10.1038/d41586-020-00341-9>.
- (185) Sierra-Valdez, F.; Azumaya, C. M.; Romero, L. O.; Nakagawa, T.; Cordero-Morales, J. F. Structure–Function Analyses of the Ion Channel TRPC3 Reveal That Its Cytoplasmic Domain Allosterically Modulates Channel Gating. *Journal of Biological Chemistry* **2018**, *293* (41), 16102–16114. <https://doi.org/10.1074/jbc.RA118.005066>.
- (186) Azumaya, C. M.; Sierra-Valdez, F.; Cordero-Morales, J. F.; Nakagawa, T. Cryo-EM Structure of the Cytoplasmic Domain of Murine Transient Receptor Potential Cation Channel Subfamily C Member 6 (TRPC6). *Journal of Biological Chemistry* **2018**, *293* (26), 10381–10391. <https://doi.org/10.1074/jbc.RA118.003183>.
- (187) Tang, Q.; Guo, W.; Zheng, L.; Wu, J.-X.; Liu, M.; Zhou, X.; Zhang, X.; Chen, L. Structure of the Receptor-Activated Human TRPC6 and TRPC3 Ion Channels. *Cell Res* **2018**, *28* (7), 746–755. <https://doi.org/10.1038/s41422-018-0038-2>.
- (188) Duan, J.; Li, J.; Zeng, B.; Chen, G.-L.; Peng, X.; Zhang, Y.; Wang, J.; Clapham, D. E.; Li, Z.; Zhang, J. Structure of the Mouse TRPC4 Ion Channel. *Nat Commun* **2018**, *9* (1), 3102. <https://doi.org/10.1038/s41467-018-05247-9>.
- (189) Vinayagam, D.; Mager, T.; Apelbaum, A.; Bothe, A.; Merino, F.; Hofnagel, O.; Gatsogiannis, C.; Raunser, S. Electron Cryo-Microscopy Structure of the Canonical TRPC4 Ion Channel. *eLife* **2018**, *7*, e36615. <https://doi.org/10.7554/eLife.36615>.
- (190) Duan, J.; Li, J.; Chen, G.-L.; Zeng, B.; Xie, K.; Peng, X.; Zhou, W.; Zhong, J.; Zhang, Y.; Xu, J.; Xue, C.; Zhu, L.; Liu, W.; Tian, X.-L.; Wang, J.; Clapham, D. E.; Li, Z.; Zhang, J. *Cryo-EM Structure of the Receptor-Activated TRPC5 Ion Channel at 2.9 Angstrom Resolution*; preprint; Biophysics, 2018. <https://doi.org/10.1101/467969>.
- (191) Bacsa, B.; Tiapko, O.; Stockner, T.; Groschner, K. Mechanisms and Significance of Ca²⁺ Entry through TRPC Channels. *Current Opinion in Physiology* **2020**, *17*, 25–33. <https://doi.org/10.1016/j.cophys.2020.06.005>.
- (192) Kim, J.; Ko, J.; Myeong, J.; Kwak, M.; Hong, C.; So, I. TRPC1 as a Negative Regulator for TRPC4 and TRPC5 Channels. *Pflugers Arch - Eur J Physiol* **2019**, *471* (8), 1045–1053. <https://doi.org/10.1007/s00424-019-02289-w>.
- (193) Storch, U.; Forst, A.-L.; Philipp, M.; Gudermann, T.; Mederos y Schnitzler, M. Transient Receptor Potential Channel 1 (TRPC1) Reduces Calcium Permeability in Heteromeric Channel Complexes. *Journal of Biological Chemistry* **2012**, *287* (5), 3530–3540. <https://doi.org/10.1074/jbc.M111.283218>.
- (194) Hong, C.; Seo, H.; Kwak, M.; Jeon, J.; Jang, J.; Jeong, E. M.; Myeong, J.; Hwang, Y. J.; Ha, K.; Kang, M. J.; Lee, K. P.; Yi, E. C.; Kim, I.-G.; Jeon, J.-H.; Ryu, H.; So, I. Increased TRPC5 Glutathionylation Contributes to Striatal Neuron Loss in Huntington's Disease. *Brain* **2015**, *138* (10), 3030–3047. <https://doi.org/10.1093/brain/aww188>.
- (195) Kollwe, A.; Schwarz, Y.; Oleinikov, K.; Raza, A.; Haupt, A.; Wartenberg, P.; Wyatt, A.; Boehm, U.; Ectors, F.; Bildl, W.; Zolles, G.; Schulte, U.; Bruns, D.; Flockerzi, V.; Fakler, B. Subunit Composition, Molecular Environment, and Activation of Native TRPC Channels Encoded by Their *Interactomes*. *Neuron* **2022**, *110* (24), 4162–4175.e7. <https://doi.org/10.1016/j.neuron.2022.09.029>.
- (196) Riccio, A.; Li, Y.; Moon, J.; Kim, K.-S.; Smith, K. S.; Rudolph, U.; Gapon, S.; Yao, G. L.; Tsvetkov, E.; Rodig, S. J.; Van't Veer, A.; Meloni, E. G.; Carlezon, W. A.; Bolshakov, V. Y.; Clapham, D. E. Essential Role for TRPC5 in Amygdala Function and Fear-Related Behavior. *Cell* **2009**, *137* (4), 761–772. <https://doi.org/10.1016/j.cell.2009.03.039>.
- (197) Riccio, A.; Li, Y.; Tsvetkov, E.; Gapon, S.; Yao, G. L.; Smith, K. S.; Engin, E.; Rudolph, U.; Bolshakov, V. Y.; Clapham, D. E. Decreased Anxiety-Like Behavior and Gαq/11-Dependent Responses in the Amygdala of Mice Lacking TRPC4 Channels. *J Neurosci* **2014**, *34* (10), 3653–3667. <https://doi.org/10.1523/JNEUROSCI.2274-13.2014>.
- (198) *Cocaine self-administration in rats lacking a...* | *F1000Research*. <https://f1000research.com/articles/2-110/v1> (accessed 2024-04-19).
- (199) TRPC5 Channel Instability Induced by Depalmitoylation Protects Striatal Neurons against Oxidative Stress in Huntington's Disease. *Biochimica et Biophysica Acta (BBA) - Molecular Cell Research* **2020**, *1867* (2), 118620. <https://doi.org/10.1016/j.bbamcr.2019.118620>.
- (200) Zhou, Y.; Castonguay, P.; Sidhom, E.-H.; Clark, A. R.; Dvela-Levitt, M.; Kim, S.; Sieber, J.; Wieder, N.; Jung, J. Y.; Andreeva, S.; Reichardt, J.; Dubois, F.; Hoffmann, S. C.; Basgen, J. M.; Montesinos, M. S.; Weins, A.; Johnson, A. C.; Lander, E. S.; Garrett, M. R.; Hopkins, C. R.; Greka, A. A Small-Molecule Inhibitor of TRPC5 Ion Channels Suppresses Progressive Kidney Disease in Animal Models. *Science* **2017**. <https://doi.org/10.1126/science.aal4178>.
- (201) *TRP'ing up chronic kidney disease* | *Science*. <https://www-science-org.emedien.ub.uni-muenchen.de/doi/10.1126/science.aar3572> (accessed 2024-04-19).
- (202) Bernal, L.; Sotelo-Hitschfeld, P.; König, C.; Sinica, V.; Wyatt, A.; Winter, Z.; Hein, A.; Touska, F.; Reinhardt, S.; Tragl, A.; Kusuda, R.; Wartenberg, P.; Sclaroff, A.; Pfeifer, J. D.; Ectors, F.; Dahl, A.; Freichel, M.; Vlachova, V.; Brauchi, S.; Roza, C.; Boehm, U.; Clapham, D. E.; Lennerz, J. K.; Zimmermann, K. Odontoblast TRPC5 Channels Signal Cold Pain in Teeth. *Science Advances* **2021**, *7* (13), eabf5567. <https://doi.org/10.1126/sciadv.abf5567>.
- (203) Sadler, K. E.; Moehring, F.; Shiers, S. I.; Laskowski, L. J.; Mikesell, A. R.; Plautz, Z. R.; Brezinski, A. N.; Mecca, C. M.; Dussor, G.; Price, T. J.; McCorvy, J. D.; Stucky, C. L. Transient Receptor Potential Canonical 5 Mediates Inflammatory Mechanical and Spontaneous Pain in Mice. *Science Translational Medicine* **2021**, *13* (595), eabd7702. <https://doi.org/10.1126/scitranslmed.abd7702>.
- (204) Denk, F. TRPC5 and the Path towards Analgesic Drug Development. *Trends in Neurosciences* **2021**, *44* (9), 687–688. <https://doi.org/10.1016/j.tins.2021.06.010>.
- (205) Bon, R. S.; Beech, D. J. In Pursuit of Small Molecule Chemistry for Calcium-Permeable Non-Selective TRPC Channels – Mirage or Pot of Gold? *Br. J. Pharmacol.* **2013**, *170* (3), 459–474. <https://doi.org/10.1111/bph.12274>.

- (206) Li, J. W.-H.; Vederas, J. C. Drug Discovery and Natural Products: End of an Era or an Endless Frontier? *Science* **2009**. <https://doi.org/10.1126/science.1168243>.
- (207) Ratnayake, R.; Covell, D.; Ransom, T. T.; Gustafson, K. R.; Beutler, J. A. Englerin A, a Selective Inhibitor of Renal Cancer Cell Growth, from *Phyllanthus Engleri*. *Org. Lett.* **2009**, *11* (1), 57–60. <https://doi.org/10.1021/ol802339w>.
- (208) Akbulut, Y.; Gaunt, H. J.; Muraki, K.; Ludlow, M. J.; Amer, M. S.; Bruns, A.; Vasudev, N. S.; Radtke, L.; Willot, M.; Hahn, S.; Seitz, T.; Ziegler, S.; Christmann, M.; Beech, D. J.; Waldmann, H. (–)-Englerin A Is a Potent and Selective Activator of TRPC4 and TRPC5 Calcium Channels. *Angew. Chem. Int. Ed.* **2015**, *54* (12), 3787–3791. <https://doi.org/10.1002/anie.201411511>.
- (209) Radtke, L.; Willot, M.; Sun, H.; Ziegler, S.; Sauerland, S.; Strohmam, C.; Fröhlich, R.; Habenberger, P.; Waldmann, H.; Christmann, M. Total Synthesis and Biological Evaluation of (–)-Englerin A and B: Synthesis of Analogues with Improved Activity Profile. *Angewandte Chemie International Edition* **2011**, *50* (17), 3998–4002. <https://doi.org/10.1002/anie.201007790>.
- (210) Nicolaou, K. C.; Kang, Q.; Ng, S. Y.; Chen, D. Y.-K. Total Synthesis of Englerin A. *J. Am. Chem. Soc.* **2010**, *132* (23), 8219–8222. <https://doi.org/10.1021/ja102927n>.
- (211) Willot, M.; Radtke, L.; Könnig, D.; Fröhlich, R.; Gessner, V. H.; Strohmam, C.; Christmann, M. Total Synthesis and Absolute Configuration of the Guaiane Sesquiterpene Englerin A. *Angewandte Chemie International Edition* **2009**, *48* (48), 9105–9108. <https://doi.org/10.1002/anie.200905032>.
- (212) Guo, L.; Plietker, B. β -Ketoesters as Mono- or Bisnucleophiles: A Concise Enantioselective Total Synthesis of (–)-Englerin A and B. *Angewandte Chemie International Edition* **2019**, *58* (25), 8346–8350. <https://doi.org/10.1002/anie.201900401>.
- (213) Rubaiy, H. N.; Seitz, T.; Hahn, S.; Choidas, A.; Habenberger, P.; Klebl, B.; Dinkel, K.; Nussbaumer, P.; Waldmann, H.; Christmann, M.; Beech, D. J. Identification of an (–)-Englerin A Analogue, Which Antagonizes (–)-Englerin A at TRPC1/4/5 Channels. *British Journal of Pharmacology* **2018**, *175* (5), 830–839. <https://doi.org/10.1111/bph.14128>.
- (214) Beckmann, H.; Richter, J.; Hill, K.; Urban, N.; Lemoine, H.; Schaefer, M. A Benzothiadiazine Derivative and Methylprednisolone Are Novel and Selective Activators of Transient Receptor Potential Canonical 5 (TRPC5) Channels. *Cell Calcium* **2017**, *66*, 10–18. <https://doi.org/10.1016/j.ceca.2017.05.012>.
- (215) Richter, J. M.; Schaefer, M.; Hill, K. Clemizole Hydrochloride Is a Novel and Potent Inhibitor of Transient Receptor Potential Channel TRPC5. *Mol Pharmacol* **2014**, *86* (5), 514–521. <https://doi.org/10.1124/mol.114.093229>.
- (216) Rubaiy, H. N. Treasure Troves of Pharmacological Tools to Study Transient Receptor Potential Canonical 1/4/5 Channels. *Br. J. Pharmacol.* **2019**, *176* (7), 832–846. <https://doi.org/10.1111/bph.14578>.
- (217) Chenard, B.; Gallaschun, R. Substituted Xanthines and Methods of Use Thereof. WO2014143799A2, September 18, 2014. <https://patents.google.com/patent/WO2014143799A2/en> (accessed 2024-03-08).
- (218) Just, S.; Chenard, B. L.; Ceci, A.; Strassmaier, T.; Chong, J. A.; Blair, N. T.; Gallaschun, R. J.; del Camino, D.; Cantin, S.; D'Amours, M.; Eickmeier, C.; Fanger, C. M.; Hecker, C.; Hessler, D. P.; Hengerer, B.; Kroker, K. S.; Malekiani, S.; Mihalek, R.; McLaughlin, J.; Rast, G.; Witek, J.; Sauer, A.; Pryce, C. R.; Moran, M. M. Treatment with HC-070, a Potent Inhibitor of TRPC4 and TRPC5, Leads to Anxiolytic and Antidepressant Effects in Mice. *PLoS ONE* **2018**, *13* (1), e0191225. <https://doi.org/10.1371/journal.pone.0191225>.
- (219) Rubaiy, H. N.; Ludlow, M. J.; Henrot, M.; Gaunt, H. J.; Miteva, K.; Cheung, S. Y.; Tanahashi, Y.; Hamzah, N.; Musialowski, K. E.; Blythe, N. M.; Appleby, H. L.; Bailey, M. A.; McKeown, L.; Taylor, R.; Foster, R.; Waldmann, H.; Nussbaumer, P.; Christmann, M.; Bon, R. S.; Muraki, K.; Beech, D. J. Picomolar, Selective, and Subtype-Specific Small-Molecule Inhibition of TRPC1/4/5 Channels. *J. Biol. Chem* **2017**, *292* (20), 8158–8173. <https://doi.org/10.1074/jbc.M116.773556>.
- (220) Bon, R. S.; Wright, D. J.; Beech, D. J.; Sukumar, P. Pharmacology of TRPC Channels and Its Potential in Cardiovascular and Metabolic Medicine. *Annu. Rev. Pharmacol. Toxicol.* **2022**, *62* (1), 427–446. <https://doi.org/10.1146/annurev-pharmtox-030121-122314>.
- (221) Minard, A.; Bauer, C. C.; Chuntharpursat-Bon, E.; Pickles, I. B.; Wright, D. J.; Ludlow, M. J.; Burnham, M. P.; Warriner, S. L.; Beech, D. J.; Muraki, K.; Bon, R. S. Potent, Selective, and Subunit-Dependent Activation of TRPC5 Channels by a Xanthine Derivative. *Br. J. Pharmacol.* **2019**, *176* (20), 3924–3938. <https://doi.org/10.1111/bph.14791>.
- (222) Dryn, D. O.; Melnyk, M. I.; Bon, R. S.; Beech, D. J.; Zholos, A. V. Pico145 Inhibits TRPC4-Mediated mICAT and Postprandial Small Intestinal Motility. *Biomedicine & Pharmacotherapy* **2023**, *168*, 115672. <https://doi.org/10.1016/j.biopha.2023.115672>.
- (223) Bauer, C. C.; Minard, A.; Pickles, I. B.; Simmons, K. J.; Chuntharpursat-Bon, E.; Burnham, M. P.; Kapur, N.; Beech, D. J.; Muench, S. P.; Wright, M. H.; Warriner, S. L.; Bon, R. S. Xanthine-Based Photoaffinity Probes Allow Assessment of Ligand Engagement by TRPC5 Channels. *RSC Chem. Biol.* **2020**, *10*, 1039.D0CB00126K. <https://doi.org/10.1039/D0CB00126K>.
- (224) Xu, Y.; Ren, Y.; Zhang, J.; Niu, B.; Liu, M.; Xu, T.; Zhang, X.; Shen, J.; Wang, K.; Cao, Z. Discovery of Pyridazinone Derivatives Bearing Tetrahydroimidazo[1,2-a]pyrazine Scaffold as Potent Inhibitors of Transient Receptor Potential Canonical 5 to Ameliorate Hypertension-Induced Renal Injury in Rats. *European Journal of Medicinal Chemistry* **2024**, *275*, 116565. <https://doi.org/10.1016/j.ejmech.2024.116565>.
- (225) Small Molecules Targeting Canonical Transient Receptor Potential Channels: An Update. *Drug Discovery Today* **2024**, *29* (5), 103951. <https://doi.org/10.1016/j.drudis.2024.103951>.
- (226) Sharma, S.; Hopkins, C. R. Review of Transient Receptor Potential Canonical (TRPC5) Channel Modulators and Diseases. *J. Med. Chem.* **2019**, *62* (17), 7589–7602. <https://doi.org/10.1021/acs.jmedchem.8b01954>.
- (227) Wright, D. J.; Simmons, K. J.; Johnson, R. M.; Beech, D. J.; Muench, S. P.; Bon, R. S. Human TRPC5 Structures Reveal Interaction of a Xanthine-Based TRPC1/4/5 Inhibitor with a Conserved Lipid Binding Site. *Commun. Biol.* **2020**, *3* (1), 704. <https://doi.org/10.1038/s42003-020-01437-8>.
- (228) Vinayagam, D.; Quentin, D.; Yu-Strzelczyk, J.; Sitsel, O.; Merino, F.; Stabrin, M.; Hofnagel, O.; Yu, M.; Ledebauer, M. W.; Nagel, G.; Malojcic, G.; Raunser, S. Structural Basis of TRPC4 Regulation by Calmodulin and Pharmacological Agents. *eLife* **2020**, *9*, e60603. <https://doi.org/10.7554/eLife.60603>.
- (229) Song, K.; Wei, M.; Guo, W.; Quan, L.; Kang, Y.; Wu, J.-X.; Chen, L. Structural Basis for Human TRPC5 Channel Inhibition by Two Distinct Inhibitors. *eLife* **2021**, *10*, e63429. <https://doi.org/10.7554/eLife.63429>.
- (230) Storch, U.; Mederos y Schnitzler, M.; Gudermann, T. A Greasy Business: Identification of a Diacylglycerol Binding Site in Human TRPC5 Channels by Cryo-EM. *Cell Calcium* **2021**, *97*, 102414. <https://doi.org/10.1016/j.ceca.2021.102414>.
- (231) Banghart, M.; Borges, K.; Isacoff, E.; Trauner, D.; Kramer, R. H. Light-Activated Ion Channels for Remote Control of Neuronal Firing. *Nat Neurosci* **2004**, *7* (12), 1381–1386. <https://doi.org/10.1038/nn1356>.
- (232) Donthamsetti, P.; Konrad, D. B.; Hetzler, B.; Fu, Z.; Trauner, D.; Isacoff, E. Y. Selective Photoswitchable Allosteric Agonist of a G Protein-Coupled Receptor. *J. Am. Chem. Soc.* **2021**, *143* (24), 8951–8956. <https://doi.org/10.1021/jacs.1c02586>.
- (233) Müller-Deku, A.; Meiring, J. C. M.; Loy, K.; Kraus, Y.; Heise, C.; Bingham, R.; Jansen, K. I.; Qu, X.; Bartolini, F.; Kapitein, L. C.; Akhmanova, A.; Ahlfeld, J.; Trauner, D.; Thorn-Seshold, O. Photoswitchable Paclitaxel-Based Microtubule Stabilisers

- Allow Optical Control over the Microtubule Cytoskeleton. *Nat. Commun.* **2020**, *11* (1), 4640. <https://doi.org/10.1038/s41467-020-18389-6>.
- (234) Gao, L.; Meiring, J. C. M.; Heise, C.; Rai, A.; Müller-Deku, A.; Akhmanova, A.; Thorn-Seshold, J.; Thorn-Seshold, O. Photoswitchable Epithilone-Based Microtubule Stabilisers Allow GFP-Imaging-Compatible, Optical Control over the Microtubule Cytoskeleton**. *Angewandte Chemie International Edition* **2022**, *61* (10), e202114614. <https://doi.org/10.1002/anie.202114614>.
- (235) Reynders, M.; Matsuura, B. S.; Bérouti, M.; Simoneschi, D.; Marzio, A.; Pagano, M.; Trauner, D. PHOTACs Enable Optical Control of Protein Degradation. *Science Advances* **2020**. <https://doi.org/10.1126/sciadv.aay5064>.
- (236) Deisseroth, K. Optogenetics. *Nat Methods* **2011**, *8* (1), 26–29. <https://doi.org/10.1038/nmeth.f.324>.
- (237) Sakmar, T. P. Structure of Rhodopsin and the Superfamily of Seven-Helical Receptors: The Same and Not the Same. *Current Opinion in Cell Biology* **2002**, *14* (2), 189–195. [https://doi.org/10.1016/S0955-0674\(02\)00306-X](https://doi.org/10.1016/S0955-0674(02)00306-X).
- (238) Kiser, P. D.; Golczak, M.; Maeda, A.; Palczewski, K. Key Enzymes of the Retinoid (Visual) Cycle in Vertebrate Retina. *Biochimica et Biophysica Acta (BBA) - Molecular and Cell Biology of Lipids* **2012**, *1821* (1), 137–151. <https://doi.org/10.1016/j.bbalip.2011.03.005>.
- (239) Zhang, F.; Vierock, J.; Yizhar, O.; Fenno, L. E.; Tsunoda, S.; Kianianmomeni, A.; Prigge, M.; Berndt, A.; Cushman, J.; Polle, J.; Magnuson, J.; Hegemann, P.; Deisseroth, K. The Microbial Opsin Family of Optogenetic Tools. *Cell* **2011**, *147* (7), 1446–1457. <https://doi.org/10.1016/j.cell.2011.12.004>.
- (240) Deisseroth, K. Optogenetics: 10 Years of Microbial Opsins in Neuroscience. *Nat Neurosci* **2015**, *18* (9), 1213–1225. <https://doi.org/10.1038/nn.4091>.
- (241) Zemelman, B. V.; Lee, G. A.; Ng, M.; Miesenböck, G. Selective Photostimulation of Genetically ChARGed Neurons. *Neuron* **2002**, *33* (1), 15–22. [https://doi.org/10.1016/S0896-6273\(01\)00574-8](https://doi.org/10.1016/S0896-6273(01)00574-8).
- (242) Nagel, G.; Ollig, D.; Fuhrmann, M.; Kateriya, S.; Musti, A. M.; Bamberg, E.; Hegemann, P. Channelrhodopsin-1: A Light-Gated Proton Channel in Green Algae. *Science* **2002**. <https://doi.org/10.1126/science.1072068>.
- (243) Nagel, G.; Szellas, T.; Huhn, W.; Kateriya, S.; Adeishvili, N.; Berthold, P.; Ollig, D.; Hegemann, P.; Bamberg, E. Channelrhodopsin-2, a Directly Light-Gated Cation-Selective Membrane Channel. *Proceedings of the National Academy of Sciences* **2003**, *100* (24), 13940–13945. <https://doi.org/10.1073/pnas.1936192100>.
- (244) Boyden, E. S.; Zhang, F.; Bamberg, E.; Nagel, G.; Deisseroth, K. Millisecond-Timescale, Genetically Targeted Optical Control of Neural Activity. *Nat Neurosci* **2005**, *8* (9), 1263–1268. <https://doi.org/10.1038/nn1525>.
- (245) Hegemann, P.; Nagel, G. From Channelrhodopsins to Optogenetics†. *EMBO Molecular Medicine* **2013**. <https://doi.org/10.1002/emmm.201202387>.
- (246) Miesenböck, G. The Optogenetic Catechism. *Science* **2009**. <https://doi.org/10.1126/science.1174520>.
- (247) Deisseroth, K.; Feng, G.; Majewska, A. K.; Miesenböck, G.; Ting, A.; Schnitzer, M. J. Next-Generation Optical Technologies for Illuminating Genetically Targeted Brain Circuits. *J. Neurosci.* **2006**, *26* (41), 10380–10386. <https://doi.org/10.1523/JNEUROSCI.3863-06.2006>.
- (248) Gunaydin, L. A.; Yizhar, O.; Berndt, A.; Sohal, V. S.; Deisseroth, K.; Hegemann, P. Ultrafast Optogenetic Control. *Nat Neurosci* **2010**, *13* (3), 387–392. <https://doi.org/10.1038/nn.2495>.
- (249) Zhang, F.; Prigge, M.; Beyrière, F.; Tsunoda, S. P.; Mattis, J.; Yizhar, O.; Hegemann, P.; Deisseroth, K. Red-Shifted Optogenetic Excitation: A Tool for Fast Neural Control Derived from *Volvox* Carteri. *Nat Neurosci* **2008**, *11* (6), 631–633. <https://doi.org/10.1038/nn.2120>.
- (250) Airan, R. D.; Thompson, K. R.; Fenno, L. E.; Bernstein, H.; Deisseroth, K. Temporally Precise in Vivo Control of Intracellular Signalling. *Nature* **2009**, *458* (7241), 1025–1029. <https://doi.org/10.1038/nature07926>.
- (251) Oppermann, J.; Rozenberg, A.; Fabrin, T.; GonzalezCabrera, C.; Béja, O.; Prigge, M.; Hegemann, P. Robust Optogenetic Inhibition with Red-Light-Sensitive Anion-Conducting Channelrhodopsins. *eLife* **2023**, *12*. <https://doi.org/10.7554/eLife.90100.1>.
- (252) Emiliani, V.; Entcheva, E.; Hedrich, R.; Hegemann, P.; Konrad, K. R.; Lüscher, C.; Mahn, M.; Pan, Z.-H.; Sims, R. R.; Vierock, J.; Yizhar, O. Optogenetics for Light Control of Biological Systems. *Nat Rev Methods Primers* **2022**, *2* (1), 1–25. <https://doi.org/10.1038/s43586-022-00136-4>.
- (253) Konrad, K. R.; Gao, S.; Zurbruggen, M. D.; Nagel, G. Optogenetic Methods in Plant Biology. *Annual Review of Plant Biology* **2023**, *74* (Volume 74, 2023), 313–339. <https://doi.org/10.1146/annurev-arplant-071122-094840>.
- (254) Sahel, J.-A.; Boulanger-Scemama, E.; Pagot, C.; Arleo, A.; Galluppi, F.; Martel, J. N.; Esposti, S. D.; Delaux, A.; de Saint Aubert, J.-B.; de Montleau, C.; Gutman, E.; Audo, I.; Duebel, J.; Picaud, S.; Dalkara, D.; Blouin, L.; Tiel, M.; Roska, B. Partial Recovery of Visual Function in a Blind Patient after Optogenetic Therapy. *Nat Med* **2021**, *27* (7), 1223–1229. <https://doi.org/10.1038/s41591-021-01351-4>.
- (255) Klán, P.; Šolomek, T.; Bochet, C. G.; Blanc, A.; Givens, R.; Rubina, M.; Popik, V.; Kostikov, A.; Wirz, J. Photoremovable Protecting Groups in Chemistry and Biology: Reaction Mechanisms and Efficacy. *Chem. Rev.* **2013**, *113* (1), 119–191. <https://doi.org/10.1021/cr300177k>.
- (256) Hansen, M. J.; Velema, W. A.; Lerch, M. M.; Szymanski, W.; Feringa, B. L. Wavelength-Selective Cleavage of Photoprotecting Groups: Strategies and Applications in Dynamic Systems. *Chem. Soc. Rev.* **2015**, *44* (11), 3358–3377. <https://doi.org/10.1039/C5CS00118H>.
- (257) Ellis-Davies, G. C. R. Caged Compounds: Photorelease Technology for Control of Cellular Chemistry and Physiology. *Nat Methods* **2007**, *4* (8), 619–628. <https://doi.org/10.1038/nmeth1072>.
- (258) Weinstain, R.; Slanina, T.; Kand, D.; Klán, P. Visible-to-NIR-Light Activated Release: From Small Molecules to Nanomaterials. *Chem. Rev.* **2020**, *120* (24), 13135–13272. <https://doi.org/10.1021/acs.chemrev.0c00663>.
- (259) Patchornik, A.; Amit, B.; Woodward, R. B. Photosensitive Protecting Groups. *J. Am. Chem. Soc.* **1970**, *92* (21), 6333–6335. <https://doi.org/10.1021/ja00724a041>.
- (260) Barton, D. H. R.; Chow, Y. L.; Cox, A.; Kirby, G. W. Photosensitive Protection of Functional Groups. *Tetrahedron Letters* **1962**, *3* (23), 1055–1057. [https://doi.org/10.1016/S0040-4039\(00\)70957-9](https://doi.org/10.1016/S0040-4039(00)70957-9).
- (261) Kaplan, J. H.; Forbush, B. I.; Hoffman, J. F. Rapid Photolytic Release of Adenosine 5'-Triphosphate from a Protected Analog: Utilization by the Sodium:Potassium Pump of Human Red Blood Cell Ghosts. *Biochemistry* **1978**, *17* (10), 1929–1935. <https://doi.org/10.1021/bi00603a020>.
- (262) Berroy, P.; Viriot, M. L.; Carré, M. C. Photolabile Group for 5'-OH Protection of Nucleosides: Synthesis and Photodeprotection Rate. *Sensors and Actuators B: Chemical* **2001**, *74* (1), 186–189. [https://doi.org/10.1016/S0925-4005\(00\)00731-0](https://doi.org/10.1016/S0925-4005(00)00731-0).
- (263) Donato, L.; Mourot, A.; Davenport, C. M.; Herbivo, C.; Warther, D.; Léonard, J.; Bolze, F.; Nicoud, J.-F.; Kramer, R. H.; Goeldner, M.; Specht, A. Water-Soluble, Donor–Acceptor Biphenyl Derivatives in the 2-(o-Nitrophenyl)Propyl Series: Highly Efficient Two-Photon Uncaging of the Neurotransmitter γ -Aminobutyric Acid at $\lambda=800$ Nm. *Angewandte Chemie International Edition* **2012**, *51* (8), 1840–1843. <https://doi.org/10.1002/anie.201106559>.

- (264) Šolomek, T.; Wirz, J.; Klán, P. Searching for Improved Photoreleasing Abilities of Organic Molecules. *Acc. Chem. Res.* **2015**, *48* (12), 3064–3072. <https://doi.org/10.1021/acs.accounts.5b00400>.
- (265) Givens, R. S.; Rubina, M.; Wirz, J. Applications of P-Hydroxyphenacyl (pHP) and Coumarin-4-Ylmethyl Photoremovable Protecting Groups. *Photochem Photobiol Sci* **2012**, *11* (3), 472–488. <https://doi.org/10.1039/c2pp05399c>.
- (266) Gorka, A. P.; Yamamoto, T.; Zhu, J.; Schnermann, M. J. Cyanine Photocages Enable Spatial Control of Inducible Cre-Mediated Recombination. *ChemBioChem* **2018**, *19* (12), 1239–1243. <https://doi.org/10.1002/cbic.201800061>.
- (267) Janeková, H.; Russo, M.; Ziegler, U.; Štacko, P. Photocaging of Carboxylic Acids from Cyanine Dyes with Near-Infrared Light**. *Angewandte Chemie International Edition* **2022**, *61* (33), e202204391. <https://doi.org/10.1002/anie.202204391>.
- (268) Klöcker, N.; Weissenboeck, F. P.; van Dülmen, M.; Špaček, P.; Hüwel, S.; Rentmeister, A. Photocaged 5' Cap Analogues for Optical Control of mRNA Translation in Cells. *Nat. Chem.* **2022**, *14* (8), 905–913. <https://doi.org/10.1038/s41557-022-00972-7>.
- (269) Liu, L.; Zhang, D.; Johnson, M.; Devaraj, N. K. Light-Activated Tetrazines Enable Precision Live-Cell Bioorthogonal Chemistry. *Nat. Chem.* **2022**, *14* (9), 1078–1085. <https://doi.org/10.1038/s41557-022-00963-8>.
- (270) Gorka, A. P.; Nani, R. R.; Schnermann, M. J. Harnessing Cyanine Reactivity for Optical Imaging and Drug Delivery. *Acc. Chem. Res.* **2018**, *51* (12), 3226–3235. <https://doi.org/10.1021/acs.accounts.8b00384>.
- (271) Schmitt, C.; Mauker, P.; Vepřek, N. A.; Gierse, C.; Meiring, J. C. M.; Kuch, J.; Akhmanova, A.; Dehmelt, L.; Thorn-Seshold, O. A Photocaged Microtubule-Stabilising Epothilone Allows Spatiotemporal Control of Cytoskeletal Dynamics. *Angewandte Chemie International Edition n/a (n/a)*, e202410169. <https://doi.org/10.1002/anie.202410169>.
- (272) Kobauri, P.; Dekker, F. J.; Szymanski, W.; Feringa, B. L. Rational Design in Photopharmacology with Molecular Photoswitches. *Angewandte Chemie International Edition* **2023**, *62* (30), e202300681. <https://doi.org/10.1002/anie.202300681>.
- (273) Broichhagen, J.; Frank, J. A.; Trauner, D. A Roadmap to Success in Photopharmacology. *Acc. Chem. Res.* **2015**, *48* (7), 1947–1960. <https://doi.org/10.1021/acs.accounts.5b00129>.
- (274) Kaufman, H.; Vratsanos, S. M.; Erlanger, B. F. Photoregulation of an Enzymic Process by Means of a Light-Sensitive Ligand. *Science* **1968**. <https://doi.org/10.1126/science.162.3861.1487>.
- (275) Bartels, E.; Wassermann, N. H.; Erlanger, B. F. Photochromic Activators of the Acetylcholine Receptor. *Proceedings of the National Academy of Sciences* **1971**, *68* (8), 1820–1823. <https://doi.org/10.1073/pnas.68.8.1820>.
- (276) Erlanger, B. F. Photoregulation of Biologically Active Macromolecules. *Annual Review of Biochemistry* **1976**, *45* (Volume 45, 1976), 267–284. <https://doi.org/10.1146/annurev.bi.45.070176.001411>.
- (277) Lester, H. A.; Krouse, M. E.; Nass, M. M.; Wassermann, N. H.; Erlanger, B. F. Light-Activated Drug Confirms a Mechanism of Ion Channel Blockade. *Nature* **1979**, *280* (5722), 509–510. <https://doi.org/10.1038/280509a0>.
- (278) Volgraf, M.; Gorostiza, P.; Numano, R.; Kramer, R. H.; Isacoff, E. Y.; Trauner, D. Allosteric Control of an Ionotropic Glutamate Receptor with an Optical Switch. *Nat Chem Biol* **2006**, *2* (1), 47–52. <https://doi.org/10.1038/nchembio756>.
- (279) Fehrentz, T.; Schönberger, M.; Trauner, D. Optochemical Genetics. *Angewandte Chemie International Edition* **2011**, *50* (51), 12156–12182. <https://doi.org/10.1002/anie.201103236>.
- (280) Velema, W. A.; Szymanski, W.; Feringa, B. L. Photopharmacology: Beyond Proof of Principle. *J. Am. Chem. Soc.* **2014**, *136* (6), 2178–2191. <https://doi.org/10.1021/ja413063e>.
- (281) Pittolo, S.; Gómez-Santacana, X.; Eckelt, K.; Rovira, X.; Dalton, J.; Goudet, C.; Pin, J.-P.; Llobet, A.; Giraldo, J.; Llebaria, A.; Gorostiza, P. An Allosteric Modulator to Control Endogenous G Protein-Coupled Receptors with Light. *Nat Chem Biol* **2014**, *10* (10), 813–815. <https://doi.org/10.1038/nchembio.1612>.
- (282) Borowiak, M.; Nahaboo, W.; Reynders, M.; Nekolla, K.; Jalinot, P.; Hasserodt, J.; Rehberg, M.; Delattre, M.; Zahler, S.; Vollmar, A.; Trauner, D.; Thorn-Seshold, O. Photoswitchable Inhibitors of Microtubule Dynamics Optically Control Mitosis and Cell Death. *Cell* **2015**, *162* (2), 403–411. <https://doi.org/10.1016/j.cell.2015.06.049>.
- (283) Stein, M.; Middendorp, S. J.; Carta, V.; Pejo, E.; Raines, D. E.; Forman, S. A.; Sigel, E.; Trauner, D. Azo-Propofols: Photochromic Potentiators of GABAA Receptors. *Angew. Chem. Int. Ed.* **2012**, *51* (42), 10500–10504. <https://doi.org/10.1002/anie.201205475>.
- (284) Velema, W. A.; Hansen, M. J.; Lerch, M. M.; Driessen, A. J. M.; Szymanski, W.; Feringa, B. L. *Ciprofloxacin-Photoswitch Conjugates: A Facile Strategy for Photopharmacology*. ACS Publications. <https://doi.org/10.1021/acs.bioconjchem.5b00591>.
- (285) Velema, W. A.; van der Berg, J. P.; Hansen, M. J.; Szymanski, W.; Driessen, A. J. M.; Feringa, B. L. Optical Control of Antibacterial Activity. *Nature Chem* **2013**, *5* (11), 924–928. <https://doi.org/10.1038/nchem.1750>.
- (286) Frank, J. A.; Moroni, M.; Moshourab, R.; Sumser, M.; Lewin, G. R.; Trauner, D. Photoswitchable Fatty Acids Enable Optical Control of TRPV1. *Nat. Commun* **2015**, *6* (1), 7118. <https://doi.org/10.1038/ncomms8118>.
- (287) Stein, M.; Breit, A.; Fehrentz, T.; Gudermann, T.; Trauner, D. Optical Control of TRPV1 Channels. *Angewandte Chemie International Edition* **2013**, *52* (37), 9845–9848. <https://doi.org/10.1002/anie.201302530>.
- (288) Baell, J. B.; Holloway, G. A. New Substructure Filters for Removal of Pan Assay Interference Compounds (PAINS) from Screening Libraries and for Their Exclusion in Bioassays. *J. Med. Chem.* **2010**, *53* (7), 2719–2740. <https://doi.org/10.1021/jm901137j>.
- (289) Fuchter, M. J. On the Promise of Photopharmacology Using Photoswitches: A Medicinal Chemist's Perspective. *J. Med. Chem.* **2020**, *63* (20), 11436–11447. <https://doi.org/10.1021/acs.jmedchem.0c00629>.
- (290) Gutzeit, V. A.; Acosta-Ruiz, A.; Munguba, H.; Häfner, S.; Landra-Willm, A.; Mathes, B.; Mony, J.; Yarotski, D.; Börjesson, K.; Liston, C.; Sandoz, G.; Levitz, J.; Broichhagen, J. A Fine-Tuned Azobenzene for Enhanced Photopharmacology in Vivo. *Cell Chem. Biol.* **2021**, *28* (11), 1648–1663.e16. <https://doi.org/10.1016/j.chembiol.2021.02.020>.
- (291) Küllmer, F.; Gregor, L.; Arndt, H.-D. Systematic Modifications of Substitution Patterns for Property Tuning of Photoswitchable Asymmetric Azobenzenes. *Org. Biomol. Chem.* **2022**, *20* (20), 4204–4214. <https://doi.org/10.1039/D2OB00214K>.
- (292) Weston, C. E.; Richardson, R. D.; Haycock, P. R.; White, A. J. P.; Fuchter, M. J. *Arylazopyrazoles: Azoheteroarene Photoswitches Offering Quantitative Isomerization and Long Thermal Half-Lives*. ACS Publications. <https://doi.org/10.1021/ja505444d>.
- (293) Küllmer, F.; Vepřek, N. A.; Borowiak, M.; Nasufović, V.; Barutzki, S.; Thorn-Seshold, O.; Arndt, H.-D.; Trauner, D. Next Generation Opto-Jasplakinolides Enable Local Remodeling of Actin Networks**. *Angewandte Chemie International Edition* **2022**, *61* (48), e202210220. <https://doi.org/10.1002/anie.202210220>.
- (294) Curcic, S.; Tiapko, O.; Groschner, K. Photopharmacology and Opto-Chemogenetics of TRPC Channels-Some Therapeutic Visions. *Pharmacol. Ther.* **2019**, *200*, 13–26. <https://doi.org/10.1016/j.pharmthera.2019.04.003>.
- (295) Frank, J. A.; Yushchenko, D. A.; Hodson, D. J.; Lipstein, N.; Nagpal, J.; Rutter, G. A.; Rhee, J.-S.; Gottschalk, A.; Brose, N.; Schultz, C.; Trauner, D. Photoswitchable Diacylglycerols Enable Optical Control of Protein Kinase C. *Nature Chemical Biology* **2016**, *12* (9), 755–762. <https://doi.org/10.1038/nchembio.2141>.

- (296) Leinders-Zufall, T.; Storch, U.; Bleyemehl, K.; Mederos y Schnitzler, M.; Frank, J. A.; Konrad, D. B.; Trauner, D.; Gudermann, T.; Zufall, F. PhoDAGs Enable Optical Control of Diacylglycerol-Sensitive Transient Receptor Potential Channels. *Cell Chem. Bio.* **2018**, *25* (2), 215–223. e3. <https://doi.org/10.1016/j.chembiol.2017.11.008>.
- (297) Leinders-Zufall, T.; Storch, U.; Mederos y Schnitzler, M.; Ojha, N. K.; Koike, K.; Gudermann, T.; Zufall, F. A Diacylglycerol Photoswitching Protocol for Studying TRPC Channel Functions in Mammalian Cells and Tissue Slices. *STAR Protocols* **2021**, *2* (2), 100527. <https://doi.org/10.1016/j.xpro.2021.100527>.
- (298) Lichtenegger, M.; Tiapko, O.; Svobodova, B.; Stockner, T.; Glasnov, T. N.; Schreiber, W.; Platzer, D.; de la Cruz, G. G.; Krenn, S.; Schober, R.; Shrestha, N.; Schindl, R.; Romanin, C.; Groschner, K. An Optically Controlled Probe Identifies Lipid-Gating Fenestrations within the TRPC3 Channel. *Nature Chemical Biology* **2018**, *14* (4), 396–404. <https://doi.org/10.1038/s41589-018-0015-6>.
- (299) Tiapko, O.; Shrestha, N.; Lindinger, S.; Cruz, G. G. de la; Graziani, A.; Klec, C.; Butorac, C.; Graier, W. F.; Kubista, H.; Freichel, M.; Birnbaumer, L.; Romanin, C.; Glasnov, T.; Groschner, K. Lipid-Independent Control of Endothelial and Neuronal TRPC3 Channels by Light. *Chem. Sci.* **2019**, *10* (9), 2837–2842. <https://doi.org/10.1039/C8SC05536J>.
- (300) Thorn-Seshold, O.; Meiring, J. C. M. Photocontrolling Microtubule Dynamics with Photoswitchable Chemical Reagents. In *Microtubules: Methods and Protocols*; Inaba, H., Ed.; Springer US: New York, NY, 2022; pp 403–430. https://doi.org/10.1007/978-1-0716-1983-4_26.
- (301) Sailer, A.; Meiring, J. C. M.; Heise, C.; Pettersson, L. N.; Akhmanova, A.; Thorn-Seshold, J.; Thorn-Seshold, O. Pyrrole Hemithioindigo Antimitotics with Near-Quantitative Bidirectional Photoswitching That Photocontrol Cellular Microtubule Dynamics with Single-Cell Precision**. *Angewandte Chemie International Edition* **2021**, *60* (44), 23695–23704. <https://doi.org/10.1002/anie.202104794>.
- (302) Calbo, J.; Weston, C. E.; White, A. J. P.; Rzepa, H. S.; Contreras-García, J.; Fuchter, M. J. *Tuning Azoheteroarene Photoswitch Performance through Heteroaryl Design*. ACS Publications. <https://doi.org/10.1021/jacs.6b11626>.
- (303) Heindl, A. H.; Wegner, H. A. Rational Design of Azothiophenes—Substitution Effects on the Switching Properties. *Chemistry – A European Journal* **2020**, *26* (60), 13730–13737. <https://doi.org/10.1002/chem.202001148>.
- (304) Gómez-Santacana, X.; de Munnik, S. M.; Vijayachandran, P.; Da Costa Pereira, D.; Bebelman, J. P. M.; de Esch, I. J. P.; Vischer, H. F.; Wijtmans, M.; Leurs, R. Photoswitching the Efficacy of a Small-Molecule Ligand for a Peptidergic GPCR: From Antagonism to Agonism. *Angewandte Chemie International Edition* **2018**, *57* (36), 11608–11612. <https://doi.org/10.1002/anie.201804875>.
- (305) Gómez-Santacana, X.; Munnik, S. M. de; Mocking, T. A. M.; Hauwert, N. J.; Sun, S.; Vijayachandran, P.; Esch, I. J. P. de; Vischer, H. F.; Wijtmans, M.; Leurs, R. A Toolbox of Molecular Photoswitches to Modulate the CXCR3 Chemokine Receptor with Light. *Beilstein J. Org. Chem.* **2019**, *15* (1), 2509–2523. <https://doi.org/10.3762/bjoc.15.244>.
- (306) Bahamonde, M. I.; Taura, J.; Paoletta, S.; Gakh, A. A.; Chakraborty, S.; Hernando, J.; Fernández-Dueñas, V.; Jacobson, K. A.; Gorostiza, P.; Ciruela, F. Photomodulation of G Protein-Coupled Adenosine Receptors by a Novel Light-Switchable Ligand. *Bioconjugate Chem.* **2014**, *25* (10), 1847–1854. <https://doi.org/10.1021/bc5003373>.
- (307) Hansen, M. J.; Hille, J. I. C.; Szymanski, W.; Driessen, A. J. M.; Feringa, B. L. Easily Accessible, Highly Potent, Photocontrolled Modulators of Bacterial Communication. *Chem* **2019**, *5* (5), 1293–1301. <https://doi.org/10.1016/j.chempr.2019.03.005>.
- (308) Westphal, M. V.; Schaefroth, M. A.; Sarott, R. C.; Imhof, M. A.; Bold, C. P.; Leippe, P.; Dhopeshwarkar, A.; Grandner, J. M.; Katrich, V.; Mackie, K.; Trauner, D.; Carreira, E. M.; Frank, J. A. Synthesis of Photoswitchable Δ^9 -Tetrahydrocannabinol Derivatives Enables Optical Control of Cannabinoid Receptor 1 Signaling. *J. Am. Chem. Soc.* **2017**, *139* (50), 18206–18212. <https://doi.org/10.1021/jacs.7b06456>.
- (309) Steinmüller, S. A. M.; Fender, J.; Deventer, M. H.; Tutov, A.; Lorenz, K.; Stove, C. P.; Hislop, J. N.; Decker, M. Visible-Light Photoswitchable Benzimidazole Azo-Arenes as β -Arrestin2-Biased Selective Cannabinoid 2 Receptor Agonists. *Angewandte Chemie International Edition* **2023**, *62* (49), e202306176. <https://doi.org/10.1002/anie.202306176>.
- (310) Agnetta, L.; Kauk, M.; Canizal, M. C. A.; Messerer, R.; Holzgrabe, U.; Hoffmann, C.; Decker, M. A Photoswitchable Dualsteric Ligand Controlling Receptor Efficacy. *Angewandte Chemie International Edition* **2017**, *56* (25), 7282–7287. <https://doi.org/10.1002/anie.201701524>.
- (311) Riefolo, F.; Matera, C.; Garrido-Charles, A.; Gomila, A. M. J.; Sortino, R.; Agnetta, L.; Claro, E.; Masgrau, R.; Holzgrabe, U.; Battle, M.; Decker, M.; Guasch, E.; Gorostiza, P. Optical Control of Cardiac Function with a Photoswitchable Muscarinic Agonist. *J. Am. Chem. Soc.* **2019**, *141* (18), 7628–7636. <https://doi.org/10.1021/jacs.9b03505>.
- (312) Colquhoun, D. Binding, Gating, Affinity and Efficacy: The Interpretation of Structure-Activity Relationships for Agonists and of the Effects of Mutating Receptors. *British Journal of Pharmacology* **1998**, *125* (5), 923–947. <https://doi.org/10.1038/sj.bjp.0702164>.
- (313) Arkhipova, V.; Fu, H.; Hoorens, M. W. H.; Trinco, G.; Lameijer, L. N.; Marin, E.; Feringa, B. L.; Poelarends, G. J.; Szymanski, W.; Slotboom, D. J.; Guskov, A. Structural Aspects of Photopharmacology: Insight into the Binding of Photoswitchable and Photocaged Inhibitors to the Glutamate Transporter Homologue. *J. Am. Chem. Soc.* **2021**, *143* (3), 1513–1520. <https://doi.org/10.1021/jacs.0c11336>.
- (314) Pospich, S.; Küllmer, F.; Nasufović, V.; Funk, J.; Bely, A.; Bieling, P.; Arndt, H.-D.; Raunser, S. Cryo-EM Resolves Molecular Recognition Of An Optojasp Photoswitch Bound To Actin Filaments In Both Switch States. *Angewandte Chemie International Edition* **2021**, *60* (16), 8678–8682. <https://doi.org/10.1002/anie.202013193>.
- (315) D'Autréaux, B.; Toledano, M. B. ROS as Signalling Molecules: Mechanisms That Generate Specificity in ROS Homeostasis. *Nat Rev Mol Cell Biol* **2007**, *8* (10), 813–824. <https://doi.org/10.1038/nrm2256>.
- (316) Miller, E. W.; Albers, A. E.; Pralle, A.; Isacoff, E. Y.; Chang, C. J. Boronate-Based Fluorescent Probes for Imaging Cellular Hydrogen Peroxide. *J. Am. Chem. Soc.* **2005**, *127* (47), 16652–16659. <https://doi.org/10.1021/ja054474f>.
- (317) Gatin-Fraudet, B.; Ottenwelter, R.; Le Saux, T.; Norsikian, S.; Pucher, M.; Lombès, T.; Baron, A.; Durand, P.; Doisneau, G.; Bourdoux, Y.; Iorga, B. I.; Erard, M.; Jullien, L.; Guianvarc'h, D.; Urban, D.; Vauzeilles, B. Evaluation of Borinic Acids as New, Fast Hydrogen Peroxide-Responsive Triggers. *Proceedings of the National Academy of Sciences* **2021**, *118* (50), e2107503118. <https://doi.org/10.1073/pnas.2107503118>.
- (318) Zhu, W.; Chai, X.; Wang, B.; Zou, Y.; Wang, T.; Meng, Q.; Wu, Q. Spiroboronate Si-Rhodamine as a near-Infrared Probe for Imaging Lysosomes Based on the Reversible Ring-Opening Process. *Chem. Commun.* **2015**, *51* (47), 9608–9611. <https://doi.org/10.1039/C5CC02496J>.
- (319) Thorn-Seshold, O.; Vargas-Sanchez, M.; McKeon, S.; Hasserodt, J. A Robust, High-Sensitivity Stealth Probe for Peptidases. *Chem. Commun.* **2012**, *48* (50), 6253–6255. <https://doi.org/10.1039/C2CC32227G>.
- (320) Zeisel, L.; Felber, J. G.; Scholzen, K. C.; Schmitt, C.; Wiegand, A. J.; Komissarov, L.; Arnér, E. S. J.; Thorn-Seshold, O. Piperazine-Fused Cyclic Disulfides Unlock High-Performance Bioreductive Probes of Thioredoxins and Bifunctional Reagents for Thiol Redox Biology. *J. Am. Chem. Soc.* **2024**, *146* (8), 5204–5214. <https://doi.org/10.1021/jacs.3c11153>.

- (321) Kamiya, M.; Asanuma, D.; Kuranaga, E.; Takeishi, A.; Sakabe, M.; Miura, M.; Nagano, T.; Urano, Y. β -Galactosidase Fluorescence Probe with Improved Cellular Accumulation Based on a Spirocyclized Rhodol Scaffold. *J. Am. Chem. Soc.* **2011**, *133* (33), 12960–12963. <https://doi.org/10.1021/ja204781t>.
- (322) Cui, D.; Mi, J.; Zhang, Z.; Su, X.; Sun, X.; Mu, G.; Shi, Y.; Yang, S. Ultrafast Photoacoustic Cavitation Pumped by Picosecond Laser for High-Efficient and Long-Term Shockwave Theranostics. *Photoacoustics* **2023**, *33*, 100546. <https://doi.org/10.1016/j.pacs.2023.100546>.
- (323) Morstein, J.; Hill, R. Z.; Novak, A. J. E.; Feng, S.; Norman, D. D.; Donthamsetti, P. C.; Frank, J. A.; Harayama, T.; Williams, B. M.; Parrill, A. L.; Tigyi, G. J.; Riezman, H.; Isacoff, E. Y.; Bautista, D. M.; Trauner, D. Optical Control of Sphingosine-1-Phosphate Formation and Function. *Nat Chem Biol* **2019**, *15* (6), 623–631. <https://doi.org/10.1038/s41589-019-0269-7>.
- (324) Morstein, J.; Dacheux, M. A.; Norman, D. D.; Shemet, A.; Donthamsetti, P. C.; Citir, M.; Frank, J. A.; Schultz, C.; Isacoff, E. Y.; Parrill, A. L.; Tigyi, G. J.; Trauner, D. Optical Control of Lysophosphatidic Acid Signaling. *J. Am. Chem. Soc.* **2020**, *142* (24), 10612–10616. <https://doi.org/10.1021/jacs.0c02154>.
- (325) Yue, L.; Pawlowski, M.; Dellal, S. S.; Xie, A.; Feng, F.; Otis, T. S.; Bruzik, K. S.; Qian, H.; Pepperberg, D. R. Robust Photoregulation of GABAA Receptors by Allosteric Modulation with a Propofol Analogue. *Nat Commun* **2012**, *3* (1), 1095. <https://doi.org/10.1038/ncomms2094>.
- (326) Lam, P.-Y.; Thawani, A. R.; Balderas, E.; White, A. J. P.; Chaudhuri, D.; Fuchter, M. J.; Peterson, R. T. TRPswitch—A Step-Function Chemo-Optogenetic Ligand for the Vertebrate TRPA1 Channel. *J. Am. Chem. Soc.* **2020**, *142* (41), 17457–17468. <https://doi.org/10.1021/jacs.0c06811>.
- (327) Won, S. M.; Song, E.; Reeder, J. T.; Rogers, J. A. Emerging Modalities and Implantable Technologies for Neuromodulation. *Cell* **2020**, *181* (1), 115–135. <https://doi.org/10.1016/j.cell.2020.02.054>.
- (328) Gutruf, P.; Krishnamurthi, V.; Vázquez-Guardado, A.; Xie, Z.; Banks, A.; Su, C.-J.; Xu, Y.; Haney, C. R.; Waters, E. A.; Kandela, I.; Krishnan, S. R.; Ray, T.; Leshock, J. P.; Huang, Y.; Chanda, D.; Rogers, J. A. Fully Implantable Optoelectronic Systems for Battery-Free, Multimodal Operation in Neuroscience Research. *Nat Electron* **2018**, *1* (12), 652–660. <https://doi.org/10.1038/s41928-018-0175-0>.

